

IRON(III) COMPLEXES OF AMINE-BIS(PHENOLATE)
LIGANDS AS CATALYSTS FOR THE C-C CROSS-COUPLING
OF ARYL GRIGNARD REAGENTS WITH BENZYL HALIDES

ELLIOTT CHARD

**Iron(III) Complexes of Amine-bis(phenolate) Ligands as Catalysts for
the C-C Cross-Coupling of Aryl Grignard Reagents with Benzyl Halides**

by

© Elliott Chard

A dissertation submitted to the

School of Graduate Studies

in partial fulfillment of the requirements for the degree of

Master of Science (M.Sc.)

Department of Chemistry
Memorial University of Newfoundland
St. John's, Newfoundland and Labrador, Canada

August 2012

St. John's

Newfoundland and Labrador

Table of Contents

Abstract.....	iv
Acknowledgements.....	v
List of Abbreviations	vi
List of Schemes.....	viii
List of Figures.....	xi
List of Tables	xvi
 Chapter 1 Introduction.....	 1
1.1 Introduction to Catalytic Cross-Coupling Reactions.....	1
1.1.1 Sonogashira Coupling.....	2
1.1.2 Suzuki Coupling	6
1.1.3 Heck Coupling	9
1.2 Introduction to Iron-Catalyzed C-C Cross-Coupling	11
1.2.1 Iron-Catalyzed Sonogashira Cross-Coupling	13
1.2.2 Iron-Catalyzed Suzuki Cross-Coupling.....	14
1.2.3 Iron-Catalyzed Heck Cross-Coupling.....	18
1.2.4 Iron-Catalyzed Kumada Cross-Coupling	19
1.2.4.1 Acyl Electrophiles	19
1.2.4.2 Alkenyl Electrophiles	21
1.2.4.3 Aryl Electrophiles.....	23
1.2.4.4 Alkyl Electrophiles.....	25
1.2.5 Mechanistic Considerations.....	28
1.3 Iron Complexes Supported by Amine-bis(phenolate) Ligands as Catalysts for C-C Cross-Coupling Reactions.....	31
1.4 Iron-Catalyzed Cross-Coupling of Benzyl Halides with Aryl Grignards.....	40
1.5 References.....	44
 Chapter 2 Synthesis and Characterization	 51
2.1 Synthesis and Characterization of Tridentate Amine-bis(phenol) Ligands.....	51
2.2 Synthesis of Iron(III) Complexes Supported by Tridentate Amine-bis(phenolate) Ligands	58

2.2.1	Synthesis of Amine-bis(phenolate) Iron(III)(acac) Complexes	58
2.2.2	Synthesis of Amine-bis(phenolate) Iron(III) Halide and Iron(III) Hydroxy Complexes	62
2.2.3	Characterization	74
2.2.3.1	Elemental Analysis	74
2.2.3.2	Mass Spectrometry	76
2.2.3.3	Structural Characterization	88
2.2.3.4	UV-visible Spectroscopy	112
2.2.3.5	Inductively Coupled Plasma Mass Spectrometry	114
2.2.3.6	Magnetic Data	115
2.3	Experimental Section	118
2.3.1	General Methods and Materials	118
2.3.2	Instrumentation	118
2.3.3	Synthesis	119
2.4	References	128
Chapter 3 Catalysis Studies		131
3.1	Introduction	131
3.2	Results and Discussion	133
3.2.1	General Procedure	133
3.2.2	Catalysis Results	134
3.2.3	Percent Yield Calculations	145
3.3	Experimental	148
3.3.1	General Methods and Materials	148
3.3.2	Instrumentation	149
3.3.3	Catalytic Method at Room Temperature	149
3.4	References	161
Chapter 4 Conclusions and Future Work		163
4.1	Complex Syntheses	163
4.2	Catalysis	170
4.3	References	173
Chapter 5 Appendix		174
5.1	Ligands and Complexes	174
5.2	Cross-Coupling Reactions	243

ABSTRACT

Traditionally, complexes containing heavy and precious metals such as palladium have been used to catalyze a wide range of C-C cross-coupling reactions. However, there are many drawbacks to using these types of catalysts because of their toxicity and/or price. More recently, in the interest of sustainability, there has been a rapid increase in the study of iron-based catalysts. Iron is inexpensive, non-toxic, environmentally benign, and readily available as it is one of the most abundant elements on Earth.¹

The catalytic formation of diarylmethane motifs is a very important synthetic tool, with applications in pharmaceuticals and biologically active compounds. To date, the formation of diarylmethane motifs by the iron-catalyzed C-C cross-coupling of benzyl halides with aryl Grignard reagents has been reported to be unsatisfactory, giving low yields and poor selectivity resulting in the formation of homocoupled by-products. The development of an air stable, non-hygroscopic, single component iron-based catalyst which can effectively generate diarylmethane motifs is of particular interest.

Recent research in the Kozak group has focused on the use of iron(III) complexes supported by amine-bis(phenolate) ligands as potential catalysts for C-C cross-coupling reactions. A series of structurally authenticated iron(III) complexes of tridentate amine-bis(phenolate) ligands have been prepared and their potential as catalysts for the C-C cross-coupling of aryl Grignards with benzyl halides, including chlorides, has been explored. The results of catalysis studies, as well as structural and spectroscopic characterization of the metal complexes will be presented.

¹ B. D. Sherry, A. Fürstner, *Acc. Chem. Res.* **2008**, 41, 1500-1511.

ACKNOWLEDGEMENTS

At this time, I would like to personally thank my supervisor Dr. Christopher Kozak for making this Masters project an enjoyable experience. It has been a true privilege to work under the guidance of a professor who has an obvious passion for the chemistry field. I would like to thank you for all of your insight, and always being there to answer my questions.

Thank you to all of the members of the Green Chemistry and Catalysis Group who have offered me help with my research, and have made me feel at home in the lab. Specifically, I would like to acknowledge Justin Belanger and Khaled Omari who have taken the time to answer any questions I might have had. I would also like to personally thank Dr. Louise Dawe for all of her insight regarding my project, and always being there for encouragement.

To all of the Chemistry professors at Memorial University, it is with your knowledge and support that I have been able to make it through this degree; thank you for everything.

List of Abbreviations

DABCO – 1,4-diazabicyclo[2.2.2]octane

Et₂O – diethyl ether

GC-MS – gas chromatography mass spectrometry

h – hour (s)

ICP-MS – inductively coupled plasma mass spectrometry

IR – infrared spectroscopy

LMCT – ligand metal charge transfer

MALDI-TOF MS – matrix-assisted laser desorption/ionization time of flight mass spectrometry

min – minute

mL – millilitre

mol – mole

MW – microwave

m/z – mass-to-charge ratio

NMR – nuclear magnetic resonance

OTf – triflate

OTs – tosylate

ppm – parts per million

rt – room temperature

sp – septet

THF – tetrahydrofuran

TMEDA – tetramethylethylenediamine

TMS – tetramethylsilane

UV – ultraviolet

Vis – visible

List of Schemes

Scheme 1.1.....	1
A general representation of some metal-catalyzed cross-coupling reactions.	
Scheme 1.2.....	2
A typical Sonogashira cross-coupling reaction.	
Scheme 1.3.....	6
A typical Suzuki cross-coupling reaction.	
Scheme 1.4.....	9
A typical Heck cross-coupling reaction.	
Scheme 1.5.....	12
The alkenylation of methylmagnesium bromide with both <i>cis</i> - and <i>trans</i> -1-bromopropene.	
Scheme 1.6.....	13
The iron catalyzed cross-coupling of phenylacetylene with phenyl iodide.	
Scheme 1.7.....	14
Iron catalyzed Sonogashira reactions reported by Vogel and co-workers.	
Scheme 1.8.....	15
Iron catalyzed Suzuki cross-coupling reactions reported by Darcel and co-workers.	
Scheme 1.9.....	15
Iron catalyzed Suzuki cross-coupling reaction of phenyl iodide with phenylboronic acid.	
Scheme 1.10.....	16
Iron catalyzed Suzuki biaryl cross-coupling reactions performed under high pressure.	
Scheme 1.11.....	18
The iron catalyzed cross-coupling of 4-iodotoluene with styrene.	
Scheme 1.12.....	20
[Fe(acac) ₃]-catalyzed reactions of functionalized magnesium reagents with acyl chlorides.	

Scheme 1.13.....	20
[Fe(acac) ₃]-catalyzed reactions of functionalized magnesium reagents with acyl cyanides.	
Scheme 1.14.....	21
The iron-catalyzed alkenylation of alkylmagnesium chlorides.	
Scheme 1.15.....	22
Iron-catalyzed cross-coupling reactions of alkenyl triflates with Grignard reagents.	
Scheme 1.16.....	23
Iron-catalyzed cross-coupling of alkyl Grignard reagents with aryl chlorides, tosylates, and triflates.	
Scheme 1.17.....	24
Iron-catalyzed oxidative homo-coupling of aryl Grignard reagents.	
Scheme 1.18.....	24
Iron-catalyzed oxidative homo-coupling of aryl Grignard reagents with atmospheric oxygen as an oxidant.	
Scheme 1.19.....	26
Iron-catalyzed cross-coupling reaction of an alkyl halide with phenylmagnesium bromide.	
Scheme 1.20.....	27
Iron-catalyzed cross-coupling of 4-methylphenyl magnesium bromide and cyclohexyl bromide in the presence of an amine.	
Scheme 1.21.....	27
Iron(III) salen-catalyzed cross-coupling of 4-methylphenyl magnesium bromide and cyclohexyl bromide.	
Scheme 1.22.....	41
Negishi-type arylations reported by Bedford <i>et al.</i>	
Scheme 2.1.....	51
Synthesis of tridentate diamine-bis(phenol) pro-ligands via a Mannich condensation reaction.	
Scheme 2.2.....	59
Synthesis of (acac)Fe[ONO] complexes.	

Scheme 2.3.....	63
Synthesis of halide-bridged dimers following a literature procedure reported by Kozak <i>et al.</i>	
Scheme 2.4.....	69
The synthesis of Fe(III) halide-bridged dimers using NaH as the base.	
Scheme 2.5.....	72
The synthesis of Fe(III) bromide-bridged dimers using ⁿ BuLi as the base.	
Scheme 3.1.....	132
Iron-catalyzed Negishi-type arylations reported by Bedford <i>et al.</i>	
Scheme 3.2.....	144
Plausible catalytic cycle for the generation of bibenzyl homocoupled by-products (Path A) and diarylmethane compounds (Path B).	

List of Figures

Figure 1.1	3
A plausible catalytic cycle for the copper-cocatalyzed Sonogashira reaction.	
Figure 1.2	5
A plausible catalytic cycle for the copper-free Sonogashira reaction.	
Figure 1.3	7
A general catalytic cycle for the Suzuki coupling reaction.	
Figure 1.4	8
Catalytic cycle for the cross-coupling of organic halides and organoboranes.	
Figure 1.5	10
A general catalytic cycle for the palladium-catalyzed Heck reaction.	
Figure 1.6	29
A plausible catalytic cycle for the iron-catalyzed cross-coupling of aryl halides with inorganic Grignard reagents.	
Figure 1.7	30
A plausible catalytic cycle for the iron-catalyzed cross-coupling of alkyl halides with aryl Grignard reagents.	
Figure 1.8	31
Two plausible catalytic cycles for the iron-catalyzed cross-coupling of aryl halides with alkyl Grignard reagents.	
Figure 1.9	32
Some examples of typical tetradentate amine-bis(phenol) ligands.	
Figure 1.10	33
Some examples of typical tridentate amine-bis(phenol) ligands.	
Figure 1.11	34
An iron(III) halide catalyst ($\text{FeCl}[\text{ONNO}]^{\text{BuMeFurf}}$) reported by Kozak and co-workers.	
Figure 1.12	36
Amine-bis(phenolato)iron(acac) complexes reported by Kozak and co-workers.	
Catalyst 1; R' = ^t Bu. Catalyst 2; R' = Me.	

Figure 1.13	36
Amine-bis(phenolato)iron(acac) complexes reported by Kozak and co-workers. Catalyst 3 ; R = R' = 'Bu. Catalyst 4 ; R = 'Bu, R' = Me. Catalyst 5 ; R = R' = Me.	
Figure 1.14	37
iron(III) chloride-bridged dimer $[\text{Fe}[\text{O}_2\text{N}]^{\text{BuMenPr}}(\mu\text{-Cl})]_2$ reported by Kozak and co-workers.	
Figure 2.1	52
Library of tridentate amine-bis(phenol) ligands synthesized.	
Figure 2.2	53
^1H -NMR spectrum of $\text{H}_2[\text{O}_2\text{N}]^{\text{BuBuPr}}(\text{L3})$.	
Figure 2.3	54
Different proton environments for $\text{H}_2[\text{ONO}]^{\text{BuBuPr}}(\text{L3})$.	
Figure 2.4	55
Single crystal X-ray structure of $\text{H}_2[\text{O}_2\text{N}]^{\text{BuBuPr}}(\text{L3})$. H-bonding exists between the hydrogen bond acceptor N(1), and the hydrogen donor located on O(2). H-atoms omitted for clarity (except on atoms O1 and O2). Ellipsoids at 50% probability.	
Figure 2.5	56
High-resolution mass spectrum of $\text{H}_2[\text{O}_2\text{N}]^{\text{BuBuPr}}(\text{L3})$.	
Figure 2.6	57
IR spectrum of $\text{H}_2[\text{O}_2\text{N}]^{\text{BuBuPr}}(\text{L3})$.	
Figure 2.7	60
UV-vis spectrum for $\text{Fe}(\text{acac})_3$ in methanol.	
Figure 2.8	61
UV-vis spectrum for $(\text{acac})\text{Fe}[\text{ONO}]^{\text{BuBuPr}}$ in methanol.	
Figure 2.9	65
Library of iron(III) amine-bis(phenolate) complexes synthesized. For C1 , C3 , C5 , C6 and C7 , co-crystallized solvent molecules omitted for clarity.	
Figure 2.10	68
A zwitterionic tetrahedral iron(III) complex bearing two bromide ligands and a quaternized ammonium fragment reported by Kozak and co-workers.	
Figure 2.11	71
A plausible mechanism for the synthesis of C5 ($\text{FeBr}_2\text{L1H}$).	

Figure 2.12.....	77
MALDI-TOF mass spectrum of C2 ([Fe L5 (μ -Cl)] ₂).	
Figure 2.13.....	79
MALDI-TOF mass spectrum of C3 (FeCl(THF) L2).	
Figure 2.14(A)	80
Theoretical isotope pattern for C3 .	
Figure 2.14(B).....	81
Experimental isotope pattern for C3 .	
Figure 2.15.....	82
MALDI-TOF mass spectrum of C4 (FeBr(THF) L2).	
Figure 2.16.....	84
MALDI-TOF mass spectrum of C5 (FeBr ₂ L1H).	
Figure 2.17.....	85
MALDI-TOF mass spectrum of C7 (FeBr ₂ L3H).	
Figure 2.18.....	87
MALDI-TOF mass spectrum of C6 ([Fe L3 (μ -OH)] ₂).	
Figure 2.19.....	90
Molecular structure (ORTEP) and partial atom labeling of C1 . Ellipsoids shown at 50% probability. Hydrogen atoms omitted for clarity (except at N(2)) along with the co-crystallized toluene molecule.	
Figure 2.20.....	93
Molecular structure (ORTEP) and partial atom labeling of [Fe(ONO) ^{BuMeⁿPr} (μ -Cl)] ₂ (Dimer A), which was previously reported in the Kozak group. Ellipsoids shown at 50% probability. Hydrogen atoms omitted for clarity.	
Figure 2.21.....	93
Molecular structure (ORTEP) and partial atom labeling of [Fe(ONO) ^{BuMeⁿBn} (μ -Cl)] ₂ (Dimer B), which was previously reported in the Kozak group. Ellipsoids shown at 50% probability. Hydrogen atoms omitted for clarity.	
Figure 2.22.....	96
A structural representation of {FeCl[^t BuN(SiMe ₂)] ₂ O} ₂ reported by Leznoff and co-workers.	

Figure 2.23	98
Molecular structure (ORTEP) and partial atom labeling of C3 . Ellipsoids shown at 50% probability. Hydrogen atoms omitted for clarity.	
Figure 2.24	98
Molecular structure (ORTEP) and partial atom labeling of C4 . Ellipsoids shown at 50% probability. Hydrogen atoms omitted for clarity.	
Figure 2.25	100
X-ray crystal structure of $\text{FeCl}[\text{O}_2\text{NO}]^{\text{BuMeFurf}}$ previously reported in the Kozak group. Ellipsoids shown at 50% probability. Hydrogen atoms omitted for clarity.	
Figure 2.26	104
Molecular structure (ORTEP) and partial atom labeling of C5 . Ellipsoids shown at 30% probability. Hydrogen atoms omitted for clarity (except for H(1)) along with the co-crystallized toluene and pentane molecules.	
Figure 2.27	104
Molecular structure (ORTEP) and partial atom labeling of C7 . Ellipsoids shown at 30% probability. Hydrogen atoms omitted for clarity (except for H(1)) along with the co-crystallized toluene molecule.	
Figure 2.28	105
Molecular structure (ORTEP) and partial atom labeling of $\text{FeBr}_2[\text{O}_2\text{NH}]^{\text{BuMenPr}}$ previously reported in the Kozak group. Ellipsoids shown at 50% probability. Hydrogen atoms omitted for clarity.	
Figure 2.29	107
A structural representation of iron(III) bromide-bridged dimers previously reported by Leznoff and co-workers.	
Figure 2.30	110
Molecular structure (ORTEP) and partial atom labeling of C6 . Ellipsoids shown at 30% probability. Hydrogen atoms omitted for clarity (except for H on O(3) and O(3)*) along with the co-crystallized toluene molecule.	
Figure 2.31	112
A structural representation of $[\text{Fe}(\text{ONO})^{\text{BuMeMe}}(\mu\text{-OH})]_2$ reported by Chaudhuri and co-workers.	
Figure 2.32	113
UV-vis spectrum of C3 . Methanol used as the solvent.	

Figure 2.33	115
Magnetic moment per mol of dimer vs. temperature for C6 .	
Figure 2.34	116
Magnetic moment per mol of dimer vs. temperature for $[\text{Fe}[\text{ONO}]^{\text{BuMeMe}}(\mu\text{-OH})]_2$.	
Figure 3.1	131
$\text{Fe}(\text{II})\text{Cl}_2\text{bis}(\text{dpbz})$ reported by Bedford and co-workers.	
Figure 3.2	133
A structural representation of C3 .	
Figure 3.3	145
A calibration curve for the determination of yields of cross-coupled products (rsqr = 0.998). Product refers to diphenylmethane.	
Figure 4.1	165
A representation of C1 $([\text{NEt}_3\text{H}]^+[\text{FeCl}_2\text{L1}])$.	
Figure 4.2	165
A representation of C3 $(\text{FeCl}(\text{THF})\text{L2})$.	
Figure 4.3	166
A representation of C4 $(\text{FeBr}(\text{THF})\text{L2})$.	
Figure 4.4	167
A representation of C5 $(\text{FeBr}_2\text{L1H})$.	
Figure 4.5	168
A representation of C6 $([\text{FeL3}(\mu\text{-OH})]_2)$.	
Figure 4.6	168
A representation of C7 $(\text{FeBr}_2\text{L3H})$.	
Figure 4.6	169
A representation of $\text{H}_2[\text{ONO}]^{\text{AmAmPr}}$.	

List of Tables

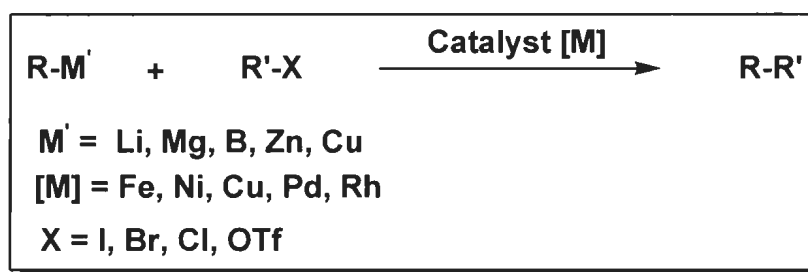
Table 1.1	35
Cross-coupling of ArMgBr with alkyl halides reported by Kozak <i>et al.</i>	
Table 1.2	37
Cross-coupling of <i>o</i> -tolylmagnesium bromide with cyclohexyl chloride reported by Kozak <i>et al.</i>	
Table 1.3	39
Cross-coupling of ArMgBr with alkyl halides reported by Kozak <i>et al.</i>	
Table 1.4	42
Iron-catalyzed cross coupling of aryl Grignard reagents and benzyl halides.	
Table 2.1	54
Assignment of resonances for the ¹ H NMR spectrum of L3 .	
Table 2.2	55
Crystallographic data and refinements for L3 .	
Table 2.3	58
Melting point (MP) data for L1 , L2 , L3 .	
Table 2.4	75
Elemental analysis of iron(III) amine-bis(phenolate) complexes. For C1 , theoretical % includes 1.3 equivalents of co-crystallized toluene.	
Table 2.5	89
Crystallographic and Structure Refinement Data for C1 and C3-C7 .	
Table 2.6	94
Selected bond lengths (Å) and bond angles (°) of C1 , [Fe[ONO] ^{BuMenPr} (μ-Cl)] ₂ (Dimer A) and [Fe[ONO] ^{BuMenPr} (μ-Cl)] ₂ (Dimer B). Symmetry operators used to generate equivalent atoms: (*) -x + 1, -y + 1, -z + 1.	
Table 2.7	99
Selected bond lengths (Å) and bond angles (°) of C3 , C4 and FeCl[O ₂ NO'] ^{BuMeFurf} .	
Table 2.8	106
Selected bond lengths (Å) and bond angles (°) of C5 , C7 and FeBr ₂ [O ₂ NH] ^{BuMenPr} .	

Table 2.9	107
Selected bond lengths (Å) observed in {FeBr[MesN(SiMe ₂) ₂ O]} ₂ and {FeBr ₂ Li[Me ₃ PhN(SiMe ₂) ₂ O]} ₂ .	
Table 2.10	111
Selected bond lengths (Å) and bond angles (°) of [Fe(ONO) ^{BuMeMe} (μ-OH)] ₂ and C6 .	
Table 2.11	114
ICP-MS analysis of FeCl ₃ , Fe(acac) ₃ and C3 .	
Table 3.1	137
The cross-coupling of benzyl bromide or benzyl chloride with Grignard reagents.	
Table 3.2	139
The cross-coupling of <i>para</i> -substituted benzyl halides with aryl Grignard reagents.	
Table 3.3	140
The cross-coupling of <i>meta</i> -substituted benzyl halides with aryl Grignard reagents.	
Table 3.4	142
The cross-coupling of <i>ortho</i> -substituted benzyl halides and (1-bromoethyl)benzene with aryl Grignard reagents.	

Chapter 1 - Introduction

1.1 Introduction to Catalytic Cross-Coupling Reactions

Catalysts, which help increase the rate of chemical reactions by lowering their activation energy barrier and selectively generating only the desired product, result in fast, clean, efficient and selective processes with minimal waste.¹ Complexes containing nickel and palladium have been studied extensively as catalysts for the construction of carbon-carbon bonds, however, there are many drawbacks to using these types of catalysts because of their toxicity and/or price.² The use of transition metal catalysts for the reaction of organometallic reagents with organic electrophiles is the method of choice for a wide range of carbon-carbon bond forming processes (**Scheme 1.1**). These reactions provide a common class of synthetic transformations, commonly referred to as “cross-coupling reactions”.³

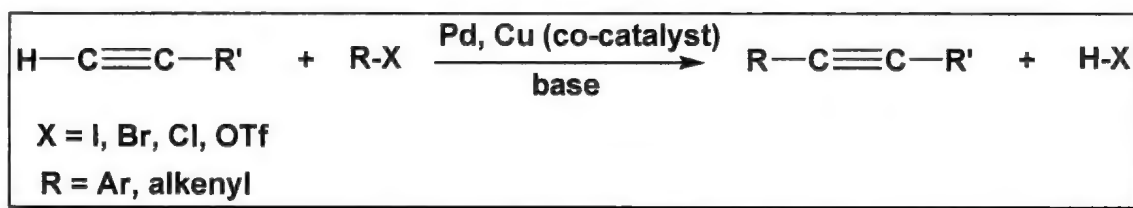


Scheme 1.1: A general representation of some metal-catalyzed cross-coupling reactions.³ The catalyst [M] represents a metal on its own or a complex supported by a ligand framework.

Transition metal catalyzed C-C bond forming reactions are among the most useful and versatile in organic synthesis. In recent years, various methodologies have been developed, such as Sonogashira, Suzuki and Heck protocols, which permit the cross-coupling of a large variety of reactants.⁴ The catalytic formation of C-C bonds is a very important synthetic tool for the preparation of pharmaceuticals, natural products and biologically active compounds. As a result, efficient and practical methods by which the target compounds can be assembled are synthetically significant.

1.1.1 Sonogashira Coupling

In 1975, Kenkichi Sonogashira reported a palladium-catalyzed substitution reaction which would become the most popular procedure for the alkynylation of aryl or alkenyl halides (**Scheme 1.2**).⁵ Sonogashira reactions, which have milder experimental conditions than previous acetylene substitution reactions, have remained a useful tool for synthetic methodology development. Sonogashira coupling has been used in the synthesis of arylalkynes and conjugated enynes, which are precursors for natural products, pharmaceuticals, and molecular organic materials.⁵ The exact mechanism of the Sonogashira reaction is still unknown, but many plausible mechanisms have been reported.⁶



Scheme 1.2: A general representation of the Sonogashira cross-coupling reaction.⁵

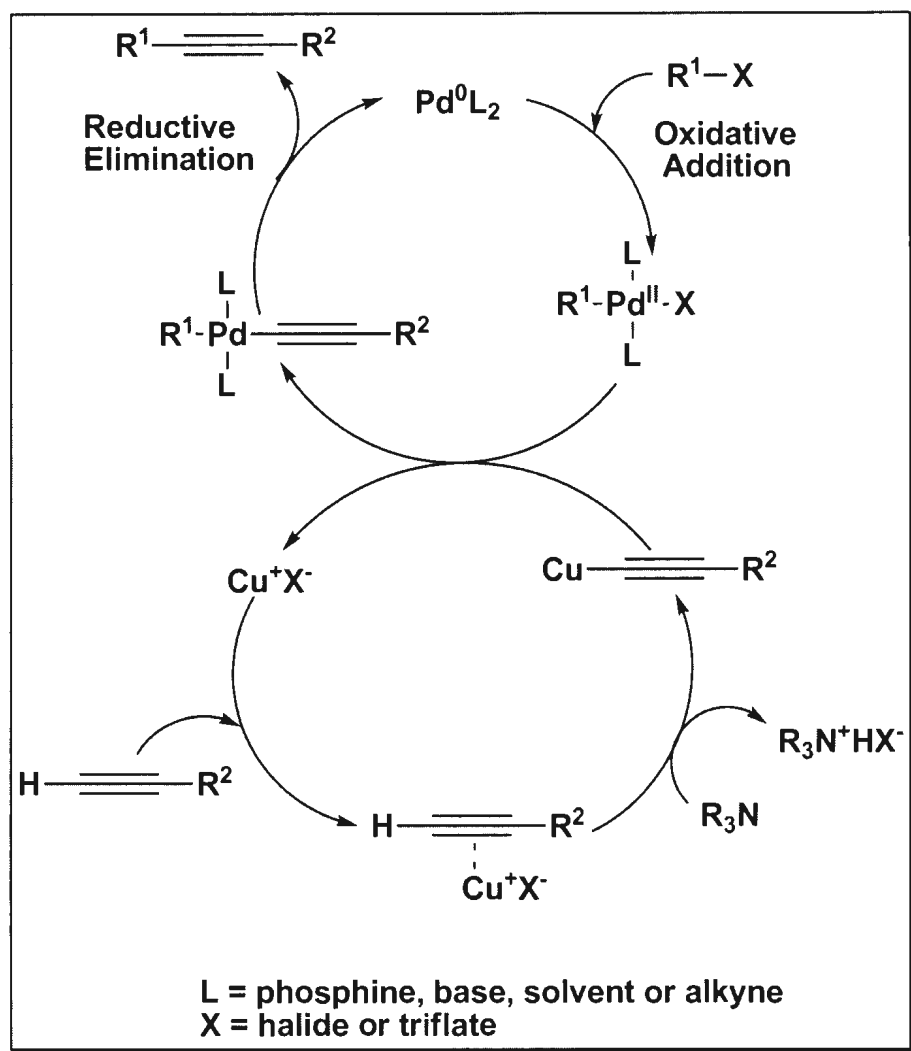


Figure 1.1: A plausible catalytic cycle for the copper-co-catalyzed Sonogashira reaction.⁵

When the Sonogashira reaction is performed in the presence of a copper co-catalyst (copper halide or triflate), the reaction is found to proceed rapidly at room temperature. The copper co-catalyzed Sonogashira reaction is believed to take place through two independent catalytic cycles (**Figure 1.1**).⁵ In the first step of the catalytic cycle, there exists a rapid oxidative addition of $R^1\text{-X}$ (R^1 = aryl, heteroaryl, vinyl; X = I, Br, Cl, OTf) to the 14-electron Pd^0L_2 catalyst. The oxidative addition step is influenced

substantially by the nature of the substrate. Since the R^1-X bond must be broken, relatively stable anions such as iodide and triflate, which are more likely to dissociate, are often required. In order to promote the dissociation, electron withdrawing substituents are typically introduced on the substrate to reduce the amount of electron density on the C-X bond.

Originally, the tertiary amine (base) was expected to directly abstract the acetylenic proton of the terminal alkyne generating a copper acetylide. However, since many tertiary amines are not basic enough to deprotonate the alkyne, a π -alkyne Cu complex is suspected to form, increasing the acidity of the alkyne proton promoting the abstraction.⁵ Once connection with the Cu-cycle is established, the rate determining transmetalation from the copper acetylide formed will ultimately generate the final coupled alkene along with the regenerated catalyst.⁵ While direct evidence has not yet proved the existence of a π -alkyne Cu complex, recent NMR studies of Sonogashira reactions with silver in place of copper have shown the presence of π -alkyne Ag complexes.⁷

Sonogashira cross-coupling reactions have many drawbacks when used in conjunction with copper salts. First of all, copper co-catalysts are often environmentally unfriendly and are extremely difficult to recover from the reaction mixture. Also, the *insitu* generation of copper acetylides often generates homocoupled by-products. Typically, these homocoupled products result from a reaction between the terminal alkyne and main reaction product.⁵ As a result, the development of a Sonogashira cross-coupling reaction which allows the elimination of a copper co-catalyst is advantageous from an environmental and economical perspective.

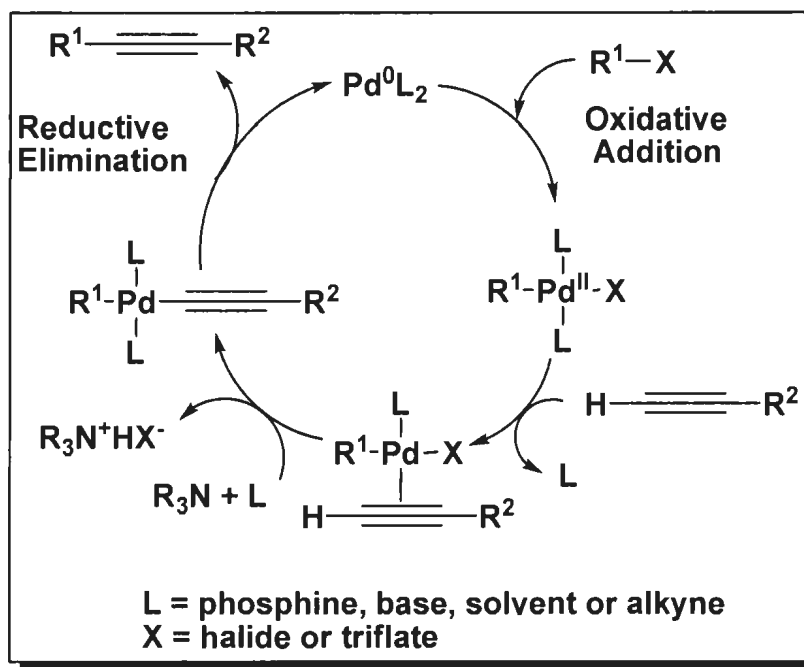
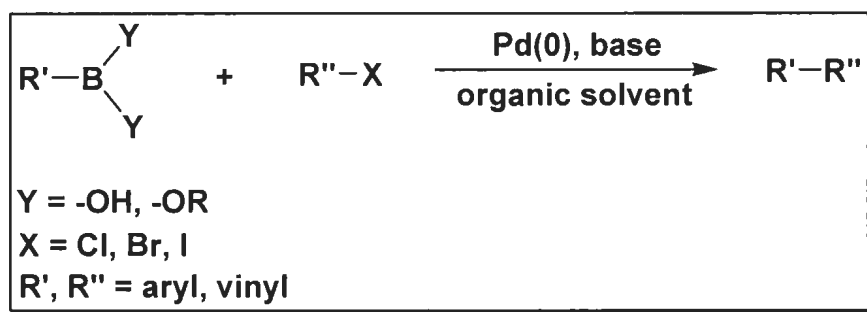


Figure 1.2: A plausible catalytic cycle for the copper-free Sonogashira reaction.⁵

Like the catalytic cycle proposed for the copper co-catalysed Sonogashira cross-coupling reaction, the copper-free Sonogashira catalytic cycle is also suspected to involve complexation of the alkyne (**Figure 1.2**).⁵ Complexation is expected to proceed after the displacement of one of the ligands (L), generating the intermediate complex $(\eta^2-R^2C\equiv CH)-PdXLR^1$. Once the desired intermediate complex is formed, the ligated alkyne can be deprotonated by the amine generating the new complex $R^1-Pd(-C\equiv CR^2)L_2$. Through a reductive elimination process, the desired coupling product can be generated along with regeneration of the catalyst.

1.1.2 Suzuki Coupling

The palladium-catalyzed Suzuki cross-coupling reaction is one of the most efficient methods for the construction of C-C bonds. Although several other methods exist, the Suzuki cross-coupling reaction, which is used widely for the synthesis of polyolefins, styrenes and substituted biphenyls, has proven to be the most popular in recent times (**Scheme 1.3**).⁸ A large variety of palladium(0) catalysts or precursors can be used for the Suzuki cross-coupling reaction. Pd(0)L₄ (where L is a phosphine) complexes are most commonly employed since they are robust.⁹ The Suzuki cross-coupling reaction possesses many key advantages when compared to other traditional methods such as Negishi and Stille cross-coupling.



Scheme 1.3: A typical Suzuki cross-coupling reaction.⁹

The Suzuki reaction involves the use of a wide range of boronic acids, which are environmentally benign (compared to other organometallic reagents) and commercially available. The reaction proceeds under mild reaction conditions, being largely unaffected by the presence of water, tolerating a broad range of functionality, and yielding nontoxic byproducts.⁹ When compared to other organometallic reagents, boron-containing byproducts are easily handled, and can be recovered completely from the reaction

mixture.⁸ Suzuki cross-coupling reactions have gained prominence in recent times since the conditions have many desirable features for large-scale synthesis and are amenable to the industrial synthesis of pharmaceuticals and fine chemicals.⁸

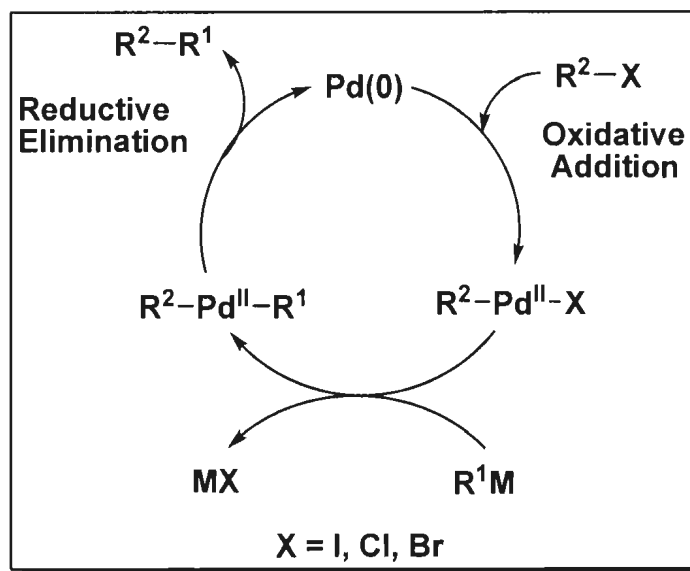


Figure 1.3: A general catalytic cycle for the Suzuki cross-coupling reaction.⁹

By analogy to other cross-coupling reactions, the catalytic cycle for the Suzuki cross-coupling reaction involves an oxidative addition-transmetalation-reductive elimination sequence (**Figure 1.3**).⁹ The efficiency of palladium originates from its ability (when it is zero-valent) to activate C-X bonds ($\text{X} = \text{I}, \text{Cl}, \text{Br}$) by an oxidative addition reaction which provides a stable *trans*- σ -organopalladium(II) complex ($\text{R}^2\text{-Pd}^{\text{II}}\text{-X}$) prone to react with nucleophiles.^{10,11} The reaction proceeds with complete retention of configuration for alkenyl halides and with inversion for allylic and benzylic halides. Alkyl halides which possess β -hydrogens are typically avoided since the oxidative addition step is very slow and may compete with β -hydride elimination from the σ -organopalladium(II) species.⁹ Aryl and 1-alkenyl halides activated by the proximity of

electron-withdrawing groups are more susceptible to oxidative addition than those with donating groups, thus allowing the use of chlorides such as 3-chloroenones for the cross-coupling reaction.⁹ The mechanism of the oxidative addition step has been characterized by means of electrochemical techniques such as steady-state voltammetry, transient voltammetry, cyclic voltammetry and reaction kinetics.¹²

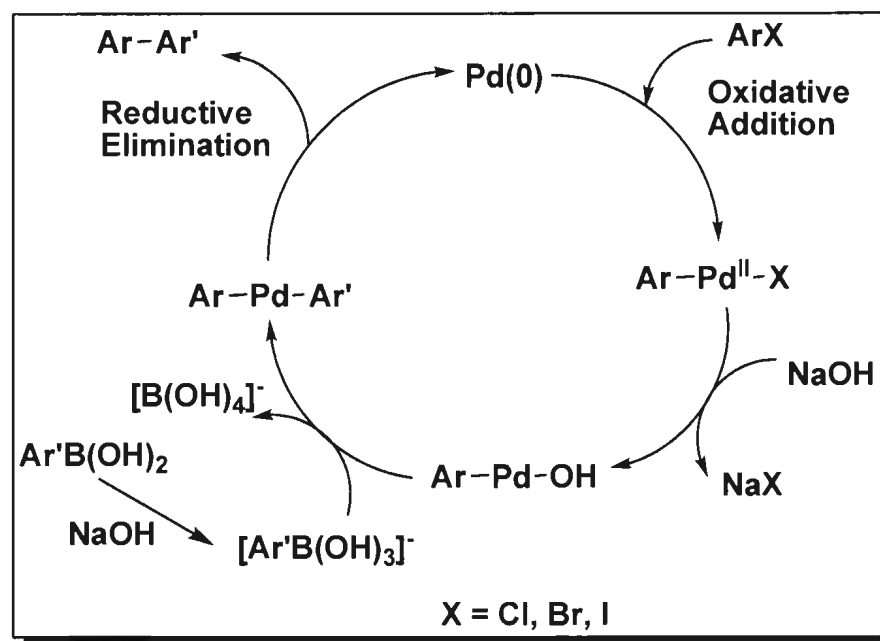


Figure 1.4: Catalytic cycle for the cross-coupling of organic halides and organoboranes.⁸

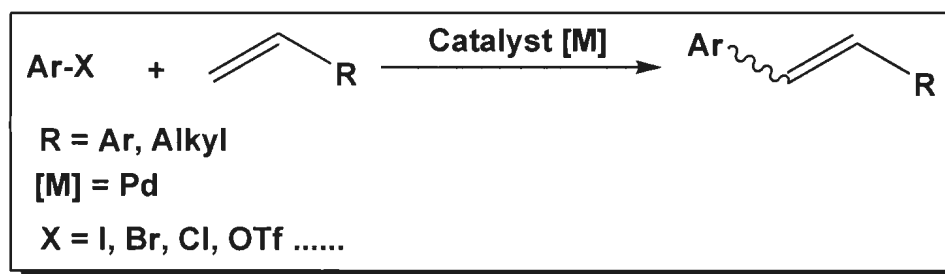
Unlike the general catalytic cycle depicted in **Figure 1.3**, the organo-borane cross-coupling catalytic cycle presented in **Figure 1.4** is highly dependent on the reaction conditions used.⁸ The choice of base and the presence of the ligands on the transition-metal complex are essential due to the low nucleophilicity of the organic group on the boron atom.⁸ The nucleophilicity can be greatly enhanced by quarternization of the boron atom with negatively charged bases generating the corresponding "ate" complex.¹³ As seen in **Figure 1.4**, the displacement of the halide ion to give the more reactive

organopalladium alkoxide (Ar-Pd-OR) or organopalladium hydroxide (Ar-Pd-OH) (depending on the base used) is a crucial step in the catalytic cycle.⁸

The transmetalation of a primary alkylborane to Pd occurs with retention of stereochemistry. Through the hydroboration of diastereomeric dideuterioalkenes, followed by coupling of the diastereomeric borane to α -iodocyclohexenone, the retention of stereochemistry was confirmed through spectral studies of the resulting cyclohexenones.¹⁴

1.1.3 Heck Coupling

The Heck reaction has been extensively exploited by synthetic chemists since its debut in the late 1960s and presents one of the simplest ways to obtain variously substituted olefins, dienes, and other unsaturated compounds (**Scheme 1.4**).¹⁵ This versatile reaction has many applications in pharmaceuticals and is also useful in polymerization chemistry.¹⁶



Scheme 1.4: A typical Heck cross-coupling reaction.¹⁵

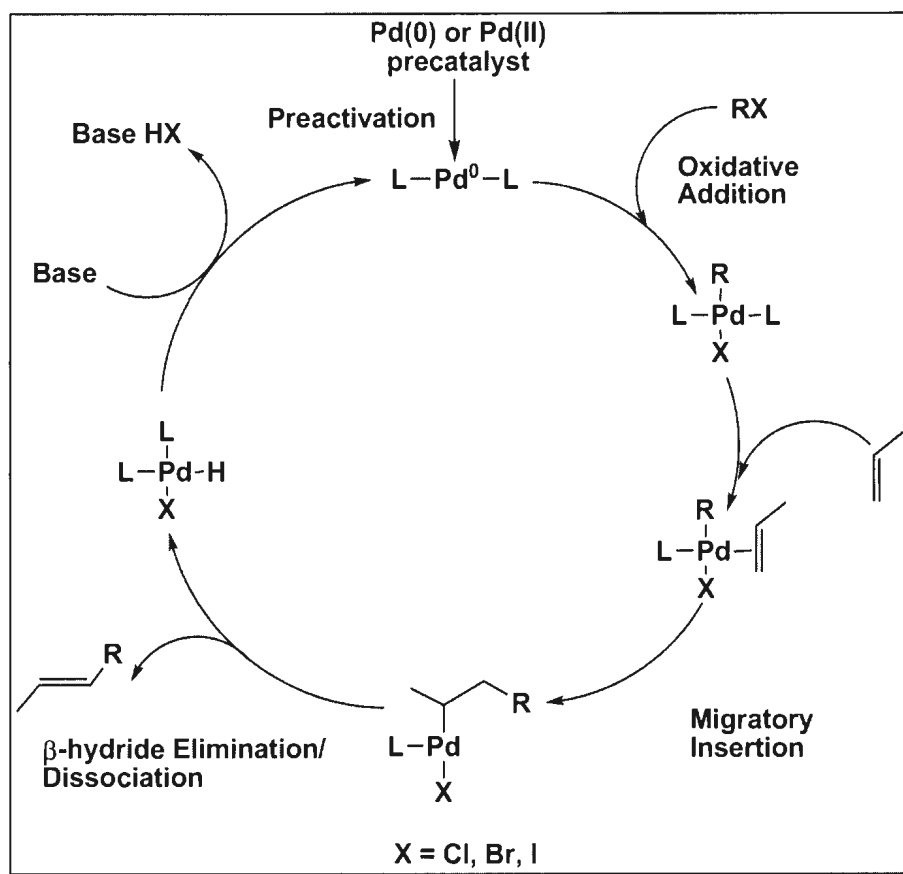


Figure 1.5: A general catalytic cycle for the palladium-catalyzed Heck reaction.¹⁶

Traditionally, the Heck reaction had been catalyzed by palladium complexes supported by phosphine ligands. The primary role of the phosphine ligand is to support palladium in its stable zero oxidation state. However, the use of palladium complexes supported by phosphine ligands is often problematic since phosphine ligands are expensive, toxic, and difficult to recover from the reaction mixture. More recently, there has been interest in designing a phosphine-free catalytic system which would present a more efficient and economically feasible process.¹⁶

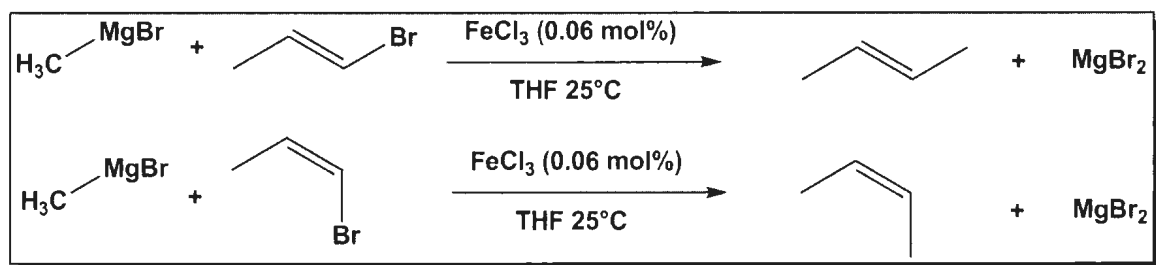
Over the last few decades, the Heck catalytic cycle has been studied extensively and many plausible mechanisms have been reported. The first step of the Heck catalytic cycle

is suspected to involve preactivation of the palladium(II) precatalyst (**Figure 1.5**). The primary reduction of Pd(II) to Pd(0) is most likely accomplished by phosphine in the phosphine-assisted catalytic cycle, but the reduction can also be assisted by hard nucleophiles such as hydroxide¹⁷⁻¹⁹ and alkoxide ions.²⁰ Following oxidative addition of R-X to the 14-electron Pd catalyst and coordination of the alkene, a typical migratory insertion reaction is expected to occur (**Figure 1.5**). β -Hydride elimination of the coordinated nucleophile can then generate the desired cross-coupling product. In the presence of a base, regeneration of the Pd(0) precatalyst can be achieved.

1.2 Introduction to Iron-Catalyzed C-C Cross-coupling

Traditionally, palladium and nickel complexes have provided the broadest utility and the deepest mechanistic insight into cross-coupling reactions,²¹ however, there are many drawbacks to using these types of catalysts because of their toxicity and/or price. From an environmental and economic point of view, developing metal-catalyzed cross-coupling methods with an emphasis on “greener” processes are of particular interest.

More recently, in the interest of sustainability, there has been a rapid increase in the study of iron-based catalysts.²² The increasing number of cross-coupling reactions using catalytic amounts of iron complexes indicates a renaissance of this metal in catalysis.²³ Iron is inexpensive, nontoxic, environmentally benign, and readily available as it is one of the most abundant elements on Earth.²¹



Scheme 1.5: The alkenylation of methylmagnesium bromide with both *cis*- and *trans*-1-bromopropene.²⁴

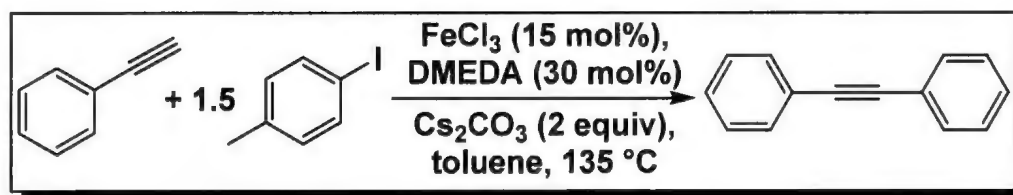
Iron catalyzed cross-coupling reactions (using Grignard nucleophiles) were first discovered in 1971 when Kochi and Tamura reported the cross-coupling of alkenyl bromides with alkyl Grignards using iron salts (**Scheme 1.5**).²⁴ In the presence of catalytic amounts of FeCl_3 , the reaction was found to be stereoselective. Compared to cross-coupling systems with palladium or nickel catalysts, iron catalysts are often advantageous since they can successfully couple alkyl halides with Grignard reagents, without competing β -hydride elimination side reactions. Today, only limited examples of C-C bond formation using alkyl chlorides have been reported,²⁵⁻²⁷ and the use of unactivated alkyl halides^{24,28} (such as alkyl chlorides) is still problematic. A catalytic system that can help address these shortcomings is required.

There are both advantages and disadvantages when using simple iron salts, such as FeCl_3 , as pre-catalysts. FeCl_3 leads to variable yields depending on its commercial origin and purity,²⁹ and is highly hygroscopic making it inconvenient for direct use on a large scale. Although $\text{Fe}(\text{acac})_3$ is a more robust, less hygroscopic iron salt,³⁰ amine additives are often required to achieve high conversions and yields of cross-coupled

products.^{29,31} Therefore, the development of an air stable, non-hygroscopic, single component iron catalyst precursor is highly desirable.

1.2.1 Iron-Catalyzed Sonogashira Cross-Coupling

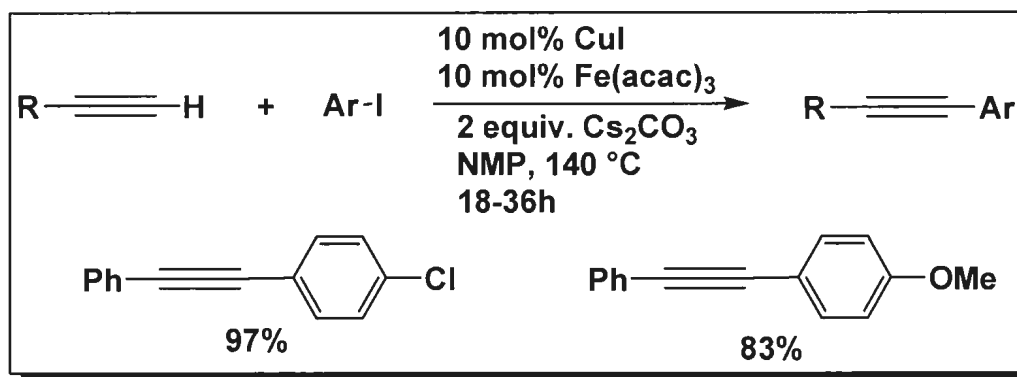
Today, the Sonogashira reaction is known as the most straightforward and efficient method for the formation of $C(sp^2)$ - $C(sp)$ bonds,³² specifically for the synthesis of aryl alkynes and conjugated enynes; alkynes are very important synthetic tools throughout the pharmaceutical and chemical industry.^{5, 33-36}



Scheme 1.6: The iron catalyzed cross-coupling of phenylacetylene with phenyl iodide.³²

The first iron catalyzed C-C cross-coupling reaction of a terminal alkyne and an arylating agent was reported in 2007 by Taillefer and co-workers.³⁷ By 2008, Bolm and co-workers discovered that $FeCl_3$, when used in conjunction with a nontoxic and cheap amine, DMEDA (*N,N*-dimethylethylenediamine), could successfully couple aryl iodides and terminal alkynes (**Scheme 1.6**).³² Two equivalents of Cs_2CO_3 is also added to the reaction mixture to help neutralize any acid (HCl) that are generated. These reaction conditions have also been found to successfully couple various terminal alkynes (both electron-rich and electron-deficient) and other substituted aryl halides.³²

In 2008, Vogel and co-workers developed an efficient Sonogashira reaction when using $\text{Fe}(\text{acac})_3$ as a catalyst, and CuI as a co-catalyst (**Scheme 1.7**). For this particular system, the use of polar aprotic solvents such as DMF (*N,N*-dimethylformamide), DMSO (dimethyl sulfoxide) and NMP (*N*-methyl-2-pyrrolidone) are crucial, since these solvents are expected to act as potential ligands to help stabilize the catalytic system.³⁸ Once again, Cs_2CO_3 is added as a base. Like the catalytic system developed by Vogel, Mao and co-workers also developed an efficient catalytic system. However, Mao and co-workers used K_3PO_4 as its base, while still maintaining excellent yields up to 99%.³⁹

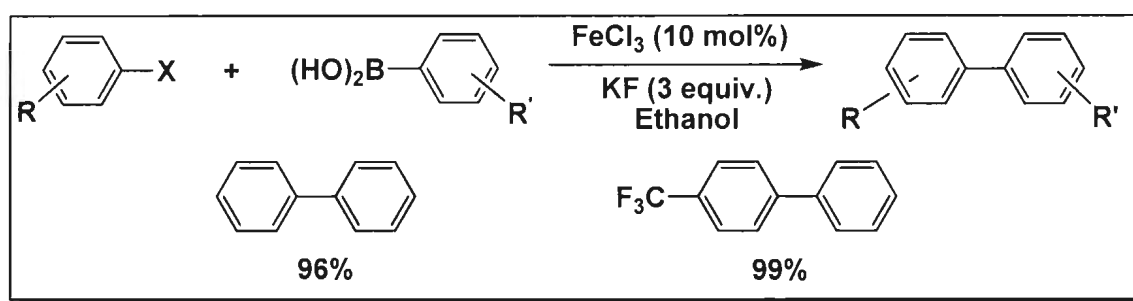


Scheme 1.7: Iron catalyzed Sonogashira reactions reported by Vogel and co-workers.³⁸

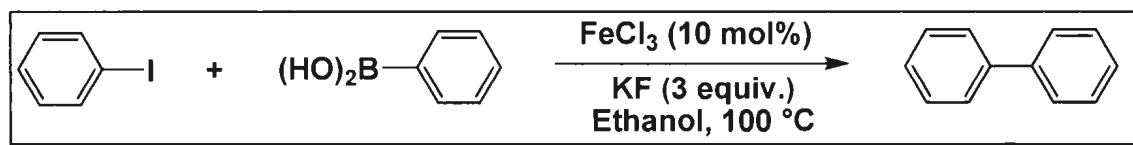
1.2.2 Iron Catalyzed Suzuki Cross-Coupling

Over the past few decades, the Suzuki cross-coupling reaction has become one of the most efficient methods for selective biaryl C-C bond formation.⁹ The transition-metal-catalyzed cross-coupling reaction of organoboron compounds is one of the most prevalent organic synthetic reactions for the production of functional molecules, which are often present as partial structures in natural products and pharmaceuticals.^{40,41} Traditionally,

palladium complexes have been used widely as catalysts for the Suzuki reaction.⁴² One major drawback with the palladium system is that most palladium complexes are expensive and toxic which makes production on a large scale impractical. Also, many palladium complexes are air sensitive, which can be very inconvenient. In recent times, there has been a significant rise in the use of iron-based catalysts for the Suzuki cross-coupling reaction, to help promote environmentally benign synthetic methodologies.⁴⁰



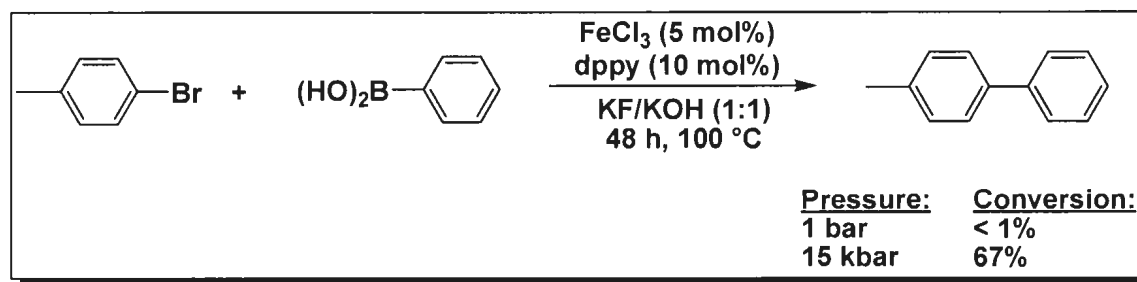
Scheme 1.8: Iron catalyzed Suzuki cross-coupling reactions reported by Darcel and co-workers.⁴⁰



Scheme 1.9: Iron catalyzed Suzuki cross-coupling reaction of phenyl iodide with phenylboronic acid.⁴⁰

In 2009, Darcel and co-workers reported an efficient, mild, and simple method for the iron-catalyzed Suzuki cross-coupling reaction between iodo- or bromoaryl derivatives and arylboronic acids.⁴⁰ In the presence of iron(III) chloride, and a stoichiometric amount of potassium fluoride, aryl iodides and bromides can react with arylboronic acids to give the corresponding biaryl compounds with good to excellent yields (**Scheme 1.8**).⁴⁰ Interestingly, when a hydrated precursor $\text{FeCl}_3 \cdot 6\text{H}_2\text{O}$ was used, only moderate yields of

the biphenyl derivative was obtained.⁴⁰ Darcel and coworkers also reported the crucial role of pressure on the cross-coupling process. When the reaction between iodobenzene and phenylboronic acid was performed in an open flask (**Scheme 1.9**), only 25% conversion was observed. On the contrary, when the same reaction was conducted in a sealed tube, 100% conversion was observed.⁴⁰ A year prior, Young and co-workers reported that the Suzuki cross-coupling reaction between bromobenzene and phenylboronic acid can be promoted at high pressure in the presence of FeCl_3 and dppy (2-(diphenylphosphino)pyridine) (**Scheme 1.10**).⁴³ They suggested that the main influence of pressure on the iron-catalyzed reaction is to accelerate the reduction of the metal center to its low valent catalytically active oxidation state.⁴³



Scheme 1.10: Iron catalyzed Suzuki biaryl cross-coupling reactions performed under high pressure.⁴³

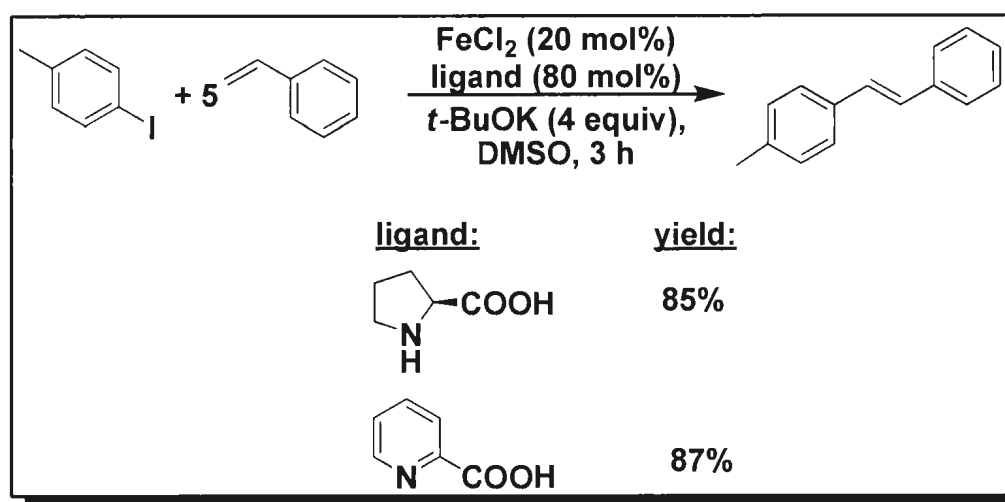
In 2010, two independent laboratories failed to reproduce the results reported by Darcel and Bézier.⁴⁴ Consequently, the Darcel group decided to re-examine the reaction. Surprisingly, Darcel and co-workers discovered that the reaction (**Scheme 1.8**) was highly dependent on the source of potassium fluoride used due to the presence of trace amounts of palladium. In 2010, the communication was retracted. According to the

literature, several other iron-catalyzed Suzuki cross-coupling reactions have been troubled by contaminant/impurity concerns. For example, in 2008, Franzén and co-workers reported the first iron-catalyzed Suzuki cross-coupling reaction involving iron-pyridine complexes.⁴⁵ This particular system was reported to be highly effective for the cross-coupling of various aryl bromides and phenyl boronic acid. However, when Bedford and Nakamura examined this catalytic system they determined that the results reported were impossible to reproduce.⁴⁶ Bedford and co-workers discovered that trace palladium contamination was the active catalytic component and not the suspected iron-pyridine complex. Eventually, Franzén and co-workers retracted their article.⁴⁷

The observation that reactions can be catalyzed by trace metal impurities is not a new phenomenon. An early and notable example was the discovery of the “nickel effect” in the 1950s, which led to the development of the Ziegler catalysts.⁴⁸ According to recent reports by Bolm and co-workers, certain iron-catalyzed cross-coupling reactions with FeCl_3 may be significantly affected by trace quantities of other metals, particularly copper.⁴⁹ These findings suggested that both the purity and source of the FeCl_3 can play a crucial role in the cross-coupling process.⁴⁹ In order to strengthen the credibility of iron-catalyzed cross-coupling reactions, it would be desirable to analyze the purity of all reagents and starting materials employed. Techniques such as inductively coupled plasma mass spectrometry (ICP-MS) can be used to analyze the purity of all materials with detection limits at sub parts per billion (ppb) levels.⁵⁰

1.2.3 Iron-Catalyzed Heck Cross-Coupling

Today, the Mizoroki-Heck cross-coupling reaction is one of the most efficient methods for designing aryl-substituted olefins. Traditionally, palladium^{51,52} and nickel^{53,54} complexes have been used extensively, in combination with phosphine based ligands. However, due to recent economical and environmental concerns, more benign alternatives have been developed.



Scheme 1.11: The iron catalyzed cross-coupling of 4-iodotoluene with styrene.⁵⁵

In 2008, Vogel and co-workers determined that simple iron salts such as FeCl_2 are active catalysts for the arylation of alkenes with aryl halides.⁵⁵ Iron(II) starting materials were found to have better catalytic activity for this transformation than iron(III) salts. For this particular reaction, $t\text{-BuOK}$ is used as the base, while DMSO is used as the reaction medium. Cheap and environmentally friendly ligands such as proline or picolinic acid are generally present. For the cross-coupling of 4-iodotoluene with styrene (**Scheme 1.11**), 20 mol% of FeCl_2 and 80 mol% of ligand is required. The desired product can be achieved in

a short period of time (3 h), under mild reaction conditions (60 °C), and in good to excellent yields.⁵⁵ However, one major drawback with this particular reaction is the requirement of excess styrene to help drive the arylation process. When excess styrene is present, the polymerization of styrene is inevitable. In the future, generating a reaction procedure which requires less ligand, and less styrene, would be both environmentally and economically beneficial.

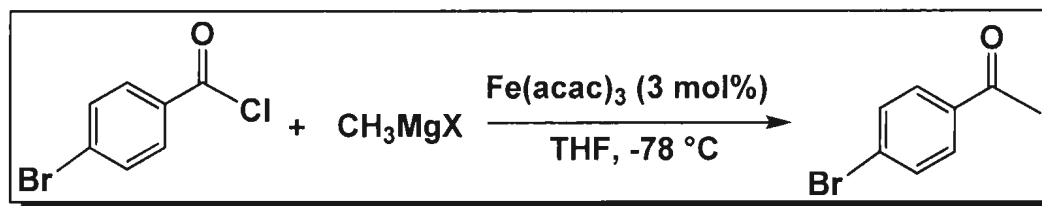
1.2.4 Iron-Catalyzed Kumada Cross-Coupling

In 1972, Makoto Kumada reported a nickel-catalyzed reaction of Grignard reagents with alkenyl and aryl halides.⁵⁶ The advantages gained by replacing nickel with palladium were discovered shortly thereafter.⁵⁷ Over the past 30 years, there has been a rapid development in the use of iron catalysts for Kumada-type cross-coupling reactions. Previous reports have shown that Kumada-type reactions can occur very rapidly at low temperatures, and are distinguished by broad functional group tolerance.^{58,59} Today, the iron-catalyzed Kumada-type cross-coupling reaction is very diverse, and many different methods exist.

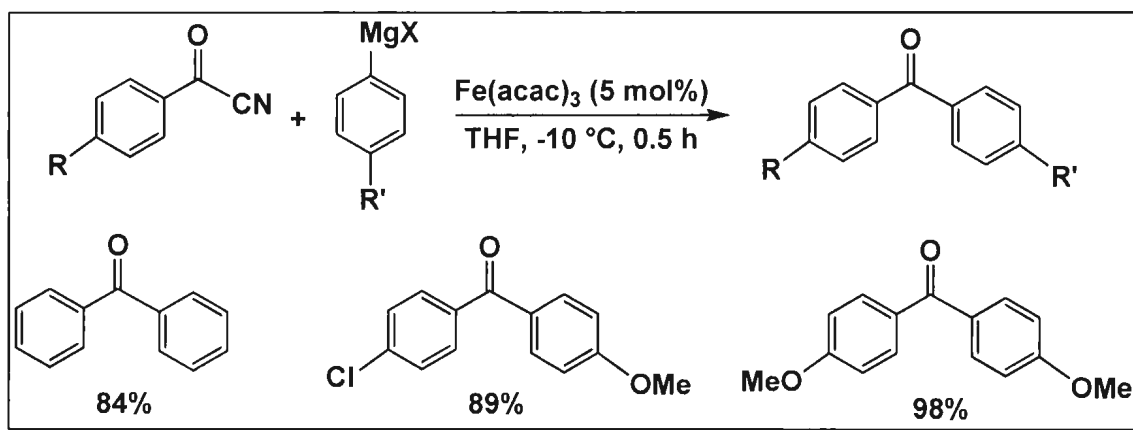
1.2.4.1 Acyl Electrophiles

In the first half of the 20th century, the reaction of nucleophiles (Grignard reagents) with activated acid derivatives posed a significant challenge to synthetic chemists. However, in 1953, Cook and co-workers discovered that catalytic FeCl₃ was highly effective for the alkylation of acetyl chloride, generating 2-hexanone (> 70% yield).⁶⁰ This was a very significant discovery, opening a gateway for the iron-catalyzed

cross-coupling of acid chlorides, acid cyanides and thioesters, with alkyl and aryl Grignard reagents.^{61,62}



Scheme 1.12: $[\text{Fe}(\text{acac})_3]$ -catalyzed reactions of functionalized magnesium reagents with acyl chlorides.⁶¹

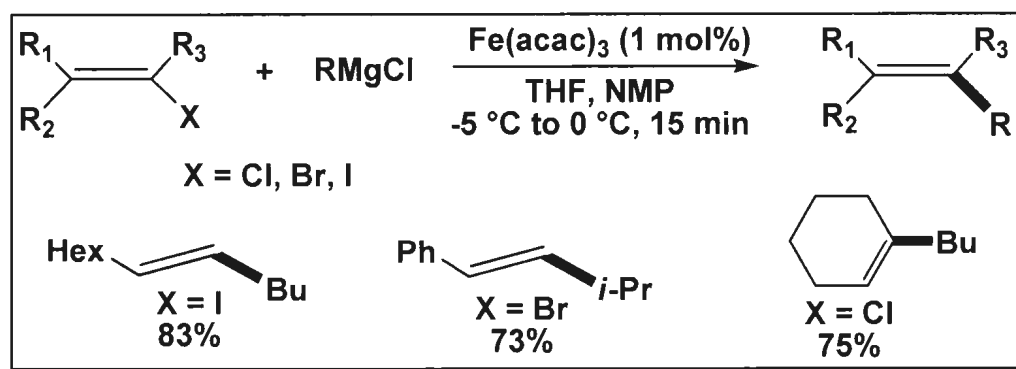


Scheme 1.13: $[\text{Fe}(\text{acac})_3]$ -catalyzed reactions of functionalized magnesium reagents with acyl cyanides.⁶²

In 2004, Fürstner and co-workers discovered that the air stable and nontoxic iron salt, $\text{Fe}(\text{acac})_3$, was an excellent precatalyst for the cross-coupling of Grignard reagents with acid chlorides.⁶¹ When methylmagnesium bromide was reacted with *p*-bromobenzoyl chloride in the presence of $\text{Fe}(\text{acac})_3$ (3 mol%) at -78°C , *p*-bromoacetophenone was generated with a yield of 86% (**Scheme 1.12**).⁶¹ In the same

year, Knochel and co-workers discovered that $\text{Fe}(\text{acac})_3$ was also an excellent precatalyst for the cross-coupling of functionalized aryl and heteroaryl Grignard reagents with aryl and heteroaryl acyl cyanides (**Scheme 1.13**).⁶² This reaction represents a very efficient method for the development of polyfunctional diaryl ketones which are widely used throughout the pharmaceutical industry.⁶³

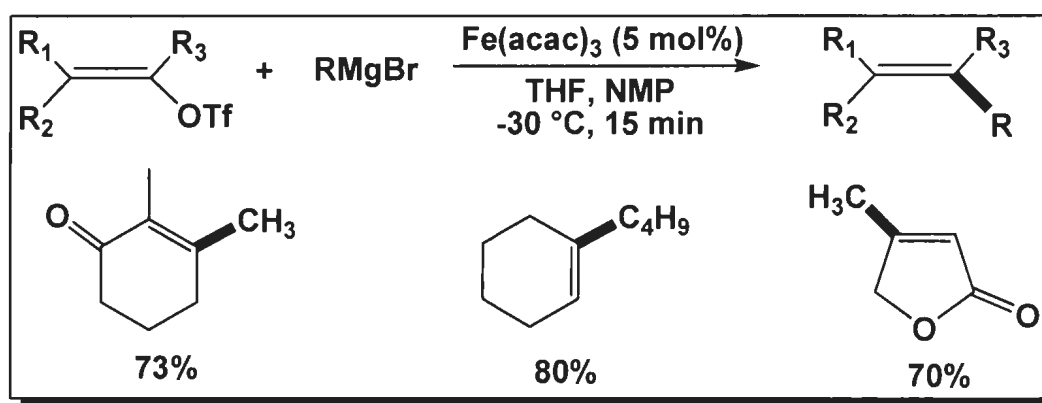
1.2.4.2 Alkenyl Electrophiles



Scheme 1.14: The iron-catalyzed alkenylation of alkylmagnesium chlorides.⁶⁴

The iron-catalyzed alkenylation of Grignard reagents was first described by Kochi and co-workers in 1971.²⁴ In the presence of catalytic amounts of FeCl_3 , alkenyl halides were found to react with organomagnesium halides. One major drawback with the method reported by Kochi and co-workers was the requirement of excess alkenyl halide. The iron-catalyzed cross-coupling reaction between alkenyl electrophiles and alkyl Grignard reagents was significantly improved in 1998, when Cahiez and co-workers discovered the beneficial use of *N*-methylpyrrolidinone (NMP) as a co-solvent (**Scheme**

1.14).⁶⁴ In the presence of NMP, $\text{Fe}(\text{acac})_3$ is capable of catalyzing the alkenylation of Grignard reagents, while providing shorter reaction times, higher yields and increased selectivity.⁶⁴ Co-solvents, such as NMP, have the potential to directly coordinate to a vacant site on the metal complex and function as axially stabilizing ligands or “place holders” which can help prevent decomposition of the catalyst (*i.e.* via β -hydrogen elimination).

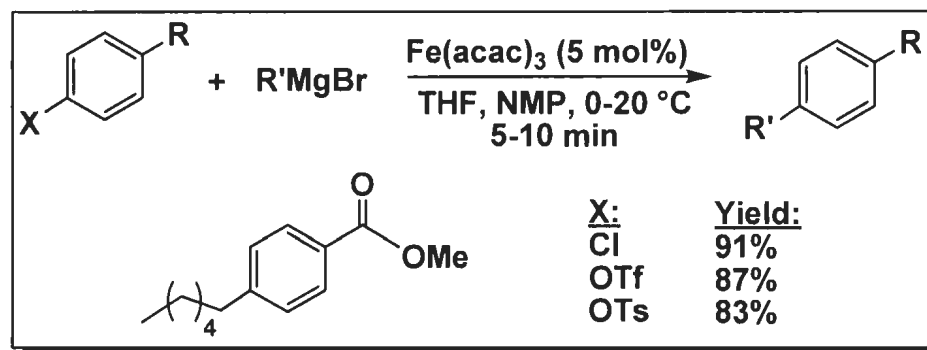


Scheme 1.15: Iron-catalyzed cross-coupling reactions of alkenyl triflates with Grignard reagents.⁶¹

In 2004, Scheiper and co-workers discovered that $\text{Fe}(\text{acac})_3$ was also an efficient catalyst for the cross-coupling reaction between alkenyl triflates and Grignard reagents (**Scheme 1.15**).⁶¹ This particular reaction demonstrates exceptional functional group tolerance, allowing the use of alkenyl substrates bearing esters, enones, ethers, acetals and lactones. Likewise, organomagnesium halides bearing ether, acetal, alkyne, or chloride entities have also been successfully employed.⁶¹

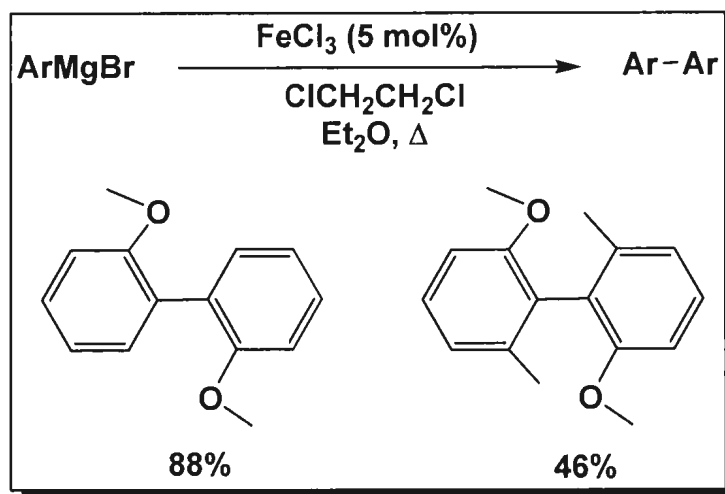
1.2.4.3 Aryl Electrophiles

In 2002, Fürstner and co-workers reported an efficient iron-catalyzed cross-coupling reaction between alkylmagnesium halides and aromatic electrophiles.⁶⁵ When moderately electron-deficient aryl chlorides, triflates and tosylates were reacted with alkylmagnesium halides in the presence of $\text{Fe}(\text{acac})_3$, good to excellent yields were obtained (**Scheme 1.16**). Unfortunately, the reaction is sensitive to steric effects, as aryl chlorides bearing *ortho* substituents generally result in lower yields than their *para*-substituted counterparts.⁶⁵

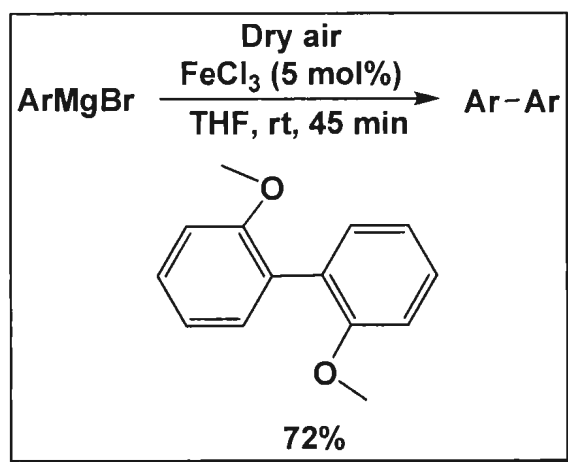


Scheme 1.16: Iron-catalyzed cross-coupling of alkyl Grignard reagents with aryl chlorides, tosylates, and triflates.⁶⁵

The oxidative homo-coupling of aryl-metal reagents is one of the most efficient synthetic methods for the construction of a symmetrical biaryl backbone.⁶⁶ In 2005, Hayashi and co-workers reported an efficient and practical reaction system for the iron-catalyzed oxidative homo-coupling of aryl Grignard reagents.⁶⁷ When FeCl_3 was used as a catalyst in the presence of an oxidant such as 1,2-dichloroethane, the oxidative homo-coupling of 2-methoxyphenylmagnesium bromide was found to give an 88% yield of the desired biaryl product (**Scheme 1.17**). Once again, introduction of alkyl groups at the *ortho* position of the aryl Grignard resulted in a lower yield of the biaryl product.⁶⁷



Scheme 1.17: Iron-catalyzed oxidative homo-coupling of aryl Grignard reagents.⁶⁷



Scheme 1.18: Iron-catalyzed oxidative homo-coupling of aryl Grignard reagents with atmospheric oxygen as an oxidant.⁶⁹

In the same year (2005), Cahiez and co-workers decided to modify the catalytic system reported by Hayashi. Since diethyl ether is inconvenient for large-scale application (especially at reflux) and the preparation of aromatic Grignard reagents is much easier in THF, Cahiez and co-workers investigated the use of THF as the reaction medium. When THF is used instead of diethyl ether, only 0.6 equivalents of the oxidant is

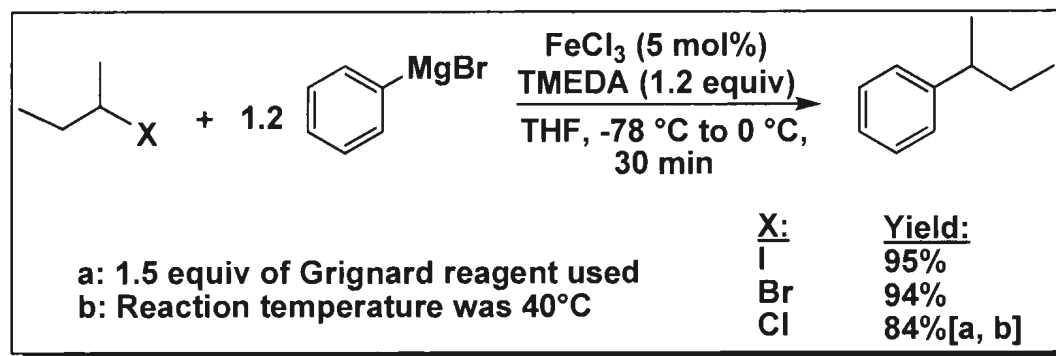
required (compared to 1.2 reported by Hayashi *et al.*) to achieve comparable yields reported by Hayashi.⁶⁸ By 2007, Cahiez and co-workers developed a more economical method for the preparation of biaryl compounds. By using atmospheric air as the oxidant (instead of 1,2-dichloroethane), the iron-catalyzed homo-coupling of 2-methoxyphenylmagnesium bromide was found to generate the desired biaryl product with a yield greater than 70% (**Scheme 1.18**).⁶⁹

1.2.4.4 Alkyl Electrophiles

Traditionally, the metal-catalyzed cross-coupling of alkyl halides with aryl Grignard reagents has posed many challenges for synthetic chemists. Primary and secondary halides tend to be less reactive than aryl halides and the intermediate alkyl complexes formed tend to be prone to rapid β -elimination reactions generating undesirable alkene products. However, over the last few decades, substantial advances have been developed to help address these shortcomings.⁷⁰

In 2004, Nakumara and co-workers reported an efficient catalytic system for the cross-coupling of primary or secondary alkyl halides with aryl Grignard reagents.⁷⁰ In the presence of 1.2 equivalents of the additive *N,N,N',N'*-tetramethylethylenediamine (TMEDA), FeCl₃ (5 mol%) was found to be an active catalyst for the coupling of aryl Grignard reagents with primary and secondary alkyl halides, generating products in yields greater than 80%. The more polarizable alkyl iodides were more reactive than the corresponding alkyl bromides, with the least reactive being the alkyl chlorides (**Scheme**

1.19).⁷⁰ For this particular reaction system, primary alkyl halides were much less reactive than the corresponding secondary alkyl halides.

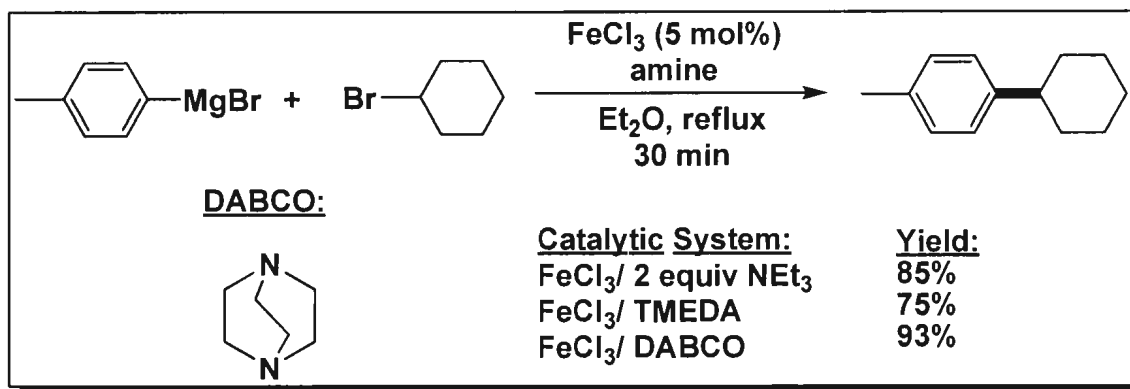


Scheme 1.19: Iron-catalyzed cross-coupling reaction of an alkyl halide with phenylmagnesium bromide.⁷⁰

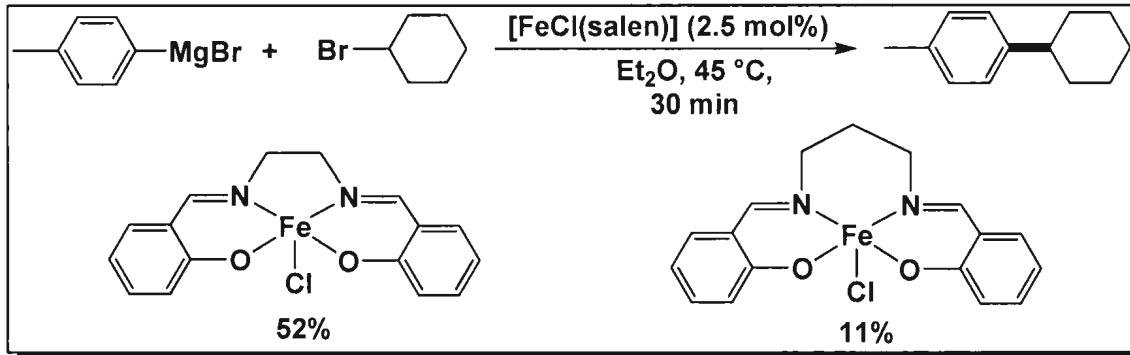
Unfortunately, there are some distinct disadvantages with the catalytic system reported by Nakamura and co-workers. First of all, an excess amount of amine is required, which needs to be added with the Grignard reagent. Second, the Grignard/amine mixture must be added very slowly *via* the use of a syringe pump. Lastly, the reaction must be cooled to low temperatures.

In 2006, Bedford and co-workers developed a catalytic system which would prove to be superior to the one previously reported by Nakumara and co-workers. Unlike the catalytic system reported by Nakumara,⁷⁰ Bedford and co-workers reported the use of amines in catalytic quantities. Also, slow addition of Grignard reagent and low temperature conditions were determined not to be prerequisites for good catalytic activity. In the presence of ligands such as triethylamine, TMEDA and DABCO, FeCl_3 (5 mol%)

was found to be an effective catalyst for the cross-coupling of 4-methylphenylmagnesium bromide and cyclohexyl bromide (Scheme 1.20).⁷¹



Scheme 1.20: Iron-catalyzed cross-coupling of 4-methylphenylmagnesium bromide and cyclohexyl bromide in the presence of an amine.⁷¹



Scheme 1.21: Iron(III) salen-catalyzed cross-coupling of 4-methylphenylmagnesium bromide and cyclohexyl bromide.⁷²

Inspired by previous work by Fürstner,⁶⁵ Bedford and co-workers discovered that iron(III) salen complexes were active catalysts for the coupling of aryl Grignard reagents with primary and secondary alkyl halides bearing β -hydrogens (Scheme 1.21).⁷² The

salen ligand is very versatile as the substituents on the phenolate ring can be easily varied, along with the diimine functionality. Bedford and co-workers demonstrated that catalytic activity is dependent on the nature of the diimine backbone. As the diimine backbone becomes more bulky and electron donating in nature, the activity of the catalyst was reported to decrease.⁷²

1.2.5 Mechanistic Considerations

Today, nickel and palladium metal complexes provide the broadest utility and deepest mechanistic insight into cross-coupling reactions. In fact, iron cross-coupling catalysis was largely unexplored until the mid-1990s and the mechanistic study of iron catalyzed cross-coupling is still underdeveloped. Iron-catalyzed reactions are typically very difficult to study mechanistically due to the paramagnetic nature of iron and the instability of alkyl-iron intermediates.⁷³ However, over the past few decades, there have been many advances in the area of iron-catalyzed cross-coupling and some plausible mechanisms have been reported. This section will focus specifically on the mechanistic study of C-C cross-coupling reactions promoted by iron.

In 2002, Fürstner and co-workers reported a plausible mechanism for the iron-catalyzed cross-coupling reaction between aryl halides and alkylmagnesium halides. Unlike previous reports which speculate that Fe(0) or Fe(I) species constitute the catalytically active intermediate, Fürstner proposed that “super-ate” complexes of Fe(-II) act as the catalytically active component.⁶⁵ When FeCl₂ reacts with 4 equivalents of RMgX, a new species is generated (Fe(MgX)₂) bearing a formal negative charge at the iron center. This species, which lacks any stabilizing ligands, can oxidatively add to aryl

halides (**Figure 1.6**).⁶⁵ The organometallic iron compound can then be alkylated by excess Grignard reagent. Subsequent reductive coupling of the organic ligands should then generate the desired cross-coupling product along with regeneration of the Fe(-II) species.⁶⁵

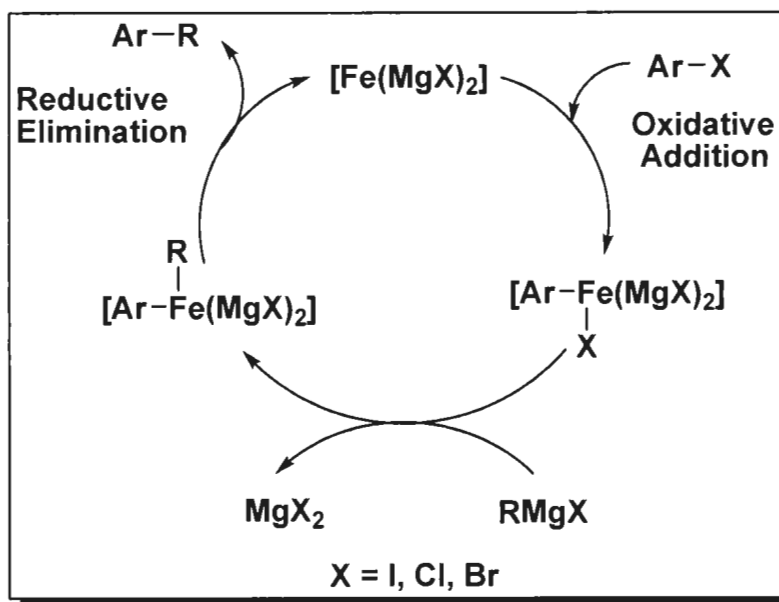


Figure 1.6: A plausible catalytic cycle for the iron-catalyzed cross-coupling of aryl halides with inorganic Grignard reagents.⁶⁵

Previously, Nakamura and Fürstner reported that the mechanism for the iron-catalyzed coupling of alkyl halides with aryl Grignard reagents may in fact proceed *via* a radical process.^{25,72} In both cases, there was an observation that the coupling of 2-bromooctane with phenylmagnesium bromide leads to the formation of a racemic product. In 2006, Bedford and co-workers proposed a similar mechanism.⁷⁴ Only after the Grignard reagent reacts with the iron pre-catalyst, the active iron species in oxidation state n reacts with an alkyl halide (by the transfer of a single electron) to generate an alkyl radical and an $[\text{Fe}^{(n+1)}\text{X}]$ species (**Figure 1.7**). Transmetalation with the Grignard reagent,

followed by a reductive elimination process, is then expected to generate the desired cross-coupling product along with regeneration of the catalyst.⁷⁴

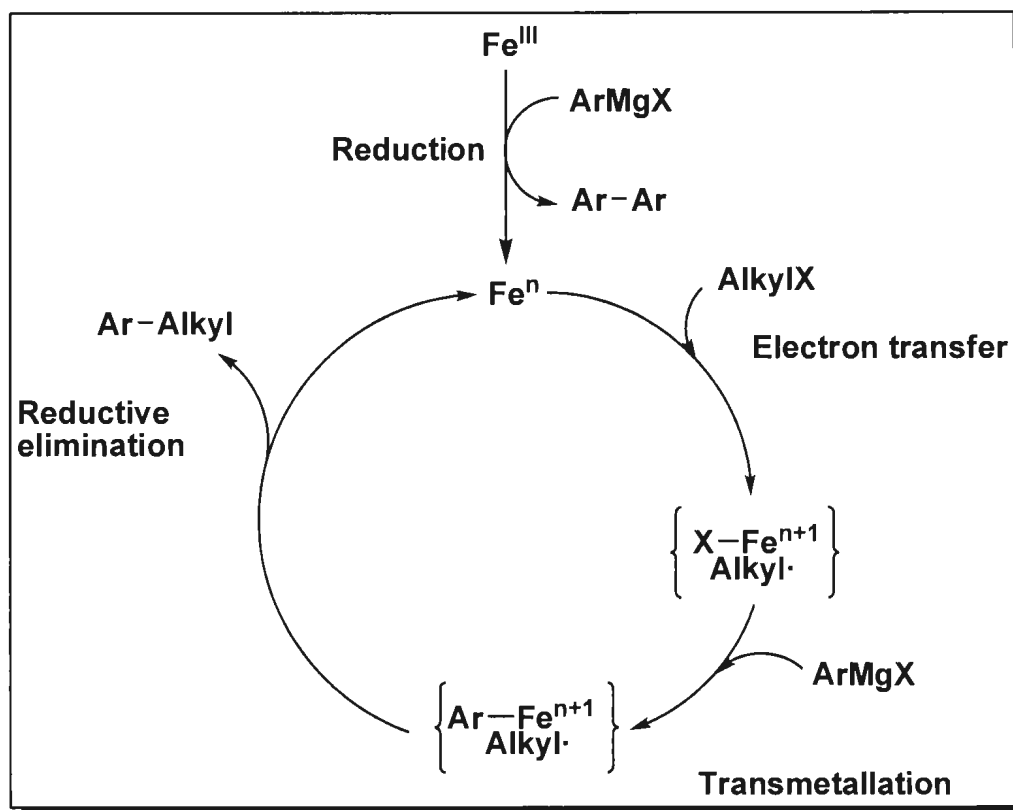


Figure 1.7: A plausible catalytic cycle for the iron-catalyzed cross-coupling of alkyl halides with aryl Grignard reagents.⁷⁴

More recently, in 2009, Norrby and co-workers reported a mechanism for the iron catalyzed cross-coupling of aryl electrophiles with alkyl Grignard reagents. Using density functional theory (DFT) calculations and Hammett competition experiments, two potential mechanistic pathways have been reported (**Figure 1.8**).⁷⁵ According to Norrby *et al.*, the reaction follows a pathway where an Fe(I) complex (a reduced iron catalyst formed *in situ* and labeled $[\text{Fe}]$) reacts in a rate-limiting oxidative addition with the aryl electrophile (**Path A**). After rapid thermoneutral transmetalation from a Grignard reagent

occurs, reductive elimination of the resulting alkyl-aryl Fe(III) complex generates the desired cross-coupling product, along with regeneration of the catalyst. Unfortunately, at this time, there is no direct method for distinguishing between the order of the oxidative addition and transmetalation steps. Therefore, initial transmetalation from the Grignard reagent (**Path B**) should also be considered as a valid proposal since both cycles (**Path A** and **Path B**) fit the observed kinetics.⁷⁵

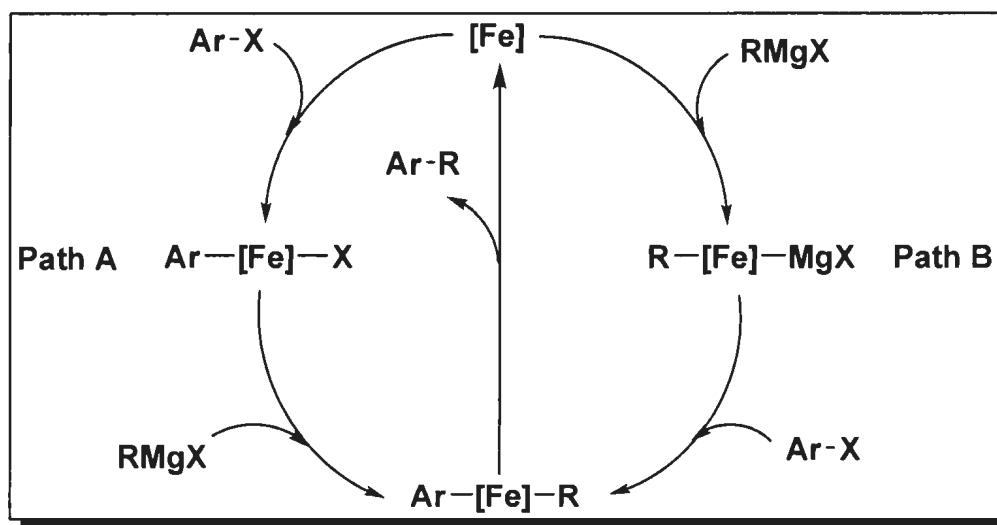


Figure 1.8: Two plausible catalytic cycles for the iron-catalyzed cross-coupling of aryl halides with alkyl Grignard reagents.⁷⁵

1.3 Iron Complexes supported by Amine-bis(phenolate) Ligands as Catalysts for C-C cross-coupling

Recently, the use of chelating amine-bis(phenolate) ligands has played a very important role in transition metal catalyst design. These dianionic compounds form a diverse set of ligands that have been predominantly used with high-valent early transition

metals.⁷⁶⁻⁸¹ When used in combination with group 4 and 5 transition metals, high activity towards olefin or cyclic ester polymerization has been previously reported.⁸²⁻⁹¹

Today, there has been very limited use of amine-bis(phenolate) ligands with first row late transition metals such as iron.⁹²⁻⁹⁹ However, a number of Fe(III) complexes supported by these ligands have been investigated as a result of their close relationship with phenol-containing ligands found in non-heme iron containing metalloenzymes.^{98, 100-103} Iron(III) amine-bis(phenolate) systems have also been used to mimic iron-tyrosinate proteins such as catechol 1,2-dioxygenase (CTD), which catalyze the oxidative cleavage of catechol or its derivatives with the incorporation of molecular oxygen.¹⁰⁴ Recently, iron(III) complexes supported by tetradentate and tridentate (amine)bis(phenolato) ligands have been used as effective catalysts for cross-coupling of aryl Grignard reagents with alkyl halides, including primary and secondary alkyl halides.¹⁰⁵⁻¹⁰⁷ This section will focus primarily on these iron-catalyzed cross-coupling systems, along with some of the catalysis results reported.

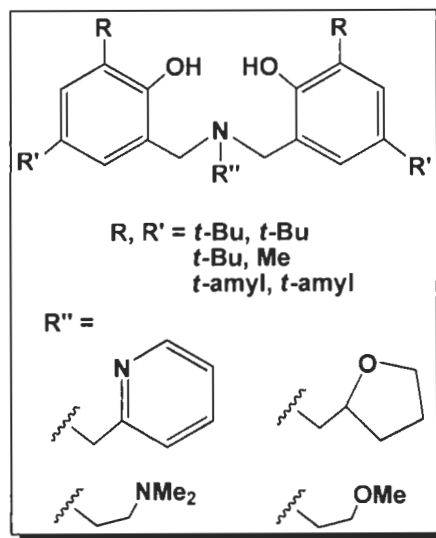


Figure 1.9: Some examples of typical tetradentate amine-bis(phenol) ligands.

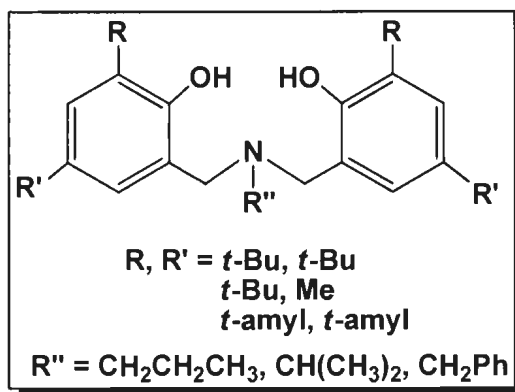


Figure 1.10: Some examples of typical tridentate amine-bis(phenol) ligands.

Amine-bis(phenol) ligands, which possess “hard” nitrogen and oxygen donor atoms, contain two dialkyl-substituted phenol groups bearing either *tert*-butyl, *tert*-amyl or methyl substituents, *ortho* and *para* (or *ortho* and *meta*) to a hydroxyl group. When tetradentate in nature, amine-bis(phenol) ligands also contain a pendant donor arm which generates a relatively constrained tripodal environment (**Figure 1.9**). These tetradentate ligands have a general formulation of $\text{H}_2[\text{O}_2\text{NN}']^{\text{RR}'\text{R}''}$ when the pendant donor is dialkylamino or pyridyl based. A general formulation of $\text{H}_2[\text{O}_2\text{NO}]^{\text{RR}'\text{R}''}$ is used when the pendant donor is tetrahydrofuranyl. Here, R and R' represent the alkyl substituents on the phenol ring, while R'' represents the nature of the pendant donor arm. Tridentate amine-bis(phenol) ligand precursors are abbreviated $\text{H}_2[\text{O}_2\text{N}]^{\text{RR}'\text{R}''}$. Once again, R and R' represent the alkyl substituents on the phenol ring, while R'' represents the alkyl group coordinated to the central amine donor (**Figure 1.10**).

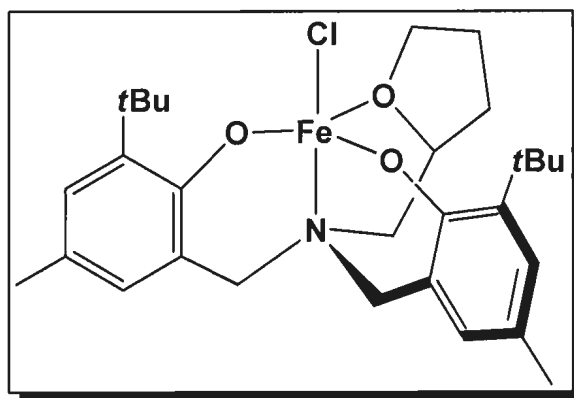
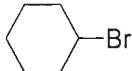
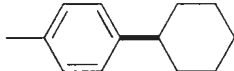
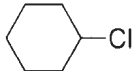
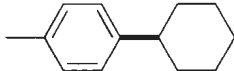
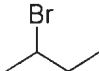
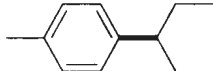
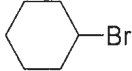
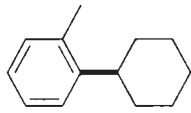
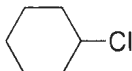
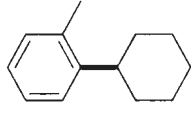
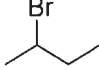
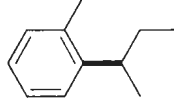
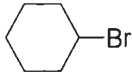
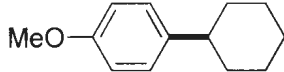

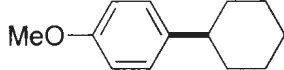
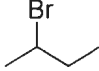
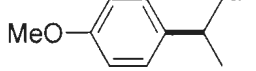


Figure 1.11: An iron(III) halide catalyst ($\text{FeCl}[\text{O}_2\text{NO}]^{\text{BuMeFurf}}$) reported by Kozak and co-workers.¹⁰⁵

In 2008, Kozak and co-workers reported that iron(III) halide compounds supported by tetradentate amine-bis(phenolate) ligands ($\text{FeCl}[\text{O}_2\text{NO}]^{\text{BuMeFurf}}$) showed good activity as catalysts for the cross-coupling of aryl Grignard reagents with primary and secondary alkyl halides (**Figure 1.11**).¹⁰⁵ For these particular reactions, diethyl ether was found to be superior to THF as the solvent. When the Grignard reagent (4.0 mmol) was reacted with the alkyl halide (2.0 mmol) in the presence of a catalytic amount of $\text{FeCl}[\text{O}_2\text{NO}]^{\text{BuMeFurf}}$ (5.0 mol%), moderate to excellent yields were reported (**Table 1.1**).¹⁰⁵ Bromocyclohexane gave excellent yields (99%) when reacted with *p*-tolyl, *o*-tolyl and *p*-anisyl Grignard reagents respectively (**Table 1.1**, entries 1, 4 and 7), while chlorocyclohexane gave only moderate yields with all three Grignard reagents (**Table 1.1**, entries 2, 5 and 8). Similarly, only moderate yields were observed when 2-bromobutane was reacted with all three Grignard reagents (**Table 1.1**, entries 3, 6, and 9).¹⁰⁵

Table 1.1: Cross-coupling of ArMgBr with alkyl halides reported by Kozak *et al.*¹⁰⁵

Entry	ArMgBr	Alkyl Halide	Product	Yield (%)
1	<i>p</i> -Tolyl			99
2	<i>p</i> -Tolyl			48
3	<i>p</i> -Tolyl			79
4	<i>o</i> -Tolyl			99
5	<i>o</i> -Tolyl			62
6	<i>o</i> -Tolyl			50
7	<i>p</i> -Anisyl			99
8	<i>p</i> -Anisyl			22
9	<i>p</i> -Anisyl			37

More recently, in 2011, Kozak and co-workers investigated a series of octahedral amine-bis(phenolato)iron(acac) complexes as single-component catalysts for the cross-coupling of aryl Grignard reagents with alkyl halides.¹⁰⁶ When cyclohexyl chloride (1.00 mmol) was reacted with *o*-tolylmagnesium bromide (2.00 mmol) in diethyl ether, yields of cross-coupled product varied depending on the nature of the amine-bis(phenolate) ligand employed. By introducing an amine pendant arm on the amine-bis(phenolate)

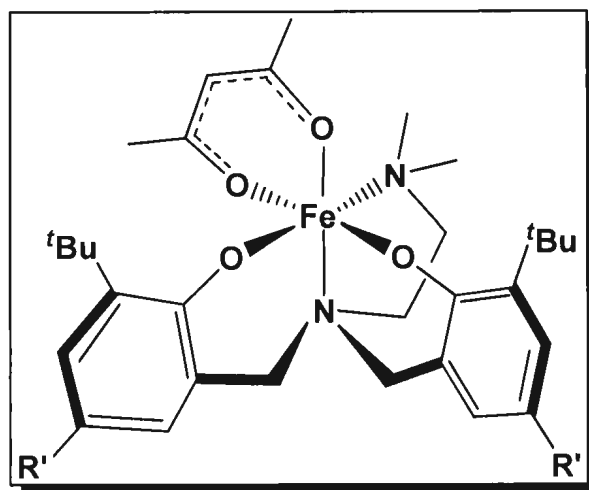


Figure 1.12: Amine-bis(phenolato)iron(acac) complexes reported by Kozak and co-workers. Catalyst **1**; R' = ^tBu. Catalyst **2**; R' = Me.¹⁰⁶

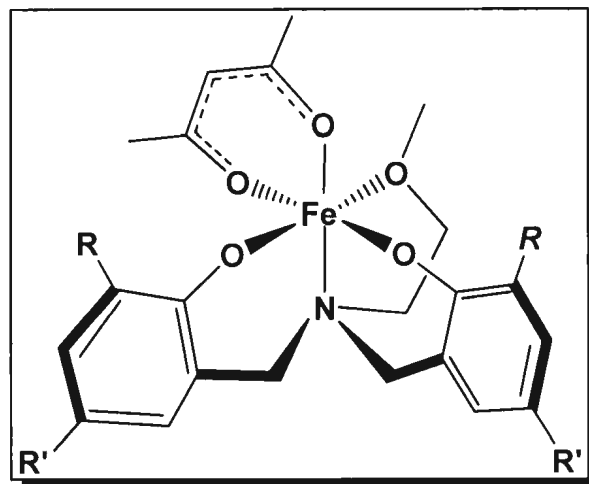
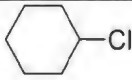
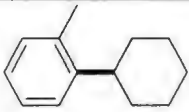


Figure 1.13: Amine-bis(phenolato)iron(acac) complexes reported by Kozak and co-workers. Catalyst **3**; R = R' = ^tBu. Catalyst **4**; R = ^tBu, R' = Me. Catalyst **5**; R = R' = Me.¹⁰⁶

backbone (**Figure 1.12**), relatively lower yields of the cross-coupling products were obtained (**Table 1.2**, catalysts **1** and **2**). However, when ether pendant arms were employed (**Figure 1.13**), excellent yields (up to 96%) were reported (**Table 1.2**, catalysts

3, 4 and 5).¹⁰⁶ Previously, Bedford and co-workers found moderate yields (70-80%) for the cross-coupling reaction between cyclohexyl chloride and *p*-tolylmagnesium bromide using different iron catalysts such as Fe(salen) complexes and Fe nanoparticles.^{72, 108}

Table 1.2: Cross-coupling of *o*-tolylmagnesium bromide with cyclohexyl chloride reported by Kozak *et al.*¹⁰⁶

Catalyst	ArMgBr	Alkyl Halide	Product	%Yield
1	<i>o</i> -Tolyl			33
2	"	"	"	55
3	"	"	"	96
4	"	"	"	80
5	"	"	"	79

Reaction conditions: Microwave heating for 10 min at 100 °C, catalyst (0.05 mmol).

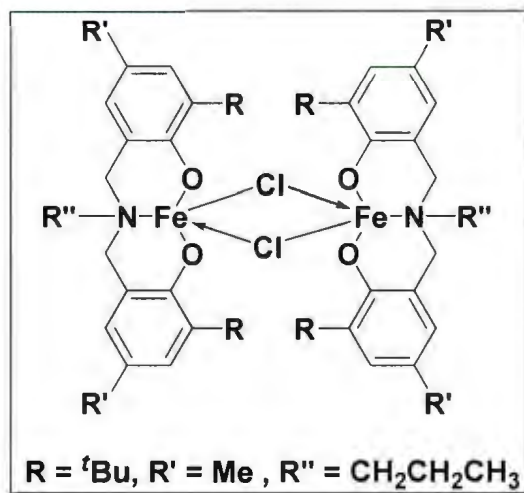



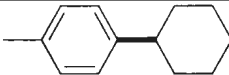
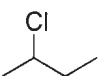
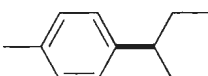
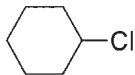
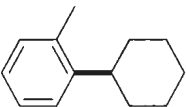
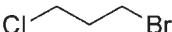
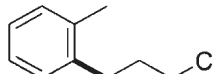
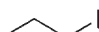
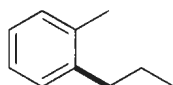
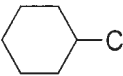
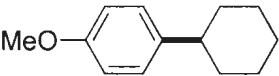
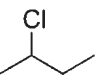
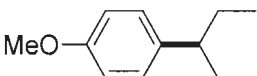
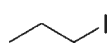
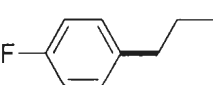
Figure 1.14: An iron(III) chloride-bridged dimer $[\text{Fe}(\text{O}_2\text{N})^{\text{BuMenPr}}(\mu\text{-Cl})_2]$ reported by Kozak and co-workers.¹⁰⁷

In order to generate more reactive catalysts, while maintaining the robust nature of the catalyst precursor, Kozak and co-workers focused their attention on tridentate amine-bis(phenolate) ligands.¹⁰⁷ In 2010, Kozak and co-workers reported the synthesis of a Fe(III) chloride-bridged dimer (**Figure 1.14**), which was used as an air stable, non-hygroscopic, single-component catalyst (0.05 mmol) for the C-C cross-coupling of aryl Grignard reagents (4.0 mmol) with primary and secondary alkyl halides (2.0 mmol), including chlorides. For some reactions, higher yields were reported under microwave heating.¹⁰⁷

When cyclohexyl chloride was investigated as a substrate, modest to good yields were reported depending on the Grignard reagent used. When *p*-tolylmagnesium bromide was used as the Grignard reagent (**Table 1.3**, entry 1), a poorer yield of the cross-coupled product was obtained compared to *o*-tolylmagnesium bromide (**Table 1.3**, entry 3).¹⁰⁷ A yield of 86% (**Table 1.3**, entry 3) was found to be superior to previous results reported in the Kozak group.¹⁰⁵ Cyclohexyl chloride gave poor yields with *p*-anisylmagnesium bromide (**Table 1.3**, entry 6). However, microwave-assisted heating (100 °C for 10 minutes) drastically improved the conversion for cyclohexyl chloride, giving the desired cross-coupled product in 91% yield.¹⁰⁷

Today, there are only limited reports of Kumada-type cross-coupling using secondary alkyl chlorides. According to Nakamura and co-workers, when phenylmagnesium bromide was reacted with 2-chlorobutane in the presence of FeCl₃/TMEDA, an 84% yield of the cross-coupled product was obtained. However, slow addition of the Grignard reagent was required along with heating to 40 °C.²⁴ Surprisingly,

Table 1.3: Cross-coupling of ArMgBr with alkyl halides reported by Kozak *et al.*¹⁰⁷

Entry	ArMgBr	Alkyl Halide	Product	%Yield
1	<i>p</i> -Tolyl			47
2	<i>p</i> -Tolyl			64
3	<i>o</i> -Tolyl			86
4	<i>o</i> -Tolyl			61
5	<i>o</i> -Tolyl			76
6	<i>p</i> -Anisyl			22 91 ^a
7	<i>p</i> -Anisyl			35
8	<i>p</i> -FPh			67

^a Microwave heating, 100 °C, 10 minutes.

when Fe(acac)₃/TMEDA was employed by Cahiez and co-workers, only traces of the cross-coupled product were observed when phenylmagnesium bromide was reacted with 2-chlorobutane.³¹ When 2-chlorobutane was reacted with various Grignard reagents in the presence of [Fe(O₂N)^{BuMenPr}(μ-Cl)]₂, modest yields were reported at room temperature (Table 1.3, entries 2 and 7).¹⁰⁷

Primary alkyl halides were also screened by Kozak and co-workers. When 1-iodopropane was reacted with *o*-tolylmagnesium bromide (Table 1.3, entry 5) and *p*-

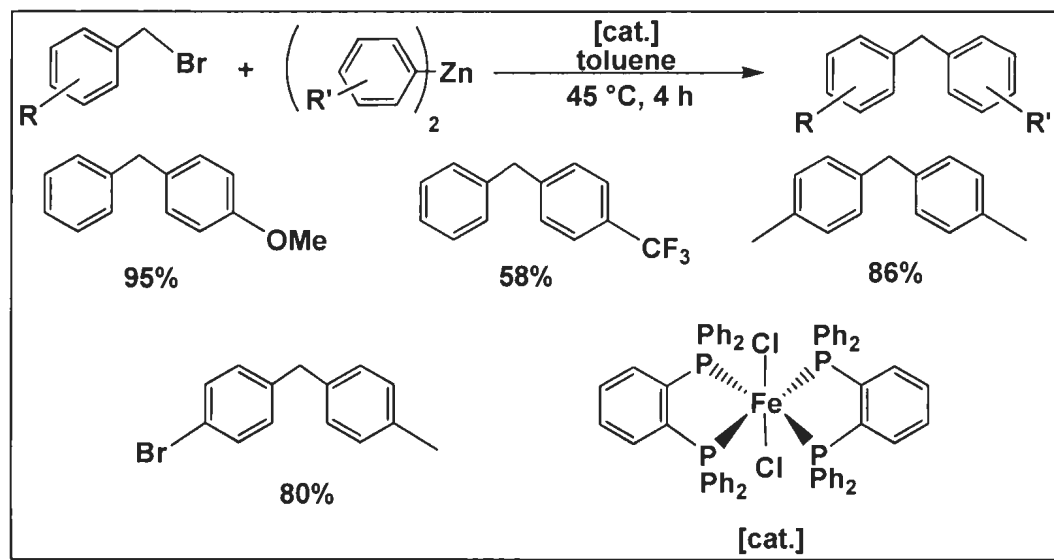
fluorophenylmagnesium bromide (**Table 1.3**, entry 8), 76% and 67% yields were reported respectively.¹⁰⁷ During a competitive arylation reaction of 1-bromo-3-chloropropane, selective attack at the bromide site resulted in a moderate yield of 1-(3-chloropropyl)-2-methylbenzene (**Table 1.3**, entry 4).¹⁰⁷

1.4 Iron-Catalyzed Cross-Coupling of Benzyl Halides with Aryl Grignards

The catalytic formation of diarylmethane motifs is a very important synthetic tool, with applications in pharmaceuticals and biologically active compounds.¹⁰⁹⁻¹¹⁰ Traditionally, the formation of diarylmethane motifs by the iron-catalyzed coupling of benzyl halides with aryl Grignard reagents has been reported to be unsatisfactory, giving low yields and poor selectivity resulting in the formation of homo-coupled by-products. The copper-catalyzed coupling of aryl Grignard reagents has been found to be more effective, but many systems are limited by low functional group tolerance.¹¹¹ The use of arylboron-based compounds has also been employed as an effective method.¹¹² However, these particular systems require expensive and toxic palladium-based catalysts which are impractical for large scale application. Due to recent environmental and economic concerns, the development of an iron-based catalyst which can effectively generate diarylmethane motifs is of particular interest.

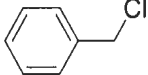
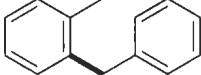
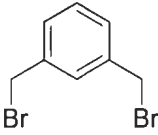
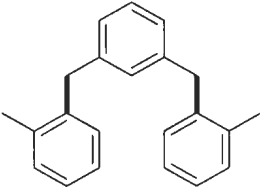
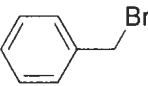
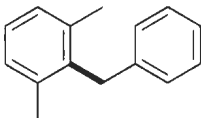
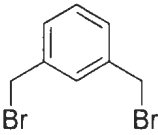
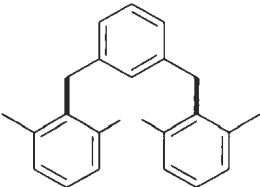
Recently, Bedford and co-workers investigated the construction of diarylmethane motifs using iron-based catalysts. Initial attempts focused on the iron-catalyzed cross-coupling of benzyl halides with aryl Grignard reagents. When iron-phosphine catalysts

containing either 1,2-bis(diphenylphosphino)benzene (dpbz) or 1,3-bis(diphenylphosphino)propane (dppp) were employed, low yields and poor selectivities with respect to homo-coupled by-products resulted. However, in the presence of softer aryl zinc nucleophiles, Bedford and co-workers reported that Fe(II)Cl₂bis(dp bz) was an active catalyst for the Negishi coupling of arylzinc reagents with benzyl halides (**Scheme 1.22**).¹¹³ Unfortunately, there are some economic disadvantages with this particular catalytic system. Firstly, the use of diarylzinc reagents requires an additional step in the reaction procedure (compared to using the Grignard reagent directly) since all the diarylzinc reagents employed are prepared from the corresponding Grignard reagents. Second, only one aryl group from Ar₂Zn is transferred during the course of the reaction. Therefore, it would be more practical on an economic basis to develop an iron-based catalytic system in which aryl Grignard reagents can be used directly.



Scheme 1.22: Negishi-type arylations reported by Bedford *et al.*¹¹³

Table 1.4: Iron-catalyzed cross-coupling of aryl Grignard reagents and benzyl halides.¹⁰⁷

Entry	ArMgBr	Alkyl Halide	Product	% Yield
1	<i>o</i> -Tolyl			>95
2	"			>95
3	2,6-Me ₂ Ph			78
4	"			19

Unlike the previous system reported by Bedford and co-workers, which requires the use of aryl zinc reagents, in 2010, Kozak and co-workers reported an effective iron-based catalytic system for the cross-coupling of benzyl halides with aryl Grignard reagents.¹⁰⁷ When benzyl chloride was reacted with *o*-tolylmagnesium bromide in the presence of $[\text{Fe}[\text{O}_2\text{N}]^{\text{BuMenPr}}(\mu\text{-Cl})_2]$ (**Figure 1.14**), an excellent yield of the cross-coupled product was obtained (**Table 1.4**, entry 1).¹⁰⁷ Previous reports resulted in only 68% conversion when benzyl bromide was used.¹⁰⁵ Surprisingly, the cross-coupling reaction between benzyl bromide and sterically crowded 2,6-dimethylphenylmagnesium bromide resulted in a 78% yield of the desired cross-coupled product (**Table 1.4**, entry 3).¹⁰⁷ The double arylation of 1,3-bis(bromomethyl)benzene with *o*-tolylmagnesium bromide was also achieved in high yield (**Table 1.4**, entry 2), requiring 2.0 equivalents of Grignard reagent per halide functional group. However, the double arylation of 1,3-

bis(bromomethyl)benzene with 2,6-dimethylphenylmagnesium bromide resulted in a poor yield of cross-coupled product (**Table 1.4**, entry 4).¹⁰⁷

Unfortunately, at this time, preliminary investigations (using $[\text{Fe}(\text{O}_2\text{N})^{\text{BuMe}^n\text{Pr}}(\mu\text{-Cl})_2]$ as the catalyst) only include a limited combination of benzyl halides and aryl Grignard reagents.¹⁰⁷ The primary goal of this Master's project is to prepare a series of iron(III) complexes supported by tridentate amine-bis(phenolate) ligands and investigate their ability to catalyze the cross-coupling of benzyl halides with aryl Grignard reagents. By studying the introduction of electron-donating and electron-withdrawing groups on both the benzylic substrate and the aryl Grignard reagent, a more thorough understanding of the iron-catalyzed cross-coupling reaction may be determined. In addition, an investigation to determine whether or not steric requirements play a significant role in the catalysis will also be considered.

1.5 References

- ¹ C. Bolm, J. Legros, J. L. Paih and L. Zani, *Chem. Rev.*, **2004**, 104, 6217.
- ² *Metal-Catalyzed Cross-Coupling Reactions*, 2nd ed., A. de Meijere and F. Diederich, Eds, Wiley-VCH, Weinheim, 2004.
- ³ K. Tamao, N. Miyaura, *Top. Curr. Chem.*, **2002**, 219, 1.
- ⁴ R. Franzén, *Can. J. Chem.*, **2000**, 78, 957.
- ⁵ R. Chinchilla, C. Najera, *Chem. Rev.*, **2007**, 107, 874.
- ⁶ V. Bohm, W. Herrmann, *Eur. J. Org. Chem.*, **2000**, 3679.
- ⁷ S. Berger, P. Pale, U. Létinois-Halbes, *J. Org. Chem.*, **2005**, 70, 9185.
- ⁸ S. Kotha, K. Lahiri, D. Kashinath, *Tetrahedron Lett.*, **2002**, 58, 9633.
- ⁹ N. Miyaura, A. Suzuki, *Chem. Rev.*, **1995**, 95, 2457.
- ¹⁰ J. F. Fauvarque, A. Jutand, *J. Org. Chem.*, **1977**, C-17.
- ¹¹ A. Gille, J.K. Stille, *J. Am. Chem. Soc.*, **1980**, 102, 4933.
- ¹² C. Amatore, A. Jutand, *J. Org. Chem.*, **1999**, 64, 254.
- ¹³ A. Pelter, K. Smith, H. C. Brown, *Borane Reagents.*, AP, New York, **1988**.
- ¹⁴ B. H. Ridgway, K.A. Woerpel, *J. Org. Chem.*, **1998**, 63, 458.
- ¹⁵ R. F. Heck, *J. Am. Chem. Soc.*, **1968**, 90, 5518.
- ¹⁶ I. P. Beletskaya, A. V. Cheprakov, *Chem. Rev.*, **2000**, 100, 3009.
- ¹⁷ M. Ioele, G. Ortaggi, M. Scarsella, G. Sleiter, *Polyhedron*, **1991**, 10, 2475.
- ¹⁸ V. Grushin, H. Alper, *Organometallics*, **1993**, 12, 1890.
- ¹⁹ V. Grushin, *J. Am. Chem. Soc.*, **1999**, 121, 5831.

- ²⁰ P. Roffia, G. Gregorio, F. Conti, G. Pregaglia, *J. Mol. Catal.*, **1977**, 2, 191.
- ²¹ B. D. Sherry, A. Furstner, *Acc. Chem. Res.*, **2008**, 41, 1500.
- ²² A. C. Frisch, M. Beller, *Angew. Chem. Int. Ed.*, **2005**, 44, 674.
- ²³ *Iron Catalysis in Organic Chemistry*, B. Plietker, Eds, Wiley-VCH, Weinheim, 2008.
- ²⁴ M. Tamura, J. K. Kochi, *Synthesis*, **1971**, 6, 303.
- ²⁵ M. Nakamura, K. Matsuo, S. Ito, B. Nakamura, *J. Am. Chem. Soc.*, **2004**, 126, 3686.
- ²⁶ R. Martin, A. Furstner, *Angew. Chem. Int. Ed.*, **2004**, 43, 3955.
- ²⁷ A. C. Frisch, N. Shaikh, A. Zapf, M. Beller, *Angew. Chem. Int. Ed.*, **2002**, 41, 4056.
- ²⁸ M. R. Netherton, G. C. Fu, *Adv. Synth. Catal.*, **2004**, 346, 1525.
- ²⁹ G. Cahiez, V. Habiak, C. Duplais, A. Moyeux, *Angew. Chem. Int. Ed.*, **2007**, 46, 4364.
- ³⁰ T. Nagano, T. Hayashi, *Org. Lett.*, **2004**, 6, 1297.
- ³¹ G. Cahiez, C. Duplais, A. Moyeux, *Org. Lett.*, **2007**, 9, 3253.
- ³² M. Carril, A. Correa, C. Bolm, *Angew. Chem. Int. Ed.*, **2008**, 47, 4862.
- ³³ C. Li, Z. Xie, Y. Zhang, J. Chen, Z. Yang, *J. Org. Chem.*, **2003**, 68, 8500.
- ³⁴ K. Hiroya, S. Matsumoto, T. Sakamoto, *Org. Lett.*, **2004**, 6, 2953.
- ³⁵ K. Nicolaou, P. Bulger, D. Sarlah, *Angew. Chem. Int. Ed.*, **2005**, 44, 4442.
- ³⁶ K. Odlo, J. Klaveness, P. Rongved, T. Hansen, *Tetrahedron Lett.*, **2006**, 47, 1101.
- ³⁷ M. Taillefer, N. Xia, A. Ouail, *Angew. Chem. Int. Ed.*, **2007**, 46, 8862.
- ³⁸ C. Rao Volla, P. Vogel, *Tetrahedron Lett.*, **2008**, 49, 5961.
- ³⁹ J. Mao, G. Xie, M. Wu, J. Guo, S. Ji, *Adv. Synth. Catal.*, **2008**, 350, 2477.
- ⁴⁰ D. Bézier, C. Darcel, *Adv. Synth. Catal.*, **2009**, 351, 1732.
- ⁴¹ T. Hatakeyama, T. Hashimoto, Y. Kondo, Y. Fujiwara, H. Seike, H. Takaya, Y. Tamada, T. Ono, M. Nakamura, *J. Am. Chem. Soc.*, **2010**, 132, 10674.

- ⁴² E. Negishi, Z. Huang, G. Wang, S. Mohan, C. Wang, H. Hattori, *Acc. Chem. Res.*, **2008**, 41, 1474.
- ⁴³ Y. Guo, D. Young, T. Hor, *Tetrahedron Lett.*, **2008**, 49, 5620.
- ⁴⁴ D. Bézier, C. Dracel, *Adv. Synth. Catal.*, **2010**, 352, 1081.
- ⁴⁵ T. Kylvälä, A. Valkonen, K. Rissanen, Y. Xu, R. Franzén, *Tetrahedron Lett.*, **2008**, 49, 6679.
- ⁴⁶ R. Bedford, M. Nakamura, N. Gower, M. Haddow, M. Hall, M. Huwe, T. Hashimoto, R. Okopie, *Tetrahedron Lett.*, **2009**, 50, 6110.
- ⁴⁷ T. Kylvälä, A. Valkonen, K. Rissanen, Y. Xu, R. Franzén, *Tetrahedron Lett.*, **2009**, 50, 5692.
- ⁴⁸ K. Ziegler, H. Gellert, E. Holzkamp, G. Wilke, *Brennst.-Chem.*, **1954**, 35, 321.
- ⁴⁹ C. Bolm, S. Buchwald, *Angew. Chem. Int. Ed.*, **2009**, 48, 2.
- ⁵⁰ *Isotopic Analysis, Fundamentals and Applications using ICP-MS*, 1st ed, F. Vanhaecke, P. Degryse, Eds, Wiley-VCH, Weinheim, 2012.
- ⁵¹ G. Fu, *Acc. Chem. Res.*, **2008**, 41, 1555.
- ⁵² A. Trzeciak, J. Ziolkowski, *Coord. Chem. Rev.*, **2005**, 249, 2308.
- ⁵³ K. Inamoto, J. Kuroda, T. Danjo, T. Sakamoto, *Synlett*, **2005**, 1624.
- ⁵⁴ S. Ma, H. Wang, K. Gao, F. Zhao, *J. Mol. Catal A: Chem.*, **2006**, 248, 17.
- ⁵⁵ R. Loska, C. Volla, P. Vogel, *Adv. Synth. Catal.*, **2008**, 350, 2859.
- ⁵⁶ K. Tamao, Y. Kiso, K. Sumitani, M. Kumada, *M. J. Am. Chem. Soc.*, **1972**, 94, 9268.
- ⁵⁷ M. Yamamura, I. Moritani, S. Murahashi, *J. Org. Chem.*, **1975**, 91, C39.
- ⁵⁸ R. Martin, A. Fürstner, *Angew. Chem. Int. Ed.*, **2004**, 43, 3955.
- ⁵⁹ M. Nakamura, K. Matsuo, S. Ito, E. Nakamura, *J. Am. Chem. Soc.*, **2004**, 126, 3686.

- ⁶⁰ W. Percival, R. Wagner, N. Cook, *J. Am. Chem. Soc.*, **1953**, 75, 3731.
- ⁶¹ A. Fürstner, B. Scheiper, M. Bonnekessel, A. Krause, *J. Org. Chem.*, **2004**, 69, 3943.
- ⁶² C. Duplais, F. Bures, I. Sapountzis, T. Korn, G. Cahiez, P. Knochel, *Angew. Chem. Int. Ed.*, **2004**, 43, 2968.
- ⁶³ R. Dieter, *Tetrahedron Lett.*, **1999**, 55, 4177.
- ⁶⁴ G. Cahiez, H. Avedissian, *Synthesis*, **1998**, 1199.
- ⁶⁵ A. Fürstner, A. Leitner, M. Méndez, H. Krause, *J. Am. Chem. Soc.*, **2002**, 124, 13856.
- ⁶⁶ J. Hassan, M. Sevignon, C. Gozzi, E. Schulz, M. Lemaire, *Chem. Rev.*, **2002**, 102, 1359.
- ⁶⁷ T. Nagano, T. Hayashi, *Org. Lett.*, **2005**, 7, 491.
- ⁶⁸ G. Cahiez, C. Chaboche, F. Mahuteau-Betzer, M. Ahr, *Org. Lett.*, **2005**, 7, 1943.
- ⁶⁹ G. Cahiez, A. Moyeux, J. Buendia, C. Duplais, *J. Am. Chem. Soc.*, **2007**, 129, 13788.
- ⁷⁰ M. Nakamura, K. Matsuo, S. Ito, E. Nakamura, *J. Am. Chem. Soc.*, **2004**, 126, 3686.
- ⁷¹ R. B. Bedford, D. Bruce, R. Frost, M. Hird, *Chem. Commun.*, **2005**, 4161.
- ⁷² R. B. Bedford, D. Bruce, R. Frost, M. Hird, J. Goodby, *Chem. Commun.*, **2005**, 2822.
- ⁷³ J. Kleimark, A. Hedström, P. Larsson, C. Johansson, P. Norrby, *ChemCatChem*, **2009**, 152.
- ⁷⁴ R. B. Bedford, M. Betham, D. Bruce, A. Danopoulos, R. Frost, M. Hird, *J. Org. Chem.*, **2006**, 71, 1104.
- ⁷⁵ P. Norrby, J. Kleimark, A. Hedstrom, P. Larsson, C. Johansson, *ChemCatChem*, **2009**, 1, 152.
- ⁷⁶ L. Gade, *Chem. Commun.*, **2000**, 173.
- ⁷⁷ L. Gade, *Acc. Chem. Res.*, **2002**, 35, 575.

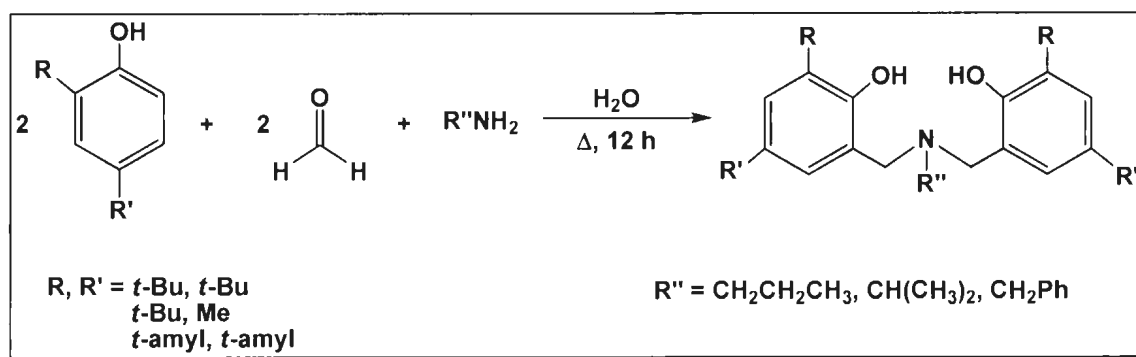
- ⁷⁸ V. Gibson, S. Spitzmesser, *Chem. Rev.*, **2003**, 103, 283.
- ⁷⁹ H. Kawaguchi, T. Matsuo, *J. Org. Chem.*, **2004**, 69, 4228.
- ⁸⁰ R. Kempe, *Angew. Chem. Int. Ed.*, **2000**, 39, 469.
- ⁸¹ W. Piers, D. Emslie, *Coord. Chem. Rev.*, **2002**, 233, 131.
- ⁸² A. Yeori, I. Goldberg, M. Kol, *Macromolecules*, **2007**, 40, 8521.
- ⁸³ A. Yeori, I. Goldberg, M. Shuster, M. Kol, *J. Am. Chem. Soc.* **2006**, 128, 13062.
- ⁸⁴ S. Gendler, S. Segal, I. Goldberg, M. Kol, Z. Goldschmidt, *Inorg. Chem.*, **2006**, 45, 4783.
- ⁸⁵ S. Segal, I. Goldberg, M. Kol, *Organometallics*, **2005**, 24, 200.
- ⁸⁶ S. Groysman, E. Tshuva, I. Goldberg, M. Kol, Z. Goldschmidt, M. Shuster, *Organometallics*, **2004**, 23, 5291.
- ⁸⁷ S. Groysman, I. Goldberg, M. Kol, E. Genizi, Z. Goldschmidt, *Inorg. Chim. Acta.*, **2003**, 345, 137.
- ⁸⁸ C. Lorber, F. Wolff, R. Choukroun, L. Vendier, *Eur. J. Org. Chem.*, **2005**, 8250.
- ⁸⁹ A. Chmura, M. Davidson, M. Jones, M. Lunn, M. Mahon, A. Johnson, P. Khunkamchoo, S. Roberts, S. Wong, *Macromolecules*, **2006**, 39, 7250.
- ⁹⁰ E. Tshuva, I. Goldberg, M. Kol, *J. Am. Chem. Soc.*, **2000**, 122, 10706.
- ⁹¹ Y. Sarazin, R. Howard, D. Hughes, S. Humphrey, M. Bochmann, *Dalton Trans.*, **2006**, 340.
- ⁹² U. K. Das, J. Bobak, C. Fowler, S. E. Hann, C. F. Petten, L. N. Dawe, A. Decken, F. M. Kerton, C. M. Kozak, *Dalton Trans.*, **2010**, 39, 5462.
- ⁹³ T. Nagataki, S. Itoh, *Chem. Lett.*, **2007**, 36, 748

- ⁹⁴ L. Rodriguez, E. Labisbal, A. Sousa-Pedrares, J. A. Garcia-Vazquez, J. Romero, M. L. Duran, J. Real, A. Sousa, *Inorg. Chem.*, **2006**, 45, 7903.
- ⁹⁵ A. Philibert, F. Thomas, C. Philouze, S. Hamman, E. Saint-Aman, J. Pierre, *Chem. Eur. J.*, **2003**, 9, 3803.
- ⁹⁶ O. Rotthaus, F. Thomas, O. Jarjayes, C. Philouze, E. Saint-Aman, J. Pierre, *Chem. Eur. J.*, **2006**, 12, 6953.
- ⁹⁷ J. Strautmann, S. George, E. Bothe, E. Bill, T. Weyhermüller, A. Stämmler, H. Bogge, T. Glaser, *Inorg. Chem.*, **2006**, 12, 6953.
- ⁹⁸ T. Weyhermüller, T. Paine, E. Bothe, E. Bill, P. Chaudhuri, *Inorg. Chim. Acta.*, **2002**, 337, 344.
- ⁹⁹ E. Safaei, T. Weyhermüller, E. Bothe, K. Wieghardt, P. Chaudhuri, *Eur. J. Org. Chem.*, **2007**, 2334.
- ¹⁰⁰ M. Velusamy, M. Palaniandavar, R. Gopalan, G. Kulkarni, *Inorg. Chem.*, **2003**, 42, 8283.
- ¹⁰¹ R. Viswanathan, M. Palaniandavar, T. Balasubramanian, T. Muthiah, *Inorg. Chem.*, **1998**, 37, 2943.
- ¹⁰² P. Mialane, E. Anxolabéhère-Mallart, G. Blondin, A. Nivorojkine, J. Guilhem, L. Tchertanova, M. Cesario, N. Ravi, E. Bominaar, J. Girerd, E. Munck, *Inorg. Chim. Acta.*, **1997**, 263, 367.
- ¹⁰³ T. Kurahashi, K. Oda, M. Sugimoto, T. Ogura, H. Fujii, *Inorg. Chem.*, **2006**, 45, 7709.
- ¹⁰⁴ M. Velusamy, R. Mayilmurugan, M. Palaniandavar, *Inorg. Chem.*, **2004**, 43, 6284.
- ¹⁰⁵ R. R. Chowdhury, A. K. Crane, C. Fowler, P. Kwong, C. M. Kozak, *Chem. Commun.*, **2008**, 94.

- ¹⁰⁶ K. Hassan, L. N. Dawe, C. M. Kozak, *Eur. J. Org. Chem.*, **2011**, 4610.
- ¹⁰⁷ X. Qian, L. N. Dawe, C. M. Kozak, *Dalton Trans.*, **2011**, 40, 933.
- ¹⁰⁸ R. B. Bedford, M. Betham, D. W. Bruce, S. A. Davis, R. M. Frost, M. Hird, *Chem. Commun.*, **2006**, 1398.
- ¹⁰⁹ K. McPhail, D. Rivett, D. Lack, M. Davies-Coleman, *Tetrahedron*, **2000**, 56, 9391.
- ¹¹⁰ Y. Long, X. Jiang, R. Dayam, T. Sacher, R. Shoemaker, S. Sei, N. Neamati, *J. Med. Chem.*, **2004**, 47, 2561.
- ¹¹¹ W. Dohle, D. Lindsay, P. Knochel, *Org. Lett.*, **2001**, 3, 2871.
- ¹¹² M. Burns, I. Fairlamb, A. Kapdi, P. Sehnal, R. Taylor, *Org. Lett.*, **2007**, 9, 5397.
- ¹¹³ R. B. Bedford, M. Huwe, M. C. Wilkinson, *Chem. Commun.*, **2009**, 600.

Chapter 2 – Synthesis and Characterization

2.1 Synthesis and Characterization of Tridentate Amine-bis(phenol) Ligands



Scheme 2.1: Synthesis of tridentate diamine-bis(phenol) pro-ligands via a Mannich condensation reaction.

The tridentate amine-bis(phenol) ligand precursors were readily synthesized by a modified Mannich condensation reaction, in which the required 2,4-disubstituted phenol, amine and formaldehyde were heated to reflux in water for 12 hours (**Scheme 2.1**).¹ The literature procedure used methanol as the solvent;^{2,3} however, higher yields and shorter reaction times were achieved when water is used as the reaction medium. In order to generate more reactive catalysts (compared to tetradentate counterparts), while still maintaining the robust nature of the catalyst precursor, tridentate amine-bis(phenol) ligands were synthesized with relatively bulky substituents on the phenol rings.

Six different amine-bis(phenol) ligand precursors were synthesized (**Figure 2.1**) and were characterized via numerous analytical and spectroscopic techniques. As a general

representation, the characterization of $\text{H}_2[\text{ONO}]^{\text{BuBuPr}} (\text{H}_2\text{L3})$ will be discussed in detail below.

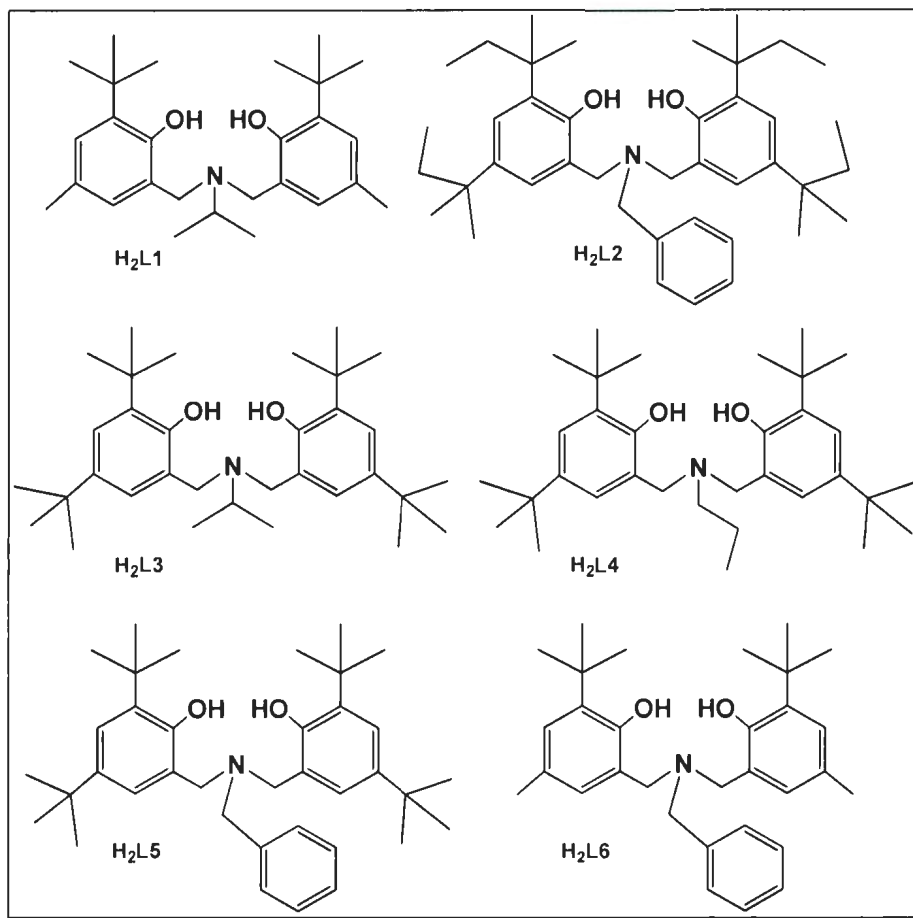


Figure 2.1: Library of tridentate amine-bis(phenol) ligands synthesized.

The ligands were characterized using both ^1H and ^{13}C NMR. A representative ^1H NMR spectrum of $\text{H}_2\text{L3}$ is shown in **Figure 2.2**. The ^1H NMR spectrum for $\text{H}_2\text{L3}$ (measured in CDCl_3) exhibited two singlets at 7.21 ppm and 6.92 ppm respectively. These singlets correspond to the aromatic hydrogen atoms of the benzene ring (**Figure 2.3**; H^{C} and H^{D}). The singlet located at 3.71 ppm arises from the ArCH^{E}_2 groups. This suggests that there is free rotation in solution resulting in equivalent proton environments.

The septet at 3.17 ppm is assigned to $\text{CH}^{\text{F}}(\text{CH}_3)_2$, which is split due to coupling to the neighboring methyl groups (H^{G}). The singlets at 1.39 ppm and 1.28 ppm, correspond to the H atoms (H^{A} and H^{B}) of the *t*-butyl groups on the benzene ring. As seen in **Figure 2.2**, a signal corresponding to the hydroxyl protons is broad and found at 8.15 ppm. Since CDCl_3 is an acidic solvent (contains a small quantity of DCl) the hydroxyl groups of the proligand undergo exchange and broaden. The ^1H NMR spectrum for $\text{H}_2[\text{ONO}]^{\text{BuBu/Pr}}$ ($\text{H}_2\text{L3}$) is summarized in **Table 2.1**.

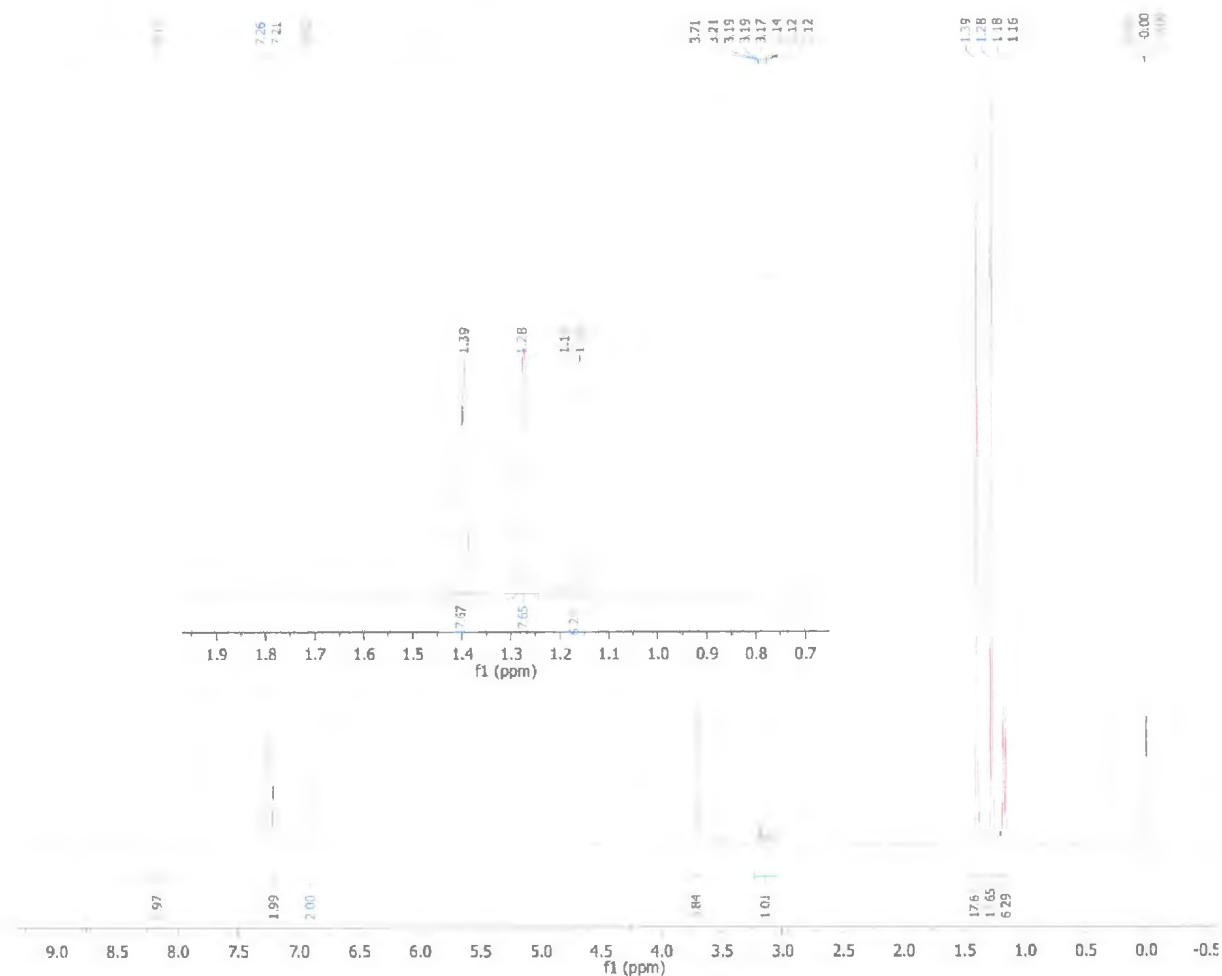


Figure 2.2: ^1H -NMR spectrum of $\text{H}_2[\text{O}_2\text{N}]^{\text{BuBu/Pr}}$ ($\text{H}_2\text{L3}$).

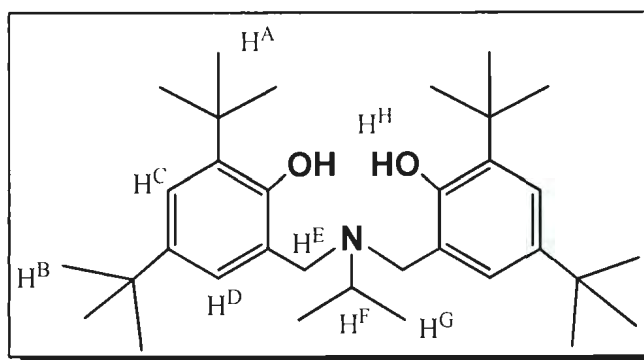


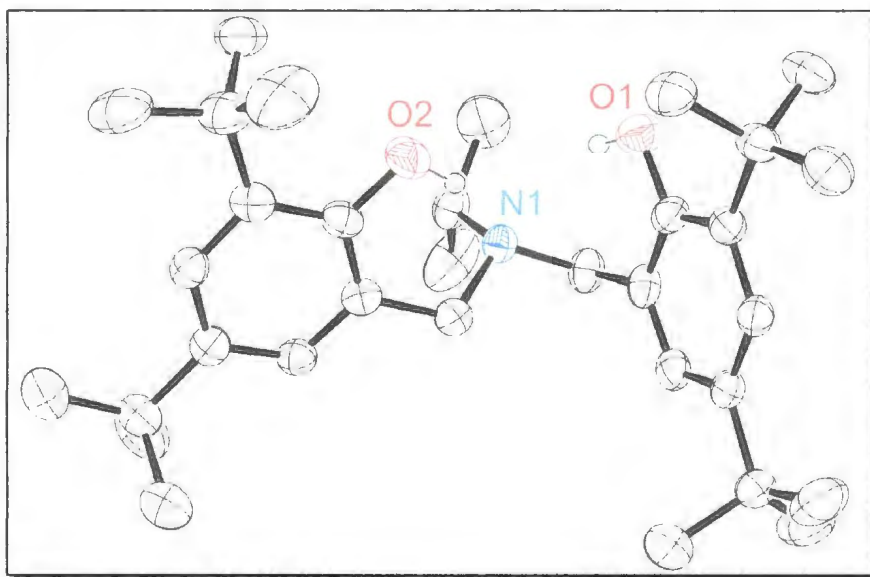
Figure 2.3: Different proton environments for $\text{H}_2[\text{ONO}]^{\text{BuBuPr}}$ ($\text{H}_2\text{L3}$).

Table 2.2: Assignment of resonances for the ^1H NMR spectrum of $\text{H}_2\text{L3}$.

Protons	No. of equiv. protons	Chemical Shift (δ)	Peak	Proton types	Coupling Constant
H^{A}	18	1.39	Singlet	$\text{C}(\text{CH}^{\text{A}}_3)_3$	
H^{B}	18	1.28	Singlet	$\text{C}(\text{CH}^{\text{B}}_3)_3$	
H^{C}	2	7.21	Singlet	Aromatic	
H^{D}	2	6.92	Singlet	Aromatic	
H^{E}	4	3.71	Singlet	ArCH^{E}_2	
H^{F}	1	3.17	Septet	$\text{CH}^{\text{F}}(\text{CH}_3)_2$	$^3J = 5 \text{ Hz}$
H^{G}	6	1.18	Doublet	$\text{CH}(\text{CH}^{\text{G}}_3)_2$	$^3J = 5 \text{ Hz}$
H^{H}	1	8.15	Singlet	ArOH^{H}	

Table 2.3: Crystallographic data and refinements for H₂L3.

Chemical formula	C ₃₃ H ₅₃ NO ₂	<i>V</i> / Å ³	3138.7(12)
Formula weight	496.76	<i>Z</i>	4
<i>T</i> /K	158	<i>D</i> /g cm ⁻³	1.049
Crystal color, Habit	Colorless, prism	μ(Mo-Kα)/cm ⁻¹	0.63
Crystal dimensions/mm	0.46 × 0.15 × 0.11	<i>F</i> (000)	1096
Crystal system	monoclinic	θ range for collection/°	-75.0 to 105.0
Space group	<i>P</i> 2 ₁ /c (#14)	Reflections collected	40638
<i>a</i> /Å	15.185(4)	Independent reflections	6483
<i>b</i> /Å	11.707(3)	<i>R</i> (int)	0.0369
<i>c</i> /Å	18.596(4)	<i>R</i> ₁ [<i>I</i> > 2σ(<i>I</i>)]	0.0830
α/°	90	<i>wR</i> ² [<i>I</i> > 2σ(<i>I</i>)]	0.2384
β/°	108.298(4)	GOF on <i>F</i> ²	1.157
γ/°	90		

**Figure 2.4:** Single crystal X-ray structure of H₂[O₂N]^{BuBuPr} (H₂L3). H-bonding exists between the hydrogen bond acceptor N(1), and the hydrogen donor located on O(2). H-atoms omitted for clarity (except on atoms O1 and O2). Ellipsoids at 50% probability.

Single crystals of $\text{H}_2\text{L3}$ suitable for X-ray diffraction were isolated from a saturated methanol solution (**Figure 2.4**). Detailed crystallographic data and refinements for $\text{H}_2\text{L3}$ are shown in **Table 2.2**, while selected bond lengths and angles are presented in the appendix at the end of this thesis. Interestingly, the molecular structure of $\text{H}_2\text{L3}$ exhibits intramolecular hydrogen-bonding (**Figure 2.4**) which has also been observed in other amine-bis(phenol) ligands.⁴

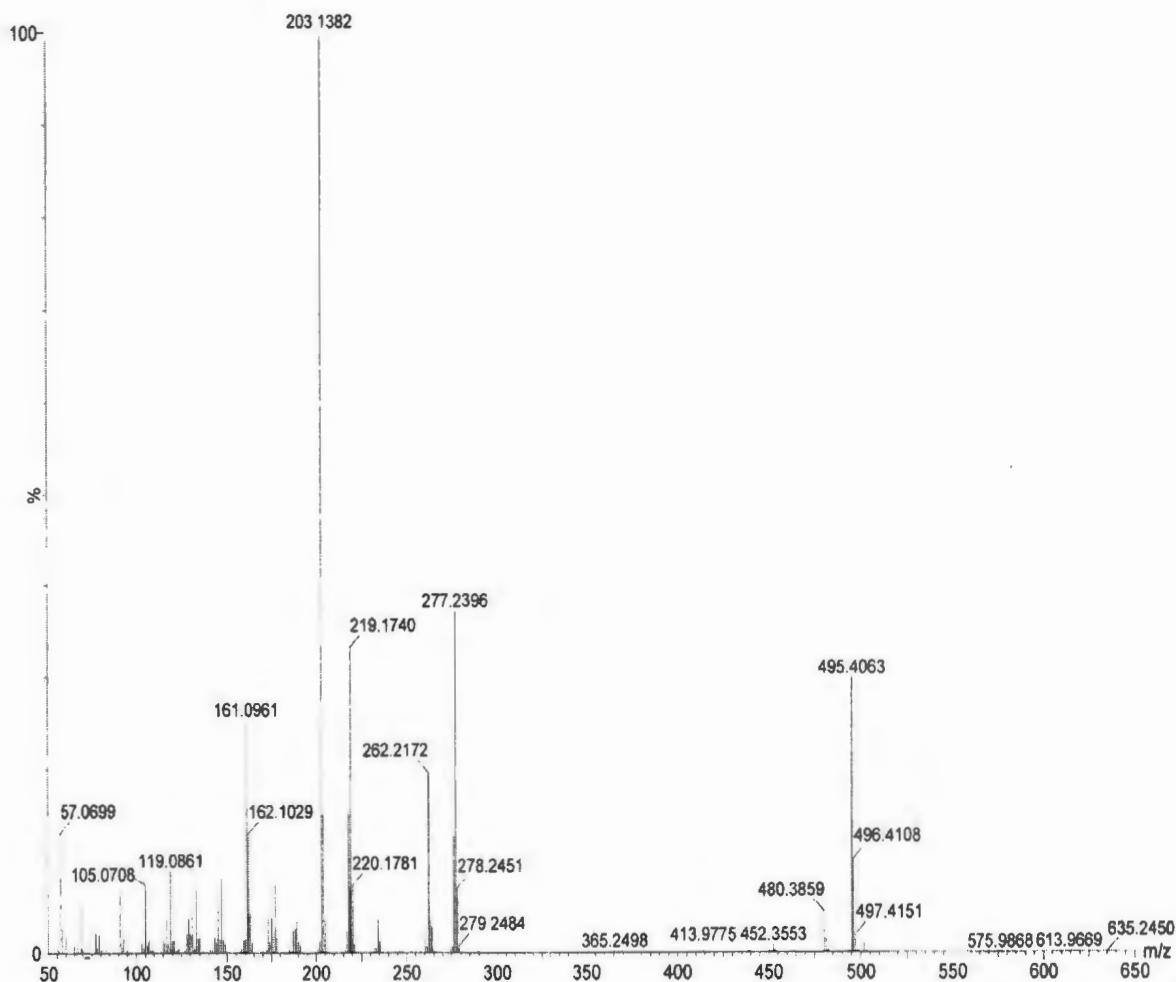


Figure 2.5: High-resolution mass spectrum of $\text{H}_2[\text{O}_2\text{N}]^{\text{BuBuPr}}(\text{H}_2\text{L3})$.

High-resolution mass spectrometry (HRMS) and infrared (IR) spectroscopy were also used to characterize H_2L3 . As seen in **Figure 2.5**, a molecular ion peak for $H_2[O_2N]^{BuBuPr}(H_2L3)$ is observed at 495.4063 m/z. Peaks found at lower masses can be attributed to fragment ions of the molecule. The IR spectrum of H_2L3 is presented in **Figure 2.6**. At approximately 3196 cm^{-1} , there exists a broad peak (absorption band) which indicates the presence of a hydroxyl group. The sharp peaks observed at 2958 cm^{-1} and 2865 cm^{-1} represent C-H stretching vibrations originating from aromatic and alkane functional groups, respectively. The absorption bands located in the fingerprint region ($1400\text{--}600\text{ cm}^{-1}$) also indicate the presence of both aromatic and alkane functional groups.

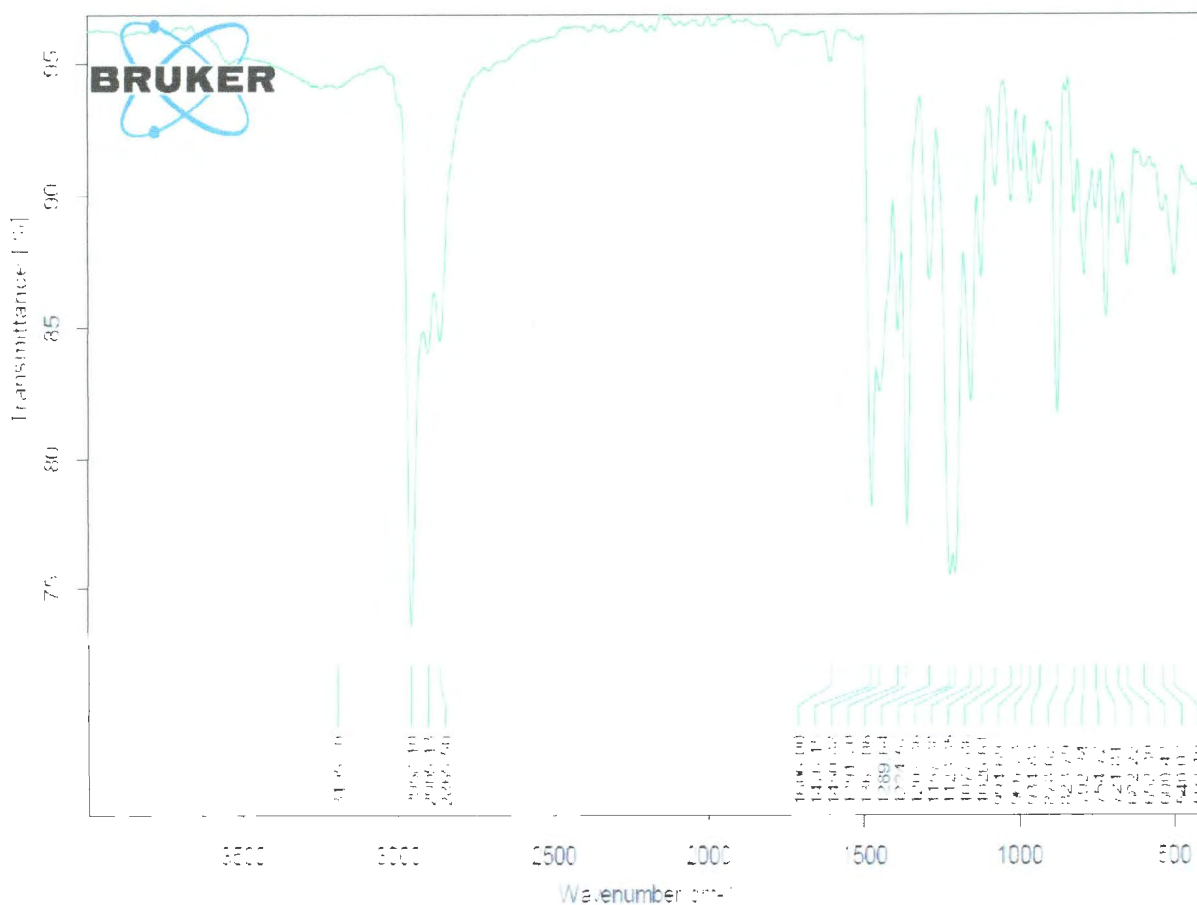


Figure 2.6: IR spectrum of $H_2[O_2N]^{BuBuPr}(H_2L3)$.

A melting point (MP) analysis was also performed on $\text{H}_2[\text{O}_2\text{N}]^{\text{BuBuPr}}$ (**H₂L3**), along with **H₂L1** and **H₂L2**. As seen in **Table 2.3**, the MP of **H₂L1** is more than 10 °C lower than the MP for the more sterically congested analogue (**H₂L3**) derived from 2,4-di-*tert*-butyl phenol. Surprisingly, sterically hindered $\text{H}_2[\text{O}_2\text{N}]^{\text{AmAmBn}}$ (**H₂L2**) was found to have the lowest MP of the three ligands investigated with a MP range of 127.4-128.9 °C. The higher MP of **H₂L3** may be attributed to the presence of intermolecular hydrogen-bonding. Of course, other intermolecular forces (such as dipole-dipole interactions) and existing packing constraints in the solid state are also likely to play a crucial role.

Table 2.3: Melting point (MP) data for **H₂L1**, **H₂L2**, **H₂L3**.

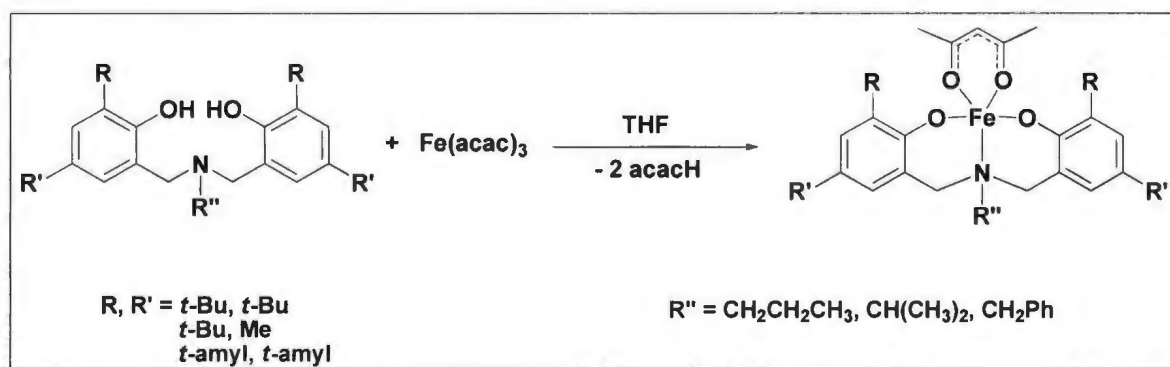
Ligand	MP range (°C)
H₂L1	130.2-131.7
H₂L2	127.4-128.9
H₂L3	142.5-143.3

2.2 Synthesis and Characterization of Iron(III) Complexes Supported by Tridentate Amine-bis(phenolate) Ligands

2.2.1 Synthesis of Amine-bis(phenolate) Iron(III)(acac) Complexes

The first series of Fe(III) amine-bis(phenolate) complexes ((acac)Fe[ONO]) was synthesized via a modified literature procedure reported by Chaudhuri and co-workers.⁵ The desired complexes were prepared by reacting the tridentate amine-bis(phenol) pro-ligand directly with $\text{Fe}(\text{acac})_3$ in THF in the presence of air (**Scheme 2.2**). The reaction of a protic ligand with $\text{Fe}(\text{acac})_3$ generates two equivalents of acetylacetone. After stirring

the reaction mixture for 2 hours, a clear dark brown solution was generated with some unreacted ligand generally present. Once the ligand was removed via suction filtration, the resulting dark brown filtrate was concentrated down to dryness via rotavap to give a dark waxy purple material. Since acetylacetone is a liquid at room temperature and has a boiling point of 140 °C, most of the byproduct should evaporate during this process. After washing the purple material with a minimal amount of heptane, a dark red crystalline solid was isolated via gravity filtration along with a dark brown filtrate. A sample of the red solid was dissolved in minimal hot methanol and was placed in the freezer to help induce crystal growth. Crystals were obtained, but X-ray diffraction analysis of the sample resulted in a single crystal structure of the starting material, Fe(acac)₃. The dark brown filtrate was also placed in the freezer to help induce crystal growth. After a few days in the freezer, dark brown crystals were evident and were also analyzed via X-ray crystallography, which confirmed the presence of the amine-bis(phenol) starting material. The unreacted ligand was separated from the brown solution via suction filtration, and the brown solution was concentrated down to dryness overnight on the Schlenk line to give a dark brown oily material.



Scheme 2.2: Synthesis of (acac)Fe[ONO] complexes.

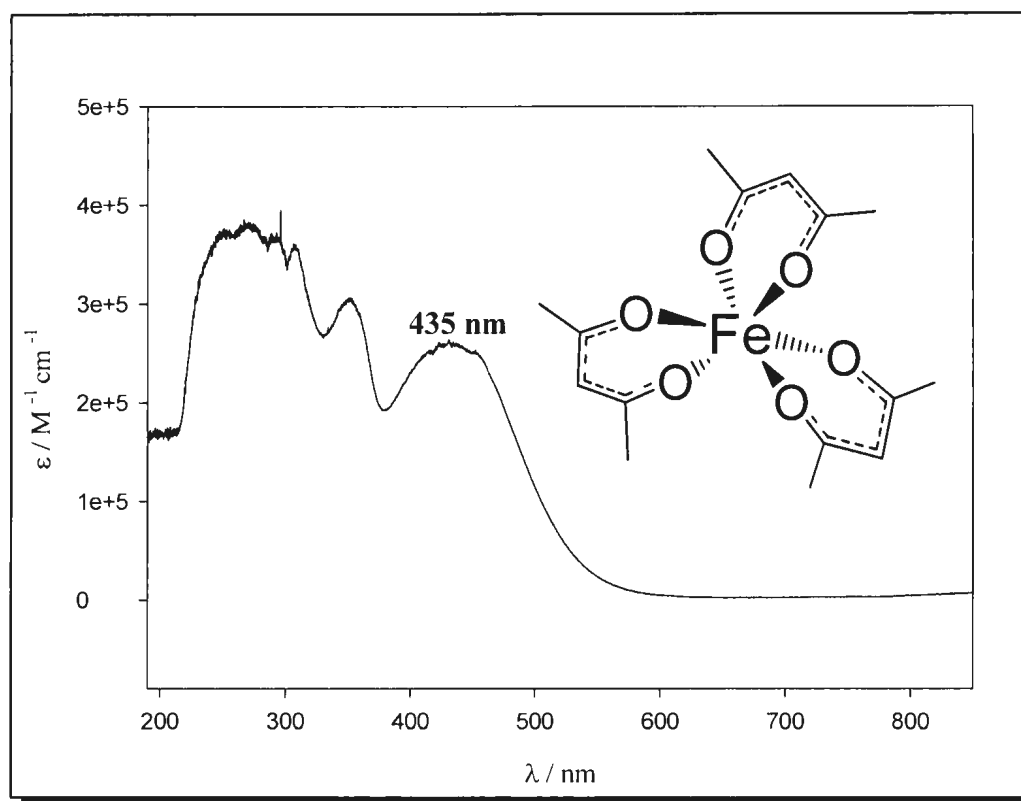


Figure 2.7: UV-vis spectrum for $\text{Fe}(\text{acac})_3$ in methanol.

Since both $\text{Fe}(\text{acac})_3$ and $(\text{acac})\text{Fe}[\text{ONO}]$ exhibit different coordination environments, both compounds were analyzed via UV-vis spectroscopy. An electronic absorption spectrum of $\text{Fe}(\text{acac})_3$ in methanol shows multiple intense bands in the UV and visible regions (**Figure 2.7**). The absorption maxima observed in the UV region (below 300 nm) are attributed to $\pi \rightarrow \pi^*$ transitions originating from the acetylacetonate units. Two intense absorptions are observed between 300-500 nm, and are assigned as ligand-to-metal ($\text{L} \rightarrow \text{M}$) charge transfer transitions. When compared to the UV-vis spectrum of the potential product $(\text{acac})\text{Fe}[\text{ONO}]^{\text{BuBuPr}}$ (**Figure 2.8**), some noticeable differences are evident. For instance, the LMCT band at approximately 435 nm in the spectrum of $\text{Fe}(\text{acac})_3$ has shifted to approximately 455 nm in the spectrum of the

potential product which may indicate the presence of a different coordination environment about the iron center. In addition, in the spectrum representing the potential product, the LMCT band at approximately 455 nm is only one-third the intensity of the peak at 435 nm in the spectrum of $\text{Fe}(\text{acac})_3$. If this ratio represents the probability of a LMCT band occurring, then the ratio of intensity may also be 3:1 which agrees with the results obtained (since the ratio of acac ligand in the starting material and product is 3:1 respectively).

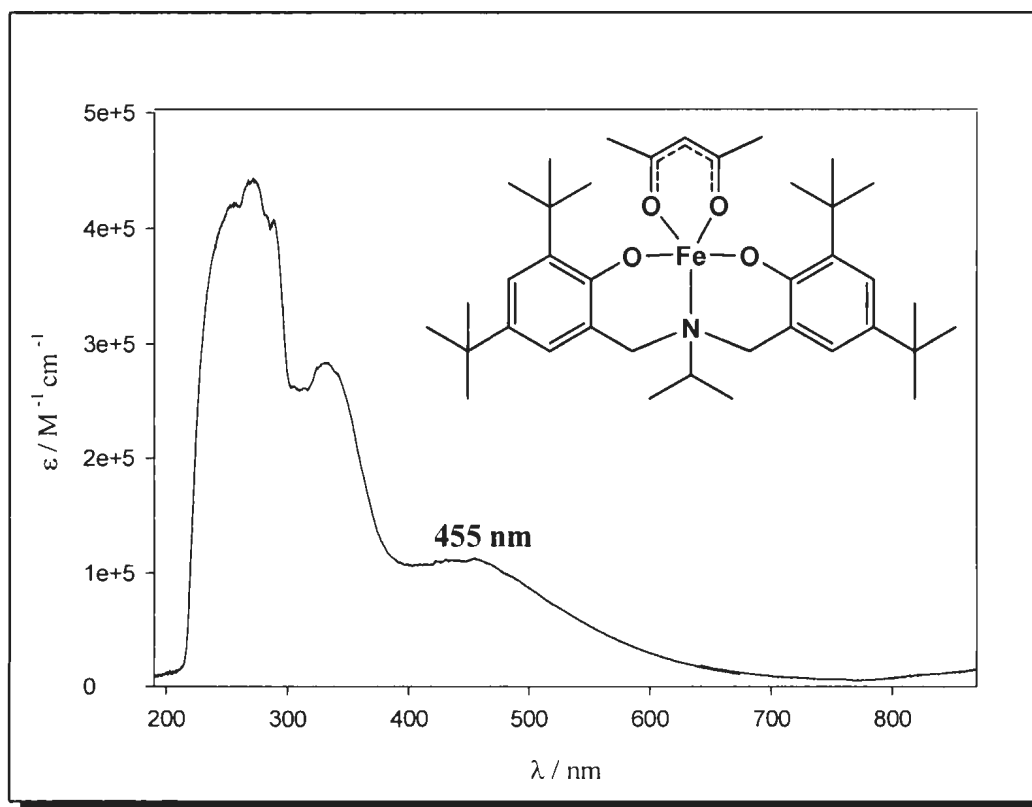


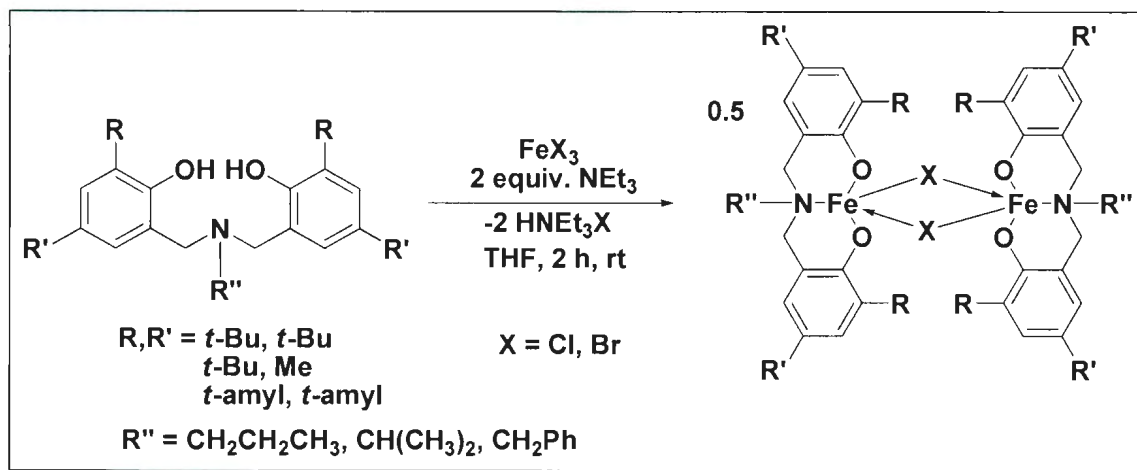
Figure 2.8: UV-vis spectrum for $(\text{acac})\text{Fe}[\text{ONO}]^{\text{BuBuPr}}$ in methanol.

In theory, the reaction (**Scheme 2.2**) is satisfied both electronically (Fe can exist as a five coordinate species) and thermodynamically (entropy increases since there is an increase in the number of molecules formed upon going from reactants to products). However, isolating the desired trigonal bipyramidal amine-bis(phenolate) Fe(acac) compound via the discussed method was unsuccessful to-date (even with the use of a base). Since Fe(acac)₃ and the ligand were much less soluble in the reaction medium than the desired product, the reaction may not have gone to completion causing the starting materials to precipitate out of the THF solution. This might explain why large quantities of both starting materials were removed during the purification procedure. If the desired complexes possess a low melting point, they may exist as oily materials. This might explain why the final product was isolated as a dark brown oil for each reaction attempted. Further investigations need to be performed in order to determine whether or not trigonal bipyramidal amine-bis(phenolate)Fe(acac) complexes can be successfully synthesized by the chemical reaction shown in **Scheme 2.2**.

2.2.2 Synthesis of Amine-bis(phenolate) Iron(III) Halide and Iron(III) Hydroxy Complexes

Following a general procedure reported by Kozak and co-workers,⁶ a second series of iron(III) complexes was synthesized (**Scheme 2.3**). The Fe(III) complexes were generated by reacting a diamine-bis(phenol) proligand directly with FeCl₃ in the presence of two equivalents of NEt₃ in THF via standard Schlenk techniques. The reaction of the protic ligand with FeCl₃ generates two equivalents of hydrogen chloride as a by-product; therefore two equivalents of NEt₃ are required to neutralize the acid (producing two

equivalents of NEt_3HCl). After stirring the reaction mixture for 2 hours under an inert atmosphere of nitrogen, a dark purple solution was generated with some light brown solid throughout. Once the brown solid was removed via filtration, the THF was removed via vacuum to yield a dark purple powder. The crude powder was then brought into a glove box where several purification steps were performed. Since the by-product (NEt_3HCl) was expected to be insoluble in non-polar toluene, washings with minimal toluene were performed so the by-product could be easily separated via suction filtration. This process was often performed many times in order to enhance purification. According to previous work in the Kozak group, the complexes exist as halide-bridged dimers in the solid state giving distorted trigonal bipyramidal iron(III) ions.⁶ However, recent results suggest that other Fe(III) complexes can be generated depending on the purification procedures employed and the steric requirements of the amine-bis(phenolate) backbone.



Scheme 2.3: The intended synthesis of halide-bridged dimers following a literature procedure reported by Kozak *et al.*⁶

When FeCl_3 reacted with $\text{H}_2[\text{ONO}]^{\text{BuMeiPr}}(\text{H}_2\text{L1})$ (as described in **Scheme 2.3**), an unexpected result was obtained when a sample of the dark purple crystal (recrystallized from toluene) was analyzed via X-ray crystallography. Instead of generating a chloride-bridged dimer as originally predicted, a trigonal bipyramidal iron(III) “ate” complex was isolated with a triethylammonium cation (**Figure 2.9, C1** ($[\text{NEt}_3\text{H}]^+[\text{FeCl}_2\text{L1}]^-$)). Characterization of **C1** will be discussed in detail in the next section. Unfortunately, this specific complex will not be practical as a catalyst for C-C cross coupling because the triethylammonium cation can act as a source of H^+ and react with the Grignard reagent. Nonetheless, this specific reaction does provide some beneficial information. Mainly, that purification could be problematic during the synthesis of these complexes and that a efficient method of purification needs to be developed.

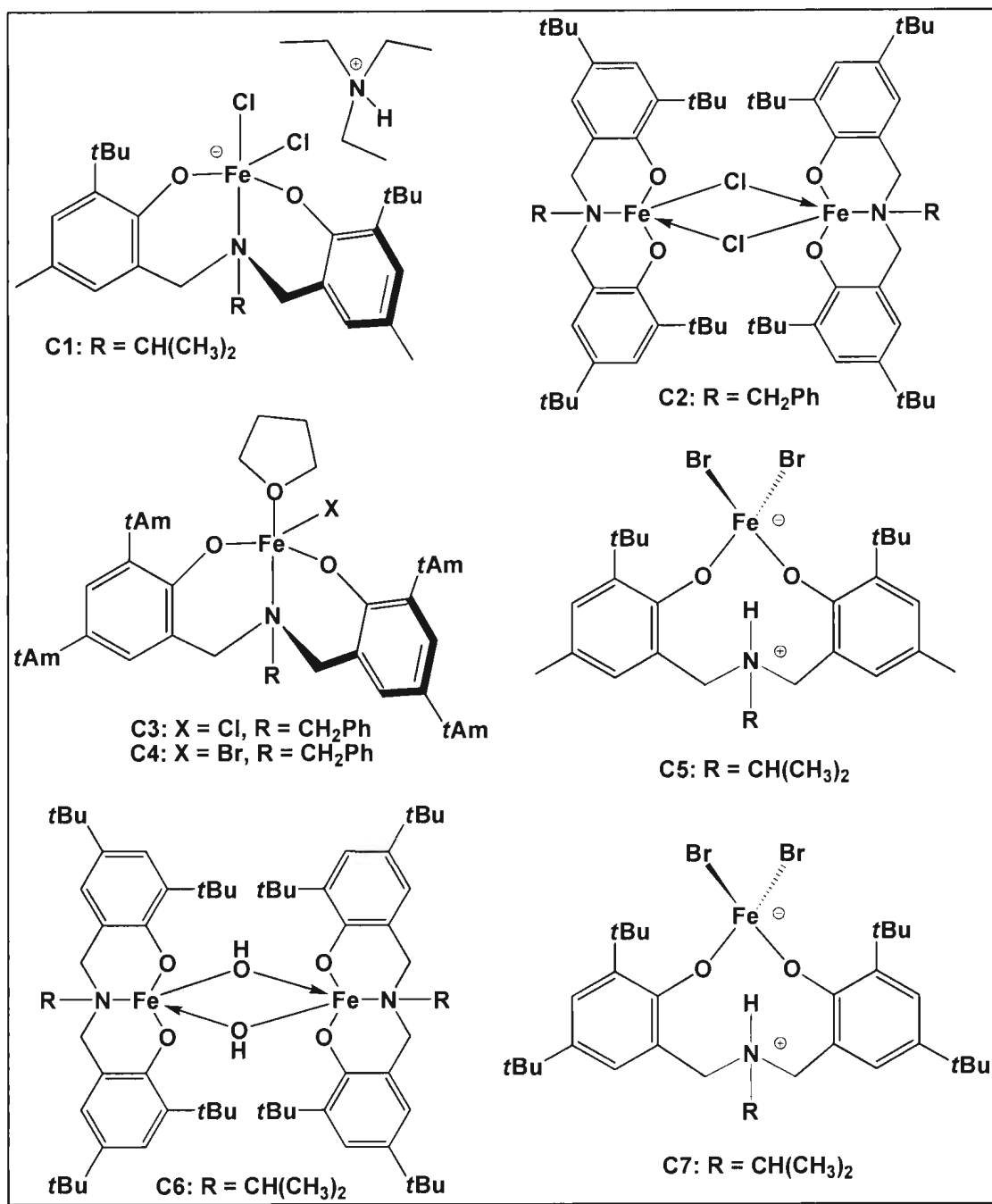


Figure 2.9: Collection of iron(III) amine-bis(phenolate) complexes synthesized. For C1, C3, C5, C6 and C7, co-crystallized solvent molecules omitted for clarity.

Problems with purification were also identified when FeCl_3 was reacted with $\text{H}_2[\text{ONO}]^{\text{BuBuBz}}$ ($\text{H}_2\text{L5}$) following the same procedure described above. Unlike the iron(III) “ate” complex shown in **Figure 2.9 (C1)**, X-ray analysis of the recrystallized product resulted in a single crystal X-ray structure of the triethylammonium salt. Obviously at this point, further purification steps were required. One desirable quality of these Fe(III) complexes, is that they are non-hygroscopic and quite robust. Therefore, due to the limitation of solvents available inside the glove box for purification, the sample was brought outside the glove box and was washed three times with acetone. The newly purified product was a dark brown crystalline solid. The color change from purple to brown is possibly a result of acetone coordination to the iron center. When MALDI-TOF MS analysis was performed on a sample of the brown solid, evidence supporting the generation of an iron(III) amine-bis(phenolate) chloride complex was obtained (**Figure 2.9, C2** ($[\text{FeL5}(\mu\text{-Cl})_2]$)). $[\text{FeL5}(\mu\text{-Cl})_2]$ has been previously synthesized and characterized in the Kozak group.⁶ Characterization of **C2** will be discussed in the next section.

Recently, a more efficient method of purification was established when FeCl_3 was reacted with $\text{H}_2[\text{ONO}]^{\text{AmAmBz}}$ ($\text{H}_2\text{L2}$). Unlike previous reactions, where triethylammonium chloride was separated via repeated toluene washings, the crude purple powder from this particular reaction was dissolved in minimal toluene and placed directly in the freezer inside the glove box. After approximately 48 hours in the freezer, a thin layer of a white crystalline solid was evident at the bottom of the recrystallization flask. Results to date suggest that unreacted ligand and triethylammonium chloride tend to precipitate out of the toluene solution at a faster rate than the desired iron(III) complex.

Therefore, decanting off the mother liquor and passing the dark purple solution through a Celite plug can establish a more effective method of purification.

Once the mother liquor was passed through a Celite plug, the dark purple solution was placed back into the freezer to help induce crystal growth. Eventually, dark purple crystals were evident throughout the reaction flask, and a sample was analyzed via X-ray crystallography. Surprisingly, an iron(III) THF adduct was isolated (**Figure 2.9**, **C3** ($\text{FeCl}(\text{THF})\text{L2}$)) instead of the expected chloride-bridged dimer. Since the iron(III) center has a high-spin (amine-bis(phenolate) ligands are considered weak field) d^5 coordination environment (hence is kinetically labile), it is surprising to see a THF adduct which is only weakly coordinating to high-spin iron(III) (even more so than chloride ligands). In general, chloride-bridged dimers of iron amine-bis(phenolate) complexes are sterically crowded about the two iron(III) centers. Since the ligand backbone here contains very bulky *t*-amyl substituents, one reason why the iron(III) THF adduct is formed in favor of the chloride-bridged dimer may be that the dimer formation is sterically disfavored. Characterization of **C3** will be discussed in the next section.

Surprisingly, when Kozak and co-workers attempted to synthesize an iron(III) bromide-bridged dimer (**Scheme 2.3**), a zwitterionic tetrahedral iron(III) complex bearing two bromide ligands and a quaternized ammonium fragment was generated (**Figure 2.10**).⁶ Protonation of the central nitrogen donor is an unexpected result and may ultimately be a result of incomplete deprotonation of the amine-bis(phenol) ligand (possibly due to water contamination). In an attempt to generate the desired iron(III) bromide-bridged dimer, this synthesis was revisited, but a stronger base (NaH or $^t\text{BuLi}$) was employed.

Following a modified literature procedure reported by Mountford and co-workers,⁷ a THF solution of the desired tridentate amine-bis(phenol) ligand was added dropwise to a NaH suspension in THF at -78 °C via standard Schlenk techniques (**Scheme 2.4**). Upon returning to room temperature (hydrogen gas was released as a by-product), the sodium salt of the amine-bis(phenolate) ligand was then added dropwise to a THF solution of FeX₃ (X = Cl, Br) at -78 °C (with the aid of a cannula filter) generating two equivalents of NaX and an immediate color change to dark purple. After stirring for 2 hours at room temperature (under an atmosphere of nitrogen), the THF was removed under vacuum to yield a dark purple powder. The crude powder was then brought into a glove box where a series of purification steps was performed. Since the by-product (NaX) was expected to be insoluble in non-polar toluene, washings with minimal toluene were performed. After passing the reaction mixture through a frit containing a Celite pad (to remove NaX), the dark purple filtrate was placed in the freezer for recrystallization.

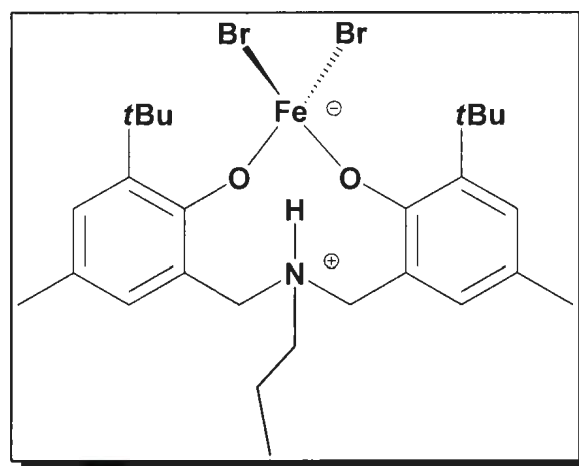
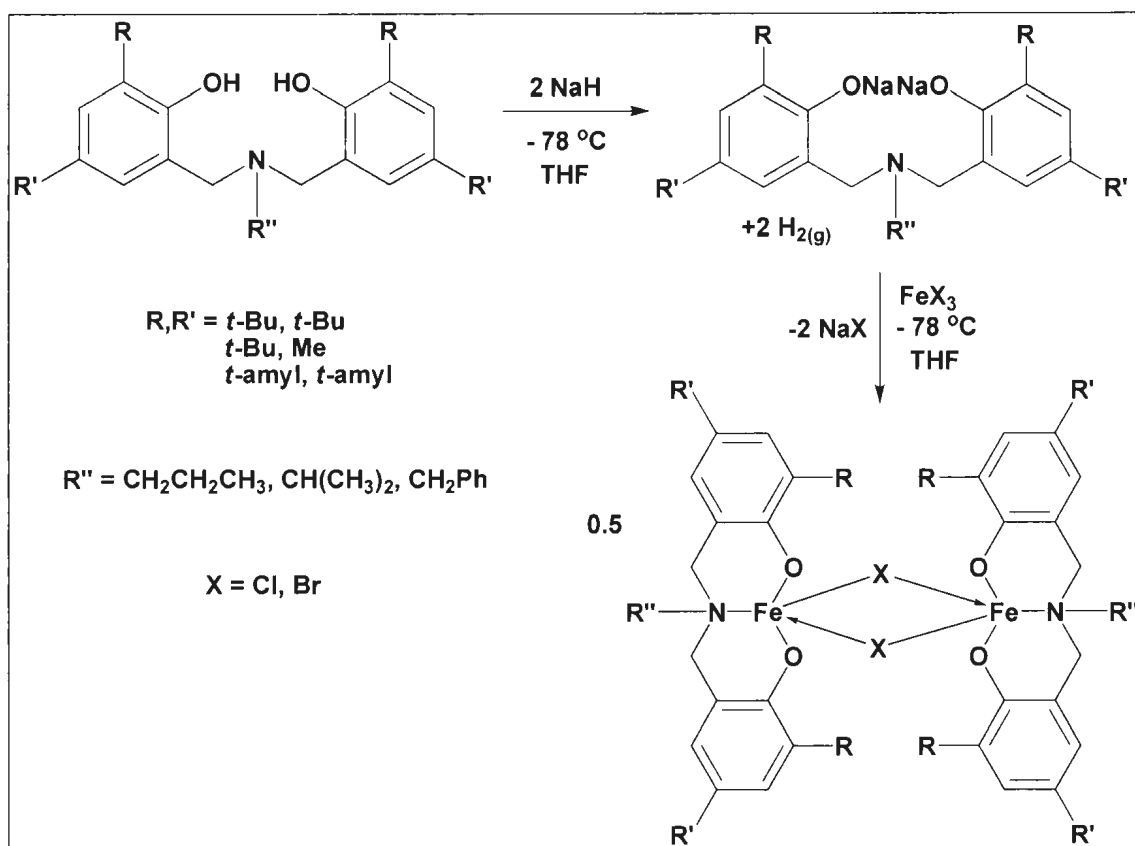


Figure 2.10: A zwitterionic tetrahedral iron(III) complex bearing two bromide ligands and a quaternized ammonium fragment reported by Kozak and co-workers.⁶



Scheme 2.4: The intended synthesis of Fe(III) halide-bridged dimers using NaH as the base.

When FeBr_3 reacts with $\text{Na}_2[\text{ONO}]^{\text{AmAmBz}}$ (as described in **Scheme 2.4**) a surprising result was obtained when a sample of the dark purple crystal (recrystallized from toluene) was analyzed via X-ray crystallography. Interestingly, a bromide analog of **C3** was isolated (**Figure 2.9**, **C4** ($\text{FeBr}(\text{THF})\text{L2}$)) instead of the expected bromide-bridged dimer. Once again, since the ligand backbone contains very bulky *t*-amyl substituents, the monomer species is presumably too hindered to dimerize (but there is

enough space for THF to coordinate). Characterization of **C4** will be discussed in the next section.

Surprisingly, following the same reaction procedure depicted in **Scheme 2.4**, X-ray diffraction of single crystals (obtained from slow evaporation of a toluene solution inside the glove box freezer) isolated from the reaction between FeBr_3 and the sodium salt of $\text{H}_2[\text{ONO}]^{\text{BuMe/Pr}}$ (**H₂L1**), resulted in a zwitterionic tetrahedral iron(III) complex bearing two bromide ligands and a quaternized ammonium fragment (**Figure 2.9**, **C5** ($\text{FeBr}_2\text{L1H}$)). Like the zwitterionic tetrahedral iron(III) complex shown in **Figure 2.10**, the generation of **C5** is likely a result of the incomplete deprotonation of the amine-bis(phenol) ligand due to water contamination (possibly from wet glassware or the cannula filter). A plausible mechanism for the synthesis of **C5** can be found in **Figure 2.11**. As shown in **Figure 2.11**, water ($\text{pK}_a = 15.7$) can potentially react with the sodium salt of the amine-bis(phenolate) ligand to generate NaOH and one equivalent of $\text{NaH}[\text{ONO}]$. Since NaOH is a strong base and the phenol groups ($\text{pK}_a \sim 10$) of the amine-bis(phenolate) ligand are acidic, it is very unlikely that the equilibrium would lie in favor of NaOH formation. However, NaOH is prone to react with FeBr_3 (generating NaBr and highly insoluble $\text{Fe}(\text{OH})_3$) which may drive the equilibrium to the right. For this particular mechanism, abstraction of the proton from the phenolic hydroxyl group will likely depend on the basicity of the central amine donor. Characterization of **C5** will be discussed in the next section.

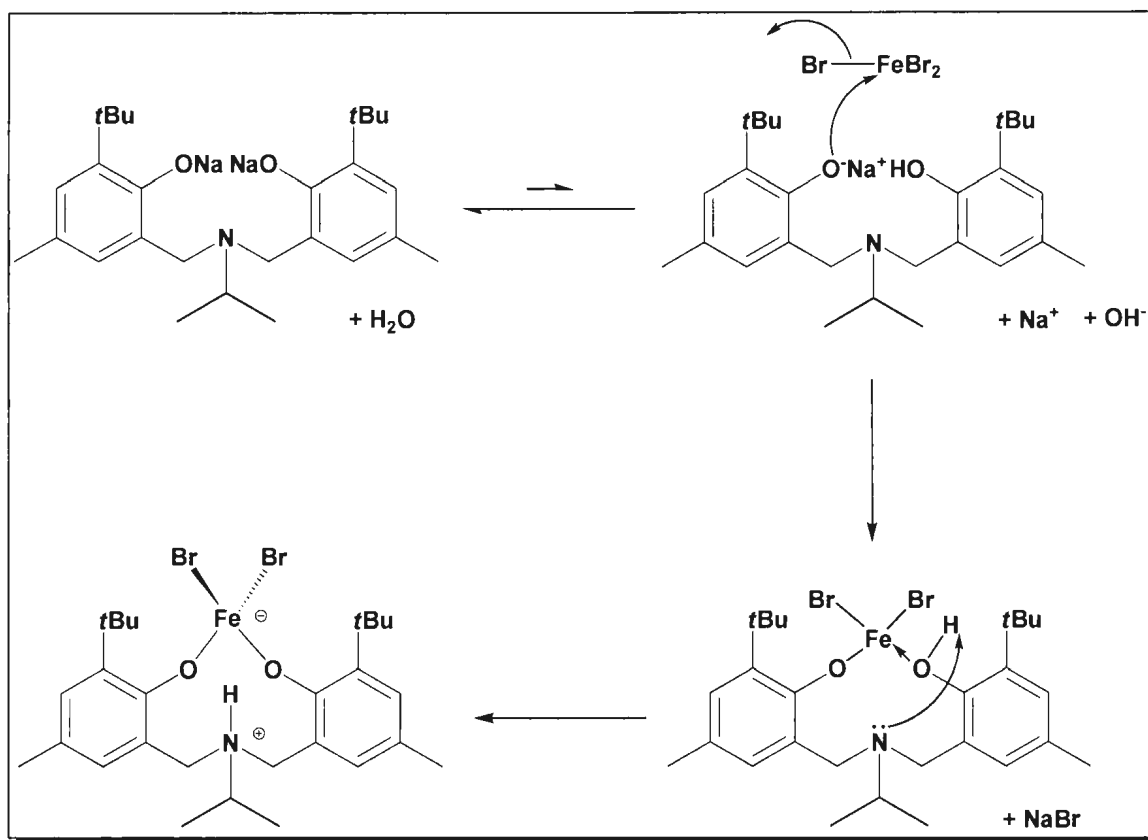
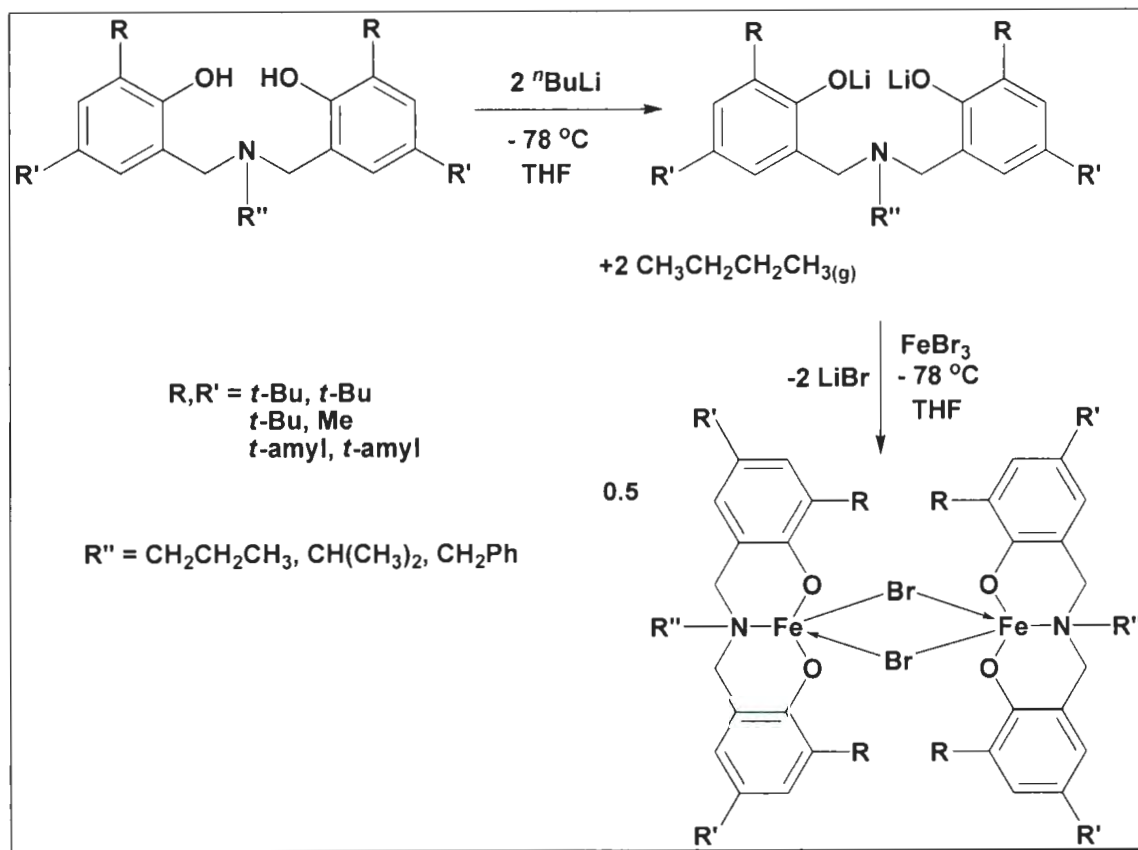


Figure 2.11: A plausible mechanism for the synthesis of **C5** ($\text{FeBr}_2\text{L1H}$).

When $\text{H}_2[\text{ONO}]^{\text{BuBu}i\text{Pr}}$ was lithiated using $n\text{BuLi}$ at $-78\text{ }^\circ\text{C}$ in THF (**Scheme 2.5**), a clear yellow solution was generated. Upon warming the reaction mixture to room temperature and releasing butane gas as a by-product, the lithiated ligand was transferred via a cannula filter to a solution of FeBr_3 in THF at $-78\text{ }^\circ\text{C}$ (immediate color change to dark purple) generating two equivalents of LiBr . After stirring for 2 hours at room temperature (under an atmosphere of nitrogen), the THF was removed via vacuum to yield a dark purple powder. Inside the glove box, the crude product was dissolved in minimal toluene, and the reaction mixture was passed through a frit containing a Celite

pad to remove any LiBr present. The isolated purple powder was then dissolved in minimal toluene and placed in the freezer for recrystallization. After one month in the freezer, dark brown crystals appeared throughout a dark brown solution. When a sample of the brown crystal was analyzed via X-ray crystallography, an iron(III) hydroxy-bridged dimer was observed (**Figure 2.9, C6** ($[\text{FeL3}(\mu\text{-OH})_2]$)) instead of the desired bromide-bridged dimer.



Scheme 2.5: The intended synthesis of Fe(III) bromide-bridged dimers using $^n\text{BuLi}$ as the base.

According to the work reported by Attia and co-workers, treatment of a monomeric Fe(III) species (with coordinated monoanionic ligands) with a strong base (such as KOH) at room temperature leads to a μ -dihydroxo bridging structure core.⁸ One of the major drawbacks when using cannula filters (and frits inside the glovebox) is the possibility of contamination due to the presence of water. If water was present when the solution of lithiated ligand was passed through the cannula filter (or from another source of contamination), LiOH could have been generated (due to hydrolysis of the lithiated amine-bis(phenolate) ligand). In theory, if the strong base LiOH was present, the desired product (likely monomeric in solution) would most likely react with the base to generate the iron(III) hydroxyl-bridged dimer as reported by Attia and co-workers.⁸ Of course, hydrolysis of the desired product could have also generated the observed hydroxyl species. This might help explain why the reaction mixture changed from dark purple to dark brown over the month-long period in the freezer.

In an attempt to successfully isolate $[\text{FeL3}(\mu\text{-Br})]_2$ (instead of $[\text{FeL3}(\mu\text{-OH})]_2$), the reaction between the lithiated ligand of $\text{H}_2\text{L3}$ and FeBr_3 was repeated as described above. Once again, the purified crude purple powder was dissolved in minimal toluene and placed in the freezer for recrystallization inside the glove box. After six months in the freezer, dark purple crystals appeared throughout a dark purple solution. This was a very promising result since the recrystallized product of **C6** ($[\text{FeL3}(\mu\text{-OH})]_2$) resulted in dark brown crystals. Unfortunately, when a sample of the purple crystal was analyzed via X-ray crystallography, a zwitterionic tetrahedral iron(III) complex bearing two bromide ligands and a quaternized ammonium fragment (**Figure 2.9**, **C7** ($\text{FeBr}_2\text{L3H}$)) was discovered instead of the desired bromide-bridged dimer. Even though great precaution

was taken, it seems that incomplete deprotonation of the ligand likely resulted due to the contamination of water as discussed previously.

2.2.3 Characterization

The iron(III) amine-bis(phenolate) complexes (**C1-C7**) were characterized using several analytical and spectroscopic techniques including elemental analysis, MALDI-TOF mass-spectrometry, single crystal X-ray diffraction, UV-vis spectroscopy, inductively coupled plasma mass spectrometry and magnetic measurements. A thorough discussion of the results obtained can be found in the following sections.

2.2.3.1 Elemental Analysis

Elemental Analysis was performed on recrystallized samples (from a saturated toluene solution) of **C1** and **C3-C7** (**Table 2.4**). Since toluene has a relatively high boiling point (110.6 °C), all samples were dried overnight on a high vacuum line to help remove residual toluene. As seen in **Table 2.4**, the experimental values (%) obtained are in good agreement with calculated values. Differences between theoretical and experimental values may be attributed to experimental error or residual solvent molecules. Also, metal nitrides may have formed during the elemental analysis leading to the observed discrepancy.

Table 2.4: Elemental analysis of iron(III) amine-bis(phenolate) complexes. For **C1**, theoretical % includes 1.3 equivalents of co-crystallized toluene.

Compound	Theoretical % Carbon (Experimental)	Theoretical % Hydrogen (Experimental)	Theoretical % Nitrogen (Experimental)
C1 (C ₃₃ H ₅₅ Cl ₂ FeN ₂ O ₂)	66.68 (66.73)	8.69 (8.92)	3.69 (3.44)
C3 (C ₄₅ H ₆₇ ClFeNO ₃)	70.99 (71.25)	8.87 (9.03)	1.84 (2.10)
C4 (C ₄₅ H ₆₇ BrFeNO ₃)	67.08 (66.87)	8.38 (8.12)	1.74 (2.05)
C5 (C ₂₇ H ₄₀ Br ₂ FeNO ₂)	51.78 (51.53)	6.44 (6.18)	2.24 (2.07)
C6 (C ₆₆ H ₁₀₄ Fe ₂ N ₂ O ₆)	69.95 (70.12)	9.25 (8.98)	2.47 (2.65)
C7 (C ₃₃ H ₅₂ Br ₂ FeNO ₂)	55.79 (55.61)	7.38 (7.19)	1.97 (2.11)

In the crystal structure of **C1**, there exists a toluene molecule sandwiched between repeating units of the anion (“ate” complex) and cation (triethylammonium). Since there are no distinguishable π - π interactions within the structure, it is likely that the toluene molecule is caged within the structure. This conclusion can help explain the elemental results obtained (**Table 2.4**). If toluene is caged within the structure, it is very unlikely that drying the sample overnight via a high vacuum will help remove the co-crystallized solvent. In fact, when the theoretical % includes 1.3 equivalents of co-crystallized toluene, experimental and theoretical percentages agree respectively.

2.2.3.2 Mass Spectrometry

MALDI-TOF MS (matrix assisted laser desorption ionization mass spectrometry with a time-of-flight detector) was used to analyze recrystallized samples of the metal complexes **C2-C7**. Since MALDI-TOF MS is a soft ionization technique, the fragmentation of metal complexes is generally minimal providing useful structural information.^{9,10} All sample solutions were prepared using a 1:1 ratio of matrix to analyte in toluene. Anthracene was a convenient choice for the matrix, since both anthracene and the iron(III) amine-bis(phenolate) complexes are readily soluble in toluene. MALDI-TOF MS analysis of iron(III) amine-bis(phenolate) complexes previously reported by the Kozak group display an intense peak ($[M-X]^+$) representing the loss of a halide ligand and a weak molecular ion peak ($[M]^+$).⁶ Since both the halide ligand and the phenolate-oxygen donors possess additional lone pairs (capable of forming bridges between two iron centres), multimetallic species, such as dimers, are often seen in the gas phase during analysis.⁶

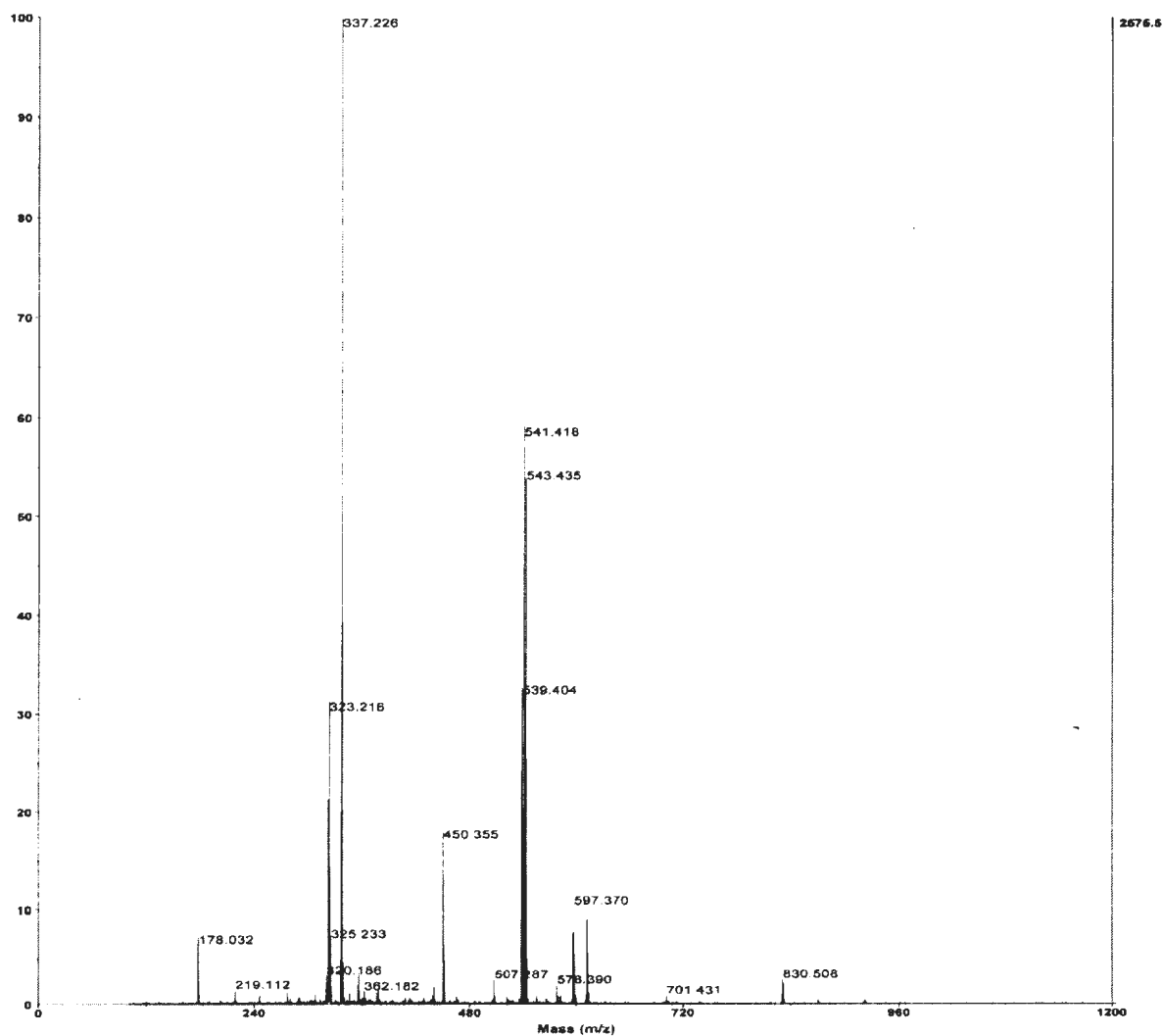


Figure 2.12: MALDI-TOF mass spectrum of **C2** ($[\text{FeL5}(\mu\text{-Cl})]_2$).

The MALDI-MS spectrum for **C2** ($[\text{FeL5}(\mu\text{-Cl})]_2$) is shown in **Figure 2.12**. No molecular ion peak ($[\text{M}]^+$) at 632.300 m/z is evident, however, a fragment ion is observed at 597.370 m/z, which represents the loss of Cl ($[\text{M-Cl}]^+$). This can be attributed to the fact that the chloride ligand is only weakly coordinating. The peaks observed at 541.418 m/z and 337.226 m/z (base peak) represent $[\text{M-FeCl}]^+$ and a fragment of the amine-

bis(phenol) ligand backbone ($[M-FeCl-phenol]^+$) respectively. In the mass spectrum of **C2**, there are no observed peaks indicating the presence of the dimer ($[2M]^+$). The higher mass peaks found at approximately 850 m/z, likely represent fragments of dimers formed in the gas phase during the analysis. Theoretical isotopic patterns for the proposed structure also agree with experimental values. This result shows the coordination of the amine-bis(phenolate) ligand to the iron centre.

MALDI-TOF MS analysis was also performed on complexes **C3-C4** and supports the proposed formulations. As seen in the mass spectrum of **C3** ($FeCl(THF)L2$) (**Figure 2.13**), the THF ligand was lost from the parent ion ($[M-THF]^+$, 688.328 m/z). At 653.374 m/z, there also exists a peak which represents the loss of both THF and Cl ($[M-THF-Cl]^+$). Here, the loss of Cl and THF is attributed to the fact that both ligands are only weakly coordinating. Theoretical isotope patterns (**Figure 2.14(A)**) for **C3** were also compared with experimental values (**Figure 2.14(B)**) in order to further confirm the coordination of the amine-bis(phenolate) ligand to the iron centre. As seen in **Figures 2.14(A)** and **Figure 2.14(B)**, there are some discrepancies between the theoretical and experimental isotope patterns shown, specifically in the isotope patterns at about 653.374 m/z. In the experimental isotope pattern, there exists a much more intense peak at 650.388 m/z than the one found in the theoretical isotope pattern of $[M-THF-Cl-H]^+$. This gives reason to believe that the experimental isotope pattern (**Figure 2.14(B)**) is actually a mixture of two overlapping isotope patterns originating from two molecules of very similar masses, differing by one mass unit, H. The jagged baseline area in the experimental isotope pattern provides further evidence of this conclusion.

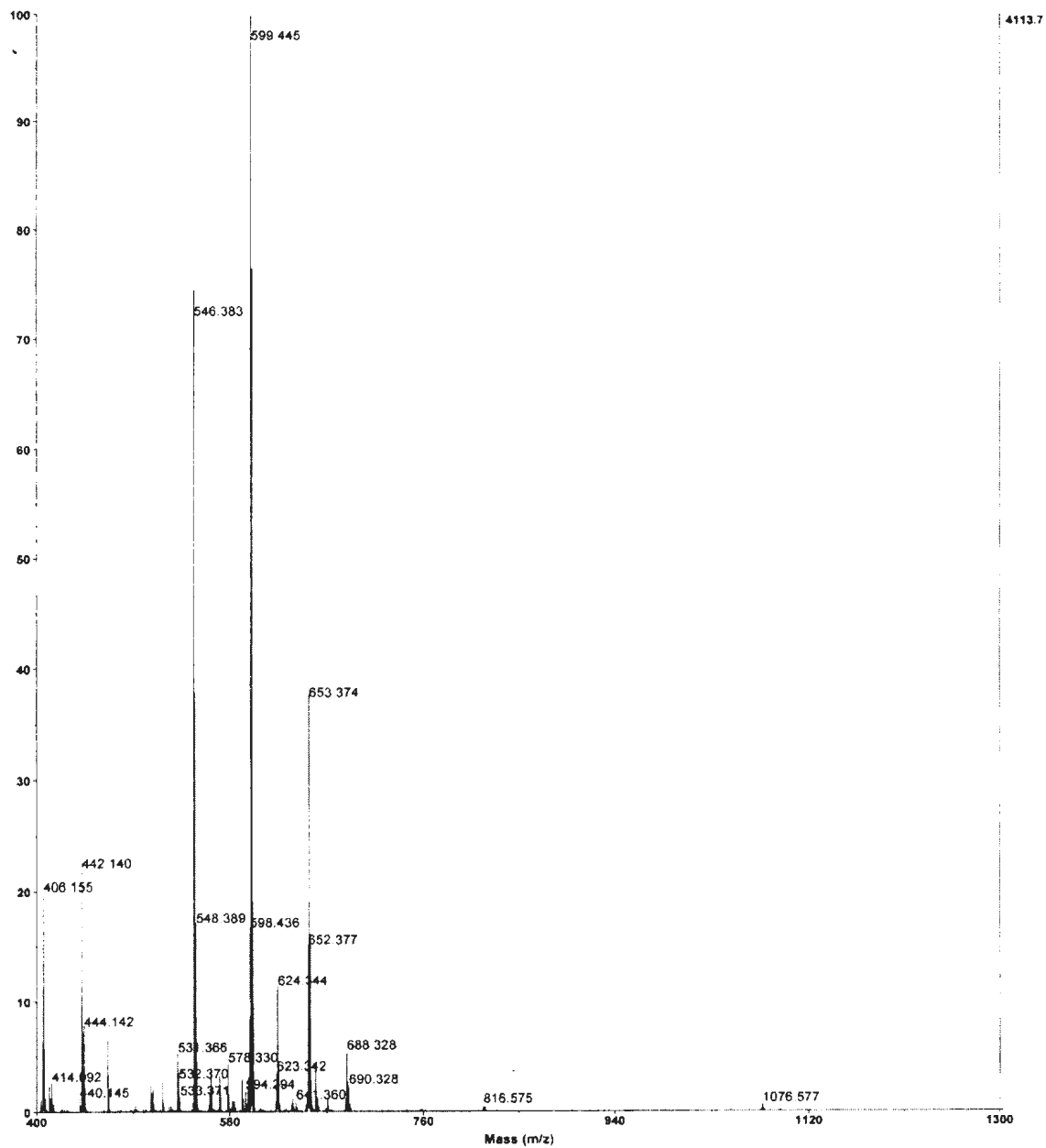


Figure 2.13: MALDI-TOF mass spectrum of C3 (FeCl(THF)L2).

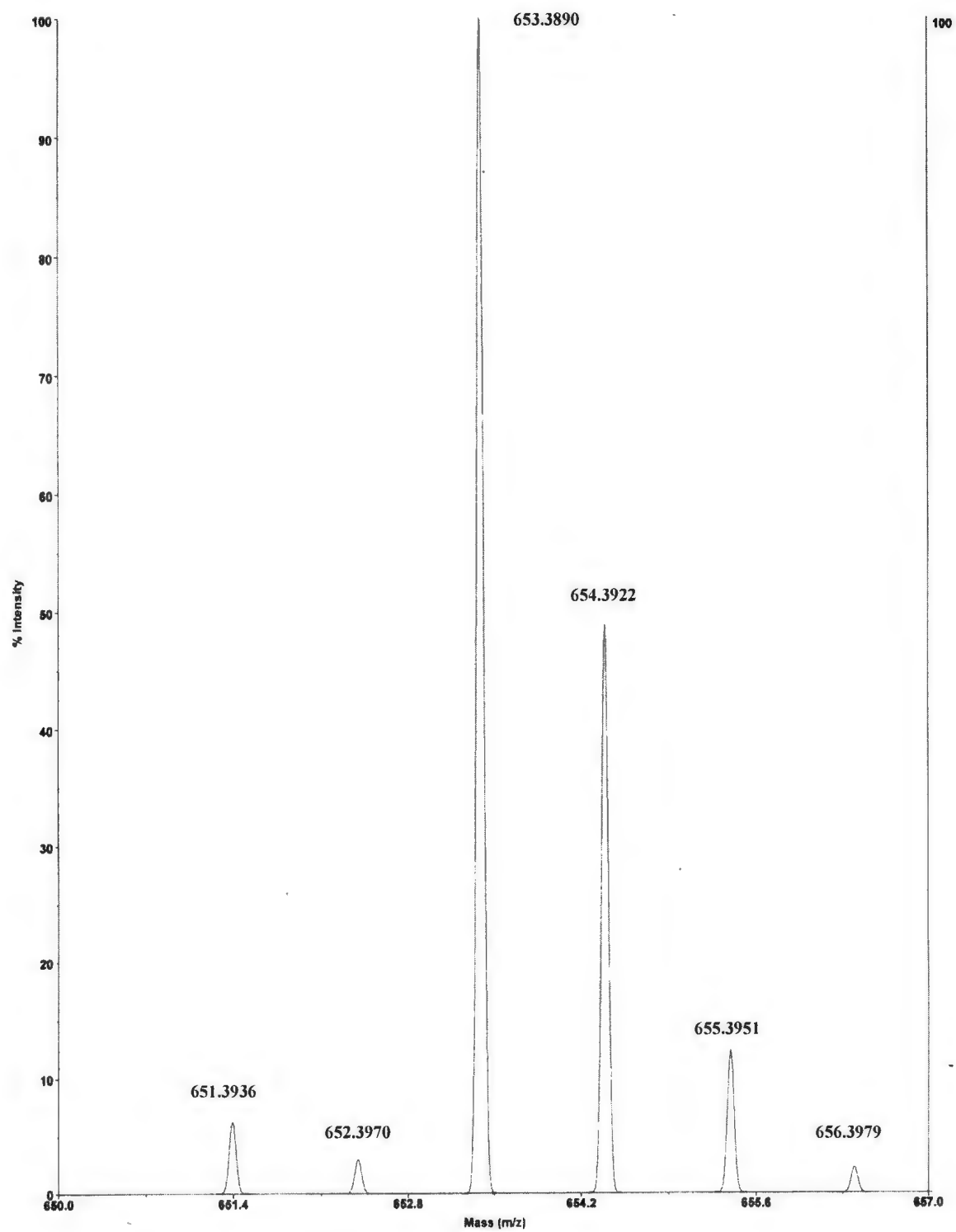


Figure 2.14(A): Theoretical isotope pattern for C3.

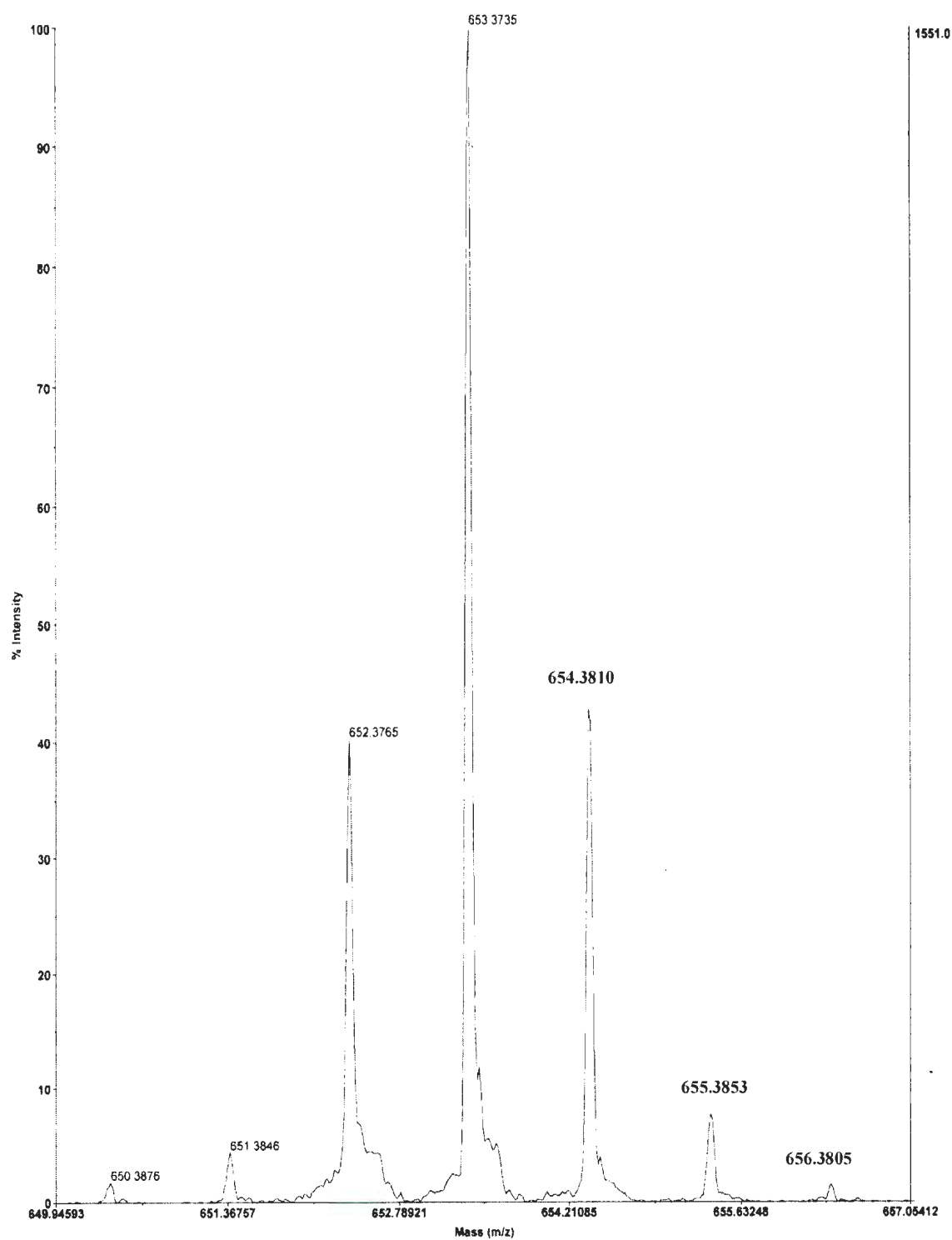


Figure 2.14(B): Experimental isotope pattern for C3.

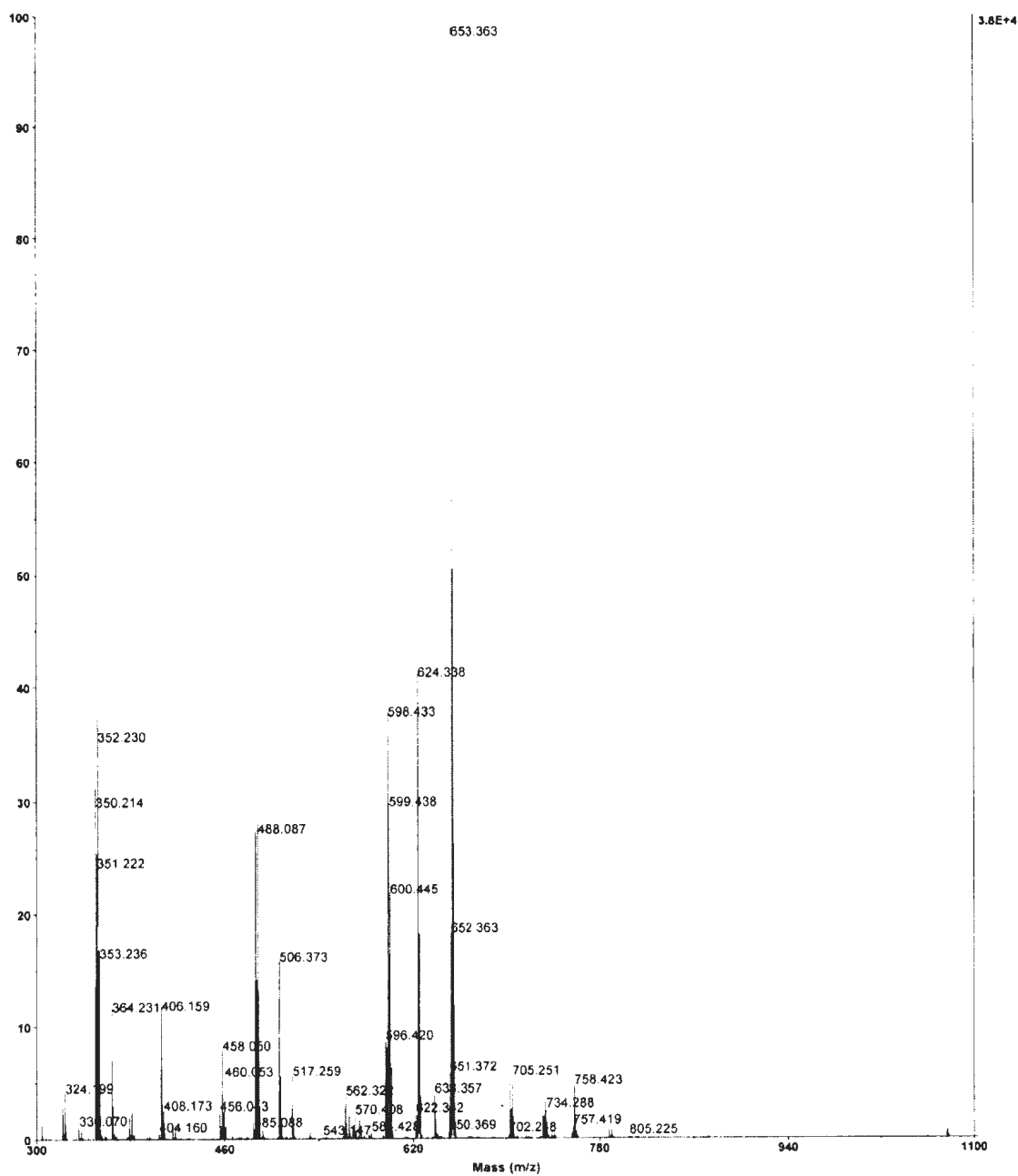


Figure 2.15: MALDI-TOF mass spectrum of **C4** (FeBr(THF)L2).

The mass spectrum of **C4** can be found in **Figure 2.15**. Unlike the mass spectrum of **C3**, the mass spectrum of **C4** shows a very weak molecular ion peak ($[M]^+$) which is located at 805.225 m/z. Once again, as seen in **Figure 2.15**, the THF ligand is lost from the parent ion ($[M-THF]^+$, m/z = 734.288). At 653.363 m/z, there also exists a peak (base peak) which represents the loss of both THF and Br ($[M-THF-Br]^+$). Theoretical isotopic patterns for the proposed structure also agree with experimental values.

MALDI-TOF MS analysis was also performed on complexes **C5** and **C7** and supports the proposed formulations. As seen in the mass spectrum of **C5** (**Figure 2.16**), no molecular ion peak ($[M]^+$) at 626.265 m/z is evident. However, peaks corresponding to characteristic fragment ions are observed. As shown in **Figure 2.16**, there exists a peak at 545.135 m/z which represents the loss of one bromide ligand from the parent ion along with the proton of the central nitrogen atom ($[M-Br-H]^+$, m/z = 545.135). At 465.215 m/z, there also exists a peak which represents the loss of both bromide ligands and the proton of the central nitrogen atom ($[M-2Br-H]^+$). The observed fragmentation pattern (**Figure 2.16**) has also been found in the MALDI-TOF mass spectrum of a similar complex reported previously by the Kozak group (**Figure 2.10**).⁶ The mass spectrum of **C7** can be found in **Figure 2.17**. As seen in the mass spectrum of **C7**, there exists a very weak molecular ion peak ($[M]^+$) at 710.468 m/z. At 549.260 m/z, there also exists a peak which represents the loss of both bromide ligands and the proton of the central nitrogen atom ($[M-2Br-H]^+$). The higher mass peaks found above 710 m/z likely represent fragments of dimers formed in the gas phase during the analysis. Theoretical isotopic patterns for **C5** and **C7** also agree with experimental values.

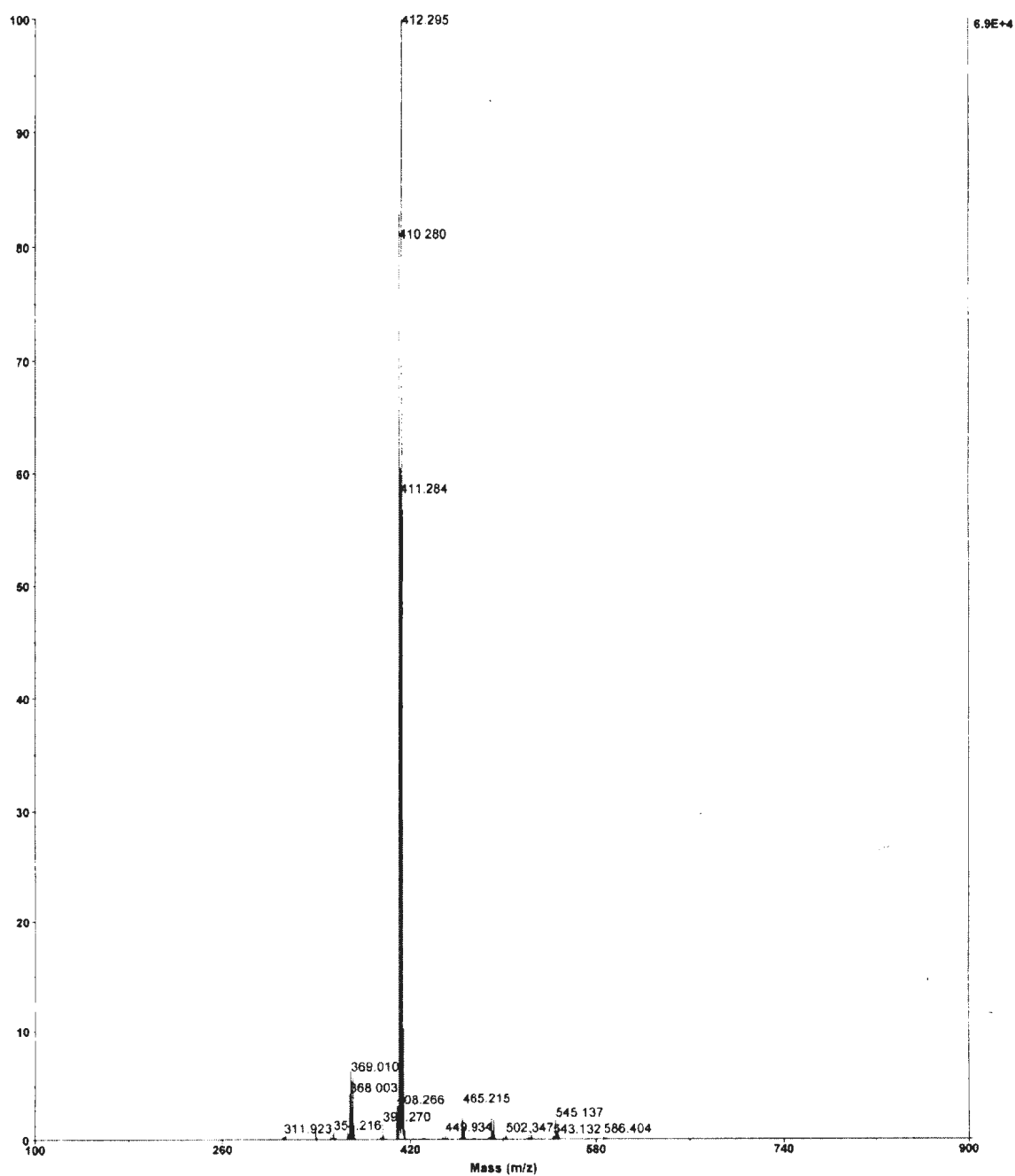


Figure 2.16: MALDI-TOF mass spectrum of C5 (FeBr₂L1H).

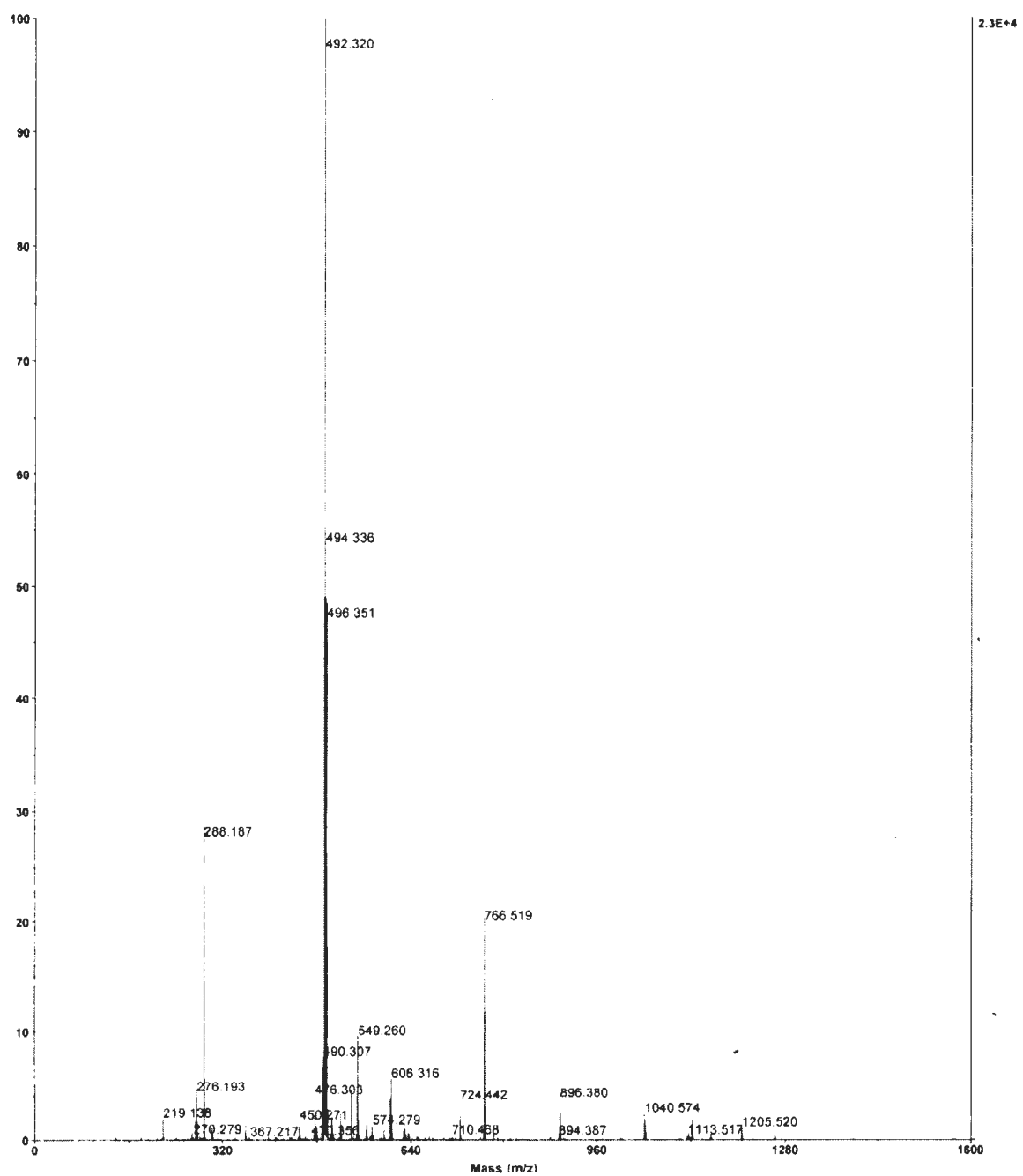


Figure 2.17: MALDI-TOF mass spectrum of C7 (FeBr₂L3H).

The MALDI-MS spectrum for **C6** ($[\text{FeL3}(\mu\text{-OH})]_2$) is shown in **Figure 2.18**. As seen in the mass spectrum, a molecular ion peak ($[\text{M}]^+$) is evident at 564.394 m/z. Also, a characteristic fragment ion is observed at 549.399 m/z, which represents the loss of the hydroxyl ligand ($[\text{M-OH}]^+$). The peaks observed at 496.479 m/z (base peak) and 219.166 m/z, represent $[\text{M-FeOH}]^+$ and a fragment ion of the amine-bis(phenol) backbone respectively. In the mass spectrum of **C6**, there are no observed peaks indicating the presence of the dimer ($[2\text{M}]^+$). The higher mass peaks found at approximately 650 m/z, likely represent fragments of dimers formed in the gas phase during the analysis. Theoretical isotopic patterns for the proposed structure also agree with experimental values (please see appendix). This result shows the coordination of the amine-bis(phenolate) ligand to the iron centre.

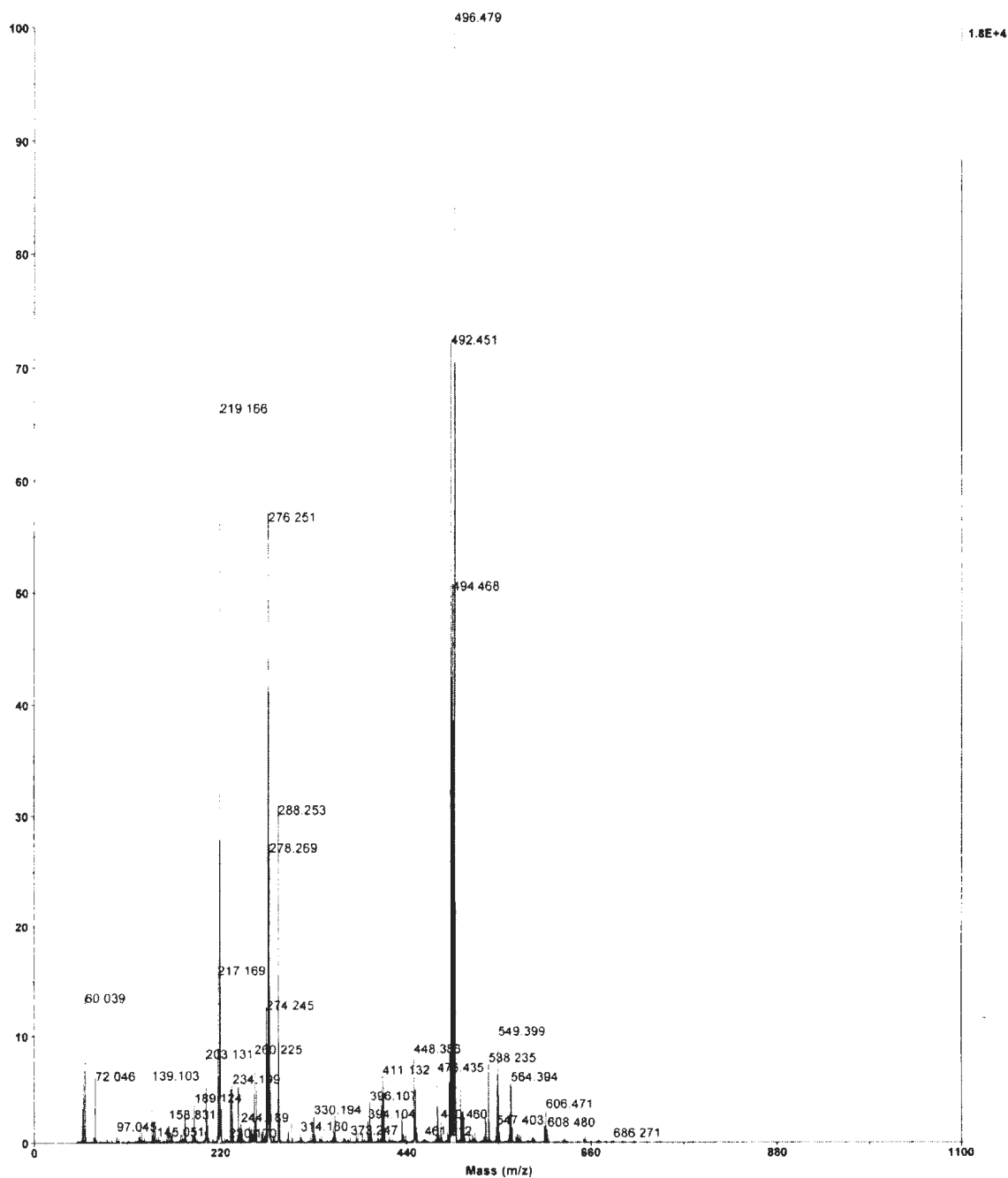


Figure 2.18: MALDI-TOF mass spectrum of C6 ($[\text{FeL3}(\mu\text{-OH})]_2$).

2.2.3.3 Structural Characterization

Molecular Structure of C1:

Single crystals of **C1** suitable for X-ray diffraction were obtained from a saturated toluene solution at -35 °C inside a nitrogen filled glove box. The solid state molecular structure of **C1** is shown in **Figure 2.19**, while crystallographic data and selected metric parameters are shown in **Table 2.5** and **Table 2.6**, respectively. In the solid state, **C1** exhibits a monomeric structure having a trigonal bipyramidal iron(III) centre with a formal negative charge (“ate” complex). In the solid state molecular structure of **C1**, there exists a toluene molecule sandwiched between repeating units of the anion (“ate” complex) and cation (triethylammonium). Since there are no distinguishable π - π interactions within the structure, it is likely that the toluene molecule is caged within the structure as the result of ionic (Coulombic) intermolecular forces between the anion and cation units. Elemental analysis performed on a recrystallized sample of **C1** supports this reasoning (see section 2.2.2.1). The equatorial plane of the Fe^{III} ion in **C1** consists of two phenolate oxygens, O(1) and O(2), and a chloride ion, Cl(2), where the sum of bond angles is 359.69° indicating near perfect planarity. The iron atom is displaced 0.06 Å above the equatorial plane. The amine nitrogen donor (N(1)) and the chloride ion Cl(1) occupy the apical sites, giving a Cl(1)-Fe(1)-N(1) bond angle of 178.85(7)° which is close to the ideal linear geometry. The *cis*-orientated chloride ligands are nearly orthogonal with a Cl(1)-Fe(1)-Cl(2) bond angle of 91.42(5)°. The distorted trigonal bipyramidal coordination environment of the Fe^{III} ion possesses a trigonality index parameter, τ , value of 0.837 [as defined by Addison and Reedijk, $\tau = (\beta - \alpha)/60$, where β represents the largest

angle about the metal centre and α represents the second largest angle about the metal centre. For perfect trigonal bipyramidal and square pyramidal geometries the τ values are one and zero, respectively].¹¹

Table 2.5: Crystallographic and Structure Refinement Data for **C1** and **C3-C7**.

Compound reference	C1	C3	C4	C5	C6	C7
Chemical formula	C ₄₀ H ₆₃ Cl ₂ FeN ₂ O ₂	C ₄₅ H ₆₇ ClFeNO ₃	C ₄₅ H ₆₇ BrFeNO ₃	C _{44.50} H ₆₀ Br ₂ FeNO ₂	C ₈₀ H ₁₂₀ Fe ₂ N ₂ O ₆	C ₄₀ H ₆₀ Br ₂ FeNO ₂
Colour	Dark Red	Red	Dark Red	Black	Red	Dark Red
Habit	Prism	Prism	Prism	Prism	Prism	Prism
Formula Mass	730.70	761.33	805.78	856.62	1317.53	802.57
Crystal system	Triclinic	Monoclinic	Monoclinic	Monoclinic	Orthorhombic	Triclinic
<i>a</i> [Å]	11.162(3)	25.441(12)	39.512(3)	14.816(4)	24.3216(17)	10.5127(10)
<i>b</i> [Å]	11.397(4)	10.907(4)	10.9112(4)	16.729(4)	18.1938(11)	13.6960(14)
<i>c</i> [Å]	17.686(6)	31.379(15)	25.084(2)	18.202(5)	18.8654(12)	15.3413(15)
α [°]	83.003(14)	90	90	90	90	68.421(5)
β [°]	75.944(13)	94.00(3)	126.271(3)	107.386(3)	90	79.693(6)
γ [°]	69.005(11)	90	90	90	90	77.951(6)
Unit cell <i>V</i> [Å ³]	2036.1(11)	8686(7)	8718.8(11)	4305.4(20)	8348.0(9)	1996.1(3)
Temperature [K]	163(1)	163(1)	163(1)	163(1)	193(1)	163(1)
Space group	<i>P</i> -1 (#2)	12/a (#15)	C2/c (#15)	P2 ₁ /c (#14)	Pccn (#56)	<i>P</i> -1 (#2)
<i>Z</i>	2	8	8	4	4	2
<i>D_c</i> /g cm ⁻³	1.192	1.164	1.228	1.321	1.048	1.335
Radiation type	MoK α	MoK α	MoK α	MoK α	MoK α	MoK α
Absorption, μ [mm ⁻¹]	0.535	0.446	1.302	2.246	0.393	2.412
<i>F</i> (000)	786	3288	3432	1784	2856	838
Reflections measured	17721	16461	54433	54221	24717	14400
Independant refl's	8338	7386	9027	8910	5448	6952
<i>R_{int}</i>	0.0574	0.1000	0.0364	0.0588	0.1590	0.0962
<i>R_i</i> (<i>I</i> > 2 σ (<i>I</i>)) ^[a]	0.0634	0.1181	0.0622	0.0554	0.1586	0.0991
<i>wR</i> (<i>F</i> ²) (<i>I</i> > 2 σ (<i>I</i>)) ^[b]	0.1905	0.3701	0.1715	0.1413	0.4243	0.2578
<i>R_i</i> (all data)	.0902	0.1918	0.0656	0.0690	0.2272	0.1683
Goodness of fit on <i>F</i> ²	1.093	1.094	1.093	1.104	1.177	1.035

[a] $R_I = \Sigma(|F_o| - |F_c|) / \Sigma|F_o|$. [b] $wR_2 = [\Sigma(w(F_o^2 - F_c^2)^2) / \Sigma w(F_o^2)^2]^{1/2}$.

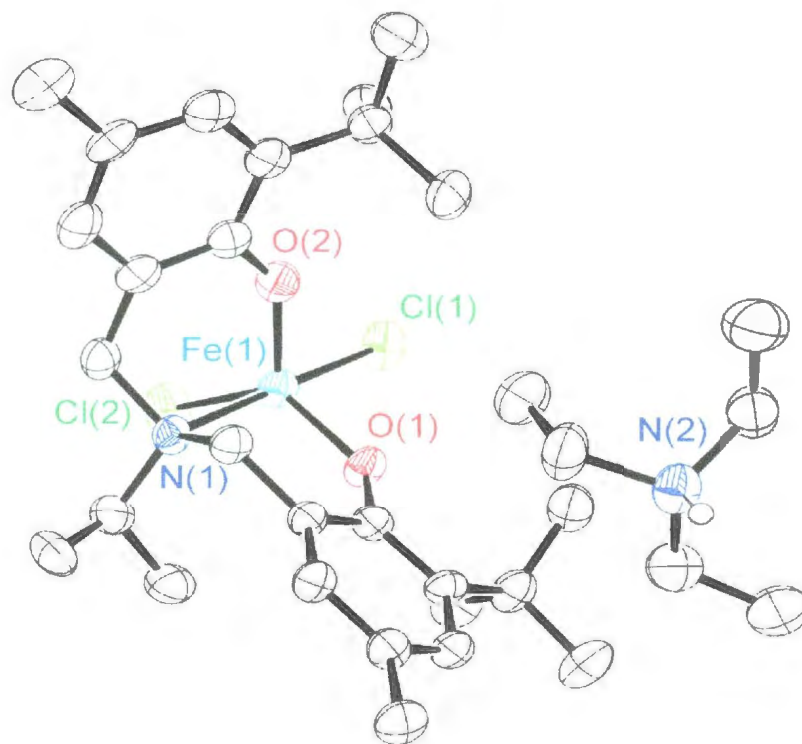


Figure 2.19: Molecular structure (ORTEP) and partial atom labeling of **C1**. Ellipsoids shown at 50% probability. The co-crystallized toluene molecule and hydrogen atoms omitted for clarity (except at N(2)).

Previously, Kozak and co-workers reported mononuclear trigonal bipyramidal iron(III) complexes of related tetradentate diamine-bis(phenolate) ligands (abbreviated $[O_2NN']$, where N' represents a pendant dimethylaminoethyl or pyridyl arm).¹² The Fe-Cl bond lengths in $FeCl[O_2NN']^{BuMePy}$ and $FeCl[O_2NN']^{BuMeNMe_2}$ were found to be 2.3051(10) and 2.2894(5) Å respectively, which are very similar to the Fe-Cl(2) interaction observed in the equatorial plane of **C1**. The Fe-Cl(1) bond length (2.3618(13) Å) in **C1**, where Cl(1) is *trans* to a hard nitrogen donor, is slightly longer than the Fe-Cl bond length observed in $FeCl[O_2NN']^{BuMePy}$ and also slightly longer than the Fe-Cl bond length observed in $FeCl[O_2NN']^{BuMeNMe_2}$ (where Cl is also *trans* to a hard nitrogen donor).

C1 has a Fe-N(1) distance of 2.255(3) Å which is very similar to the Fe-N bond lengths reported in FeCl[O₂NN']^{BuMePy} (2.2706(15) Å) and FeCl[O₂NN']^{BuMeNMe₂} (2.248(2) Å). The phenolate oxygen atoms in **C1** exhibit bond distances of 1.855(2) and 1.848(2) Å for Fe(1)-O(1) and Fe(1)-O(2), respectively. These interactions are only slightly shorter than those observed in Kozak's FeCl[O₂NN'] complexes, where average Fe-O distances of 1.86 Å are observed.

The coordination geometry around iron(III) in **C1** is very closely related to a series of iron(III) chloride-bridged dimers previously reported in the Kozak group.⁶ A molecular structure (ORTEP) representation of [Fe[ONO]^{BuMenPr}(μ-Cl)]₂ (**Dimer A**) and [Fe[ONO]^{BuMcBn}(μ-Cl)]₂ (**Dimer B**) can be found in **Figure 2.20** and **Figure 2.21**, respectively, while selected metric parameters can be found in **Table 2.6**. Like **C1**, the five-coordinate trigonal bipyramidal iron(III) centre(s) in **Dimer A** and **Dimer B** are composed of two chloride ions along with two phenolate oxygen donor atoms and a central amine nitrogen atom originating from a tridentate amine-bis(phenolate) backbone. The axial Fe-Cl bond length in **C1** (2.3618(4) Å) is slightly shorter than the axial Fe-Cl bond lengths found in **Dimer A** (2.4911(8) Å) and **Dimer B** (2.5025(3) Å). The equatorial Fe-Cl(2) bond length in **C1** (2.3038(14) Å) is intermediate to the equatorial Fe-Cl bond lengths reported in **Dimer A** (2.298(2) Å) and **Dimer B** (2.3290(4) Å). The Fe-N(1) distance of 2.255(3) Å observed in **C1** is longer than the observed Fe-N distances found in both chloride-bridged dimers. The Fe-O distances in **C1** are 1.855(2) and 1.848(3) Å for Fe(1)-O(1) and Fe(1)-O(2), respectively, which are longer than the distances reported between iron and the phenolate oxygen atoms in **Dimer A** and **Dimer B**. Since the iron centre in **C1** has a formal negative charge, the anionic oxygen donors

may be slightly repelled by the metal centre. From an electronic perspective, this may account for the longer Fe-O distances observed in **C1**. Of course, in the case of both **Dimer A** and **Dimer B**, steric hindrance originating from the presence of two large amine-bis(phenolate) ligands about the two iron(III) centres may also be a major contributor. As seen in **Figure 2.20** and **Figure 2.21**, two phenolate oxygen donor atoms and a bridging chloride occupy the equatorial plane around each iron ion, where the sum of bond angles is 359.89° in **Dimer A** and 359.84° in **Dimer B**. In comparison to both chloride-bridged dimers, the sum of bond angles about the equatorial plane in **C1** (359.69°) is slightly lower. The amine nitrogen donor and a bridging chloride ion take up the axial positions, giving a Cl(1)*-Fe(1)-N(1) bond angle of 178.32(9)° in **Dimer A** and Cl(2)-Fe(1)-N(1) bond angle of 177.28(3)° in **Dimer B**. Complex **C1** has a Cl(1)-Fe(1)-N(1) bond angle of 178.85(7)° which is closer to the ideal linear geometry. The *cis*-oriented chloride ligands are nearly orthogonal with a Cl-Fe-Cl bond angle of 87.36(4)° in **Dimer A** and 84.341(14)° in **Dimer B**. The Cl-Fe-Cl bond angle in **C1** is 91.42(5)°, which is closer to the perfect orthogonal angle of 90°.

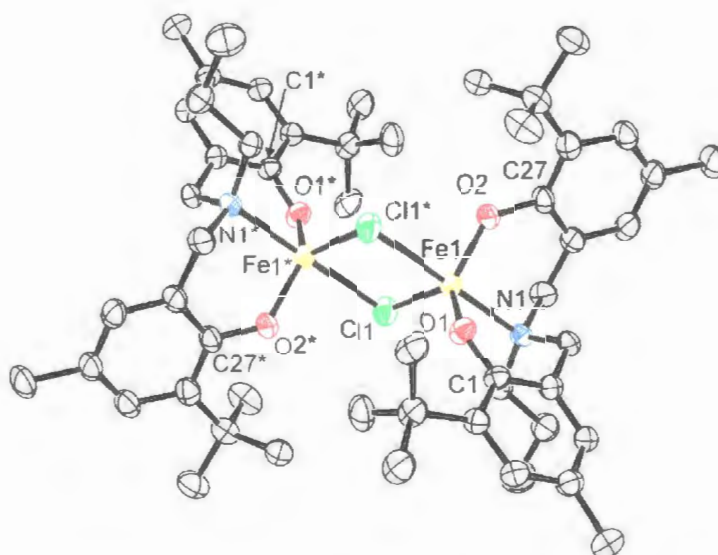


Figure 2.20: Molecular structure (ORTEP) and partial atom labeling of $[\text{Fe}(\text{ONO})^{\text{BuMeBn}}(\mu\text{-Cl})_2]$ (**Dimer A**), which was previously reported in the Kozak group. Ellipsoids shown at 50% probability. Hydrogen atoms omitted for clarity.⁶

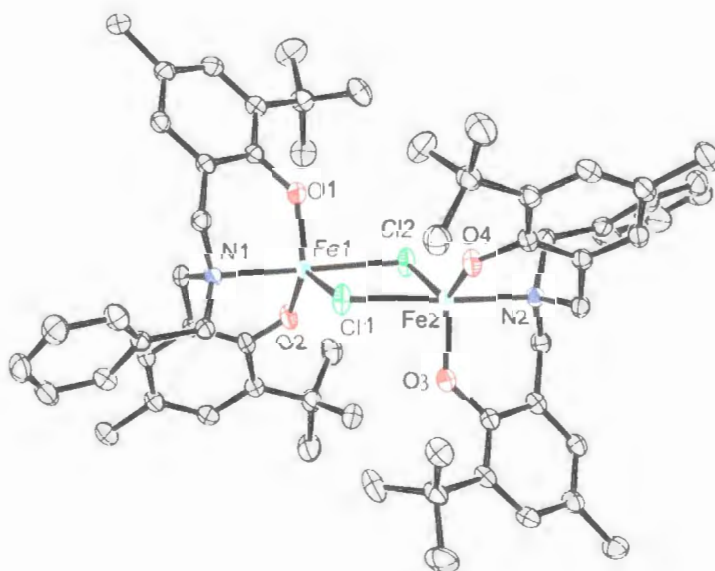


Figure 2.21: Molecular structure (ORTEP) and partial atom labeling of $[\text{Fe}(\text{ONO})^{\text{BuMeBn}}(\mu\text{-Cl})_2]$ (**Dimer B**), which was previously reported in the Kozak group. Ellipsoids shown at 50% probability. Hydrogen atoms omitted for clarity.⁶

Table 2.6: Selected bond lengths (Å) and bond angles (°) of **C1**, [Fe(ONO)^{BuMenPr}(μ-Cl)]₂ (**Dimer A**) and [Fe(ONO)^{BuMenPr}(μ-Cl)]₂ (**Dimer B**). Symmetry operators used to generate equivalent atoms: (*) -x + 1, -y + 1, -z + 1.

	Dimer A	Dimer B	C1
Fe(1)-O(1)	1.818(3)	1.8276(13)	1.855(2)
Fe(1)-O(2)	1.817(3)	1.8222(12)	1.848(3)
Fe(1)-N(1)	2.183(4)	2.1819(10)	2.255(3)
Fe(1)-Cl(1)	2.298(2)	2.3290(4)	2.3618(4)
Fe(1)-Cl(1)*	2.4911(18)		
Fe(1)-Cl(2)		2.5025(3)	2.3038(14)
O(1)-Fe(1)-O(2)	124.63(14)	119.36(5)	114.58(12)
N(1)-Fe(1)-Cl(1)	93.92(10)	93.59(3)	178.85(7)
N(1)-Fe(1)-Cl(1)*	178.32(9)		
N(1)-Fe(1)-Cl(2)		177.28(3)	89.35(9)
Cl(1)-Fe(1)-Cl(1)*	87.36(6)		
Cl(1)-Fe(1)-Cl(2)		84.341(14)	91.42(5)
Fe(1)-Cl(1)-Fe(1)*	92.64(6)		
Fe(1)-Cl(1)-Fe(2)		95.384(14)	
O(1)-Fe(1)-Cl(1)	113.18(11)	114.96(4)	91.49(8)
O(1)-Fe(1)-Cl(1)*	89.86(11)		
O(1)-Fe(1)-Cl(2)		88.91(3)	128.60(10)
O(2)-Fe(1)-Cl(1)	122.08(12)	125.52(4)	92.71(9)
O(2)-Fe(1)-Cl(1)*	89.41(11)		
O(2)-Fe(1)-Cl(2)		92.60(3)	116.51(8)
O(1)-Fe(1)-N(1)	88.99(13)	90.38(4)	87.35(10)
O(2)-Fe(1)-N(1)	90.62(13)	90.03(4)	87.71(11)

In 2002, Leznoff and co-workers reported a five-coordinate iron(III) chloride-bridged dimer with a distorted trigonal bipyramidal geometry.¹³ Unlike the coordination environment of **C1**, which contains two anionic oxygen donor atoms and a central nitrogen donor, the iron(III) centre in $\{\text{FeCl}[\text{iBuN}(\text{SiMe}_2)]_2\text{O}\}_2$ is composed of two anionic nitrogen donor atoms and a central, neutral O-donor (**Figure 2.22**). The Fe-Cl bond lengths in $\{\text{FeCl}[\text{iBuN}(\text{SiMe}_2)]_2\text{O}\}_2$ are 2.3181(19) and 2.4652(17) Å whereas the corresponding distances in **C1** are 2.3618(4) and 2.3038(14) Å. The Cl-Fe-Cl bond angle in $\{\text{FeCl}[\text{iBuN}(\text{SiMe}_2)]_2\text{O}\}_2$ is 86.75(6)°, which is lower than the Cl-Fe-Cl angle observed in **C1** (91.42(5)°) and intermediate to those observed in **Dimer A** (87.36(6)°) and **Dimer B** (84.341(14)°). The central, neutral O-donor in $\{\text{FeCl}[\text{iBuN}(\text{SiMe}_2)]_2\text{O}\}_2$ is only weakly bonded to the iron centre, showing a Fe-O bond distance of 2.597(4) Å. However, the anionic nitrogen donors in $\{\text{FeCl}[\text{iBuN}(\text{SiMe}_2)]_2\text{O}\}_2$ show Fe-N bond lengths of 1.894(4) and 1.887(5) Å which are slightly longer than the Fe-N distance of 2.255(3) Å found in **C1**. The sum of bond angles about the equatorial plane in $\{\text{FeCl}[\text{iBuN}(\text{SiMe}_2)]_2\text{O}\}_2$ is only 332.23°, compared to nearly 360° in **C1**, **Dimer A** and **Dimer B**. This suggests that the iron centre in $\{\text{FeCl}[\text{iBuN}(\text{SiMe}_2)]_2\text{O}\}_2$ is more closely tetrahedral in geometry whereas the iron centres in **C1**, **Dimer A** and **Dimer B** possess five strong metal-ligand interactions.

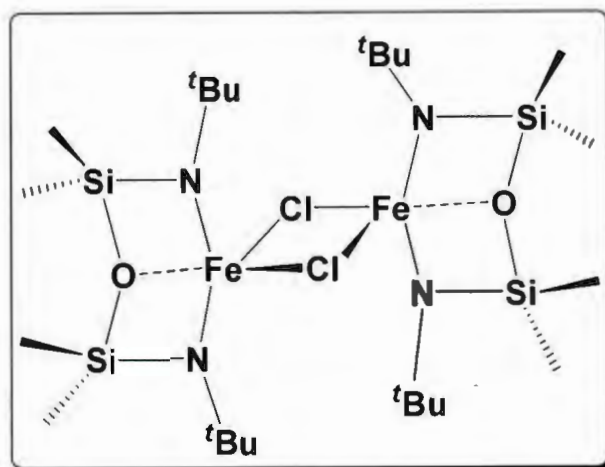


Figure 2.22: A structural representation of $\{\text{FeCl}[\text{tBuN}(\text{SiMe}_2)]_2\text{O}\}_2$ reported by Leznoff and co-workers.¹³

Molecular Structure of C3 and C4:

Slow evaporation of toluene solutions of **C3** and **C4** under a N_2 atmosphere in a glove box provided single crystals suitable for X-ray diffraction analysis. The solid state molecular structures of **C3** and **C4** are shown in **Figure 2.23** and **Figure 2.24**, respectively. The crystallographic data and selected metric parameters of **C3** and **C4** are shown in **Table 2.5** and **Table 2.7**. For **C3** and **C4**, the coordination around the iron atom is distorted trigonal bipyramidal with the trigonality index value (τ) of 0.805 in **C3** and 0.783 in **C4**. The metal is bonded to two phenolate oxygen atoms and a halide ion (a chloride ion in **C3** and a bromide ion in **C4**), which define the trigonal plane of the bipyramid. In **C3** and **C4**, the sum of bond angles about the equatorial plane is 359.89° and 359.85° respectively, indicating near perfect planarity. The central nitrogen atom of the ligand and the oxygen atom of the THF ligand occupy the apical sites of **C3** and **C4**,

giving a O(3)-Fe(1)-N(1) bond angle of $172.0(2)^\circ$ and $171.77(12)^\circ$, respectively. The O(3)-Fe(1)-N(1) angle (for both **C3** and **C4**) is considerably distorted from the ideal linear geometry; it is bent away from the phenolate groups and directed toward the halide ion. The Fe-O distances in **C3** are 1.854(6) and 1.848(6) Å for Fe(1)-O(1) and Fe(1)-O(2), respectively. The iron(III) bromide complex **C4** displays shorter Fe-O bond lengths of 1.8491(18) Å for Fe(1)-O(1) and 1.842(4) Å for Fe(1)-O(2) implying the presence of a slightly stronger iron-oxygen overlap. The Fe(1)-Cl(1) distance of 2.237(3) Å in **C3** is shorter than the Fe-Cl distances found in **C1**, **Dimer A** and **Dimer B**. In addition, the Fe-Cl distance observed in **C3** is slightly shorter than the Fe-Cl distances reported in similar iron(III) trigonal bipyramidal complexes possessing tetradentate amine-bis(phenolate) ligands.¹² The Fe(1)-Br(1) distance of 2.3808(8) Å in **C4** is longer than the Fe(1)-Cl(1) distance of 2.237(3) Å in **C3**. However, the Fe(1)-Br(1) distance in **C4** is shorter than Fe-Br distances reported in other five-coordinate iron(III)-bromide complexes.^{14,15} The central nitrogen donor in the ligand backbone exhibits a Fe-N(1) bond length of 2.190(6) Å in **C3** and 2.185(2) Å in **C4**. These Fe-N distances are slightly shorter than the Fe-N(1) bond length found in **C1** (2.255(3) Å). For **C3** and **C4**, the Fe(1)-O(3) bond lengths are 2.151(6) and 2.145(2) Å respectively, implying that the oxygen atom of the THF ligand in both complexes share approximately the same degree of overlap with the iron(III) centre.

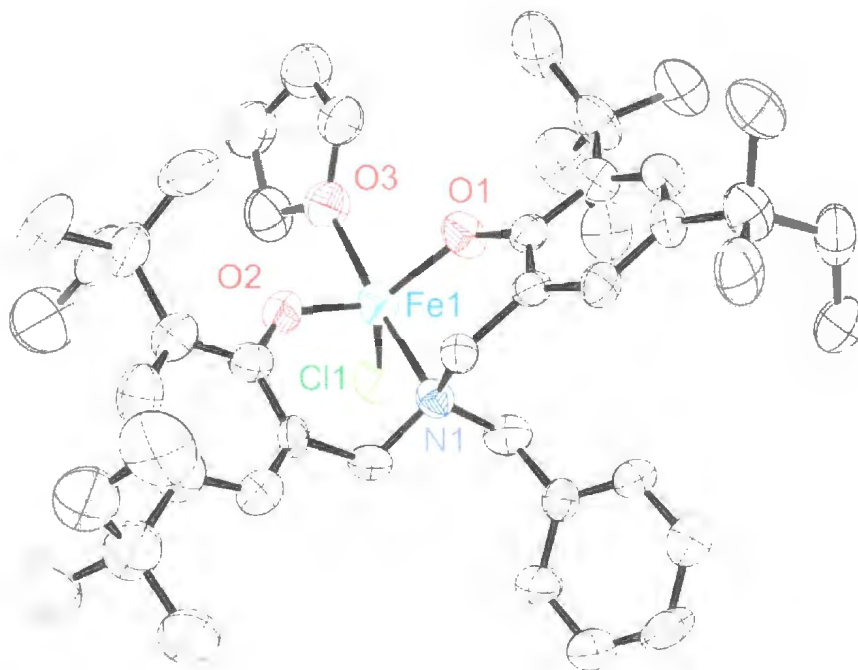


Figure 2.23: Molecular structure (ORTEP) and partial atom labeling of C3. Ellipsoids shown at 50% probability. Hydrogen atoms omitted for clarity.

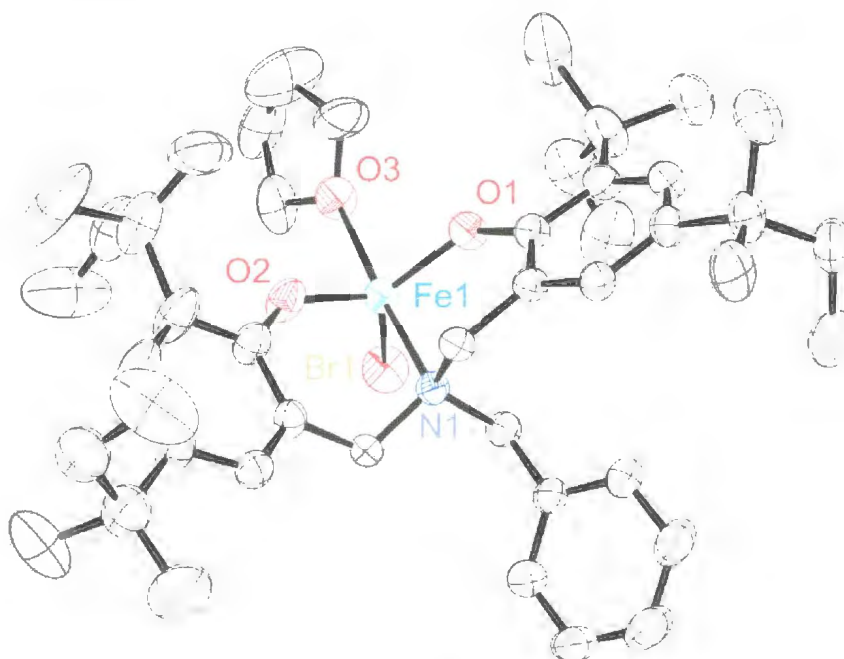


Figure 2.24: Molecular structure (ORTEP) and partial atom labeling of C4. Ellipsoids shown at 50% probability. Hydrogen atoms omitted for clarity.

Table 2.7: Selected bond lengths (Å) and bond angles (°) of **C3**, **C4** and $\text{FeCl}[\text{O}_2\text{NO}']^{\text{BuMeFurf}}$.

	C3	C4	$\text{FeCl}[\text{O}_2\text{NO}']^{\text{BuMeFurf}}$
Fe(1)-O(1)	1.854(6)	1.8491(18)	1.850(2)
Fe(1)-O(2)	1.848(6)	1.842(4)	1.854(2)
Fe(1)-O(3)	2.151(6)	2.145(2)	2.074(3)
Fe(1)-N(1)	2.190(6)	2.185(2)	2.223(3)
Fe(1)-Cl(1)	2.237(3)		2.2739(10)
Fe(1)-Br(1)		2.3808(8)	
O(1)-Fe(1)-O(2)	123.7(3)	124.80(14)	118.39(10)
N(1)-Fe(1)-Cl(1)	96.12(17)		165.69(8)
N(1)-Fe(1)-Br(1)		96.79(8)	
N(1)-Fe(1)-O(3)	172.0(2)	171.77(12)	75.79(10)
Cl(1)-Fe(1)-O(3)	91.72(18)		89.98(8)
Br(1)-Fe(1)-O(3)		91.36(10)	
O(1)-Fe(1)-Cl(1)	121.49(20)		100.81(8)
O(1)-Fe(1)-Br(1)		120.17(11)	
O(1)-Fe(1)-O(3)	86.7(2)	86.89(9)	119.00(11)
O(2)-Fe(1)-Cl(1)	114.7(2)		96.60(8)
O(2)-Fe(1)-Br(1)		114.88(9)	
O(2)-Fe(1)-O(3)	88.6(2)	88.17(12)	119.60(11)
O(1)-Fe(1)-N(1)	88.0(2)	88.03(8)	87.62(10)
O(2)-Fe(1)-N(1)	89.4(2)	89.41(11)	89.37(10)

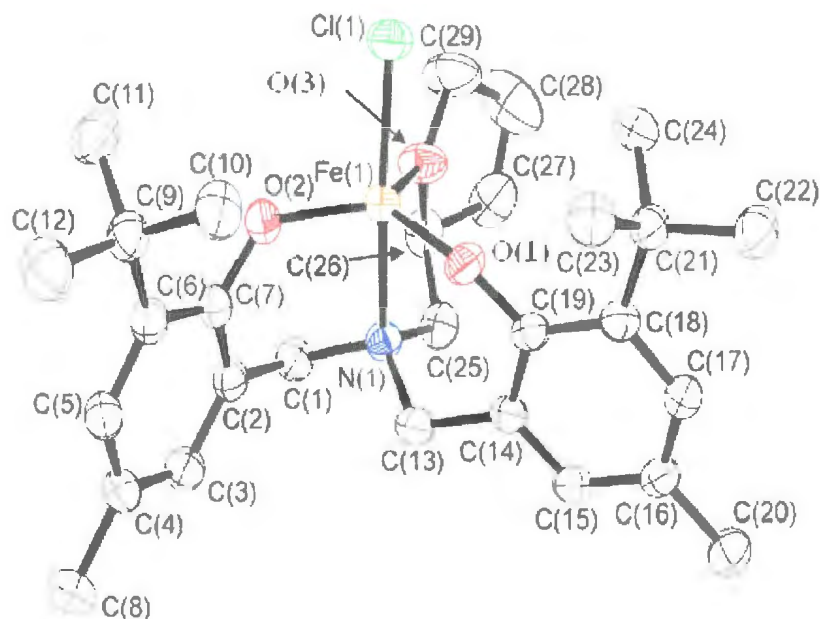


Figure 2.25: X-ray crystal structure of $\text{FeCl}[\text{O}_2\text{NO}']^{\text{BuMeFurf}}$ previously reported in the Kozak group.¹⁶ Ellipsoids shown at 50% probability. Hydrogen atoms omitted for clarity.

The coordination environment of **C3** shares striking similarities with an iron(III)-chloride complex previously reported by the Kozak group. Like **C3**, the coordination geometry around the iron atom in $\text{FeCl}[\text{O}_2\text{NO}']^{\text{BuMeFurf}}$ is trigonal bipyramidal (**Figure 2.25**).¹⁶ However, unlike **C3**, which possesses a tridentate amine-bis(phenolate) ligand (with bulky *tert*-amyl substituents), the iron atom in $\text{FeCl}[\text{O}_2\text{NO}']^{\text{BuMeFurf}}$ is supported by a tetradentate amine-bis(phenolate) ligand containing a pendant tetrahydrofurfuryl group. A comparison of selected metric parameters can be found in **Table 2.7**. In $\text{FeCl}[\text{O}_2\text{NO}']^{\text{BuMeFurf}}$, two phenolate oxygen atoms and the furfuryl oxygen atom define the bipyramid. As seen in **Figure 2.23**, the THF ligand in **C3** is located in the axial position. The chloride ion of **C3** and $\text{FeCl}[\text{O}_2\text{NO}']^{\text{BuMeFurf}}$ are also located in different planes about the iron(III) centre; the chloride ion is located in the equatorial plane of **C3**

and in the axial plane of $\text{FeCl}[\text{O}_2\text{NO}']^{\text{BuMeFurf}}$. In **C3**, a shorter Fe-Cl bond length (2.237(3) Å) is observed compared to the Fe-Cl distance in $\text{FeCl}[\text{O}_2\text{NO}']^{\text{BuMeFurf}}$ (2.2739(10) Å) since the chloride ion in the latter compound is *trans* to the amine nitrogen donor. The Fe-O(3) bond length in $\text{FeCl}[\text{O}_2\text{NO}']^{\text{BuMeFurf}}$ (which originates from the chelating tetrahydrofurfuryl pendant arm) is shorter than the Fe-O(3) distance observed in **C3**. For **C3** and $\text{FeCl}[\text{O}_2\text{NO}']^{\text{BuMeFurf}}$, the coordination around the iron atom is distorted trigonal bipyramidal with the trigonality index value (τ) of 0.805 in **C3** and 0.768 in $\text{FeCl}[\text{O}_2\text{NO}']^{\text{BuMeFurf}}$.

Molecular Structure of C5 and C7:

Single crystals of **C5** and **C7** suitable for X-ray diffraction were obtained from saturated toluene solutions at -35 °C inside a nitrogen filled glove box. The solid state molecular structures of **C5** and **C7** are shown in **Figure 2.26** and **Figure 2.27**, respectively. The crystallographic data and selected metric parameters of **C5** and **C7** are shown in **Table 2.5** and **Table 2.8**, respectively. In the solid state, complexes **C5** and **C7** exhibit monomeric structures having tetrahedral iron(III) centres. Unlike complexes **C1-C4**, and also unlike the previously reported iron(III) complexes of amine-bis(phenolate) ligands,^{12,17,18} the bis(phenolate) ligand in **C5** and **C7** binds in a bidentate fashion. In both complexes (**C5** and **C7**), the central nitrogen donor is protonated giving a quaternized ammonium group. The oxygen donors of the phenolate groups remain anionic, giving a net monoanionic ammonium-bis(phenolate) ligand. Two bromide ions and the phenolate oxygen donor atoms make up the tetrahedral coordination environment about the iron(III)

centre in both **C5** and **C7**. The four-coordinate tetrahedral iron(III) centre is thereby formally anionic, resulting in an overall zwitterionic iron(III) complex. The bond angles around the metal range from 106.38(13)° to 110.90(9)° in **C5**, and 105.9(3)° to 112.0(2)° in **C7**, which are only moderately distorted from the ideal tetrahedral angle of 109.5°. The bond lengths of Fe-Br(1) and Fe-Br(2) are slightly asymmetrical in **C5** and **C7**. The Fe-Br distances in **C5** are 2.3596(9) and 2.3491(8) Å for Fe-Br(1) and Fe-Br(2) respectively, while the Fe-Br distances in **C7** are 2.355(2) and 2.3697(19) Å for Fe-Br(1) and Fe-Br(2), respectively. The Fe-Br distances observed in **C5** are slightly shorter than the terminally bonded Fe-Br bond length (2.3683(11) Å) found in a mononuclear square pyramidal iron(III) bromide complex (FeBr[O₂N₂]^{BuBu}) containing a salan ligand, previously reported in the Kozak group.¹⁴ The Fe-Br distance of 2.3683(11) Å is intermediate to the Fe-Br bond lengths observed in the more sterically congested **C7**. In **C5**, the phenolate oxygen atoms exhibit bond distances to iron of 1.822(2) and 1.832(3) Å for Fe-O(1) and Fe-O(2), respectively. The Fe-O(1) and Fe-O(2) bond lengths observed in the related complex **C7** (containing bulkier 2,4-di-*tert*-butylphenolate groups) are slightly longer, with distances of 1.843(6) and 1.851(6) Å, respectively. The Fe-O interactions observed in **C5** and **C7** are similar to those observed in FeBr[O₂N₂]^{BuBu}, where average Fe-O distances of 1.837 Å are observed.¹⁴

The coordination geometry of **C5** and **C7** are similar to a tetrahedral iron(III) complex previously reported by Kozak and co-workers.⁶ Like **C5**, FeBr₂[O₂NH]^{BuMenPr} contains 2-*tert*-butyl-4-methylphenolate groups. However, unlike both **C5** and **C7**, which possess an isopropyl alkyl group on the central nitrogen donor, the central nitrogen donor of FeBr₂[O₂NH]^{BuMenPr} contains a *n*-propyl alkyl substituent. The molecular structure of

$\text{FeBr}_2[\text{O}_2\text{NH}]^{\text{BuMenPr}}$ and selected metric parameters can be found in **Figure 2.28** and **Table 2.8**, respectively. As seen in **Table 2.8**, the Fe-O bond lengths observed in $\text{FeBr}_2[\text{O}_2\text{NH}]^{\text{BuMenPr}}$ are slightly shorter than the corresponding Fe-O distances found in **C7**. However, the Fe-O bond lengths are very similar to those observed in **C5**. Similarly, as found in both **C5** and **C7**, the Fe-Br bond lengths observed in $\text{FeBr}_2[\text{O}_2\text{NH}]^{\text{BuMenPr}}$ are slightly asymmetrical. The Fe-Br(2) bond length (2.3723(7) Å) observed in $\text{FeBr}_2[\text{O}_2\text{NH}]^{\text{BuMenPr}}$ is slightly longer than the Fe-Br distances found in **C5** and **C7**. The bond angles around the iron centre range from 105.24(15)° to 112.87(10)° in $\text{FeBr}_2[\text{O}_2\text{NH}]^{\text{BuMenPr}}$ and 106.38(13)° to 110.90(9)° in **C5**. Since both complexes share the same substituents on the phenolate rings, the differences in bond angles observed may be attributed to the differences in sterics originating from the alkyl substituents on the central nitrogen donor.

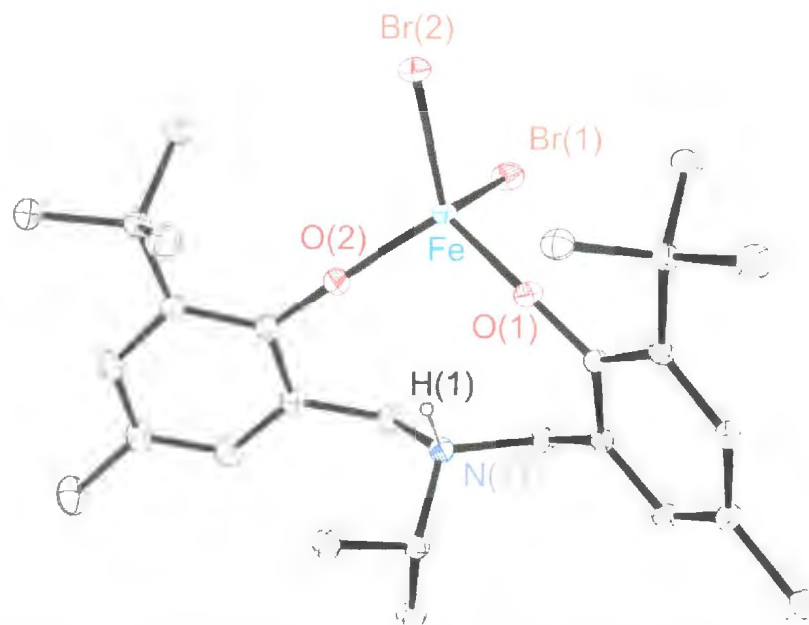


Figure 2.26: Molecular structure (ORTEP) and partial atom labeling of C5. Ellipsoids shown at 30% probability. The co-crystallized toluene, pentane molecules and hydrogen atoms omitted for clarity (except for H(1)).

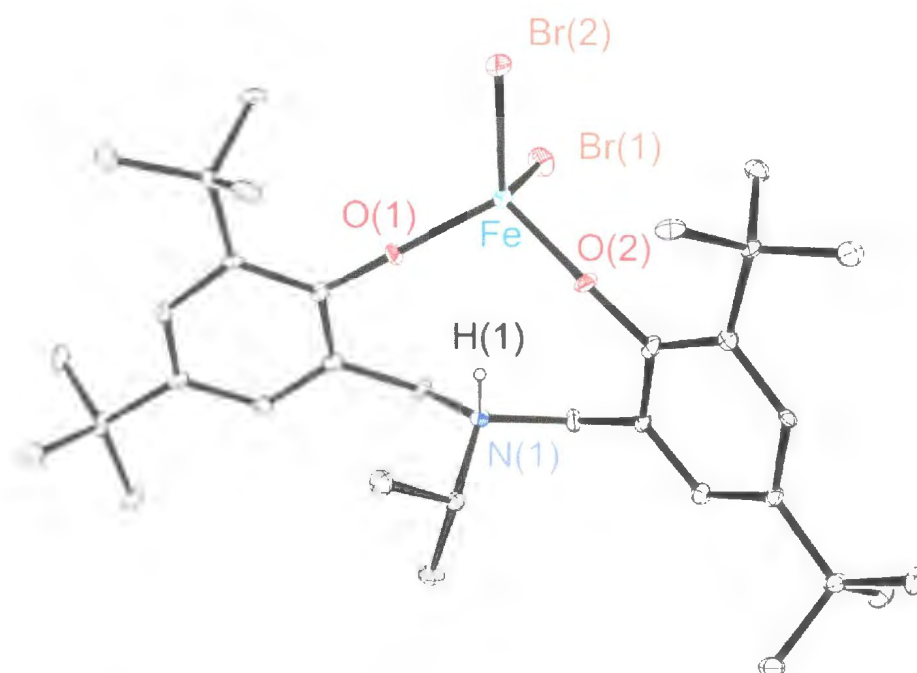


Figure 2.27: Molecular structure (ORTEP) and partial atom labeling of C7. Ellipsoids shown at 30% probability. The co-crystallized toluene molecule and hydrogen atoms omitted for clarity (except for H(1)).

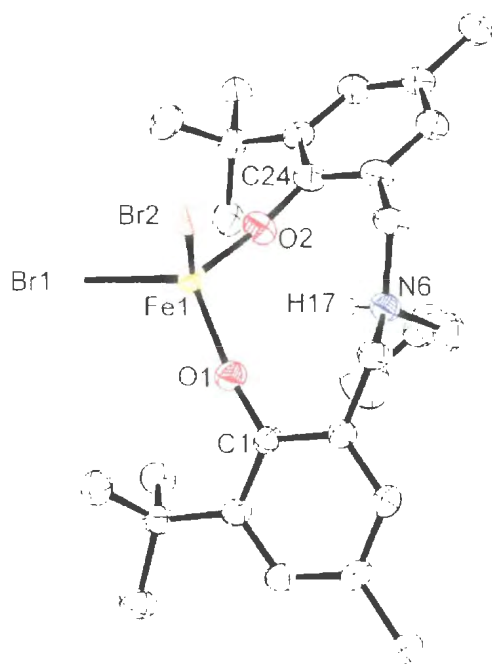


Figure 2.28: Molecular structure (ORTEP) and partial atom labeling of $\text{FeBr}_2[\text{O}_2\text{NH}]\text{BuMenPr}$ previously reported in the Kozak group.⁶ Ellipsoids shown at 50% probability. Hydrogen atoms omitted for clarity

Table 2.8: Selected bond lengths (Å) and bond angles (°) of **C5**, **C7** and $\text{FeBr}_2[\text{O}_2\text{NH}]^{\text{BuMenPr}}$.

	C5	C7	$\text{FeBr}_2[\text{O}_2\text{NH}]^{\text{BuMenPr}}$
Fe(1)-O(1)	1.822(2)	1.843(6)	1.828(3)
Fe(1)-O(2)	1.832(3)	1.851(6)	1.836(3)
Fe(1)-Br(1)	2.3596(9)	2.355(2)	2.3569(7)
Fe(1)-Br(2)	2.3491(8)	2.3697(19)	2.3723(7)
Fe...N	3.439(4)	3.429(7)	3.435(3)
O(1)-Fe(1)-O(2)	106.38(13)	105.9(3)	105.24(15)
O(1)-Fe(1)-Br(1)	108.43(8)	108.9(2)	110.72(9)
O(1)-Fe(1)-Br(2)	110.90(9)	110.8(2)	109.24(15)
O(2)-Fe(1)-Br(1)	110.71(9)	107.5(3)	112.87(10)
O(2)-Fe(1)-Br(2)	110.08(9)	112.0(2)	108.93(9)
Br(1)-Fe(1)-Br(2)	110.26(3)	111.53(7)	109.54(2)

Previously, Leznoff and co-workers reported two different tetrahedral iron(III) bromide complexes which share a similar coordination geometry with **C5** and **C7**.^{19,20} However, unlike the monomeric structure observed in **C5** and **C7**, the iron (III) complexes reported by the Leznoff group exhibit dimeric structures resulting in tetrahedral iron(III) centres bridged by bromide ligands. Structural representations of $\{\text{FeBr}[\text{MesN}(\text{SiMe}_2)]_2\text{O}\}_2$ and $\{\text{FeBr}_2\text{Li}[\text{Me}_3\text{PhN}(\text{SiMe}_2)]_2\text{O}\}_2$ can be found in **Figure 2.29**, while selected metric parameters can be located in **Table 2.9**. Compared to the bromide-bridged dimers reported by Leznoff and co-workers, **C5** and **C7** exhibit an unusual, neutral iron(III) dibromide tetrahedral environment. As seen in **Table 2.9**, the

Fe-Br distances observed in $\{\text{FeBr}[\text{MesN}(\text{SiMe}_2)]_2\text{O}\}_2$ and $\{\text{FeBr}_2\text{Li}[\text{Me}_3\text{PhN}(\text{SiMe}_2)]_2\text{O}\}_2$ are slightly longer than the Fe-Br bond lengths found in **C5** and **C7** (Table 2.9).

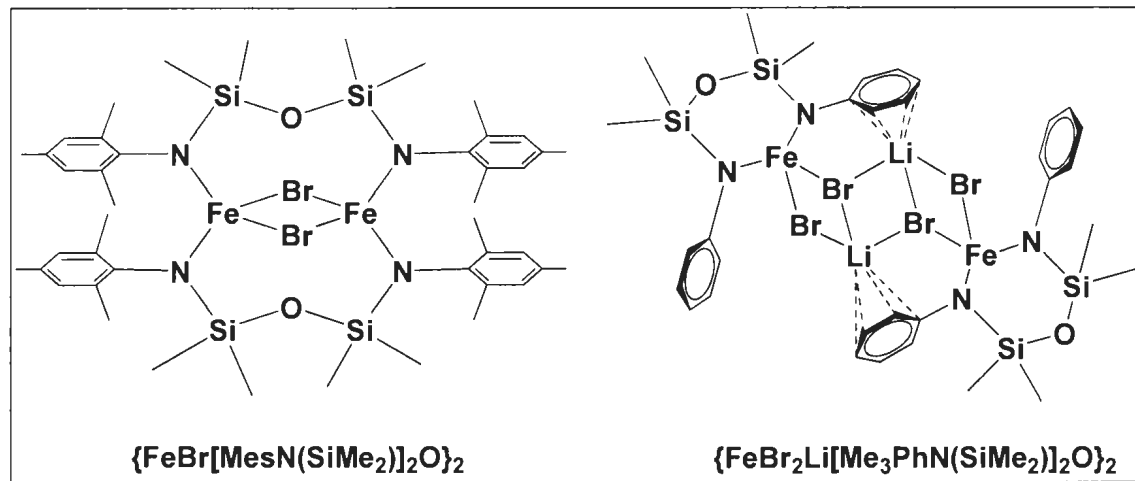


Figure 2.29: A structural representation of iron(III) bromide-bridged dimers previously reported by Leznoff and co-workers.^{19, 20}

Table 2.9: Selected bond lengths (Å) observed in $\{\text{FeBr}[\text{MesN}(\text{SiMe}_2)]_2\text{O}\}_2$ and $\{\text{FeBr}_2\text{Li}[\text{Me}_3\text{PhN}(\text{SiMe}_2)]_2\text{O}\}_2$.^{21, 22}

Bond	$\{\text{FeBr}[\text{MesN}(\text{SiMe}_2)]_2\text{O}\}_2$	$\{\text{FeBr}_2\text{Li}[\text{Me}_3\text{PhN}(\text{SiMe}_2)]_2\text{O}\}_2$
Fe-Br(1)	2.471(2)	2.4601(11)
Fe-Br(2)	2.503(2)	2.4313(11)
Fe-N(1)	1.864(8)	1.905(4)
Fe-N(2)	1.880(7)	1.877(5)

Molecular Structure of C6:

Single crystals of **C6** suitable for X-ray diffraction were obtained from a saturated toluene solution at -35 °C inside a nitrogen filled glove box. The solid state molecular structure of **C6** is shown in **Figure 2.30**, while crystallographic data and selected metric parameters are shown in **Table 2.5** and **Table 2.10**, respectively. In the solid state, **C6** exhibits a dimeric structure resulting in a trigonal bipyramidal iron(III) centre bridged by hydroxide ligands. A similar compound ($[\text{Fe}(\text{ONO})^{\text{BuMeMe}}(\mu\text{-OH})]_2$) has been previously reported by Chaudhuri and co-workers (**Figure 2.31**).²³ However, unlike **C6**, which contains 2,4-di-*tert*-butylphenolate groups, $[\text{Fe}(\text{ONO})^{\text{BuMeMe}}(\mu\text{-OH})]_2$ possesses less sterically congested 2-*tert*-butyl-4-methylphenolate groups. In addition, the central nitrogen donors of $[\text{Fe}(\text{ONO})^{\text{BuMeMe}}(\mu\text{-OH})]_2$ contain a methyl alkyl substituent, while the central nitrogen donors of **C6** possess bulkier isopropyl alkyl groups. A structural representation of $[\text{Fe}(\text{ONO})^{\text{BuMeMe}}(\mu\text{-OH})]_2$ can be found in **Figure 2.31**, while selected metric parameters can be located in **Table 2.10**. The Fe...Fe* distance of 3.13645(17) Å in **C6**, which is slightly longer than the Fe...Fe* distance (3.066 Å) observed in $[\text{Fe}(\text{ONO})^{\text{BuMeMe}}(\mu\text{-OH})]_2$, precludes any bonding interaction between the metal centres. Like $[\text{Fe}(\text{ONO})^{\text{BuMeMe}}(\mu\text{-OH})]_2$, two phenolate oxygen donor atoms and a bridging hydroxo oxygen atom occupy the equatorial plane around each iron ion in **C6**. The sum of bond angles about the equatorial plane is 359.70° in **C6** and 359.97° in $[\text{Fe}(\text{ONO})^{\text{BuMeMe}}(\mu\text{-OH})]_2$, indicating near perfect planarity. The amine nitrogen and the bridging hydroxo oxygen atom O(3)* take up the axial positions, giving an O(3)*-Fe-N bond angle of 169.9(3)° in **C6** and 171.72(4)° in $[\text{Fe}(\text{ONO})^{\text{BuMeMe}}(\mu\text{-OH})]_2$, which is considerably distorted from the ideal linear geometry; it is bent away from the phenolate

groups and directed towards the other bridging hydroxo group. The *cis*-orientated oxygen atoms of the bridging hydroxo groups possess an O(3)-Fe-O(3)* bond angle of 76.38(5)° in **C6**. The comparable angle is 77.64(5) ° in [Fe[ONO]^{BuMeMe}(μ-OH)]₂, which deviates considerably from an orthogonal bonding angle of 90°. The Fe-O(3)-Fe* bridge angle in **C6** is 103.6(4)°, which is slightly larger than the Fe-O(3)-Fe* angle of 102.36(5)° observed in [Fe[ONO]^{BuMeMe}(μ-OH)]₂. The asymmetric nature of the bridging hydroxo oxygen atoms in **C6** and [Fe[ONO]^{BuMeMe}(μ-OH)]₂ is demonstrated by the different Fe-O bond lengths observed for Fe-O(3) and Fe-O(3)*. In **C6**, the Fe-O(3) and Fe-O(3)* bond lengths are 2.010(8) Å and 1.980(8) Å, respectively. As seen in **Table 2.10**, these bond distances are slightly longer than the corresponding bond lengths observed in [Fe[ONO]^{BuMeMe}(μ-OH)]₂. In **C6**, the Fe-O(1) distance of 1.857(8) Å and Fe-O(2) length of 1.870(8) Å are very similar to the Fe-O(1) and Fe-O(2) distances in [Fe[ONO]^{BuMeMe}(μ-OH)]₂ of 1.8570(11) and 1.8605(11) Å, respectively.

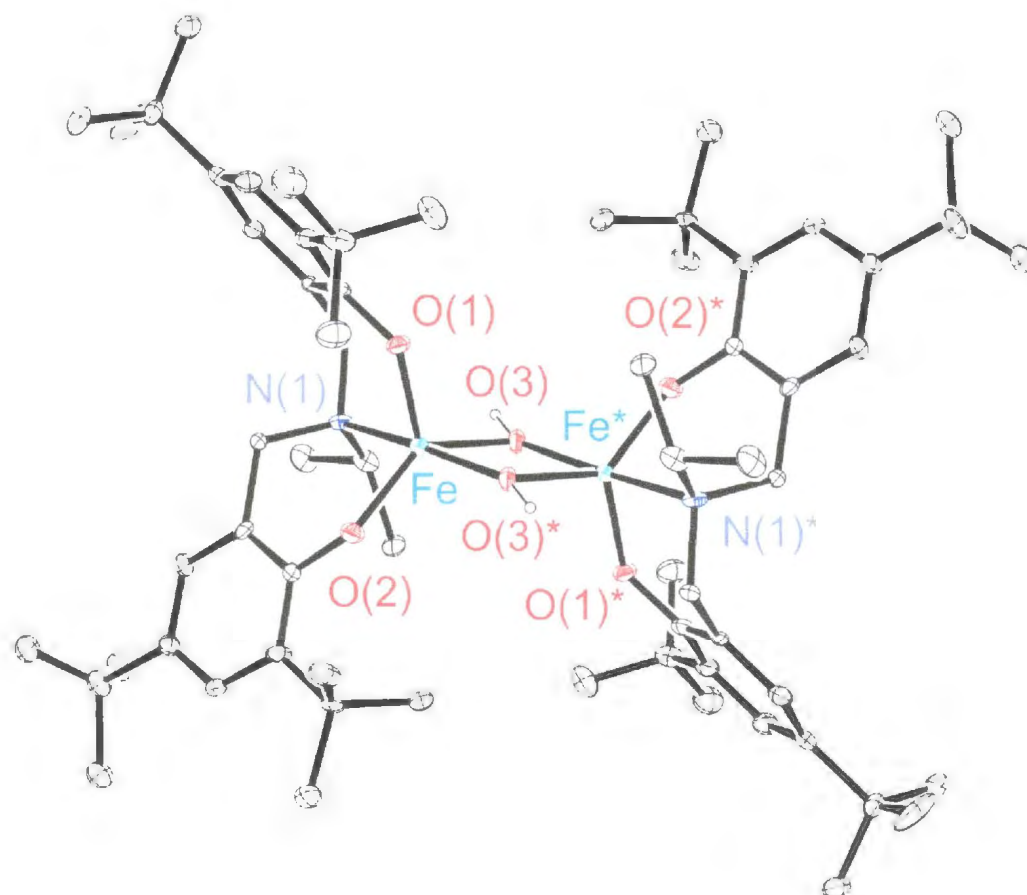


Figure 2.30: Molecular structure (ORTEP) and partial atom labeling of C6. Ellipsoids shown at 30% probability. The co-crystallized toluene molecule and hydrogen atoms omitted for clarity (except for H on O(3) and O(3)*). Symmetry operators used to generate equivalent atoms: (*) $-x + 1, -y + 1, -z + 1$.

Table 2.10: Selected bond lengths (Å) and bond angles (°) of [Fe(ONO)^{BuMeMe}(μ-OH)₂ and C6.²³

	C6	[Fe(ONO) ^{BuMeMe} (μ-OH) ₂
Fe-O(1)	1.857(8)	1.8570(11)
Fe-O(2)	1.870(8)	1.8605(11)
Fe-O(3)	1.980(8)	1.9305(10)
Fe-O(3)*	2.010(8)	2.0037(11)
Fe-N	2.214(10)	2.1942(12)
Fe...Fe*	3.13645(17)	3.066
O(1)-Fe-O(2)	116.9(4)	121.03(5)
O(1)-Fe-O(3)	110.2(4)	117.54(5)
O(2)-Fe-O(3)	132.6(4)	121.40(5)
O(1)-Fe-O(3)*	96.4(3)	96.15(5)
O(2)-Fe-O(3)*	93.5(3)	94.41(5)
O(3)-Fe-O(3)*	76.38(5)	77.64(5)
O(1)-Fe-N(1)	91.4(3)	89.25(5)
O(2)-Fe-N(1)	88.6(3)	88.14(5)
O(3)-Fe-N(1)	95.0(3)	94.31(5)
O(3)*-Fe-N(1)	169.9(3)	171.72(4)
Fe-O(3)-Fe*	103.6(4)	102.36(5)

For C6: There is likely to be some inaccuracy in bond distances and angles due to the low cut-off in 2θ (45°). This was done due to very weak diffraction at high angles.

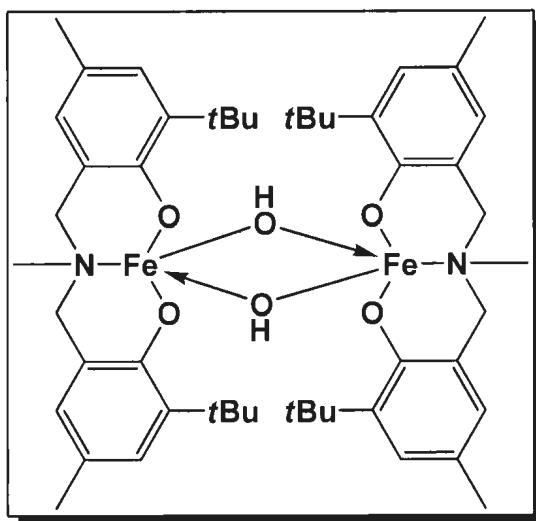


Figure 2.31: A structural representation of $[\text{Fe}(\text{ONO})^{\text{BuMeMe}}(\mu\text{-OH})]_2$ reported by Chaudhuri and co-workers.²³

2.2.3.4 UV-visible Spectroscopy

The complex **C3**, which is an intensely purple-coloured solid, was analyzed via UV-visible spectroscopy. An electronic absorption spectrum shows multiple intense bands in the UV (ultraviolet) and visible regions (**Figure 2.32**) which is consistent with other iron(III) amine-bis(phenolate) complexes reported in the literature.⁶ The absorption maxima observed in the UV region (below 250 nm) are attributed to $\pi \rightarrow \pi^*$ transitions originating from the phenolate units. In fact, absorptions in this region have been previously observed in the spectra of the unmetallated ligand precursors.²⁴ Other intense absorptions are also observed between 300-375 nm (UV region), and are assigned as ligand-to-metal ($\text{L} \rightarrow \text{M}$) charge transfer transitions from the out of plane p_π orbital (HOMO) of the phenolate oxygen to the partially-filled dx^2-y^2/dz^2 orbital of high spin

iron(III). The lowest energy bands (visible region) arise from $L \rightarrow M$ charge transfer transitions from the in-plane p_π orbital of the phenolate oxygen to the half-filled d_{π^*} orbital of iron(III).

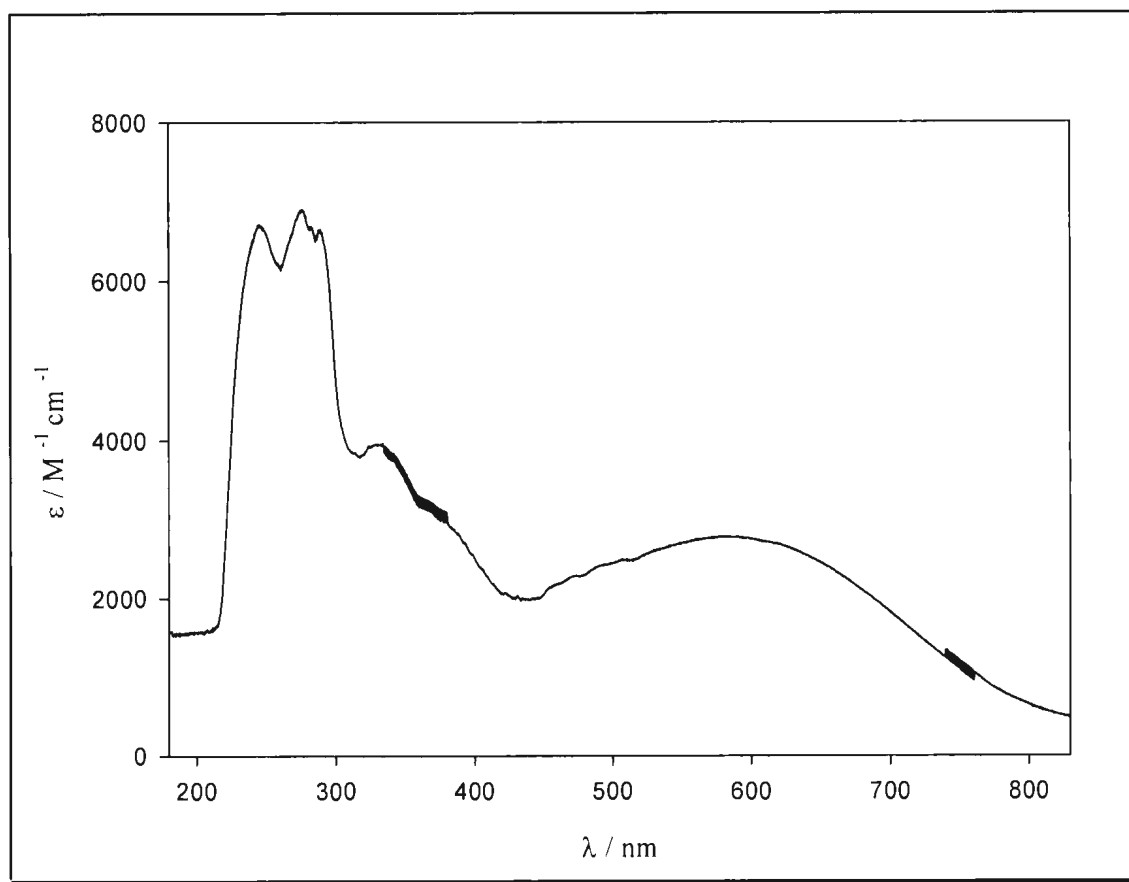


Figure 2.32: UV-vis spectrum of **C3**. Methanol used as the solvent.

2.2.3.5 Inductively Coupled Plasma Mass Spectrometry

According to previous reports in the literature, C-C cross-coupling reactions can be largely affected by trace metal impurities.²⁵ The use of FeCl_3 as a catalyst has become controversial in recent times, since yields often vary according to its purity and commercial origin.²⁶ In 2009, Bolm and co-workers investigated different sources of FeCl_3 in the couplings of pyrazole, phenyl amide, phenol and thiophenol with aryl iodides. Bolm determined that the cross-coupling reactions may in certain cases be significantly affected by trace quantities of other metals, particularly copper.²⁷

Table 2.11: ICP-MS analysis of FeCl_3 , $\text{Fe}(\text{acac})_3$ and **C3**.

Compound	Pd (ppm)	Ni (ppm)	Pt (ppm)	Cu (ppm)
$\text{Fe}(\text{acac})_3$	0.342	13.98	0.518	15.3
FeCl_3	0.011	107.19	0.000	99.0
C3	0.026	0.00	0.000	1.6

In this project, complex **C3** will be used in the catalysis studies. In order to assess the purity of **C3**, a recrystallized sample was analyzed via inductively coupled plasma mass spectrometry (ICP-MS) and the level(s) of trace metal impurities were compared to $\text{Fe}(\text{acac})_3$ and FeCl_3 , which were used as starting materials in the synthesis of the complexes. As seen in **Table 2.6**, both $\text{Fe}(\text{acac})_3$ and FeCl_3 have a considerably higher level of Ni and Cu than **C3**. The lower level of Cu and Ni in **C3**, compared to the starting material FeCl_3 , is likely attributed to the purification procedure employed during its isolation. Surprisingly, **C3** contains a slightly higher level of palladium than FeCl_3 .

However, this is likely a result of contamination during the complex synthesis. According to the ICP-MS analysis, both FeCl_3 and **C3** have no level of Pt present (within the parts per million (ppm) detection limit).

2.2.3.6 Magnetic Data

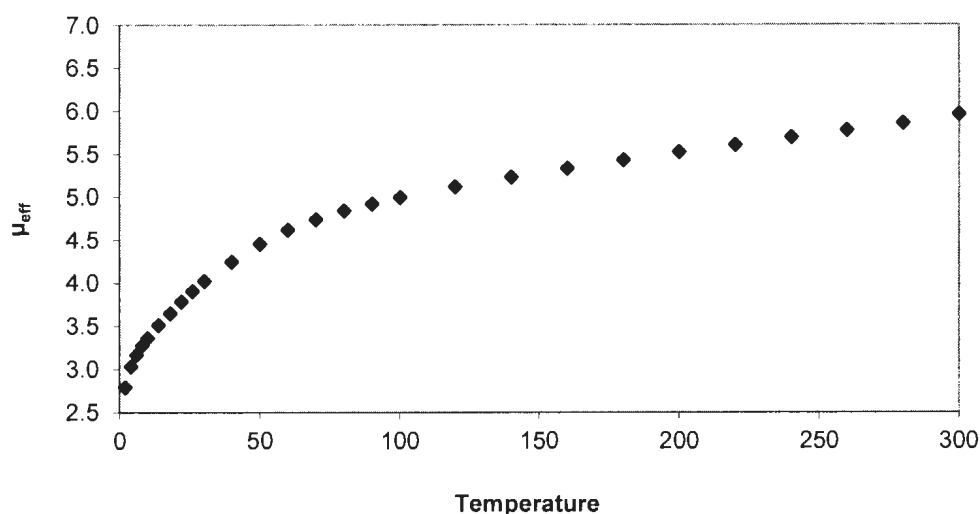


Figure 2.33: Magnetic moment per mol of dimer vs. temperature for **C6**.

The temperature dependent magnetic behavior of **C6** was examined in the temperature range of 2 to 300 K in an applied magnetic field of 1 T. The magnetic behavior of **C6** is characteristic of an antiferromagnetically coupled dinuclear complex. Variable temperature magnetic studies show the μ_{eff} value of $5.96 \mu_B$ at 300 K to decrease monotonically with decreasing temperature until it reaches a value of $2.79 \mu_B$ at 2 K.

(Figure 2.33). This suggests a small degree of exchange coupling between two paramagnetic high-spin iron(III) centres ($S_{\text{Fe}} = 5/2$). Also, since there is no maximum observed in the plot of susceptibility, χ , vs. T (see appendix), the exchange coupling between the two metal centers would be very small. The moment at 2 K is higher than expected for a $S_T = 0$ ground state and suggests the presence of a temperature independent paramagnetic impurity. In fact, when variable temperature magnetic studies were performed on a similar complex ($[\text{Fe}(\text{ONO})^{\text{BuMeMe}}(\mu\text{-OH})]_2$) reported by Chaudhuri and co-workers,²³ the magnetic moment at 2 K was determined to be approximately $1.20 \mu_{\text{B}}$ (Figure 2.34).

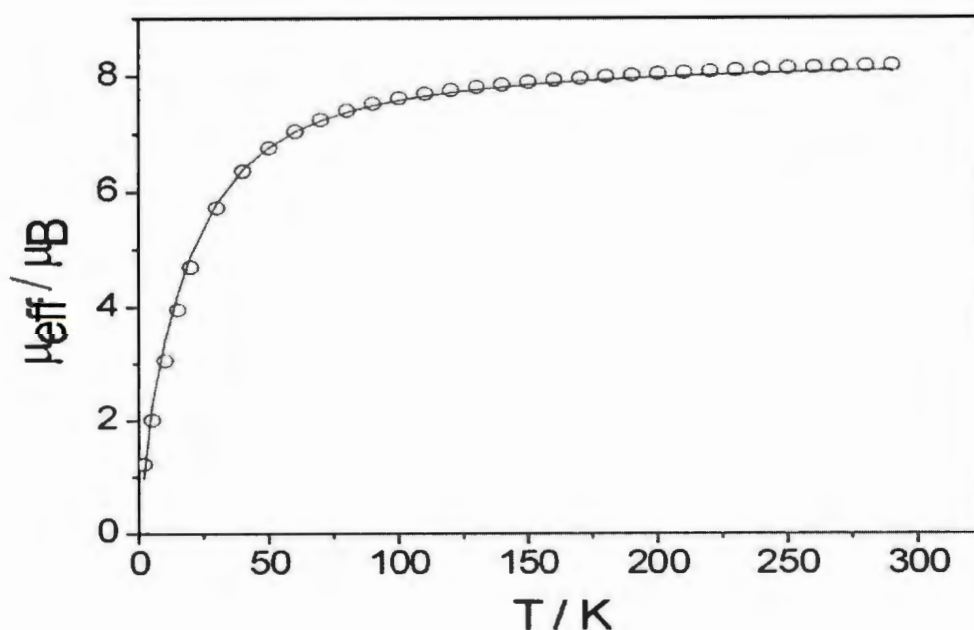


Figure 2.34: Magnetic moment per mol of dimer vs. temperature for $[\text{Fe}(\text{ONO})^{\text{BuMeMe}}(\mu\text{-OH})]_2$. [Reprinted with permission from P. Chaudhuri, T. Weyhermüller, R. Wagner, *Eur. J. Inorg. Chem.*, **2011**, 2547.]

Similar weak antiferromagnetic coupling has also been observed in $[\text{Fe}(\text{ONO})^{\text{BuMeMe}}(\mu\text{-OH})]_2$.²³ According to Chaudhuri and co-workers, the bridging Fe-O-Fe angle is a major factor in determining the strength of the exchange interaction between the two iron centres.²³ The Fe-O-Fe bridging angle ($103.6(4)^\circ$) in **C6** is slightly larger than the bridging angle ($102.36(5)^\circ$) observed in the iron(III) hydroxy-bridged dimer $[\text{Fe}(\text{ONO})^{\text{BuMeMe}}(\mu\text{-OH})]_2$ (**Figure 2.31**) reported by the Chaudhuri group which exhibits a rare case of exchange-coupled five-coordinate ferric(III) centres.²³ In the plot of μ_{eff} vs. temperature for $[\text{Fe}(\text{ONO})^{\text{BuMeMe}}(\mu\text{-OH})]_2$ (**Figure 2.34**), the moment drops rapidly to $1.22 \mu_{\text{B}}$ at 2 K (below 50 K). Since both complexes (**C6** and $[\text{Fe}(\text{ONO})^{\text{BuMeMe}}(\mu\text{-OH})]_2$) possess dibridged four-membered $\text{Fe}_2(\mu\text{-OH})_2$ structure cores (along with a very similar amine-bis(phenolate) ligand backbone), the differences in antiferromagnetic coupling observed may be attributed to the different bridging angles observed in each compound or the presence of paramagnetic impurities. Of course, since the average Fe-O(bridging) bond lengths observed in **C6** (1.996 \AA) are slightly longer than the average Fe-O(bridging) bond lengths observed in $[\text{Fe}(\text{ONO})^{\text{BuMeMe}}(\mu\text{-OH})]_2$ (1.966 \AA), differences in Fe-O(bridging) bond lengths cannot be discounted as a contributor in the differences of antiferromagnetic coupling observed.

2.3 Experimental Section

2.3.1 General Methods and Materials

All ligands (**H₂L1**-**H₂L6**) were synthesized in the presence of air. Unless otherwise stated, all iron complexes were synthesized under an atmosphere of dry oxygen-free nitrogen by means of standard Schlenk techniques or by using an MBraun LabmasterDP glove box. THF was stored over sieves and distilled from sodium benzophenone ketyl under nitrogen. Anhydrous toluene was purified using an MBraun solvent purification system. Anhydrous FeCl₃ (97%) was used for the synthesis of **C1-C3**. Anhydrous FeBr₃ (99%) was obtained from Strem Chemicals for the preparation of **C4-C7**. Reagents were purchased either from Strem, Aldrich or Alfa Aesar and used without further purification.

2.3.2 Instrumentation

NMR spectra were recorded using CDCl₃ solutions with a Bruker Avance III 300 MHz instrument with a 5 mm-multinuclear broadband observe (BBFO) probe. MALDI-TOF MS spectra were performed using an ABI QSTAR XL Applied Biosystems/MDS hybrid quadrupole TOF MS/MS system equipped with an oMALDI-2 ion source. Samples were prepared at a concentration of 10.0 mg/mL in toluene. Anthracene was used as the matrix, which was mixed at a concentration of 10.0 mg/mL. UV-vis spectra were recorded with an Ocean Optics USB4000+ fiber optic spectrophotometer. IR spectra were recorded with a Bruker Alpha IR spectrometer equipped with a diamond crystal ATR module. HRMS spectra were recorded using a High Resolution MSD Waters

Micromass GCT Premier spectrometer equipped with an electron impact ion source and a time-of-flight (oa-TOF) mass analyzer. Melting point data were collected on a MPA100 OptiMelt Automated Melting Point System. Magnetic susceptibility data were acquired in the solid state using a Quantum Designs MPMS5 SQUID magnetometer. Elemental analyses were carried out by Canadian Micro-analytical Services Ltd. Delta, BC, Canada, or by Guelph Chemical Laboratories Ltd. Guelph, Ontario, Canada. The crystal structures were collected on a AFC8-Saturn 70 single crystal X-ray diffractometer from Rigaku/MSO, equipped with an X-stream 2000 low temperature system.

2.3.3 Synthesis

$\text{H}_2[\text{O}_2\text{N}]^{\text{BuMeiPr}}(\text{H}_2\text{L1})$:

To a stirred mixture of 2-*t*-butyl-4-methylphenol (20.398 g, 0.1232 mol) in 100 mL of deionized water was added 37% aqueous formaldehyde (10 mL, 0.1232 mol) followed by slow addition of isopropylamine (3.55 g, 0.0615 mol). The reaction was heated to reflux for 12 hours. Upon cooling, the reaction mixture separated into two phases. The upper phase was decanted and the remaining oily residue was triturated with cold methanol to give an analytically pure, white powder (16.25 g, 64%). ^1H NMR (300 MHz, CDCl_3 , δ): 7.00 (s, ArH, 2H); 6.73 (s, ArH, 2H); 3.65 (s, CH_2 , 4H); 3.16 (septet, $^3J = 5$ Hz, CH, 1H); 2.24 (s, CH_3 , 6H); 1.39 (s, CH_3 , 18H); 1.17 (d, $^3J = 5$ Hz, CH_3 , 6H). $^{13}\text{C}\{^1\text{H}\}$ NMR (75 MHz, 298 K, CDCl_3): δ 152.68 (Ar); 136.80 (Ar); 128.93 (Ar); 128.03 (Ar); 127.20 (Ar); 122.36 (Ar); 51.64 (CH_2); 48.33 (CH); 34.59 ($\text{C}(\text{CH}_3)_3$); 29.64

(C(CH₃)₃); 20.80 (ArCH₃); 16.64 (CH(CH₃)₂). HRMS (TOF MS EI⁺): (m/z): [M]⁺ calcd.

For H₂L1, 411.3137; found, 411.3143. MP range (°C): 130.2-131.7.

H₂[O₂N]^{AmAmBn}(H₂L2):

To a stirred mixture of 2,4-di-*t*-amylphenol (28.829 g, 0.1232 mol) in 100 mL of deionized water was added 37% aqueous formaldehyde (10 mL, 0.1232 mol) followed by slow addition of benzylamine (6.59 g, 0.0615 mol). The reaction was heated to reflux for 12 hours. Upon cooling, the reaction mixture separated into two phases. The upper phase was decanted and the remaining white mass of solid material was triturated with cold methanol to give an analytically pure, white powder (27.91 g, 76%). ¹H NMR (300 MHz, CDCl₃, δ): 7.37 (s, ArH, 1H); 7.35 (s, ArH, 1H); 7.32 (s, ArH, 1H); 7.30 (s, ArH, 1H); 7.26 (s, ArH, 1H); 7.08 (d, *J* = 1.6 Hz, ArH, 2H); 6.86 (d, *J* = 1.6 Hz, ArH, 2H); 3.73 (s, NCH₂, 2H); 3.62 (s, ArCH₂, 4H); 1.87 (m, CH₂, 4H); 1.55 (m, CH₂, 4H); 1.34 (s, CH₃, 12H); 1.22 (s, CH₃, 12H); 0.64 (m, CH₃, 12H). ¹³C {¹H} NMR (75 MHz, 298 K, CDCl₃): δ 151.98 (Ar); 139.51 (Ar); 137.62 (Ar); 134.09 (Ar); 129.59 (Ar); 128.93 (Ar); 127.85 (Ar); 125.86 (Ar); 125.80 (Ar); 121.15 (Ar); 58.51 (CH₂); 56.95 (CH₂); 38.49 ((CH₃)₂C(CH₂CH₃)); 37.27 ((CH₃)₂C(CH₂CH₃)); 37.21 ((CH₃)₂C(CH₂CH₃)); 33.00 ((CH₃)₂C(CH₂CH₃)); 28.60 ((CH₃)₂C(CH₂CH₃)); 27.75 ((CH₃)₂C(CH₂CH₃)); 9.58 ((CH₃)₂C(CH₂CH₃)); 9.20 ((CH₃)₂C(CH₂CH₃)). HRMS (TOF MS EI⁺): (m/z): [M]⁺ calcd. For H₂L2, 599.4702; found, 599.4711. MP range (°C): 127.4-128.9.

$\text{H}_2[\text{O}_2\text{N}]^{\text{BuBuPr}}(\text{H}_2\text{L3}):$

To a stirred mixture of 2,4-di-*t*-butylphenol (26.491 g, 0.1232 mol) in 100 mL of deionized water was added 37% aqueous formaldehyde (10 mL, 0.1232 mol) followed by slow addition of isopropylamine (3.55 g, 0.0615 mol). The reaction was heated to reflux for 12 hours. Upon cooling, the reaction mixture separated into two phases. The upper phase was decanted and the remaining light orange solid was triturated with cold methanol to give an analytically pure, white powder (17.32 g, 57%). ^1H NMR (300 MHz, CDCl_3 , δ): 7.21 (s, ArH, 2H); 6.92 (s, ArH, 2H); 3.71 (s, CH_2 , 4H); 3.17 (sp, $^3J = 5$ Hz, CH, 1H); 1.39 (s, CH_3 , 18H); 1.28 (s, CH_3 , 18H); 1.18 (d, $^3J = 5$ Hz, CH_3 , 6H). $^{13}\text{C}\{^1\text{H}\}$ NMR (300 MHz, 298 K, CDCl_3): δ 152.60 (ArCOH); 141.43 (Ar); 136.02 (Ar); 125.03 (Ar); 123.41 (Ar); 121.63 (Ar); 52.00 ($\text{NCH}(\text{CH}_3)_2$); 48.40 (ArCH_2); 34.88 ($\text{C}(\text{CH}_3)_3$); 34.18 ($\text{C}(\text{CH}_3)_3$); 31.67 ($\text{C}(\text{CH}_3)_3$); 29.70 ($\text{C}(\text{CH}_3)_3$); 16.66 ($\text{CH}(\text{CH}_3)_2$). HRMS (TOF MS EI+): (m/z): $[\text{M}]^+$ calcd. For $\text{H}_2\text{L3}$, 495.4076; found, 495.4063. MP range ($^\circ\text{C}$): 142.5-143.3. IR (neat): $\nu = 3196, 2958, 2905, 2865, 1606, 1476, 1451, 1391, 1362, 1290, 1225, 1207, 1157, 1123, 1078, 1027, 995, 967, 935, 879, 824, 792, 755, 722, 682, 653, 600, 540, 503\text{ cm}^{-1}$.

$\text{H}_2[\text{O}_2\text{N}]^{\text{BuBuPr}}(\text{H}_2\text{L4}):^{28,29}$

To a stirred mixture of 2,4-di-*t*-butylphenol (26.490 g, 0.1232 mol) in 100 mL of deionized water was added 37% aqueous formaldehyde (10 mL, 0.1232 mol) followed by slow addition of *n*-propylamine (3.55 g, 0.0615 mol). The reaction was heated to reflux for 12 hours. Upon cooling, the reaction mixture separated into two phases. The upper

phase was decanted and the remaining light orange solid was triturated with cold methanol to give an analytically pure, white powder (16.79 g, 55%). ^1H NMR (300 MHz, CDCl_3 , δ): 7.21 (s, ArH, 2H); 6.92 (s, ArH, 2H); 3.68 (s, CH_2 , 4H); 2.53 (t, $^3J = 7.5\text{ Hz}$, CH_2 , 2H); 1.63 (m, CH_2 , 2H); 1.40 (s, CH_3 , 18H); 1.28 (s, CH_3 , 18H); 0.90 (t, $^3J = 7.5\text{ Hz}$, CH_3 , 3H). $^{13}\text{C}\{^1\text{H}\}$ NMR (75 MHz, 298 K, CDCl_3): δ 152.41 (Ar); 141.48 (Ar); 136.01 (Ar); 128.93 (Ar); 125.05 (Ar); 123.46 (Ar); 121.73 (Ar); 57.23 (ArCH_2); 55.52 (ArCH_2); 34.87 ($\text{C}(\text{CH}_3)_3$); 34.19 ($\text{C}(\text{CH}_3)_3$); 31.67 ($\text{C}(\text{CH}_3)_3$); 29.71 ($\text{C}(\text{CH}_3)_3$); 19.39 (CH_2); 11.79 (CH_3).

$\text{H}_2[\text{O}_2\text{N}]^{\text{BuBuBn}}(\text{H}_2\text{L5})$:¹

To a stirred mixture of 2,4-di-*t*-butylphenol (25.701 g, 0.1232 mol) in 100 mL of deionized water was added 37% aqueous formaldehyde (10 mL, 0.1232 mol) followed by slow addition of benzylamine (6.59 g, 0.0615 mol). The reaction was heated to reflux for 12 hours. Upon cooling, the reaction mixture separated into two phases. The upper phase was decanted and the remaining light orange solid was triturated with cold methanol to give an analytically pure, white powder (16.69 g, 50%). ^1H NMR (300 MHz, CDCl_3 , δ): 7.38 (s, ArH, 1H); 7.35 (s, ArH, 1H); 7.33 (s, ArH, 1H); 7.30 (s, ArH, 1H); 7.26 (s, ArH, 1H); 7.18 (d, $J = 1.6\text{ Hz}$, ArH, 2H); 6.92 (d, $J = 1.6\text{ Hz}$, ArH, 2H); 3.64 (s, NCH_2 , 2H); 3.58 (s, CH_2 , 2H); 1.41 (s, CH_3 , 18H); 1.28 (s, CH_3 , 18H); $^{13}\text{C}\{^1\text{H}\}$ NMR (75 MHz, 298 K, CDCl_3): δ 152.14 (Ar); 141.46 (Ar); 135.97 (Ar); 129.61 (Ar); 128.96 (Ar); 128.43 (Ar); 125.16 (Ar); 123.61 (Ar); 121.41 (Ar); 56.88 (ArCH_2); 34.91 ($\text{C}(\text{CH}_3)_3$); 34.17 ($\text{C}(\text{CH}_3)_3$); 31.66 ($\text{C}(\text{CH}_3)_3$); 29.65 ($\text{C}(\text{CH}_3)_3$).

H₂[O₂N]^{BuMeBn}(H₂L6):¹

To a stirred mixture of 2-*t*-butyl-4-methylphenol (20.210 g, 0.1232 mol) in 100 mL of deionized water was added 37% aqueous formaldehyde (10 mL, 0.1232 mol) followed by slow addition of isopropylamine (6.62 g, 0.0615 mol). The reaction was heated to reflux for 12 hours. Upon cooling, the reaction mixture separated into two phases. The upper phase was decanted and the remaining pale orange precipitate was triturated with cold methanol to give an analytically pure, white powder (22.53 g, 80%). ¹H NMR (300 MHz, CDCl₃, δ): 7.38 (s, ArH, 1H); 7.36 (s, ArH, 1H); 7.35 (s, ArH, 1H); 7.33 (s, ArH, 1H); 7.26 (s, ArH, 1H); 6.93 (d, ArH, 2H); 6.92 (d, ArH, 2H); 3.64 (s, CH₂, 4H); 3.58 (s, CH₂, 2H); 1.60 (s, ArCH₃, 6H); 1.27 (s, CH₃, 18H). ¹³C{¹H} NMR (75 MHz, 298 K, CDCl₃): δ 152.14 (Ar); 141.46 (Ar); 135.97 (Ar); 129.60 (Ar); 128.95 (Ar); 125.15 (Ar); 123.60 (Ar); 121.41 (Ar); 58.51 (CH₂); 56.87 (CH₂); 34.90 (C(CH₃)₃); 29.64 (C(CH₃)₃); 18.47 (ArCH₃).

[NEt₃H]⁺[FeCl₂L1]⁻ (C1):

To a THF solution (50 mL) of recrystallized **H₂L1** (2.00 g, 4.87 mmol) was added a solution of anhydrous FeCl₃ (0.800 g, 4.93 mmol) in THF resulting in an intense purple solution. To this solution was added triethylamine (1.00 g, 9.86 mmol) and the resulting mixture was stirred for 2 hours. After stirring, the dark purple solution was filtered through Celite. Removal of solvent under vacuum yielded a dark purple product. Crystals suitable for X-ray diffraction were obtained by slow evaporation of a toluene solution

(1.693 g, 55%). Anal. Calcd for $C_{33}H_{55}Cl_2FeN_2O_2$ (plus 1.3 equivalents of co-crystallized toluene): C, 66.68; H, 8.69; N, 3.69. Found: C, 66.73; H, 8.92; N, 3.44.

[FeL5(μ -Cl)]₂ (C2):

To a THF solution (50 mL) of recrystallized **H₂L5** (2.00 g, 3.68 mmol) was added a solution of anhydrous FeCl₃ (0.597 g, 3.68 mmol) in THF resulting in an intense purple solution. To this solution was added triethylamine (0.744 g, 7.36 mmol) and the resulting mixture was stirred for 2 hours. After stirring, the dark purple solution was filtered through Celite. Removal of solvent under vacuum yielded a dark purple powder. The purple product was washed three times with 10 mL of acetone. Dark purple crystals were obtained by slow evaporation of a saturated toluene solution (1.306 g, 54%). MS (MALDI-TOF) m/z (% ion): 543.435 (60, [M-FeCl]⁺), 597.370 (12, [M-Cl]⁺).

FeCl(THF)L2 (C3):

To a THF solution (50 mL) of recrystallized **H₂L2** (2.00 g, 3.33 mmol) was added a solution of anhydrous FeCl₃ (0.597 g, 3.33 mmol) in THF resulting in an intense purple solution. To this solution was added triethylamine (0.674 g, 6.66 mmol) and the resulting mixture was stirred for 2 hours. After stirring, the dark purple solution was filtered through Celite. Removal of solvent under vacuum yielded a dark purple product (1.809 g, 71%). The purple product was dissolved in minimal toluene and was placed in the freezer for 48 hours where a thin layer of white precipitate appeared at the bottom of the reaction flask. The mother liquor was decanted and passed through Celite. Crystals suitable for X-ray diffraction were obtained by slow evaporation of the toluene solution (1.408 g, 56%).

Anal. Calcd for $C_{45}H_{67}ClFeNO_3$: C, 70.99; H, 8.87; N, 1.84. Found: C, 71.25; H, 9.03; N, 2.10. (MALDI-TOF) m/z (% ion): 599.445 (100, $[M-Fe-Cl-THF]^+$), 653.375 (40, $[M-Cl-THF]^+$), 688.328 (8, $[M-THF]^+$). UV-vis (methanol) λ_{max} , nm (ϵ): 600 (2750), 330 (3950), 250 (6610).

FeBr(THF)L2 (C4):

A THF solution (50 mL) of recrystallized **L2** (2.00 g, 3.33 mmol) was added dropwise to a NaH suspension (0.320 g, 13.33 mmol) in THF at $-78\text{ }^\circ\text{C}$. Upon return to room temperature, the sodium salt of the ligand was added dropwise to a THF solution of anhydrous $FeBr_3$ (0.985 g, 3.33 mmol) at $-78\text{ }^\circ\text{C}$ resulting in an intense purple solution. After stirring for 2 hours, the solvent was removed via vacuum to give a dark purple powder. The dark purple product was then extracted with minimal toluene and the resulting dark purple solution was filtered through Celite. Crystals suitable for X-ray diffraction were obtained by slow evaporation of the toluene solution (2.255 g, 84%). Anal. Calcd for $C_{45}H_{67}BrFeNO_3$: C, 67.08; H, 8.38; N, 1.74. Found: C, 66.87; H, 8.12; N, 2.05. (MALDI-TOF) m/z (% ion): 599.445 (40, $[M-Fe-Br-THF]^+$), 653.363 (100, $[M-Br-THF]^+$), 734.288 (5, $[M-THF]^+$), 805.225 (1, $[M]^+$).

FeBr₂L1H (C5):

A THF solution (50 mL) of recrystallized **L1** (2.00 g, 4.86 mmol) was added dropwise to a NaH suspension (0.467 g, 19.45 mmol) in THF at $-78\text{ }^\circ\text{C}$. Upon return to room temperature, the sodium salt of the ligand was added dropwise to a THF solution of anhydrous $FeBr_3$ (1.44 g, 4.86 mmol) at $-78\text{ }^\circ\text{C}$ resulting in an intense purple solution.

After stirring for 2 hours, the solvent was removed via vacuum to give a dark purple powder. The dark purple product was then extracted with minimal toluene and the resulting dark purple solution was filtered through Celite. Crystals suitable for X-ray diffraction were obtained by slow evaporation of the toluene solution (1.958 g, 64%). Anal. Calcd for $C_{27}H_{40}Br_2FeNO_2$: C, 51.78; H, 6.44; N, 2.24. Found: C, 51.53; H, 6.18; N, 2.07. (MALDI-TOF) m/z (% ion): 412.296 (100, $[M-Fe-2Br-H]^+$), 465.215 (7, $[M-2Br-H]^+$), 545.135 (3, $[M-Br-H]^+$).

[FeL3(μ -OH)]₂ (C6):

A 1.6 M hexane solution of *n*-butyllithium (5.50 mL, 8.87 mmol) was added via syringe to a stirred solution of **L3** (2.00 g, 4.03 mmol) in THF (50 mL) at -78 °C. Upon return to room temperature, the lithiated ligand (clear pale yellow solution) was transferred via cannula to a solution of anhydrous FeBr₃ (1.19 g, 4.03 mmol) in THF (30 mL) at -78 °C. After stirring for 2 hours, the solvent was removed via vacuum to give a dark purple powder. The dark purple product was then extracted with minimal toluene and the resulting dark purple solution was filtered through Celite. Dark brown crystals suitable for X-ray diffraction were obtained by slow evaporation of the toluene solution (1.905 g, 83%). Anal. Calcd for $C_{66}H_{104}Fe_2N_2O_6$: C, 69.95; H, 9.25; N, 2.47. Found: C, 70.12; H, 8.98; N, 2.65. (MALDI-TOF) m/z (% ion): 496.479 (100, $[M-FeOH]^+$), 549.399 (10, $[M-OH]^+$), 564.394 (7, $[M]^+$).

FeBr₂L3H (C7):

A 1.6 M hexane solution of n-butyllithium (5.50 mL, 8.87 mmol) was added via syringe to a stirred solution of **L3** (2.00 g, 4.03 mmol) in THF (50 mL) at -78 °C. Upon return to room temperature, the lithiated ligand (clear pale yellow solution) was transferred via cannula to a solution of anhydrous FeBr₃ (1.19 g, 4.03 mmol) in THF (30 mL) at -78 °C. After stirring for 2 hours, the solvent was removed via vacuum to give a dark purple powder. The dark purple product was then extracted with minimal toluene and the resulting dark purple solution was filtered through Celite. Dark purple crystals suitable for X-ray diffraction were obtained by slow evaporation of the toluene solution (2.156 g, 76%). Anal. Calcd for C₃₃H₅₂Br₂FeNO₂: C, 55.79; H, 7.38; N, 1.97. Found: C, 55.61; H, 7.19; N, 2.11. (MALDI-TOF) m/z (% ion): 710.468 (2, [M]⁺), 549.260 (10, [M-2Br-H]⁺), 492.320 (100, [M-Fe-2Br-H]⁺).

2.4 References

- ¹ F. M. Kerton, S. Holloway, A. Power, R. G. Soper, K. Sheridan, J. M. Lynam, A. C. Whitwood, C. E. Willans, *Can. J. Chem.*, **2008**, *86*, 435.
- ² E. Y. Tshuva, I. Goldberg, M. Kol, Z. Goldschmidt, *Inorg. Chem.*, **2001**, *40*, 4263.
- ³ A. Chumura, M. Davidson, M. Jones, M. Lunn, M. Mahon, *Dalton Trans.*, **2006**, 887.
- ⁴ K. Hassan, L. N. Dawe, C. M. Kozak, *Eur. J. Org. Chem.*, **2011**, 4610.
- ⁵ P. Chaudhuri, E. Safaei, T. Weyhermüller, E. Bothe, K. Wieghardt, *Eur. J. Org. Chem.*, **2007**, 2334.
- ⁶ X. Qian, L. N. Dawe, C. M. Kozak, *Dalton Trans.*, **2011**, *40*, 933.
- ⁷ P. Mountford, T. Toupance, S. Dubberley, N. Rees, B. Tyrrell, *Organometallics*, **2002**, *21*, 1367.
- ⁸ S. Attia, M. F. El-Shahat, *Polyhedron*, **2007**, *26*, 791.
- ⁹ M. D. Eelman, J. M. Blacquiere, M. M. Moriarty, D. E. Fogg, *Angew. Chem. Int. Ed.*, **2008**, *47*, 303.
- ¹⁰ N. Ikpo, S. M. Butt, K. L. Collins, F. M. Kerton, *Organometallics*, **2009**, *28*, 837.
- ¹¹ A. W. Addison, T. N. Rao, J. Reedijk, J. van Rijn, G. C. Verschoor, *J. Chem. Soc., Dalton Trans.*, **1984**, 1349.
- ¹² K. Hasan, C. Fowler, P. Kwong, A. K. Crane, J. L. Collins, C. M. Kozak, *Dalton Trans.*, **2008**, 2991.
- ¹³ G. Mund, R. J. Batchelor, R. D. Sharma, C. Jones, D. B. Leznoff, *J. Chem. Soc., Dalton Trans.*, **2002**, 136.

- ¹⁴ M. D. Fryzuk, D. B. Leznoff, E. S. F. Ma, S. J. Rettig, V. G. Young, *Organometallics*, **1998**, *17*, 2313.
- ¹⁵ G. A. Abakumov, V. K. Cherkasov, M. P. Bubnov, L. G. Abakumova, V. N. Ikorskii, G. V. Romanenko, A. I. Poddel'sky, *Russ. Chem. Bull.*, **2006**, *55*, 44.
- ¹⁶ R. R. Chowdhury, A. K. Crane, C. Fowler, P. Kwong, C. M. Kozak, *Chem. Commun.*, **2008**, 94.
- ¹⁷ P. Mialane, E. Anxolabéhère-Mallart, G. Blondin, A. Nivorojkine, J. Guilhem, L. Tchertanova, M. Cesario, N. Ravi, E. Bominaar, J. Girerd, E. Munck, *Inorg. Chim. Acta.*, **1997**, *263*, 367.
- ¹⁸ J. Strautmann, S. George, E. Bothe, E. Bill, T. Weyhermüller, A. Stämmler, H. Bögge, T. Glaser, *Inorg. Chem.*, **2008**, *47*, 6804.
- ¹⁹ A. Das, Z. Moatazedi, G. Mund, A. Bennet, R. Batchelor, D. B. Leznoff, *Inorg. Chem.*, **2007**, *46*, 366.
- ²⁰ G. Mund, D. Vidovic, R. Batchelor, J. Britten, R. Sharma, C. Jones, D. B. Leznoff, *Chem. Eur. J.*, **2003**, *9*, 4757.
- ²¹ *CrystalStructure 3.7.0: Crystal Structure Analysis Package*, Rigaku and Rigaku/MS, **2000-2005**.
- ²² D. Watkin, C. Prout, J. Carruthers, P. Betteridge, *CRYSTALS Issue 10*, Chemical Crystallography Laboratory, Oxford, UK, **1996**.
- ²³ P. Chaudhuri, T. Weyhermüller, R. Wagner, *Eur. J. Inorg. Chem.*, **2011**, 2547.

- ²⁴ R. K. Dean, S. L. Granville, L. N. Dawe, A. Decken, K. M. Hattenhauer and C. M. Kozak, *Dalton Trans.*, **2010**, 39, 548.
- ²⁵ I. Thomé, A. Nijs, C. Bolm, *Chem. Soc. Rev.*, **2012**, 41, 979.
- ²⁶ G. Cahiez, V. Habiak, C. Duplais, A. Moyeux, *Angew. Chem. Int. Ed.*, **2007**, 46, 4364.
- ²⁷ S. Buchwald, C. Bolm, *Angew. Chem. Int. Ed.*, **2009**, 48, 2.
- ²⁸ E. Y. Tshuva, I. Goldberg, M. Kol, Z. Goldschmidt, *Inorg. Chem.*, **2001**, 40, 4263.
- ²⁹ E. Y. Tshuva, I. Goldberg, M. Kol, Z. Goldschmidt, *Organometallics*, **2001**, 20, 3017.

Chapter 3 – Catalysis Studies: The Iron-Catalyzed Cross-Coupling of Benzyl Halides with Aryl Grignards

3.1 Introduction

As discussed briefly in Chapter 1, the catalytic formation of diarylmethane motifs is a very important synthetic tool, with applications in pharmaceuticals and biologically active compounds.¹⁻² To date, the formation of diarylmethane motifs by the iron-catalyzed coupling of benzyl halides with aryl Grignard reagents has been reported to be unsatisfactory, giving low yields and poor selectivity resulting in the formation of homo-coupled by-products. Compared to iron-catalyzed systems, catalytic systems containing copper or palladium-based catalysts have been found to be more effective for the cross-coupling of benzyl halides with aryl Grignard reagents.³⁻⁴ However, many of these catalytic systems are expensive and/or toxic in nature.⁵ Due to recent environmental and economical concerns, the development of an iron-based catalyst which can effectively generate diarylmethane motifs is of particular interest.

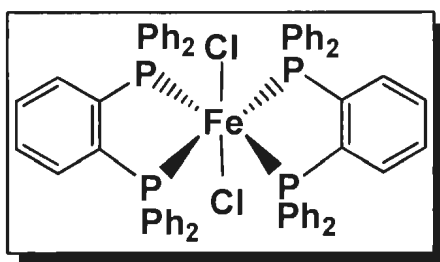
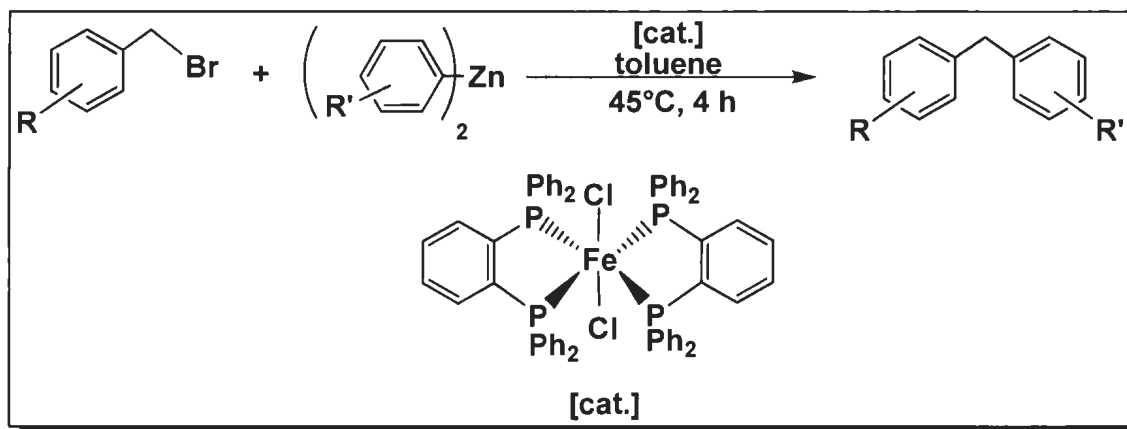


Figure 3.1: Fe(II)Cl₂bis(dpbz) reported by Bedford and co-workers.⁶

In 2009, Bedford and co-workers reported an efficient method for the construction of diarylmethane compounds.⁶ Initial attempts focused on the cross-coupling of benzyl halides with aryl Grignard reagents in the presence of iron-phosphine based catalysts. When Fe(II)Cl₂bis(dpbz) (dpbz = 1,2-bis(diphenylphosphino)benzene) (**Figure 3.1**) was employed as the catalyst, low yields and poor selectivities with respect to homo-coupled by-products resulted. However, in the presence of softer arylzinc nucleophiles, Bedford and co-workers reported that Fe(II)Cl₂bis(dpbz) was an active catalyst for the Negishi coupling of arylzinc reagents with benzyl halides (**Scheme 3.1**).⁶ Unfortunately, the use of diarylzinc reagents requires an additional step in the reaction procedure (compared to using the Grignard reagent directly) since all the diarylzinc reagents employed are prepared from the corresponding Grignard reagents. In addition, only one aryl group from Ar₂Zn is transferred during the course of the reaction. From an economical perspective, it would be more practical to develop an iron-based catalytic system in which aryl Grignard reagents can be used directly.



Scheme 3.1: Iron-catalyzed Negishi-type arylations reported by Bedford *et al.*⁶

Unlike the octahedral iron(II) catalyst reported by Bedford and co-workers, this Chapter will investigate the catalytic activity of a structurally authenticated trigonal bipyramidal amine-bis(phenolate) iron(III) complex (**Figure 3.2**) for the C-C cross coupling of aryl Grignard reagents with benzyl halides. Preliminary investigations will include the screening of electron-donating and electron-withdrawing groups on both the benzylic substrate and the aryl Grignard reagent.

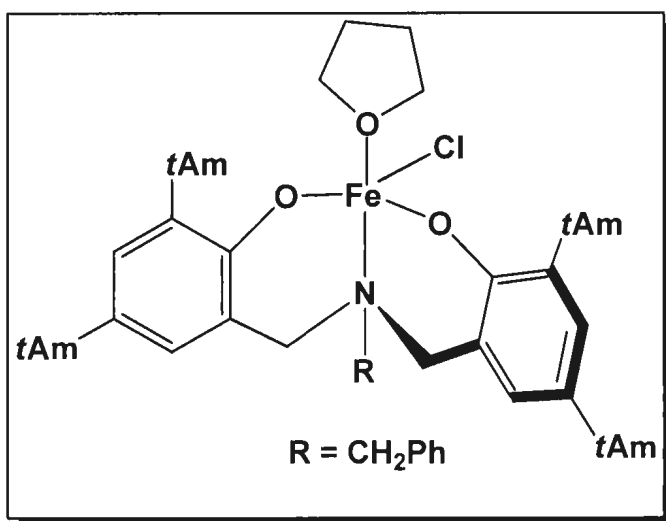


Figure 3.2: A structural representation of **C3**.

3.2 Results and Discussion

3.2.1 General Procedure

Reactions were carried out using the tridentate amine-bis(phenolate) iron(III) complex **C3** as the catalyst. 0.10 mmol of **C3** was added to a 30 mL Schlenk flask followed by the desired solvent, alkyl halide and Grignard reagent. Previous studies in the Kozak group with related Fe(III) complexes supported by tetradentate amine-

bis(phenolate)-ether ligands suggest that diethyl ether is superior to THF as a solvent for the cross-coupling of Grignard reagents with alkyl halides.⁷ In addition, it was previously found that reactions performed at room temperature gave superior results to those conducted at lower temperatures.⁷ Therefore, diethyl ether was the solvent of choice for the current study and all reactions were performed at room temperature. For each reaction, the ratio of Grignard reagent to the alkyl halide was 2:1. After stirring for 30 minutes at room temperature, the reaction mixture was quenched by adding 5 mL of HCl (2.0 M). Products were extracted with diethyl ether and product yields were quantified by GC-MS (relative to standard curves) and by ¹H NMR. GC-MS and NMR spectra can be located in the appendix at the end of this thesis.

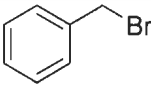
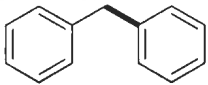
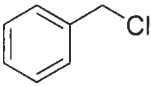
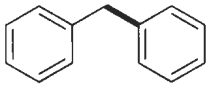
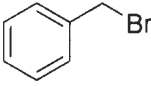
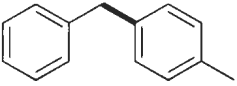
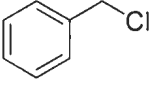
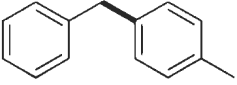
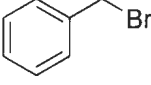
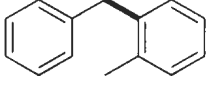
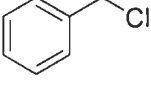
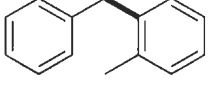
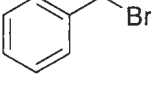
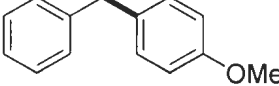
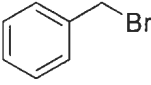
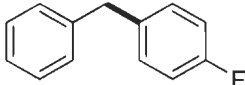
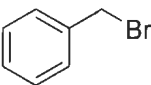
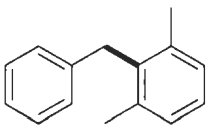
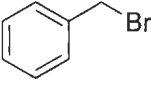
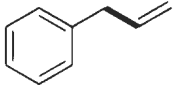
3.2.2 Catalysis Results

The first group of cross-coupling reactions investigated involved the reaction between benzyl bromide (or benzyl chloride) and a series of Grignard reagents (**Table 3.1**). An initial reaction of benzyl bromide with phenylmagnesium bromide (PhMgBr) in the presence of **C3** gave a 30% yield of cross-coupled product after 30 minutes at room temperature (**Table 3.1**, Entry 1). Low yields of the bibenzyl and biaryl homocoupled by-products were also obtained. Benzyl chloride could also be used as the electrophilic partner, generating a similar yield of the desired cross-coupled product (**Table 3.1**, Entry 2). The reaction of benzyl bromide with *o*-tolylmagnesium bromide gave a very good yield (86%) of the cross-coupled product after 30 minutes at room temperature (**Table**

3.1, Entry 5). Previously in the Kozak group, the reaction between benzyl bromide and *o*-tolylmagnesium bromide gave yields of 60% and 68% in the presence of octahedral (amine)bis(phenolato)Fe^{III}(acac) complexes and trigonal bipyramidal iron(III) halide complexes (supported by tetradentate amine-bis(phenolate) ligands), respectively.^{7,8} Surprisingly, when benzyl chloride was employed, a higher yield (94%) of the cross-coupled product was found (**Table 3.1**, Entry 6). Kozak and co-workers obtained a 95% yield of cross-coupled products from benzyl chloride and *o*-tolylmagnesium bromide in the presence of related tridentate amine-bis(phenolate) iron(III) complexes.⁹ A yield of 52% was reported in the presence of octahedral (amine)bis(phenolato)Fe^{III}(acac) complexes.⁸ Using *p*-tolylmagnesium bromide, however, gave slightly lower yields than *o*-tolylmagnesium bromide with the respective benzyl halide (**Table 3.1**, Entries 3 and 4) generating higher yields of the bibenzyl and biaryl homocoupled by-products. A similar finding was also observed in the presence of octahedral (amine)bis(phenolato)Fe^{III}(acac) complexes and trigonal bipyramidal iron(III) chloride complexes with tetradentate amine-bis(phenolate) ligands.^{7,8} According to reports by Bedford and co-workers, the iron-catalyzed Negishi coupling of benzyl bromide with the diaryl zinc reagent prepared from *p*-tolylmagnesium bromide gave a 76% isolated yield of the desired cross-coupled product.⁶ When benzyl bromide was reacted with 4-methoxyphenylmagnesium bromide (4-anisylmagnesium bromide) in the presence of **C3**, a 21% yield of the cross-coupled product was found along with large quantities of the bibenzyl by-product (**Table 3.1**, Entry 7). Previously in the Kozak group, the reaction between benzyl bromide and 4-anisylmagnesium bromide resulted in a 0% yield of the cross-coupled product when iron(III) chloride complexes with tetradentate amine-bis(phenolate) ligands were used as

the pre-catalyst.⁷ The Negishi-type arylation between benzyl bromide and the corresponding diaryl zinc reagent prepared from 4-anisylmagnesium bromide resulted in a 95% isolated yield of the cross-coupled product as reported by Bedford and co-workers.⁶ Reacting benzyl bromide with 4-fluorophenylmagnesium bromide (4-FPhMgBr) also resulted in a poor yield (21%) of the cross-coupled product (**Table 3.1**, Entry 8). High quantities of the homocoupled biaryl and bibenzyl products were formed instead. Surprisingly, benzyl bromide was found to couple with the sterically crowded 2,6-dimethylphenylmagnesium bromide (2,6-Me₂PhMgBr) in an excellent yield of 95% (**Table 3.1**, Entry 9). When the starting material FeCl₃ was employed as the catalyst for the reaction between benzyl bromide and 2,6-dimethylphenylmagnesium bromide, only trace amounts of the desired cross-coupled product was found. The reaction between benzyl bromide and 2,6-dimethylphenylmagnesium bromide without the use of a catalyst resulted in a 0% yield of the cross-coupled product. Kozak and co-workers had previously obtained a 78% yield of cross-coupled products from benzyl bromide and 2,6-dimethylphenylmagnesium bromide when using a related tridentate amine-bis(phenolate) iron(III) complex.⁹ When benzyl bromide was reacted with the *sp*² hybridized vinylmagnesium bromide (in the presence of **C3**), very poor selectivity resulting in the formation of homo-coupled by-products was found. Only trace quantities of the desired product were obtained (**Table 3.1**, Entry 10) while high quantities of the bibenzyl by-product formed instead.

Table 3.1: The cross-coupling of benzyl bromide or benzyl chloride with Grignard reagents.

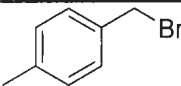
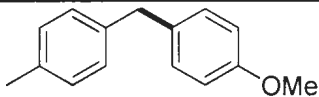
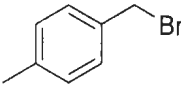
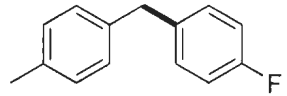
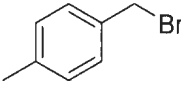
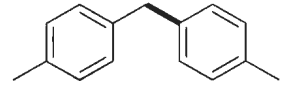
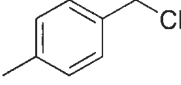
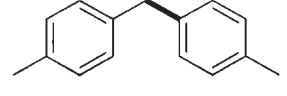
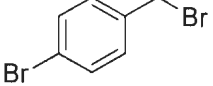
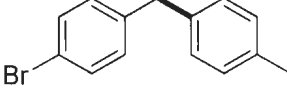
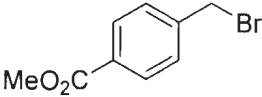
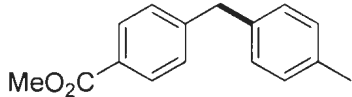
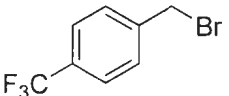
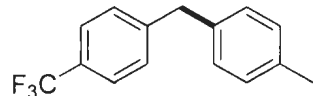
Entry	ArMgBr	Alkyl Halide	Product	% Yield ^a
1	Ph			30
2	Ph			32
3	<i>p</i> -tolyl			49
4	<i>p</i> -tolyl			41
5	<i>o</i> -tolyl			86
6	<i>o</i> -tolyl			94
7	4-anisyl			21
8	4-FPh			21
9	2,6-Me ₂ Ph			95
10	vinyl-MgBr			trace

^a Spectroscopic yields determined by GC-MS using dodecane as an internal standard.

A series of *para*-substituted benzyl halides was also screened as a cross-coupling reaction partner. When 4-methylbenzyl bromide was reacted with 4-anisylmagnesium bromide in the presence of **C3** at room temperature, a 19% yield of the desired cross-coupled product was obtained (**Table 3.2**, Entry 1). High quantities of the homocoupled bibenzyl product were formed instead. Reacting 4-methylbenzyl bromide with 4-fluorophenylmagnesium bromide (4-FPhMgBr) also resulted in a poor yield (13%) of the cross-coupled product (**Table 3.2**, Entry 2). When *p*-tolylmagnesium bromide was employed as the aryl Grignard reagent, a slightly higher yield of cross-coupled product (38%) was obtained (**Table 3.2**, Entry 3). However, high quantities of the bibenzyl and biaryl homocoupled by-products were generated. The Negishi-type arylation between 4-methylbenzyl bromide and the corresponding diaryl zinc reagent of *p*-tolylmagnesium resulted in an 86% isolated yield of the cross-coupled product as reported by Bedford and co-workers.⁶ Surprisingly, in the presence of **C3**, 4-methylbenzyl chloride was found to couple with *p*-tolylmagnesium in a high yield of 85% (**Table 3.2**, Entry 4). When the weakly electron donating methyl group of 4-methylbenzyl bromide was replaced by a weakly electron withdrawing bromide group (4-bromobenzyl bromide), the desired cross-coupling product was obtained in a moderate yield of 67% (**Table 3.2**, Entry 5) giving higher yields of the biphenyl homocoupled by-product. According to reports by Bedford and co-workers, the iron-catalyzed Negishi coupling of 4-methylbenzyl bromide with the corresponding diarylzinc reagent of *p*-tolylmagnesium bromide gave an 80% isolated yield of the desired cross-coupled product.⁶ Interestingly, when the strongly electron withdrawing substrate 4-(trifluoromethyl)benzyl bromide was employed, a higher yield (76%) of the cross-coupled product was obtained (**Table 3.2**, Entry 7). Bedford and co-

workers found a 59% isolated yield of the cross-coupled product for the Negishi coupling of 4-(trifluoromethyl)benzyl bromide with the corresponding diaryl zinc reagent of *p*-tolylmagnesium bromide.⁶ As seen in **Table 3.2**, Entry 6, the introduction of an ester group at the *para* position of the benzyl halide only gave trace quantities of the desired product resulting in the generation of high quantities of the homocoupled biaryl product instead.

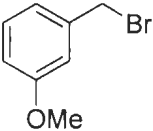
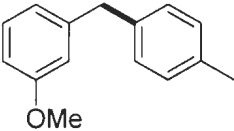
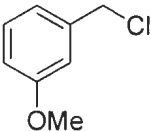
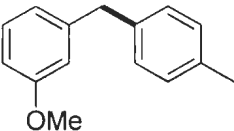
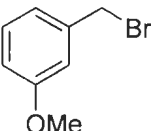
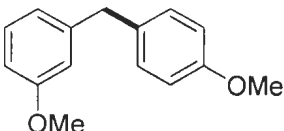
Table 3.2: The cross-coupling of *para*-substituted benzyl halides with aryl Grignard reagents.

Entry	ArMgBr	Alkyl Halide	Product	% Yield ^a
1	4-anisyl			19
2	4-FPh			13
3	<i>p</i> -tolyl			38
4	<i>p</i> -tolyl			85
5	<i>p</i> -tolyl			67
6	<i>p</i> -tolyl			trace
7	<i>p</i> -tolyl			76

^a Spectroscopic yields determined by GC-MS using dodecane as an internal standard.

Cross-coupling reactions with *meta*-substituted benzyl halides were also screened. 3-methoxybenzyl bromide was found to give low to modest yields depending on the aryl Grignard reagent used. In the presence of *p*-tolylmagnesium bromide, a good yield (72%) of the cross-coupled product was obtained (**Table 3.3**, Entry 1). A higher yield of 92% was reported for the Negishi coupling of 3-methoxybenzyl bromide with the diarylzinc reagent prepared from *p*-tolylmagnesium bromide.⁶ Surprisingly, 3-methoxybenzyl chloride could also be used as the electrophilic partner, generating an excellent yield (91%) of the desired cross-coupled product (**Table 3.3**, Entry 2). Unfortunately, 3-methoxybenzyl bromide gave a low yield of the cross-coupled product when reacted with 4-anisylmagnesium bromide in the presence of **C3** (**Table 3.3**, Entry 3). In fact, a high quantity of the unreacted starting material 3-methoxybenzyl bromide was found.

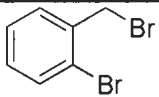
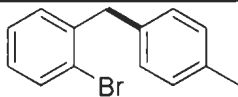
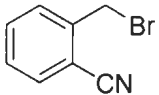
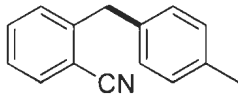
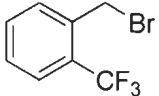
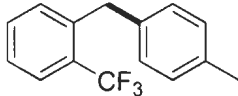
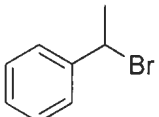
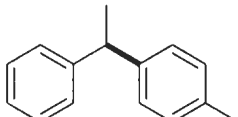
Table 3.3: The cross-coupling of *meta*-substituted benzyl halides with aryl Grignard reagents.

Entry	ArMgBr	Alkyl Halide	Product	% Yield ^a
1	<i>p</i> -tolyl			72
2	<i>p</i> -tolyl			91
3	4-anisyl			24

^a Spectroscopic yields determined by GC-MS using dodecane as an internal standard.

As seen in **Table 3.4**, iron-catalyzed cross-coupling reactions with *ortho*-substituted benzyl halides were also screened. When 2-bromobenzyl bromide was reacted with *p*-tolylmagnesium bromide in the presence of **C3**, only trace quantities of the desired cross-coupled product were generated with high yields of the biaryl homocoupled by-product. When 2-(bromomethyl) benzonitrile was reacted with *p*-tolylmagnesium bromide, a 0% yield of the cross-coupled product was obtained. In fact, the reaction exclusively generated the biaryl homocoupled by-product. The reaction between 2-(trifluoromethyl)benzyl bromide and *p*-tolylmagnesium bromide gave a low yield (24%) of the cross-coupled product (**Table 3.4**, Entry 3). Low yields of the bibenzyl and biphenyl homocoupled by-products were also obtained. The Negishi coupling of 2-(trifluoromethyl)benzyl bromide with the corresponding diarylzinc reagent of *p*-tolylmagnesium bromide gave a higher yield (64%) of the cross-coupled product.⁶ When the sterically demanding (1-bromoethyl)benzene was employed as the electrophilic substrate, only trace quantities of the desired cross-coupling product was obtained. High quantities of homocoupled biaryl byproduct were found instead.

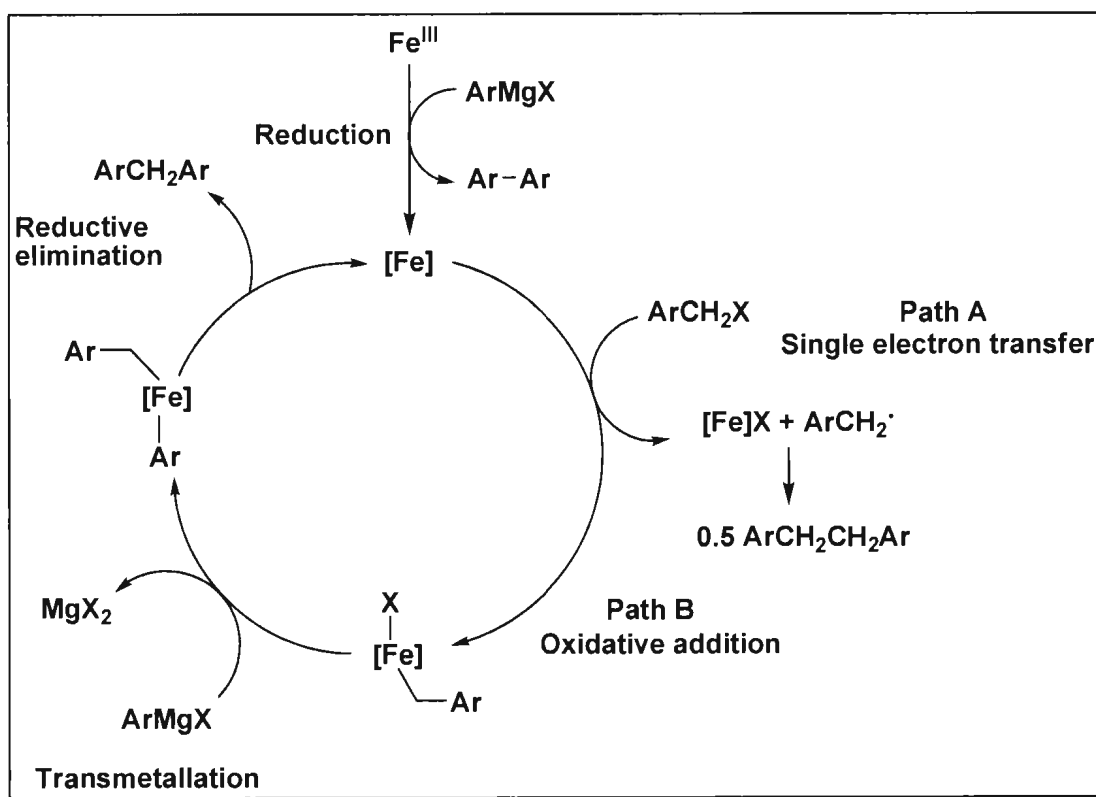
Table 3.4: The cross-coupling of *ortho*-substituted benzyl halides and (1-bromoethyl)benzene with aryl Grignard reagents.

Entry	ArMgBr	Alkyl Halide	Product	% Yield ^a
1	<i>p</i> -tolyl			trace
2	<i>p</i> -tolyl			0
3	<i>p</i> -tolyl			24
4	<i>p</i> -tolyl			trace

^a Spectroscopic yields determined by GC-MS using dodecane as an internal standard.

For many of the cross-coupling reactions attempted, bibenzyl homocoupling by-products were observed. Previously, for the reaction of dichloroethane with Grignard reagents, Hayashi and co-workers proposed a mechanism suggesting that benzyl halides could undergo radical reactions in the presence of reduced metals.¹⁰ A similar mechanism was also proposed by the Kozak group for the reaction between dichloromethane and Grignard reagents.¹¹ Nakamura and Fürstner have also reported similar mechanisms where the iron-catalyzed cross-coupling of alkyl halides with aryl Grignard reagents proceeds *via* a radical process.^{12,13} According to the literature, benzyl halides can undergo oxidative addition (OA) at a reduced iron centre or undergo a single electron transfer (SET) reaction with the reduced centre generating an arylmethyl radical, which subsequently undergoes radical coupling (**Scheme 3.2**).^{10,11} A similar mechanism may be

responsible for the bibenzyl homocoupled byproduct observed in many of the cross-coupling reactions attempted and consequently the low yields of the desired cross-coupled product. As shown in **Scheme 3.2**, after the iron(III) pre-catalyst is reduced by the aryl Grignard reagent, the catalytically active iron species can either undergo oxidative addition (**Path B**) with the benzyl halide or take part in a single electron transfer (SET) side reaction (**Path A**) with the benzyl halide generating an arylmethyl radical, and in turn, 0.5 equivalents of the bibenzyl homocoupled by-product. If oxidative addition at the reduced iron centre occurs, the resulting benzylironhalide complex is expected to undergo transmetalation with the aryl Grignard to form an arylbenzyliron complex. Reductive elimination of the arylbenzyliron complex would then generate the desired cross-coupled product along with regeneration of the reduced iron species. For more on the mechanistic considerations of iron-catalyzed cross-coupling reactions, please see Section 1.2.5 of Chapter 1.¹⁴⁻¹⁷



Scheme 3.2: Plausible catalytic cycle for the generation of bibenzyl homocoupled by-products (**Path A**) and diarylmethane compounds (**Path B**).

3.2.3 Percent Yield Calculations

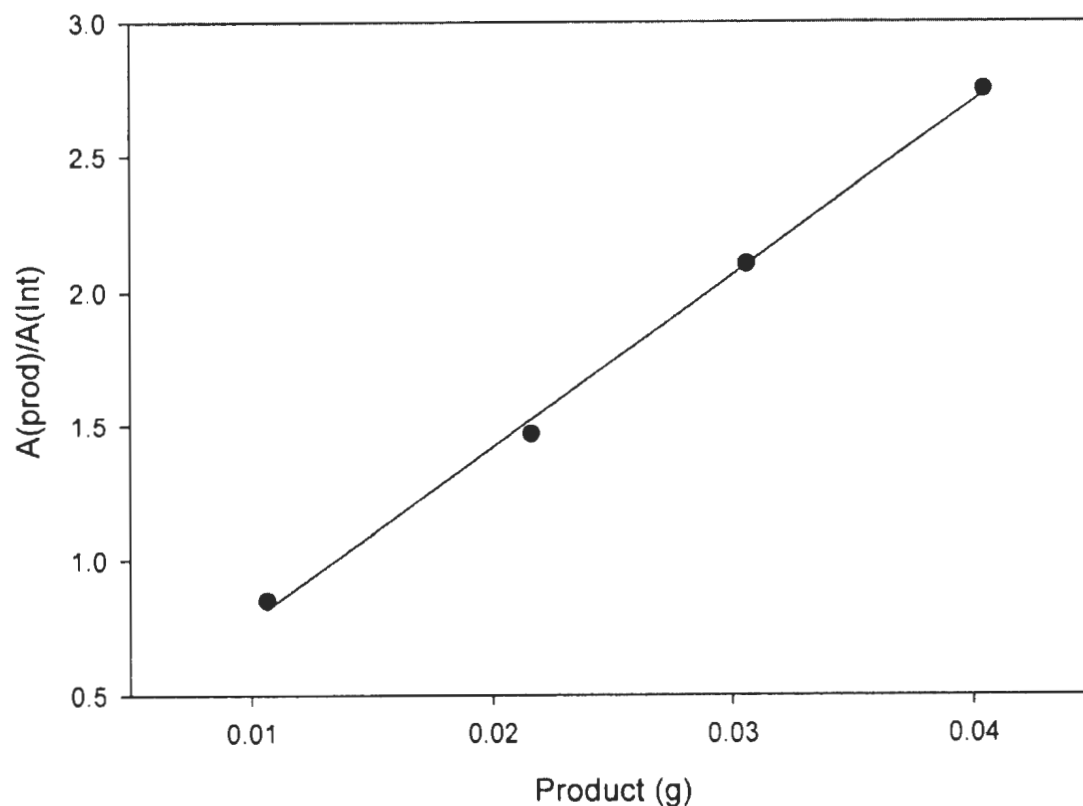


Figure 3.3: A calibration curve for the determination of yields of cross-coupled products ($r_{sq} = 0.998$). Product refers to diphenylmethane.

Accurate yield determinations of cross-coupled products were obtained from GC-MS analysis by the use of standard calibration curves. In order to generate a reliable standard curve, all points were run in duplicate (average values were used). An example of a calibration curve used during the course of this study can be found in **Figure 3.3**. After preparing a stock solution of dodecane (known concentration), a known volume of the stock solution (100 μL) was added to four separate vials each of which contained a different mass of the diarylmethane compound. By adding a different mass (known) of

the diarylmethane compound in each vial, different ratios of intensity between the internal standard dodecane and the diarylmethane product could be achieved. Approximate ratios of 1:2, 1:1, 2:1 and 3:1 (dodecane:product) were used for each calibration curve. Once GC-MS analysis was performed on each sample prepared (vial 1-4), an appropriate calibration curve was easily obtained by plotting the area of diarylmethane product over the area of internal standard (y-axis) versus the known mass of diarylmethane product in each vial (x-axis). Using Sigmaplot, a nonlinear regression analysis was obtained for each calibration curve.

To test the accuracy of the standard calibration curve shown in **Figure 3.3**, a known mass of pure diphenylmethane (0.0223 g) was placed in a GC-MS vial, along with 100 μ L of the dodecane stock solution. After performing GC-MS analysis on the mixture (samples prepared using diethyl ether), the data obtained (area of diarylmethane product over the area of internal standard) was fitted with the calibration curve shown in **Figure 3.3**. According to the nonlinear regression analysis, the mass of diphenylmethane present in the sample was .0221₄ g. This mass is extremely close to the actual mass (0.0223 g) weighed out on the analytical balance proving that the calibration curve used is very accurate.

For each cross-coupling reaction performed, reaction products were dried overnight on a Schlenk line and the dried products were weighed accurately via an analytical balance. GC-MS analysis was then performed on a portion of the reaction products which were dissolved in diethyl ether. 100 μ L of the dodecane stock solution was also added to the sample. After GC-MS data was collected, the amount of desired product in the portion used was easily calculated through the use of the appropriate

standard curve (as explained above). By extrapolation, the amount of desired product in the whole dried sample could then be calculated along with the % yield of cross-coupled products.

The percent yields of cross-coupled products were also obtained using ^1H NMR spectroscopy. As discussed above, the reaction products were first dried overnight on a Schlenk line and the dried products were weighed accurately via an analytical balance. ^1H NMR analysis was then performed on a portion of the reaction products (known mass) which were dissolved in CDCl_3 with TMS. To each portion, a known mass of acetophenone (internal standard) was also added. Acetophenone was an excellent choice as an internal standard for ^1H NMR analysis since the peaks originating from acetophenone did not interfere (overlap) with the signals from the diarylmethane compound. By integrating a known signal from the desired diarylmethane product (the singlet originating from the methylene bridge (ArCH_2Ar) at approximately 4.00 ppm) relative to a known signal originating from a proton environment of acetophenone, the number of mols of desired product in the portion analyzed could be easily measured (since the mass of acetophenone was previously determined). Once the mass of the desired product in the portion was determined, the amount of desired product in the whole dried sample could then be calculated by extrapolation, and in turn, the percent yield of cross-coupled products.

3.3 Experimental

3.3.1 General Methods and Materials

All C-C cross-coupling reactions were performed under an atmosphere of dry oxygen-free nitrogen by means of standard Schlenk techniques or by using an MBraun LabmasterDP glove box. Anhydrous diethyl ether was purified using an MBraun solvent purification system. Alkyl halides and Grignard reagents were purchased from Aldrich and used without further purification. Dodecane (purchased from Aldrich) was used as an internal standard for GC-MS analysis and diethyl ether was used for sample preparation. Acetophenone (purchased from Aldrich) was used as an internal standard for ^1H NMR analysis (CDCl_3 with TMS used as the solvent). Due to the presence of homo-coupled by-products in many of the cross-coupling reactions attempted, it was extremely difficult to analyze the cross-coupled product via NMR analysis. In fact, for most of the products analyzed, many of the peaks corresponding to the desired cross-coupled product could not be identified (due to peak overlap as a result of signals arising from the homocoupled by-products). However, for each cross-coupled product analyzed via ^1H NMR analysis, there was a distinct peak at approximately 4.00 ppm originating from the methylene bridge (ArCH_2Ar) of the diaryl compound which could be clearly identified. This specific peak was used for yield determination via ^1H NMR analysis and supports the presence of the diaryl compound(s).

3.3.2 Instrumentation

NMR spectra were recorded in CDCl_3 using a Bruker Avance III 300 MHz instrument with a 5 mm-multinuclear broadband observe (BBFO) probe. Gas chromatography mass spectrometry (GC-MS) analyses were performed using an Agilent Technologies 7890 GC system coupled to an Agilent Technologies 5975C mass selective detector (MSD). The chromatograph is equipped with electronic pressure control, split/splitless and on-column injectors, and an HP5-MS column.

3.3.3 Catalytic Method at Room Temperature (Catalytic Procedure (CP))

Catalyst **C3** (0.10 mmol) in CH_2Cl_2 (3 mL) was added to a 30 mL Schlenk flask and the solvent removed in vacuo. Et_2O (5 mL) and the alkyl halide (2.0 mmol) were added to the catalyst under dry nitrogen. A solution of Grignard reagent (4.0 mmol) (in either THF or Et_2O) was added dropwise under vigorous stirring. The resulting mixture was stirred at room temperature for 30 min and the reaction was quenched with HCl (2.0 M, 5 mL). The organic phase was extracted with Et_2O (5 mL) and dried over MgSO_4 . The organic phase was then passed through a plug of silica and the diethyl ether was removed *in vacuo*. The resulting product(s) were then analyzed by GC-MS (dodecane as internal standard) and NMR spectroscopy (acetophenone as internal standard). The characteristic methylene peak was observed in the ^1H NMR spectrum for each diarylmethane product, but the aromatic peaks were more difficult to assign due to presence of biaryl or bibenzyl contaminants. Please see the appendix (section 5.2) for representative GC-MS and NMR spectra of cross-coupled products.

Diphenylmethane (Table 3.1, Entry 1): Prepared according to **CP** using benzyl bromide (0.3421 g, 2.00 mmol) and phenylmagnesium bromide (4.00 mL, 1.0 M in THF, 4.00 mmol). Product isolated as a clear light yellow oil (0.0981 g, 30%). GC-MS retention time: m/z (% ion): 7.211 min dodecane: 170.2 (10, [M]⁺); 8.638 min biphenyl: 154.1 (100, [M]⁺); 9.016 min diphenylmethane: 167.1 (100, [M]⁺); 9.756 min bibenzyl: 182.1 (100, [M]⁺). ¹H NMR (300 MHz, CDCl₃, 298 K, δ_H): diphenylmethane 3.97 (s, 2H, ArCH₂Ar). ¹³C{¹H} NMR (75 MHz, CDCl₃, 298 K, δ_C): diphenylmethane 42.01, 126.12, 128.39, 128.99, 141.29.

Diphenylmethane (Table 3.1, Entry 2): Prepared according to **CP** using benzyl chloride (0.2532 g, 2.00 mmol) and phenylmagnesium bromide (4.00 mL, 1.0 M in THF, 4.00 mmol). Product isolated as a clear light yellow oil (0.1657 g, 32%). GC-MS retention time: m/z (% ion): 7.210 min dodecane: 170.2 (10, [M]⁺); 8.637 min biphenyl: 154.1 (100, [M]⁺); 9.015 min diphenylmethane: 167.1 (100, [M]⁺); 9.832 min bibenzyl: 182.1 (100, [M]⁺). ¹H NMR (300 MHz, CDCl₃, 298 K, δ_H): diphenylmethane 3.97 (s, 2H, ArCH₂Ar). ¹³C{¹H} NMR (75 MHz, CDCl₃, 298 K, δ_C): diphenylmethane 42.03, 126.14, 128.41, 129.01, 141.31.

1-Benzyl-4-methylbenzene (Table 3.1, Entry 3): Prepared according to **CP** using benzyl bromide (0.3421 g, 2.00 mmol) and *p*-tolylmagnesium bromide (8.00 mL, 0.5 M in Et₂O, 4.00 mmol). Product isolated as a clear light yellow oil (0.1774 g, 49%). GC-MS retention time: m/z (% ion): 7.210 min dodecane: 170.2 (10, [M]⁺); 9.752 min bibenzyl: 182.1 (30, [M]⁺); 9.899 min 4,4'-dimethylbiphenyl: 182.1 (70, [M]⁺); 10.624 min 1-

benzyl-4-methylbenzene: 182.1 (100, [M]⁺). ¹H NMR (300 MHz, CDCl₃, 298 K, δ_H): 1-benzyl-4-methylbenzene 3.93 (s, 2H, ArCH₂Ar); 2.30 (s, 3H, ArCH₃). ¹³C{¹H} NMR (75 MHz, CDCl₃, 298 K, δ_C): 1-benzyl-4-methylbenzene 21.07, 41.59, 125.96, 128.47, 128.86, 128.92, 129.19.

1-Benzyl-4-methylbenzene (Table 3.1, Entry 4): Prepared according to **CP** using benzyl chloride (0.2532 g, 2.00 mmol) and *p*-tolylmagnesium bromide (8.00 mL, 0.5 M in Et₂O, 4.00 mmol). Product isolated as a clear light yellow oil (0.1496 g, 41%). GC-MS retention time: m/z (% ion): 7.207 min dodecane: 170.2 (10, [M]⁺); 9.754 min bibenzyl: 182.1 (30, [M]⁺); 9.901 min 4,4'-dimethylbiphenyl: 182.1 (70, [M]⁺); 10.637 min 1-benzyl-4-methylbenzene: 182.1 (100, [M]⁺). ¹H NMR (300 MHz, CDCl₃, 298 K, δ_H): 1-benzyl-4-methylbenzene 3.93 (s, 2H, ArCH₂Ar); 2.30 (s, 3H, ArCH₃). ¹³C{¹H} NMR (75 MHz, CDCl₃, 298 K, δ_C): 1-benzyl-4-methylbenzene 21.09, 41.59, 125.98, 128.49, 128.87, 128.93, 129.21, 135.58, 138.34.

1-Benzyl-2-methylbenzene (Table 3.1, Entry 5): Prepared according to **CP** using benzyl bromide (0.3421 g, 2.00 mmol) and *o*-tolylmagnesium bromide (2.00 mL, 2.0 M in Et₂O, 4.00 mmol). Product isolated as a colorless oil (0.3134 g, 86%). GC-MS retention time: m/z (% ion): 7.211 min dodecane: 170.2 (10, [M]⁺); 8.935 min 4,4'-dimethylbiphenyl: 182.1 (70, [M]⁺); 9.752 min bibenzyl: 182.1 (30, [M]⁺); 9.845 min 1-benzyl-2-methylbenzene: 182.1 (100, [M]⁺). ¹H NMR (300 MHz, CDCl₃, 298 K, δ_H): 1-benzyl-2-methylbenzene 3.98 (s, 2H, ArCH₂Ar); 2.23 (s, 3H, ArCH₃). ¹³C{¹H} NMR (75 MHz,

CDCl₃, 298 K, δ_C): 1-benzyl-2-methylbenzene 19.87, 39.50, 126.49, 128.49, 128.78, 129.84, 129.91, 130.32, 133.15, 135.84, 140.43, 141.63.

1-Benzyl-2-methylbenzene (Table 3.1, Entry 6): Prepared according to **CP** using benzyl chloride (0.2532 g, 2.00 mmol) and *o*-tolylmagnesium bromide (2.00 mL, 2.0 M in Et₂O, 4.00 mmol). Product isolated as a colorless oil (0.3418 g, 94%). GC-MS retention time: m/z (% ion): 7.209 min dodecane: 170.2 (10, [M]⁺); 8.935 min 4,4'-dimethylbiphenyl: 182.1 (70, [M]⁺); 9.754 min bibenzyl: 182.1 (30, [M]⁺); 9.845 min 1-benzyl-2-methylbenzene: 182.1 (100, [M]⁺). ¹H NMR (300 MHz, CDCl₃, 298 K, δ_H): 1-benzyl-2-methylbenzene 3.98 (s, 2H, ArCH₂Ar); 2.23 (s, 3H, ArCH₃). ¹³C{¹H} NMR (75 MHz, CDCl₃, 298 K, δ_C): 1-benzyl-2-methylbenzene 19.87, 39.50, 126.49, 128.50, 128.79, 129.84, 129.99, 130.32, 133.15, 135.85, 140.44, 141.64.

4-Benzylanisole (Table 3.1, Entry 7): Prepared according to **CP** using benzyl bromide (0.3421 g, 2.00 mmol) and 4-anisylmagnesium bromide (8.00 mL, 0.5 M in Et₂O, 4.00 mmol). Product isolated as a clear light yellow oil (0.0815 g, 21%). GC-MS retention time: m/z (% ion): 7.211 min dodecane: 170.2 (10, [M]⁺); 9.753 min bibenzyl: 182.1 (30, [M]⁺); 11.761 min 4-benzylanisole: 198.1 (100, [M]⁺); 17.194 min 4,4'-dimethoxybiphenyl: 214.1 (100, [M]⁺). ¹H NMR (300 MHz, CDCl₃, 298 K, δ_H): 4-benzylanisole 3.91 (s, 2H, ArCH₂Ar); 3.82 (s, 3H, ArOCH₃). ¹³C{¹H} NMR (75 MHz, CDCl₃, 298 K, δ_C): 4-benzylanisole 41.09, 55.34, 113.93, 125.96, 128.41, 128.86, 129.80, 133.30, 141.82, 158.72.

1-Benzyl-4-fluorobenzene (Table 3.1, Entry 8): Prepared according to **CP** using benzyl bromide (0.3421 g, 2.00 mmol) and 4-fluorophenylmagnesium bromide (4.00 mL, 1.0 M in Et₂O, 4.00 mmol). Product isolated as a clear light yellow oil (0.0778 g, 21%). GC-MS retention time: m/z (% ion): 7.206 min dodecane: 170.2 (10, [M]⁺); 8.606 min 4,4'-difluorobiphenyl: 190.1 (100, [M]⁺); 9.047 min 1-benzyl-4-fluorobenzene: 186.1 (100, [M]⁺); 9.753 min bibenzyl: 182.1 (30, [M]⁺). ¹H NMR (300 MHz, CDCl₃, 298 K, δ_H): 1-benzyl-4-fluorobenzene 3.94 (s, 2H, ArCH₂Ar). ¹³C{¹H} NMR (75 MHz, CDCl₃, 298 K, δ_C): 1-benzyl-4-fluorobenzene 41.11, 115.09, 115.37, 126.23, 128.55, 128.86, 130.00, 130.01, 136.40, 136.44, 141.82, 160.22, 164.09.

1-Benzyl-2,6-dimethylbenzene (Table 3.1, Entry 9): Prepared according to **CP** using benzyl bromide (0.3421 g, 2.00 mmol) and 2,6-dimethylphenylmagnesium bromide (4.00 mL, 1.0 M in THF, 4.00 mmol). Product isolated as a clear colorless oil (0.3720 g, 95%). GC-MS retention time: m/z (% ion): 7.210 min dodecane: 170.2 (10, [M]⁺); 10.520 min 2,2',6,6'-dimethylbiphenyl: 210.1 (60, [M]⁺); 10.717 min 1-benzyl-2,6-dimethylbenzene: 196.1 (90, [M]⁺). ¹H NMR (300 MHz, CDCl₃, 298 K, δ_H): 1-benzyl-2,6-dimethylbenzene 4.05 (s, 2H, ArCH₂Ar); 2.23 (s, 6H, ArCH₃). ¹³C{¹H} NMR (75 MHz, CDCl₃, 298 K, δ_C): 1-benzyl-2,6-dimethylbenzene 20.28, 35.10, 126.37, 128.17, 128.63, 136.92, 137.20, 137.22, 137.83, 139.84.

1-Phenyl-2-propene (Table 3.1, Entry 10): Prepared according to **CP** using benzyl bromide (0.3421 g, 2.00 mmol) and vinylmagnesium bromide (4.00 mL, 1.0 M in Et₂O, 4.00 mmol). Trace amount of product found. GC-MS retention time: m/z (% ion): 5.077

min 1-Phenyl-2-propene: 117.0 (100, $[M]^+$); 7.209 min dodecane: 170.2 (10, $[M]^+$); 9.753 min bibenzyl: 182.1 (30, $[M]^+$).

1-Methoxy-4-(4-methylbenzyl)benzene (Table 3.2, Entry 1): Prepared according to CP using 4-methylbenzyl bromide (0.3721 g, 2.00 mmol) and 4-anisylmagnesium bromide (8.00 mL, 0.5 M in Et₂O, 4.00 mmol). Product isolated as a clear light yellow oil (0.0787 g, 19%). GC-MS retention time: m/z (% ion): 7.209 min dodecane: 170.2 (10, $[M]^+$); 12.228 min 4,4'-dimethylbibenzyl: 210.1 (20, $[M]^+$); 13.677 min 1-methoxy-4-(4-methylbenzyl)benzene: 212.1 (100, $[M]^+$). ¹H NMR (300 MHz, CDCl₃, 298 K, δ_H): 1-methoxy-4-(4-methylbenzyl)benzene 3.87 (s, 2H, ArCH₂Ar); 3.82 (s, 3H, ArOCH₃); 2.31 (s, 3H, ArCH₃). ¹³C{¹H} NMR (75 MHz, CDCl₃, 298 K, δ_C): 1-methoxy-4-(4-methylbenzyl)benzene 21.07, 40.64, 55.30, 113.89, 128.73, 129.16, 129.83, 133.53, 135.46, 138.55, 157.92.

1-Fluoro-4-(4-methylbenzyl)benzene (Table 3.2, Entry 2): Prepared according to CP using 4-methylbenzyl bromide (0.3721 g, 2.00 mmol) and 4-fluorophenylmagnesium bromide (4.00 mL, 1.0 M in Et₂O, 4.00 mmol). Product isolated as a clear light yellow oil (0.0537 g, 13%). GC-MS retention time: m/z (% ion): 7.210 min dodecane: 170.2 (10, $[M]^+$); 8.610 min 4,4'-difluorobiphenyl: 190.1 (100, $[M]^+$); 9.933 min 1-fluoro-4-(4-methylbenzyl)benzene: 200.1 (80, $[M]^+$); 12.231 min 4,4'-dimethylbibenzyl: 210.1 (20, $[M]^+$). ¹H NMR (300 MHz, CDCl₃, 298 K, δ_H): 1-fluoro-4-(4-methylbenzyl)benzene 3.81 (s, 2H, ArCH₂Ar); 2.23 (s, 3H, ArCH₃). ¹³C{¹H} NMR (75 MHz, CDCl₃, 298 K, δ_C): 1-

fluoro-4-(4-methylbenzyl)benzene 21.06, 40.70, 115.05, 115.53, 128.74, 129.04, 130.19, 135.32, 136.40, 136.45, 138.90, 160.83, 164.09.

Di-*p*-tolylmethane (Table 3.2, Entry 3): Prepared according to **CP** using 4-methylbenzyl bromide (0.3701 g, 2.00 mmol) and *p*-tolylmagnesium bromide (8.00 mL, 0.5 M in Et₂O, 4.00 mmol). Product isolated as a clear light yellow oil (0.1476 g, 38%). GC-MS retention time: *m/z* (% ion): 7.211 min dodecane: 170.2 (10, [M]⁺); 10.641 min 4,4'-dimethylbiphenyl: 182.2 (100, [M]⁺); 11.078 min di-*p*-tolylmethane: 196.2 (70, [M]⁺); 12.249 min 4,4'-dimethylbibenzyl: 210.2 (25, [M]⁺). ¹H NMR (300 MHz, CDCl₃, 298 K, δ_H): 1-benzyl-4-methylbenzene 3.89 (s, 2H, ArCH₂Ar); 2.38 (s, 6H, ArCH₃). ¹³C{¹H} NMR (75 MHz, CDCl₃, 298 K, δ_C): di-*p*-tolylmethane 21.07, 41.15, 128.81, 129.17, 135.48, 138.43.

Di-*p*-tolylmethane (Table 3.2, Entry 4): Prepared according to **CP** using 4-methylbenzyl chloride (0.2812 g, 2.00 mmol) and *p*-tolylmagnesium bromide (8.00 mL, 0.5 M in Et₂O, 4.00 mmol). Product isolated as a clear colorless oil (0.3329 g, 85%). GC-MS retention time: *m/z* (% ion): 7.206 min dodecane: 170.2 (10, [M]⁺); 10.627 min 4,4'-dimethylbiphenyl: 182.1 (100, [M]⁺); 11.058 min di-*p*-tolylmethane: 196.1 (70, [M]⁺); 12.249 min 4,4'-dimethylbibenzyl: 210.1 (25, [M]⁺). ¹H NMR (300 MHz, CDCl₃, 298 K, δ_H): 1-benzyl-4-methylbenzene 3.89 (s, 2H, ArCH₂Ar); 2.30 (s, 6H, ArCH₃). ¹³C{¹H} NMR (75 MHz, CDCl₃, 298 K, δ_C): di-*p*-tolylmethane 21.06, 41.14, 128.80, 129.17, 135.47, 138.42.

1-Bromo-4-(4-methylbenzyl)benzene (Table 3.2, Entry 5): Prepared according to CP using 4-bromobenzyl bromide (0.4999 g, 2.00 mmol) and *p*-tolylmagnesium bromide (8.00 mL, 0.5 M in Et₂O, 4.00 mmol). Product isolated as a clear colorless oil (0.3494 g, 38%). GC-MS retention time: *m/z* (% ion): 7.205 min dodecane: 170.2 (10, [M]⁺); 10.627 min 4,4'-dimethylbiphenyl: 182.1 (100, [M]⁺); 14.241 min 1-bromo-4-(2-phenylethyl)benzene: 262.0 (10, [M]⁺); 14.638 min 1-bromo-4-(4-methylbenzyl)benzene: 262.0 (60, [M]⁺). ¹H NMR (300 MHz, CDCl₃, 298 K, δ_H): 1-bromo-4-(4-methylbenzyl)benzene: 3.87 (s, 2H, ArCH₂Ar); 2.38 (s, 3H, ArCH₃). ¹³C{¹H} NMR (75 MHz, CDCl₃, 298 K, δ_C): 1-bromo-4-(4-methylbenzyl)benzene 21.06, 40.92, 119.80, 128.62, 129.21, 130.64, 131.51, 135.86, 137.44, 140.45.

Methyl-4-(4-methylbenzyl)benzoate (Table 3.2, Entry 6): Prepared according to CP using methyl-4-(bromomethyl)benzoate (0.4862 g, 2.00 mmol) and *p*-tolylmagnesium bromide (8.00 mL, 0.5 M in Et₂O, 4.00 mmol). Trace amount of product found. GC-MS retention time: *m/z* (% ion): 7.212 min dodecane: 170.2 (10, [M]⁺); 10.625 min 4,4'-dimethylbiphenyl: 182.1 (100, [M]⁺); 20.320 min methyl-4-(4-methylbenzyl)benzoate: 262.0 (10, [M]⁺).

1-Methyl-4-(4-(trifluoromethyl)benzyl)benzene (Table 3.2, Entry 7): Prepared according to CP using 4-(trifluoromethyl)benzyl bromide (0.4759 g, 2.00 mmol) and *p*-tolylmagnesium bromide (8.00 mL, 0.5 M in Et₂O, 4.00 mmol). Product isolated as a clear colorless oil (0.3785 g, 76%). GC-MS retention time: *m/z* (% ion): 10.029 min dodecane: 170.2 (10, [M]⁺); 14.757 min 1-methyl-4-(4-(trifluoromethyl)benzyl)benzene:

250.10 (100, [M]⁺); 14.861 min 4,4'-(trifluoromethyl)biphenyl: 318.1 (10, [M]⁺); 15.528 min 4,4'-dimethylbiphenyl: 182.1 (100, [M]⁺). ¹H NMR (300 MHz, CDCl₃, 298 K, δ_H): 1-methyl-4-(4-(trifluoromethyl)benzyl)benzene: 3.97 (s, 2H, ArCH₂Ar); 2.31 (s, 3H, ArCH₃). ¹³C{¹H} NMR (75 MHz, CDCl₃, 298 K, δ_C): 1-methyl-4-(4-(trifluoromethyl)benzyl)benzene 21.13, 41.42, 126.86, 128.62, 129.26, 129.49, 136.11, 138.35, 145.62.

1-Methoxy-3-(4-methylbenzyl)benzene (Table 3.3, Entry 1): Prepared according to **CP** using 3-methoxybenzyl bromide (0.4021 g, 2.00 mmol) and *p*-tolylmagnesium bromide (8.00 mL, 0.5 M in Et₂O, 4.00 mmol). Product isolated as a clear colorless oil (0.3069 g, 72%). GC-MS retention time: m/z (% ion): 7.213 min dodecane: 170.2 (10, [M]⁺); 10.624 min 4,4'-dimethylbiphenyl: 182.1 (100, [M]⁺); 13.214 min 1-methoxy-3-(4-methylbenzyl)benzene: 212.1 (100, [M]⁺); 19.639 min 3,3'-(dimethoxy)biphenyl: 242.1 (30, [M]⁺). ¹H NMR (300 MHz, CDCl₃, 298 K, δ_H): 1-methoxy-3-(4-methylbenzyl)benzene: 3.90 (s, 2H, ArCH₂Ar); 3.75 (s, 3H, ArOCH₃); 2.38 (s, 3H, ArCH₃). ¹³C{¹H} NMR (75 MHz, CDCl₃, 298 K, δ_C): 1-methoxy-3-(4-methylbenzyl)benzene 21.07, 41.60, 55.18, 111.28, 114.77, 121.37, 128.83, 129.19, 129.42, 135.59, 137.91, 143.05, 159.74.

1-Methoxy-3-(4-methylbenzyl)benzene (Table 3.3, Entry 2): Prepared according to **CP** using 3-methoxybenzyl chloride (0.2906 g, 2.00 mmol) and *p*-tolylmagnesium bromide (8.00 mL, 0.5 M in Et₂O, 4.00 mmol). Product isolated as a clear colorless oil (0.3879 g, 91%). GC-MS retention time: m/z (% ion): 7.208 min dodecane: 170.2 (10, [M]⁺);

10.619 min 4,4'-dimethylbiphenyl: 182.1 (100, $[M]^+$); 13.257 min 1-methoxy-3-(4-methylbenzyl)benzene: 212.1 (100, $[M]^+$). ^1H NMR (300 MHz, CDCl_3 , 298 K, δ_{H}): 1-methoxy-3-(4-methylbenzyl)benzene: 3.90 (s, 2H, ArCH_2Ar); 3.75 (s, 3H, ArOCH_3); 2.38 (s, 3H, ArCH_3). $^{13}\text{C}\{^1\text{H}\}$ NMR (75 MHz, CDCl_3 , 298 K, δ_{C}): 1-methoxy-3-(4-methylbenzyl)benzene 21.06, 41.60, 55.17, 111.29, 114.77, 121.37, 128.83, 129.19, 129.42, 135.60, 137.91, 143.05, 159.74.

1-Methoxy-3-(4-methoxybenzyl)benzene (Table 3.3, Entry 3): Prepared according to **CP** using 3-methoxybenzyl bromide (0.4021 g, 2.00 mmol) and 4-anisylmagnesium bromide (8.00 mL, 0.5 M in Et_2O , 4.00 mmol). Product isolated as a clear light yellow oil (0.1112 g, 24%). GC-MS retention time: m/z (% ion): 7.207 min dodecane: 170.2 (10, $[M]^+$); 8.395 min 3-methoxybenzyl bromide: 200.0 (10, $[M]^+$); 17.126 min 4,4'-dimethoxybiphenyl: 214.1 (100, $[M]^+$); 17.408 min 1-methoxy-3-(4-methoxybenzyl)benzene: 228.1 (100, $[M]^+$); 19.671 min 3,3'-(dimethoxy)biphenyl: 242.1 (30, $[M]^+$). ^1H NMR (300 MHz, CDCl_3 , 298 K, δ_{H}): 1-methoxy-4-(4-methylbenzyl)benzene: 3.89 (s, 2H, ArCH_2Ar); 3.79 (s, 3H, ArOCH_3); 3.75 (s, 3H, ArOCH_3). $^{13}\text{C}\{^1\text{H}\}$ NMR (75 MHz, CDCl_3 , 298 K, δ_{C}): 1-methoxy-3-(4-methoxybenzyl)benzene 26.71, 55.21, 55.37, 111.26, 114.85, 121.35, 128.64, 129.49, 129.87, 137.15, 159.79.

1-Bromo-2-(4-methylbenzyl)benzene (Table 3.4, Entry 1): Prepared according to **CP** using 2-bromobenzyl bromide (0.4999 g, 2.00 mmol) and *p*-tolylmagnesium bromide (8.00 mL, 0.5 M in Et_2O , 4.00 mmol). Trace amount of product found. GC-MS retention

time: m/z (% ion): 7.211 min dodecane: 170.2 (10, [M]⁺); 10.625 min 4,4'-dimethylbiphenyl: 182.1 (100, [M]⁺); 13.906 min 1-bromo-2-(4-methylbenzyl)benzene: 260.0 (60, [M]⁺).

2-(4-Methylbenzyl)benzonitrile (Table 3.4, Entry 2): Prepared according to CP using 2-(bromomethyl)benzonitrile (0.3921 g, 2.00 mmol) and *p*-tolylmagnesium bromide (8.00 mL, 0.5 M in Et₂O, 4.00 mmol). Product found in 0% yield. GC-MS retention time: m/z (% ion): 7.207 min dodecane: 170.2 (10, [M]⁺); 10.622 min 4,4'-dimethylbiphenyl: 182.1 (100, [M]⁺).

1-Methyl-4-(2-(trifluoromethyl)benzyl)benzene (Table 3.4, Entry 3): Prepared according to CP using 2-(trifluoromethyl)benzyl bromide (0.4759 g, 2.00 mmol) and *p*-tolylmagnesium bromide (8.00 mL, 0.5 M in Et₂O, 4.00 mmol). Product isolated as a clear light yellow oil (0.1207 g, 24%). GC-MS retention time: m/z (% ion): 7.210 min dodecane: 170.2 (10, [M]⁺); 9.709 min 4,4'-(trifluoromethyl)biphenyl: 318.1 (10, [M]⁺); 9.826 min 1-methyl-4-(2-(trifluoromethyl)benzyl)benzene: 250.1 (100, [M]⁺); 10.622 min 4,4'-dimethylbiphenyl: 182.1 (100, [M]⁺). ¹H NMR (300 MHz, CDCl₃, 298 K, δ): 1-methoxy-4-(4-methylbenzyl)benzene: 4.13 (s, 2H, ArCH₂Ar); 2.31 (s, 3H, ArCH₃).

4-(1-Methyl)-1,1'-ethylidenebenzene (Table 3.4, Entry 4): Prepared according to CP using (1-bromoethyl)benzene (0.3701 g, 2.00 mmol) and *p*-tolylmagnesium bromide (8.00 mL, 0.5 M in Et₂O, 4.00 mmol). Trace amount of product found. GC-MS retention time: m/z (% ion): 14.355 min dodecane: 170.2 (10, [M]⁺); 24.347 min 1,1'-(1,2-

dimethyl-1,2-ethanediyl)bis-benzene: 210.1 (5, $[M]^+$); 24.493 min 4-(1-methyl)-1,1'-ethylidenebenzene: 196.1 (40, $[M]^+$); 24.786 min 4,4'-dimethylbiphenyl: 182.1 (100, $[M]^+$); 24.947 min 1,1'-(1,2-dimethyl-1,2-ethanediyl)bis-benzene: 210.1 (5, $[M]^+$).

3.4 References

- ¹ K. McPhail, D. Rivett, D. Lack, M. Davies-Coleman, *Tetrahedron*, **2000**, 56, 9391.
- ² Y. Long, X. Jiang, R. Dayam, T. Sacher, R. Shoemaker, S. Sei, N. Neamati, *J. Med. Chem.*, **2004**, 47, 2561.
- ³ W. Dohle, D. Lindsay, P. Knochel, *Org. Lett.*, **2001**, 3, 2871.
- ⁴ M. Burns, I. Fairlamb, A. Kapdi, P. Sehnal, R. Taylor, *Org. Lett.*, **2007**, 9, 5397.
- ⁵ *Metal-Catalyzed Cross-Coupling Reactions*, 2nd ed., A. de Meijere and F. Diederich, Eds, Wiley-VCH, Weinheim, 2004.
- ⁶ R. B. Bedford, M. Huwe, M. C. Wilkinson, *Chem. Commun.*, **2009**, 600.
- ⁷ R. R. Chowdhury, A. K. Crane, C. Fowler, P. Kwong, C. M. Kozak, *Chem. Commun.*, **2008**, 94.
- ⁸ K. Hassan, L. N. Dawe, C. M. Kozak, *Eur. J. Org. Chem.*, **2011**, 4610.
- ⁹ X. Qian, L. N. Dawe, C. M. Kozak, *Dalton Trans.*, **2011**, 40, 93.
- ¹⁰ T. Nagano, T. Hayashi, *Org. Lett.*, **2005**, 7, 491.
- ¹¹ X. Qian, C. M. Kozak, *Synlett*, **2011**, 6, 852.
- ¹² M. Nakamura, K. Matsuo, S. Ito, B. Nakamura, *J. Am. Chem. Soc.*, **2004**, 126, 3686.
- ¹³ R. B. Bedford, D. Bruce, R. Frost, M. Hird, J. Goodby, *Chem. Commun.*, **2005**, 2822.
- ¹⁴ A. Fürstner, A. Leitner, M. Méndez, H. Krause, *J. Am. Chem. Soc.*, **2002**, 124, 13856.
- ¹⁵ J. Kleimark, A. Hedström, P. Larsson, C. Johansson, P. Norrby, *ChemCatChem*, **2009**, 152.
- ¹⁶ R. B. Bedford, M. Betham, D. Bruce, A. Danopoulos, R. Frost, M. Hird, *J. Org. Chem.*, **2006**, 71, 1104.

¹⁷ P. Norrby, J. Kleimark, A. Hedstrom, P. Larsson, C. Johansson, *ChemCatChem*, **2009**, 1, 152.

Chapter 4 – Conclusions and Future Work

4.1 Complex syntheses

In the early stages of this Master's project, the primary goal was to develop a series of air stable, non-hygroscopic, single component iron(III) catalysts for the cross-coupling of alkyl halides with aryl Grignard reagents. After many long hours in the lab, it is clear that the synthesis of iron(III) complexes supported by tridentate amine-bis(phenolate) ligands is not as straightforward as it appears in the literature. At times, not only were there issues with the purification of the complexes, there were also problems with water contamination even though all reactions were carried out on a Schlenk line (under nitrogen) and all purification procedures were performed inside a nitrogen filled glove box. During the complex synthesis, frits and cannula filters were frequently used. Insufficient drying of the frits and cannula filters may have exposed the reactions with trace amounts of water leading to the generation of unexpected complexes.

Previously in the Kozak group, a series of octahedral amine-bis(phenolate)Fe(acac) complexes was synthesized and used as catalysts for the cross-coupling of aryl Grignard reagents with alkyl halides.¹ In order to generate more reactive catalysts (compared to tetradentate counterparts), while still maintaining the robust nature of the catalyst precursor, the synthesis of iron(III) complexes supported by tridentate amine-bis(phenolate) ligands with relatively bulky substituents on the phenolate rings was attempted. Unfortunately, when Fe(acac)₃ was reacted with tridentate amine-bis(phenolate) ligands in THF or methanol (in the presence of triethylamine), isolation of the desired trigonal bipyramidal amine-bis(phenolate) Fe(acac) compound has been

unsuccessful to date. In the future, it would be interesting to attempt the synthesis of tridentate amine-bis(phenolate) Fe(acac) complexes by reacting Fe(acac)₃ with more reactive tridentate ligand precursors prepared from stronger bases such as NaH or *n*-BuLi.

During the course of this research, five authentic iron(III) halide-complexes and one iron(III) hydroxy-complex supported by tridentate amine-bis(phenolate) ligands were synthesized and characterized via several analytical and spectroscopic techniques. In order to successfully prepare these complexes, three separate reaction procedures were employed, each of which employed a different base. According to previous studies, when FeCl₃ is reacted with a tridentate amine-bis(phenol) ligand in the presence of triethylamine, the generated complexes exist as halide-bridged dimers in the solid state giving distorted trigonal bipyramidal iron(III) ions.² However, recent results obtained during the course of this study suggest that other Fe(III) complexes can be generated depending on the purification procedures employed and the steric requirements of the amine-bis(phenolate) backbone. Surprisingly, when FeCl₃ was reacted with H₂[ONO]^{BuMeiPr} as previously described by Kozak and co-workers, a trigonal bipyramidal iron(III) “ate” complex was isolated with a triethylammonium cation instead of the expected chloride-bridged dimer (**Figure 4.1**). Unfortunately, this specific complex was not practical as a catalyst for C-C cross coupling since the triethylammonium cation could react with the Grignard starting material. When FeCl₃ was reacted with H₂[ONO]^{AmAmBz} in the presence of triethylamine, a monomeric chloride species was found in the solid state, with a coordinated THF ligand (**Figure 4.2**). Due to the presence of bulky *t*-amyl substituents on the phenolate backbone, the iron(III) THF adduct was likely formed in

favor of the chloride-bridged dimer since dimer formation may be sterically unfavored (but there was enough space for THF to coordinate).

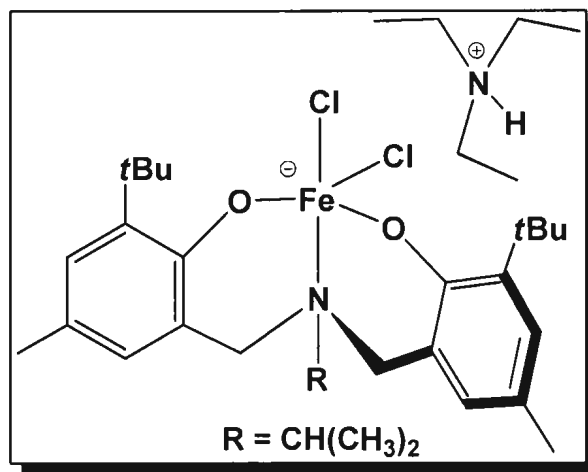


Figure 4.1: A representation of **C1** ($[\text{NEt}_3\text{H}]^+[\text{FeCl}_2\text{L1}]^-$).

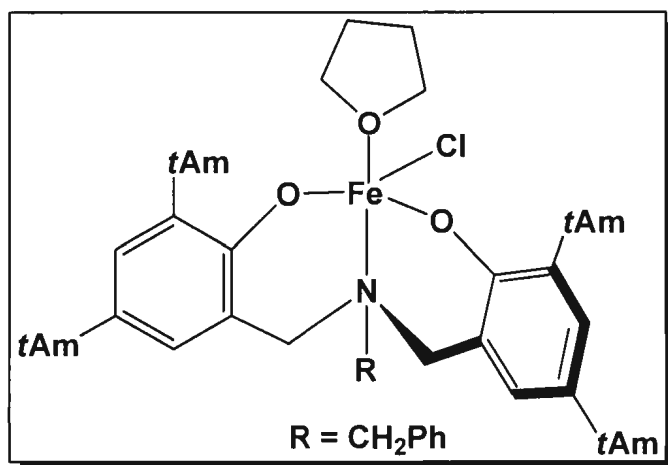


Figure 4.2: A representation of **C3** ($\text{FeCl}(\text{THF})\text{L2}$).

Previously, in an attempt to synthesize a bromide-bridged dimer using triethylamine as a base, Kozak and-coworkers had surprisingly synthesized a zwitterionic

tetrahedral iron(III) complex bearing two bromide ligands and a quarternized amonium fragment.² The generation of such a complex may be attributed to the incomplete deprotonation of the amine-bis(phenol) ligand (likely due to the unwanted presence of water). With this in mind, a stronger base (such as NaH or *n*BuLi) was also employed during the synthesis of trigonal bipyramidal iron(III) bromide complexes. When FeBr₃ was reacted with the sodium salt of H₂[ONO]^{AmAmBz}, a monomeric species was once again isolated in the solid state, with a coordinated THF ligand (**Figure 4.3**). However, when FeBr₃ was reacted with the sodium salt of H₂[ONO]^{BuMerPr}, a zwitterionic tetrahedral iron(III) complex bearing two bromide ligands and a quarternized amonium fragment was generated (**Figure 4.4**). Even though great precaution was taken, contamination with water likely occurred during the reaction procedure promoting the generation of the tetrahedral iron(III) species.

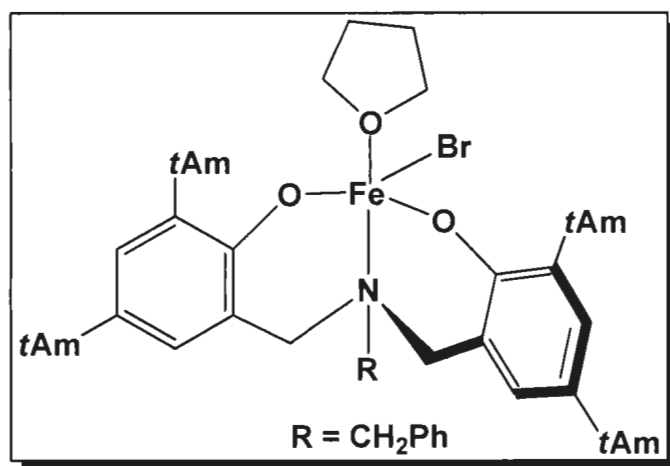


Figure 4.3: A representation of C4 (FeBr(THF)L2).

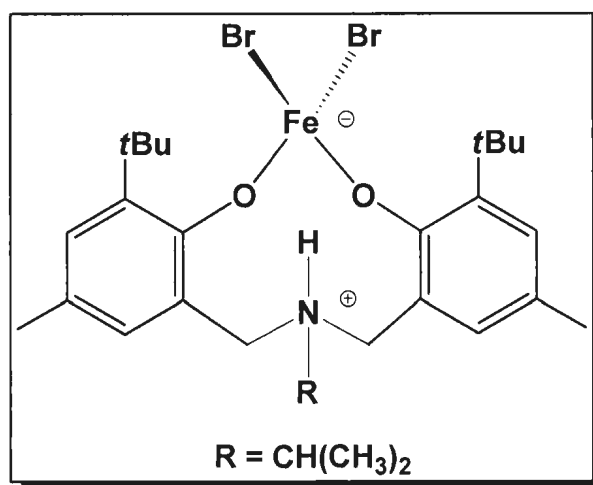


Figure 4.4: A representation of **C5** ($\text{FeBr}_2\text{L1H}$).

Problems attributable to water contamination were also found during the reaction between FeBr_3 and the lithiated salt of $\text{H}_2[\text{ONO}]^{\text{BuBurPr}}$. Instead of synthesizing the desired bromide-bridged dimer, an iron(III) hydroxy-bridged dimer was generated likely due to the contamination of water (**Figure 4.5**). According to Chaudhuri and co-workers, reacting a tridentate amine-bis(phenol) ligand with $\text{FeCl}_2 \cdot 4\text{H}_2\text{O}$ (in the presence of triethylamine) can selectively generate an iron(III) hydroxy-bridged dimer.³ For future work, it would be very interesting to prepare a series of iron(III) hydroxy-bridged dimers supported by tridentate amine-bis(phenolate) ligands and test their catalytic activity for the cross-coupling of aryl Grignards with alkyl halides.

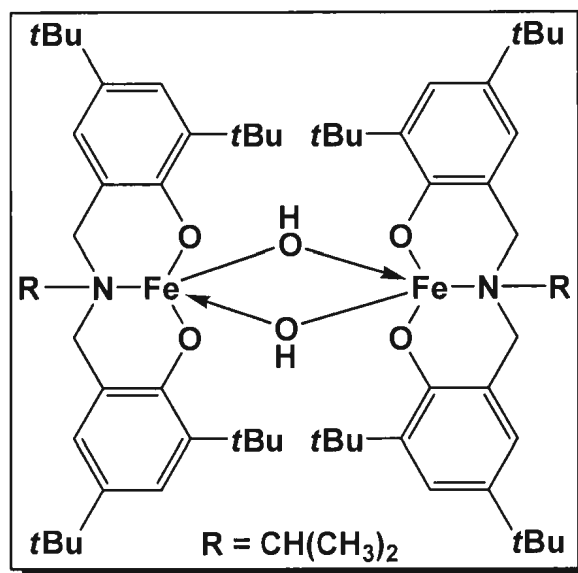


Figure 4.5: A representation of C6 ($[\text{FeL}_3(\mu\text{-OH})]_2$).

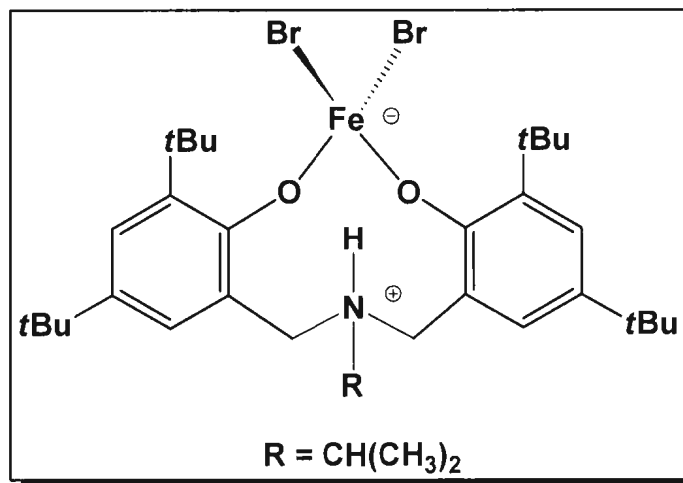


Figure 4.6: A representation of C7 ($\text{FeBr}_2\text{L}_3\text{H}$).

In a second attempt to generate $[\text{FeL}_3(\mu\text{-Br})]_2$, the reaction between FeBr_3 and the lithiated salt of $\text{H}_2[\text{ONO}]^{\text{BuBuPr}}$ resulted in a zwitterionic tetrahedral iron(III) complex bearing two bromide ligands and a quarternized ammonium fragment (**Figure 4.6**).

Frustratingly, the contamination of water likely occurred leading to the incomplete deprotonation of the amine-bis(phenol) ligand.

The complexes **C1-C7** were generated using ligands **H₂L1-H₂L3**. In the future, it would be desirable to successfully isolate iron(III) complexes supported by other tridentate amine-bis(phenolate) ligands (such as **H₂L4-H₂L6**). During the course of this research, numerous attempts were made to synthesize $\text{H}_2[\text{ONO}]^{\text{AmAmnPr}}$ (**Figure 4.7**). Unfortunately, the isolation of pure $\text{H}_2[\text{ONO}]^{\text{AmAmnPr}}$ has been unsuccessful to date due to the inability to separate phenol impurities. For future work, the isolation of pure $\text{H}_2[\text{ONO}]^{\text{AmAmnPr}}$ may be attempted by sublimation or by the use of a silica column.

\

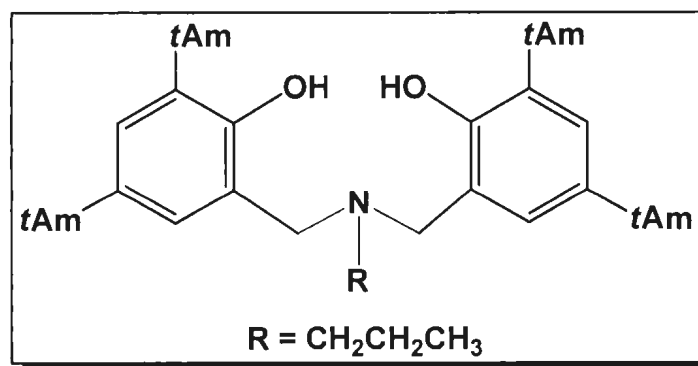


Figure 4.7: A representation of $\text{H}_2[\text{ONO}]^{\text{AmAmnPr}}$.

4.2 Catalysis

During the course of this Master's project, preliminary studies of **C3** (Figure 4.2) for the catalytic cross-coupling of aryl Grignard reagents with benzyl halides was performed. In the presence of **C3**, preliminary studies showed that the coupling of *o*-tolylmagnesium bromide with benzyl halides (including chlorides) gave cross-coupled products in very high yields. The system also showed excellent reactivity for sterically demanding nucleophiles, such as 2,6-dimethylphenylmagnesium bromide (95% yield). When *para*-substituted benzyl halides were employed, high yields of the cross-coupled products were obtained when *p*-tolylmagnesium bromide was reacted with 4-methylbenzyl chloride (85%). This was a very surprising result since the reaction between 4-methylbenzyl bromide and *p*-tolylmagnesium bromide only resulted in a 38% yield of the cross-coupled product. When the electron deficient substrate 4-(trifluoromethyl)benzyl bromide was reacted with 4-methylbenzylmagnesium bromide, a higher yield (76%) of the cross-coupled product was obtained. Some notable findings were also obtained when *meta*-substituted benzyl halides were employed. Surprisingly, 3-methoxybenzyl chloride gave a higher yield of the cross-coupled product (91%), compared to 3-methoxybenzyl bromide (72%), when reacted with *p*-tolylmagnesium bromide. Unfortunately, the reaction of the more sterically congested *ortho*-substituted benzyl halides with *p*-tolylmagnesium bromide gave very low yields of the desired cross-coupled product generating mainly homocoupled by-products. In the future, the use of microwave irradiation will be explored in hope to significantly shorten reaction times as well as to achieve the formation of cross-coupled products which may have been hindered

by high activation barriers, such as those caused by steric constraints in the cross-coupling partner.

Preliminary studies focused mainly on the use of *p*-tolylmagnesium bromide as the aryl Grignard reagent. The catalytic ability of **C3** should also be tested in the presence of other Grignards. Since benzyl bromide was found to couple with *o*-tolylmagnesium bromide in a higher yield than with *p*-tolylmagnesium bromide, there may be an “*ortho*” effect at play during the cross-coupling process. For instance, the presence of the *ortho*-methyl group may be important to the stability of Fe-aryl intermediates. With this in mind, it would be very interesting to further explore the use of *o*-tolylmagnesium bromide as the aryl Grignard reagent.

A study of catalyst loading, ratio of Grignard reagent to alkyl halide, addition rate of the Grignard reagent and temperature effects of the cross-coupling reaction should also be investigated in the future. The ability of **C4**, and the zwitterionic complexes **C5** and **C7** to catalyze the cross-coupling of aryl Grignard reagents with benzyl halides will be explored. It would also be very interesting to test the catalytic ability of iron(III) complexes supported by tridentate amine-bis(phenolate) ligands with fluorine or chlorine substituents on the phenolate rings since these groups could alter the electron density located on the metal center and hence the reactivity of the catalyst.

According to previous reports in the literature, iron-catalyzed C-C cross-coupling reactions can be largely affected by trace metal impurities.^{4,5} In order to speculate on the purity of **C3**, a recrystallized sample of **C3** was analyzed via Inductively Coupled Plasma Mass Spectrometry (ICP-MS) suggesting that **C3** contained trace amounts of metal impurities compared to the starting material FeCl₃.

At this particular time, it is uncertain whether or not the active catalytic species is homogeneous in nature or nanoparticulate iron. During the course of this research, attempts were made to analyze the iron material from the cross-coupling reactions via transmission electron microscopy (TEM) which provides surface analysis down to the nanoscale level. Unfortunately, all attempts to date were unsuccessful due to the excessive covering of the iron particulate with organic material. Since nanoparticulate iron has been proposed as the catalytic species in several iron-catalyzed cross-coupling reactions, this cannot be discounted in the present study.⁶

In conclusion, from our preliminary investigations, it was successfully demonstrated that iron(III) complexes supported by tridentate amine-bis(phenolate) ligands show great potential as catalysts for the cross-coupling of aryl Grignard reagents with benzyl halides. Even though many of the catalytic reactions resulted in a lower yield of the diaryl compound compared to the iron-catalyzed Negishi-type arylations reported by Bedford,⁷ **C3** was found to be a far superior catalyst when aryl Grignards were used directly. From an economical point of view, the results obtained are very promising and may one day shine new light into the iron-catalyzed formation of diarylmethane motifs.

4.3 References

- ¹ K. Hassan, L. N. Dawe, C. M. Kozak, *Eur. J. Org. Chem.*, **2011**, 4610.
- ² X. Qian, L. N. Dawe, C. M. Kozak, *Dalton Trans.*, **2011**, 40, 933.
- ³ P. Chaudhuri, T. Weyhermüller, R. Wagner, *Eur. J. Inorg. Chem.*, **2011**, 2547.
- ⁴ I. Thomé, A. Nijs, C. Bolm, *Chem. Soc. Rev.*, **2012**, 41, 979.
- ⁵ G. Cahiez, V. Habiak, C. Duplais, A. Moyeux, *Angew. Chem. Int. Ed.*, **2007**, 46, 4364.
- ⁶ R. B. Bedford, M. Betham, D. W. Bruce, S. A. Davis, R. M. Frost, M. Hird, *Chem. Commun.*, **2006**, 1398.
- ⁷ R. B. Bedford, M. Huwe, M. C. Wilkinson, *Chem. Commun.*, **2009**, 600.

Chapter 5 – Appendix

5.1 Ligands and Complexes

Figure A1: HRMS spectrum of H_2L1 .

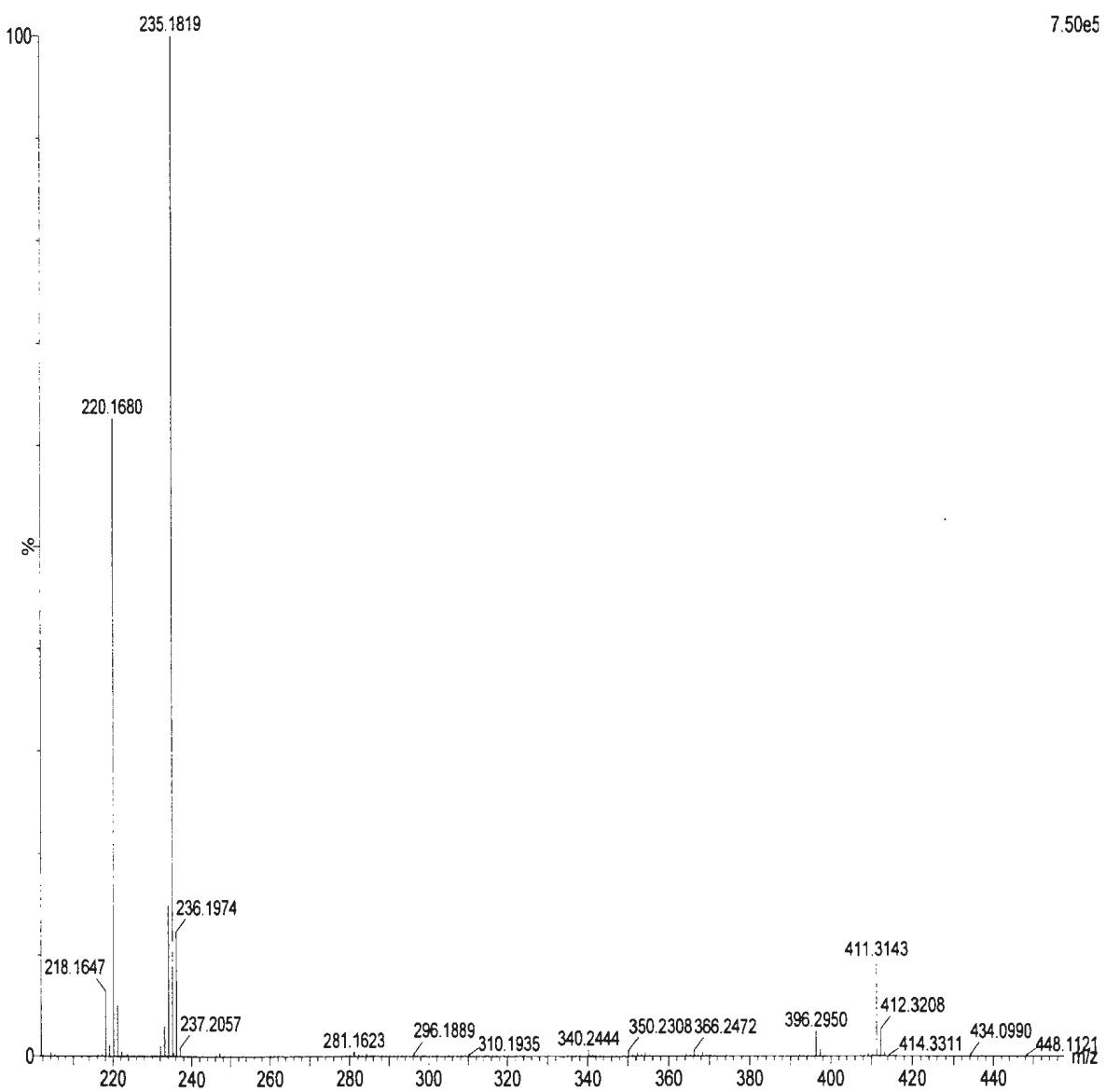


Figure A2: ^1H NMR spectrum of $\text{H}_2\text{L1}$.

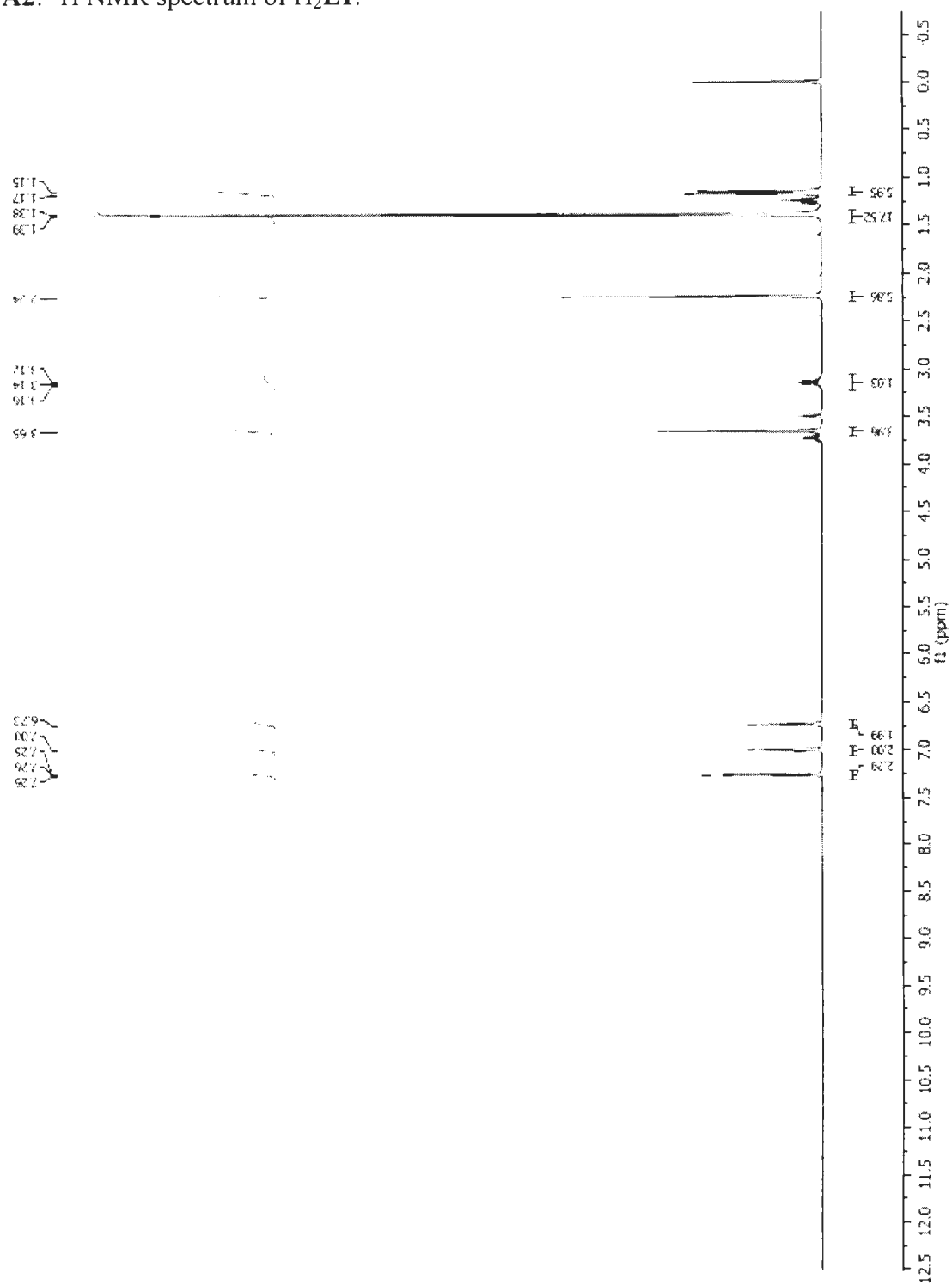
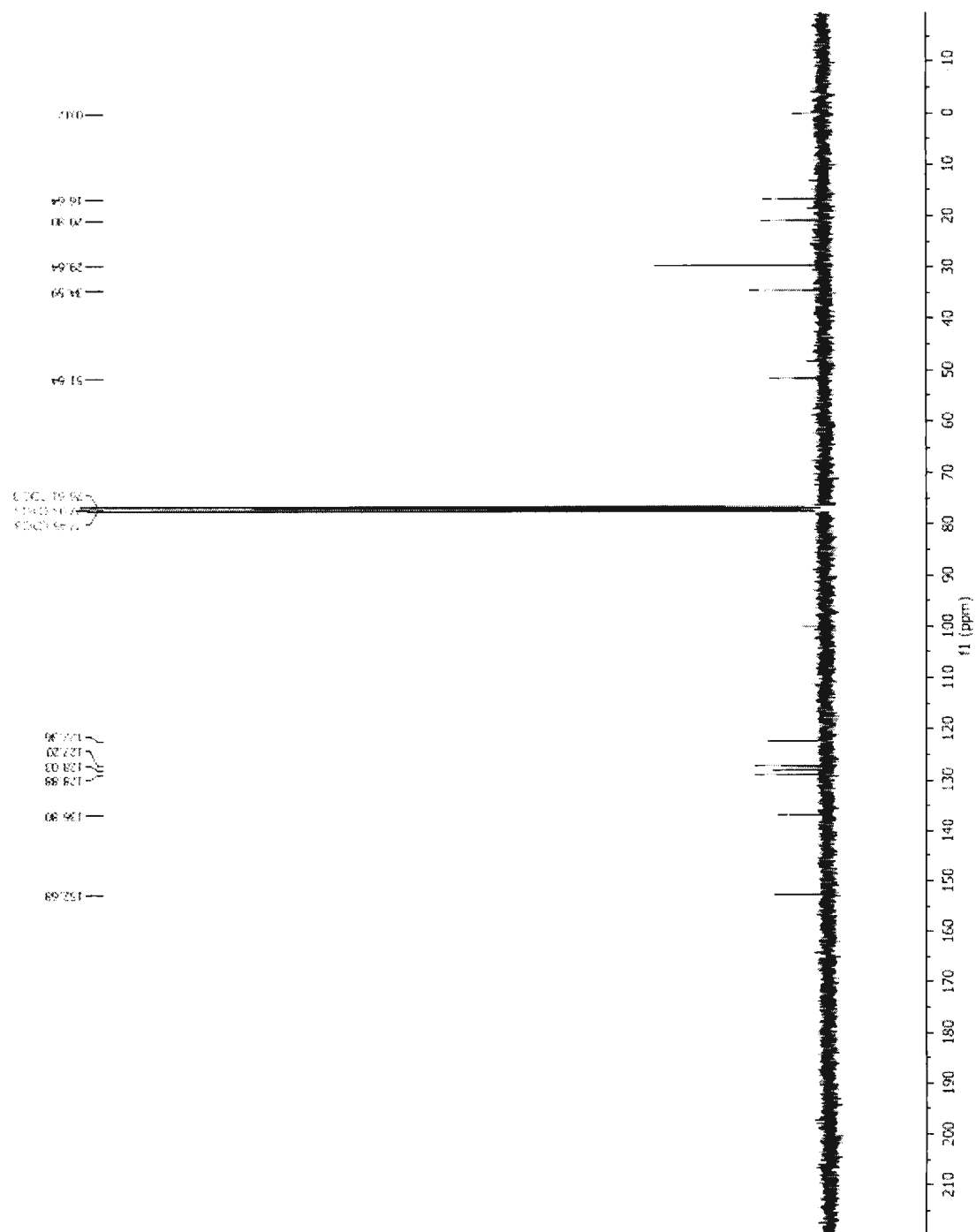


Figure A3: ^{13}C NMR spectrum of $\text{H}_2\text{L1}$.



EF040304a 152 (2.534) cm ((92.107+152.158)-(56.65+329.377))

100 MS L1
5.44e5

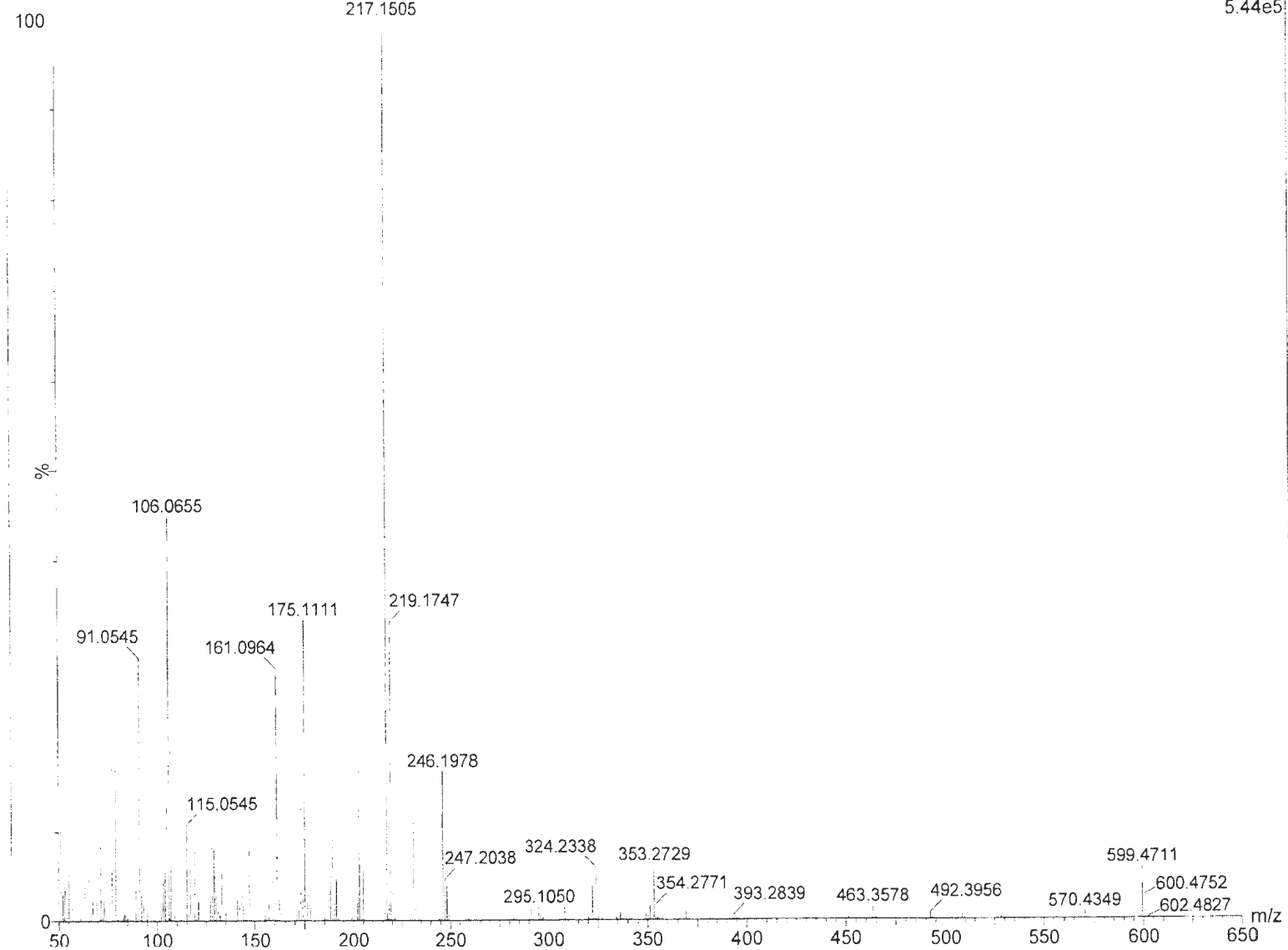


Figure A4: HRMS spectrum of H₂L₂.

Figure A5: ^1H NMR spectrum of $\text{H}_2\text{L2}$.

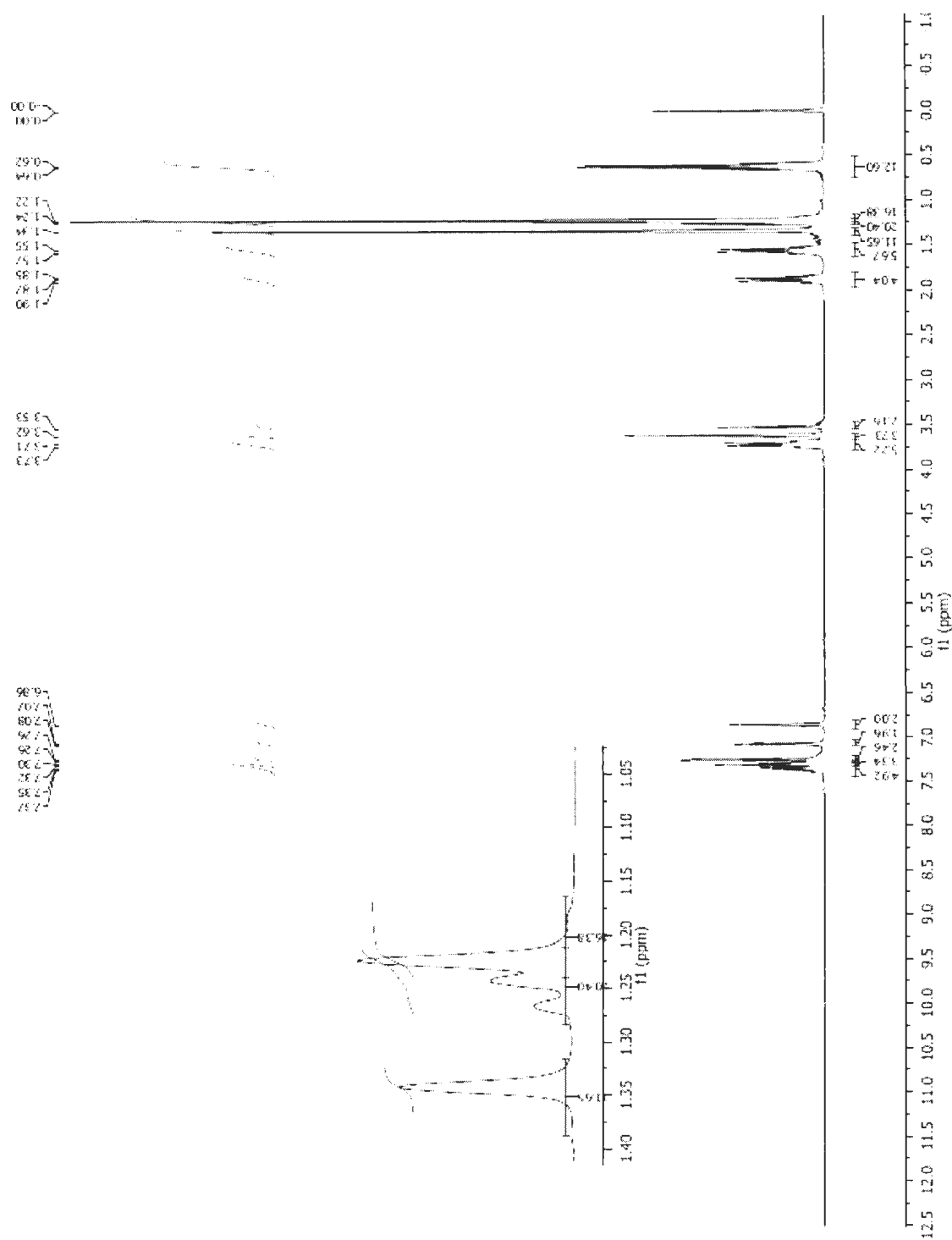


Figure A6: ^{13}C NMR spectrum of $\text{H}_2\text{L2}$.

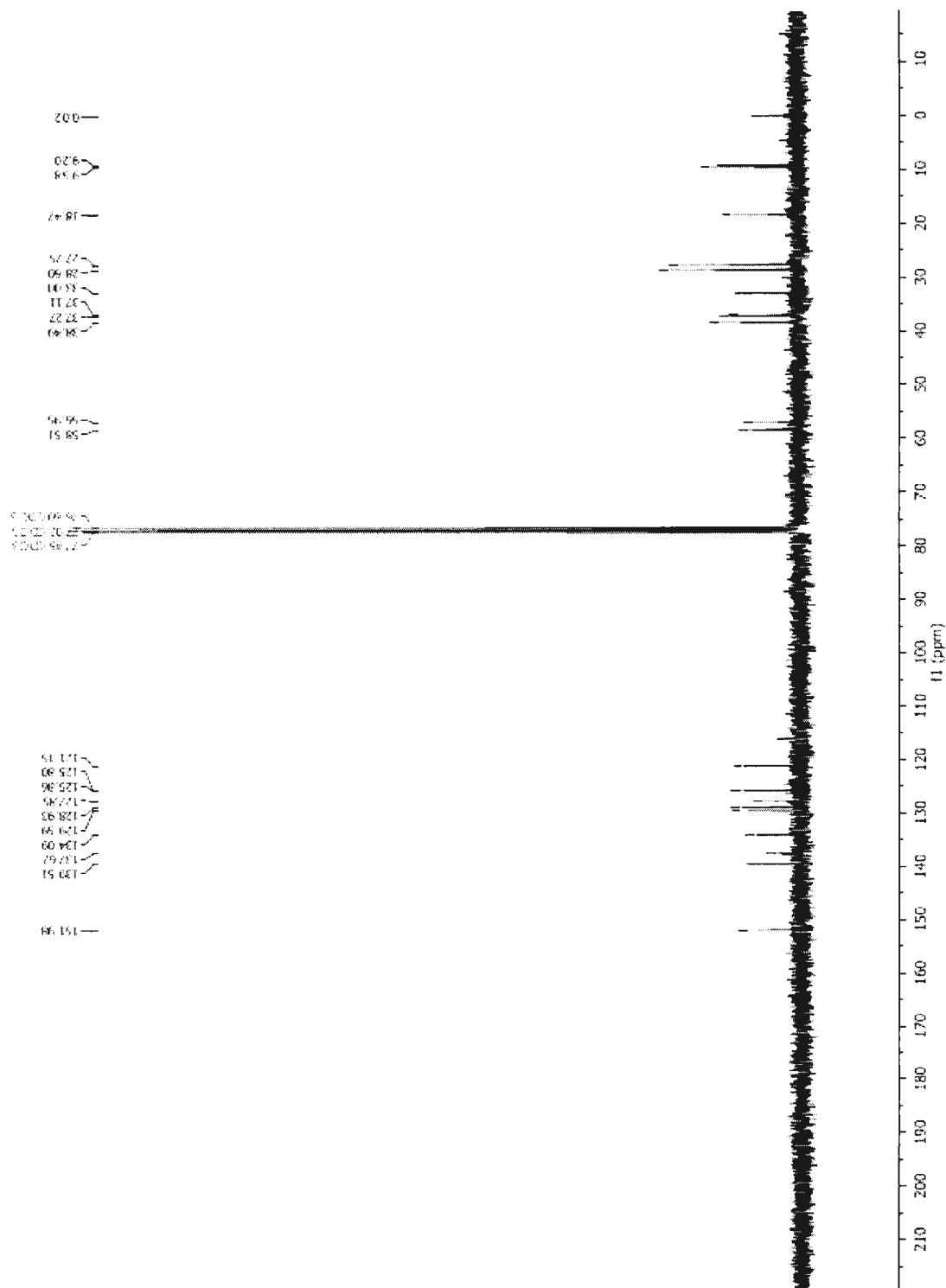
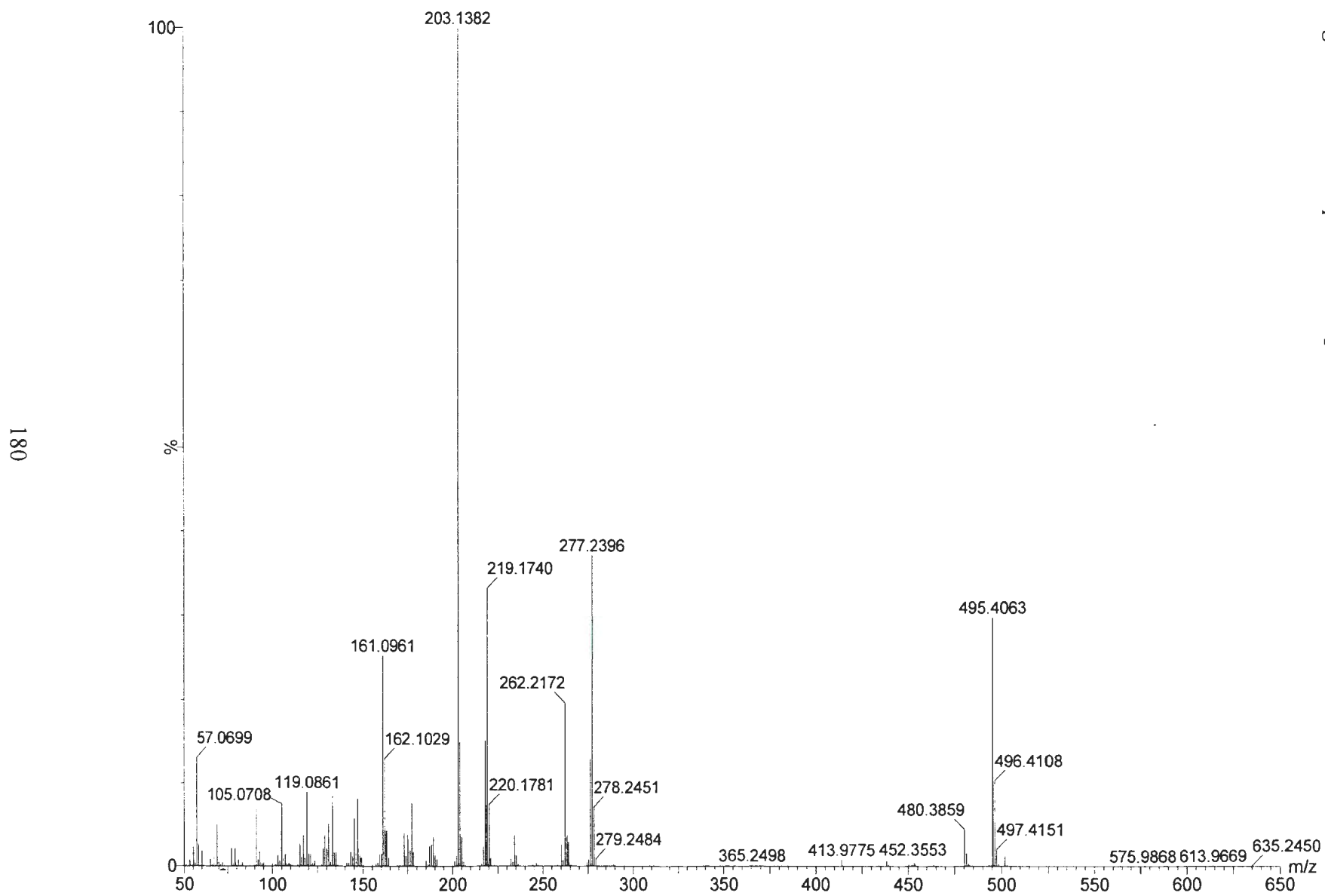


Figure A7: HRMS spectrum of H₂L3.



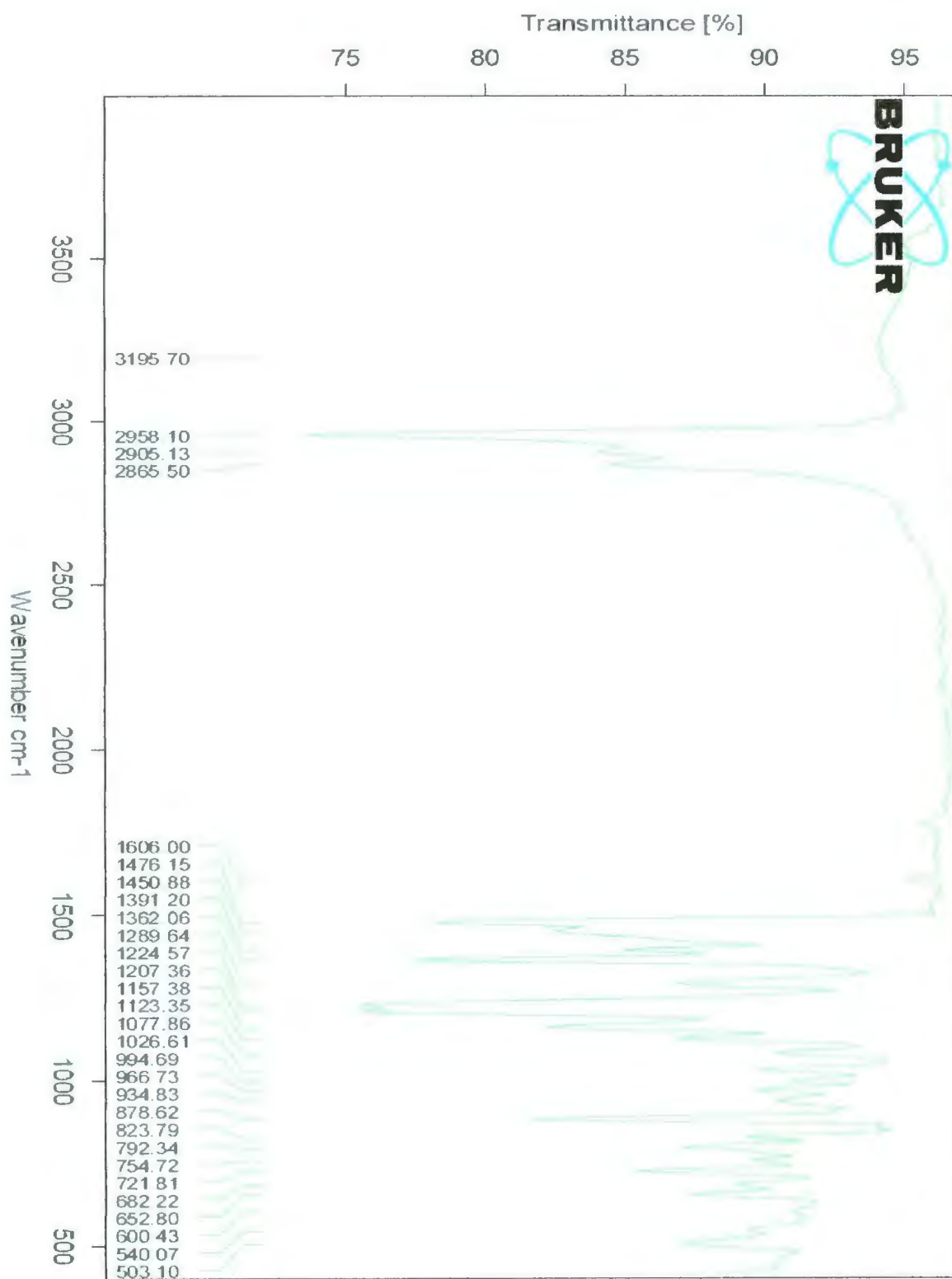
Figure A8: IR spectrum of H_2L_3 .

Figure A9: ^1H NMR spectrum of $\text{H}_2\text{L3}$.

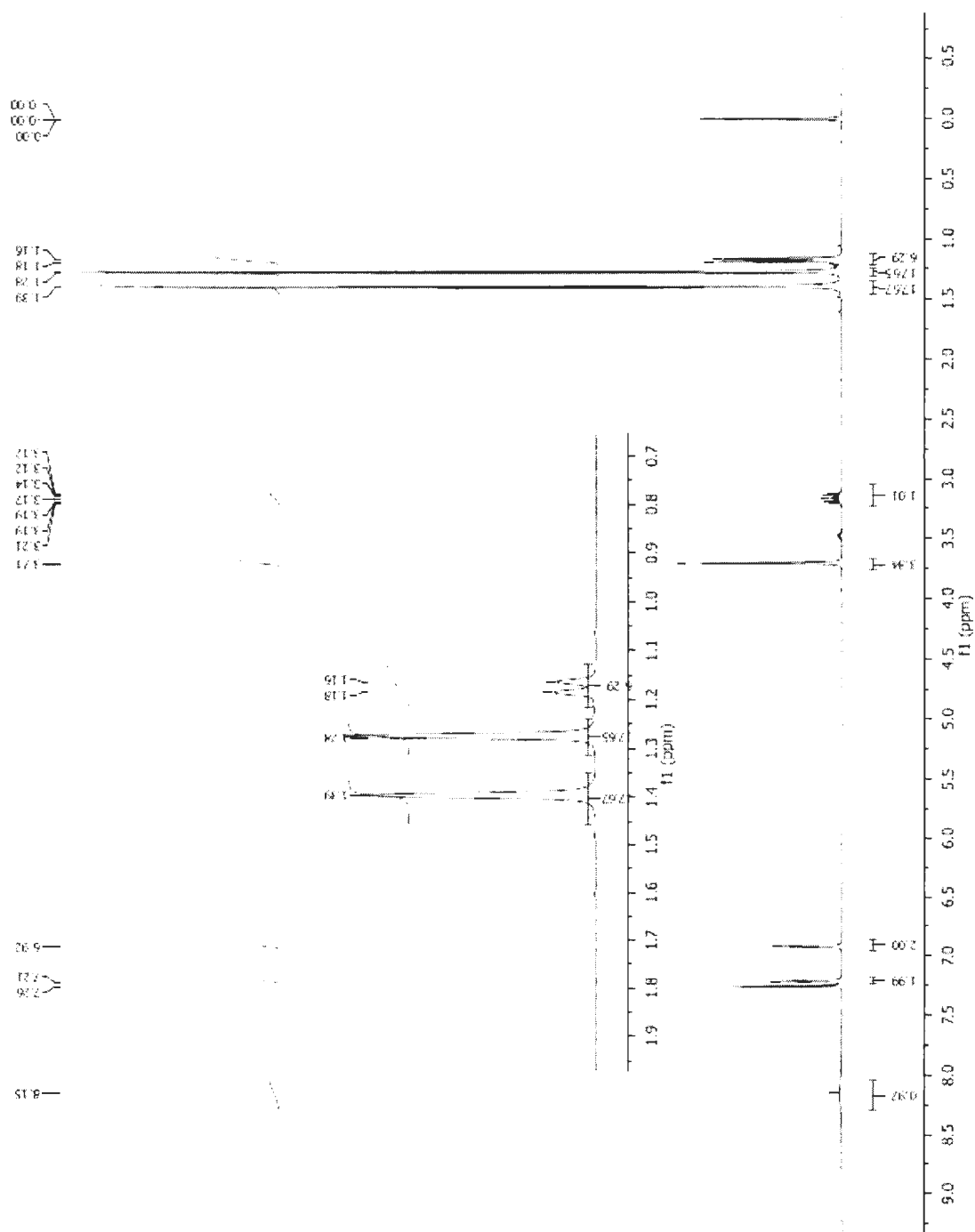


Figure A10: ^{13}C NMR spectrum of $\text{H}_2\text{L3}$.

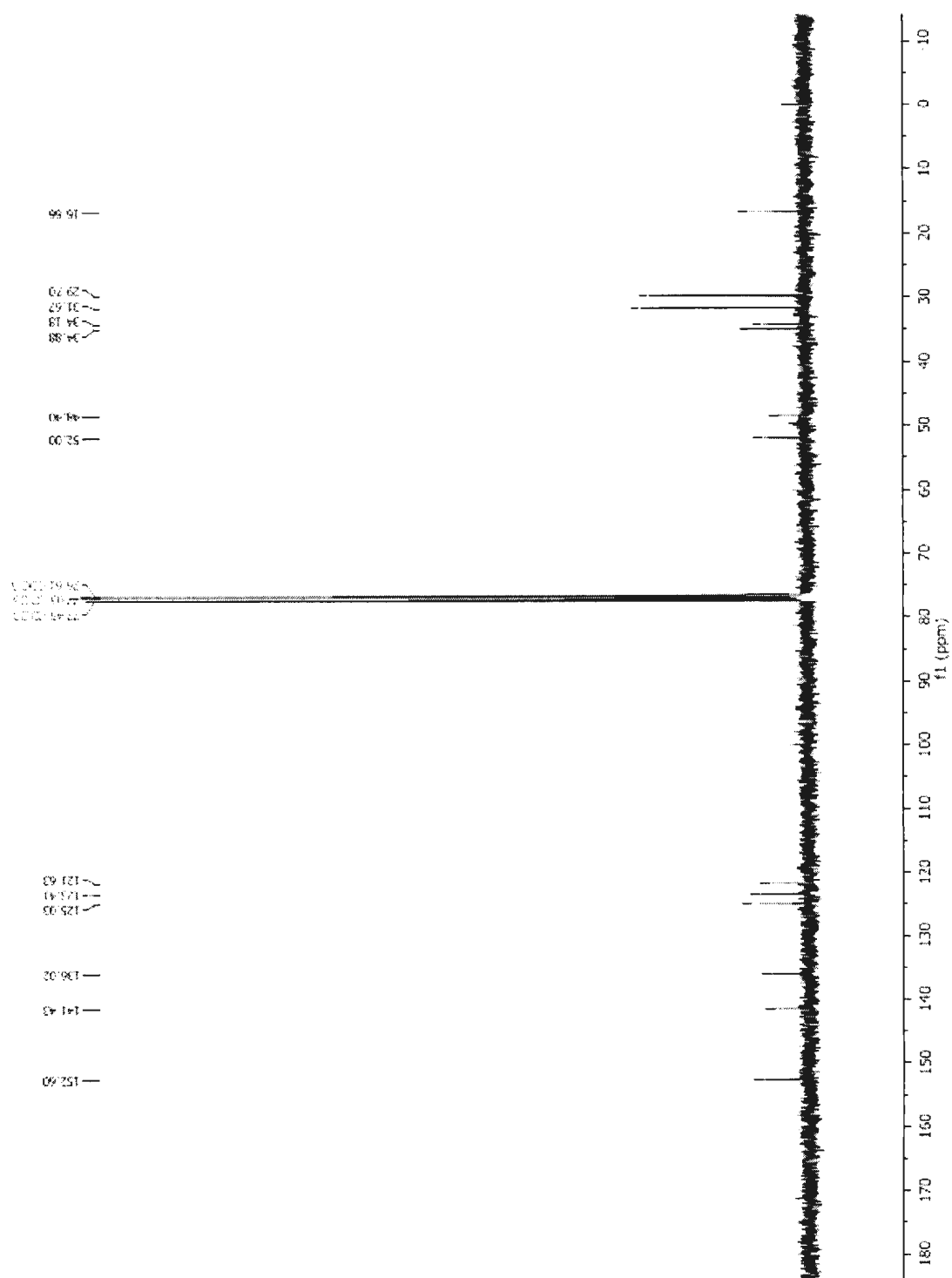


Figure A11: Single crystal X-ray structure of $\text{H}_2[\text{O}_2\text{N}]^{\text{BuBuPr}} (\text{H}_2\text{L3})$. Ellipsoids at 50% probability.

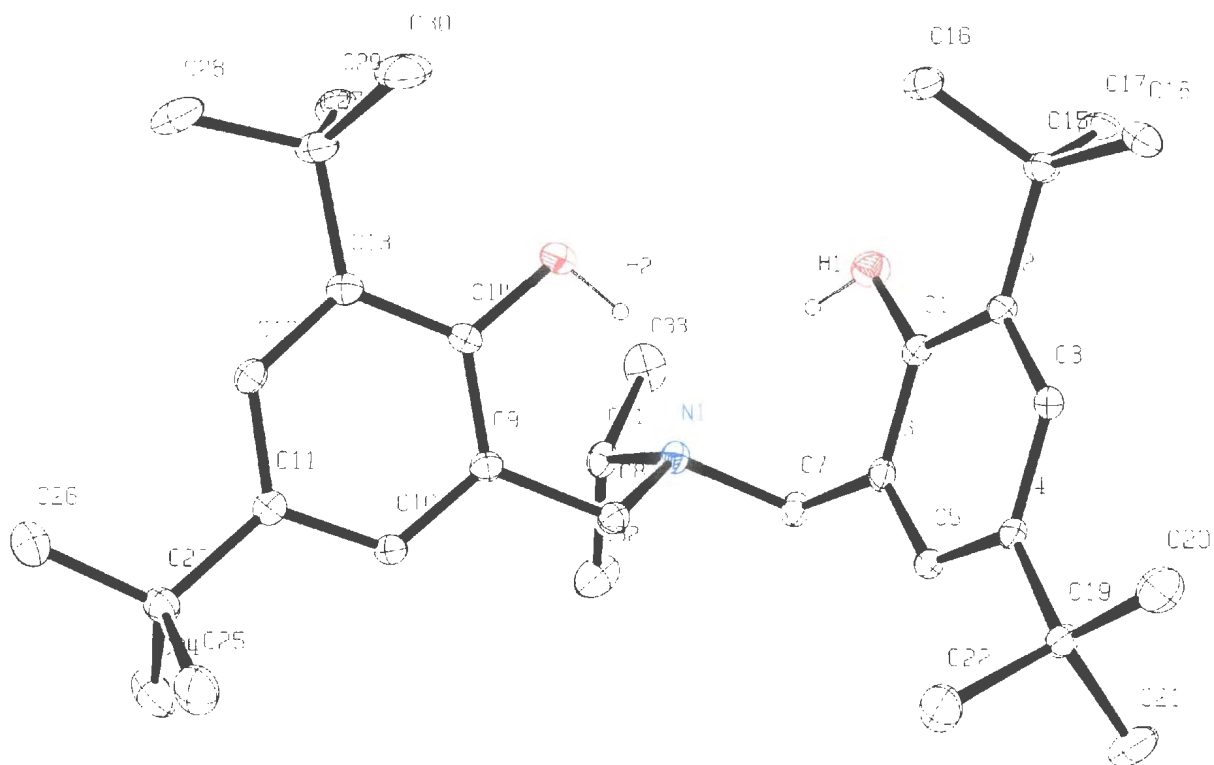


Table A1: Bond lengths (Å) for $\text{H}_2\text{L3}$.

atom	atom	distance	atom	atom	distance
O(1)	C(1)	1.373(2)	O(2)	C(14)	1.373(3)
N(1)	C(7)	1.481(2)	N(1)	C(8)	1.487(2)
N(1)	C(31)	1.486(2)	C(1)	C(2)	1.397(2)
C(1)	C(6)	1.403(3)	C(2)	C(3)	1.399(3)
C(2)	C(15)	1.537(3)	C(3)	C(4)	1.394(3)
C(4)	C(5)	1.390(3)	C(4)	C(19)	1.544(3)
C(5)	C(6)	1.381(3)	C(6)	C(7)	1.511(3)
C(8)	C(9)	1.518(2)	C(9)	C(10)	1.378(3)
C(9)	C(14)	1.392(3)	C(10)	C(11)	1.389(2)
C(11)	C(12)	1.391(3)	C(11)	C(23)	1.542(3)
C(12)	C(13)	1.385(3)	C(13)	C(14)	1.421(2)
C(13)	C(27)	1.529(3)	C(15)	C(16)	1.538(3)
C(15)	C(17)	1.541(3)	C(15)	C(18)	1.534(3)
C(19)	C(20)	1.499(3)	C(19)	C(21)	1.541(3)
C(19)	C(22)	1.529(3)	C(23)	C(24)	1.512(4)

C(23)	C(25)	1.556(4)	C(23)	C(26)	1.512(3)
C(27)	C(28)	1.534(3)	C(27)	C(29)	1.544(4)
C(27)	C(30)	1.526(5)	C(31)	C(32)	1.518(4)
C(31)	C(33)	1.525(4)	O(1)	H(1)	0.87(2)
O(2)	H(2)	0.92(2)			

Table A2: Bond angles (°) for H₂L3.

atom	atom	atom	angle
C(7)	N(1)	C(8)	108.80(17)
C(7)	N(1)	C(31)	114.15(14)
C(8)	N(1)	C(31)	112.35(17)
O(1)	C(1)	C(2)	119.8(2)
O(1)	C(1)	C(6)	118.68(18)
C(2)	C(1)	C(6)	121.5(2)
C(1)	C(2)	C(3)	116.3(2)
C(1)	C(2)	C(15)	121.7(2)
C(3)	C(2)	C(15)	121.95(19)
C(2)	C(3)	C(4)	124.03(19)
C(3)	C(4)	C(5)	117.0(2)
C(3)	C(4)	C(19)	122.64(19)
C(5)	C(4)	C(19)	120.4(2)
C(4)	C(5)	C(6)	121.8(2)
C(1)	C(6)	C(5)	119.27(19)
C(1)	C(6)	C(7)	119.9(2)
C(5)	C(6)	C(7)	120.8(2)
N(1)	C(7)	C(6)	111.14(15)
N(1)	C(8)	C(9)	114.90(18)
C(8)	C(9)	C(10)	118.9(2)
C(8)	C(9)	C(14)	120.9(2)
C(10)	C(9)	C(14)	120.12(18)
C(9)	C(10)	C(11)	121.5(2)
C(10)	C(11)	C(12)	117.2(2)
C(10)	C(11)	C(23)	119.9(2)
C(12)	C(11)	C(23)	122.88(17)
C(11)	C(12)	C(13)	124.25(18)
C(12)	C(13)	C(14)	116.4(2)
C(12)	C(13)	C(27)	121.43(19)
C(14)	C(13)	C(27)	122.2(2)
O(2)	C(14)	C(9)	120.60(18)
O(2)	C(14)	C(13)	118.8(2)
C(9)	C(14)	C(13)	120.6(2)
C(2)	C(15)	C(16)	110.18(19)
C(2)	C(15)	C(17)	110.19(17)

C(2)	C(15)	C(18)	112.1(2)
C(16)	C(15)	C(17)	108.4(2)
C(16)	C(15)	C(18)	107.93(17)
C(17)	C(15)	C(18)	108.0(2)
C(4)	C(19)	C(20)	113.0(2)
C(4)	C(19)	C(21)	109.01(19)
C(4)	C(19)	C(22)	109.1(2)
C(20)	C(19)	C(21)	108.1(2)
C(20)	C(19)	C(22)	109.7(2)
C(21)	C(19)	C(22)	107.8(2)
C(11)	C(23)	C(24)	110.2(2)
C(11)	C(23)	C(25)	108.4(2)
C(11)	C(23)	C(26)	113.4(2)
C(24)	C(23)	C(25)	107.2(2)
C(24)	C(23)	C(26)	110.1(2)
C(25)	C(23)	C(26)	107.3(2)
C(13)	C(27)	C(28)	111.9(2)
C(13)	C(27)	C(29)	108.85(19)
C(13)	C(27)	C(30)	110.2(2)
C(28)	C(27)	C(29)	106.7(2)
C(28)	C(27)	C(30)	108.0(2)
C(29)	C(27)	C(30)	111.2(3)
N(1)	C(31)	C(32)	114.5(2)
N(1)	C(31)	C(33)	109.2(2)
C(32)	C(31)	C(33)	111.4(2)
C(1)	O(1)	H(1)	106(2)
C(14)	O(2)	H(2)	101.5(19)

Table A3: Torsion angles (°) for H₂L3.

atom1	atom2	atom3	atom4	angle
C(7)	N(1)	C(8)	C(9)	176.70(18)
C(8)	N(1)	C(7)	C(6)	-68.9(2)
C(7)	N(1)	C(31)	C(32)	50.6(3)
C(7)	N(1)	C(31)	C(33)	-75.1(2)
C(31)	N(1)	C(7)	C(6)	164.7(2)
C(8)	N(1)	C(31)	C(32)	-73.9(2)
C(8)	N(1)	C(31)	C(33)	160.4(2)
C(31)	N(1)	C(8)	C(9)	-55.9(2)
O(1)	C(1)	C(2)	C(3)	178.65(16)
O(1)	C(1)	C(2)	C(15)	0.1(2)
O(1)	C(1)	C(6)	C(5)	-178.98(17)
O(1)	C(1)	C(6)	C(7)	-0.7(2)
C(2)	C(1)	C(6)	C(5)	0.6(2)

C(2)	C(1)	C(6)	C(7)	178.84(17)
C(6)	C(1)	C(2)	C(3)	-0.9(2)
C(6)	C(1)	C(2)	C(15)	-179.44(17)
C(1)	C(2)	C(3)	C(4)	-0.3(2)
C(1)	C(2)	C(15)	C(16)	60.0(2)
C(1)	C(2)	C(15)	C(17)	-59.5(2)
C(1)	C(2)	C(15)	C(18)	-179.75(18)
C(3)	C(2)	C(15)	C(16)	-118.4(2)
C(3)	C(2)	C(15)	C(17)	122.1(2)
C(3)	C(2)	C(15)	C(18)	1.8(2)
C(15)	C(2)	C(3)	C(4)	178.23(17)
C(2)	C(3)	C(4)	C(5)	1.7(2)
C(2)	C(3)	C(4)	C(19)	-176.51(17)
C(3)	C(4)	C(5)	C(6)	-2.1(2)
C(3)	C(4)	C(19)	C(20)	-1.2(2)
C(3)	C(4)	C(19)	C(21)	-121.5(2)
C(3)	C(4)	C(19)	C(22)	121.1(2)
C(5)	C(4)	C(19)	C(20)	-179.4(2)
C(5)	C(4)	C(19)	C(21)	60.3(2)
C(5)	C(4)	C(19)	C(22)	-57.1(2)
C(19)	C(4)	C(5)	C(6)	176.21(17)
C(4)	C(5)	C(6)	C(1)	1.0(2)
C(4)	C(5)	C(6)	C(7)	-177.25(17)
C(1)	C(6)	C(7)	N(1)	-66.1(2)
C(5)	C(6)	C(7)	N(1)	112.1(2)
N(1)	C(8)	C(9)	C(10)	138.7(2)
N(1)	C(8)	C(9)	C(14)	-44.3(2)
C(8)	C(9)	C(10)	C(11)	175.21(18)
C(8)	C(9)	C(14)	O(2)	3.5(3)
C(8)	C(9)	C(14)	C(13)	-176.22(19)
C(10)	C(9)	C(14)	O(2)	-179.59(19)
C(10)	C(9)	C(14)	C(13)	0.7(3)
C(14)	C(9)	C(10)	C(11)	-1.7(3)
C(9)	C(10)	C(11)	C(12)	1.7(3)
C(9)	C(10)	C(11)	C(23)	-178.16(19)
C(10)	C(11)	C(12)	C(13)	-0.7(3)
C(10)	C(11)	C(23)	C(24)	-55.0(3)
C(10)	C(11)	C(23)	C(25)	61.9(2)
C(10)	C(11)	C(23)	C(26)	-179.0(2)
C(12)	C(11)	C(23)	C(24)	125.1(2)
C(12)	C(11)	C(23)	C(25)	-117.9(2)
C(12)	C(11)	C(23)	C(26)	1.2(3)
C(23)	C(11)	C(12)	C(13)	179.2(2)
C(11)	C(12)	C(13)	C(14)	-0.3(3)
C(11)	C(12)	C(13)	C(27)	179.1(2)

C(12)	C(13)	C(14)	O(2)	-179.43(19)
C(12)	C(13)	C(14)	C(9)	0.3(3)
C(12)	C(13)	C(27)	C(28)	2.4(3)
C(12)	C(13)	C(27)	C(29)	-115.3(2)
C(12)	C(13)	C(27)	C(30)	122.5(2)
C(14)	C(13)	C(27)	C(28)	-178.3(2)
C(14)	C(13)	C(27)	C(29)	64.1(3)
C(14)	C(13)	C(27)	C(30)	-58.1(3)
C(27)	C(13)	C(14)	O(2)	1.2(3)
C(27)	C(13)	C(14)	C(9)	-179.1(2)

The sign is positive if when looking from atom 2 to atom 3 a clock-wise motion of atom 1 would superimpose it on atom 4.

Figure A12: ^1H NMR spectrum of $\text{H}_2\text{L4}$.

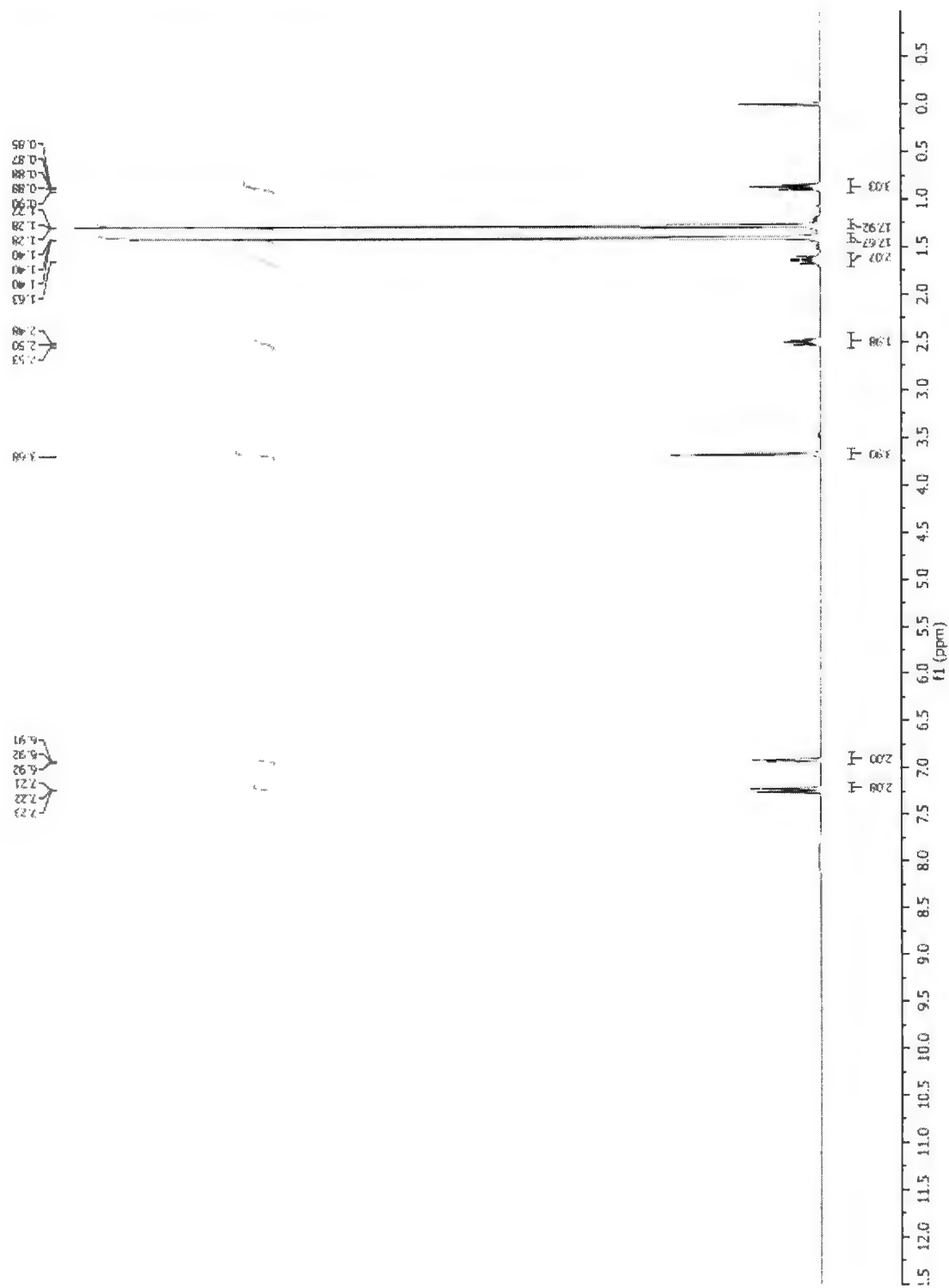


Figure A13: ^{13}C NMR spectrum of $\text{H}_2\text{L4}$.

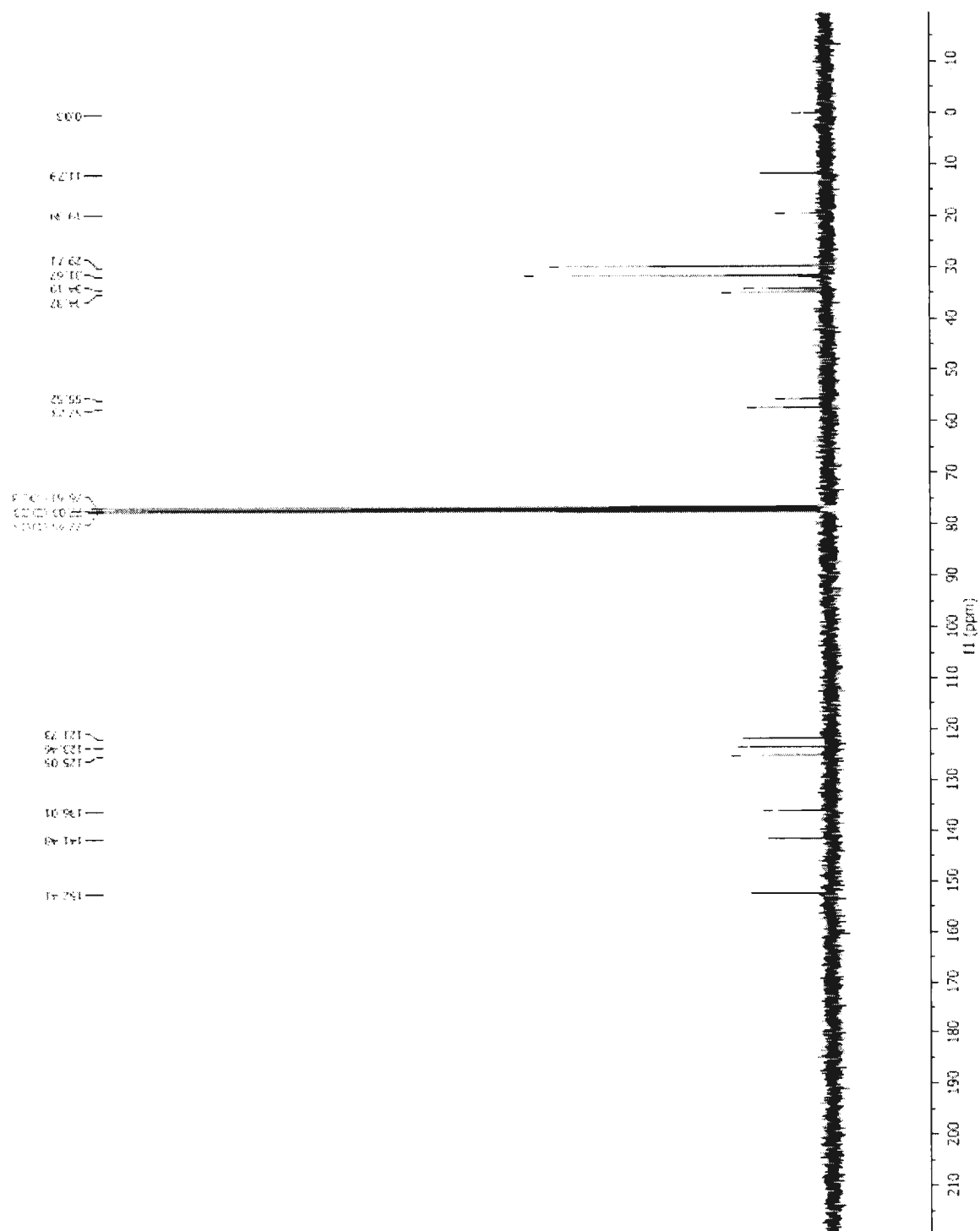


Figure A14: ^1H NMR spectrum of $\text{H}_2\text{L5}$.

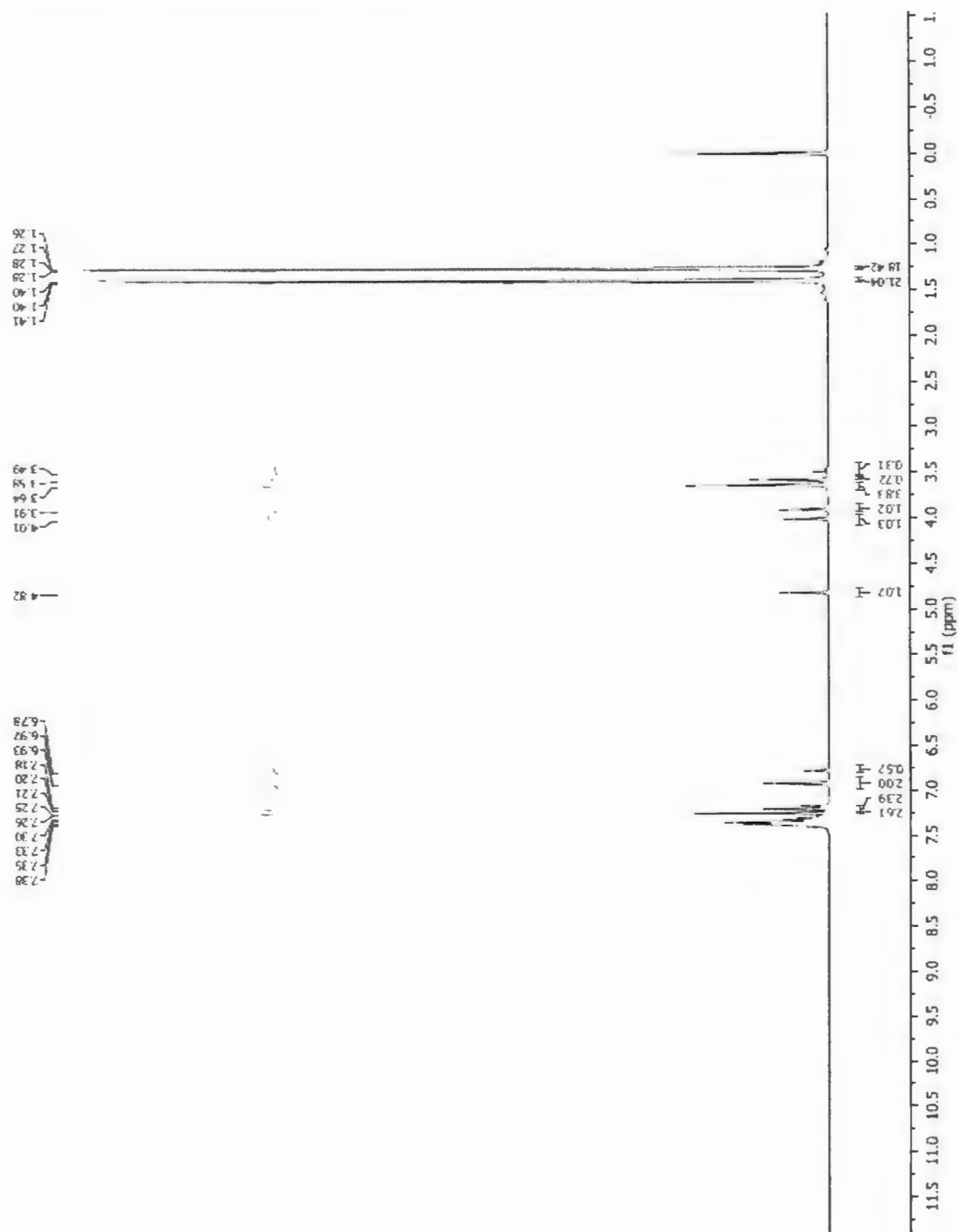


Figure A15: ^{13}C NMR spectrum of $\text{H}_2\text{L5}$.

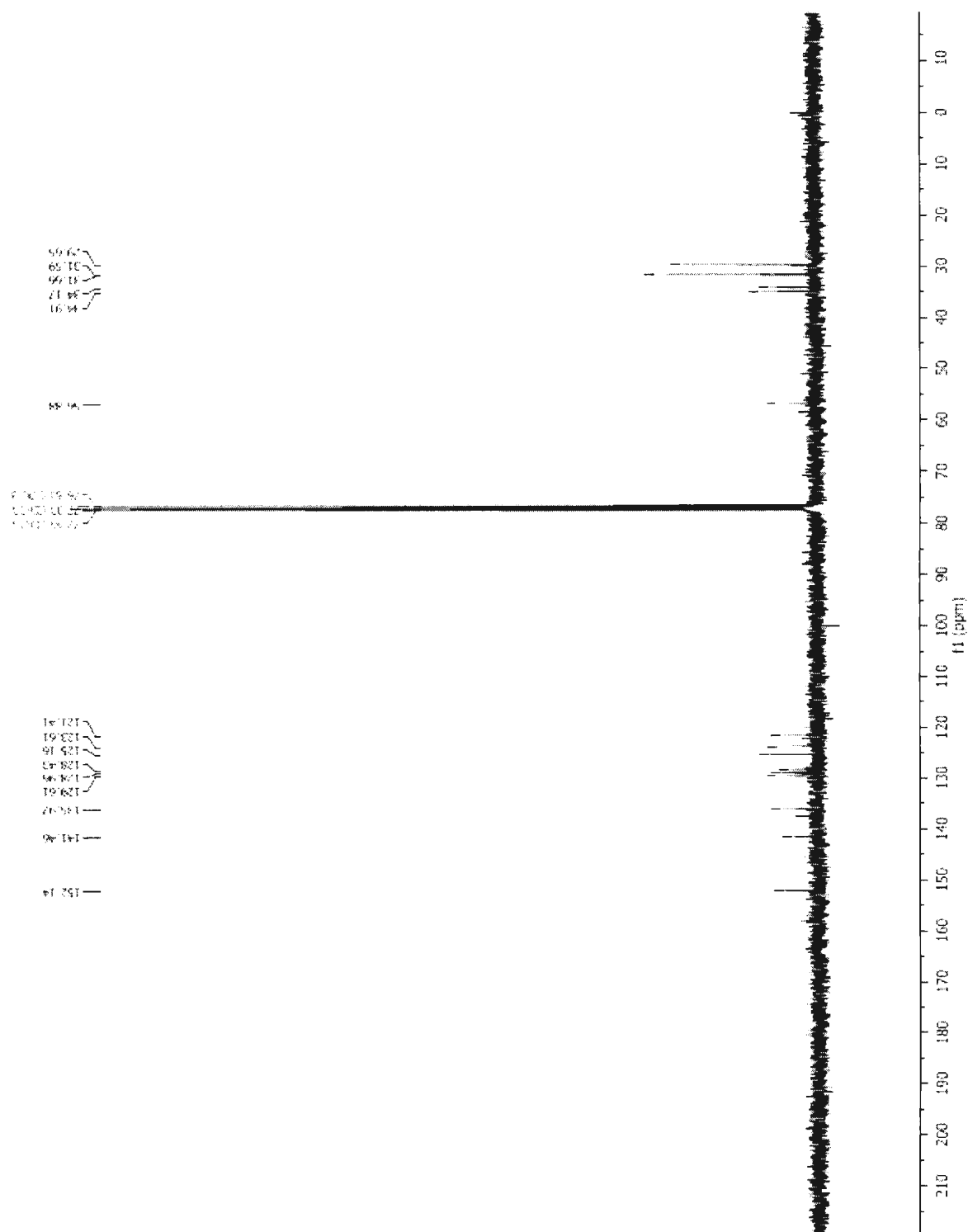


Figure A16: ^1H NMR spectrum of $\text{H}_2\text{L6}$.

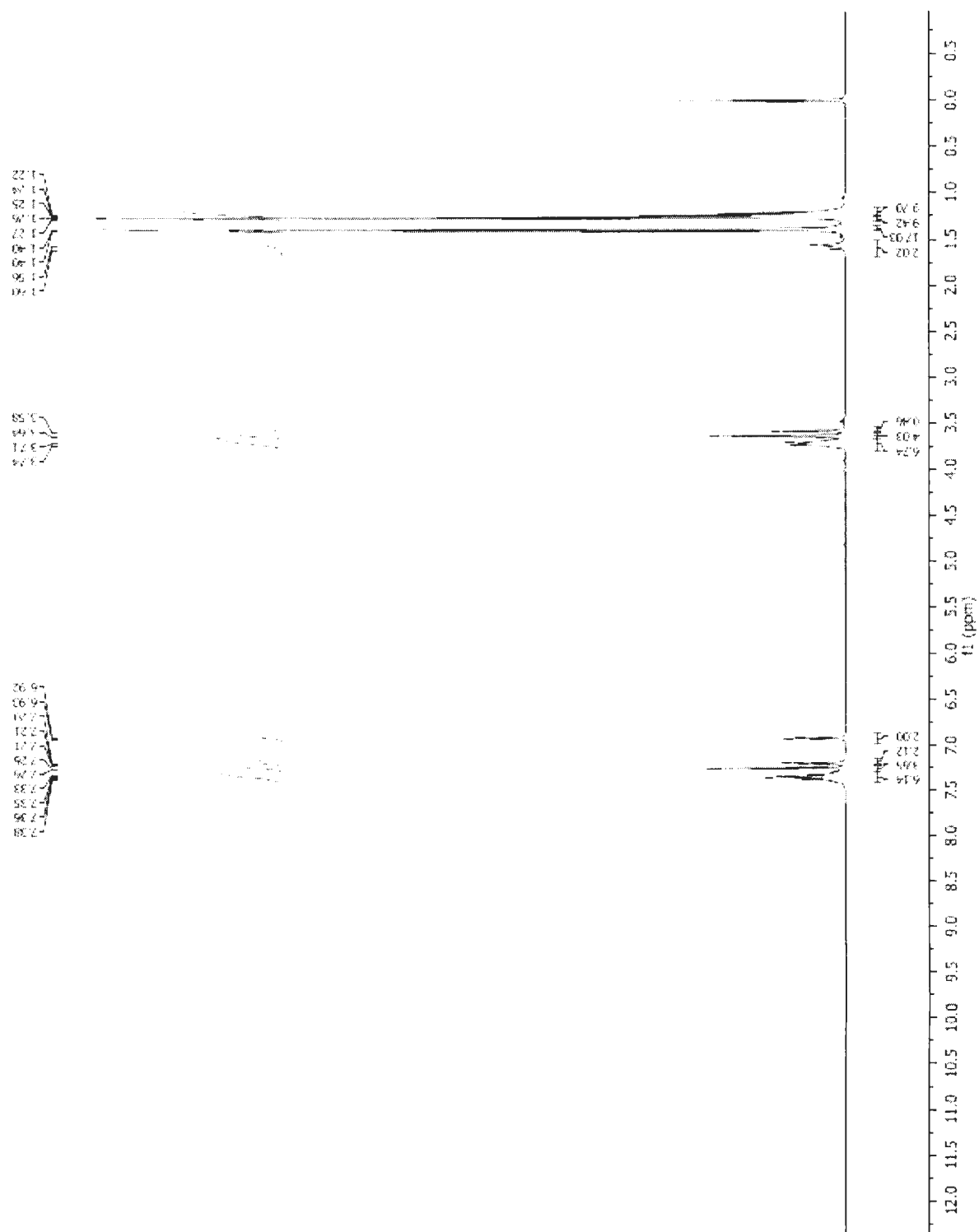


Figure A17: ^{13}C NMR spectrum of $\text{H}_2\text{L6}$.

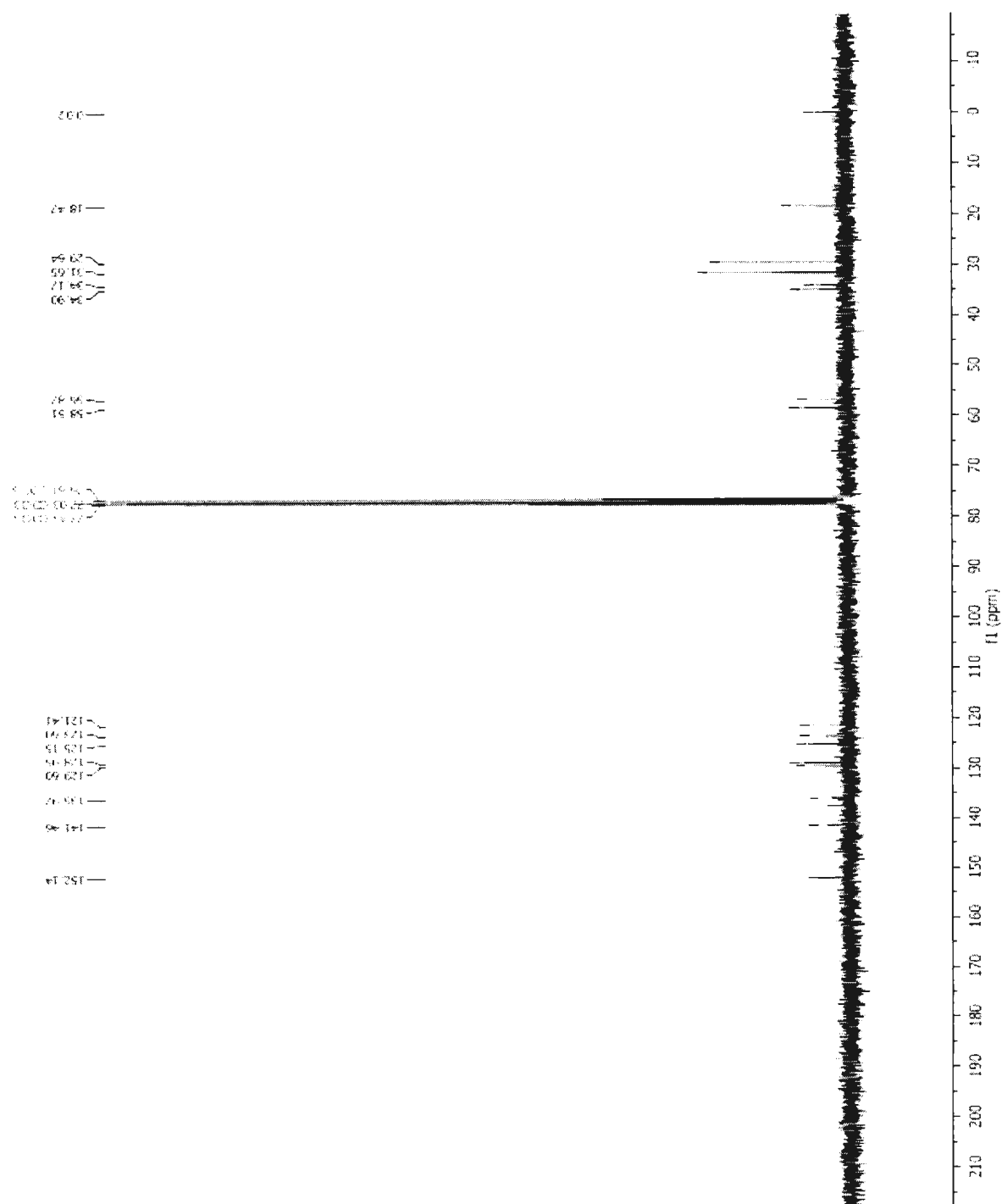


Figure A18: Single crystal X-ray structure of **C1**. Ellipsoids at 50% probability.

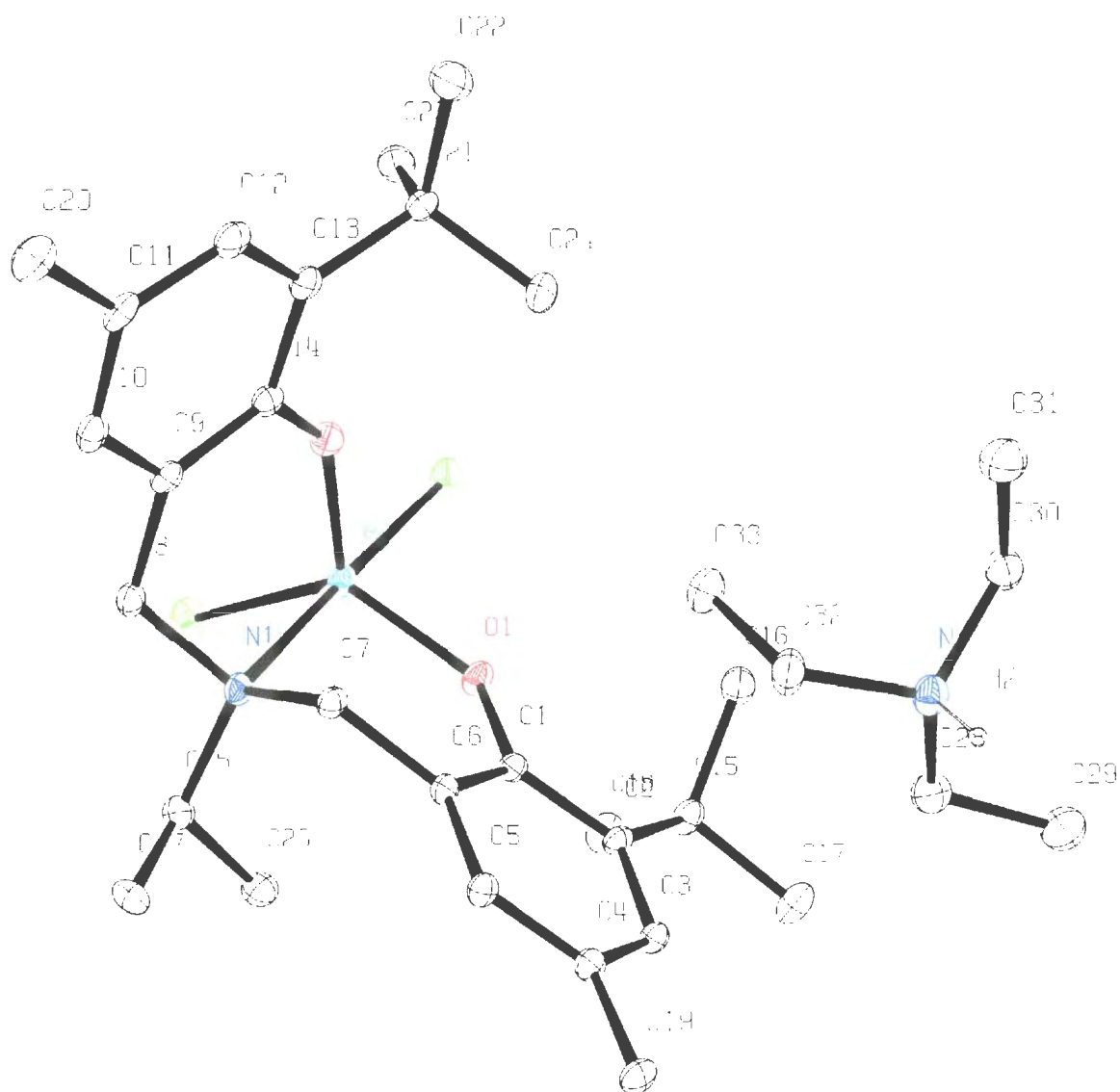


Table A4: Bond lengths (Å) for **C1**.

atom	atom	distance	atom	atom	distance
Fe(1)	Cl(1)	2.3618(13)	Fe(1)	Cl(2)	2.3038(14)
Fe(1)	O(1)	1.855(2)	Fe(1)	O(2)	1.848(3)
Fe(1)	N(1)	2.255(3)	O(1)	C(1)	1.345(4)
O(2)	C(14)	1.347(5)	N(1)	C(7)	1.497(5)
N(1)	C(8)	1.504(4)	N(1)	C(25)	1.524(5)
N(2)	C(28)	1.502(6)	N(2)	C(30)	1.475(5)

N(2)	C(32)	1.494(5)	C(1)	C(2)	1.414(4)
C(1)	C(6)	1.395(5)	C(2)	C(3)	1.408(5)
C(2)	C(15)	1.534(6)	C(3)	C(4)	1.389(6)
C(4)	C(5)	1.386(5)	C(4)	C(19)	1.520(5)
C(5)	C(6)	1.397(4)	C(6)	C(7)	1.511(4)
C(8)	C(9)	1.501(5)	C(9)	C(10)	1.393(6)
C(9)	C(14)	1.402(5)	C(10)	C(11)	1.375(6)
C(11)	C(12)	1.400(5)	C(11)	C(20)	1.518(7)
C(12)	C(13)	1.386(6)	C(13)	C(14)	1.413(5)
C(13)	C(21)	1.538(5)	C(15)	C(16)	1.543(5)
C(15)	C(17)	1.535(5)	C(15)	C(18)	1.544(7)
C(21)	C(22)	1.533(7)	C(21)	C(23)	1.532(6)
C(21)	C(24)	1.540(5)	C(25)	C(26)	1.520(6)
C(25)	C(27)	1.531(6)	C(28)	C(29)	1.481(7)
C(30)	C(31)	1.503(8)	C(32)	C(33)	1.516(6)
N(2)	H(2)	0.930			

Table A5: Bond angles (°) for **C1**.

atom	atom	atom	angle
Cl(1)	Fe(1)	Cl(2)	91.42(5)
Cl(1)	Fe(1)	O(1)	91.49(8)
Cl(1)	Fe(1)	O(2)	92.71(9)
Cl(1)	Fe(1)	N(1)	178.85(7)
Cl(2)	Fe(1)	O(1)	128.60(10)
Cl(2)	Fe(1)	O(2)	116.51(8)
Cl(2)	Fe(1)	N(1)	89.35(9)
O(1)	Fe(1)	O(2)	114.58(12)
O(1)	Fe(1)	N(1)	87.35(10)
O(2)	Fe(1)	N(1)	87.71(11)
Fe(1)	O(1)	C(1)	138.1(2)
Fe(1)	O(2)	C(14)	138.0(2)
Fe(1)	N(1)	C(7)	104.38(19)
Fe(1)	N(1)	C(8)	103.05(18)
Fe(1)	N(1)	C(25)	118.2(3)
C(7)	N(1)	C(8)	110.9(3)
C(7)	N(1)	C(25)	113.1(2)
C(8)	N(1)	C(25)	106.7(3)
C(28)	N(2)	C(30)	113.5(3)
C(28)	N(2)	C(32)	110.2(3)
C(30)	N(2)	C(32)	114.0(3)
O(1)	C(1)	C(2)	119.3(3)
O(1)	C(1)	C(6)	119.7(3)
C(2)	C(1)	C(6)	121.0(3)

C(1)	C(2)	C(3)	116.7(3)
C(1)	C(2)	C(15)	121.9(3)
C(3)	C(2)	C(15)	121.3(3)
C(2)	C(3)	C(4)	123.0(3)
C(3)	C(4)	C(5)	118.6(3)
C(3)	C(4)	C(19)	120.4(3)
C(5)	C(4)	C(19)	121.0(4)
C(4)	C(5)	C(6)	120.9(4)
C(1)	C(6)	C(5)	119.8(3)
C(1)	C(6)	C(7)	120.4(3)
C(5)	C(6)	C(7)	119.7(3)
N(1)	C(7)	C(6)	114.9(3)
N(1)	C(8)	C(9)	116.2(3)
C(8)	C(9)	C(10)	119.8(3)
C(8)	C(9)	C(14)	120.9(4)
C(10)	C(9)	C(14)	119.2(3)
C(9)	C(10)	C(11)	121.6(3)
C(10)	C(11)	C(12)	118.0(4)
C(10)	C(11)	C(20)	120.6(4)
C(12)	C(11)	C(20)	121.4(4)
C(11)	C(12)	C(13)	123.2(4)
C(12)	C(13)	C(14)	117.1(3)
C(12)	C(13)	C(21)	121.3(4)
C(14)	C(13)	C(21)	121.6(4)
O(2)	C(14)	C(9)	118.8(3)
O(2)	C(14)	C(13)	120.5(3)
C(9)	C(14)	C(13)	120.7(4)
C(2)	C(15)	C(16)	110.0(4)
C(2)	C(15)	C(17)	112.6(3)
C(2)	C(15)	C(18)	110.7(3)
C(16)	C(15)	C(17)	107.2(3)
C(16)	C(15)	C(18)	108.7(3)
C(17)	C(15)	C(18)	107.4(4)
C(13)	C(21)	C(22)	112.0(4)
C(13)	C(21)	C(23)	110.2(3)
C(13)	C(21)	C(24)	109.3(3)
C(22)	C(21)	C(23)	108.0(3)
C(22)	C(21)	C(24)	108.0(3)
C(23)	C(21)	C(24)	109.3(4)
N(1)	C(25)	C(26)	114.3(3)
N(1)	C(25)	C(27)	113.0(4)
C(26)	C(25)	C(27)	109.3(3)
N(2)	C(28)	C(29)	114.5(4)
N(2)	C(30)	C(31)	114.1(4)
N(2)	C(32)	C(33)	113.9(4)

C(28)	N(2)	H(2)	106
C(30)	N(2)	H(2)	106
C(32)	N(2)	H(2)	106

Table A6: Torsion angles (°) for **C1**.

atom1	atom2	atom3	atom4	angle
Cl(2)	Fe(1)	O(1)	C(1)	-92.6(3)
Cl(2)	Fe(1)	O(2)	C(14)	81.8(3)
Cl(2)	Fe(1)	N(1)	C(8)	-73.24(15)
Cl(2)	Fe(1)	N(1)	C(25)	44.12(14)
O(1)	Fe(1)	O(2)	C(14)	-92.4(3)
O(2)	Fe(1)	O(1)	C(1)	80.7(3)
O(1)	Fe(1)	N(1)	C(7)	42.13(16)
O(1)	Fe(1)	N(1)	C(8)	158.07(17)
O(1)	Fe(1)	N(1)	C(25)	-84.57(17)
N(1)	Fe(1)	O(1)	C(1)	-5.5(3)
O(2)	Fe(1)	N(1)	C(7)	-72.61(15)
O(2)	Fe(1)	N(1)	C(8)	43.32(16)
N(1)	Fe(1)	O(2)	C(14)	-6.4(3)
Fe(1)	O(1)	C(1)	C(6)	-14.6(5)
Fe(1)	O(2)	C(14)	C(9)	-17.3(5)
Fe(1)	N(1)	C(7)	C(6)	-69.0(2)
Fe(1)	N(1)	C(8)	C(9)	-68.9(3)
Fe(1)	N(1)	C(25)	C(26)	42.0(3)
C(7)	N(1)	C(8)	C(9)	42.3(3)
C(7)	N(1)	C(25)	C(26)	-80.4(4)
C(7)	N(1)	C(25)	C(27)	45.5(4)
C(25)	N(1)	C(7)	C(6)	60.8(3)
C(8)	N(1)	C(25)	C(26)	157.4(3)
C(8)	N(1)	C(25)	C(27)	-76.7(3)
C(30)	N(2)	C(28)	C(29)	55.1(4)
C(28)	N(2)	C(32)	C(33)	-73.2(4)
C(30)	N(2)	C(32)	C(33)	55.7(5)
C(32)	N(2)	C(30)	C(31)	51.4(5)
O(1)	C(1)	C(2)	C(15)	0.3(5)
O(1)	C(1)	C(6)	C(7)	-3.8(5)
C(2)	C(1)	C(6)	C(5)	-0.2(5)
C(6)	C(1)	C(2)	C(3)	0.6(5)
C(1)	C(2)	C(3)	C(4)	-1.2(5)
C(1)	C(2)	C(15)	C(16)	59.9(4)
C(1)	C(2)	C(15)	C(18)	-60.3(4)
C(3)	C(2)	C(15)	C(16)	-120.4(3)
C(3)	C(2)	C(15)	C(17)	-0.9(5)

C(3)	C(2)	C(15)	C(18)	119.4(3)
C(2)	C(3)	C(4)	C(5)	1.4(6)
C(3)	C(4)	C(5)	C(6)	-0.9(5)
C(4)	C(5)	C(6)	C(1)	0.4(5)
C(1)	C(6)	C(7)	N(1)	52.7(4)
C(5)	C(6)	C(7)	N(1)	-130.9(3)
N(1)	C(8)	C(9)	C(10)	-134.1(3)
N(1)	C(8)	C(9)	C(14)	49.1(4)
C(8)	C(9)	C(14)	O(2)	1.6(4)
C(10)	C(9)	C(14)	C(13)	4.9(4)
C(14)	C(9)	C(10)	C(11)	-1.9(5)
C(9)	C(10)	C(11)	C(12)	-1.7(5)
C(10)	C(11)	C(12)	C(13)	2.5(5)
C(11)	C(12)	C(13)	C(14)	0.4(5)
C(12)	C(13)	C(14)	C(9)	-4.1(4)
C(12)	C(13)	C(21)	C(22)	1.4(4)
C(12)	C(13)	C(21)	C(23)	-118.8(3)
C(12)	C(13)	C(21)	C(24)	121.0(3)
C(14)	C(13)	C(21)	C(23)	62.4(4)
C(14)	C(13)	C(21)	C(24)	-57.7(4)
C(21)	C(13)	C(14)	O(2)	-5.0(4)

Figure A19: MALDI-MS spectrum of **C2**.

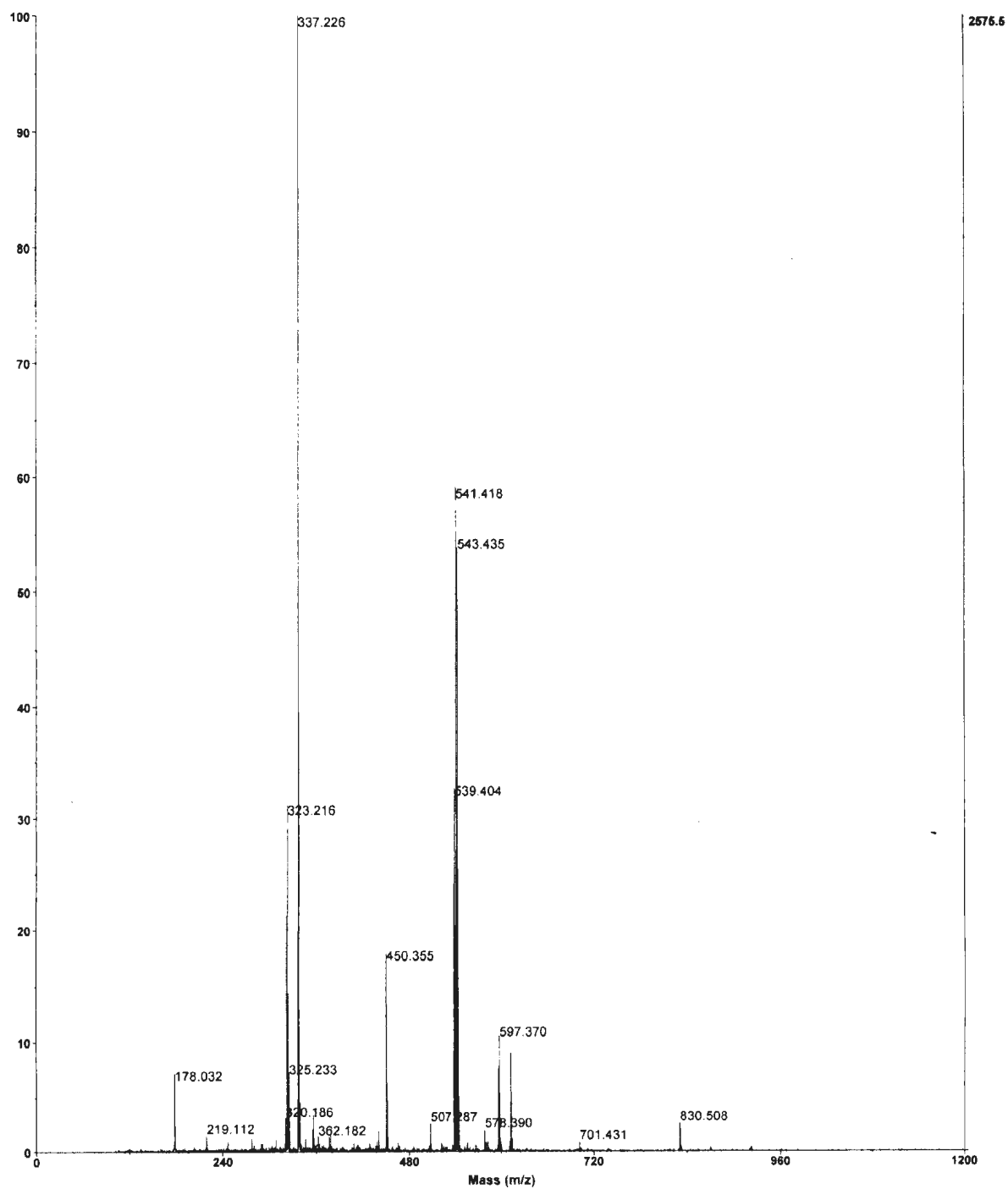


Figure A20: MALDI-MS experimental isotope pattern for **C2**.

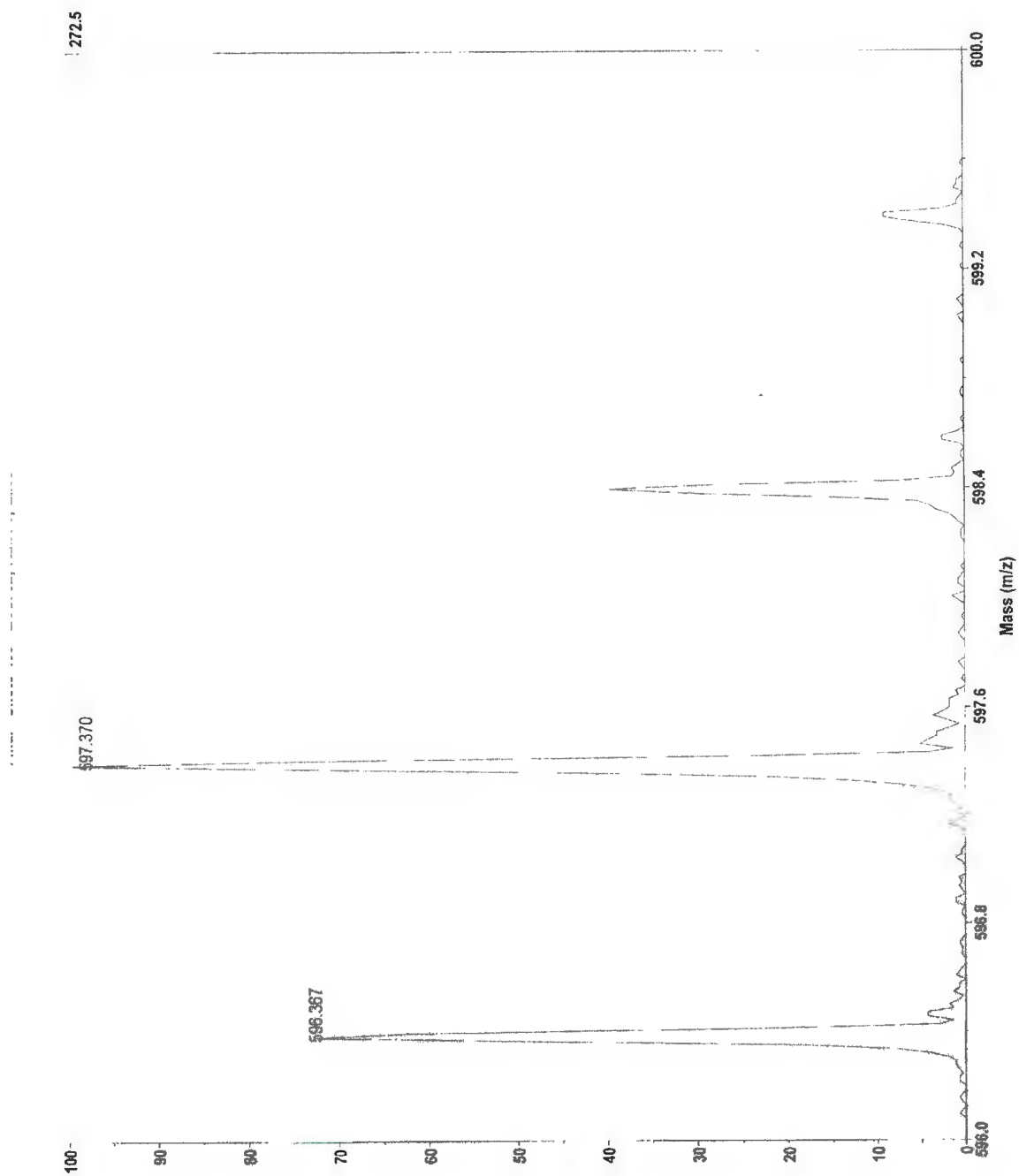


Figure A21: UV-vis spectrum of **C3** in methanol.

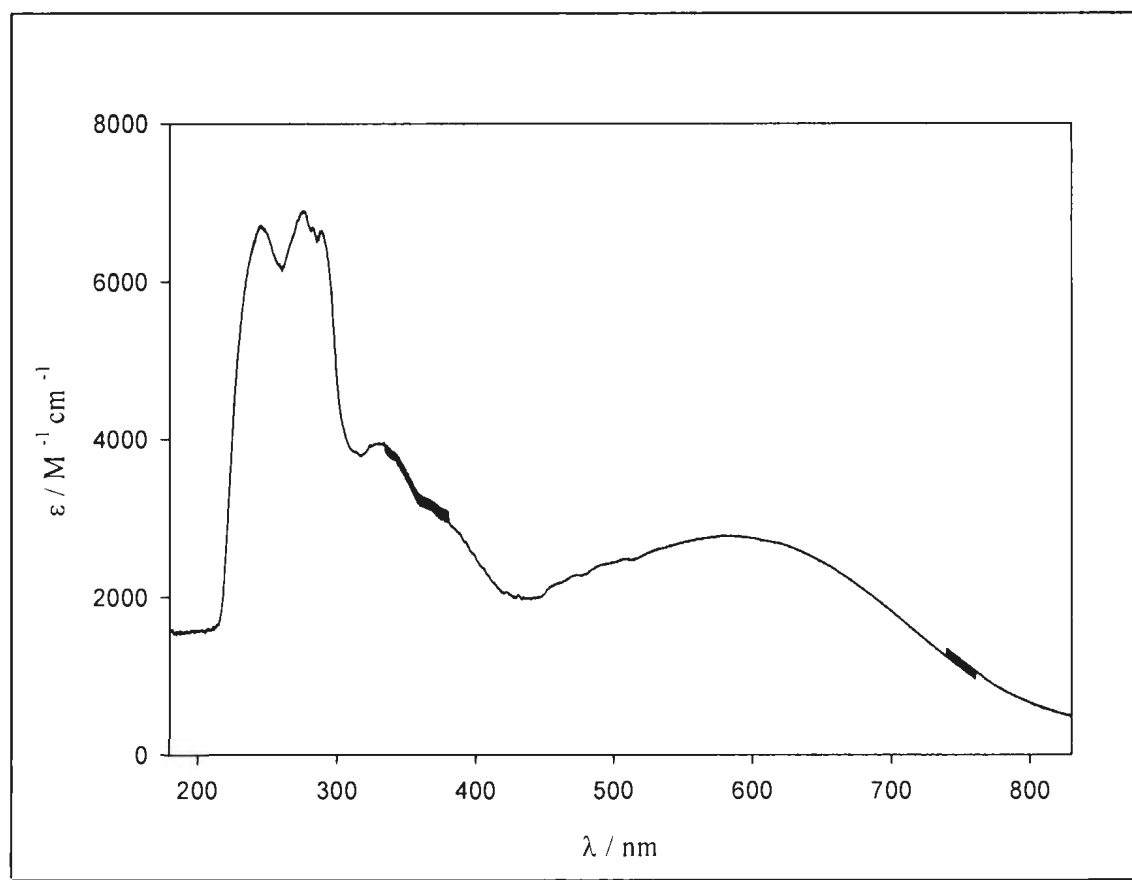


Figure A22: MALDI-MS spectrum of **C3**.

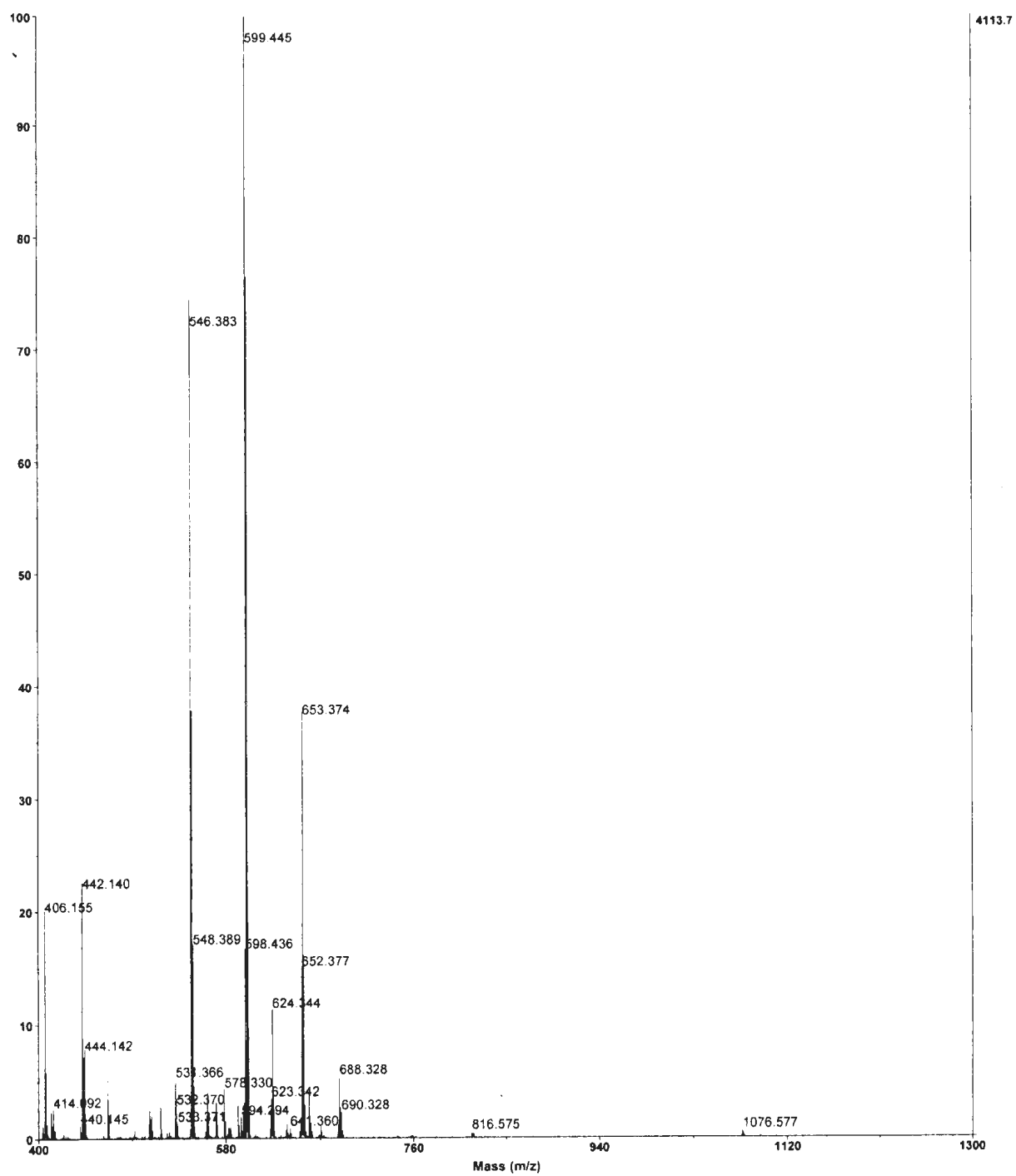


Figure A23: Theoretical isotope pattern for **C3**.

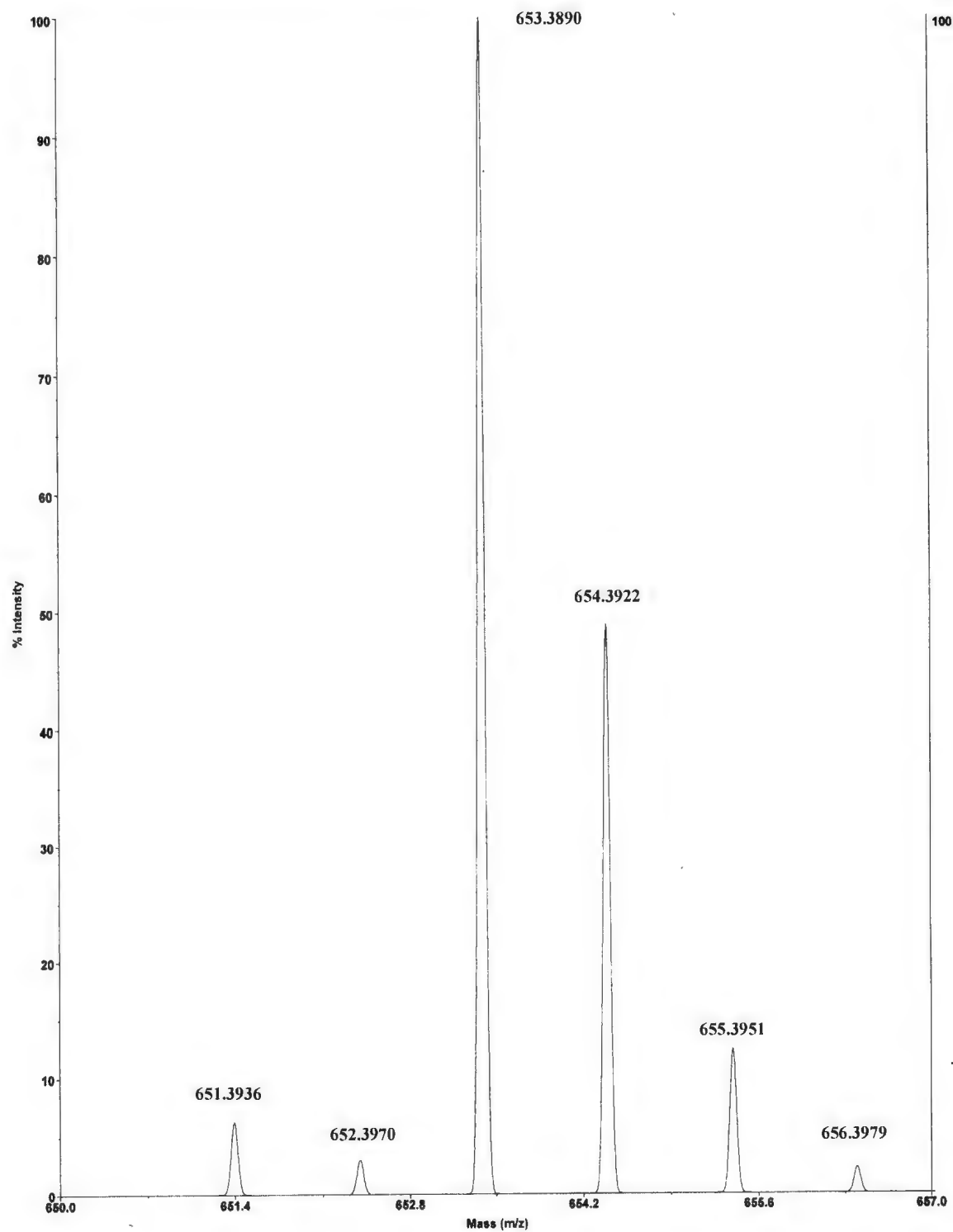


Figure A24: Experimental isotope pattern for **C3**.

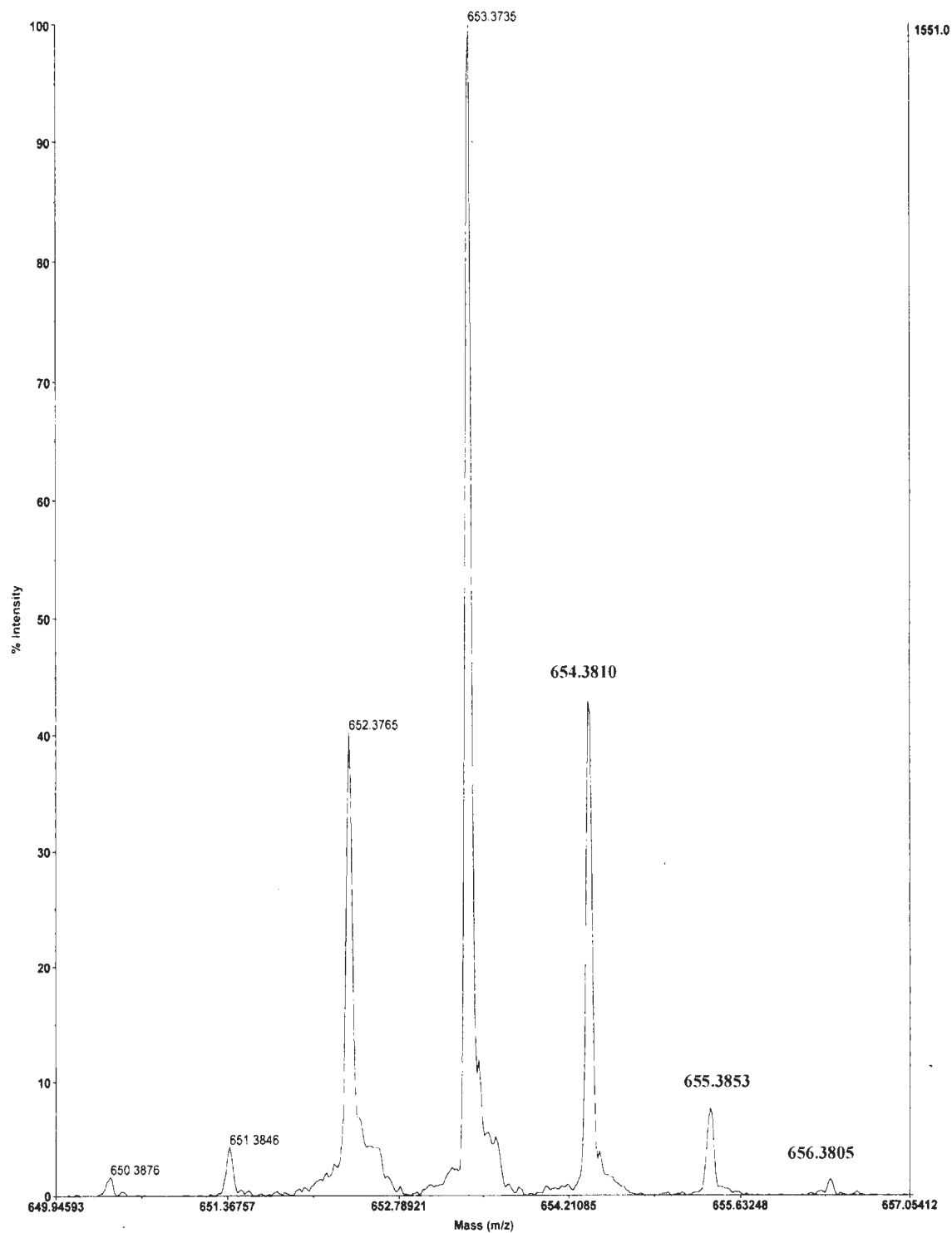


Figure A25: Single crystal X-ray structure of **C3**. Ellipsoids at 50% probability.

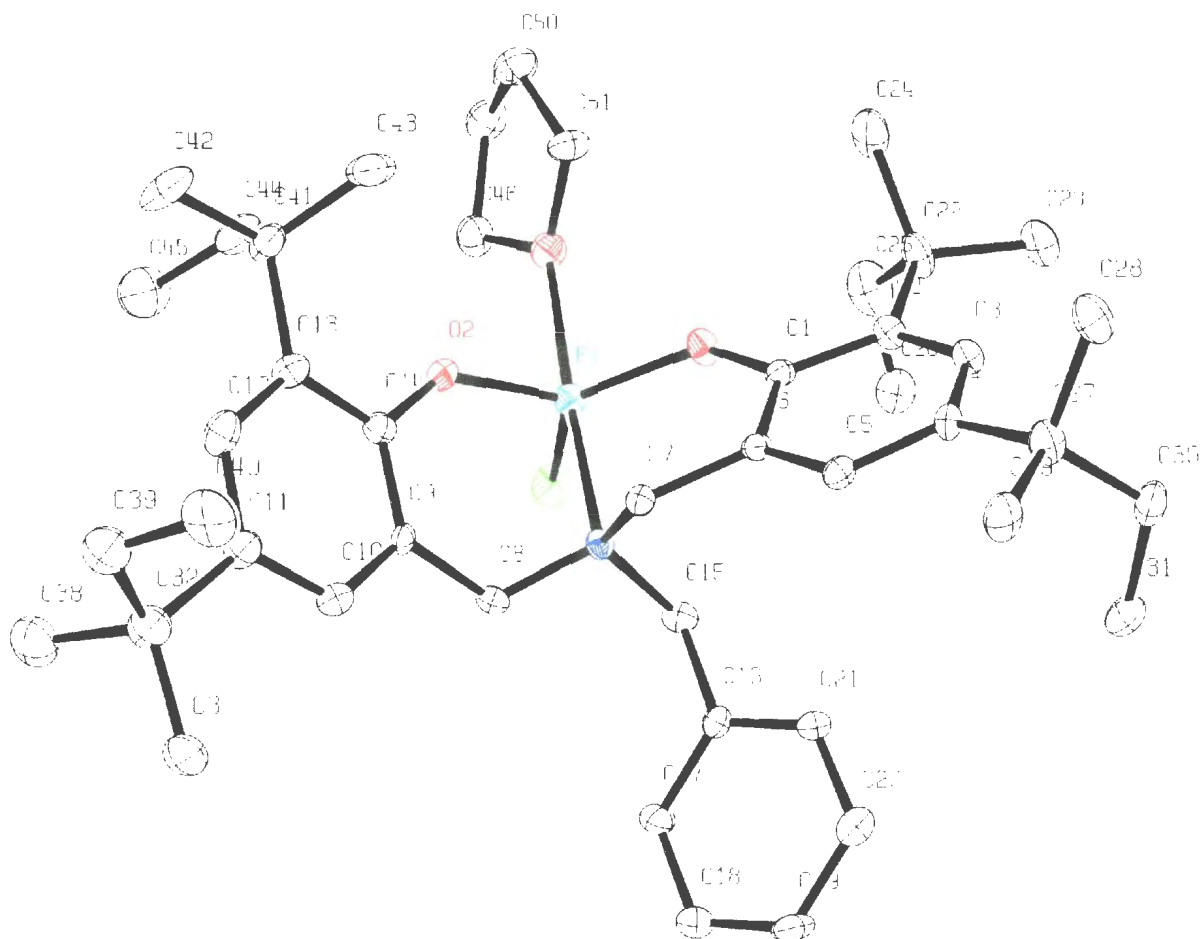


Table A7: Bond lengths (Å) for **C3**.

atom	atom	distance	atom	atom	distance
Fe(1)	Cl(1)	2.237(3)	Fe(1)	O(1)	1.854(6)
Fe(1)	O(2)	1.848(6)	Fe(1)	O(3)	2.151(6)
Fe(1)	N(1)	2.190(6)	O(1)	C(1)	1.346(9)
O(2)	C(14)	1.371(10)	O(3)	C(46)	1.453(13)
O(3)	C(49)	1.44(5)	O(3)	C(51)	1.46(2)
N(1)	C(7)	1.483(9)	N(1)	C(8)	1.481(10)
N(1)	C(15)	1.522(10)	C(1)	C(2)	1.424(11)
C(1)	C(6)	1.383(10)	C(2)	C(3)	1.379(12)
C(2)	C(22)	1.549(13)	C(3)	C(4)	1.384(12)
C(4)	C(5)	1.390(11)	C(4)	C(27)	1.524(12)
C(5)	C(6)	1.399(10)	C(6)	C(7)	1.517(11)

C(8)	C(9)	1.523(10)	C(9)	C(10)	1.385(11)
C(9)	C(14)	1.386(11)	C(10)	C(11)	1.342(12)
C(11)	C(12)	1.382(13)	C(11)	C(32)	1.601(14)
C(12)	C(13)	1.387(13)	C(13)	C(14)	1.403(12)
C(13)	C(41)	1.569(13)	C(15)	C(16)	1.520(12)
C(16)	C(17)	1.400(12)	C(16)	C(21)	1.341(12)
C(17)	C(18)	1.405(14)	C(18)	C(19)	1.376(16)
C(19)	C(20)	1.408(15)	C(20)	C(21)	1.396(14)
C(22)	C(23)	1.539(15)	C(22)	C(24)	1.636(15)
C(22)	C(25)	1.486(17)	C(25)	C(26)	1.402(19)
C(27)	C(28)	1.545(13)	C(27)	C(29)	1.550(13)
C(27)	C(30)	1.532(13)	C(30)	C(31)	1.474(16)
C(32)	C(33)	1.51(2)	C(32)	C(34)	1.59(2)
C(32)	C(35)	1.45(3)	C(32)	C(37)	1.48(3)
C(32)	C(38)	1.55(4)	C(32)	C(39)	1.59(3)
C(35)	C(36)	1.47(4)	C(39)	C(40)	1.50(4)
C(41)	C(42)	1.557(14)	C(41)	C(43)	1.524(16)
C(41)	C(44)	1.529(14)	C(44)	C(45)	1.430(18)
C(46)	C(47)	1.558(15)	C(47)	C(48)	1.51(3)
C(47)	C(50)	1.485(20)	C(48)	C(49)	1.46(4)
C(50)	C(51)	1.47(3)			

Table A8: Bond angles (°) for **C3**.

atom	atom	atom	angle
Cl(1)	Fe(1)	O(1)	121.49(20)
Cl(1)	Fe(1)	O(2)	114.7(2)
Cl(1)	Fe(1)	O(3)	91.72(18)
Cl(1)	Fe(1)	N(1)	96.12(17)
O(1)	Fe(1)	O(2)	123.7(3)
O(1)	Fe(1)	O(3)	86.7(2)
O(1)	Fe(1)	N(1)	88.0(2)
O(2)	Fe(1)	O(3)	88.6(2)
O(2)	Fe(1)	N(1)	89.4(2)
O(3)	Fe(1)	N(1)	172.0(2)
Fe(1)	O(1)	C(1)	135.7(5)
Fe(1)	O(2)	C(14)	136.1(5)
Fe(1)	O(3)	C(46)	123.7(6)
Fe(1)	O(3)	C(49)	127.3(15)
Fe(1)	O(3)	C(51)	121.4(8)
C(46)	O(3)	C(49)	108.8(16)
C(46)	O(3)	C(51)	109.5(10)
C(49)	O(3)	C(51)	19.6(18)
Fe(1)	N(1)	C(7)	104.2(4)

Fe(1)	N(1)	C(8)	106.1(4)
Fe(1)	N(1)	C(15)	110.6(4)
C(7)	N(1)	C(8)	111.2(6)
C(7)	N(1)	C(15)	113.7(6)
C(8)	N(1)	C(15)	110.6(6)
O(1)	C(1)	C(2)	120.2(7)
O(1)	C(1)	C(6)	120.1(7)
C(2)	C(1)	C(6)	119.6(7)
C(1)	C(2)	C(3)	116.6(7)
C(1)	C(2)	C(22)	122.2(7)
C(3)	C(2)	C(22)	120.8(8)
C(2)	C(3)	C(4)	125.1(8)
C(3)	C(4)	C(5)	116.5(7)
C(3)	C(4)	C(27)	120.7(7)
C(5)	C(4)	C(27)	122.7(7)
C(4)	C(5)	C(6)	121.0(7)
C(1)	C(6)	C(5)	120.5(7)
C(1)	C(6)	C(7)	120.8(7)
C(5)	C(6)	C(7)	118.7(7)
N(1)	C(7)	C(6)	114.6(6)
N(1)	C(8)	C(9)	116.3(6)
C(8)	C(9)	C(10)	119.8(7)
C(8)	C(9)	C(14)	120.2(7)
C(10)	C(9)	C(14)	119.8(7)
C(9)	C(10)	C(11)	121.3(8)
C(10)	C(11)	C(12)	119.1(9)
C(10)	C(11)	C(32)	120.8(8)
C(12)	C(11)	C(32)	120.0(8)
C(11)	C(12)	C(13)	122.2(9)
C(12)	C(13)	C(14)	117.4(8)
C(12)	C(13)	C(41)	121.6(8)
C(14)	C(13)	C(41)	121.0(8)
O(2)	C(14)	C(9)	120.1(7)
O(2)	C(14)	C(13)	119.9(7)
C(9)	C(14)	C(13)	120.0(8)
N(1)	C(15)	C(16)	115.9(6)
C(15)	C(16)	C(17)	119.1(7)
C(15)	C(16)	C(21)	120.6(8)
C(17)	C(16)	C(21)	119.9(8)
C(16)	C(17)	C(18)	119.6(8)
C(17)	C(18)	C(19)	120.0(9)
C(18)	C(19)	C(20)	119.6(9)
C(19)	C(20)	C(21)	119.0(9)
C(16)	C(21)	C(20)	121.8(9)
C(2)	C(22)	C(23)	111.4(8)

C(2)	C(22)	C(24)	106.7(7)
C(2)	C(22)	C(25)	114.4(9)
C(23)	C(22)	C(24)	107.2(8)
C(23)	C(22)	C(25)	109.4(9)
C(24)	C(22)	C(25)	107.3(9)
C(22)	C(25)	C(26)	110.6(12)
C(4)	C(27)	C(28)	108.8(7)
C(4)	C(27)	C(29)	112.0(8)
C(4)	C(27)	C(30)	110.6(7)
C(28)	C(27)	C(29)	107.6(8)
C(28)	C(27)	C(30)	107.1(8)
C(29)	C(27)	C(30)	110.5(8)
C(27)	C(30)	C(31)	116.7(9)
C(11)	C(32)	C(33)	114.5(11)
C(11)	C(32)	C(34)	106.4(11)
C(11)	C(32)	C(35)	108.8(12)
C(11)	C(32)	C(37)	113.8(12)
C(11)	C(32)	C(38)	109.5(13)
C(11)	C(32)	C(39)	108.7(13)
C(33)	C(32)	C(34)	105.9(14)
C(33)	C(32)	C(35)	114.5(14)
C(33)	C(32)	C(37)	131.5(15)
C(33)	C(32)	C(38)	57.7(16)
C(33)	C(32)	C(39)	46.7(14)
C(34)	C(32)	C(35)	106.0(15)
C(34)	C(32)	C(37)	54.8(16)
C(34)	C(32)	C(38)	51.3(15)
C(34)	C(32)	C(39)	142.5(15)
C(35)	C(32)	C(37)	51.7(17)
C(35)	C(32)	C(38)	139.9(17)
C(35)	C(32)	C(39)	74.5(15)
C(37)	C(32)	C(38)	101.1(19)
C(37)	C(32)	C(39)	119.0(16)
C(38)	C(32)	C(39)	103.7(17)
C(32)	C(35)	C(36)	110.5(19)
C(32)	C(39)	C(40)	115(2)
C(13)	C(41)	C(42)	112.7(8)
C(13)	C(41)	C(43)	110.1(8)
C(13)	C(41)	C(44)	109.3(8)
C(42)	C(41)	C(43)	105.0(9)
C(42)	C(41)	C(44)	108.0(8)
C(43)	C(41)	C(44)	111.7(8)
C(41)	C(44)	C(45)	115.9(10)
O(3)	C(46)	C(47)	102.9(8)
C(46)	C(47)	C(48)	111.2(14)

C(46)	C(47)	C(50)	104.2(10)
C(48)	C(47)	C(50)	37.5(19)
C(47)	C(48)	C(49)	100(3)
O(3)	C(49)	C(48)	115(3)
C(47)	C(50)	C(51)	106.3(15)
O(3)	C(51)	C(50)	107.9(16)

Table A9: Torsion angles (°) for **C3**.

atom1	atom2	atom3	atom4	angle
Cl(1)	Fe(1)	O(1)	C(1)	-106.4(5)
Cl(1)	Fe(1)	O(2)	C(14)	90.8(5)
Cl(1)	Fe(1)	O(3)	C(46)	39.5(4)
Cl(1)	Fe(1)	O(3)	C(49)	-146.4(4)
Cl(1)	Fe(1)	N(1)	C(8)	-74.3(3)
Cl(1)	Fe(1)	N(1)	C(15)	45.7(3)
O(1)	Fe(1)	O(2)	C(14)	-92.8(6)
O(2)	Fe(1)	O(1)	C(1)	77.5(6)
O(1)	Fe(1)	O(3)	C(49)	-25.0(5)
O(1)	Fe(1)	O(3)	C(51)	-47.7(4)
O(1)	Fe(1)	N(1)	C(7)	46.8(3)
O(1)	Fe(1)	N(1)	C(15)	-75.7(3)
N(1)	Fe(1)	O(1)	C(1)	-10.4(5)
O(2)	Fe(1)	O(3)	C(46)	-75.2(4)
O(2)	Fe(1)	O(3)	C(49)	98.9(5)
O(2)	Fe(1)	O(3)	C(51)	76.1(4)
O(2)	Fe(1)	N(1)	C(7)	-76.9(3)
O(2)	Fe(1)	N(1)	C(8)	40.5(3)
N(1)	Fe(1)	O(2)	C(14)	-5.6(5)
Fe(1)	O(1)	C(1)	C(6)	-14.1(10)
Fe(1)	O(2)	C(14)	C(9)	-13.0(11)
C(46)	O(3)	C(49)	C(48)	-12(3)
C(49)	O(3)	C(46)	C(47)	1.8(19)
C(46)	O(3)	C(51)	C(50)	-6.5(16)
C(51)	O(3)	C(46)	C(47)	22.5(12)
C(49)	O(3)	C(51)	C(50)	85(5)
C(51)	O(3)	C(49)	C(48)	-108(6)
Fe(1)	N(1)	C(7)	C(6)	-70.0(6)
Fe(1)	N(1)	C(8)	C(9)	-66.6(6)
C(7)	N(1)	C(8)	C(9)	46.1(8)
C(7)	N(1)	C(15)	C(16)	58.7(8)
C(15)	N(1)	C(7)	C(6)	50.5(8)
C(8)	N(1)	C(15)	C(16)	-67.3(8)
O(1)	C(1)	C(2)	C(22)	1.7(10)

O(1)	C(1)	C(6)	C(7)	1.6(10)
C(2)	C(1)	C(6)	C(5)	8.3(10)
C(6)	C(1)	C(2)	C(3)	-8.2(10)
C(1)	C(2)	C(3)	C(4)	1.5(11)
C(1)	C(2)	C(22)	C(24)	74.9(9)
C(1)	C(2)	C(22)	C(25)	-43.6(11)
C(3)	C(2)	C(22)	C(23)	18.9(11)
C(3)	C(2)	C(22)	C(24)	-97.9(8)
C(3)	C(2)	C(22)	C(25)	143.6(7)
C(2)	C(3)	C(4)	C(5)	5.1(12)
C(3)	C(4)	C(5)	C(6)	-5.1(11)
C(3)	C(4)	C(27)	C(28)	57.1(9)
C(3)	C(4)	C(27)	C(30)	-60.3(9)
C(5)	C(4)	C(27)	C(28)	-125.4(7)
C(5)	C(4)	C(27)	C(29)	-6.6(10)
C(5)	C(4)	C(27)	C(30)	117.2(8)
C(4)	C(5)	C(6)	C(1)	-1.5(11)
C(1)	C(6)	C(7)	N(1)	47.6(9)
C(5)	C(6)	C(7)	N(1)	-136.0(6)
N(1)	C(8)	C(9)	C(10)	-134.5(6)
N(1)	C(8)	C(9)	C(14)	50.8(9)
C(8)	C(9)	C(14)	O(2)	-4.4(11)
C(10)	C(9)	C(14)	C(13)	2.8(11)
C(14)	C(9)	C(10)	C(11)	1.6(11)
C(9)	C(10)	C(11)	C(12)	-4.4(13)
C(10)	C(11)	C(12)	C(13)	2.9(15)
C(10)	C(11)	C(32)	C(34)	-54.3(11)
C(10)	C(11)	C(32)	C(35)	59.6(12)
C(10)	C(11)	C(32)	C(37)	4.0(14)
C(10)	C(11)	C(32)	C(38)	-108.4(9)
C(10)	C(11)	C(32)	C(39)	139.0(8)
C(12)	C(11)	C(32)	C(33)	6.4(14)
C(12)	C(11)	C(32)	C(34)	123.1(9)
C(12)	C(11)	C(32)	C(35)	-123.1(9)
C(12)	C(11)	C(32)	C(38)	69.0(11)
C(12)	C(11)	C(32)	C(39)	-43.6(12)
C(11)	C(12)	C(13)	C(14)	1.4(14)
C(12)	C(13)	C(14)	C(9)	-4.1(12)
C(12)	C(13)	C(41)	C(42)	4.1(12)
C(12)	C(13)	C(41)	C(43)	120.9(9)

Figure A26: MALDI-MS spectrum of C4.

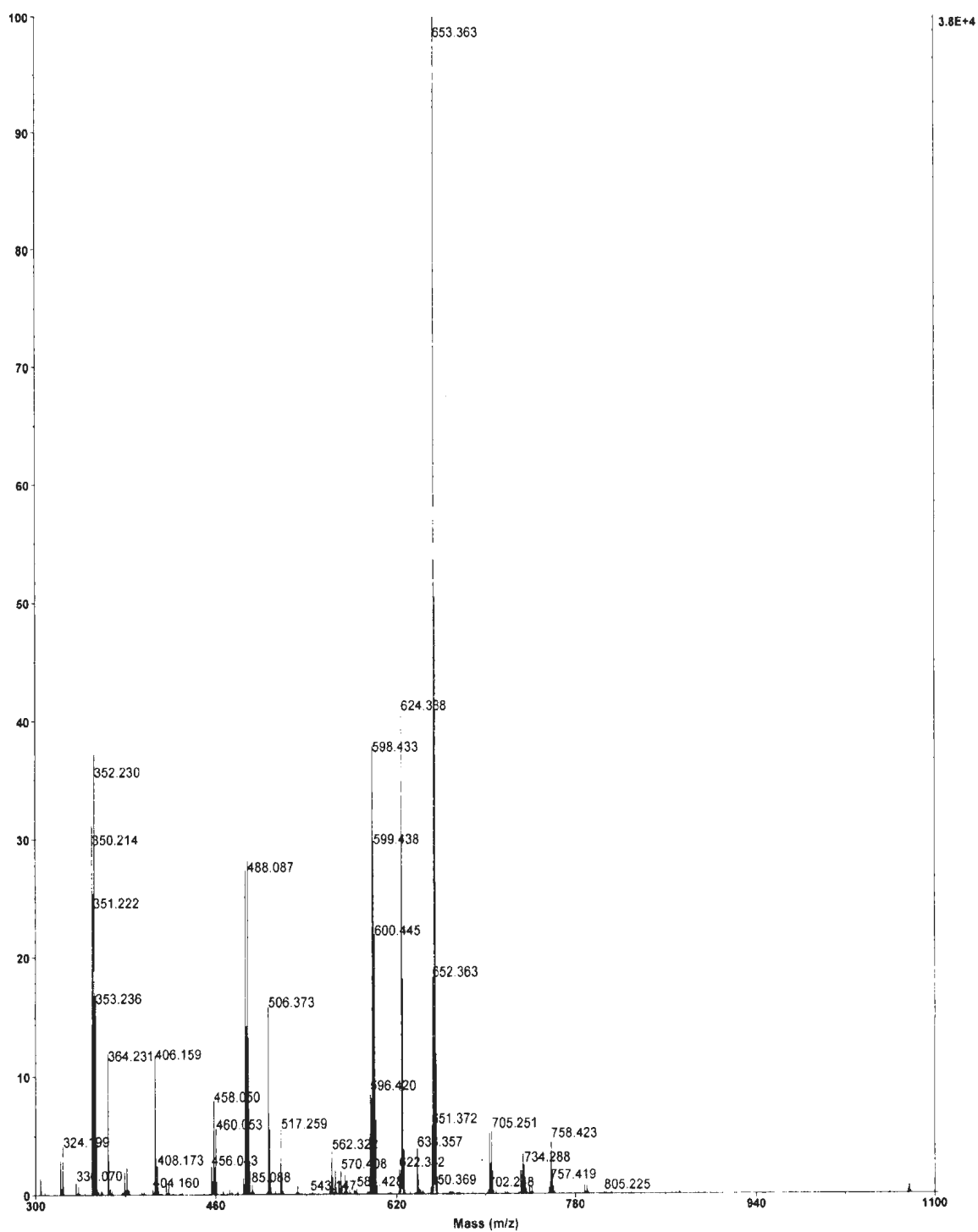


Figure A27: MALSI-MS Experimental isotope pattern for C4.

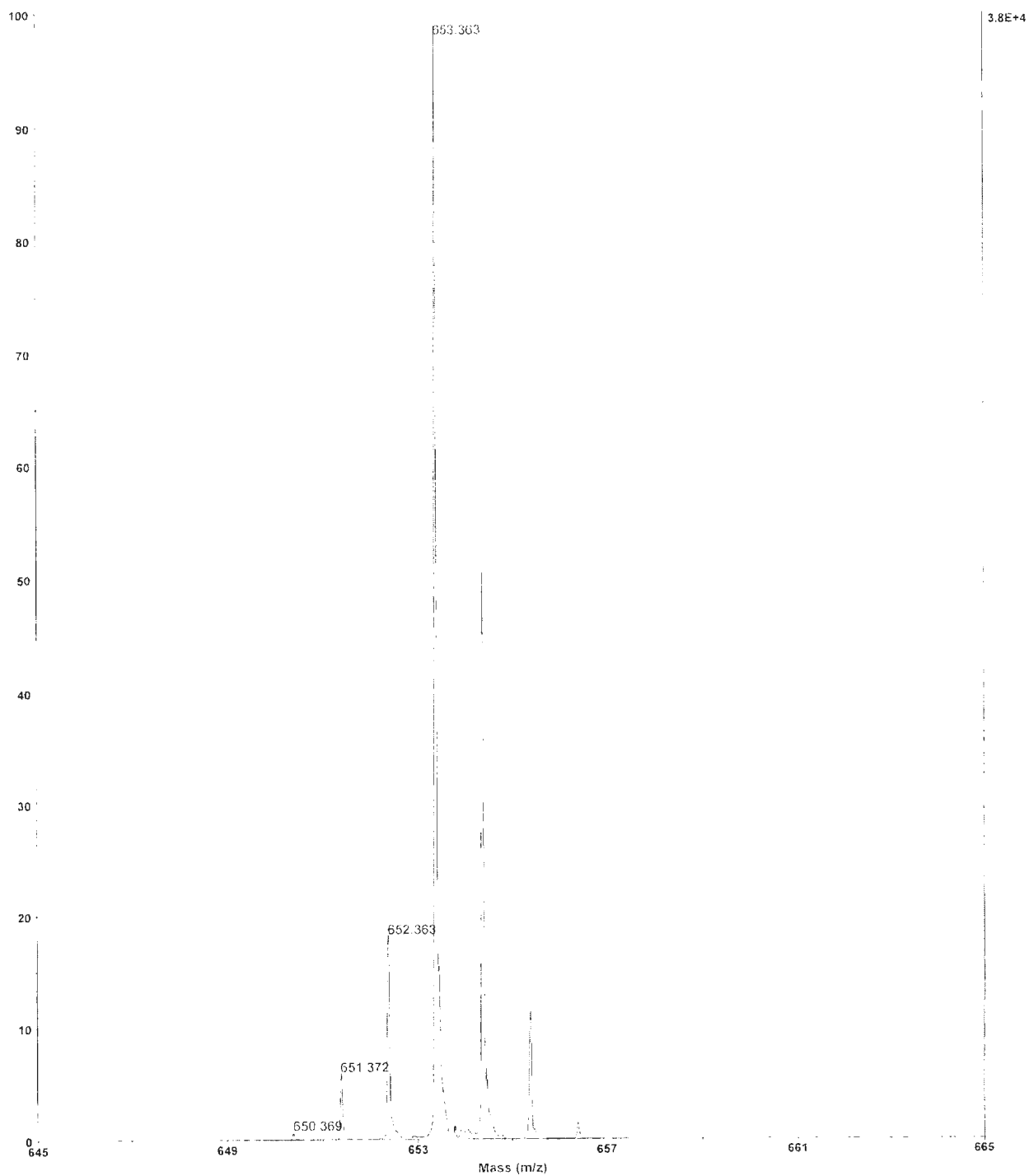


Figure A28: Single crystal X-ray structure of **C4**. Ellipsoids at 50% probability.

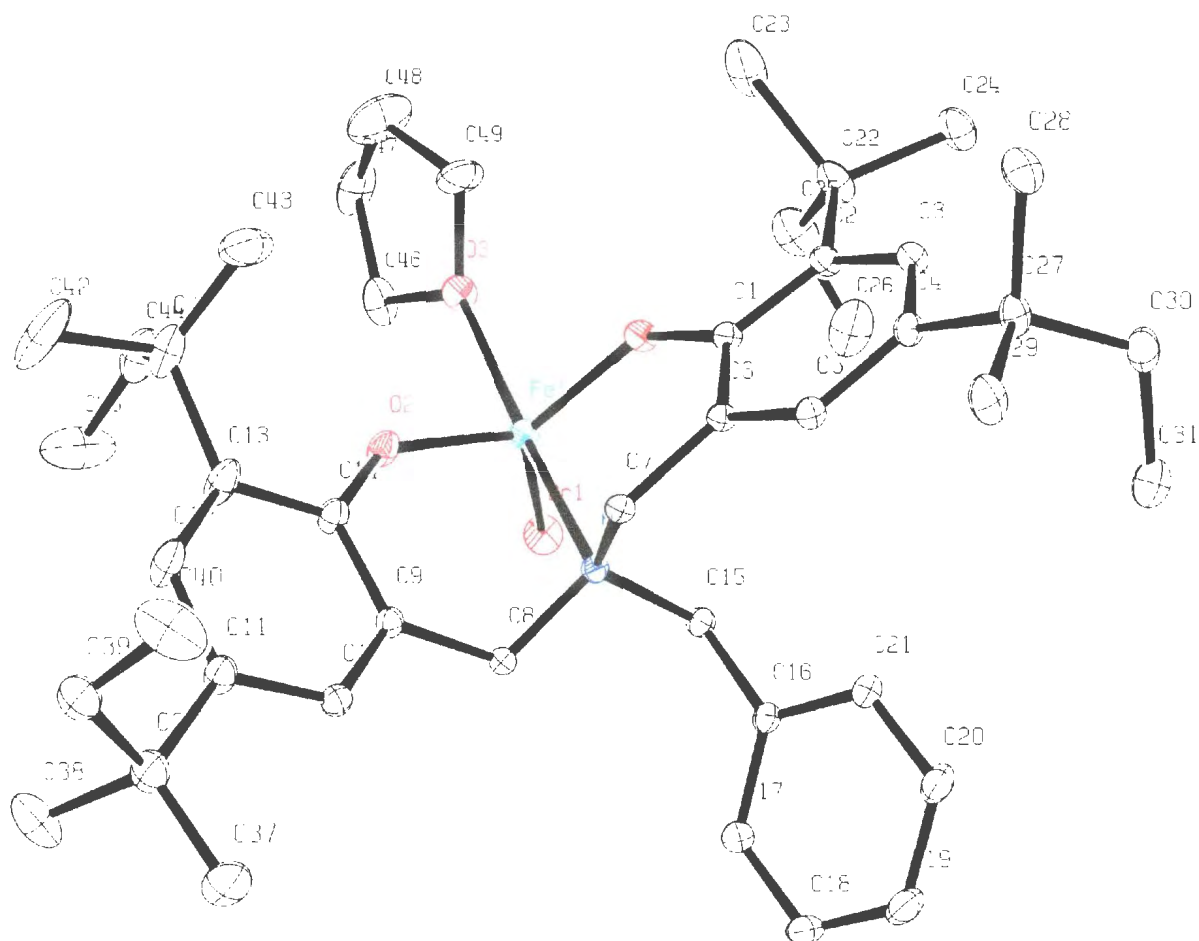


Table A10: Bond lengths (Å) for **C4**.

atom	atom	distance	atom	atom	distance
Br(1)	Fe(1)	2.3808(8)	Fe(1)	O(1)	1.8491(18)
Fe(1)	O(2)	1.842(4)	Fe(1)	O(3)	2.145(2)
Fe(1)	N(1)	2.185(2)	O(1)	C(1)	1.347(3)
O(2)	C(14)	1.346(5)	O(3)	C(46)	1.448(4)
O(3)	C(49)	1.424(7)	N(1)	C(7)	1.490(4)
N(1)	C(8)	1.494(3)	N(1)	C(15)	1.505(6)
C(1)	C(2)	1.416(4)	C(1)	C(6)	1.403(4)
C(2)	C(3)	1.385(4)	C(2)	C(22)	1.540(5)
C(3)	C(4)	1.397(5)	C(4)	C(5)	1.381(4)
C(4)	C(27)	1.539(4)	C(5)	C(6)	1.393(4)
C(6)	C(7)	1.503(4)	C(8)	C(9)	1.510(6)

C(9)	C(10)	1.386(5)	C(9)	C(14)	1.400(5)
C(10)	C(11)	1.392(7)	C(11)	C(12)	1.389(6)
C(11)	C(32)	1.533(6)	C(12)	C(13)	1.388(7)
C(13)	C(14)	1.408(9)	C(13)	C(41)	1.615(8)
C(15)	C(16)	1.512(5)	C(16)	C(17)	1.391(5)
C(16)	C(21)	1.387(4)	C(17)	C(18)	1.388(6)
C(18)	C(19)	1.369(6)	C(19)	C(20)	1.386(6)
C(20)	C(21)	1.393(6)	C(22)	C(23)	1.699(12)
C(22)	C(24)	1.548(6)	C(22)	C(25)	1.464(8)
C(25)	C(26)	1.358(13)	C(27)	C(28)	1.537(6)
C(27)	C(29)	1.530(6)	C(27)	C(30)	1.538(7)
C(30)	C(31)	1.510(9)	C(32)	C(33)	1.59(2)
C(32)	C(34)	1.475(20)	C(32)	C(35)	1.529(15)
C(32)	C(37)	1.444(16)	C(32)	C(38)	1.571(9)
C(32)	C(39)	1.568(16)	C(35)	C(36)	1.39(4)
C(39)	C(40)	1.451(16)	C(41)	C(42)	1.545(18)
C(41)	C(43)	1.492(7)	C(41)	C(44)	1.486(9)
C(44)	C(45)	1.400(8)	C(46)	C(47)	1.496(8)
C(47)	C(48)	1.450(13)	C(48)	C(49)	1.423(10)

Table A11: Bond angles (°) for **C4**.

atom	atom	atom	angle
Br(1)	Fe(1)	O(1)	120.17(11)
Br(1)	Fe(1)	O(2)	114.88(9)
Br(1)	Fe(1)	O(3)	91.36(10)
Br(1)	Fe(1)	N(1)	96.79(8)
O(1)	Fe(1)	O(2)	124.80(14)
O(1)	Fe(1)	O(3)	86.89(9)
O(1)	Fe(1)	N(1)	88.03(8)
O(2)	Fe(1)	O(3)	88.17(12)
O(2)	Fe(1)	N(1)	89.41(11)
O(3)	Fe(1)	N(1)	171.77(12)
Fe(1)	O(1)	C(1)	135.97(17)
Fe(1)	O(2)	C(14)	136.5(3)
Fe(1)	O(3)	C(46)	124.7(2)
Fe(1)	O(3)	C(49)	123.9(3)
C(46)	O(3)	C(49)	108.4(4)
Fe(1)	N(1)	C(7)	104.90(17)
Fe(1)	N(1)	C(8)	107.58(17)
Fe(1)	N(1)	C(15)	111.82(20)
C(7)	N(1)	C(8)	109.7(3)
C(7)	N(1)	C(15)	112.8(2)
C(8)	N(1)	C(15)	109.8(2)

O(1)	C(1)	C(2)	121.3(3)
O(1)	C(1)	C(6)	119.3(2)
C(2)	C(1)	C(6)	119.5(2)
C(1)	C(2)	C(3)	117.5(3)
C(1)	C(2)	C(22)	121.4(3)
C(3)	C(2)	C(22)	121.0(3)
C(2)	C(3)	C(4)	124.0(3)
C(3)	C(4)	C(5)	116.8(2)
C(3)	C(4)	C(27)	119.7(2)
C(5)	C(4)	C(27)	123.5(3)
C(4)	C(5)	C(6)	121.9(3)
C(1)	C(6)	C(5)	119.9(2)
C(1)	C(6)	C(7)	121.1(2)
C(5)	C(6)	C(7)	118.9(3)
N(1)	C(7)	C(6)	114.7(3)
N(1)	C(8)	C(9)	115.5(3)
C(8)	C(9)	C(10)	118.7(3)
C(8)	C(9)	C(14)	121.2(3)
C(10)	C(9)	C(14)	120.0(4)
C(9)	C(10)	C(11)	122.0(3)
C(10)	C(11)	C(12)	116.2(4)
C(10)	C(11)	C(32)	121.7(4)
C(12)	C(11)	C(32)	122.0(5)
C(11)	C(12)	C(13)	124.5(7)
C(12)	C(13)	C(14)	117.3(5)
C(12)	C(13)	C(41)	122.7(7)
C(14)	C(13)	C(41)	119.8(4)
O(2)	C(14)	C(9)	119.8(4)
O(2)	C(14)	C(13)	120.4(3)
C(9)	C(14)	C(13)	119.8(4)
N(1)	C(15)	C(16)	117.7(3)
C(15)	C(16)	C(17)	121.2(3)
C(15)	C(16)	C(21)	120.6(3)
C(17)	C(16)	C(21)	118.0(3)
C(16)	C(17)	C(18)	120.7(3)
C(17)	C(18)	C(19)	120.9(4)
C(18)	C(19)	C(20)	119.4(4)
C(19)	C(20)	C(21)	119.7(3)
C(16)	C(21)	C(20)	121.3(3)
C(2)	C(22)	C(23)	104.6(5)
C(2)	C(22)	C(24)	111.7(3)
C(2)	C(22)	C(25)	116.0(3)
C(23)	C(22)	C(24)	106.1(4)
C(23)	C(22)	C(25)	105.5(5)
C(24)	C(22)	C(25)	111.9(5)

C(22)	C(25)	C(26)	109.5(5)
C(4)	C(27)	C(28)	108.4(3)
C(4)	C(27)	C(29)	111.2(3)
C(4)	C(27)	C(30)	110.3(4)
C(28)	C(27)	C(29)	107.8(4)
C(28)	C(27)	C(30)	107.9(3)
C(29)	C(27)	C(30)	111.1(4)
C(27)	C(30)	C(31)	115.3(3)
C(11)	C(32)	C(33)	109.8(11)
C(11)	C(32)	C(34)	116.5(6)
C(11)	C(32)	C(35)	109.5(7)
C(11)	C(32)	C(37)	114.2(9)
C(11)	C(32)	C(38)	105.5(5)
C(11)	C(32)	C(39)	109.7(5)
C(33)	C(32)	C(34)	106.7(11)
C(33)	C(32)	C(35)	101.7(12)
C(33)	C(32)	C(37)	51.4(10)
C(33)	C(32)	C(38)	59.6(10)
C(33)	C(32)	C(39)	140.0(11)
C(34)	C(32)	C(35)	111.5(14)
C(34)	C(32)	C(37)	129.2(10)
C(34)	C(32)	C(38)	55.4(9)
C(34)	C(32)	C(39)	47.7(7)
C(35)	C(32)	C(37)	51.2(12)
C(35)	C(32)	C(38)	144.4(8)
C(35)	C(32)	C(39)	70.9(13)
C(37)	C(32)	C(38)	107.9(8)
C(37)	C(32)	C(39)	115.4(10)
C(38)	C(32)	C(39)	103.0(8)
C(32)	C(35)	C(36)	109.6(16)
C(32)	C(39)	C(40)	113.9(13)
C(13)	C(41)	C(42)	108.2(5)
C(13)	C(41)	C(43)	112.6(5)
C(13)	C(41)	C(44)	107.0(6)
C(42)	C(41)	C(43)	106.5(7)
C(42)	C(41)	C(44)	107.0(6)
C(43)	C(41)	C(44)	115.2(5)
C(41)	C(44)	C(45)	119.9(5)
O(3)	C(46)	C(47)	105.4(4)
C(46)	C(47)	C(48)	103.5(5)
C(47)	C(48)	C(49)	108.0(9)
O(3)	C(49)	C(48)	107.7(5)

Table A12: Torsion angles (°) for **C4**.

atom1	atom2	atom3	atom4	angle
Br(1)	Fe(1)	O(1)	C(1)	-104.4(3)
Br(1)	Fe(1)	O(2)	C(14)	96.5(3)
Br(1)	Fe(1)	O(3)	C(46)	44.1(3)
Br(1)	Fe(1)	O(3)	C(49)	-157.8(2)
Br(1)	Fe(1)	N(1)	C(8)	-76.95(17)
Br(1)	Fe(1)	N(1)	C(15)	43.68(10)
O(1)	Fe(1)	O(2)	C(14)	-87.9(3)
O(2)	Fe(1)	O(1)	C(1)	80.2(4)
O(1)	Fe(1)	O(3)	C(49)	-37.7(3)
O(1)	Fe(1)	N(1)	C(7)	46.07(17)
O(1)	Fe(1)	N(1)	C(15)	-76.47(14)
N(1)	Fe(1)	O(1)	C(1)	-7.7(3)
O(2)	Fe(1)	O(3)	C(46)	-70.7(3)
O(2)	Fe(1)	O(3)	C(49)	87.3(3)
O(2)	Fe(1)	N(1)	C(7)	-78.78(16)
O(2)	Fe(1)	N(1)	C(8)	38.04(18)
O(2)	Fe(1)	N(1)	C(15)	158.68(13)
N(1)	Fe(1)	O(2)	C(14)	-0.7(3)
Fe(1)	O(1)	C(1)	C(6)	-18.0(6)
Fe(1)	O(2)	C(14)	C(9)	-18.1(5)
C(46)	O(3)	C(49)	C(48)	1.0(7)
C(49)	O(3)	C(46)	C(47)	14.9(6)
Fe(1)	N(1)	C(7)	C(6)	-69.3(3)
Fe(1)	N(1)	C(8)	C(9)	-64.0(3)
C(7)	N(1)	C(8)	C(9)	49.6(3)
C(7)	N(1)	C(15)	C(16)	59.4(3)
C(15)	N(1)	C(7)	C(6)	52.7(3)
C(8)	N(1)	C(15)	C(16)	-63.4(3)
O(1)	C(1)	C(2)	C(22)	-2.8(6)
O(1)	C(1)	C(6)	C(7)	4.4(6)
C(2)	C(1)	C(6)	C(5)	6.9(6)
C(6)	C(1)	C(2)	C(3)	-6.0(6)
C(1)	C(2)	C(3)	C(4)	0.7(7)
C(1)	C(2)	C(22)	C(23)	77.3(5)
C(1)	C(2)	C(22)	C(25)	-38.4(7)
C(3)	C(2)	C(22)	C(23)	-99.6(4)
C(3)	C(2)	C(22)	C(24)	14.8(7)
C(3)	C(2)	C(22)	C(25)	144.7(4)
C(2)	C(3)	C(4)	C(5)	3.8(6)
C(3)	C(4)	C(5)	C(6)	-2.9(6)
C(3)	C(4)	C(27)	C(28)	56.1(5)
C(3)	C(4)	C(27)	C(30)	-61.8(4)

C(5)	C(4)	C(27)	C(28)	-124.2(4)
C(5)	C(4)	C(27)	C(29)	-5.8(6)
C(5)	C(4)	C(27)	C(30)	117.9(4)
C(4)	C(5)	C(6)	C(1)	-2.4(6)
C(1)	C(6)	C(7)	N(1)	45.5(5)
C(5)	C(6)	C(7)	N(1)	-136.7(3)
N(1)	C(8)	C(9)	C(10)	-135.5(2)
N(1)	C(8)	C(9)	C(14)	48.9(3)
C(8)	C(9)	C(14)	O(2)	-2.7(4)
C(10)	C(9)	C(14)	C(13)	1.7(4)
C(14)	C(9)	C(10)	C(11)	1.1(4)
C(9)	C(10)	C(11)	C(12)	-1.9(4)
C(10)	C(11)	C(12)	C(13)	-0.0(6)
C(10)	C(11)	C(32)	C(33)	-48.0(4)
C(10)	C(11)	C(32)	C(35)	62.9(5)
C(10)	C(11)	C(32)	C(37)	7.6(5)
C(10)	C(11)	C(32)	C(38)	-110.8(4)
C(10)	C(11)	C(32)	C(39)	138.9(3)
C(12)	C(11)	C(32)	C(33)	129.6(4)
C(12)	C(11)	C(32)	C(34)	8.2(6)
C(12)	C(11)	C(32)	C(35)	-119.5(4)
C(12)	C(11)	C(32)	C(38)	66.9(5)
C(12)	C(11)	C(32)	C(39)	-43.5(5)
C(11)	C(12)	C(13)	C(14)	2.7(7)
C(12)	C(13)	C(14)	C(9)	-3.4(5)
C(12)	C(13)	C(41)	C(42)	-3.5(6)
C(12)	C(13)	C(41)	C(43)	113.9(5)
C(12)	C(13)	C(41)	C(44)	-118.5(5)
C(14)	C(13)	C(41)	C(43)	-60.6(7)
C(14)	C(13)	C(41)	C(44)	67.1(5)
C(41)	C(13)	C(14)	O(2)	-8.8(5)
N(1)	C(15)	C(16)	C(17)	90.5(4)
N(1)	C(15)	C(16)	C(21)	-94.6(4)
C(17)	C(16)	C(21)	C(20)	-1.6(7)
C(21)	C(16)	C(17)	C(18)	0.8(7)
C(16)	C(17)	C(18)	C(19)	0.3(9)
C(17)	C(18)	C(19)	C(20)	-0.7(10)
C(18)	C(19)	C(20)	C(21)	-0.0(10)
C(19)	C(20)	C(21)	C(16)	1.2(9)
C(2)	C(22)	C(25)	C(26)	-56.9(7)
C(24)	C(22)	C(25)	C(26)	72.9(5)
C(4)	C(27)	C(30)	C(31)	-61.4(4)
C(29)	C(27)	C(30)	C(31)	62.4(4)
C(11)	C(32)	C(35)	C(36)	67.5(18)
C(11)	C(32)	C(39)	C(40)	-64.1(6)

C(33)	C(32)	C(39)	C(40)	126.0(14)
C(34)	C(32)	C(35)	C(36)	-63.0(15)
C(38)	C(32)	C(35)	C(36)	-123.1(15)
C(35)	C(32)	C(39)	C(40)	40.5(7)
C(39)	C(32)	C(35)	C(36)	-37.3(13)
C(37)	C(32)	C(39)	C(40)	66.6(9)
C(13)	C(41)	C(44)	C(45)	49.5(9)
C(42)	C(41)	C(44)	C(45)	-66.2(9)
O(3)	C(46)	C(47)	C(48)	-24.6(7)
C(46)	C(47)	C(48)	C(49)	25.8(10)
C(47)	C(48)	C(49)	O(3)	-17.3(10)

Figure 29A: MALDI-MS spectrum of **C5**.

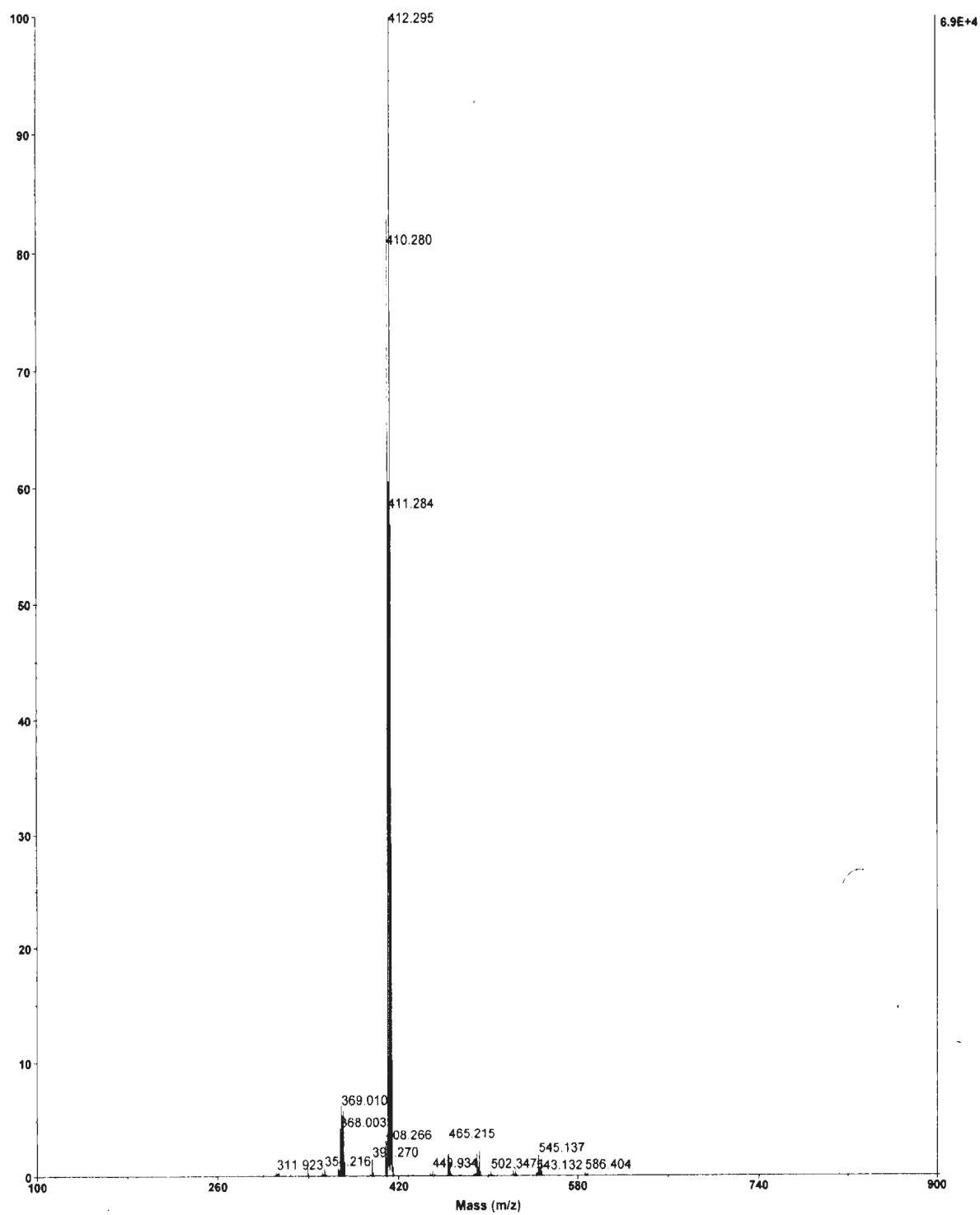


Figure 30A: MALDI-MS experimental isotope pattern of **C5**.

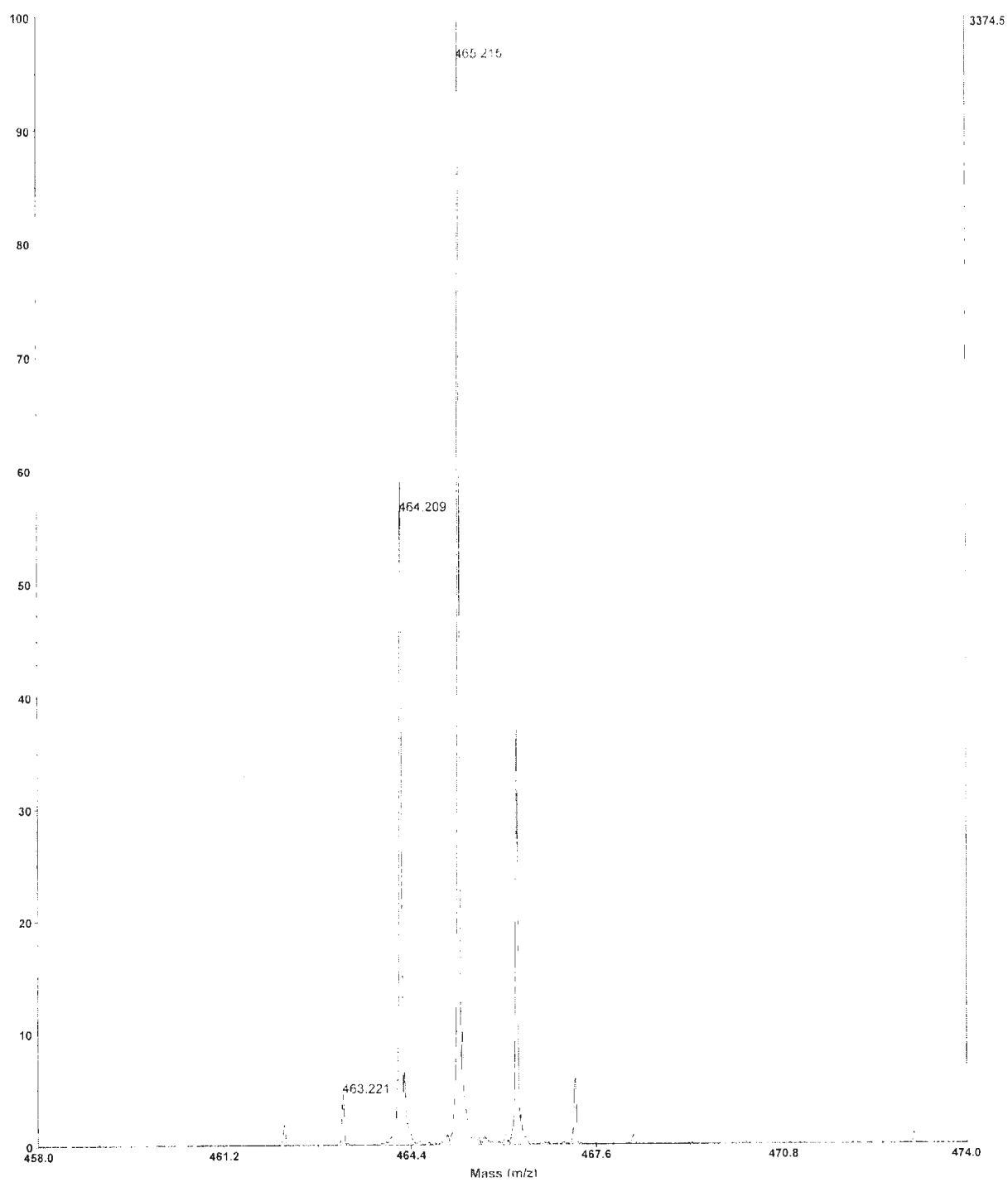


Figure A31: Single crystal X-ray structure of **C5**. Ellipsoids at 30% probability.

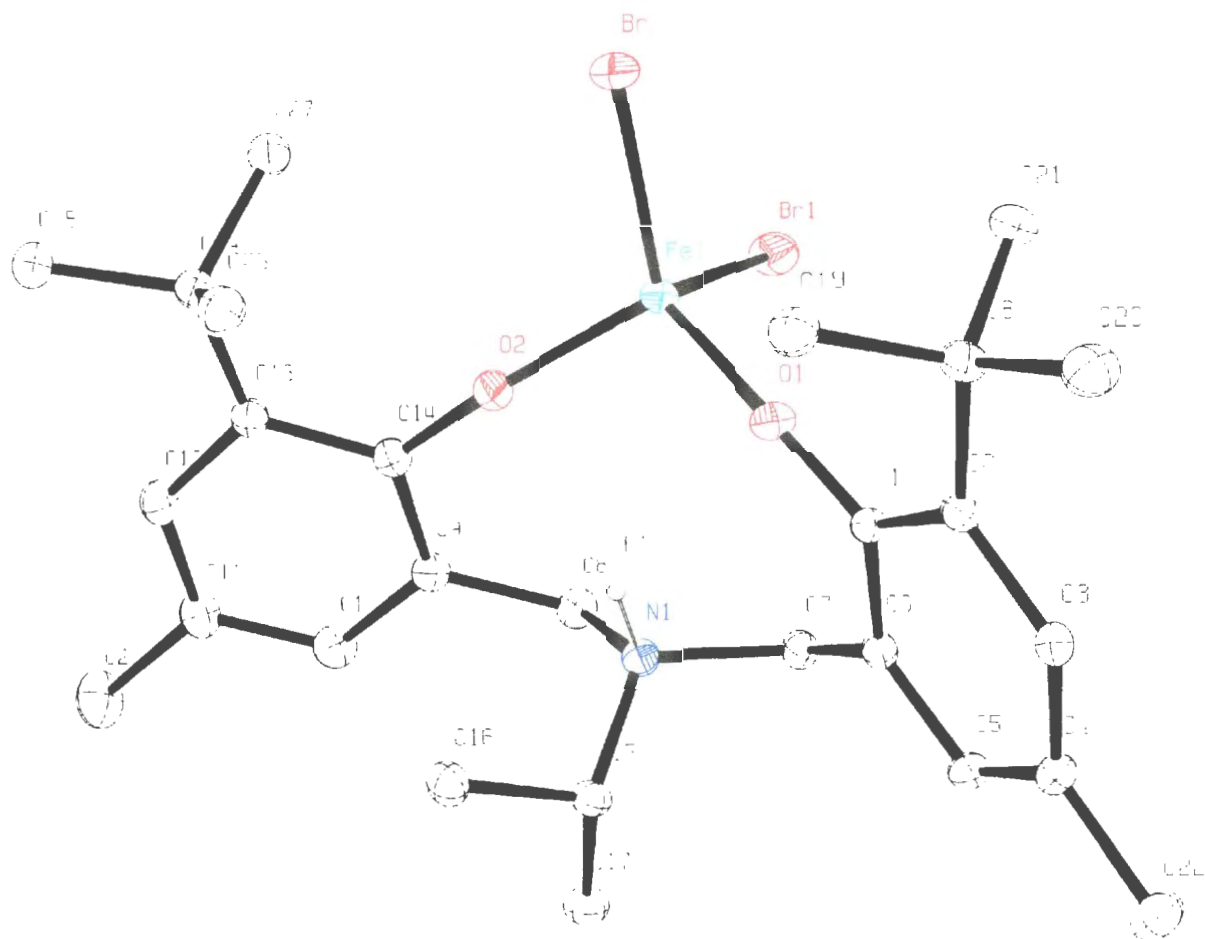


Table A13: Bond lengths (Å) for **C5**.

atom	atom	distance	atom	atom	distance
Br(1)	Fe(1)	2.3596(9)	Br(2)	Fe(1)	2.3491(8)
Fe(1)	O(1)	1.822(2)	Fe(1)	O(2)	1.832(3)
O(1)	C(1)	1.342(4)	O(2)	C(14)	1.349(5)
N(1)	C(7)	1.515(5)	N(1)	C(8)	1.523(4)
N(1)	C(15)	1.520(5)	C(1)	C(2)	1.414(5)
C(1)	C(6)	1.407(5)	C(2)	C(3)	1.401(5)
C(2)	C(18)	1.531(6)	C(3)	C(4)	1.383(6)
C(4)	C(5)	1.371(5)	C(4)	C(22)	1.513(6)
C(5)	C(6)	1.385(5)	C(6)	C(7)	1.491(5)
C(8)	C(9)	1.494(5)	C(9)	C(10)	1.389(6)
C(9)	C(14)	1.400(6)	C(10)	C(11)	1.379(5)
C(11)	C(12)	1.382(6)	C(11)	C(23)	1.517(7)

C(12)	C(13)	1.404(6)	C(13)	C(14)	1.413(5)
C(13)	C(24)	1.519(6)	C(15)	C(16)	1.519(5)
C(15)	C(17)	1.513(6)	C(18)	C(19)	1.547(5)
C(18)	C(20)	1.537(5)	C(18)	C(21)	1.537(6)
C(24)	C(25)	1.533(6)	C(24)	C(26)	1.540(5)
N(1)	H(1)	0.91(5)			

Table A14: Bond angles (°) for **C5**.

atom	atom	atom	angle
Br(1)	Fe(1)	Br(2)	110.26(3)
Br(1)	Fe(1)	O(1)	108.43(8)
Br(1)	Fe(1)	O(2)	110.71(9)
Br(2)	Fe(1)	O(1)	110.90(9)
Br(2)	Fe(1)	O(2)	110.08(9)
O(1)	Fe(1)	O(2)	106.38(13)
Fe(1)	O(1)	C(1)	166.9(2)
Fe(1)	O(2)	C(14)	163.3(2)
C(7)	N(1)	C(8)	109.7(3)
C(7)	N(1)	C(15)	111.9(3)
C(8)	N(1)	C(15)	116.6(3)
O(1)	C(1)	C(2)	121.9(3)
O(1)	C(1)	C(6)	118.1(3)
C(2)	C(1)	C(6)	119.9(3)
C(1)	C(2)	C(3)	116.2(3)
C(1)	C(2)	C(18)	122.1(3)
C(3)	C(2)	C(18)	121.7(3)
C(2)	C(3)	C(4)	123.9(3)
C(3)	C(4)	C(5)	118.6(3)
C(3)	C(4)	C(22)	120.9(4)
C(5)	C(4)	C(22)	120.5(4)
C(4)	C(5)	C(6)	120.5(4)
C(1)	C(6)	C(5)	120.7(3)
C(1)	C(6)	C(7)	118.9(3)
C(5)	C(6)	C(7)	120.4(3)
N(1)	C(7)	C(6)	111.9(3)
N(1)	C(8)	C(9)	111.9(3)
C(8)	C(9)	C(10)	120.6(4)
C(8)	C(9)	C(14)	118.6(3)
C(10)	C(9)	C(14)	120.8(3)
C(9)	C(10)	C(11)	120.8(4)
C(10)	C(11)	C(12)	117.6(4)
C(10)	C(11)	C(23)	121.1(4)

C(12)	C(11)	C(23)	121.3(4)
C(11)	C(12)	C(13)	124.7(3)
C(12)	C(13)	C(14)	116.0(4)
C(12)	C(13)	C(24)	121.4(3)
C(14)	C(13)	C(24)	122.6(4)
O(2)	C(14)	C(9)	117.8(3)
O(2)	C(14)	C(13)	122.0(3)
C(9)	C(14)	C(13)	120.1(4)
N(1)	C(15)	C(16)	111.1(3)
N(1)	C(15)	C(17)	111.7(3)
C(16)	C(15)	C(17)	113.4(4)
C(2)	C(18)	C(19)	109.8(3)
C(2)	C(18)	C(20)	111.5(3)
C(2)	C(18)	C(21)	109.9(3)
C(19)	C(18)	C(20)	107.5(3)
C(19)	C(18)	C(21)	110.9(3)
C(20)	C(18)	C(21)	107.2(4)
C(13)	C(24)	C(25)	112.6(4)
C(13)	C(24)	C(26)	109.4(3)
C(25)	C(24)	C(26)	107.2(3)
C(7)	N(1)	H(1)	106(3)
C(8)	N(1)	H(1)	107(2)
C(15)	N(1)	H(1)	105(3)

Table A15: Torsion angles (°) for **C5**.

atom1	atom2	atom3	atom4	angle
Br(1)	Fe(1)	O(1)	C(1)	-31.7(10)
Br(1)	Fe(1)	O(2)	C(14)	10.3(7)
Br(2)	Fe(1)	O(1)	C(1)	-152.9(9)
Br(2)	Fe(1)	O(2)	C(14)	132.4(6)
O(1)	Fe(1)	O(2)	C(14)	-107.3(7)
O(2)	Fe(1)	O(1)	C(1)	87.4(9)
C(7)	N(1)	C(15)	C(16)	151.3(2)
C(7)	N(1)	C(15)	C(17)	-81.1(3)
C(15)	N(1)	C(7)	C(6)	-67.2(4)
C(8)	N(1)	C(15)	C(16)	-81.3(3)
C(8)	N(1)	C(15)	C(17)	46.4(3)
C(15)	N(1)	C(8)	C(9)	68.3(4)
O(1)	C(1)	C(2)	C(18)	-4.9(5)
O(1)	C(1)	C(6)	C(7)	5.7(5)
C(2)	C(1)	C(6)	C(5)	4.0(5)
C(6)	C(1)	C(2)	C(3)	-4.0(5)
C(1)	C(2)	C(3)	C(4)	1.1(6)

C(1)	C(2)	C(18)	C(19)	63.2(4)
C(1)	C(2)	C(18)	C(21)	-59.0(4)
C(3)	C(2)	C(18)	C(19)	-117.2(4)
C(3)	C(2)	C(18)	C(20)	1.8(5)
C(3)	C(2)	C(18)	C(21)	120.5(3)
C(2)	C(3)	C(4)	C(5)	1.8(6)
C(3)	C(4)	C(5)	C(6)	-1.9(6)
C(4)	C(5)	C(6)	C(1)	-0.9(6)
C(1)	C(6)	C(7)	N(1)	-67.6(4)
C(5)	C(6)	C(7)	N(1)	113.7(4)
N(1)	C(8)	C(9)	C(10)	-116.0(3)
N(1)	C(8)	C(9)	C(14)	64.0(4)
C(8)	C(9)	C(14)	O(2)	-3.7(5)
C(10)	C(9)	C(14)	C(13)	-0.8(5)
C(14)	C(9)	C(10)	C(11)	-0.5(6)
C(9)	C(10)	C(11)	C(12)	1.7(6)
C(10)	C(11)	C(12)	C(13)	-1.6(6)
C(11)	C(12)	C(13)	C(14)	0.4(6)
C(12)	C(13)	C(14)	C(9)	0.8(5)
C(12)	C(13)	C(24)	C(25)	-3.5(5)
C(12)	C(13)	C(24)	C(26)	115.7(4)
C(14)	C(13)	C(24)	C(26)	-62.2(4)
C(24)	C(13)	C(14)	O(2)	1.8(5)

Figure 32A: MALDI-MS spectrum of C6.

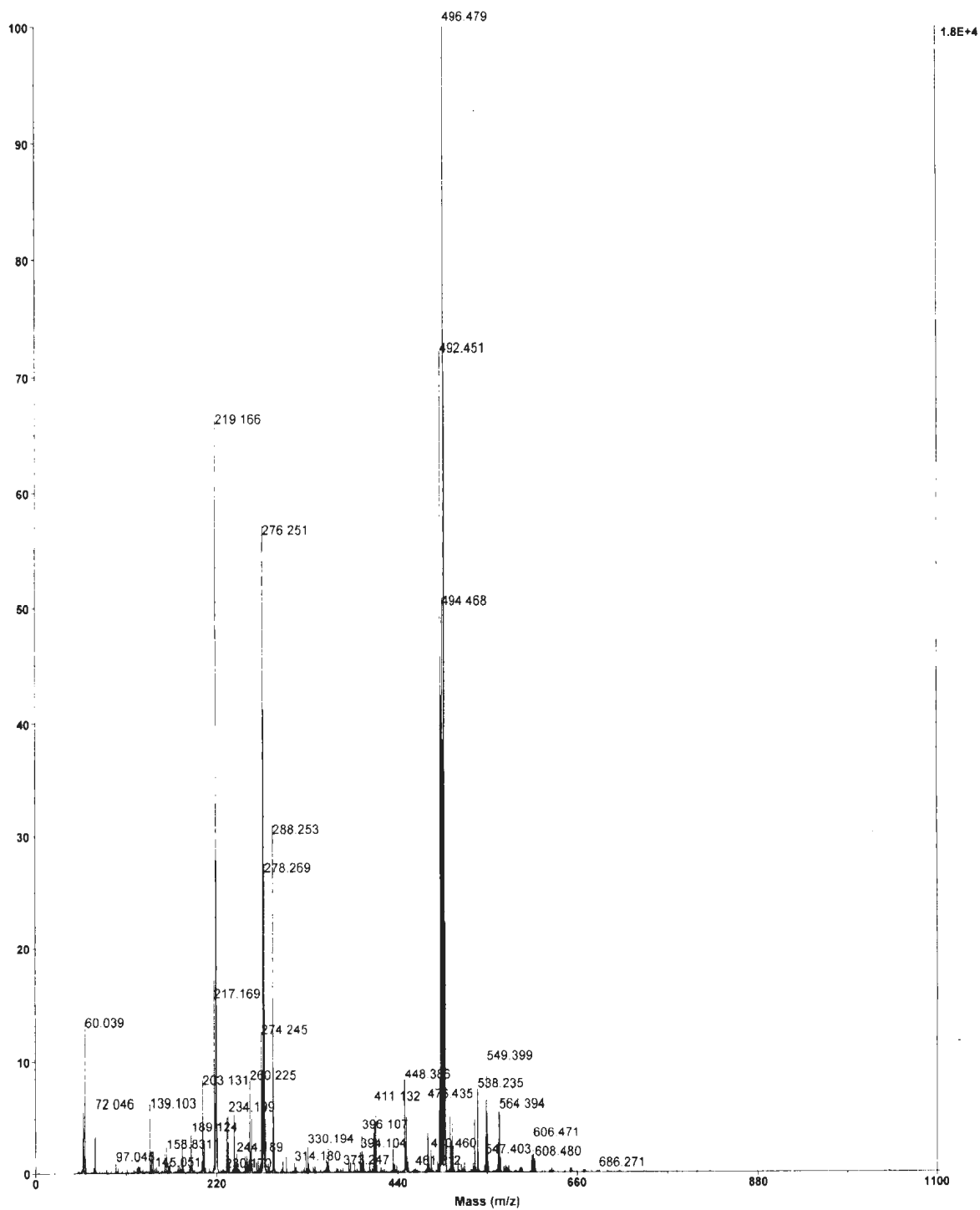


Figure 33A: MALDI-MS experimental isotope pattern of C6.

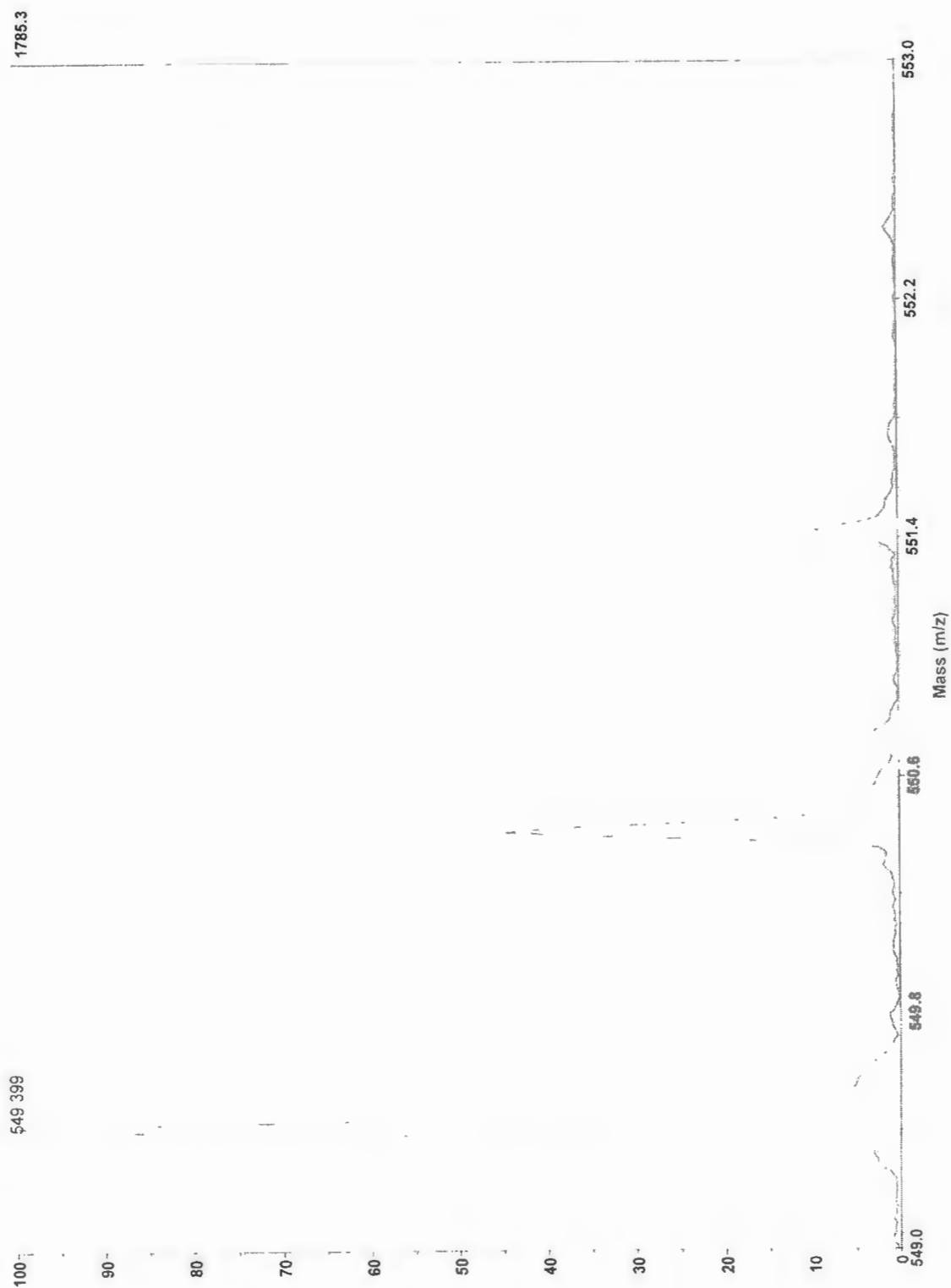


Figure A34: Magnetic moment per mol of dimer vs. temperature for **C6**

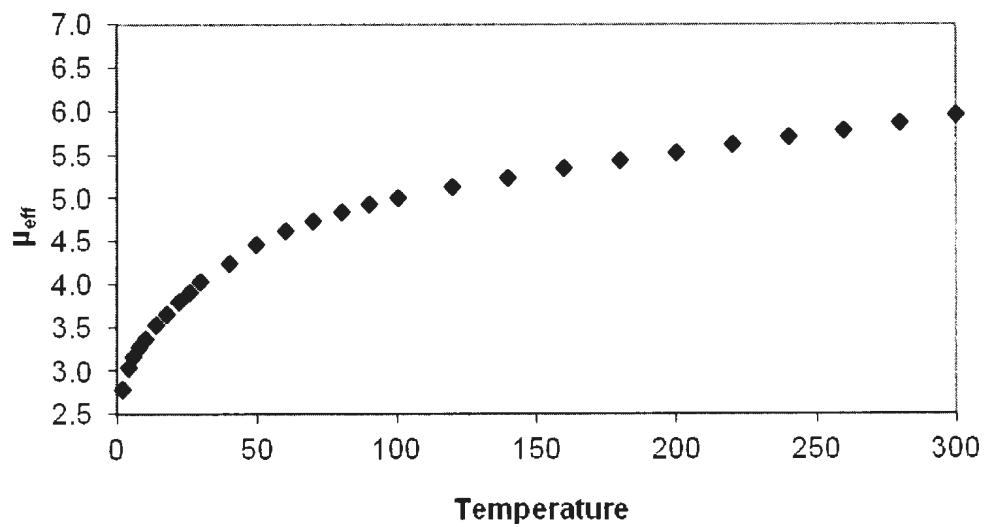


Figure A35: Susceptibility per mol of dimer vs. temperature for **C6**

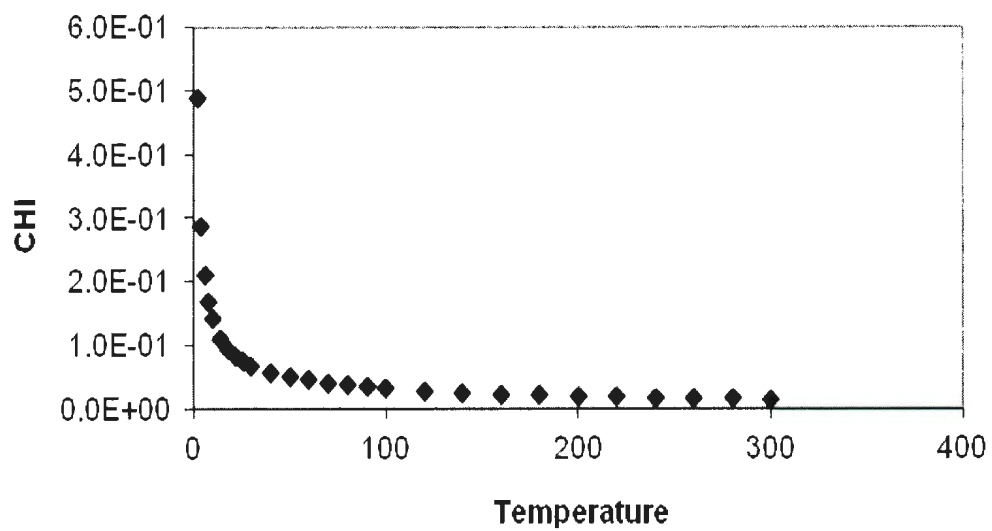


Figure A36: Single crystal X-ray structure of **C6**. Ellipsoids at 30% probability.

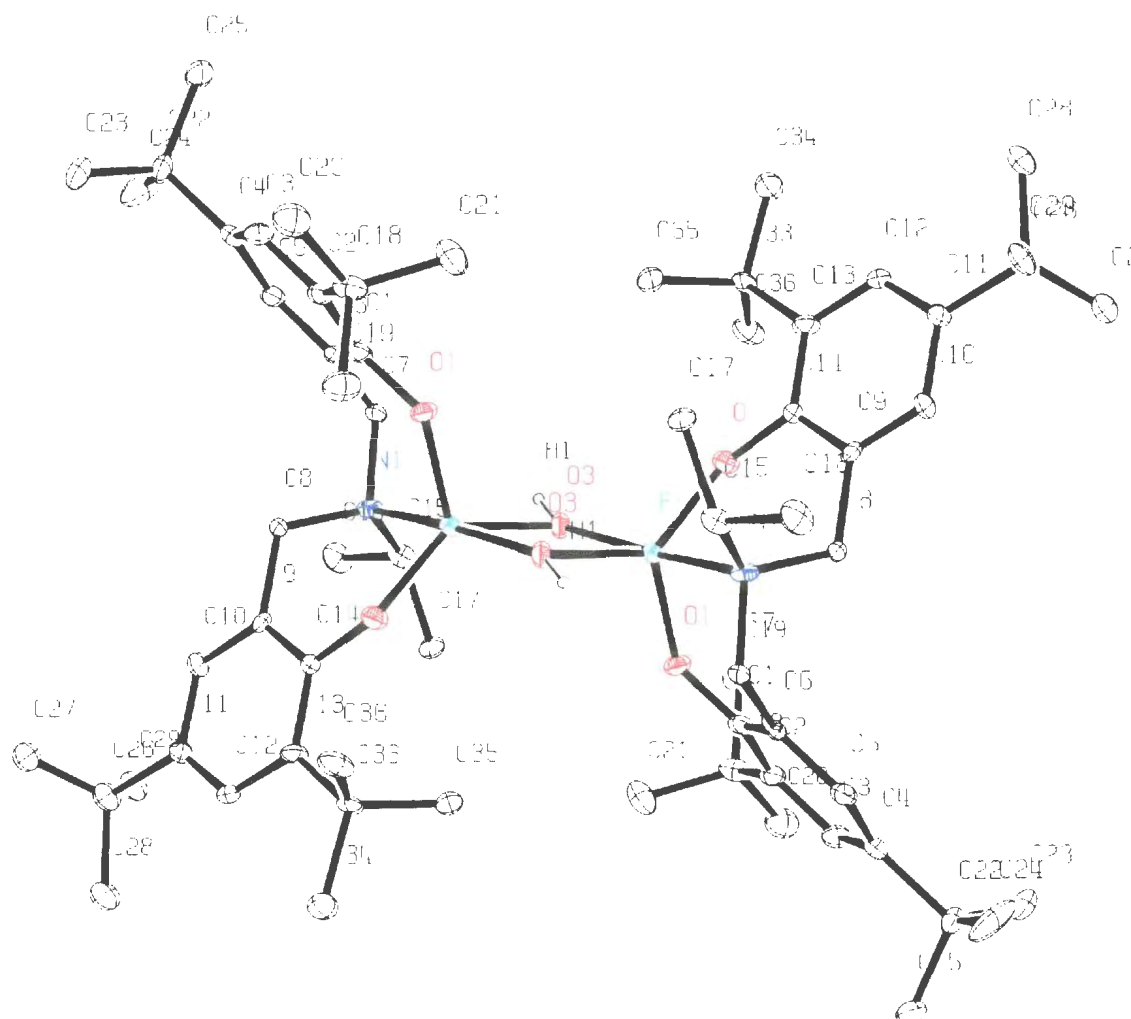


Table A16: Bond lengths (Å) for **C6**.

atom	atom	distance	atom	atom	distance
Fe(1)	Fe(1) ¹	3.13645(17)	Fe(1)	O(1)	1.857(8)
Fe(1)	O(2)	1.870(8)	Fe(1)	O(3)	1.980(8)
Fe(1)	O(3) ¹	2.010(8)	Fe(1)	N(1)	2.214(10)
O(1)	C(1)	1.358(14)	O(2)	C(14)	1.361(14)
N(1)	C(7)	1.513(15)	N(1)	C(8)	1.495(15)
N(1)	C(15)	1.548(16)	C(1)	C(2)	1.386(18)
C(1)	C(6)	1.402(16)	C(2)	C(3)	1.383(18)
C(2)	C(18)	1.494(19)	C(3)	C(4)	1.408(19)
C(4)	C(5)	1.385(19)	C(4)	C(22)	1.572(18)
C(5)	C(6)	1.374(17)	C(6)	C(7)	1.494(16)

C(8)	C(9)	1.517(17)	C(9)	C(10)	1.381(17)
C(9)	C(14)	1.385(16)	C(10)	C(11)	1.402(19)
C(11)	C(12)	1.361(17)	C(11)	C(26)	1.561(19)
C(12)	C(13)	1.403(18)	C(13)	C(14)	1.405(18)
C(13)	C(33)	1.535(17)	C(15)	C(16)	1.512(18)
C(15)	C(17)	1.562(18)	C(18)	C(19)	1.57(2)
C(18)	C(20)	1.53(2)	C(18)	C(21)	1.54(2)
C(22)	C(23)	1.51(2)	C(22)	C(24)	1.53(2)
C(22)	C(25)	1.54(2)	C(26)	C(27)	1.42(4)
C(26)	C(28)	1.57(4)	C(26)	C(29)	1.62(4)
C(26)	C(30)	1.50(3)	C(26)	C(31)	1.59(3)
C(26)	C(32)	1.50(3)	C(33)	C(34)	1.546(19)
C(33)	C(35)	1.544(19)	C(33)	C(36)	1.51(2)
O(3)	H(1)	0.87(10)			

Table A17: Bond angles (°) for **C6**.

atom	atom	atom	angle
Fe(1) ¹	Fe(1)	O(1)	106.8(2)
Fe(1) ¹	Fe(1)	O(2)	117.8(2)
Fe(1) ¹	Fe(1)	O(3)	38.5(2)
Fe(1) ¹	Fe(1)	O(3) ¹	37.9(2)
Fe(1) ¹	Fe(1)	N(1)	133.3(2)
O(1)	Fe(1)	O(2)	116.9(4)
O(1)	Fe(1)	O(3)	110.2(4)
O(1)	Fe(1)	O(3) ¹	96.4(3)
O(1)	Fe(1)	N(1)	91.4(3)
O(2)	Fe(1)	O(3)	132.6(4)
O(2)	Fe(1)	O(3) ¹	93.5(3)
O(2)	Fe(1)	N(1)	88.6(3)
O(3)	Fe(1)	O(3) ¹	76.38(5)
O(3)	Fe(1)	N(1)	95.0(3)
O(3) ¹	Fe(1)	N(1)	169.9(3)
Fe(1)	O(1)	C(1)	133.0(7)
Fe(1)	O(2)	C(14)	134.2(7)
Fe(1)	O(3)	Fe(1) ¹	103.6(4)
Fe(1)	N(1)	C(7)	103.8(7)
Fe(1)	N(1)	C(8)	106.0(6)
Fe(1)	N(1)	C(15)	114.8(7)
C(7)	N(1)	C(8)	108.2(9)
C(7)	N(1)	C(15)	107.3(9)
C(8)	N(1)	C(15)	115.9(9)
O(1)	C(1)	C(2)	120.3(11)
O(1)	C(1)	C(6)	118.1(11)

C(2)	C(1)	C(6)	121.5(11)
C(1)	C(2)	C(3)	116.7(12)
C(1)	C(2)	C(18)	122.3(12)
C(3)	C(2)	C(18)	120.9(12)
C(2)	C(3)	C(4)	123.7(12)
C(3)	C(4)	C(5)	117.0(12)
C(3)	C(4)	C(22)	119.9(12)
C(5)	C(4)	C(22)	123.1(12)
C(4)	C(5)	C(6)	121.3(12)
C(1)	C(6)	C(5)	119.6(11)
C(1)	C(6)	C(7)	120.1(10)
C(5)	C(6)	C(7)	120.1(10)
N(1)	C(7)	C(6)	114.9(9)
N(1)	C(8)	C(9)	114.0(9)
C(8)	C(9)	C(10)	119.2(10)
C(8)	C(9)	C(14)	118.7(10)
C(10)	C(9)	C(14)	122.1(11)
C(9)	C(10)	C(11)	119.1(11)
C(10)	C(11)	C(12)	118.5(12)
C(10)	C(11)	C(26)	119.4(11)
C(12)	C(11)	C(26)	122.0(12)
C(11)	C(12)	C(13)	123.9(12)
C(12)	C(13)	C(14)	116.8(11)
C(12)	C(13)	C(33)	122.4(11)
C(14)	C(13)	C(33)	120.8(11)
O(2)	C(14)	C(9)	119.5(11)
O(2)	C(14)	C(13)	120.9(10)
C(9)	C(14)	C(13)	119.6(11)
N(1)	C(15)	C(16)	111.8(10)
N(1)	C(15)	C(17)	112.1(10)
C(16)	C(15)	C(17)	109.9(11)
C(2)	C(18)	C(19)	110.7(11)
C(2)	C(18)	C(20)	114.0(12)
C(2)	C(18)	C(21)	109.6(11)
C(19)	C(18)	C(20)	105.5(11)
C(19)	C(18)	C(21)	108.3(12)
C(20)	C(18)	C(21)	108.5(12)
C(4)	C(22)	C(23)	110.1(12)
C(4)	C(22)	C(24)	111.0(13)
C(4)	C(22)	C(25)	108.2(11)
C(23)	C(22)	C(24)	110.8(13)
C(23)	C(22)	C(25)	108.4(13)
C(24)	C(22)	C(25)	108.2(14)
C(11)	C(26)	C(27)	109.2(19)
C(11)	C(26)	C(28)	109.7(16)

C(11)	C(26)	C(29)	105.0(16)
C(11)	C(26)	C(30)	115.4(15)
C(11)	C(26)	C(31)	107.1(14)
C(11)	C(26)	C(32)	110.3(14)
C(27)	C(26)	C(28)	112(2)
C(27)	C(26)	C(29)	113(2)
C(27)	C(26)	C(30)	61(2)
C(27)	C(26)	C(31)	48.3(19)
C(27)	C(26)	C(32)	138(2)
C(28)	C(26)	C(29)	108(2)
C(28)	C(26)	C(30)	133.9(19)
C(28)	C(26)	C(31)	68(2)
C(28)	C(26)	C(32)	41(2)
C(29)	C(26)	C(30)	52.2(18)
C(29)	C(26)	C(31)	146.9(17)
C(29)	C(26)	C(32)	68.4(19)
C(30)	C(26)	C(31)	105.6(17)
C(30)	C(26)	C(32)	111.1(19)
C(31)	C(26)	C(32)	106.7(19)
C(13)	C(33)	C(34)	111.1(10)
C(13)	C(33)	C(35)	110.0(11)
C(13)	C(33)	C(36)	109.5(10)
C(34)	C(33)	C(35)	105.7(11)
C(34)	C(33)	C(36)	108.9(12)
(35)	C(33)	C(36)	111.8(11)
Fe(1)	O(3)	H(1)	96(7)
Fe(1) ¹	O(3)	H(1)	155(8)

Table A18: Torsion angles (°) for **C6**.

atom1	atom2	atom3	atom4	angle
Fe(1) ¹	Fe(1)	O(1)	C(1)	-152.0(6)
O(1)	Fe(1)	Fe(1) ¹	O(2) ¹	46.1(3)
O(1)	Fe(1)	Fe(1) ¹	O(3) ¹	-78.5(3)
O(1)	Fe(1)	Fe(1) ¹	O(3)	101.5(3)
O(1)	Fe(1)	Fe(1) ¹	N(1) ¹	-71.3(3)
Fe(1) ¹	Fe(1)	O(2)	C(14)	126.1(6)
O(2)	Fe(1)	Fe(1) ¹	O(1) ¹	-46.1(3)
O(2)	Fe(1)	Fe(1) ¹	O(3) ¹	55.5(3)
O(2)	Fe(1)	Fe(1) ¹	O(3)	-124.5(3)
O(2)	Fe(1)	Fe(1) ¹	N(1) ¹	62.6(3)
O(3)	Fe(1)	Fe(1) ¹	O(1) ¹	78.5(4)
O(3)	Fe(1)	Fe(1) ¹	O(2) ¹	-55.5(4)
O(3) ¹	Fe(1)	Fe(1) ¹	O(1)	-101.5(4)

O(3) ¹	Fe(1)	Fe(1) ¹	O(2) ¹	124.5(4)
O(3) ¹	Fe(1)	Fe(1) ¹	N(1) ¹	7.2(4)
Fe(1) ¹	Fe(1)	N(1)	C(7)	83.9(5)
Fe(1) ¹	Fe(1)	N(1)	C(15)	-32.9(7)
N(1)	Fe(1)	Fe(1) ¹	O(1) ¹	71.3(3)
N(1)	Fe(1)	Fe(1) ¹	O(2) ¹	-62.6(3)
N(1)	Fe(1)	Fe(1) ¹	O(3)	-7.2(3)
O(1)	Fe(1)	O(2)	C(14)	-104.6(7)
O(2)	Fe(1)	O(1)	C(1)	73.6(8)
O(1)	Fe(1)	O(3)	Fe(1) ¹	-91.9(4)
O(3)	Fe(1)	O(1)	C(1)	-111.4(7)
O(1)	Fe(1)	O(3) ¹	Fe(1) ¹	109.3(4)
O(1)	Fe(1)	N(1)	C(7)	-31.0(5)
O(1)	Fe(1)	N(1)	C(8)	82.9(5)
O(1)	Fe(1)	N(1)	C(15)	-147.8(5)
N(1)	Fe(1)	O(1)	C(1)	-15.6(8)
O(2)	Fe(1)	O(3)	Fe(1) ¹	82.0(5)
O(3)	Fe(1)	O(2)	C(14)	81.9(8)
O(2)	Fe(1)	O(3) ¹	Fe(1) ¹	-133.1(4)
O(3) ¹	Fe(1)	O(2)	C(14)	156.5(7)
O(2)	Fe(1)	N(1)	C(7)	-147.9(5)
O(2)	Fe(1)	N(1)	C(8)	-34.0(5)
O(2)	Fe(1)	N(1)	C(15)	95.3(5)
N(1)	Fe(1)	O(2)	C(14)	-13.7(7)
O(3)	Fe(1)	N(1)	C(7)	79.4(5)
O(3)	Fe(1)	N(1)	C(15)	-37.4(6)
Fe(1)	O(1)	C(1)	C(2)	-145.2(8)
Fe(1)	O(1)	C(1)	C(6)	33.1(16)
Fe(1)	O(2)	C(14)	C(9)	33.5(15)
Fe(1)	O(2)	C(14)	C(13)	-147.0(7)
Fe(1)	N(1)	C(7)	C(6)	67.5(9)
Fe(1)	N(1)	C(8)	C(9)	69.1(9)
Fe(1)	N(1)	C(15)	C(17)	-42.6(10)
C(8)	N(1)	C(7)	C(6)	-44.8(11)
C(7)	N(1)	C(15)	C(16)	78.7(11)
C(7)	N(1)	C(15)	C(17)	-157.4(8)
C(8)	N(1)	C(15)	C(16)	-42.4(13)
C(8)	N(1)	C(15)	C(17)	81.6(11)
C(15)	N(1)	C(8)	C(9)	-59.5(12)
O(1)	C(1)	C(2)	C(18)	-3.0(18)
O(1)	C(1)	C(6)	C(7)	3.3(16)
C(2)	C(1)	C(6)	C(5)	-2.9(17)
C(6)	C(1)	C(2)	C(3)	3.4(17)
C(1)	C(2)	C(3)	C(4)	-3.3(18)
C(1)	C(2)	C(18)	C(19)	56.6(16)

C(1)	C(2)	C(18)	C(21)	-62.8(15)
C(3)	C(2)	C(18)	C(19)	-128.2(12)
C(3)	C(2)	C(18)	C(20)	-9.4(17)
C(3)	C(2)	C(18)	C(21)	112.4(13)
C(2)	C(3)	C(4)	C(5)	2.6(19)
C(3)	C(4)	C(5)	C(6)	-1.9(18)
C(3)	C(4)	C(22)	C(23)	54.4(15)
C(3)	C(4)	C(22)	C(25)	-63.9(15)
C(5)	C(4)	C(22)	C(23)	-127.0(12)
C(5)	C(4)	C(22)	C(24)	-3.9(17)
C(5)	C(4)	C(22)	C(25)	114.7(13)
C(4)	C(5)	C(6)	C(1)	2.1(17)
C(1)	C(6)	C(7)	N(1)	-59.9(13)
C(5)	C(6)	C(7)	N(1)	124.6(11)
N(1)	C(8)	C(9)	C(10)	125.0(10)
N(1)	C(8)	C(9)	C(14)	-56.8(13)
C(8)	C(9)	C(14)	O(2)	0.8(16)
C(10)	C(9)	C(14)	C(13)	-0.5(17)
C(14)	C(9)	C(10)	C(11)	0.2(18)
C(9)	C(10)	C(11)	C(12)	1.0(18)
C(10)	C(11)	C(12)	C(13)	-1.9(19)
C(10)	C(11)	C(26)	C(27)	61.6(16)
C(10)	C(11)	C(26)	C(29)	-59.5(15)
C(10)	C(11)	C(26)	C(30)	-4.6(19)
C(10)	C(11)	C(26)	C(31)	112.6(12)
C(10)	C(11)	C(26)	C(32)	-131.6(12)
C(12)	C(11)	C(26)	C(27)	-115.7(13)
C(12)	C(11)	C(26)	C(28)	7.8(18)
C(12)	C(11)	C(26)	C(29)	123.2(12)
C(12)	C(11)	C(26)	C(31)	-64.7(15)
C(12)	C(11)	C(26)	C(32)	51.0(17)
C(11)	C(12)	C(13)	C(14)	1.5(19)
C(12)	C(13)	C(14)	C(9)	-0.3(17)
C(12)	C(13)	C(33)	C(34)	-1.6(17)
C(12)	C(13)	C(33)	C(35)	-118.2(12)
C(12)	C(13)	C(33)	C(36)	118.6(12)
C(14)	C(13)	C(33)	C(35)	60.6(14)
C(14)	C(13)	C(33)	C(36)	-62.6(14)
C(33)	C(13)	C(14)	O(2)	1.5(18)

Figure 37A: MALDI-MS spectrum of **C7**.

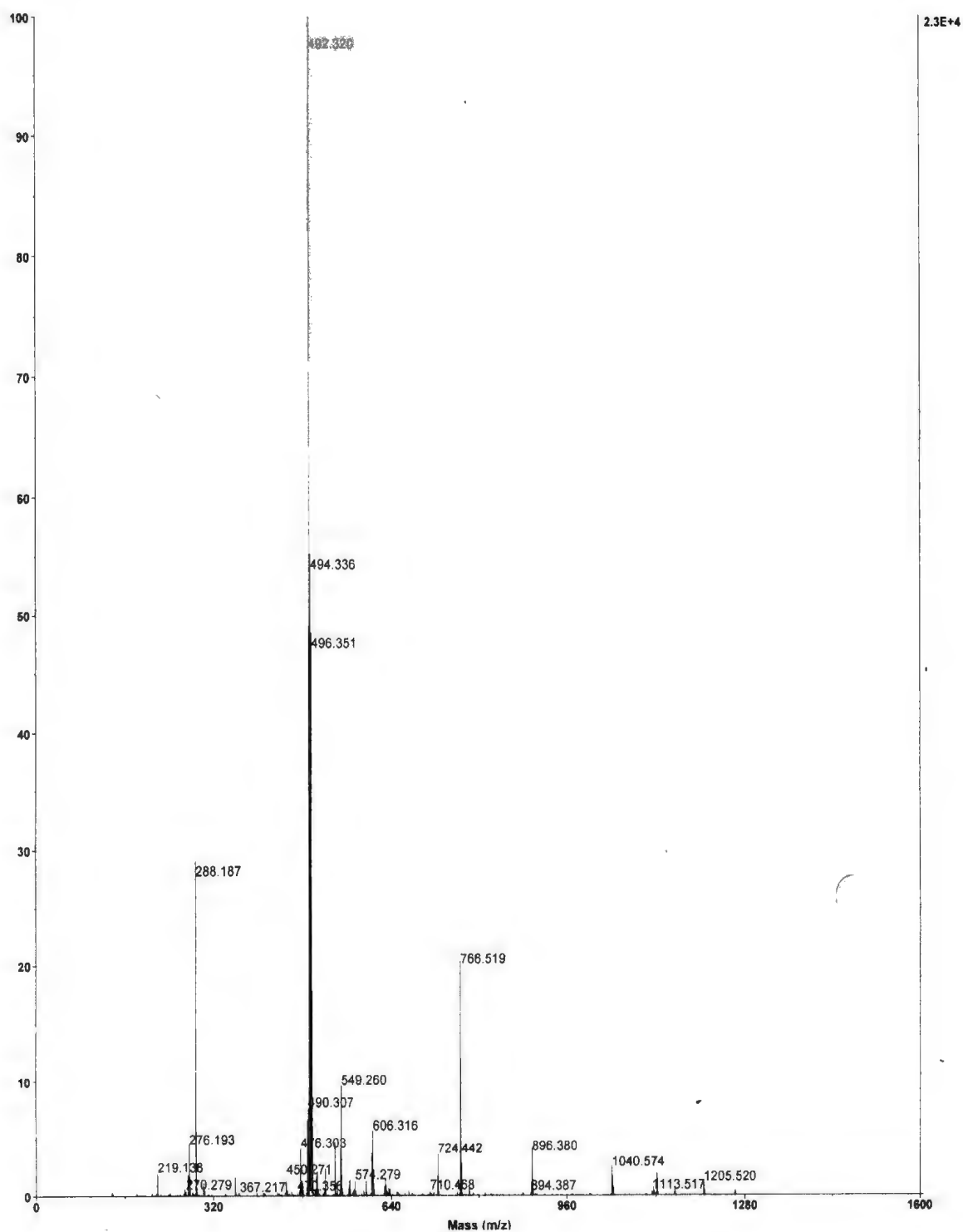


Figure 38A: MALDI-MS experimental isotope pattern for **C7**.

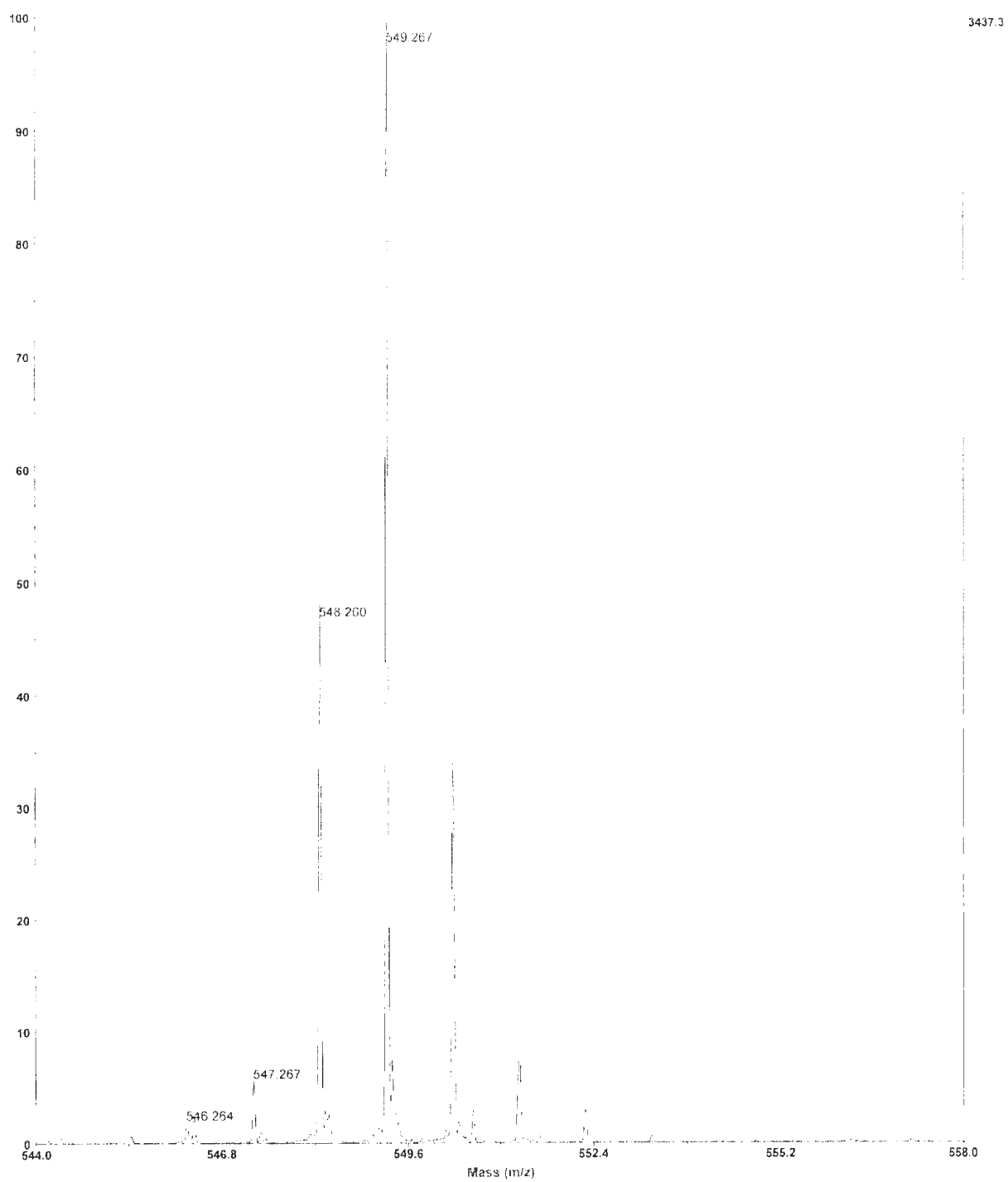


Figure A39: Single crystal X-ray structure of **C7**. Ellipsoids at 30% probability.

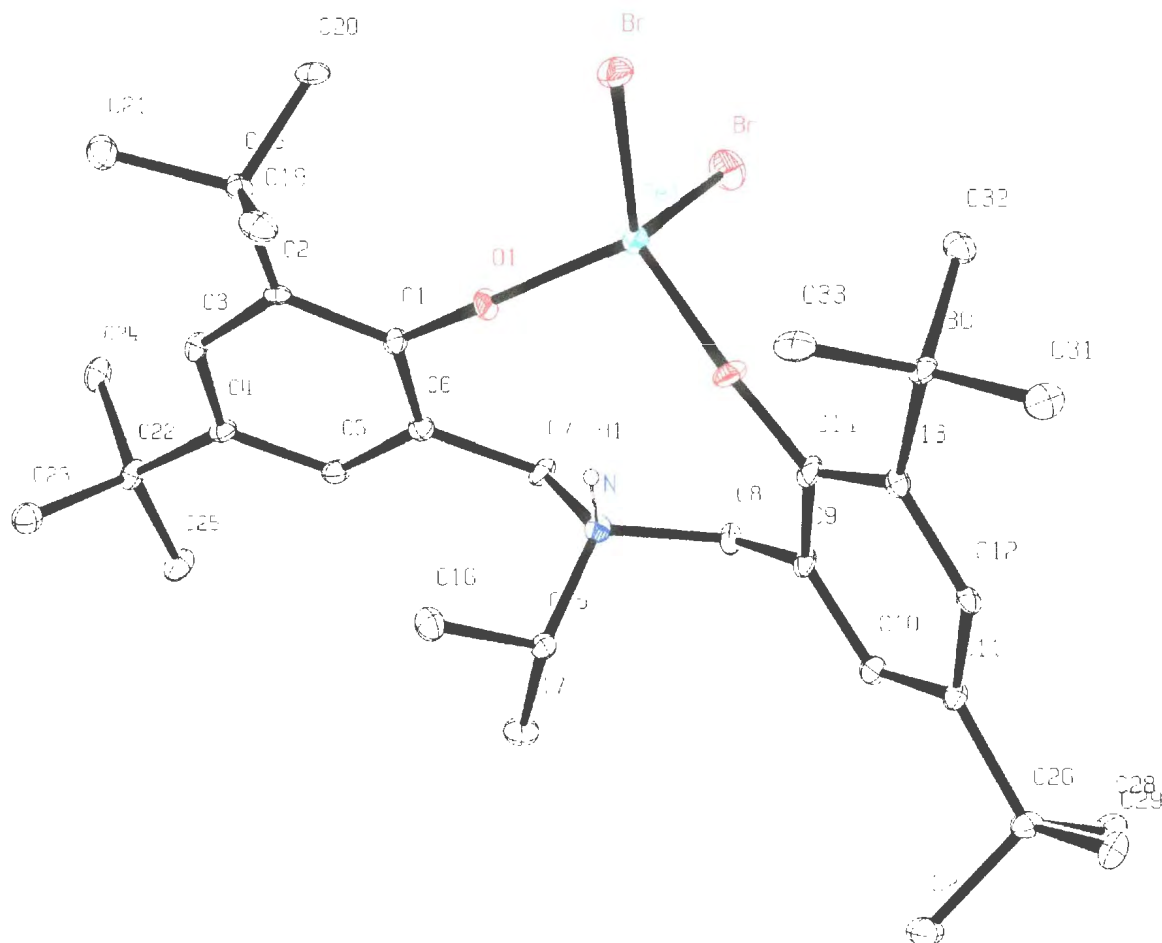


Table A19: Bond lengths (Å) for **C7**.

atom	atom	distance	atom	atom	distance
Br(1)	Fe(1)	2.355(2)	Br(2)	Fe(1)	2.3697(19)
Fe(1)	O(1)	1.843(6)	Fe(1)	O(2)	1.851(6)
O(1)	C(1)	1.349(9)	O(2)	C(14)	1.363(11)
N(1)	C(7)	1.494(11)	N(1)	C(8)	1.522(13)
N(1)	C(15)	1.519(12)	C(1)	C(2)	1.415(14)
C(1)	C(6)	1.406(14)	C(2)	C(3)	1.413(11)
C(2)	C(18)	1.545(14)	C(3)	C(4)	1.376(14)
C(4)	C(5)	1.403(14)	C(4)	C(22)	1.555(11)
C(5)	C(6)	1.404(11)	C(6)	C(7)	1.494(14)
C(8)	C(9)	1.498(12)	C(9)	C(10)	1.386(12)
C(9)	C(14)	1.394(14)	C(10)	C(11)	1.394(12)
C(11)	C(12)	1.394(13)	C(11)	C(26)	1.534(12)
C(12)	C(13)	1.408(12)	C(13)	C(14)	1.413(11)

C(13)	C(30)	1.543(13)	C(15)	C(16)	1.529(17)
C(15)	C(17)	1.510(14)	C(18)	C(19)	1.543(14)
C(18)	C(20)	1.526(14)	C(18)	C(21)	1.535(14)
C(22)	C(23)	1.516(17)	C(22)	C(24)	1.547(12)
C(22)	C(25)	1.514(15)	C(26)	C(27)	1.545(14)
C(26)	C(28)	1.553(19)	C(26)	C(29)	1.533(13)
C(30)	C(31)	1.533(11)	C(30)	C(32)	1.528(14)
C(30)	C(33)	1.544(17)	N(1)	H(1)	0.88(7)

Table A20: Bond angles (°) for **C7**.

atom	atom	atom	angle
Br(1)	Fe(1)	Br(2)	111.53(7)
Br(1)	Fe(1)	O(1)	108.9(2)
Br(1)	Fe(1)	O(2)	107.5(3)
Br(2)	Fe(1)	O(1)	110.8(2)
Br(2)	Fe(1)	O(2)	112.0(2)
O(1)	Fe(1)	O(2)	105.9(3)
Fe(1)	O(1)	C(1)	160.6(7)
Fe(1)	O(2)	C(14)	168.0(8)
C(7)	N(1)	C(8)	108.8(8)
C(7)	N(1)	C(15)	117.8(6)
C(8)	N(1)	C(15)	112.6(7)
O(1)	C(1)	C(2)	122.6(8)
O(1)	C(1)	C(6)	118.1(8)
C(2)	C(1)	C(6)	119.3(7)
C(1)	C(2)	C(3)	116.0(8)
C(1)	C(2)	C(18)	122.3(7)
C(3)	C(2)	C(18)	121.7(8)
C(2)	C(3)	C(4)	126.4(9)
C(3)	C(4)	C(5)	116.2(7)
C(3)	C(4)	C(22)	122.0(9)
C(5)	C(4)	C(22)	121.8(9)
C(4)	C(5)	C(6)	120.5(9)
C(1)	C(6)	C(5)	121.7(9)
C(1)	C(6)	C(7)	119.5(7)
C(5)	C(6)	C(7)	118.8(9)
N(1)	C(7)	C(6)	114.9(9)
N(1)	C(8)	C(9)	111.7(9)
C(8)	C(9)	C(10)	119.6(9)
C(8)	C(9)	C(14)	119.4(8)
C(10)	C(9)	C(14)	121.0(8)
C(9)	C(10)	C(11)	121.1(9)
C(10)	C(11)	C(12)	116.7(8)

C(10)	C(11)	C(26)	119.2(8)
C(12)	C(11)	C(26)	124.0(7)
C(11)	C(12)	C(13)	124.5(7)
C(12)	C(13)	C(14)	116.1(8)
C(12)	C(13)	C(30)	121.2(7)
C(14)	C(13)	C(30)	122.6(8)
O(2)	C(14)	C(9)	118.1(7)
O(2)	C(14)	C(13)	121.6(9)
C(9)	C(14)	C(13)	120.2(8)
N(1)	C(15)	C(16)	111.3(8)
N(1)	C(15)	C(17)	112.3(9)
C(16)	C(15)	C(17)	113.3(8)
C(2)	C(18)	C(19)	109.3(7)
C(2)	C(18)	C(20)	109.7(9)
C(2)	C(18)	C(21)	112.5(7)
C(19)	C(18)	C(20)	111.4(7)
C(19)	C(18)	C(21)	107.2(10)
C(20)	C(18)	C(21)	106.7(7)
C(4)	C(22)	C(23)	108.6(8)
C(4)	C(22)	C(24)	107.9(7)
C(4)	C(22)	C(25)	112.2(8)
C(23)	C(22)	C(24)	108.9(8)
C(23)	C(22)	C(25)	109.5(8)
C(24)	C(22)	C(25)	109.6(8)
C(11)	C(26)	C(27)	107.3(8)
C(11)	C(26)	C(28)	109.9(9)
C(11)	C(26)	C(29)	113.1(8)
C(27)	C(26)	C(28)	109.1(8)
C(27)	C(26)	C(29)	108.4(9)
C(28)	C(26)	C(29)	108.9(8)
C(13)	C(30)	C(31)	111.6(7)
C(13)	C(30)	C(32)	108.8(9)
C(13)	C(30)	C(33)	109.5(7)
C(31)	C(30)	C(32)	107.3(7)
C(31)	C(30)	C(33)	108.3(9)
C(32)	C(30)	C(33)	111.3(8)
C(7)	N(1)	H(1)	106(5)
C(8)	N(1)	H(1)	105(6)
C(15)	N(1)	H(1)	105(7)

Table A21: Torsion angles (°) for **C7**.

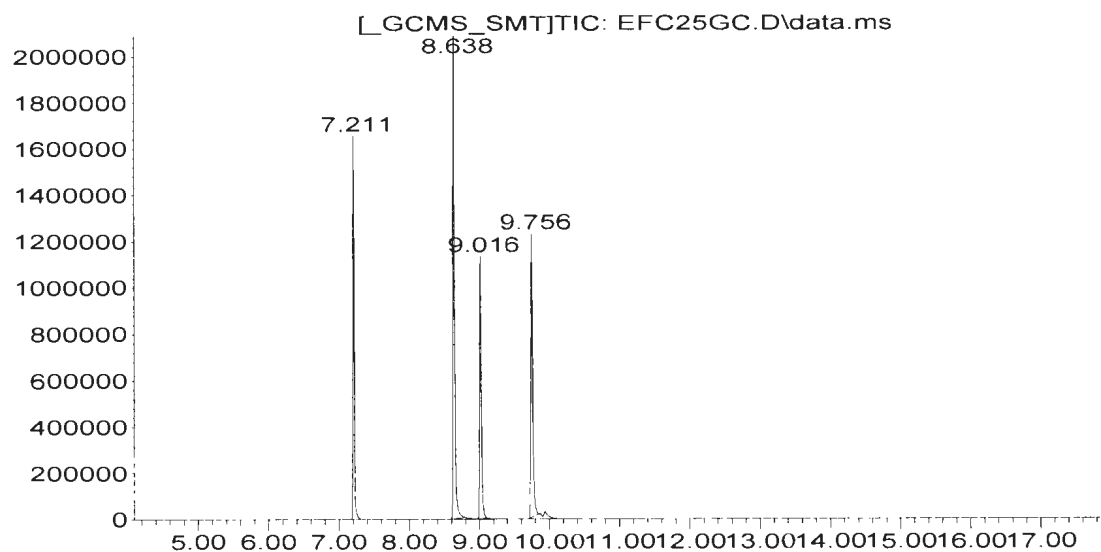
atom1	atom2	atom3	atom4	angle
Br(1)	Fe(1)	O(1)	C(1)	7.1(13)
Br(1)	Fe(1)	O(2)	C(14)	-15.4(20)
Br(2)	Fe(1)	O(1)	C(1)	130.1(12)
Br(2)	Fe(1)	O(2)	C(14)	-138.2(19)
O(1)	Fe(1)	O(2)	C(14)	100.9(20)
O(2)	Fe(1)	O(1)	C(1)	-108.2(13)
C(7)	N(1)	C(15)	C(16)	-80.5(10)
C(7)	N(1)	C(15)	C(17)	47.7(11)
C(15)	N(1)	C(7)	C(6)	65.0(10)
C(8)	N(1)	C(15)	C(16)	151.6(6)
C(8)	N(1)	C(15)	C(17)	-80.2(8)
C(15)	N(1)	C(8)	C(9)	-64.8(9)
O(1)	C(1)	C(2)	C(18)	3.8(14)
O(1)	C(1)	C(6)	C(7)	-3.9(13)
C(2)	C(1)	C(6)	C(5)	-1.1(14)
C(6)	C(1)	C(2)	C(3)	1.5(13)
C(1)	C(2)	C(3)	C(4)	-1.4(13)
C(1)	C(2)	C(18)	C(19)	-60.7(11)
C(1)	C(2)	C(18)	C(20)	61.6(10)
C(3)	C(2)	C(18)	C(19)	120.3(8)
C(3)	C(2)	C(18)	C(20)	-117.3(9)
C(3)	C(2)	C(18)	C(21)	1.3(12)
C(2)	C(3)	C(4)	C(5)	0.7(14)
C(3)	C(4)	C(5)	C(6)	-0.1(13)
C(3)	C(4)	C(22)	C(23)	-55.3(11)
C(3)	C(4)	C(22)	C(24)	62.7(12)
C(5)	C(4)	C(22)	C(23)	125.7(9)
C(5)	C(4)	C(22)	C(24)	-116.4(9)
C(5)	C(4)	C(22)	C(25)	4.5(12)
C(4)	C(5)	C(6)	C(1)	0.3(14)
C(1)	C(6)	C(7)	N(1)	58.9(11)
C(5)	C(6)	C(7)	N(1)	-122.7(9)
N(1)	C(8)	C(9)	C(10)	118.6(9)
N(1)	C(8)	C(9)	C(14)	-63.6(10)
C(8)	C(9)	C(14)	O(2)	9.2(15)
C(10)	C(9)	C(14)	C(13)	5.7(16)
C(14)	C(9)	C(10)	C(11)	-1.2(16)
C(9)	C(10)	C(11)	C(12)	-3.2(15)
C(10)	C(11)	C(12)	C(13)	3.2(15)
C(10)	C(11)	C(26)	C(27)	-55.9(13)
C(10)	C(11)	C(26)	C(28)	62.6(11)
C(12)	C(11)	C(26)	C(27)	123.8(10)

C(12)	C(11)	C(26)	C(28)	-117.7(10)
C(12)	C(11)	C(26)	C(29)	4.2(15)
C(11)	C(12)	C(13)	C(14)	1.0(15)
C(12)	C(13)	C(14)	C(9)	-5.5(15)
C(12)	C(13)	C(30)	C(31)	3.9(14)
C(12)	C(13)	C(30)	C(32)	122.1(9)
C(12)	C(13)	C(30)	C(33)	-116.1(9)
C(14)	C(13)	C(30)	C(32)	-55.5(12)
C(30)	C(13)	C(14)	O(2)	-9.0(16)
C(14)	C(13)	C(30)	C(33)	66.3(12)

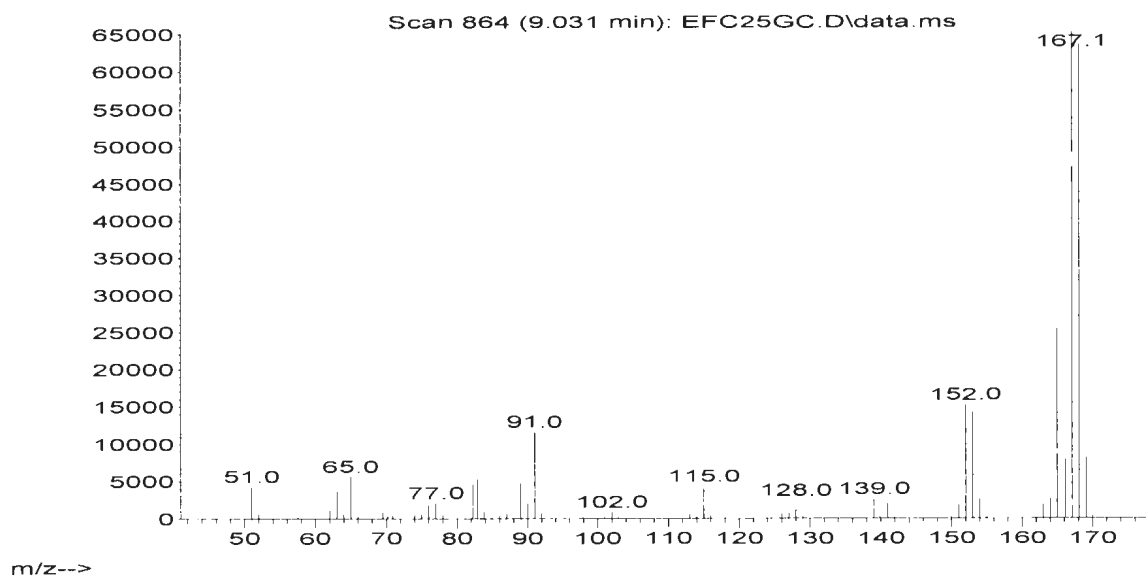
5.2 Cross-coupling reactions: GC traces, mass spectra and NMR spectra of selected cross-coupling products.

FigureA40: GC-MS analysis of **Diphenylmethane** (Table 3.1, Entry 1). GC-MS retention time: m/z (% ion): 7.211 min dodecane; 8.638 min biphenyl; 9.016 min diphenylmethane; 9.756 min bibenzyl.

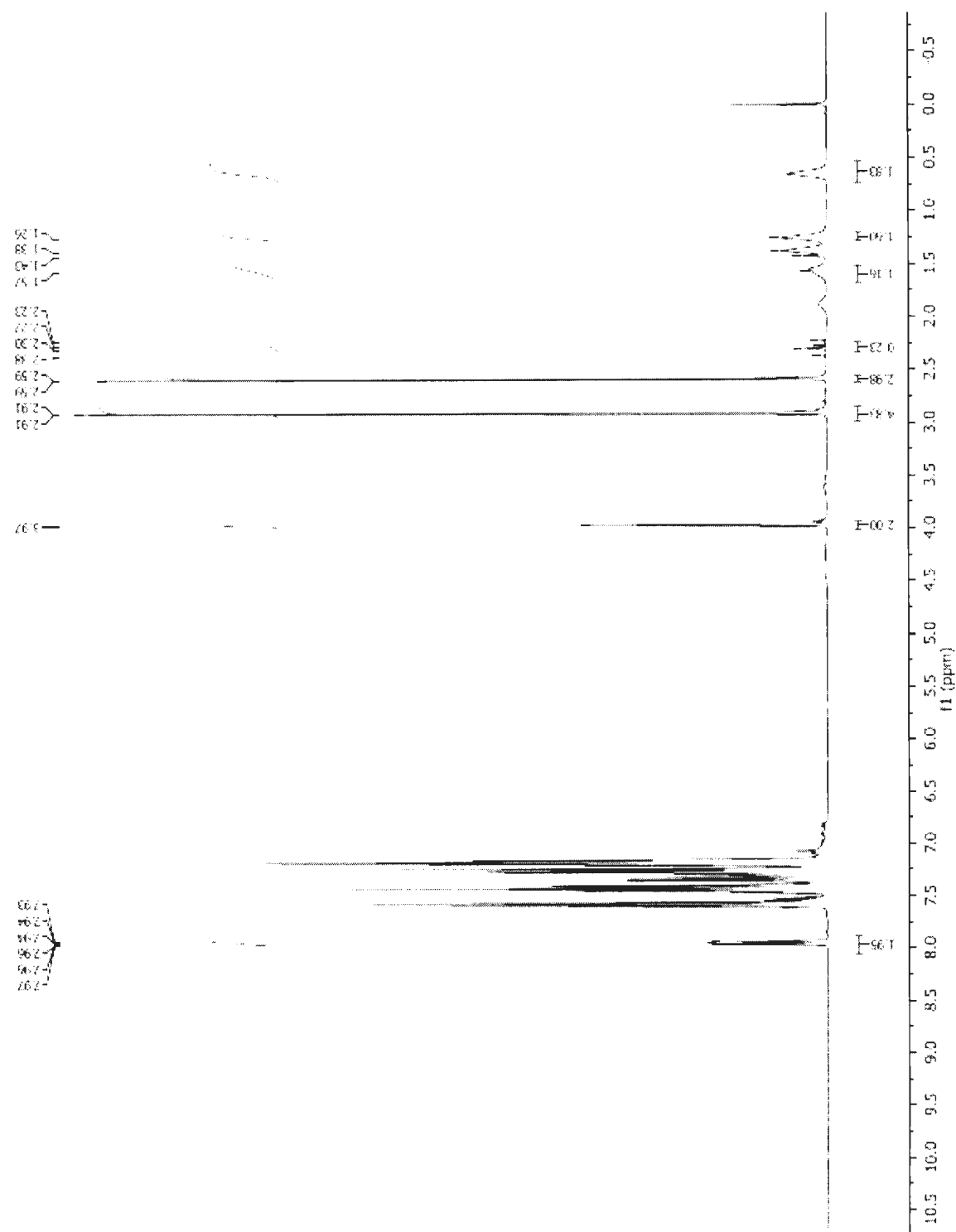
Abundance



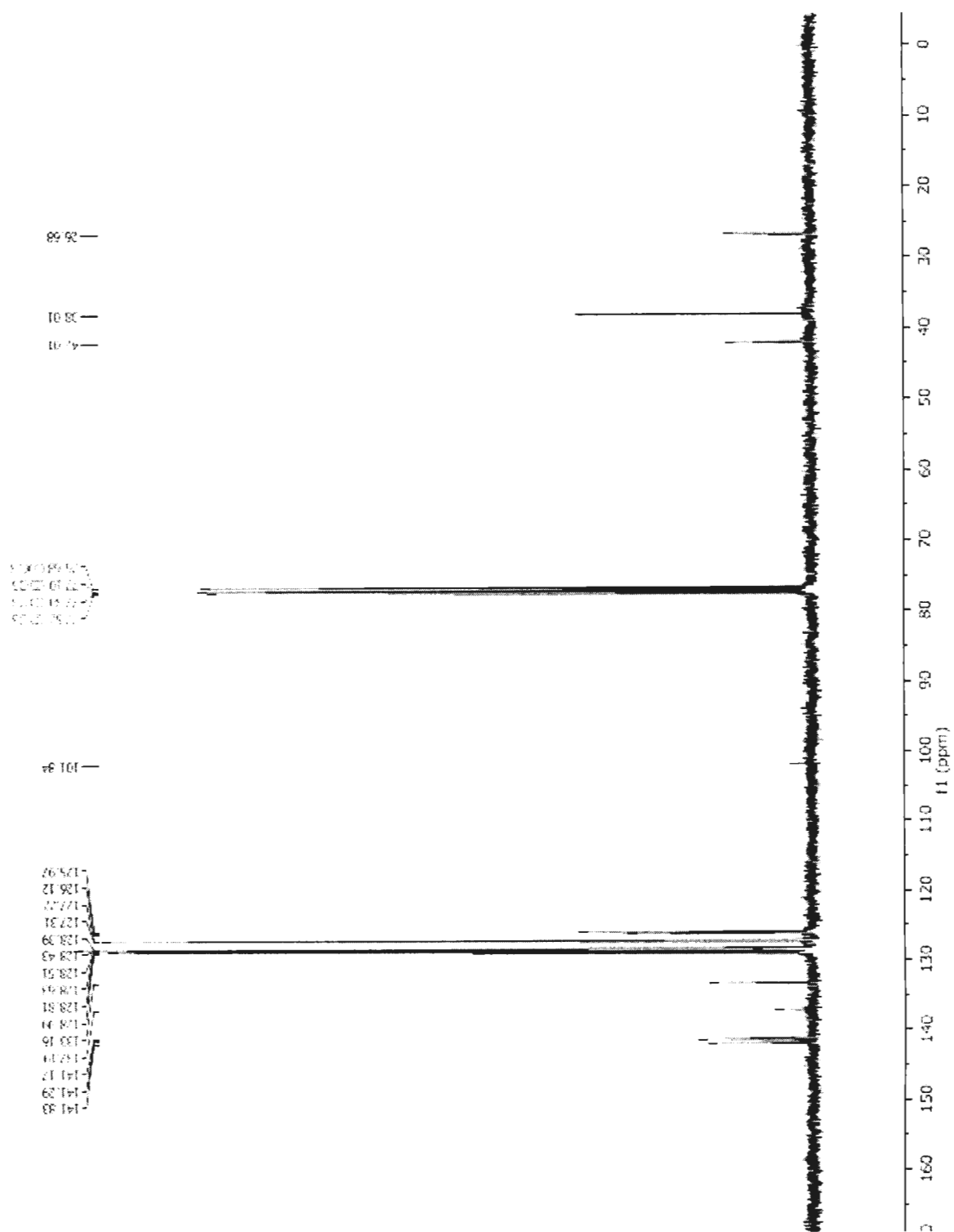
Abundance



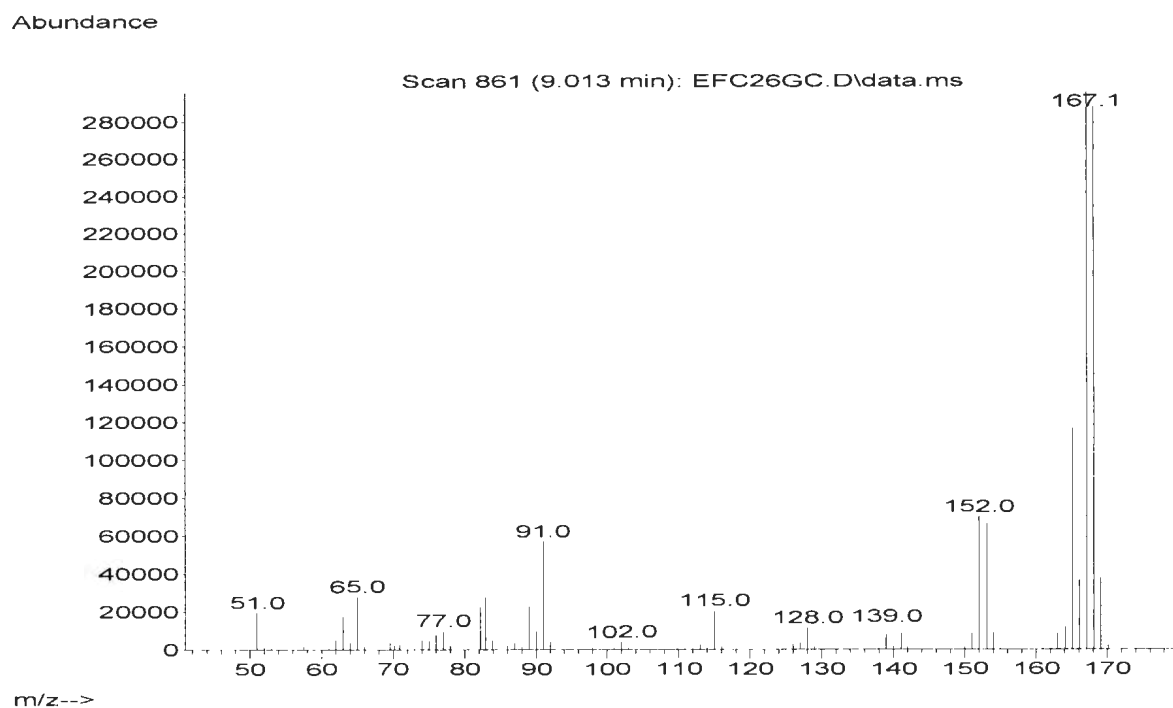
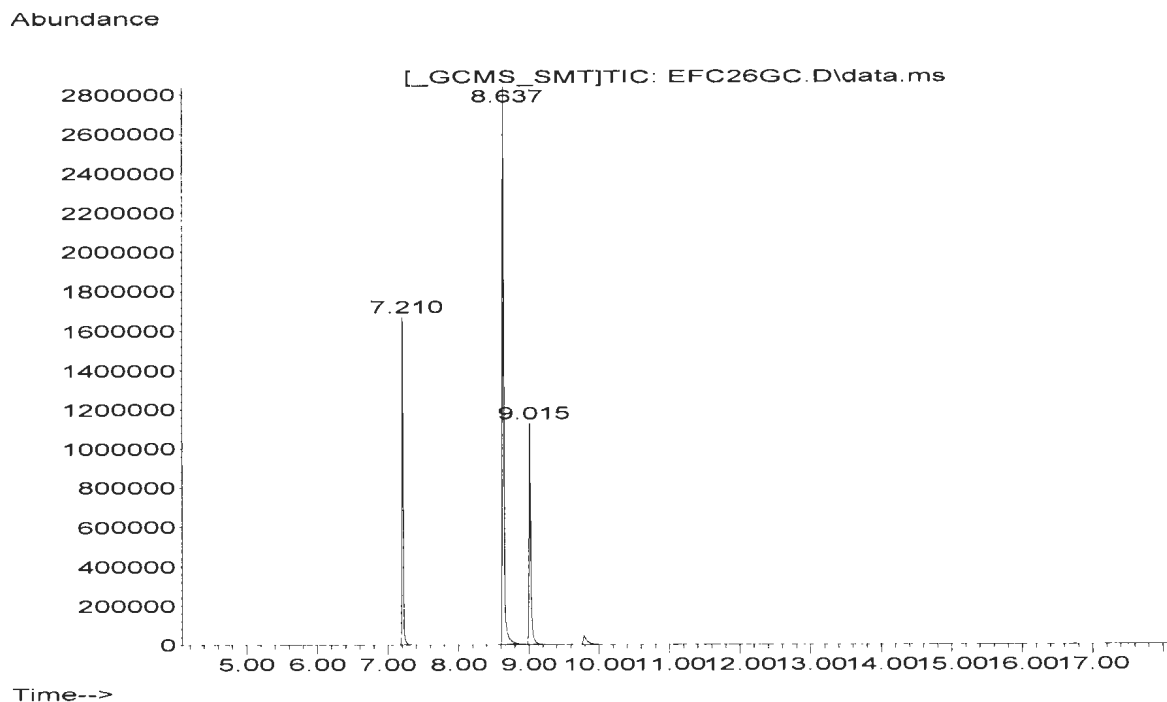
FigureA41: ^1H NMR spectrum for **Diphenylmethane** (Table 3.1, Entry 1).



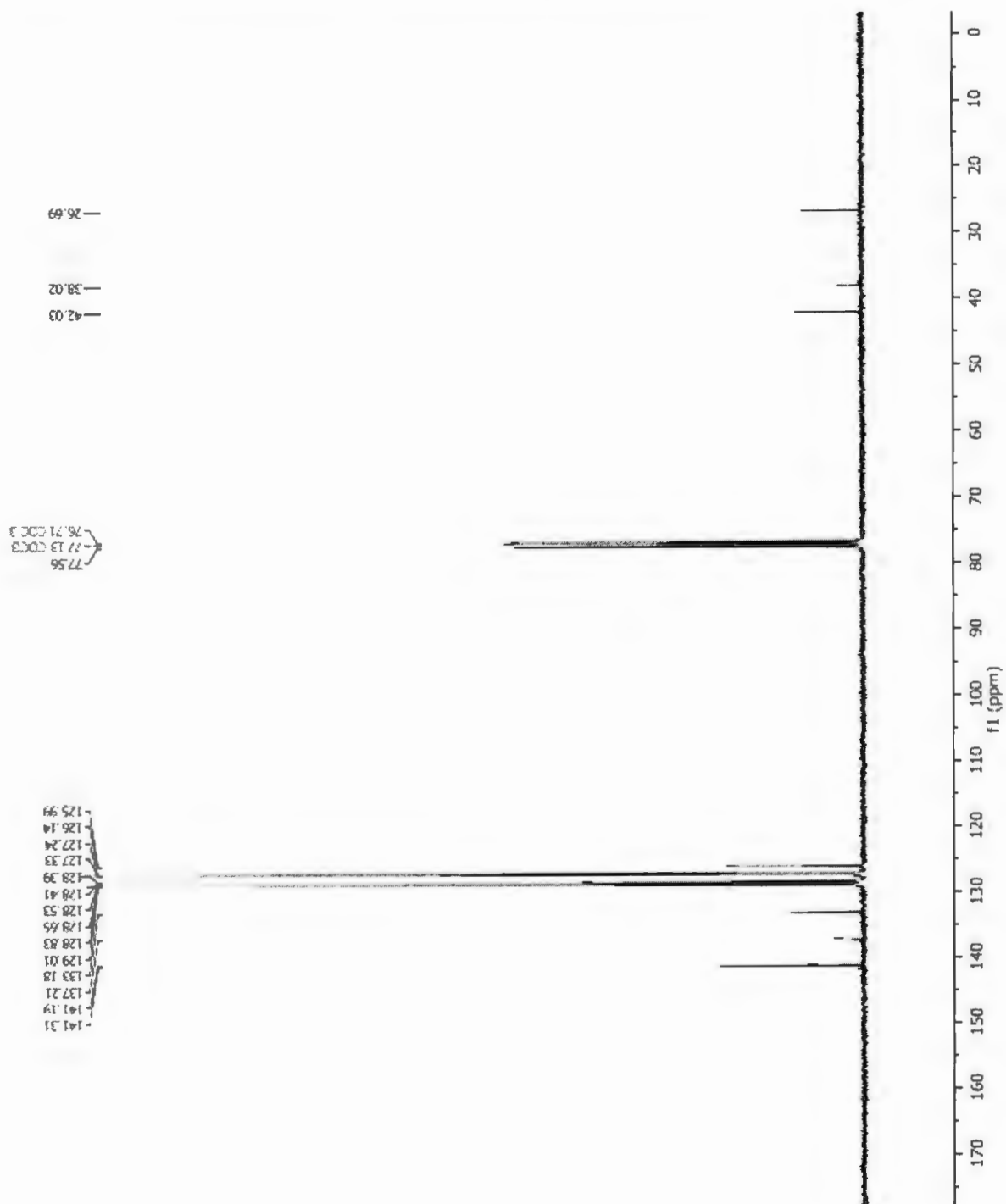
FigureA42: ^{13}C NMR spectrum for Diphenylmethane (Table 3.1, Entry 1).



FigureA43: GC-MS analysis of **Diphenylmethane** (Table 3.1, Entry 2). GC-MS retention time: m/z (% ion): 7.210 min dodecane; 8.637 min biphenyl; 9.015 min diphenylmethane; 9.756 min bibenzyl.

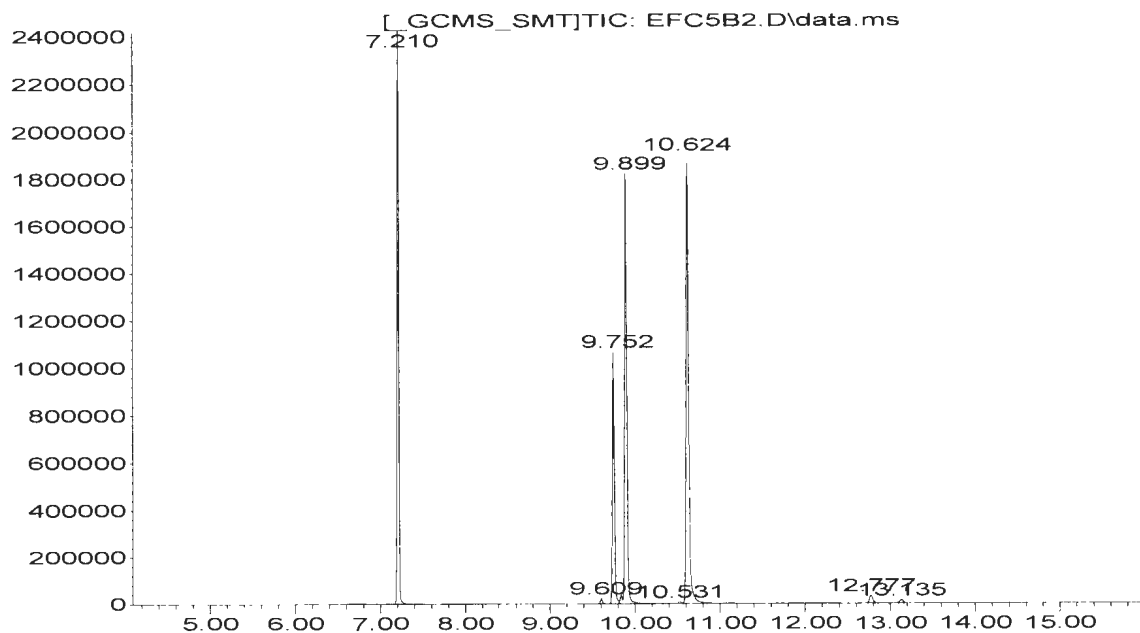


FigureA45: ^{13}C NMR spectrum for **Diphenylmethane** (Table 3.1, Entry 2).



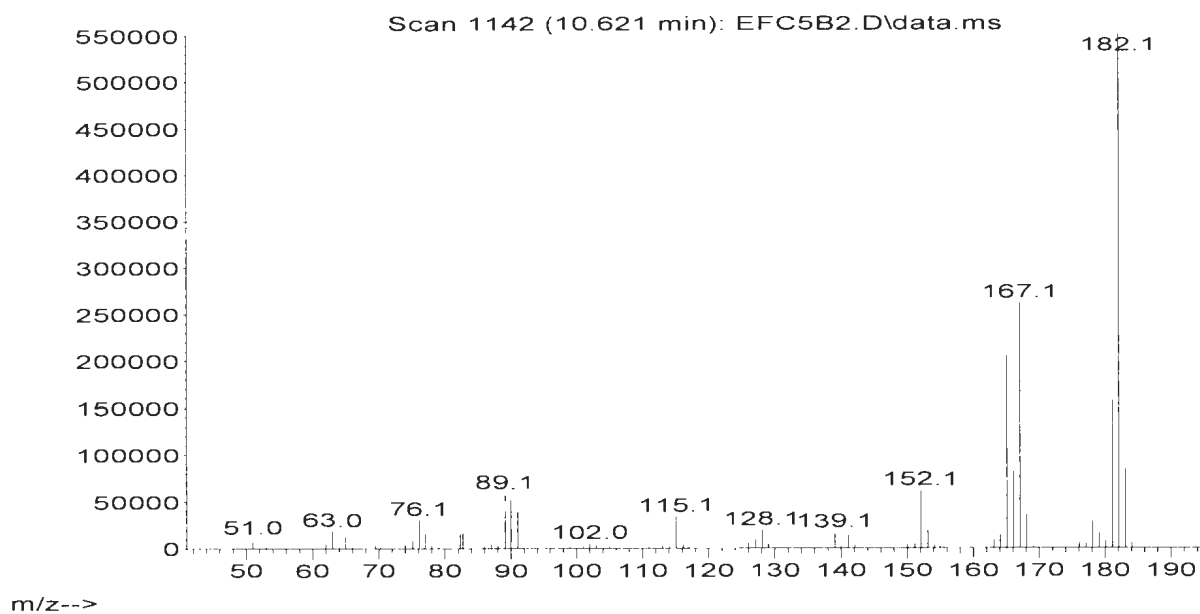
FigureA46: GC-MS analysis of **1-Benzyl-4-methylbenzene** (Table 3.1, Entry 3). GC-MS retention time: 7.210 min dodecane; 9.752 min bibenzyl; 9.899 min 4,4'-dimethylbiphenyl; 10.624 min 1-benzyl-4-methylbenzene.

Abundance



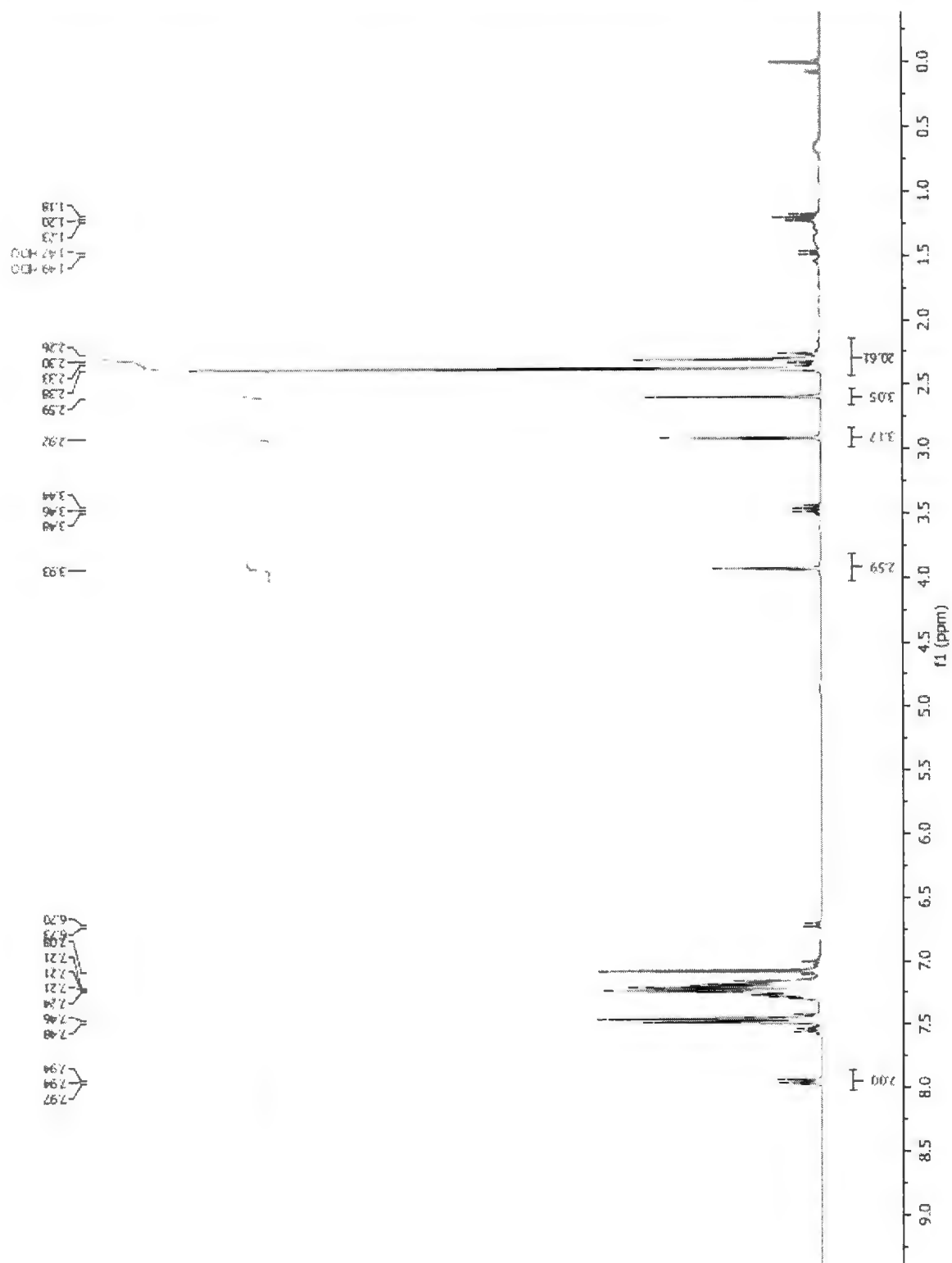
Time-->

Abundance

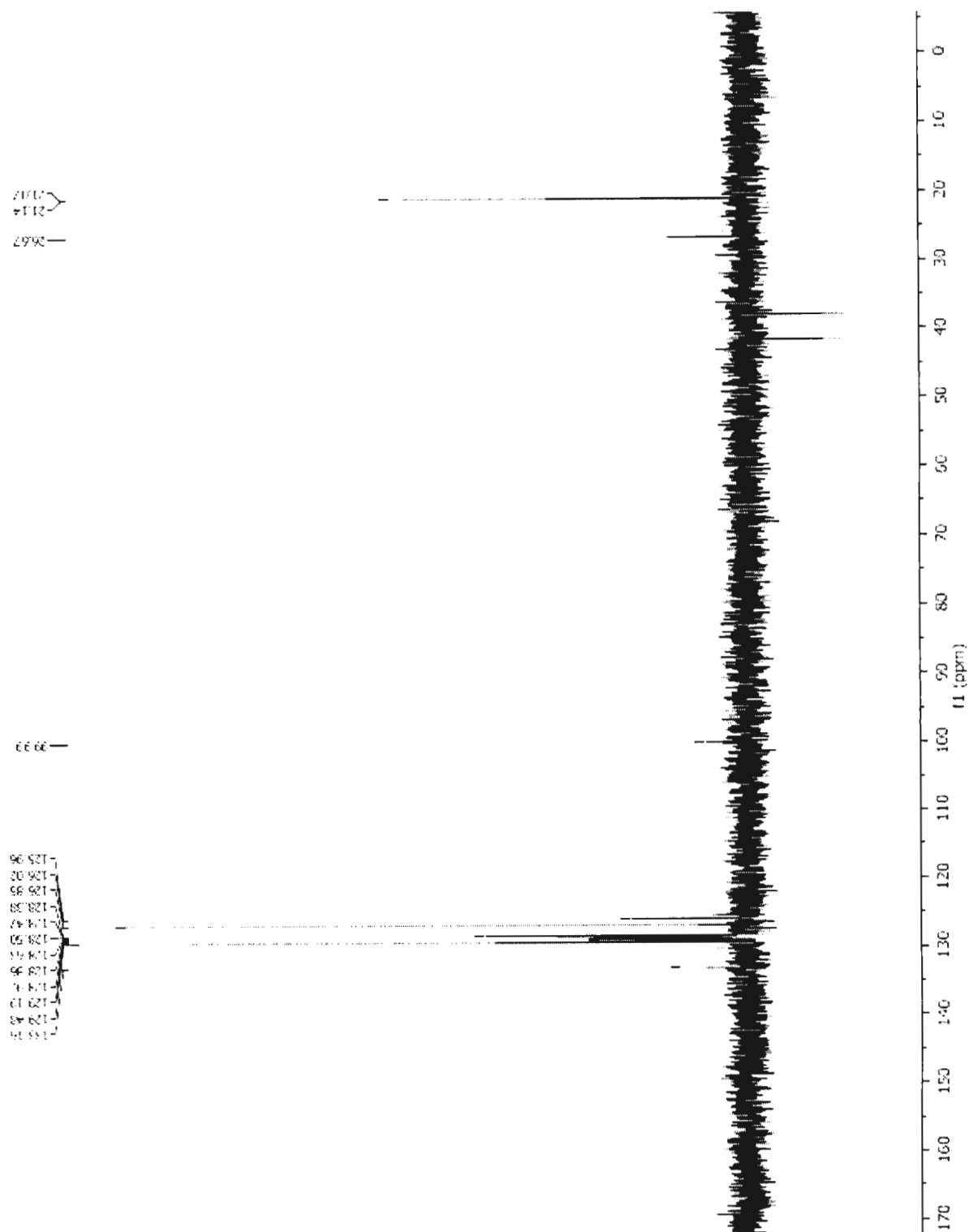


m/z-->

FigureA47: ^1H NMR spectrum for 1-Benzyl-4-methylbenzene (Table 3.1, Entry 3).

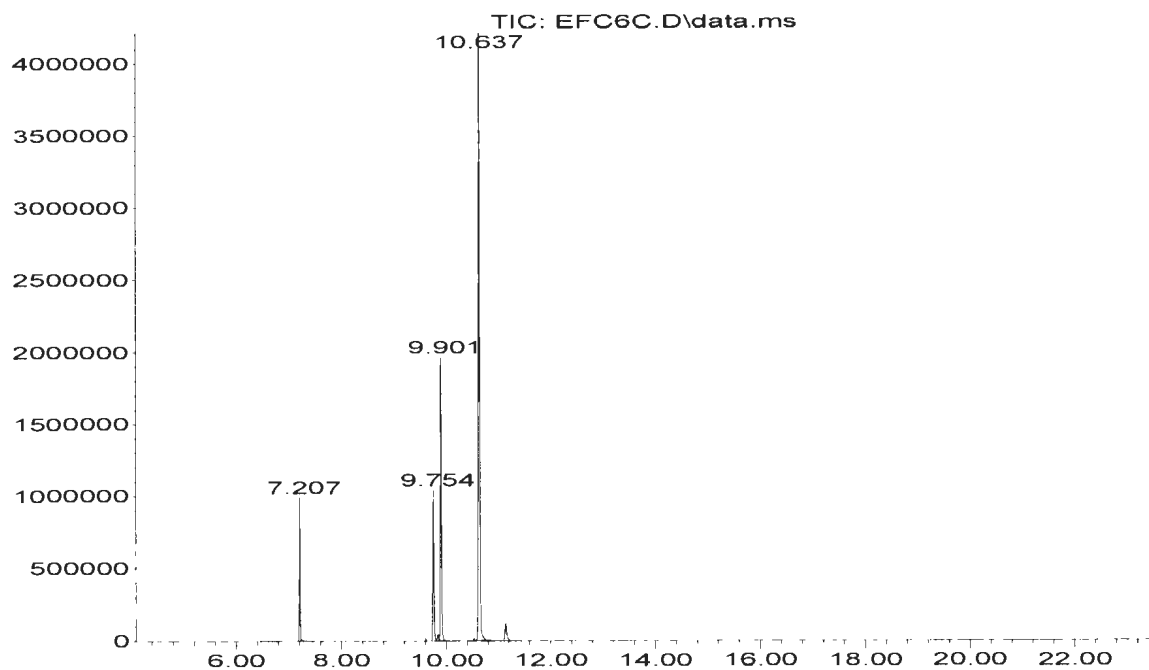


FigureA48: ^{13}C NMR spectrum for 1-Benzyl-4-methylbenzene (Table 3.1, Entry 3).

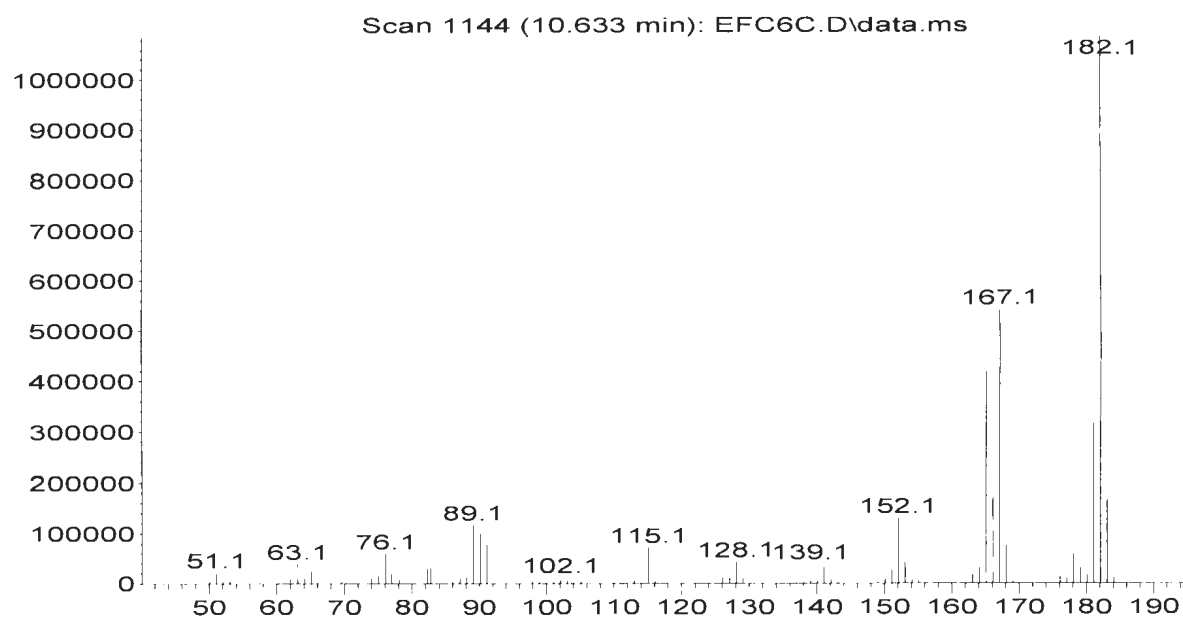


FigureA49: GC-MS analysis of **1-Benzyl-4-methylbenzene** (Table 3.1, Entry 4). GC-MS retention time: 7.207 min dodecane; 9.754 min bibenzyl; 9.901 min 4,4'-dimethylbiphenyl; 10.637 min 1-benzyl-4-methylbenzene.

Abundance

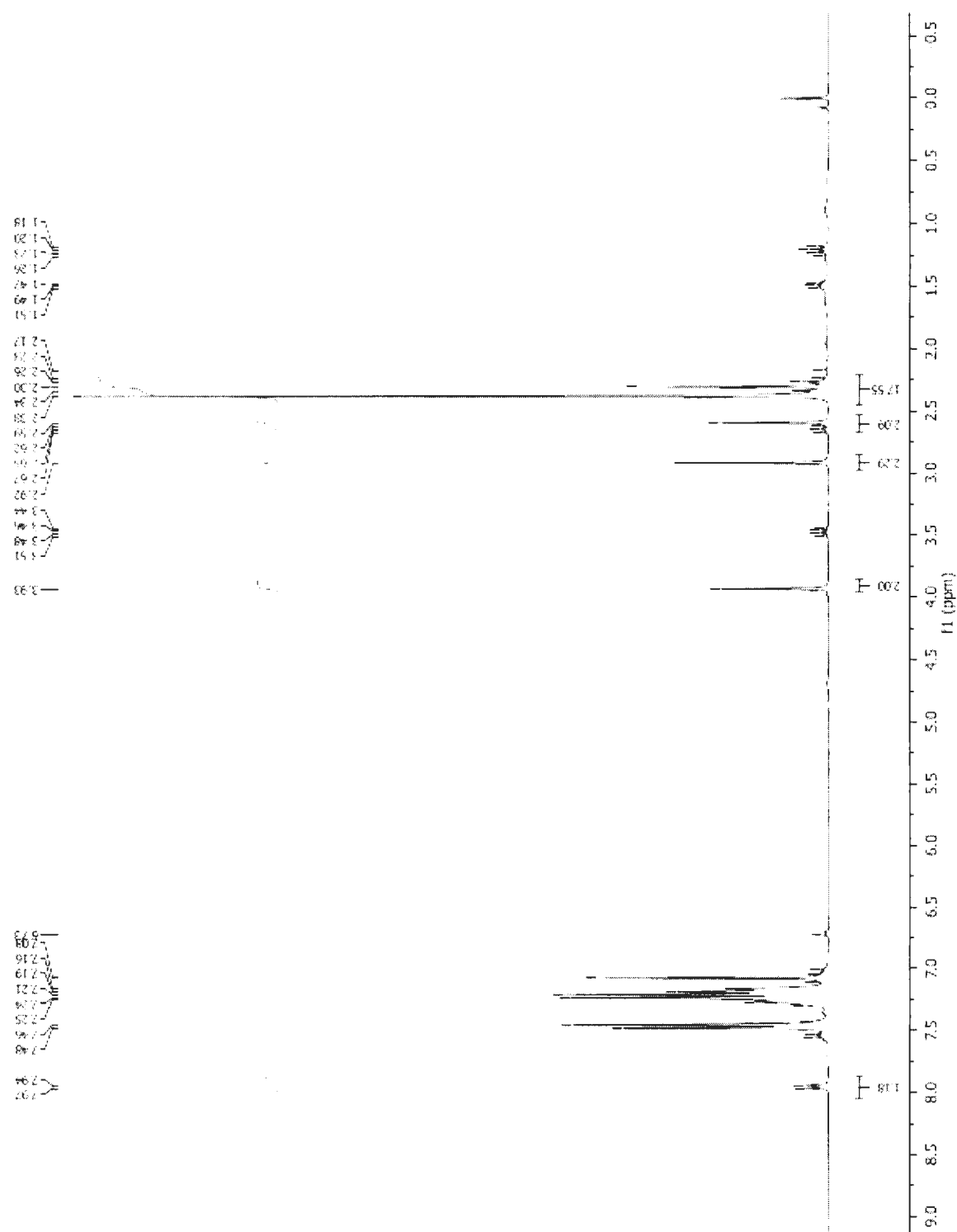


Time-->
Abundance

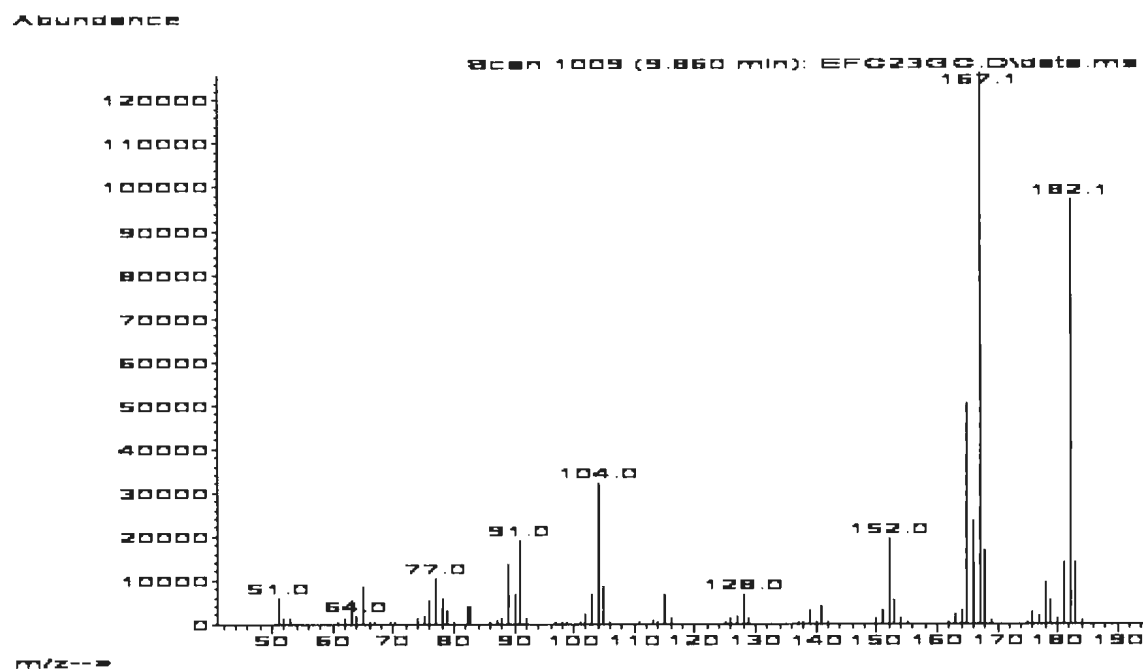
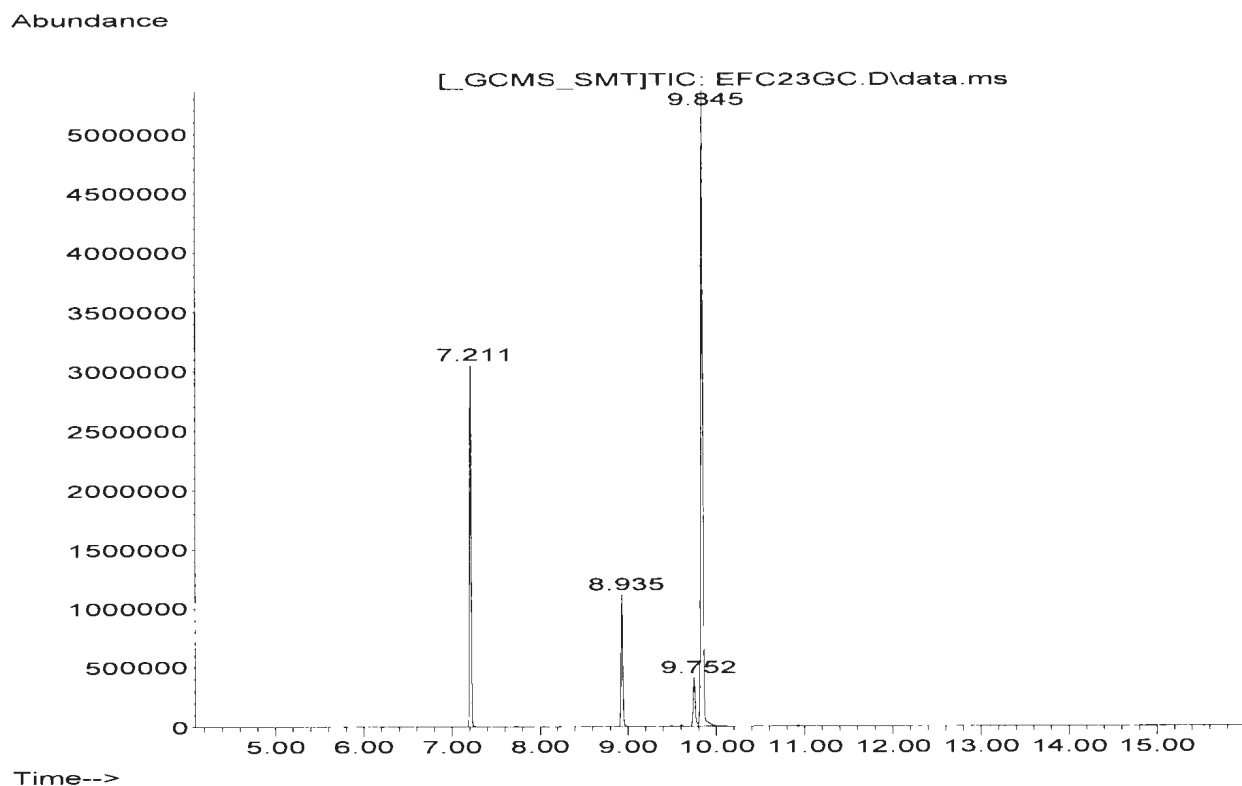


m/z-->

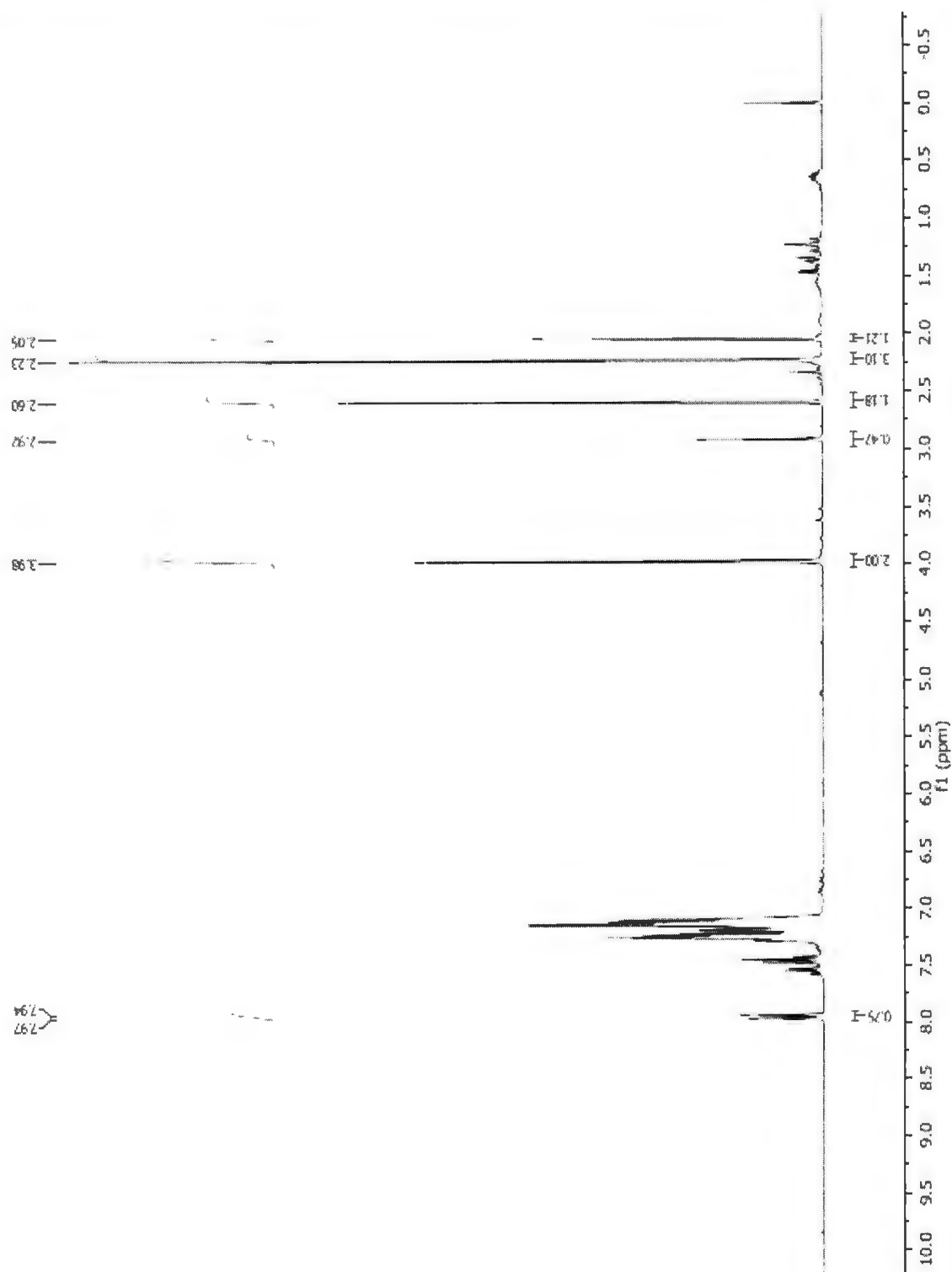
FigureA50: ^1H NMR spectrum for 1-Benzyl-4-methylbenzene (Table 3.1, Entry 4).



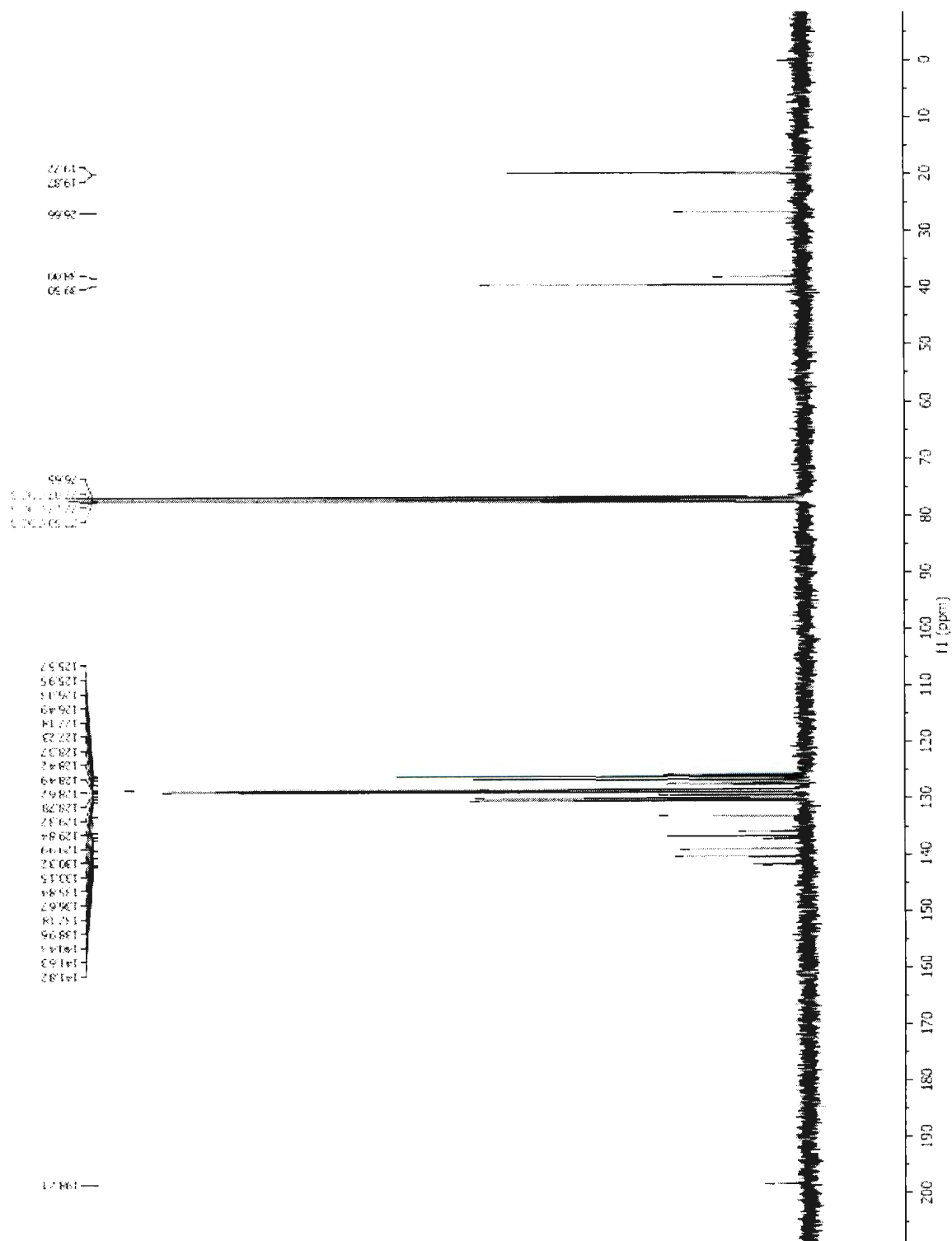
FigureA52: GC-MS analysis of **1-Benzyl-2-methylbenzene** (Table 3.1, Entry 5). GC-MS retention time: 7.211 min dodecane; 8.935 min 4,4'-dimethylbiphenyl; 9.752 min bibenzyl; 9.845 min 1-benzyl-2-methylbenzene.



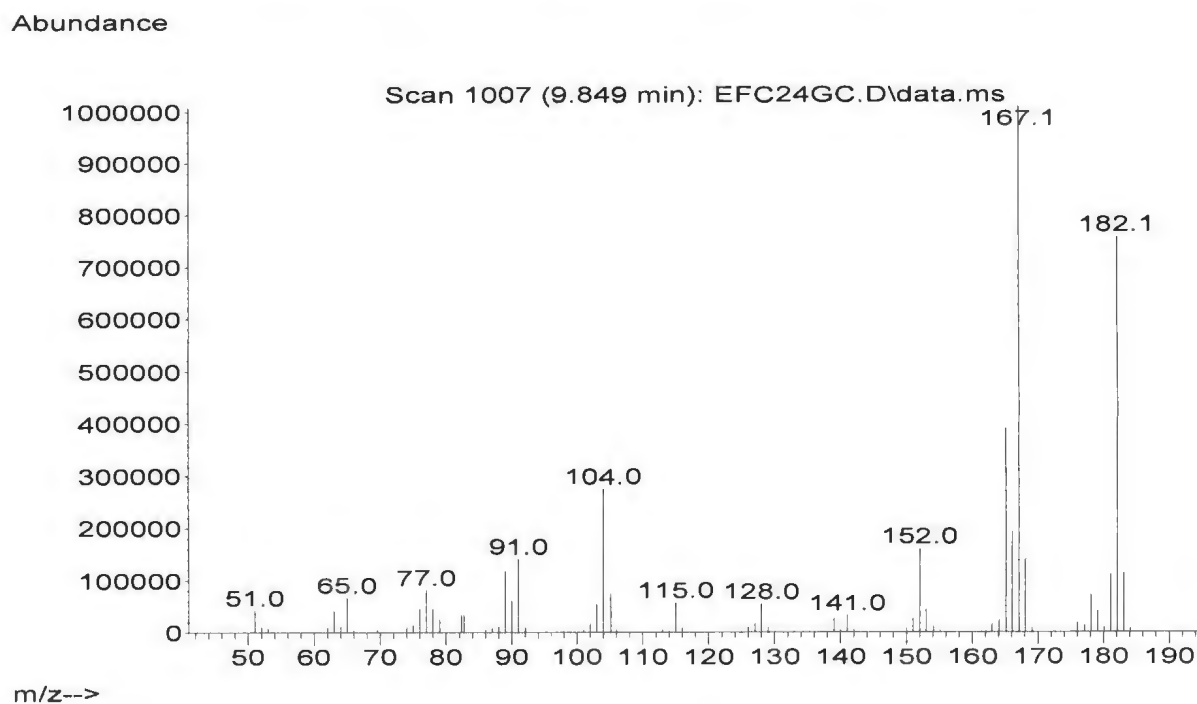
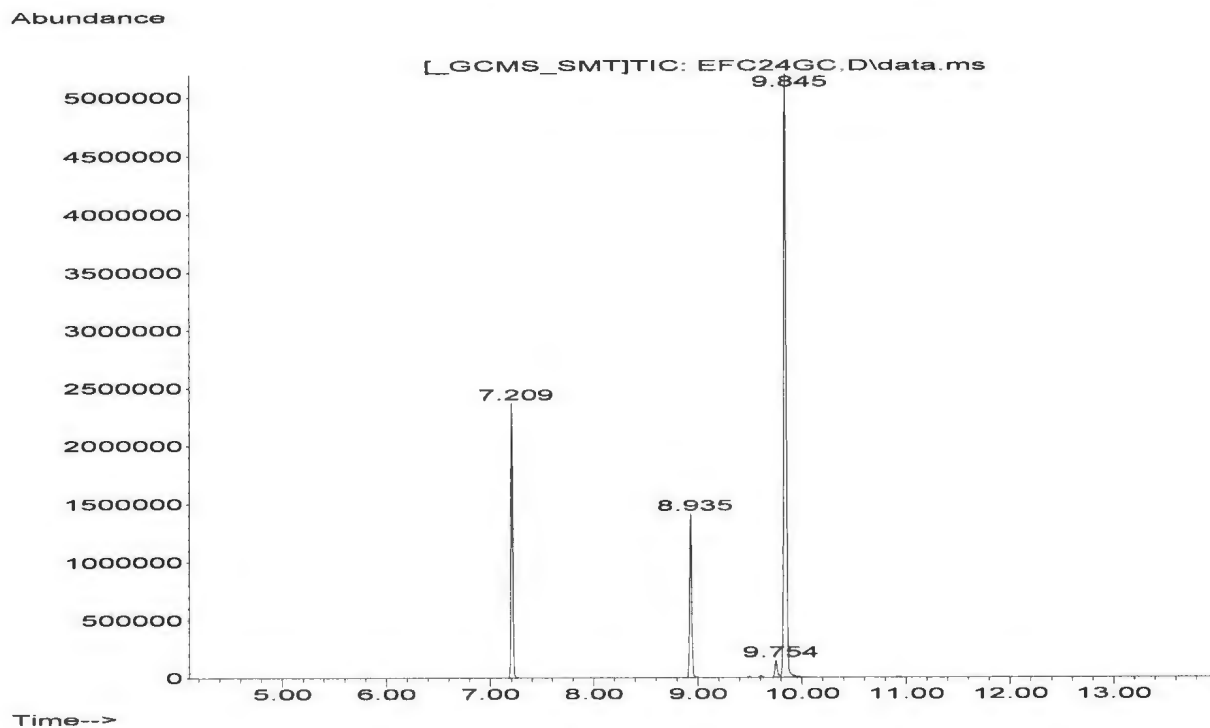
FigureA53: ^1H NMR spectrum for 1-Benzyl-2-methylbenzene (Table 3.1, Entry 5).



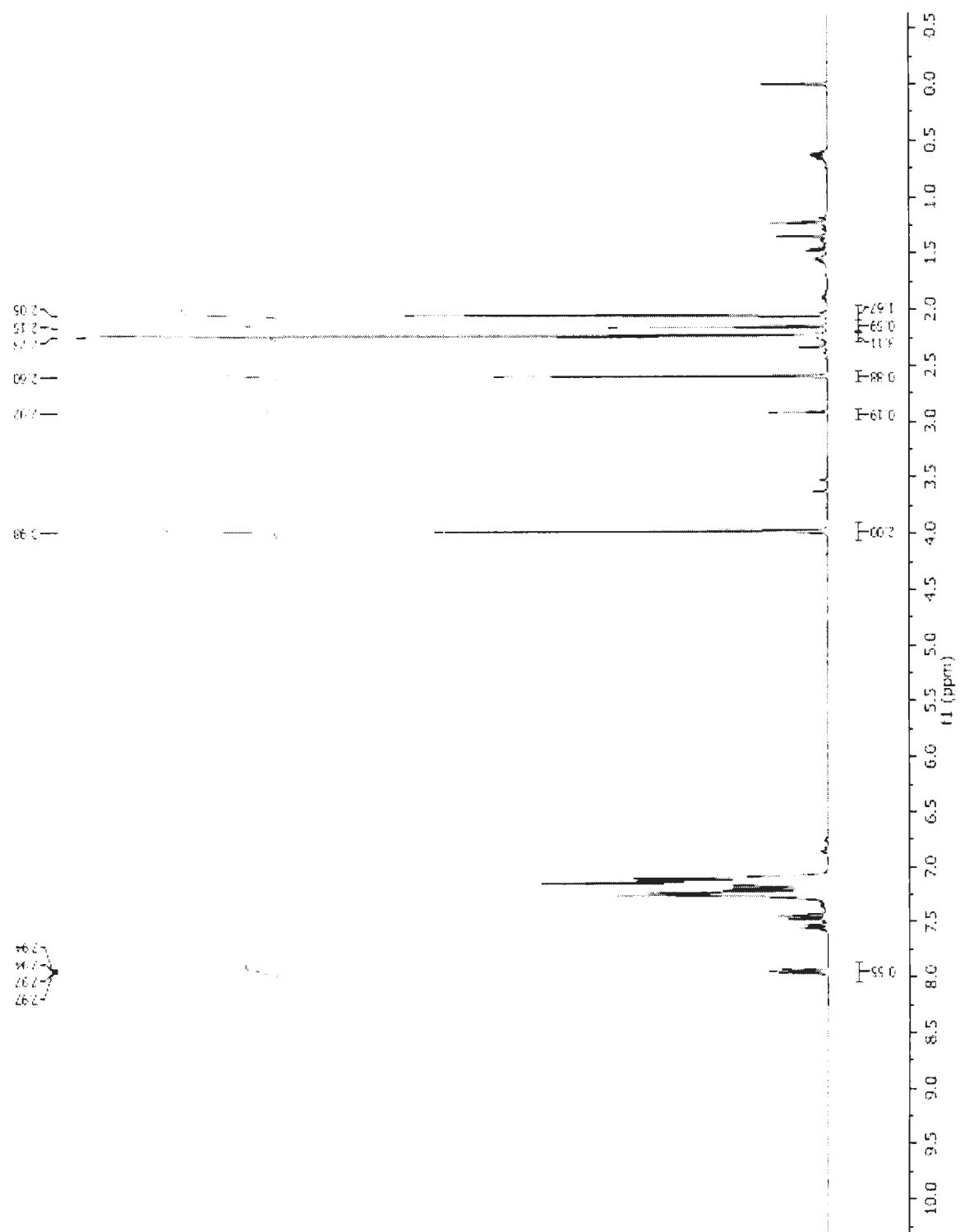
FigureA54: ^{13}C NMR spectrum for 1-Benzyl-2-methylbenzene (Table 3.1, Entry 5).



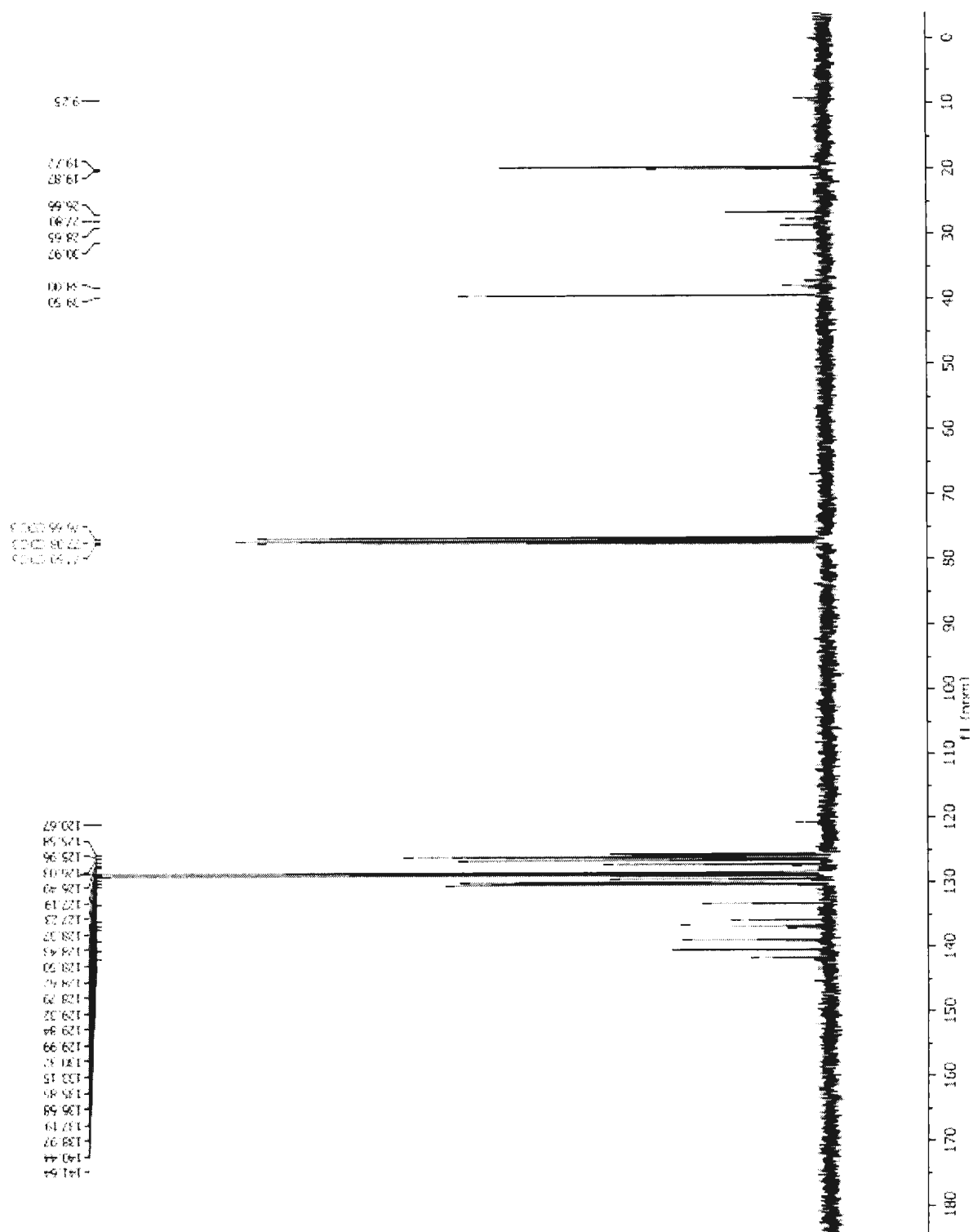
FigureA55: GC-MS analysis of **1-Benzyl-2-methylbenzene** (Table 3.1, Entry 6). GC-MS retention time: 7.209 min dodecane; 8.935 min 4,4'-dimethylbiphenyl; 9.754 min bibenzyl; 9.845 min 1-benzyl-2-methylbenzene.



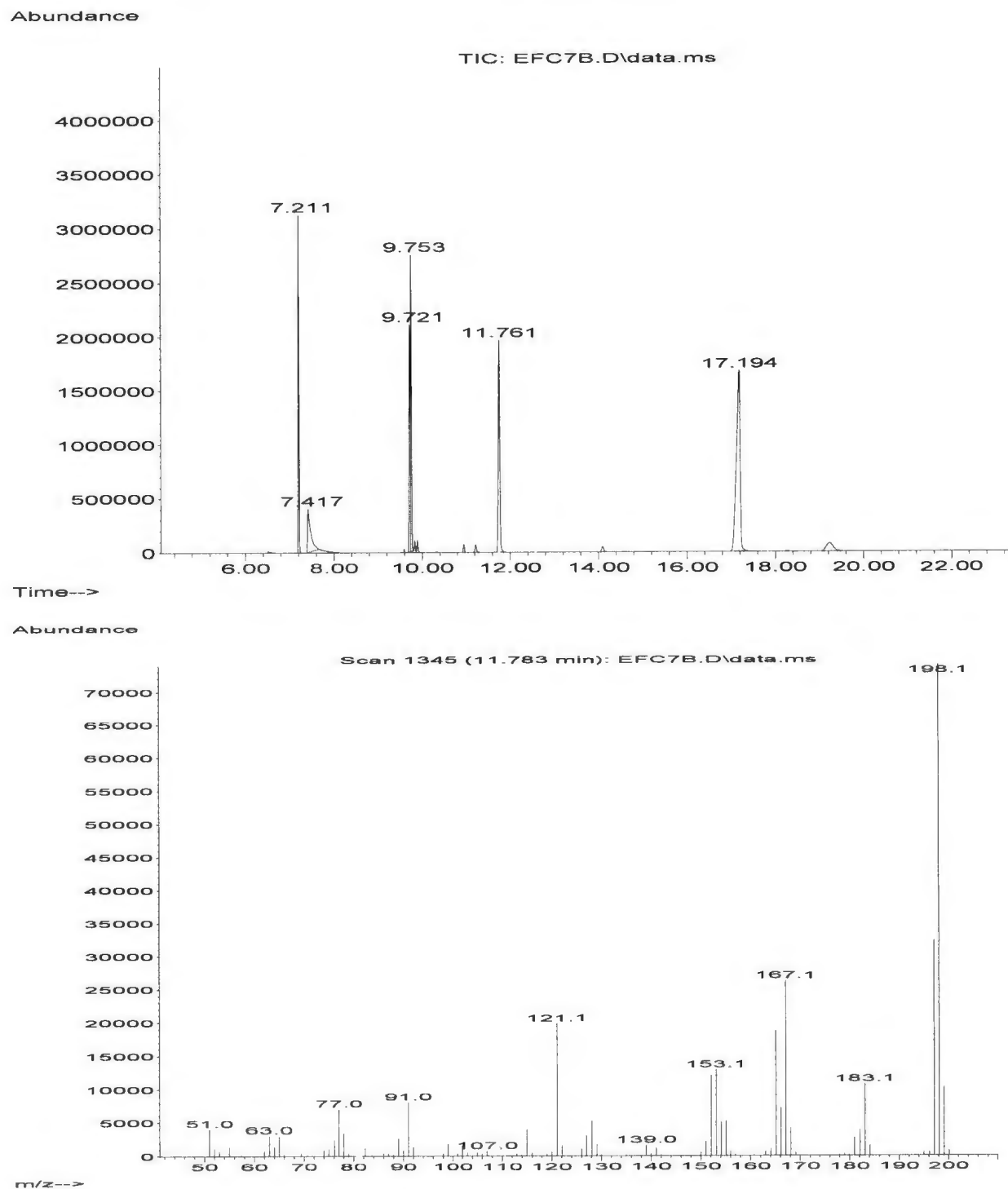
FigureA56: ^1H NMR spectrum for 1-Benzyl-2-methylbenzene (Table 3.1, Entry 6).



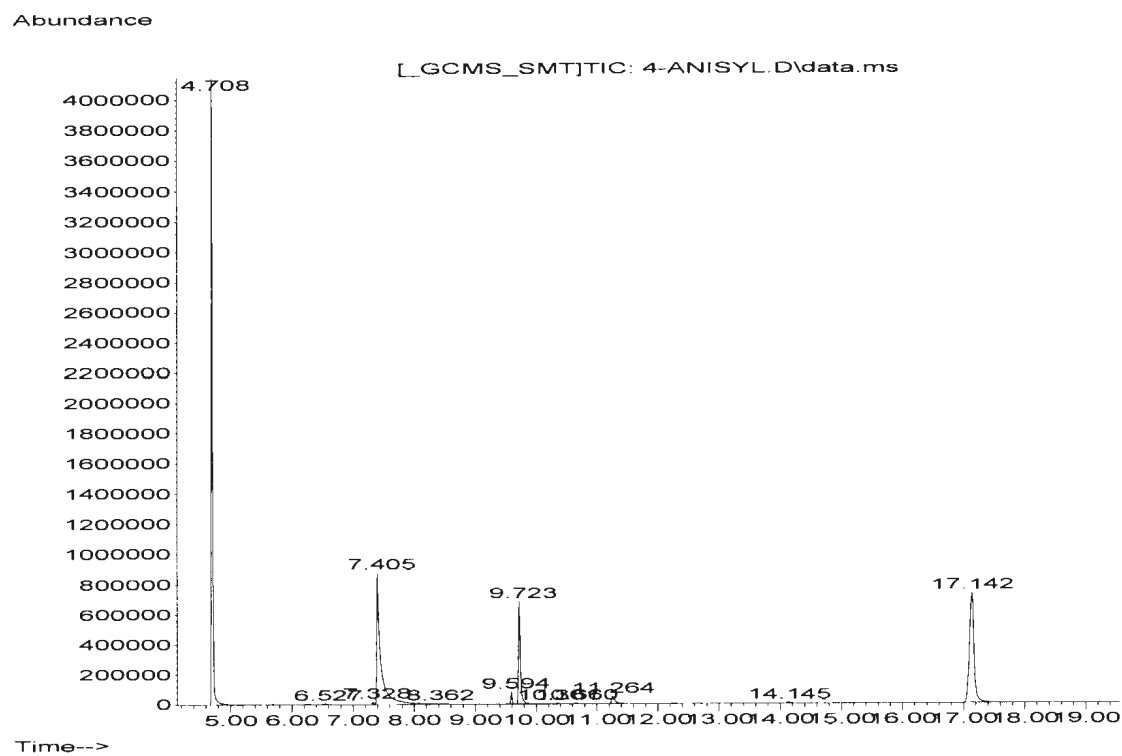
FigureA57: ^{13}C NMR spectrum for 1-Benzyl-2-methylbenzene (Table 3.1, Entry 6).



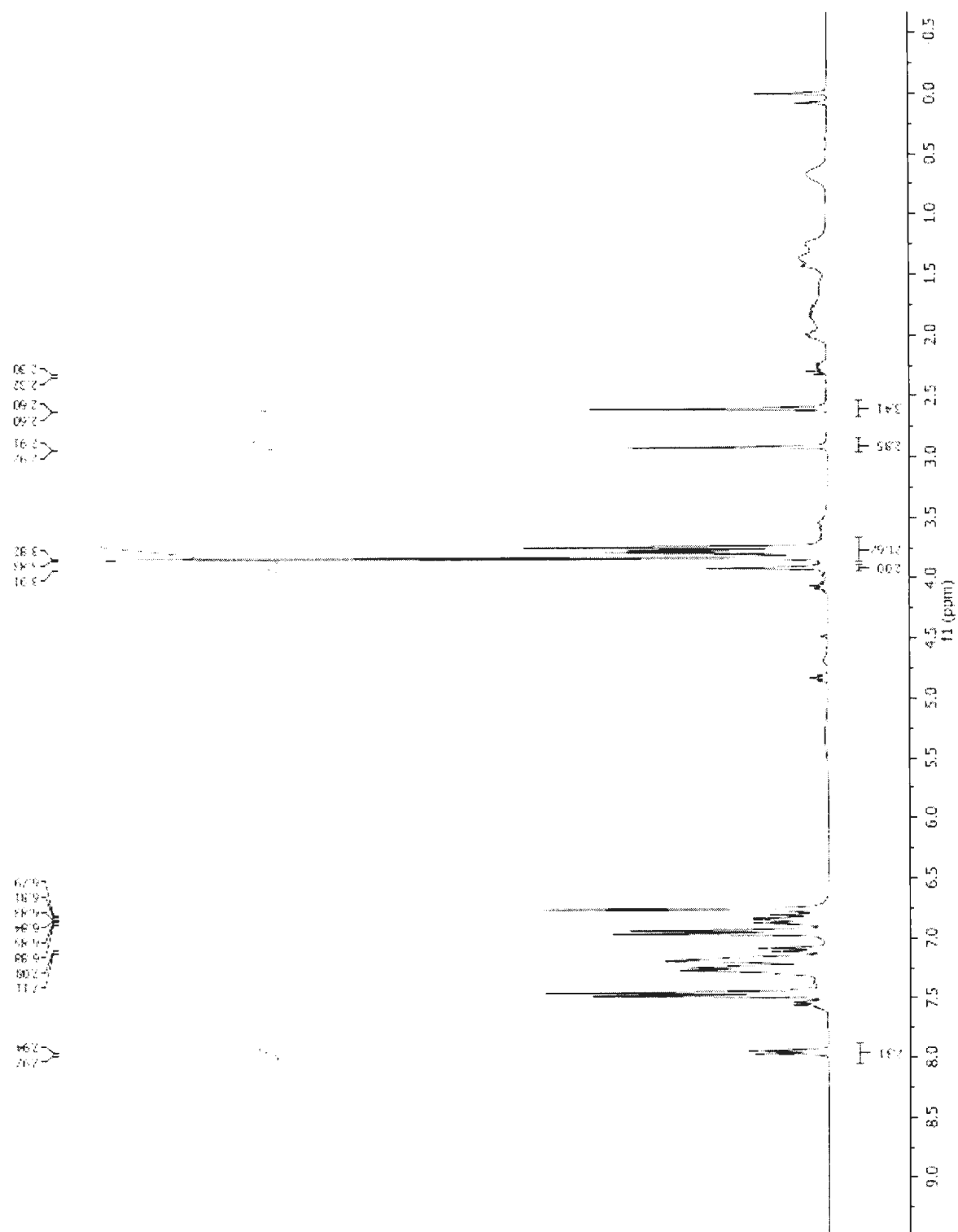
FigureA58: GC-MS analysis of **4-Benzylanisole** (Table 3.1, Entry 7). GC-MS retention time: 7.211 min dodecane; 9.753 min bibenzyl; 11.761 min 4-benzylanisole; 17.194 min 4,4'-dimethoxybiphenyl.



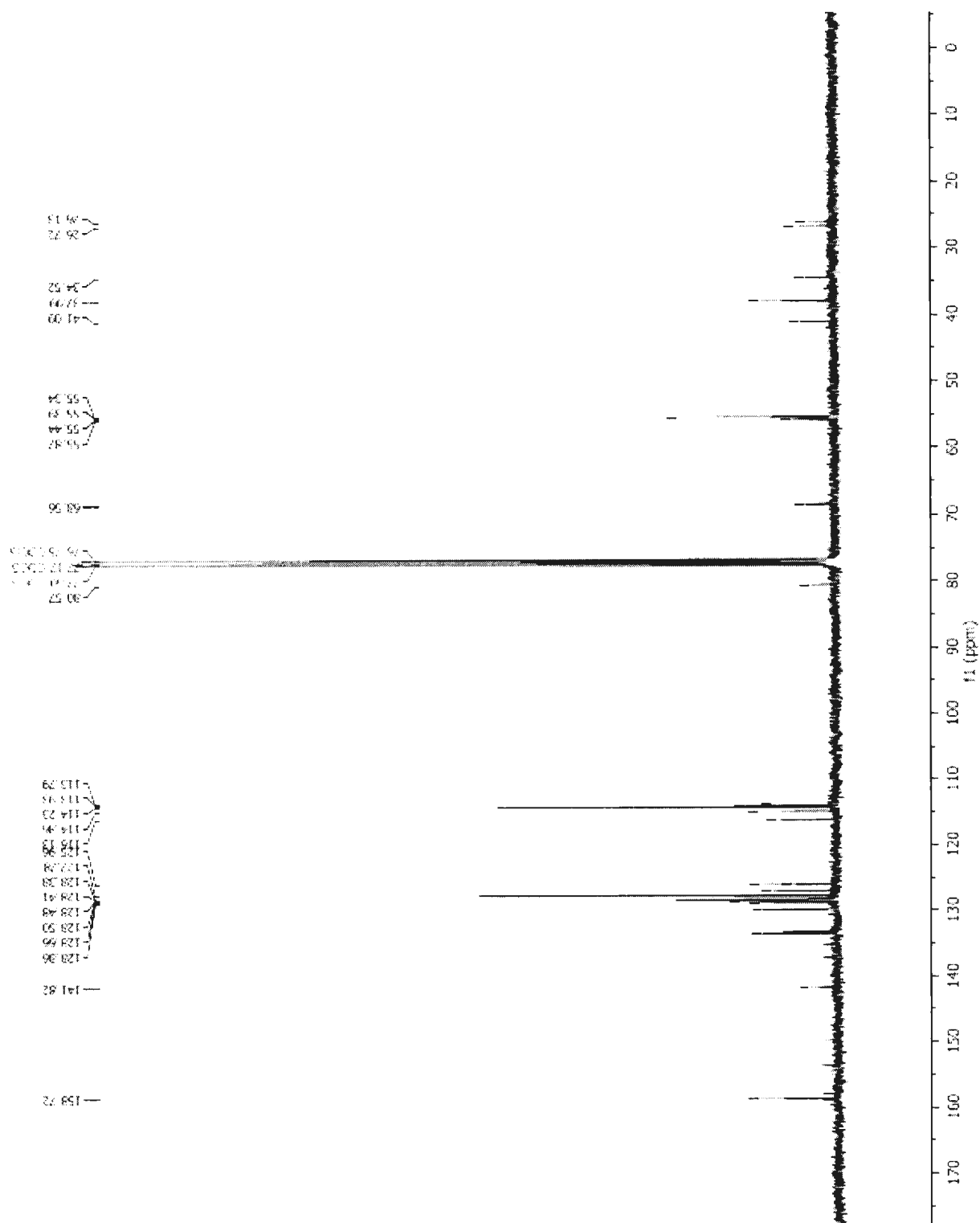
FigureA59: GC-MS analysis of 4-methoxyphenylmagnesium bromide used.



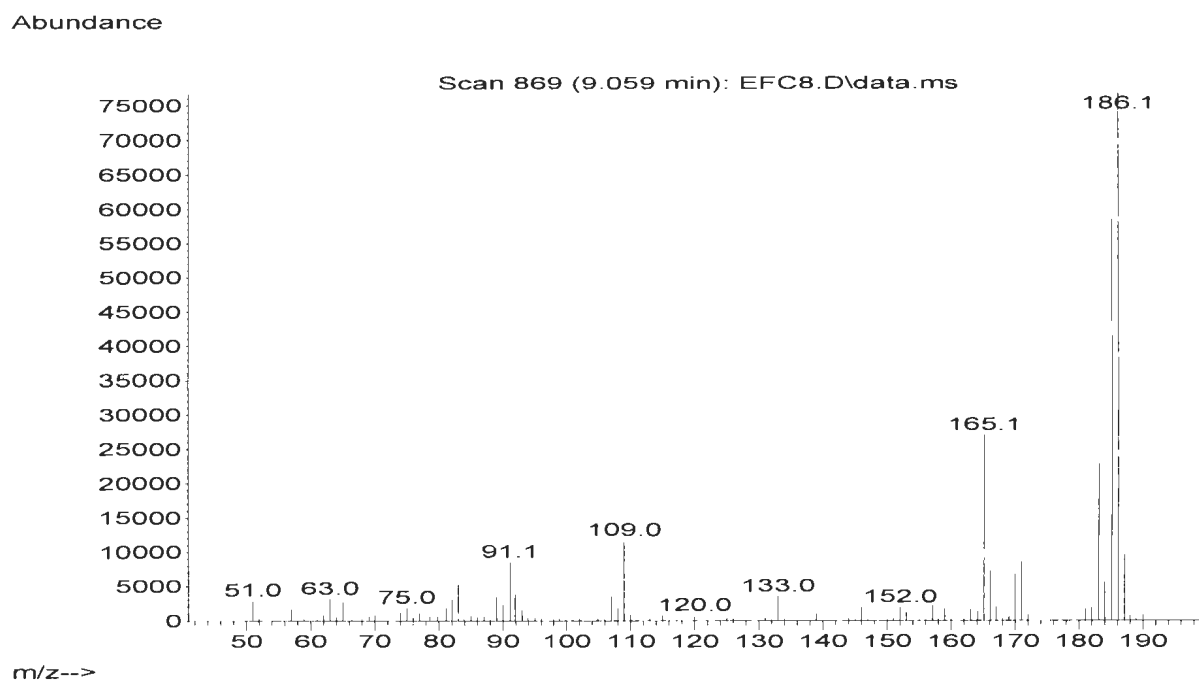
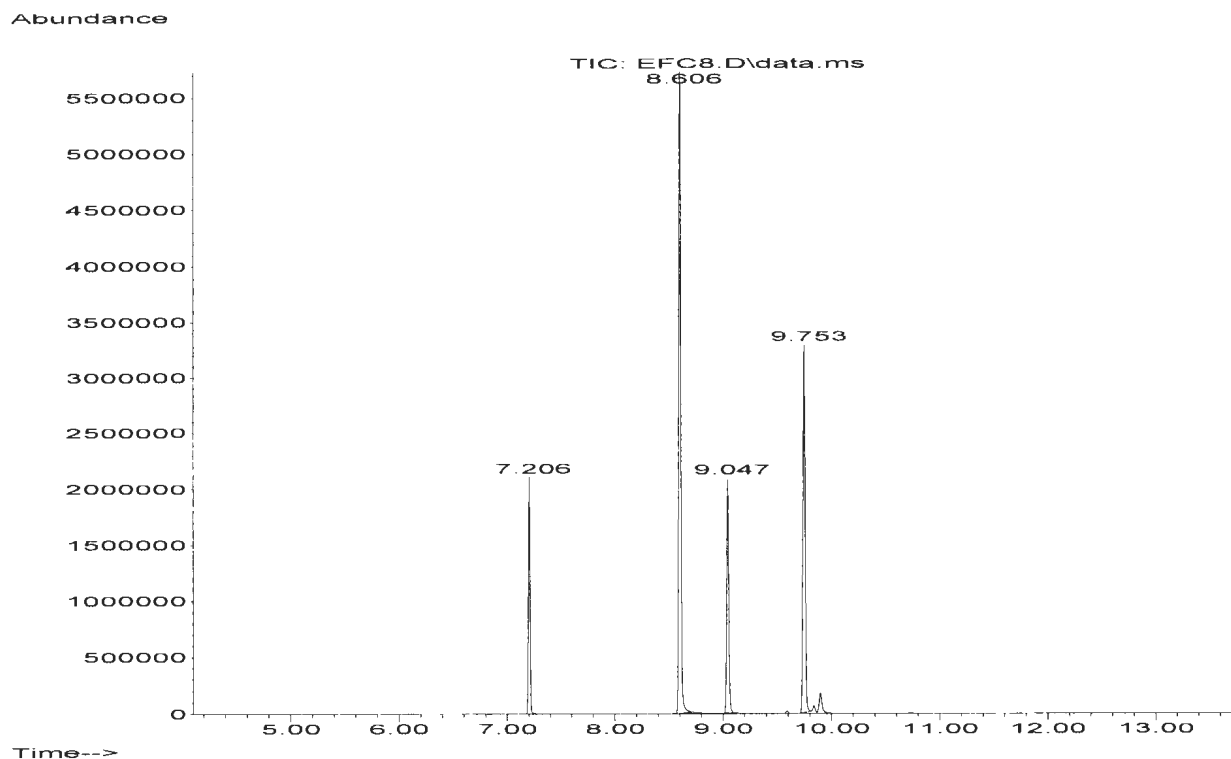
FigureA60: ^1H NMR spectrum for 4-Benzylanisole (Table 3.1, Entry 7).



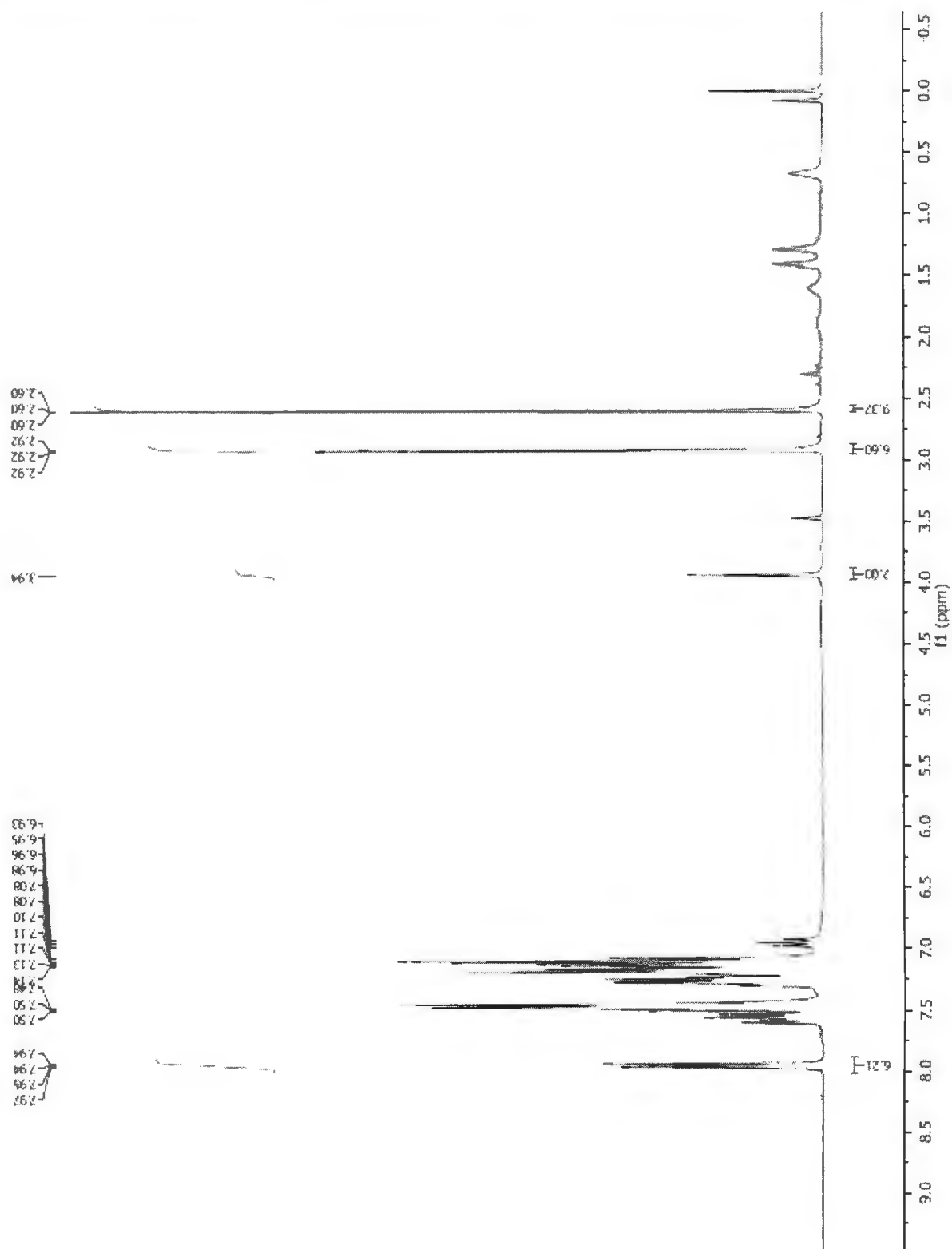
FigureA61: ^{13}C NMR spectrum for **4-Benzylanisole** (Table 3.1, Entry 7).



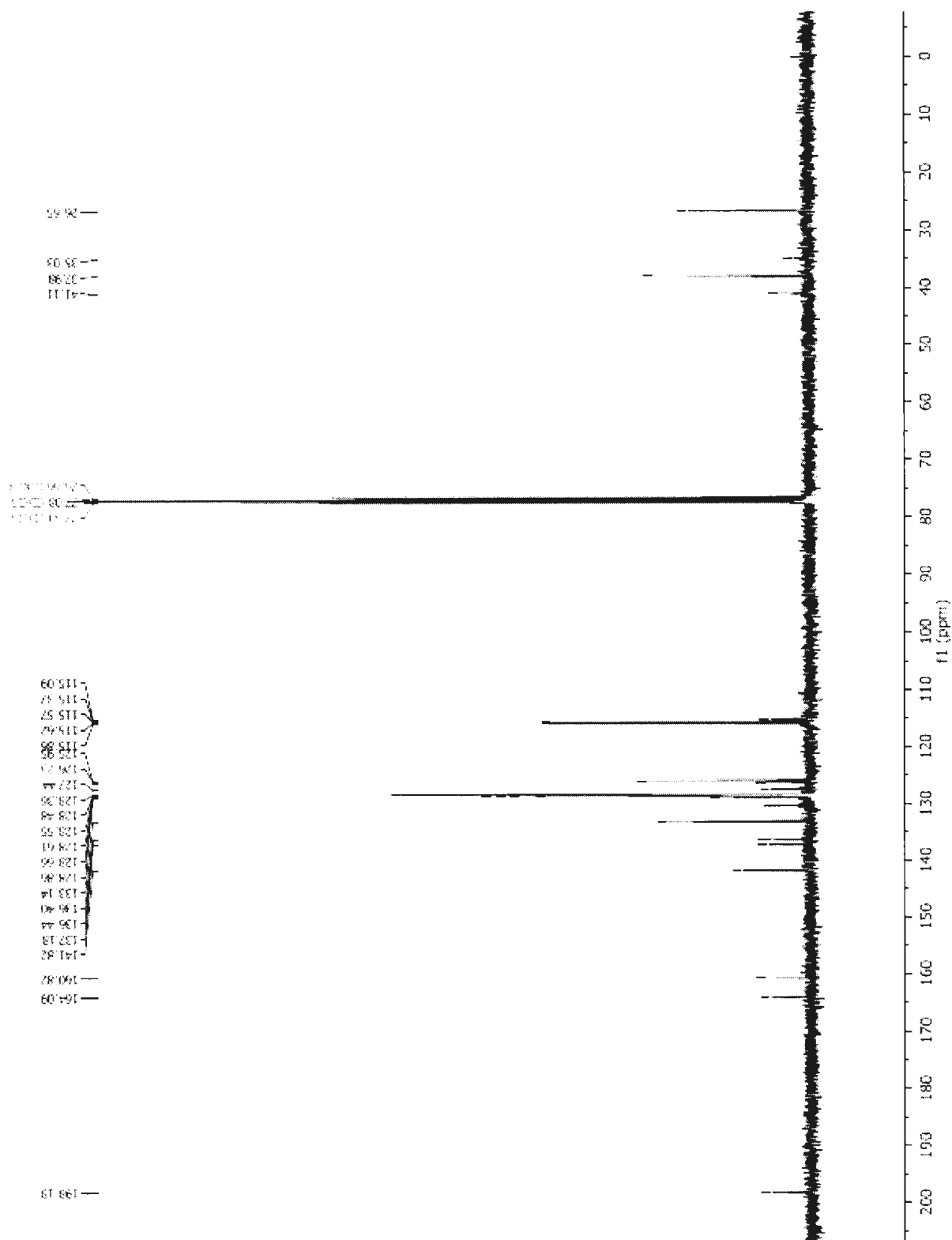
FigureA62: GC-MS analysis of **1-Benzyl-4-fluorobenzene** (Table 3.1, Entry 8). GC-MS retention time: 7.206 min dodecane; 8.606 min 4,4'-difluorobiphenyl; 9.047 min 1-benzyl-4-fluorobenzene; 9.753 min bibenzyl.



FigureA63: ^1H NMR spectrum for 1-Benzyl-4-fluorobenzene (Table 3.1, Entry 8).

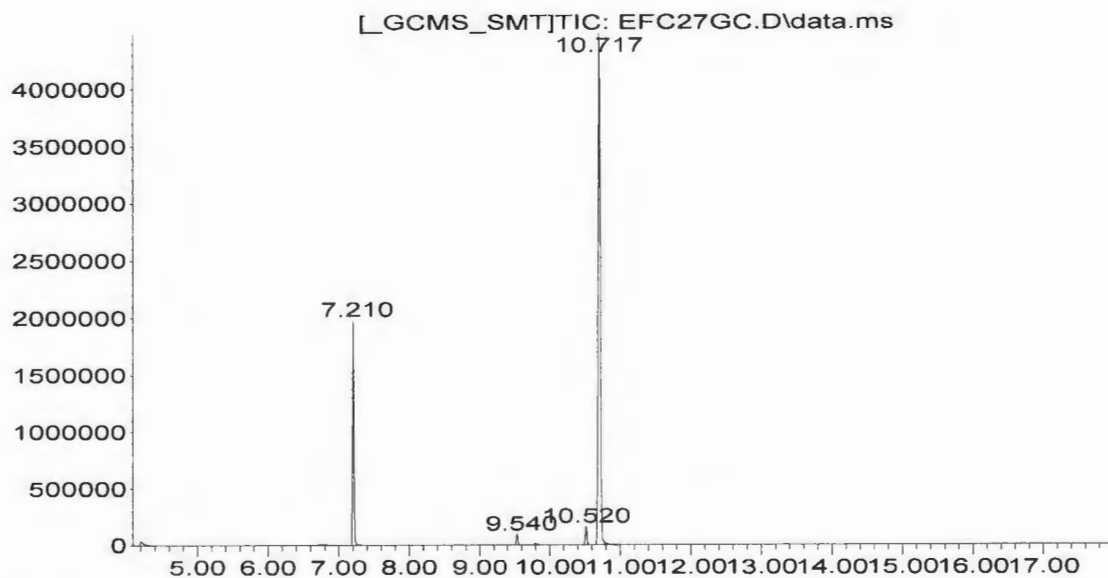


FigureA64: ^{13}C NMR spectrum for 1-Benzyl-4-fluorobenzene (Table 3.1, Entry 8).



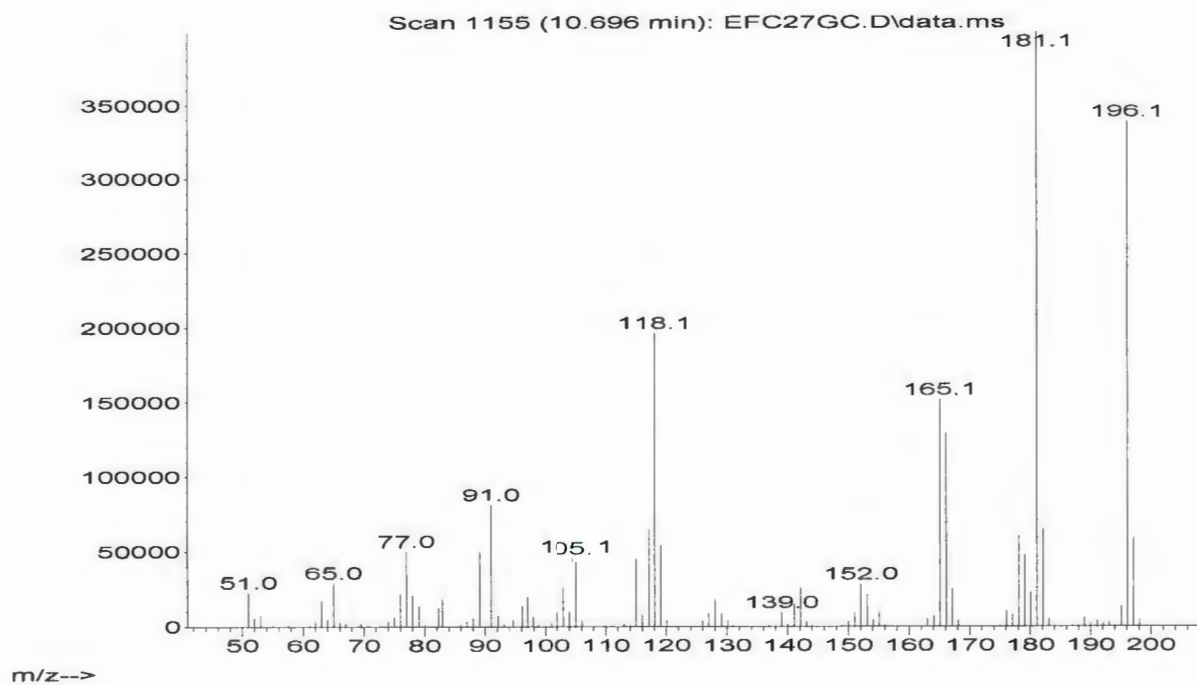
FigureA65: GC-MS analysis of **1-Benzyl-2,6-dimethylbenzene** (Table 3.1, Entry 9).
 GC-MS retention time: 7.210 min dodecane; 10.520 min 2,2',6,6'-dimethylbiphenyl;
 10.717 min 1-benzyl-2,6-dimethylbenzene.

Abundance



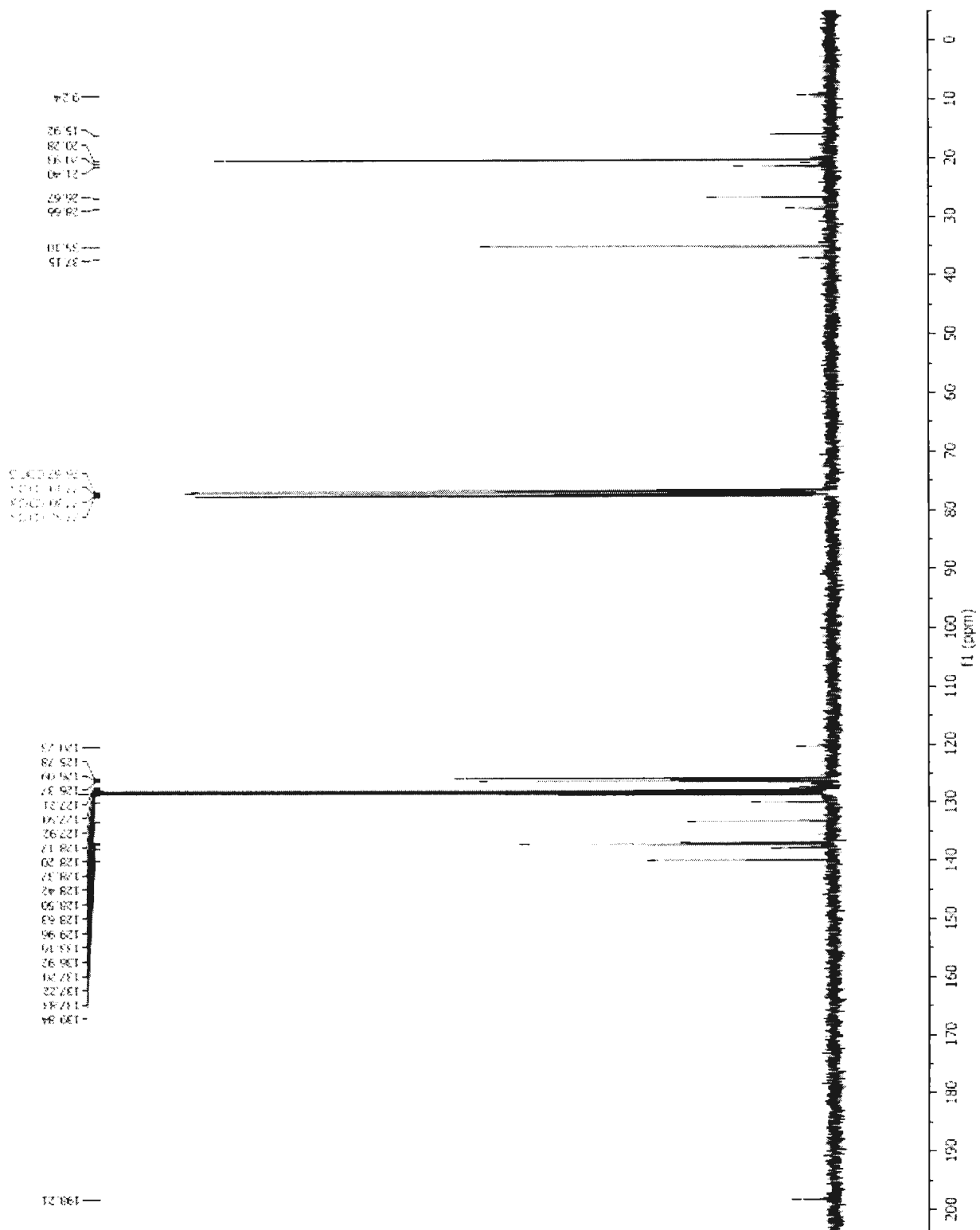
Time-->

Abundance

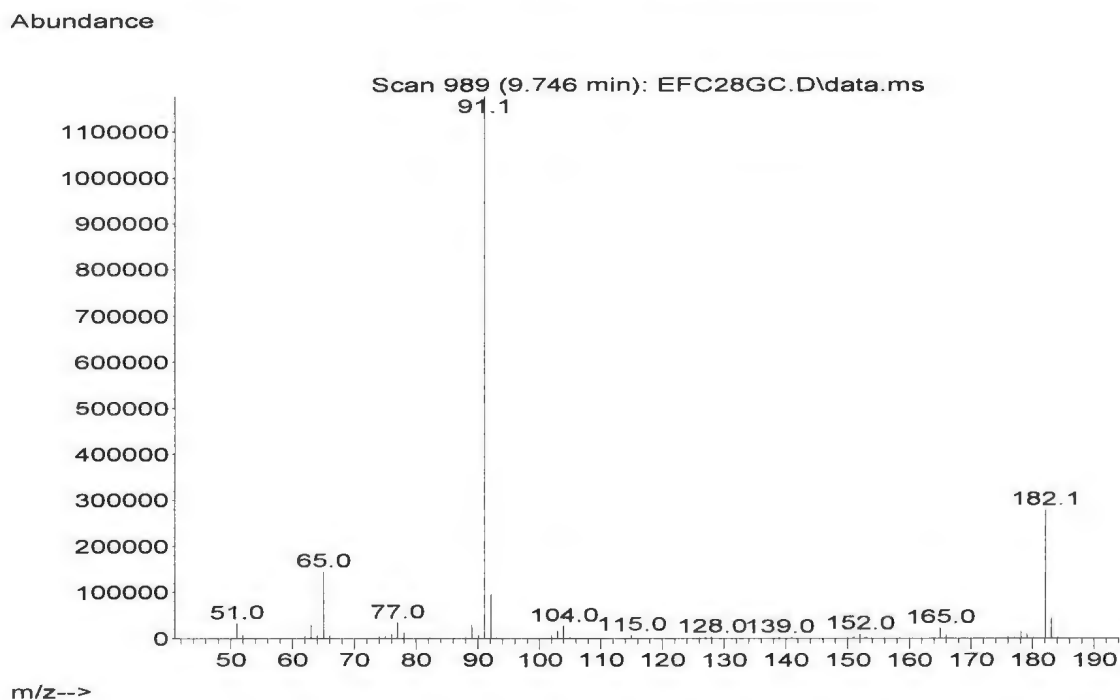
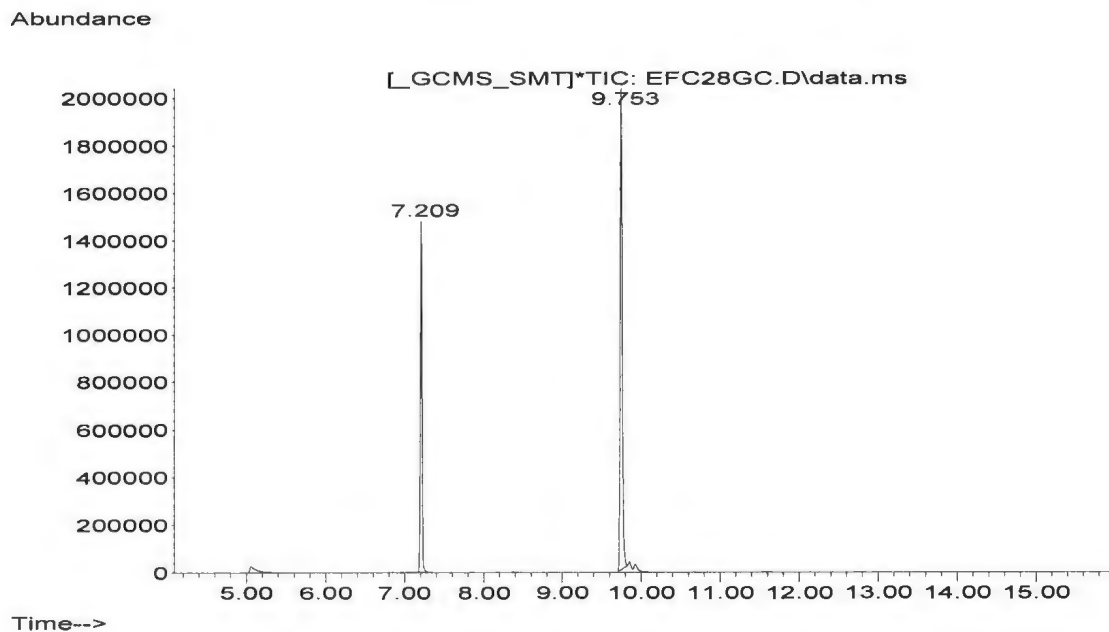


m/z-->

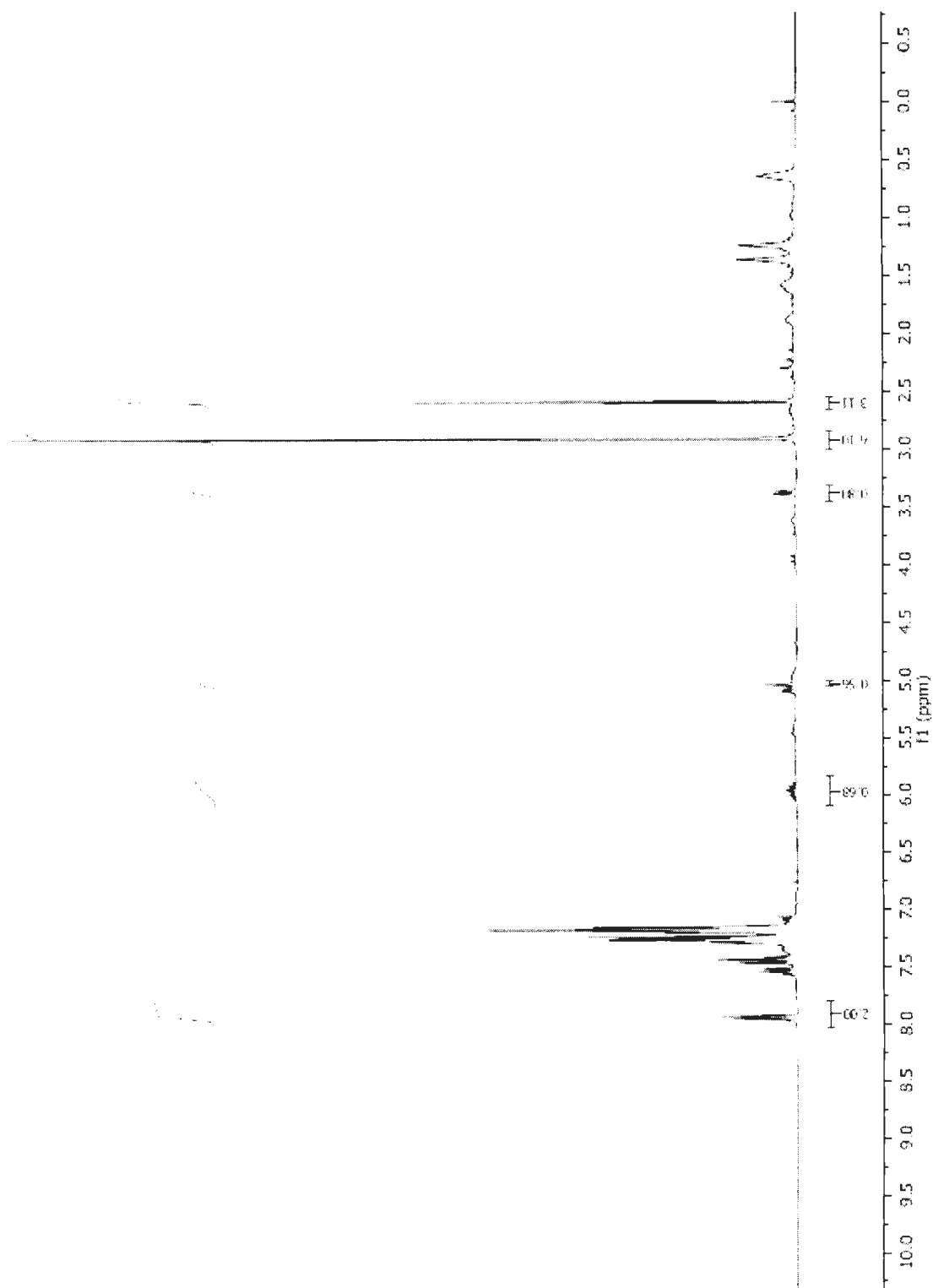
FigureA67: ^{13}C NMR spectrum for **1-Benzyl-2,6-dimethylbenzene** (Table 3.1, Entry 9).



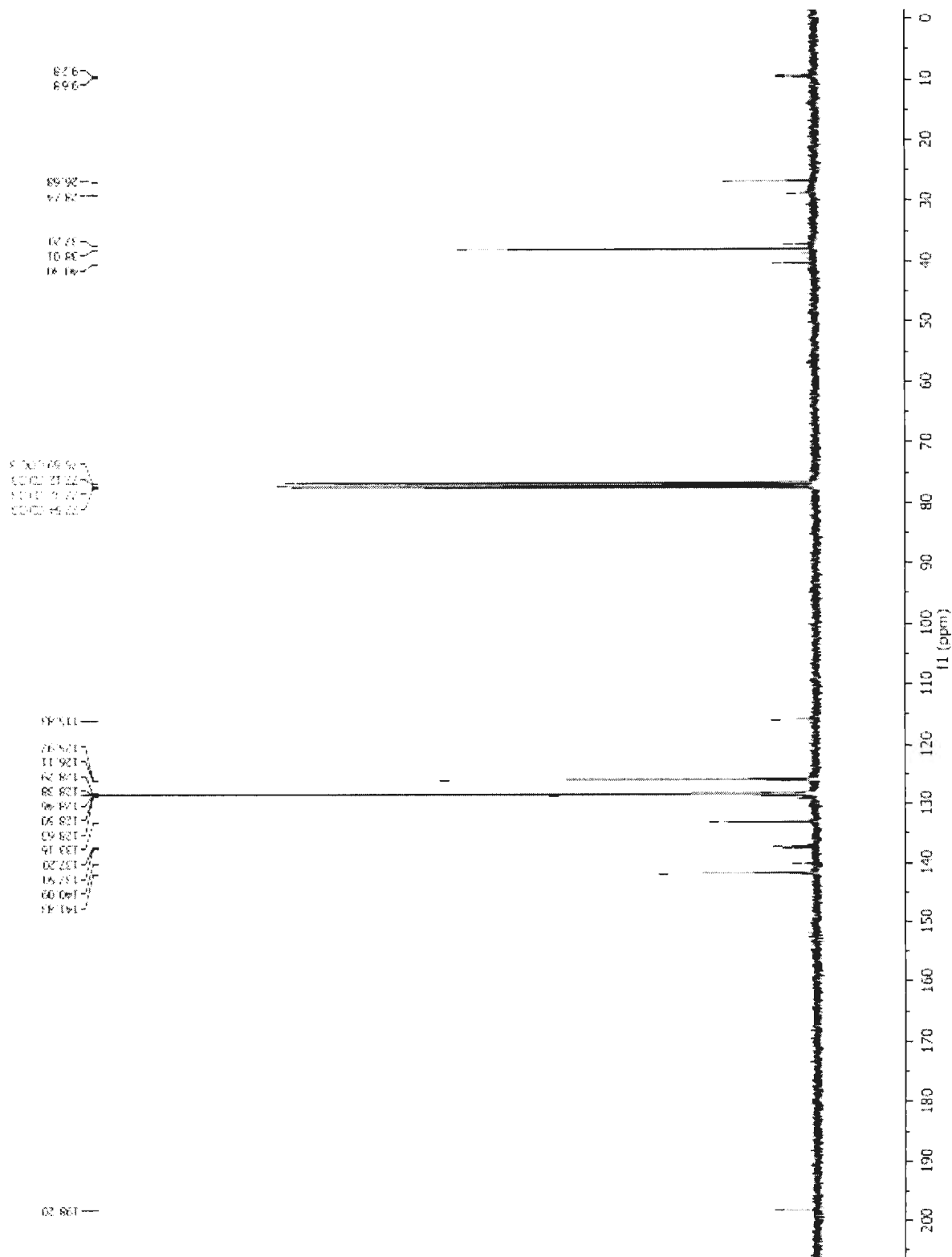
FigureA68: GC-MS analysis of **1-Phenyl-2-propene** (Table 3.1, Entry 10). GC-MS retention time: m/z: 5.077 min 1-Phenyl-2-propene; 7.209 min dodecane; 9.753 min bibenzyl.



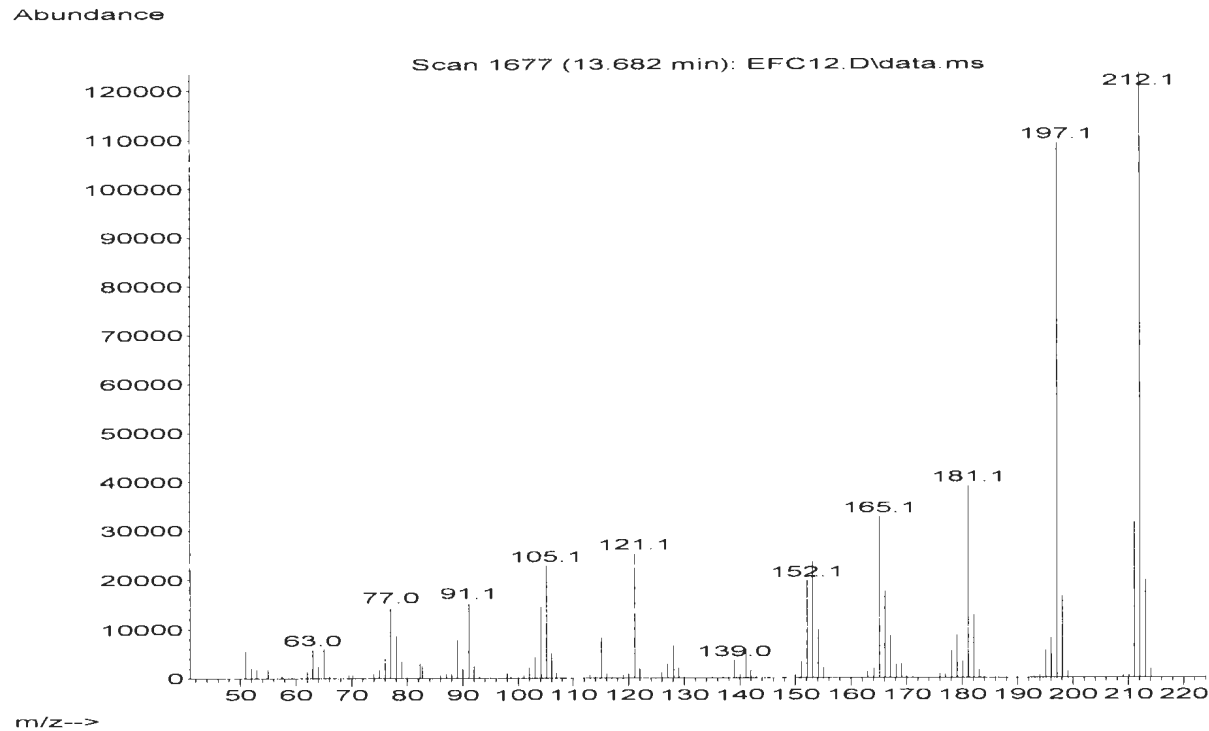
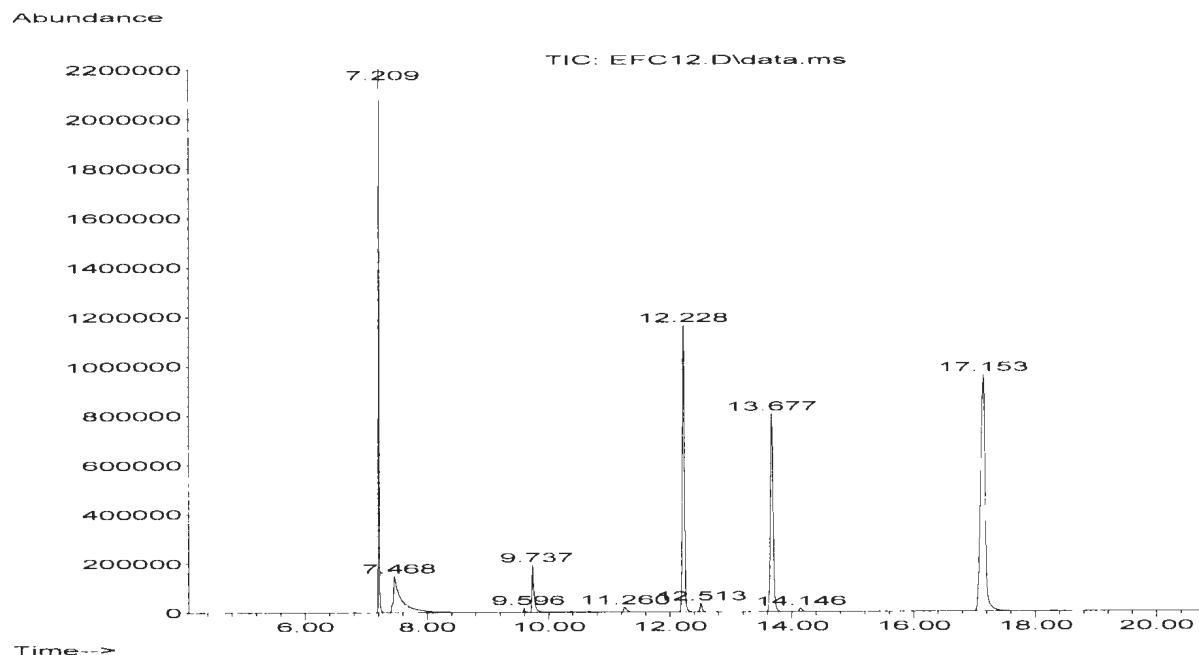
FigureA69: ^1H NMR spectrum for 1-Phenyl-2-propene (Table 3.1, Entry 10).



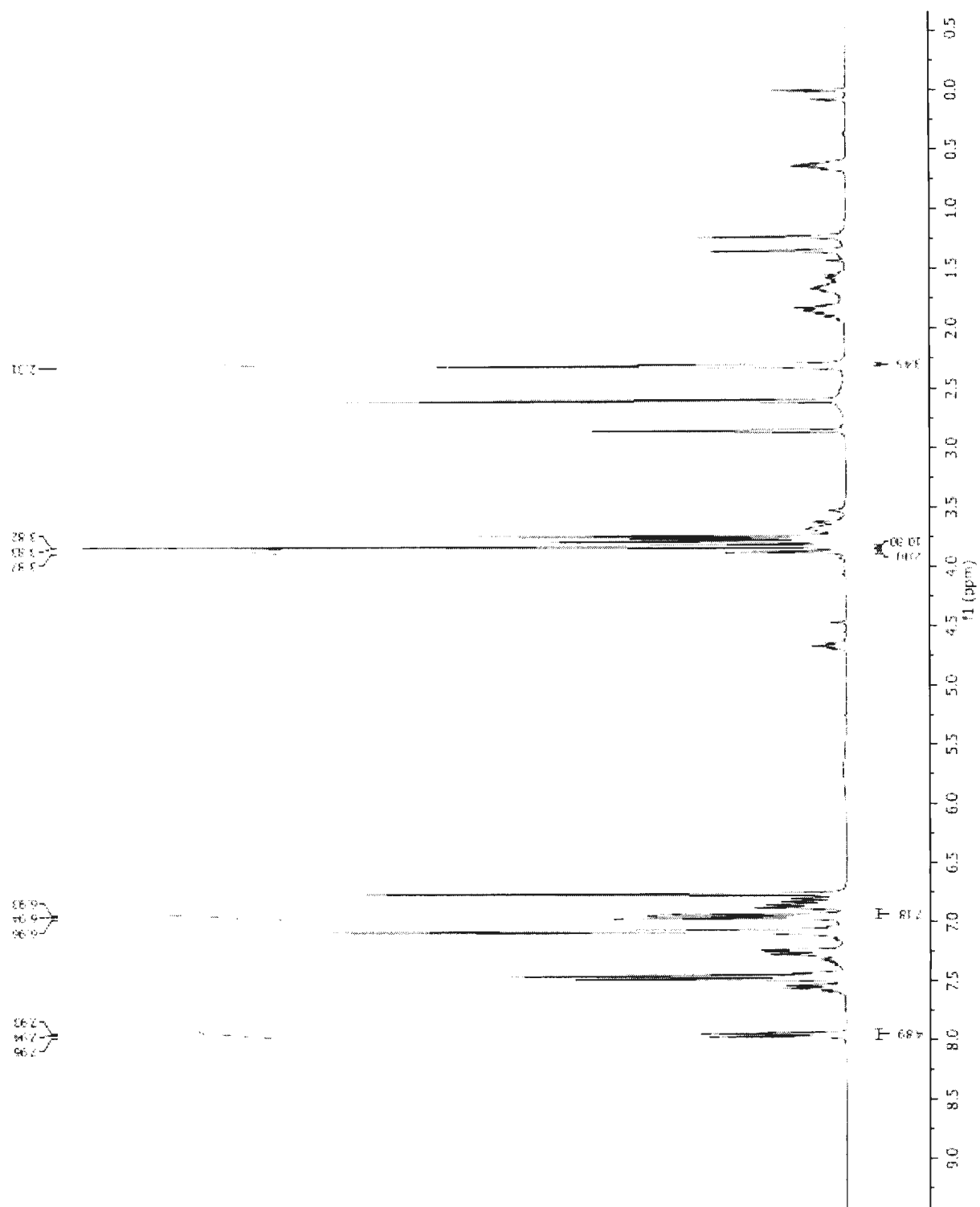
FigureA70: ^{13}C NMR spectrum for **1-Phenyl-2-propene** (Table 3.1, Entry 10).



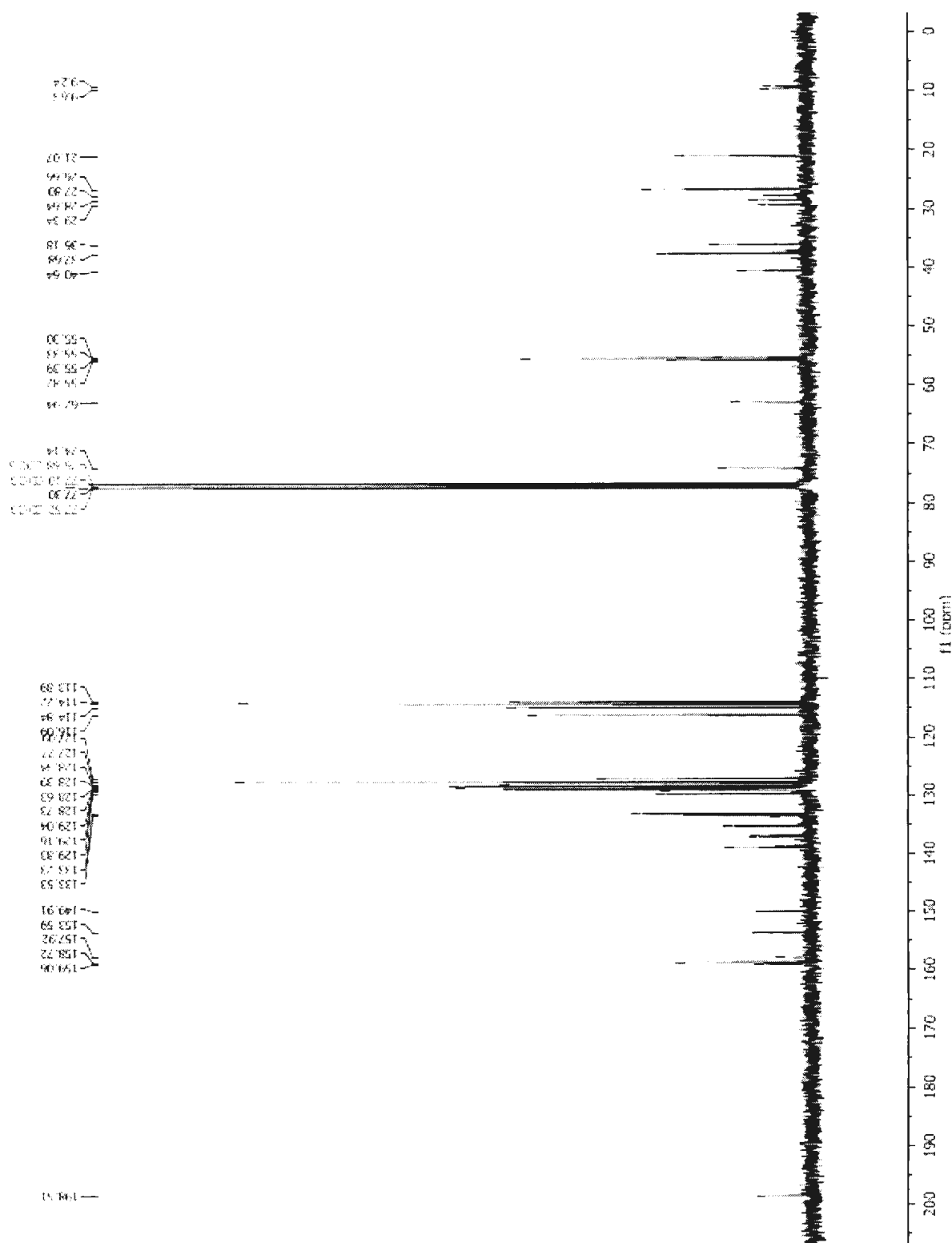
FigureA71: GC-MS analysis of **1-Methoxy-4-(4-methylbenzyl)benzene** (Table 3.2, Entry 1). GC-MS retention time: 7.209 min dodecane; 12.228 min 4,4'-dimethylbibenzyl; 13.677 min 1-methoxy-4-(4-methylbenzyl)benzene.



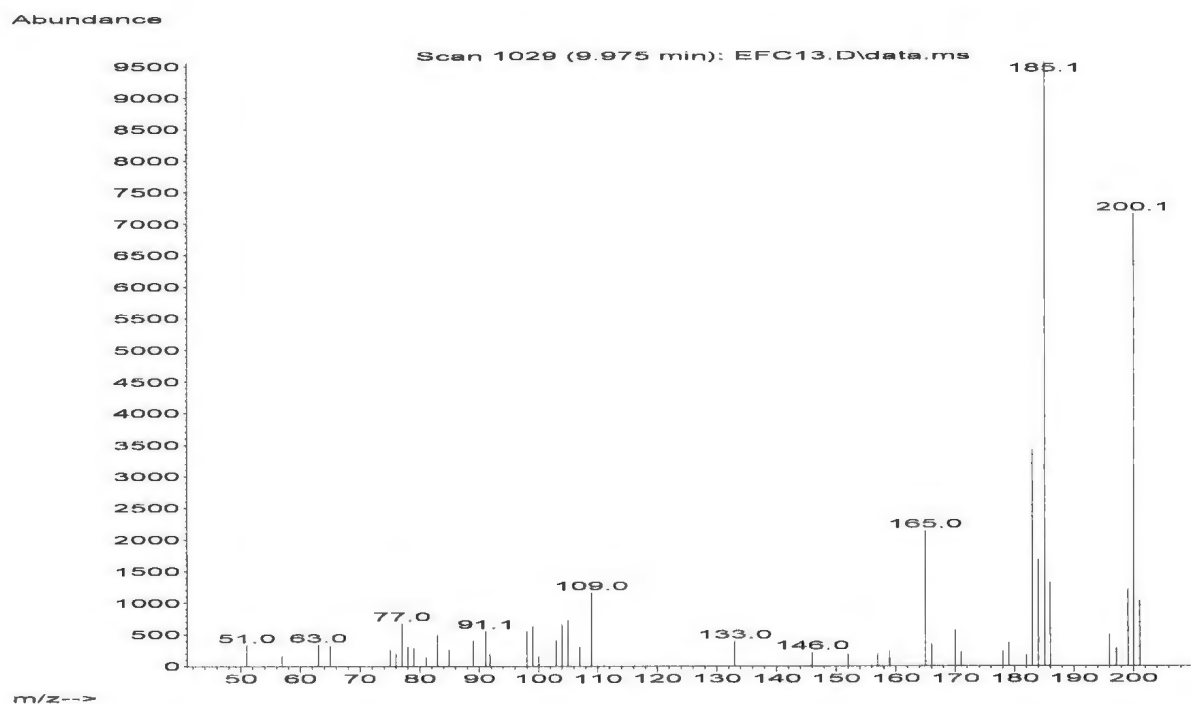
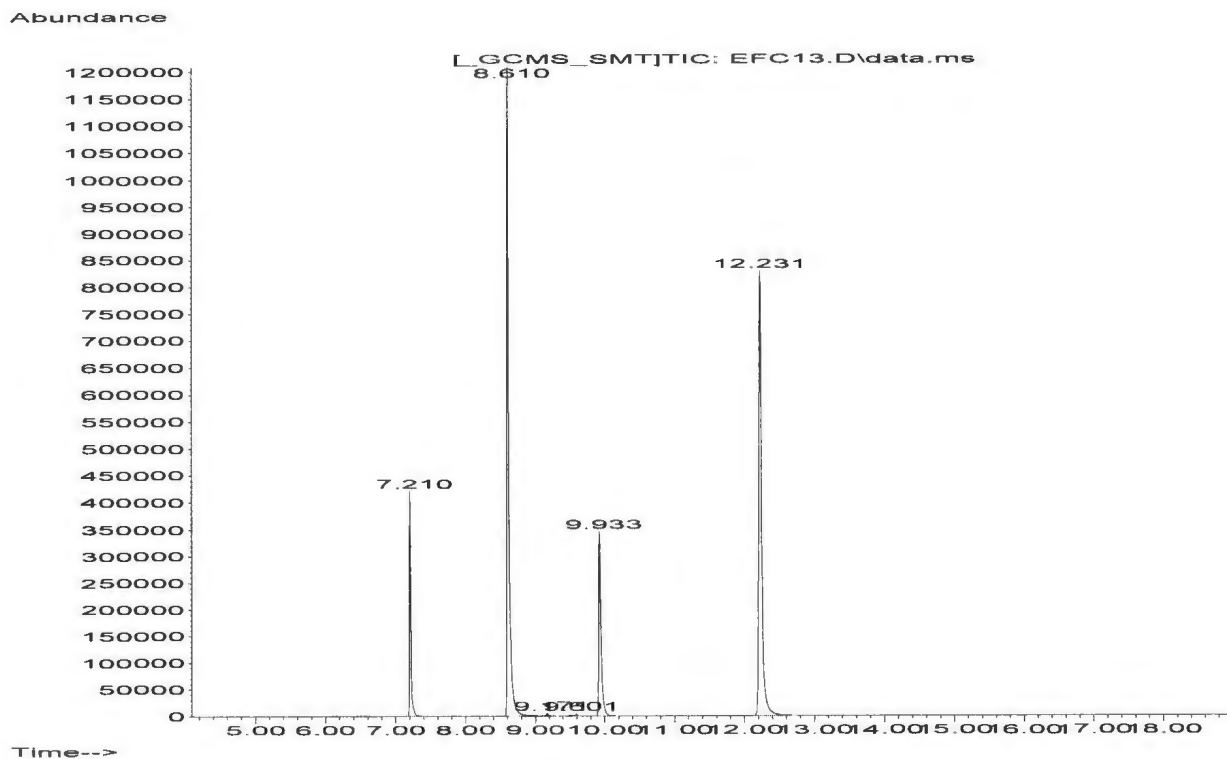
FigureA72: ^1H NMR spectrum for 1-Methoxy-4-(4-methylbenzyl)benzene (Table 3.2, Entry 1).



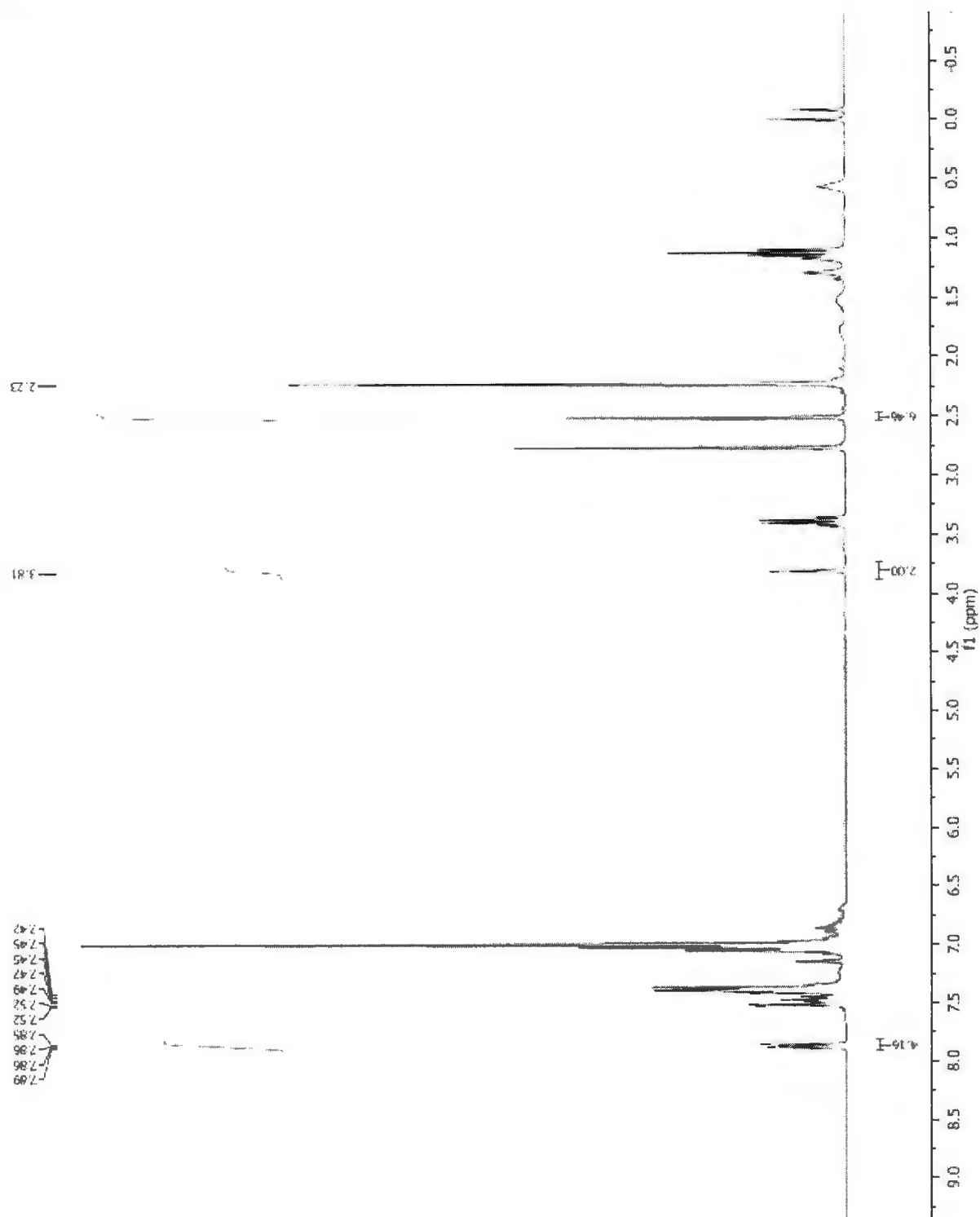
FigureA73: ^{13}C NMR spectrum for 1-Methoxy-4-(4-methylbenzyl)benzene (Table 3.2, Entry 1).



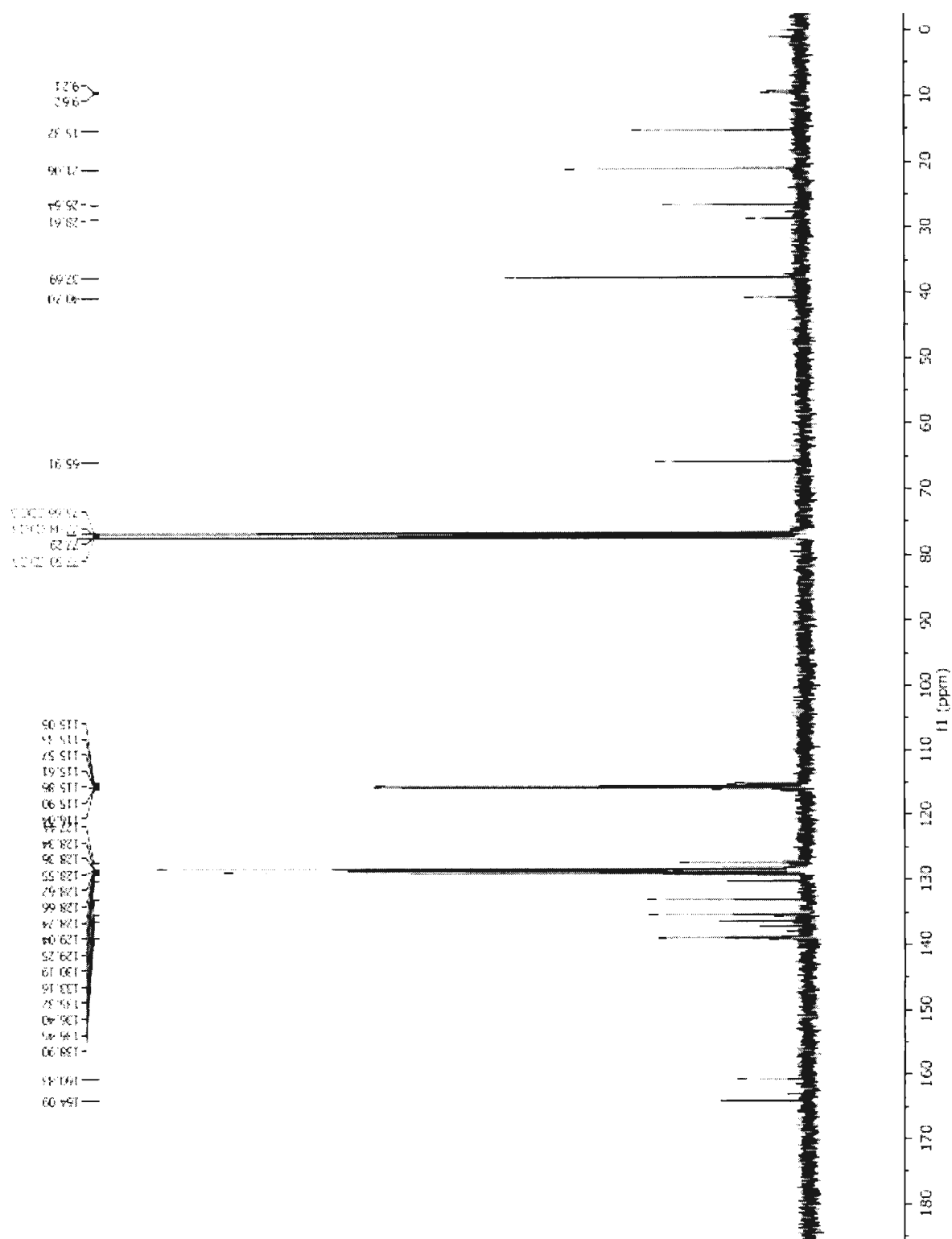
FigureA74: GC-MS analysis of 1-Fluoro-4-(4-methylbenzyl)benzene (Table 3.2, Entry 2). GC-MS retention time: 7.210 min dodecane; 8.610 min 4,4'-difluorobiphenyl; 9.933 min 1-fluoro-4-(4-methylbenzyl)benzene; 12.231 min 4,4'-dimethylbibenzyl.



FigureA75: ^1H NMR spectrum for **1-Fluoro-4-(4-methylbenzyl)benzene** (Table 3.2, Entry 2).

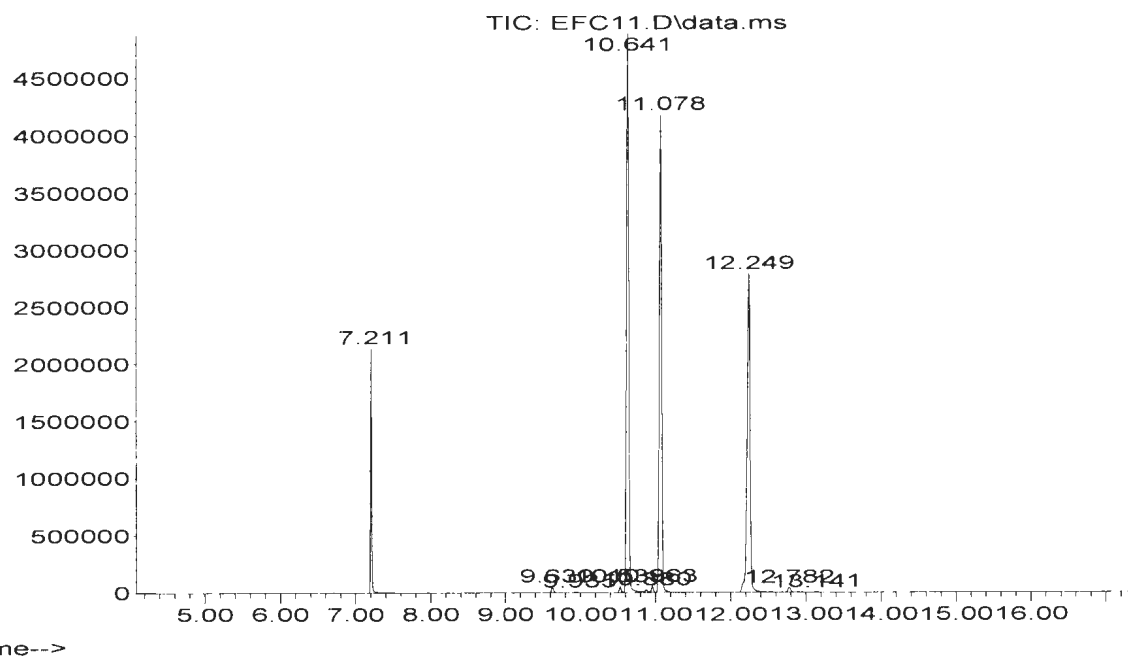


FigureA76: ^{13}C NMR spectrum for 1-Fluoro-4-(4-methylbenzyl)benzene (Table 3.2, Entry 2).

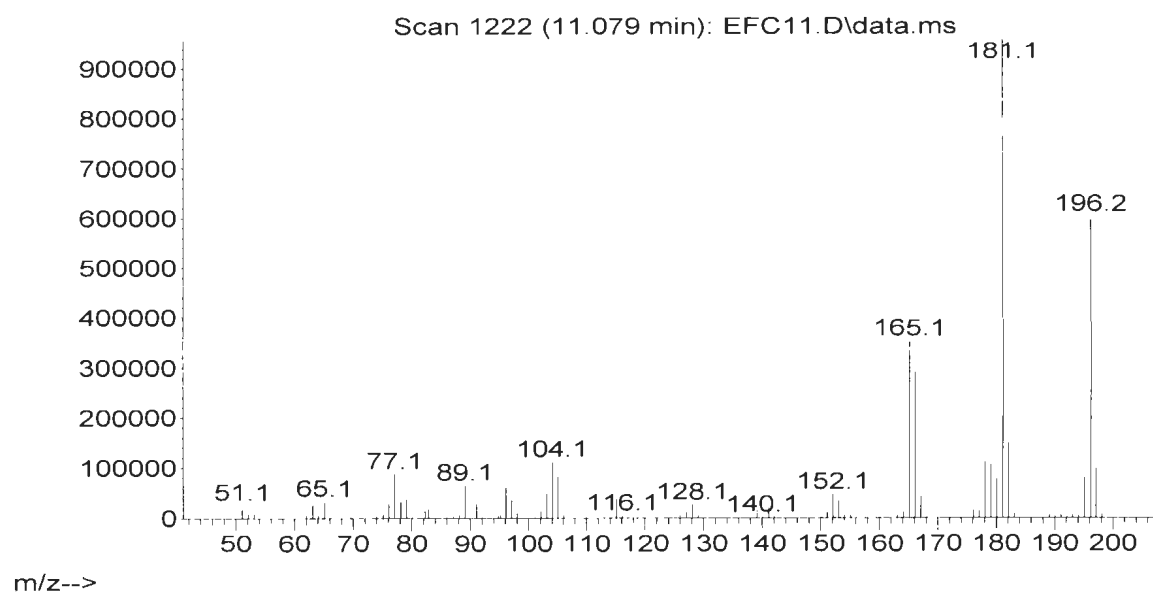


FigureA77: GC-MS analysis of **Di-*p*-tolylmethane** (Table 3.2, Entry 3). GC-MS retention time: m/z (% ion): 7.211 min dodecane; 10.641 min 4,4'-dimethylbiphenyl; 11.078 min di-*p*-tolylmethane; 12.249 min 4,4'-dimethylbibenzyl.

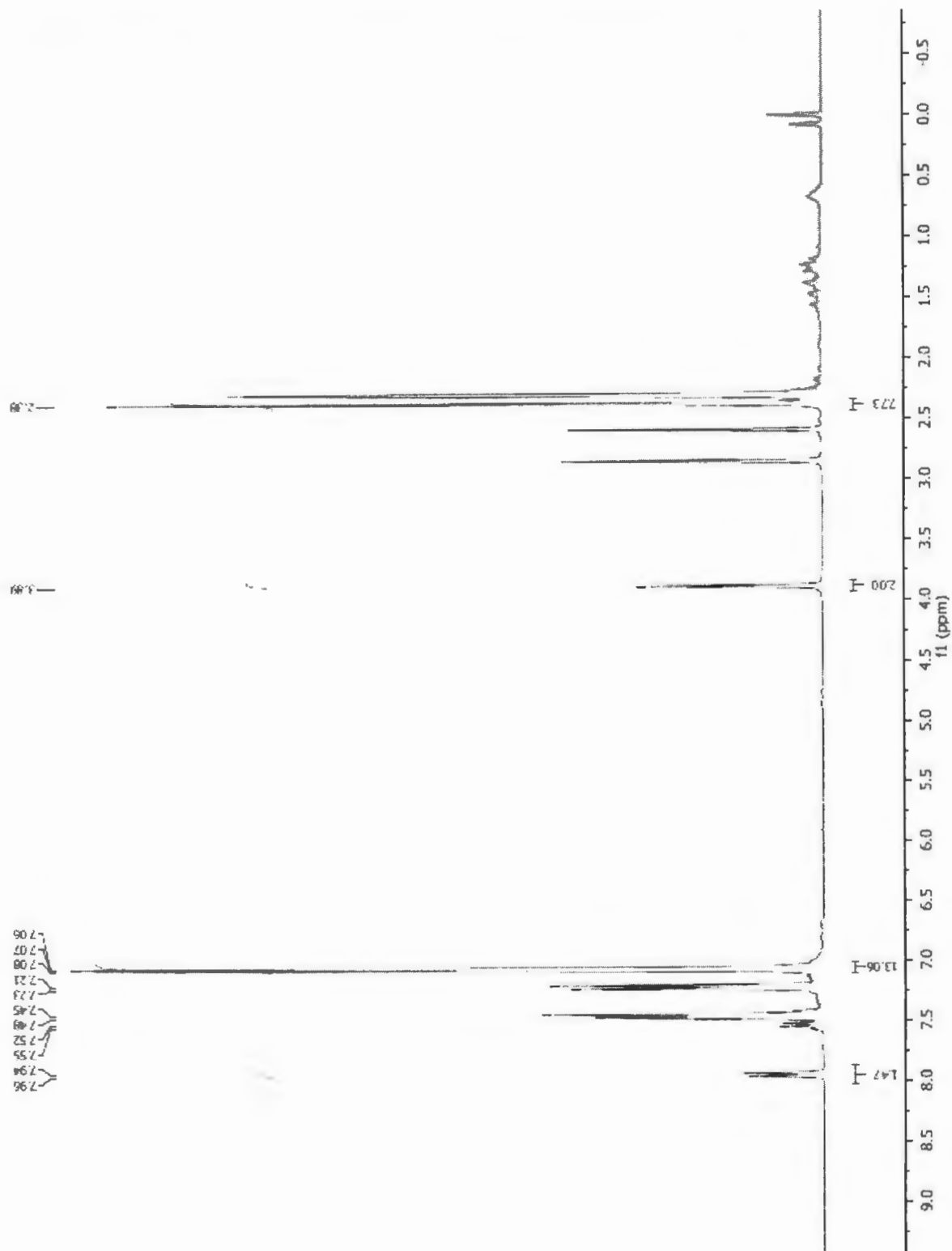
Abundance



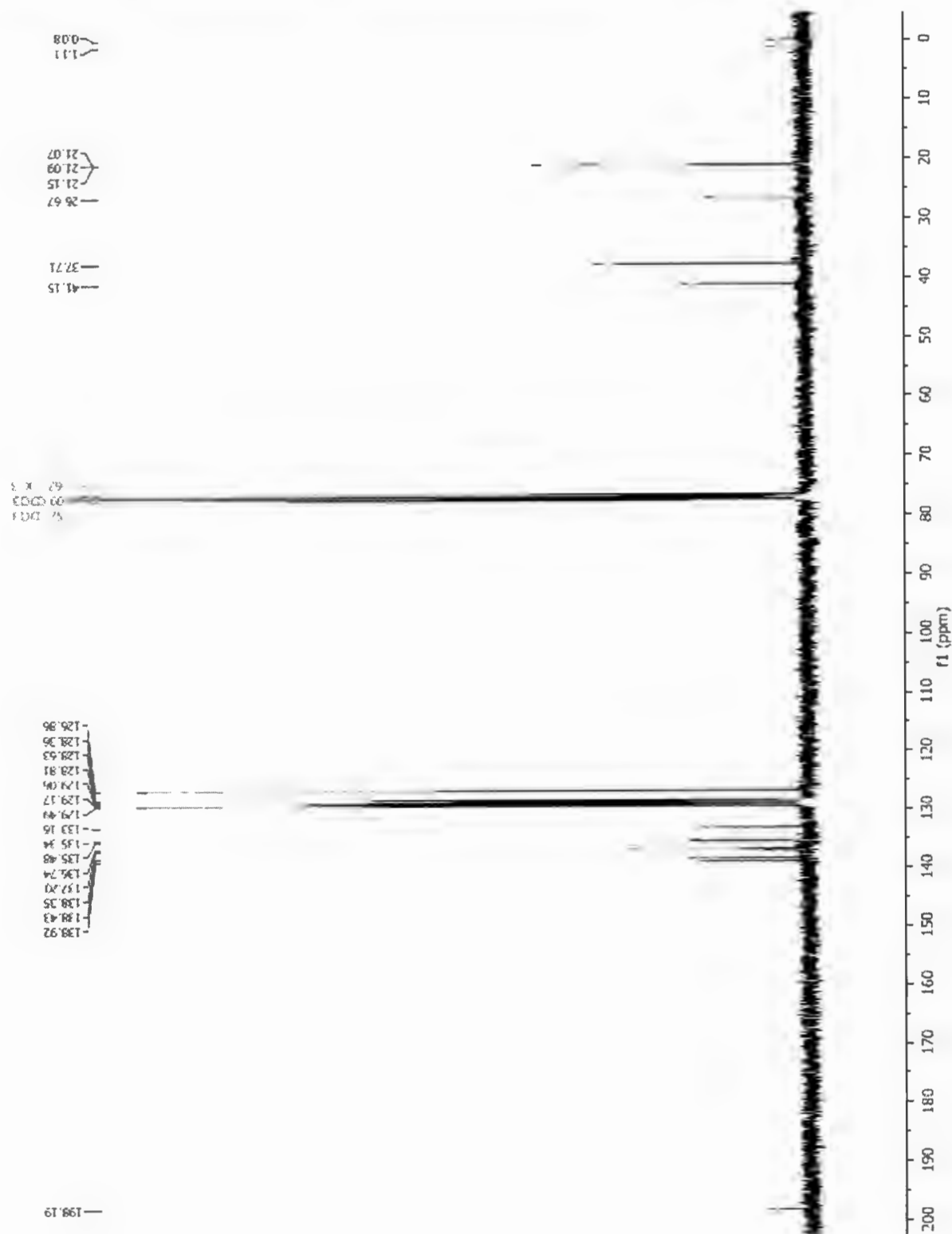
Abundance



FigureA78: ^1H NMR spectrum for Di-*p*-tolylmethane (Table 3.2, Entry 3).

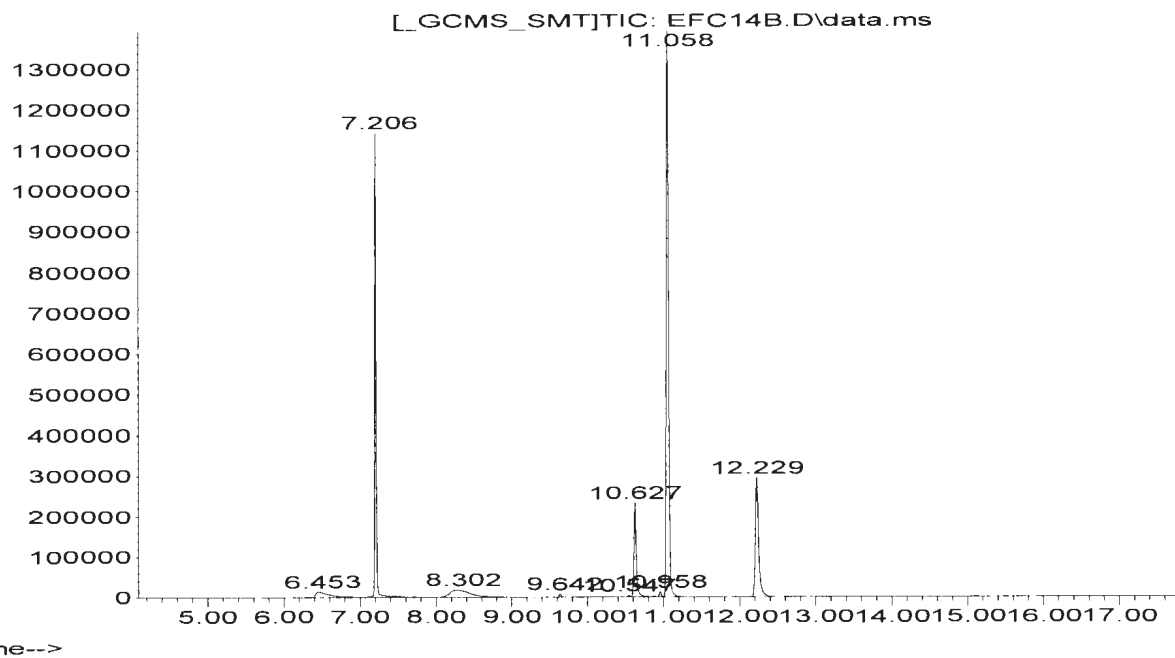


FigureA79: ^{13}C NMR spectrum for Di-*p*-tolylmethane (Table 3.2, Entry 3).

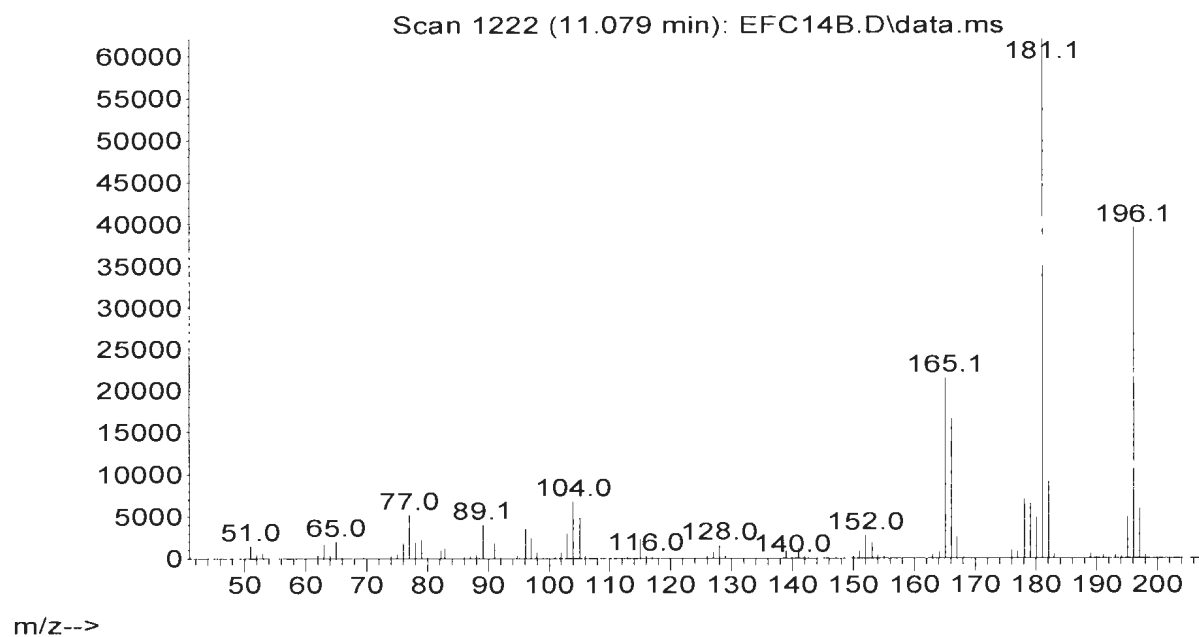


FigureA80: GC-MS analysis of **Di-*p*-tolylmethane** (Table 3.2, Entry 4). GC-MS retention time: m/z (% ion): 7.206 min dodecane; 10.627 min 4,4'-dimethylbiphenyl; 11.058 min di-*p*-tolylmethane; 12.249 min 4,4'-dimethylbibenzyl.

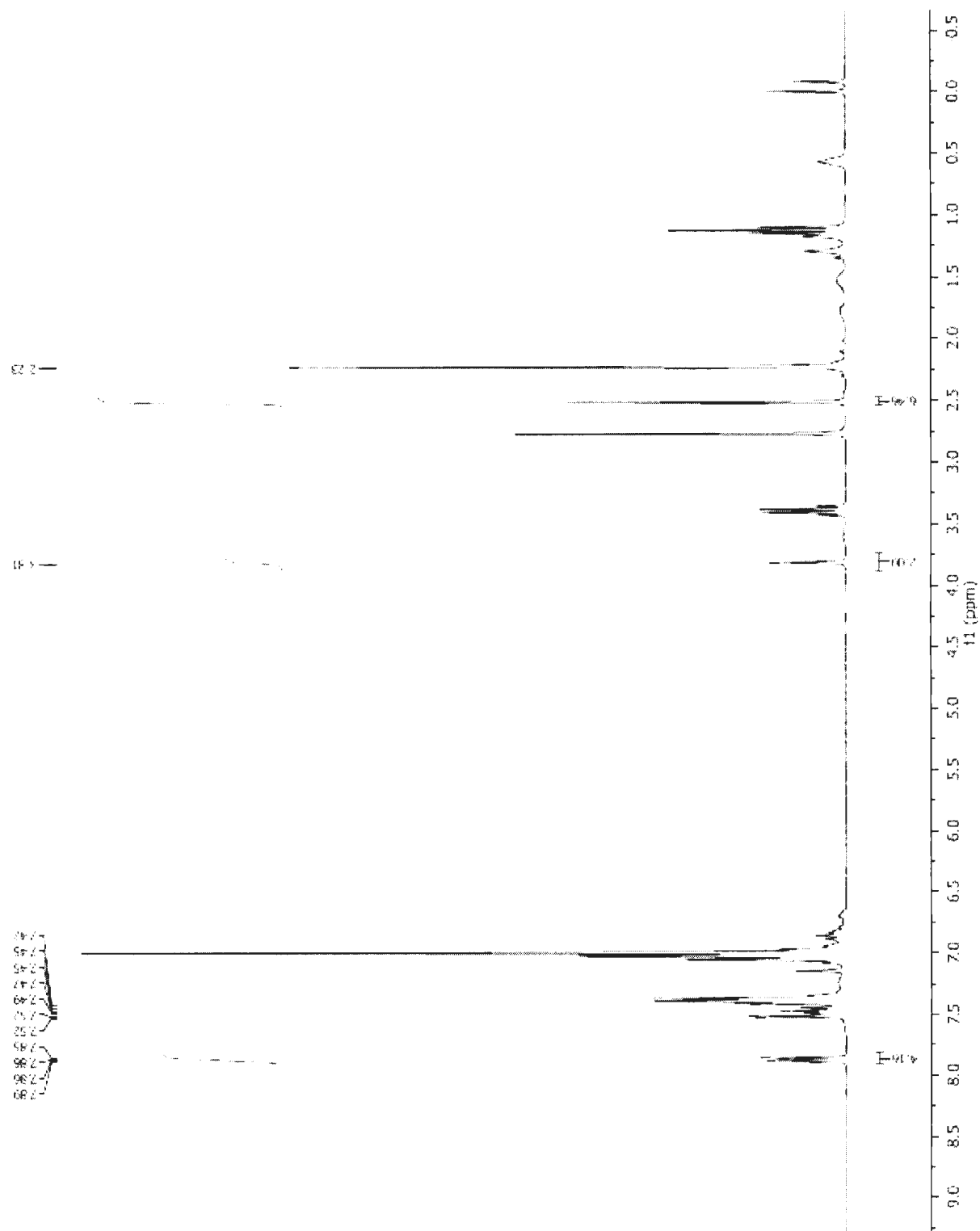
Abundance



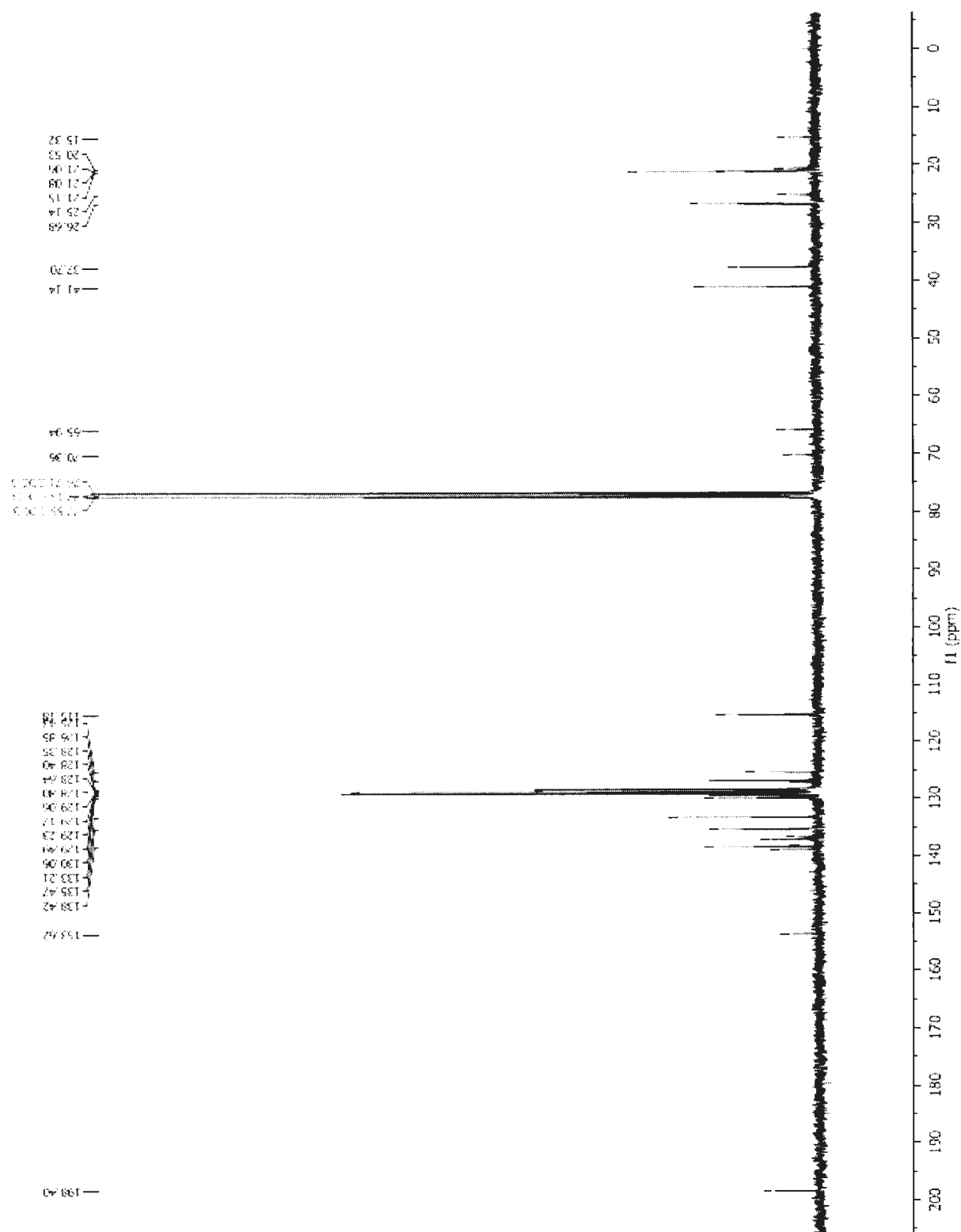
Abundance



FigureA81: ^1H NMR spectrum for Di-*p*-tolylmethane (Table 3.2, Entry 4).

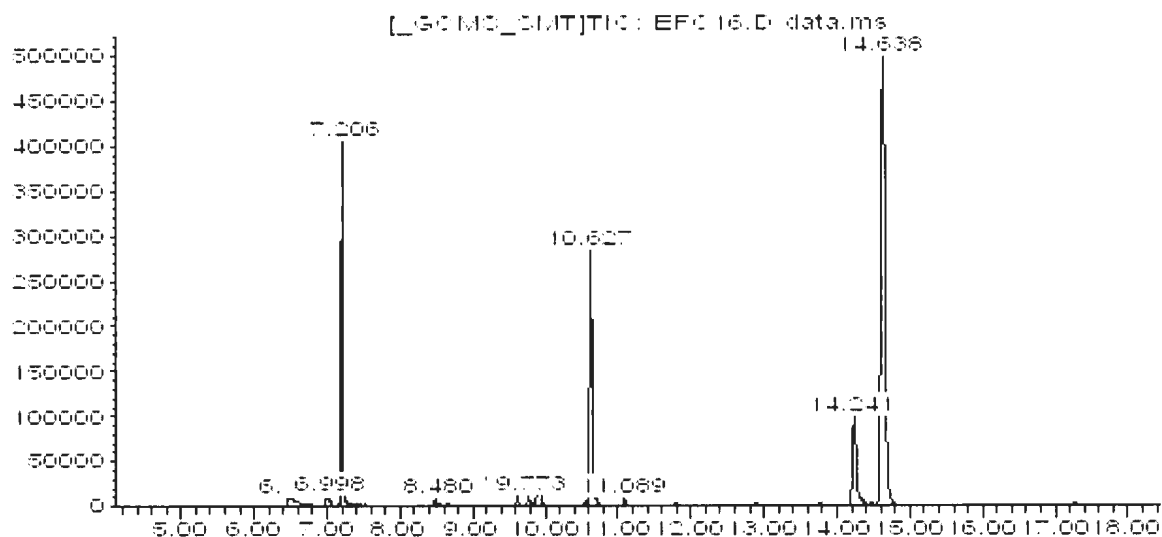


FigureA82: ^{13}C NMR spectrum for Di-*p*-tolylmethane (Table 3.2, Entry 4).

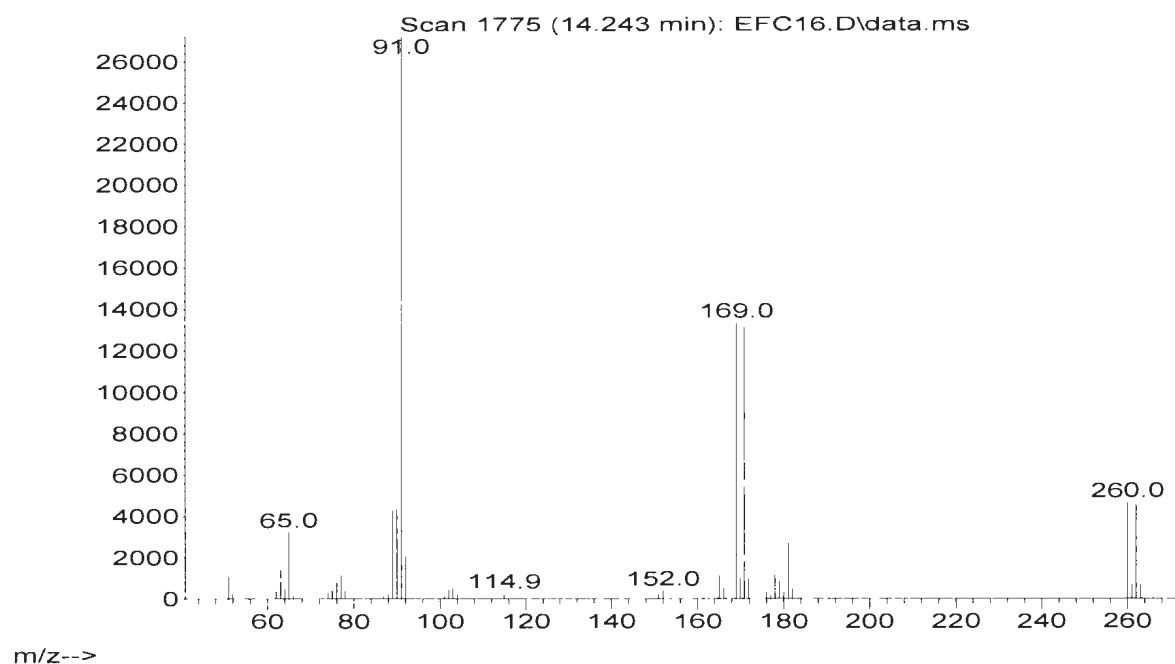


FigureA83: GC-MS analysis of **1-Bromo-4-(4-methylbenzyl)benzene** (Table 3.2, Entry 5). GC-MS retention time: 7.205 min dodecane; 10.627 min 4,4'-dimethylbiphenyl; 14.241 min 1-bromo-4-(2-phenylethyl)benzene; 14.638 min 1-bromo-4-(4-methylbenzyl)benzene.

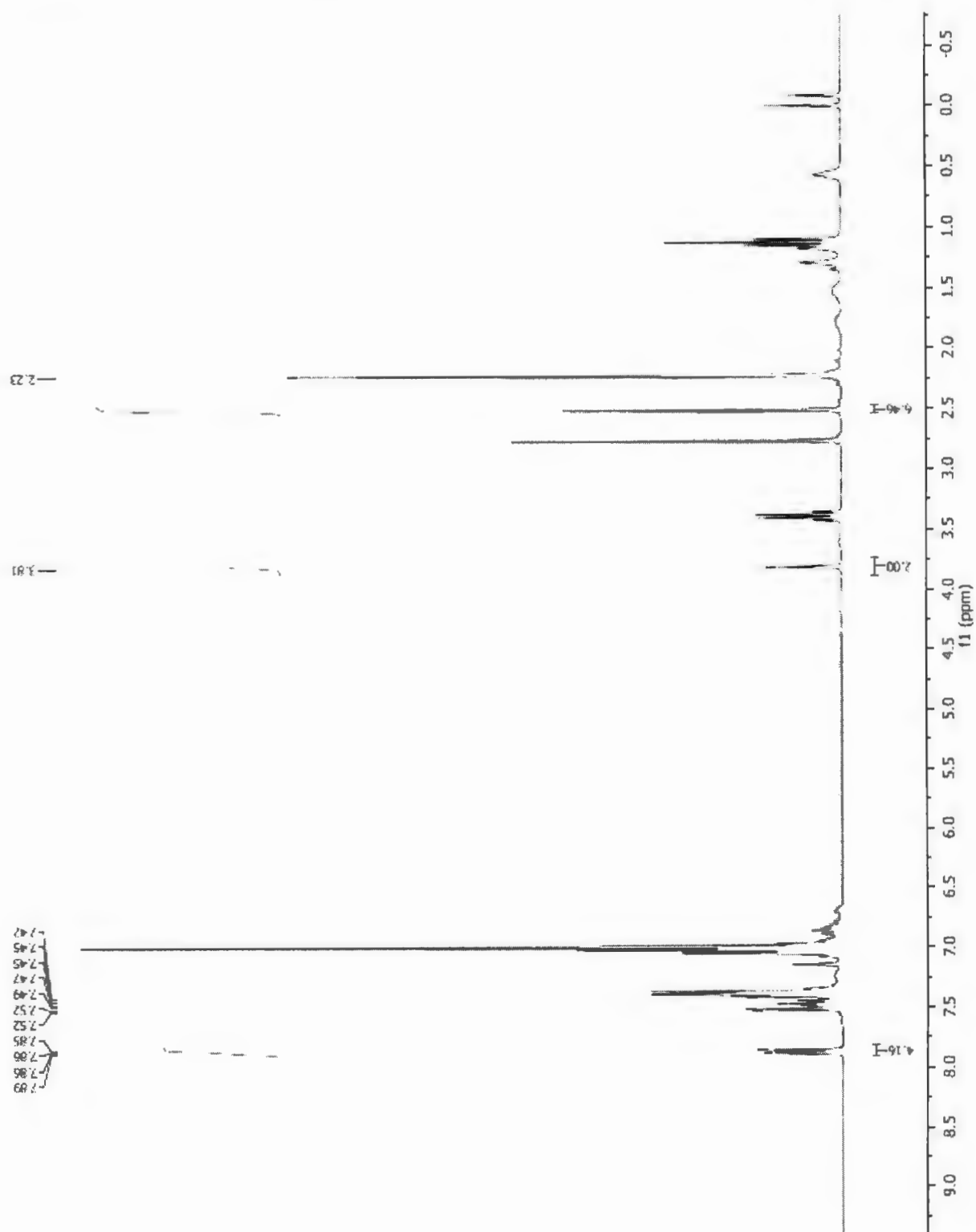
Abundance



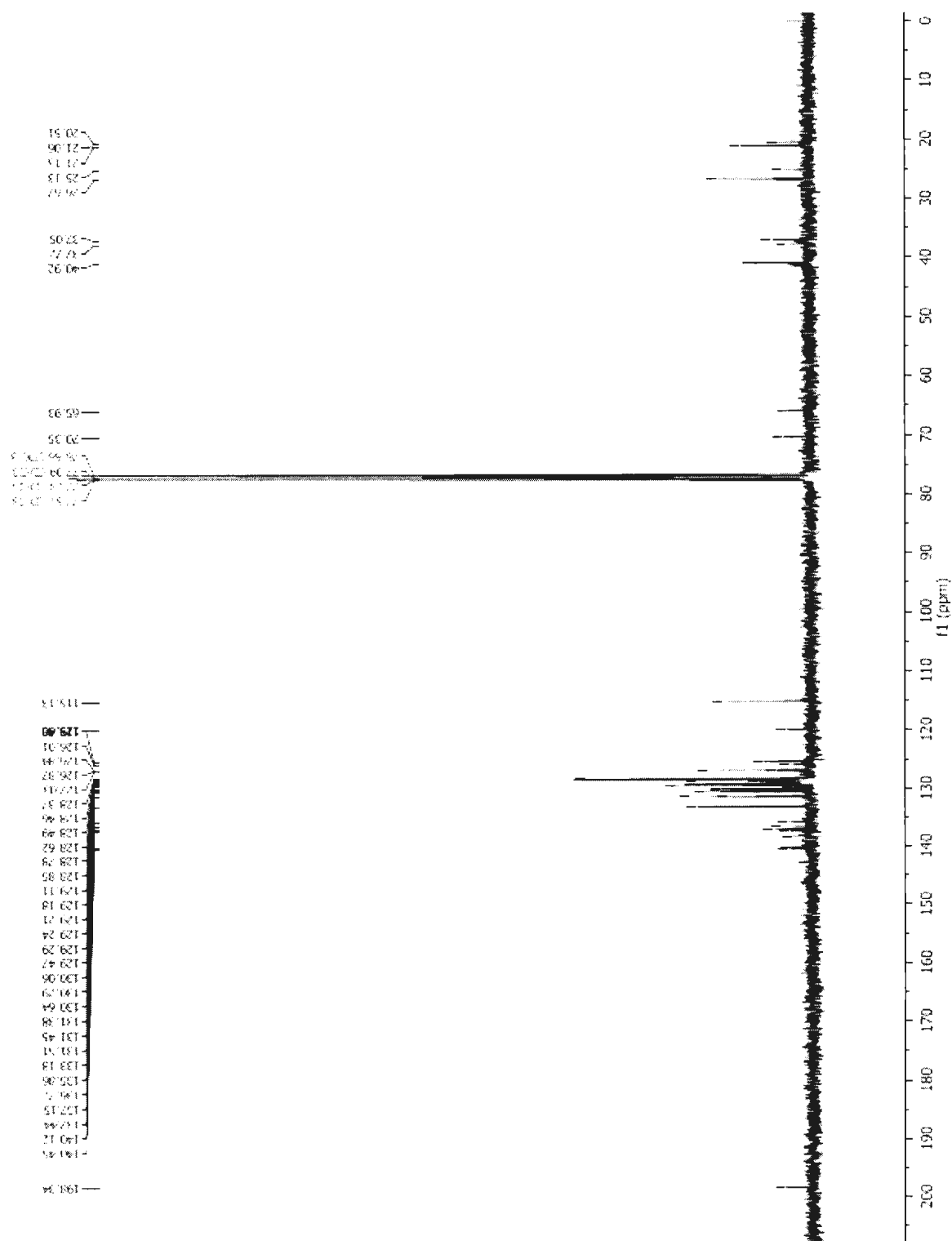
Abundance



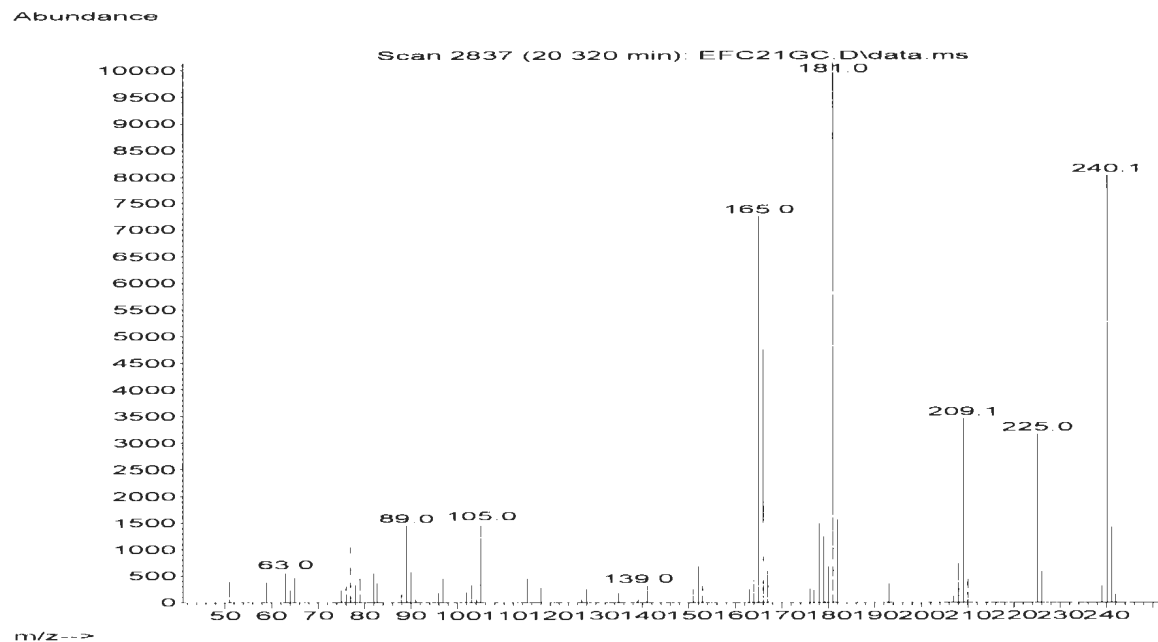
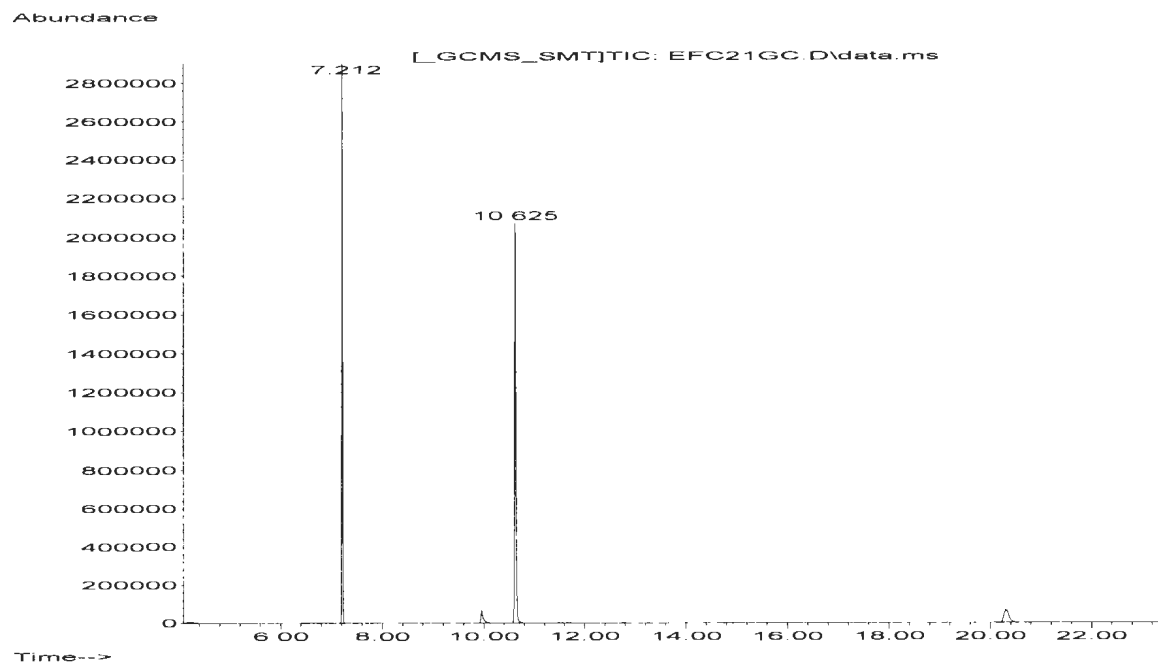
FigureA84: ^1H NMR spectrum for 1-Bromo-4-(4-methylbenzyl)benzene (Table 3.2, Entry 5).



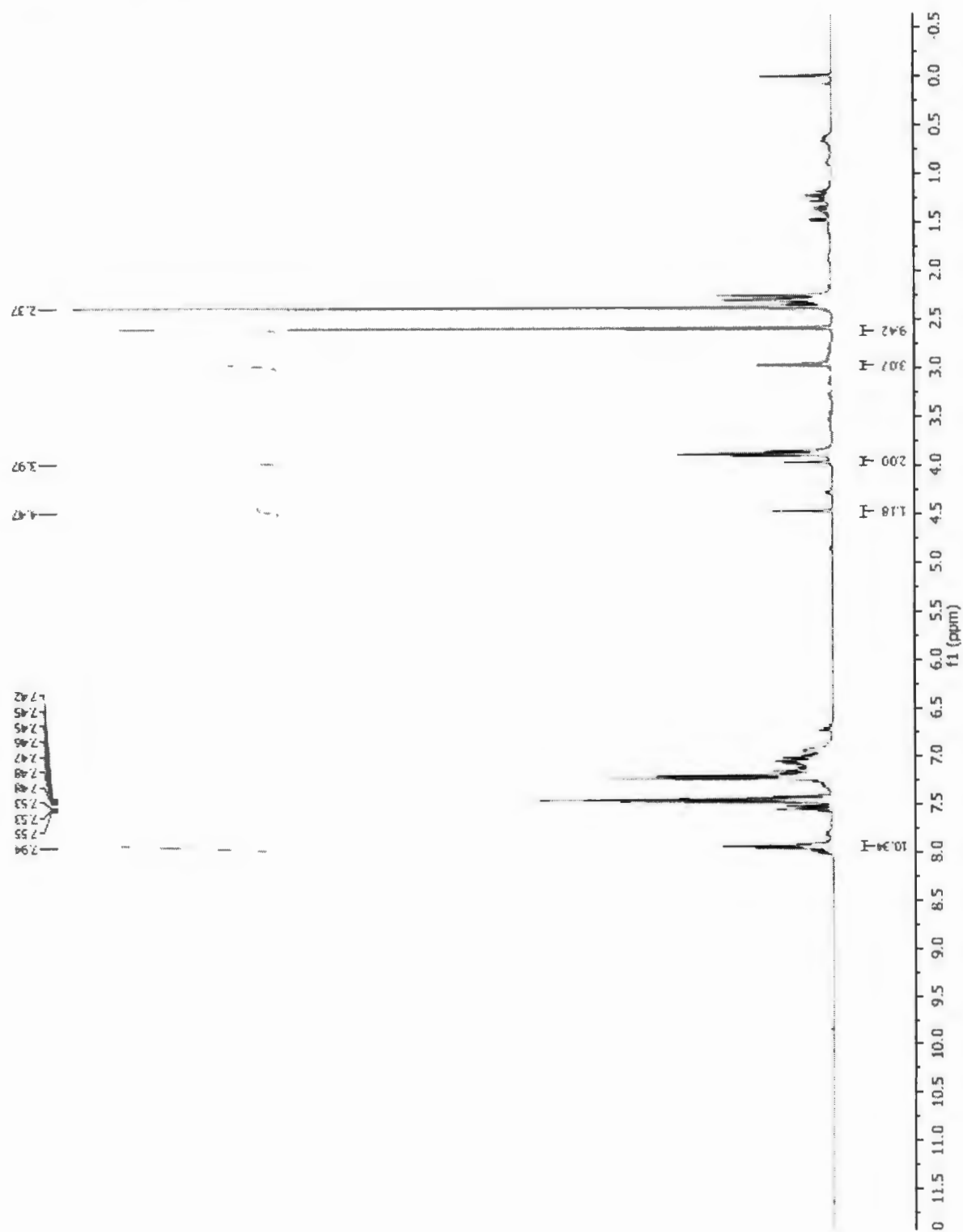
FigureA85: ¹³C NMR spectrum for **1-Bromo-4-(4-methylbenzyl)benzene** (Table 3.2, Entry 5).



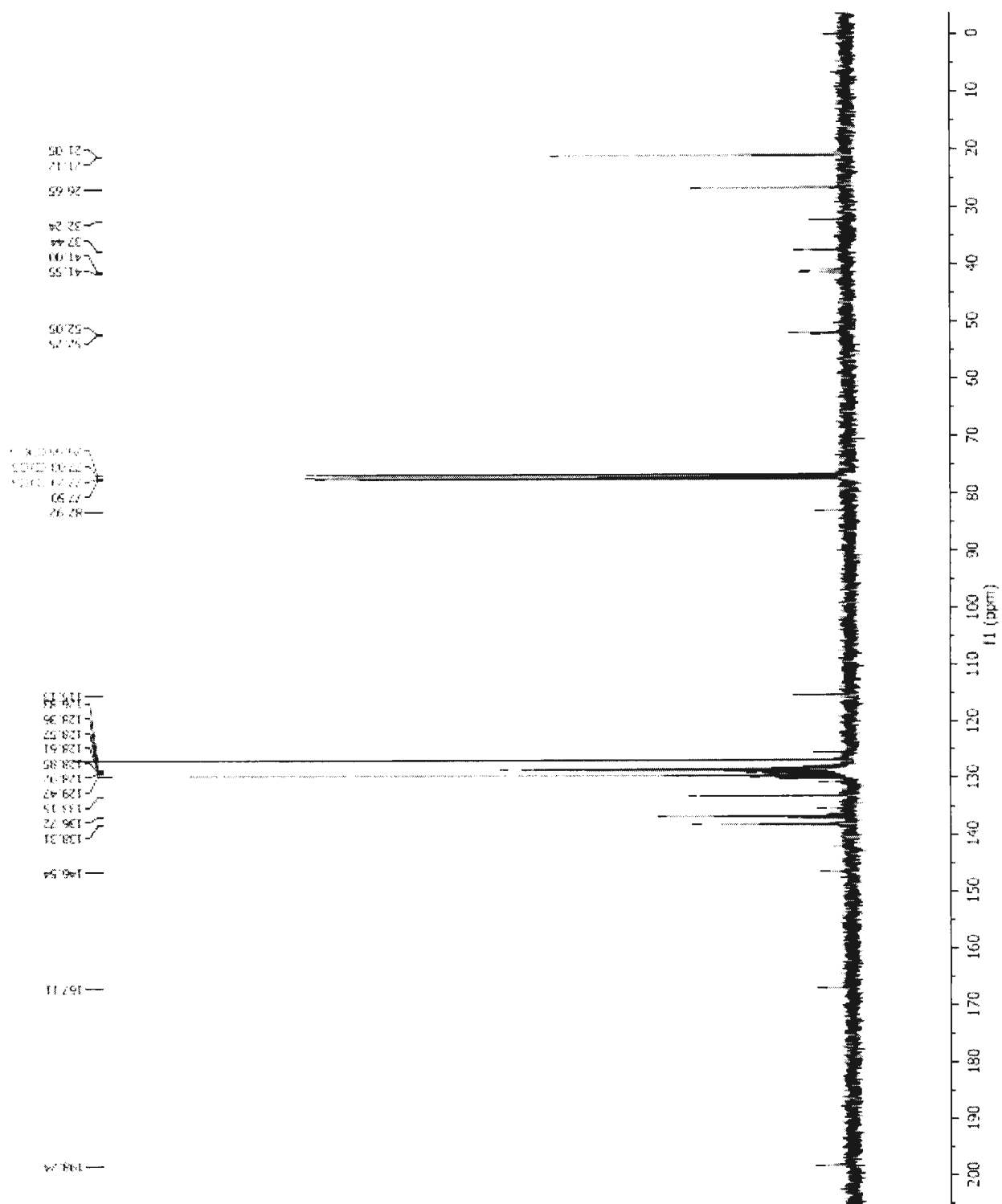
FigureA86: GC-MS analysis of **Methyl-4-(4-methylbenzyl)benzoate** (Table 3.2, Entry 6). GC-MS retention time: 7.212 min dodecane; 10.625 min 4,4'-dimethylbiphenyl; 20.320 min methyl-4-(4-methylbenzyl)benzoate.



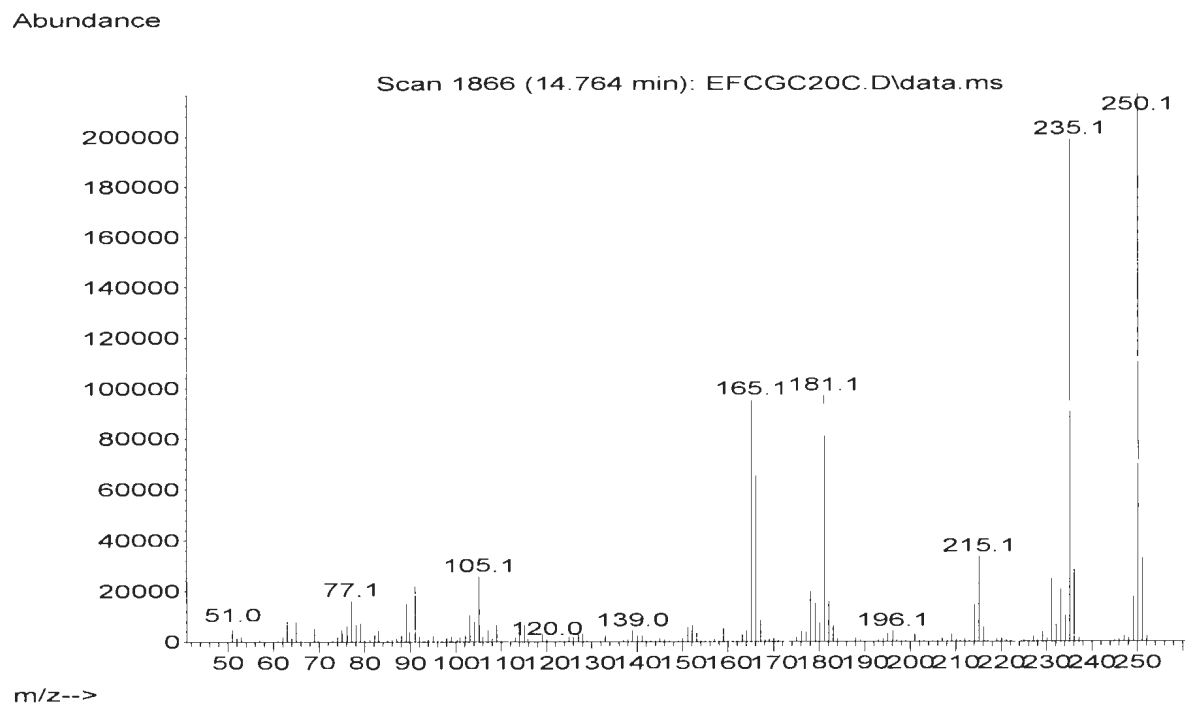
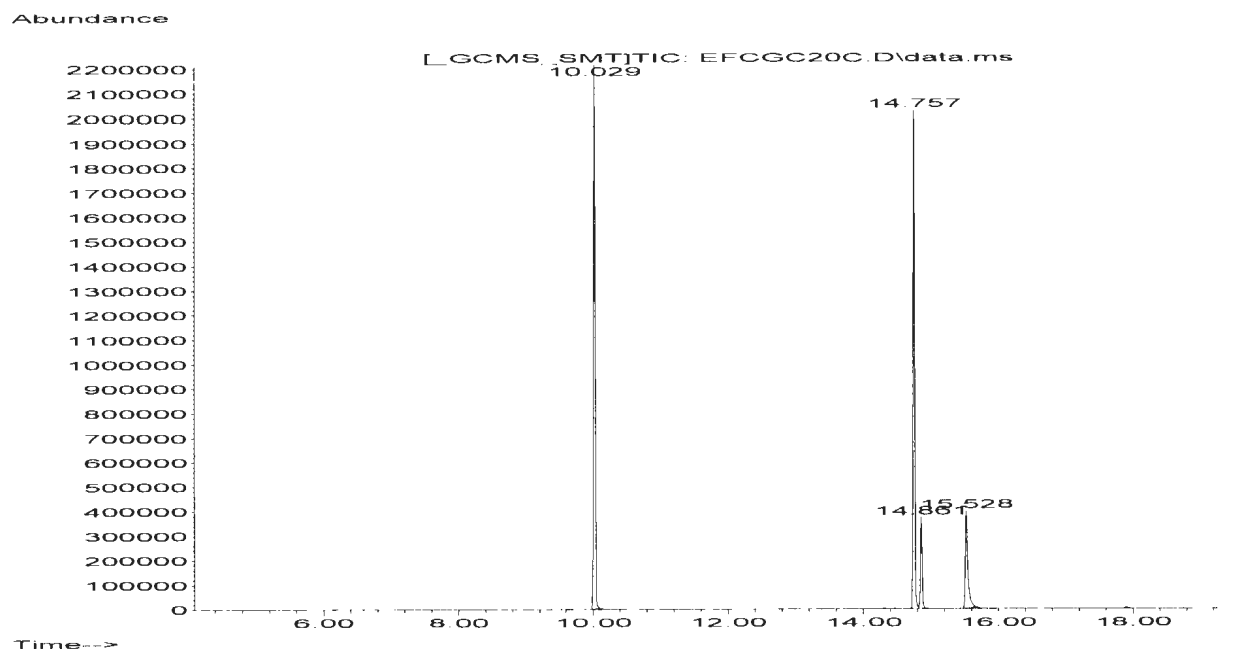
FigureA87: ^1H NMR spectrum for Methyl-4-(4-methylbenzyl)benzoate (Table 3.2, Entry 6).



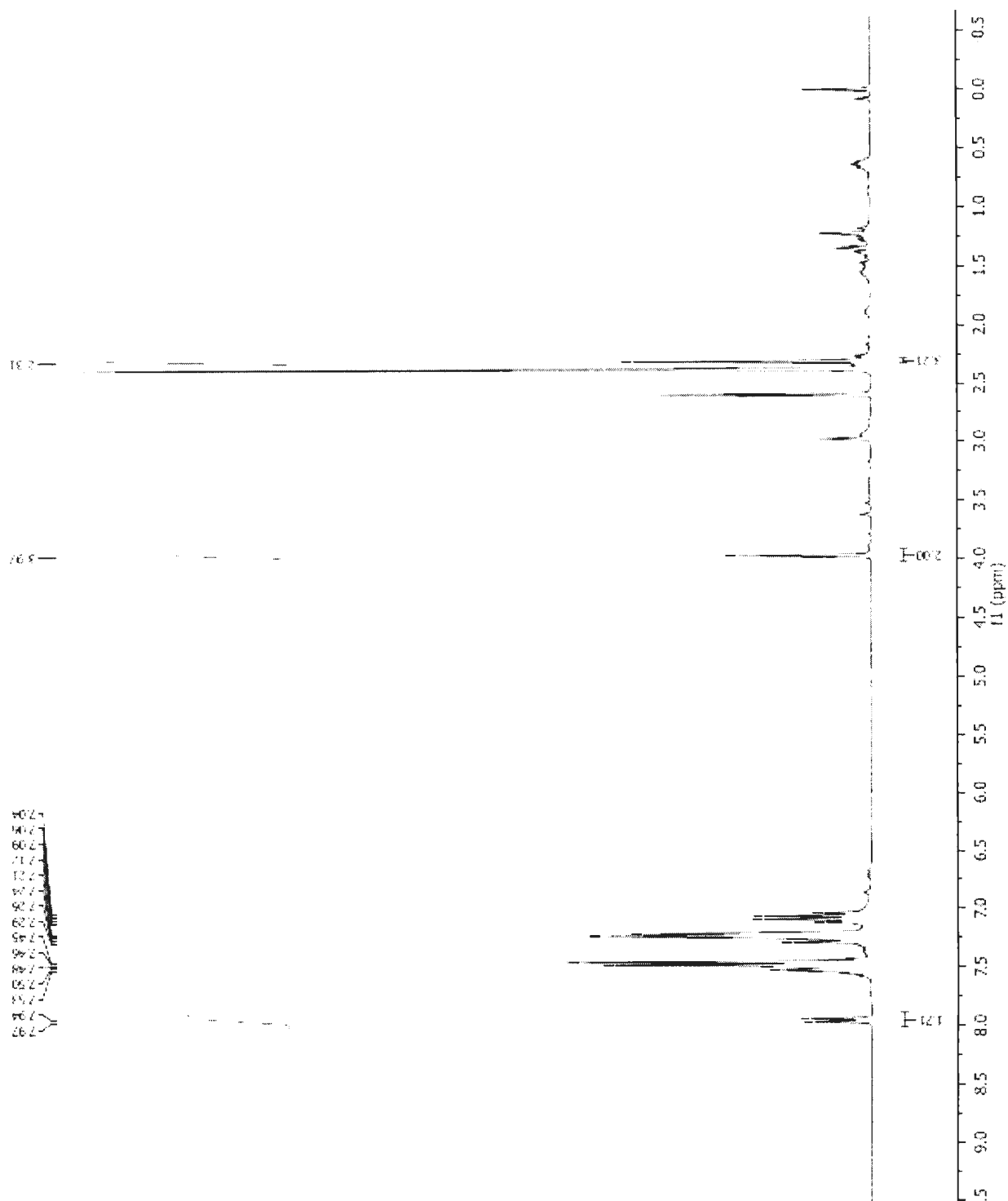
FigureA88: ^{13}C NMR spectrum for Methyl-4-(4-methylbenzyl)benzoate (Table 3.2, Entry 6).



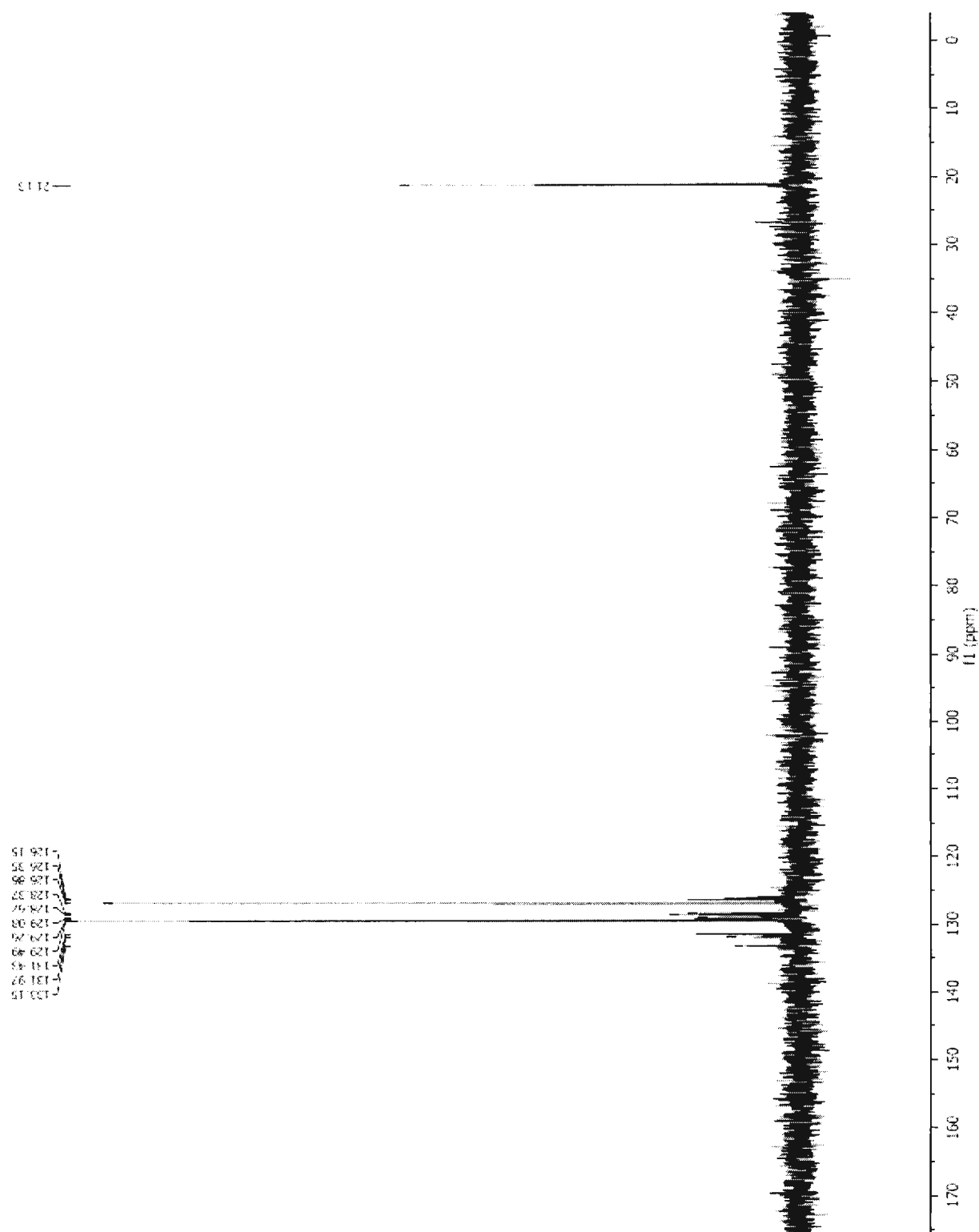
FigureA89: GC-MS analysis of **1-Methyl-4-(4-(trifluoromethyl)benzyl)benzene** (**Table 3.2, Entry 7**). GC-MS retention time: 10.029 min dodecane; 14.757 min 1-methyl-4-(4-(trifluoromethyl)benzyl)benzene; 14.861 min 4,4'-(trifluoromethyl)bibenzyl; 15.528 min 4,4'-dimethylbiphenyl.



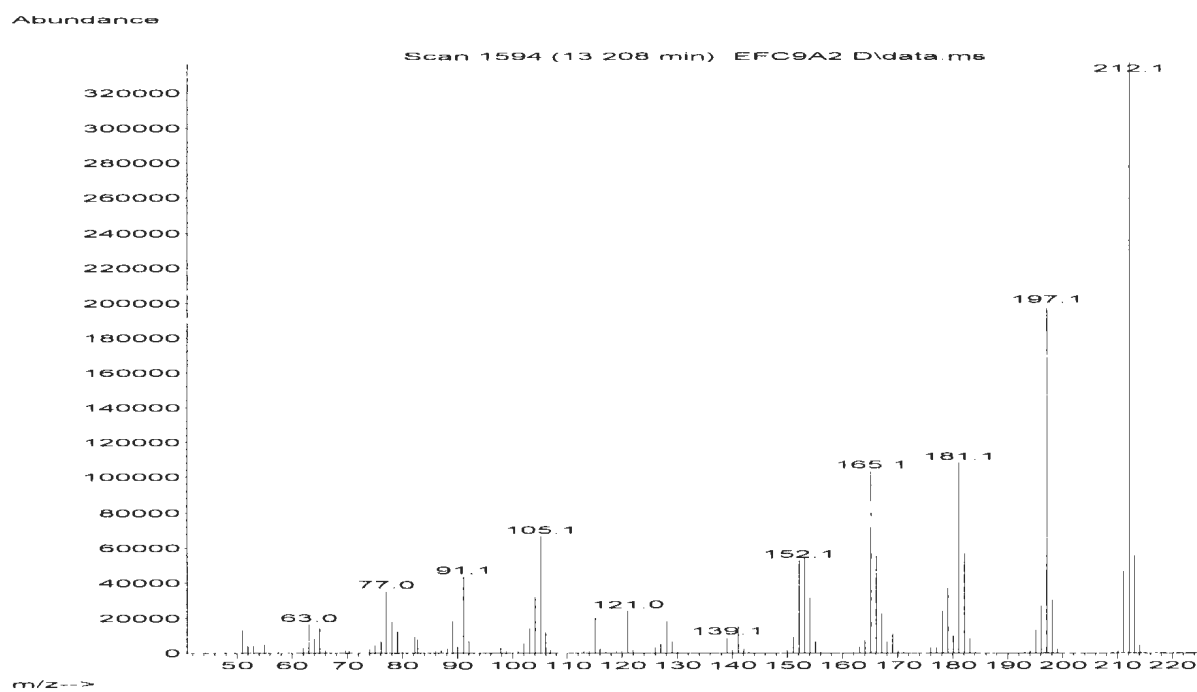
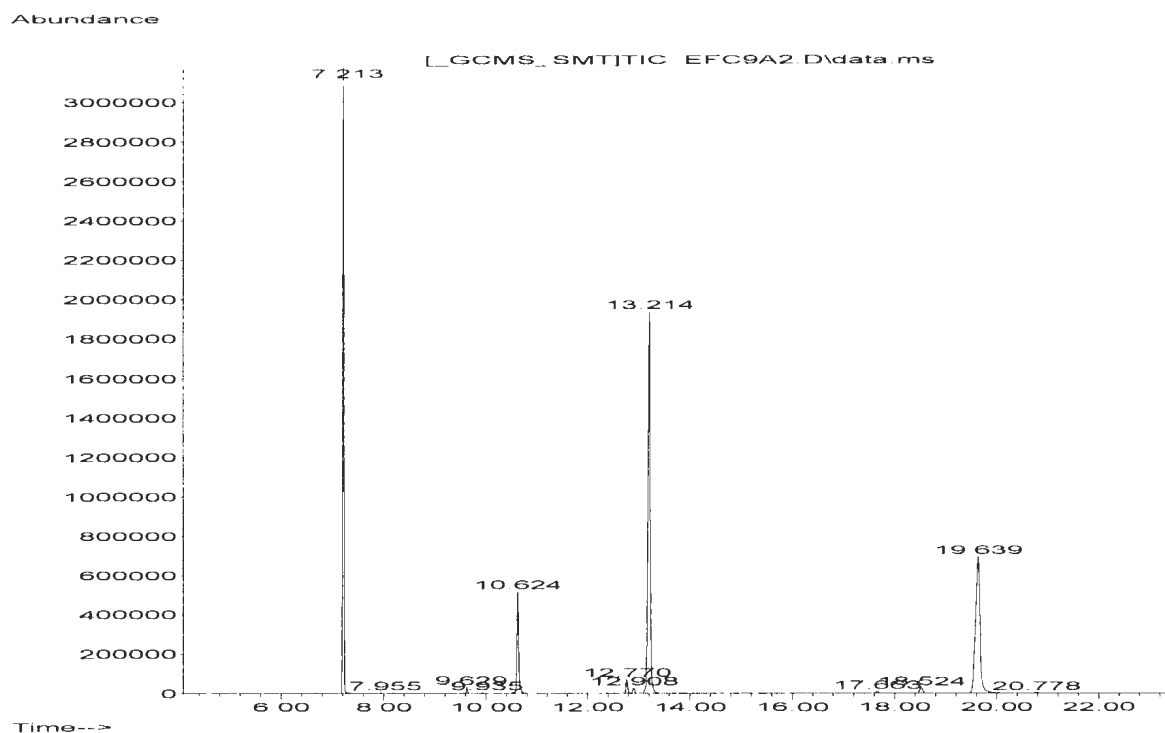
FigureA90: ¹H NMR spectrum for 1-Methyl-4-(4-(trifluoromethyl)benzyl)benzene (Table 3.2, Entry 7).



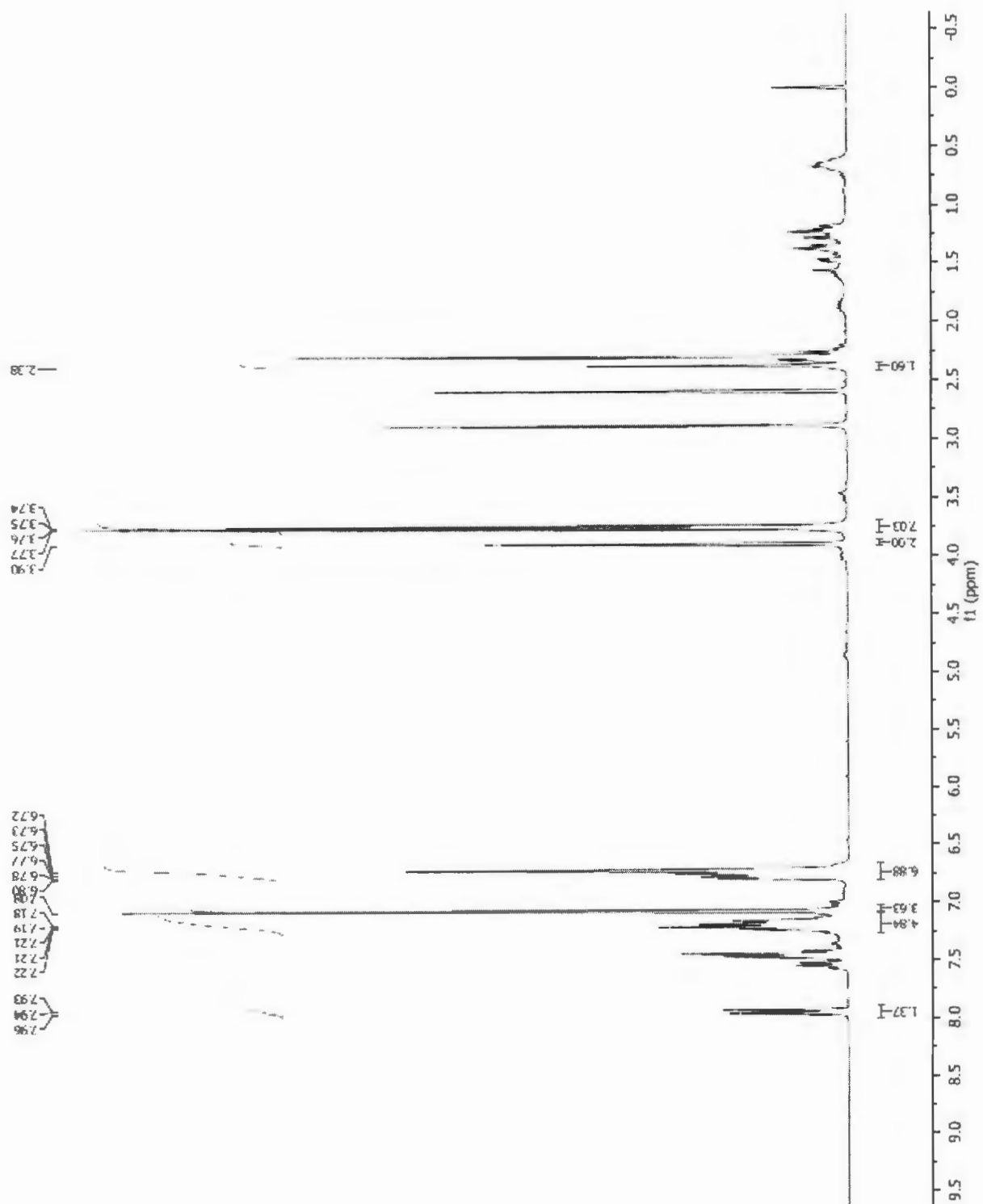
FigureA91: ^{13}C NMR spectrum for 1-Methyl-4-(4-(trifluoromethyl)benzyl)benzene (Table 3.2, Entry 7).



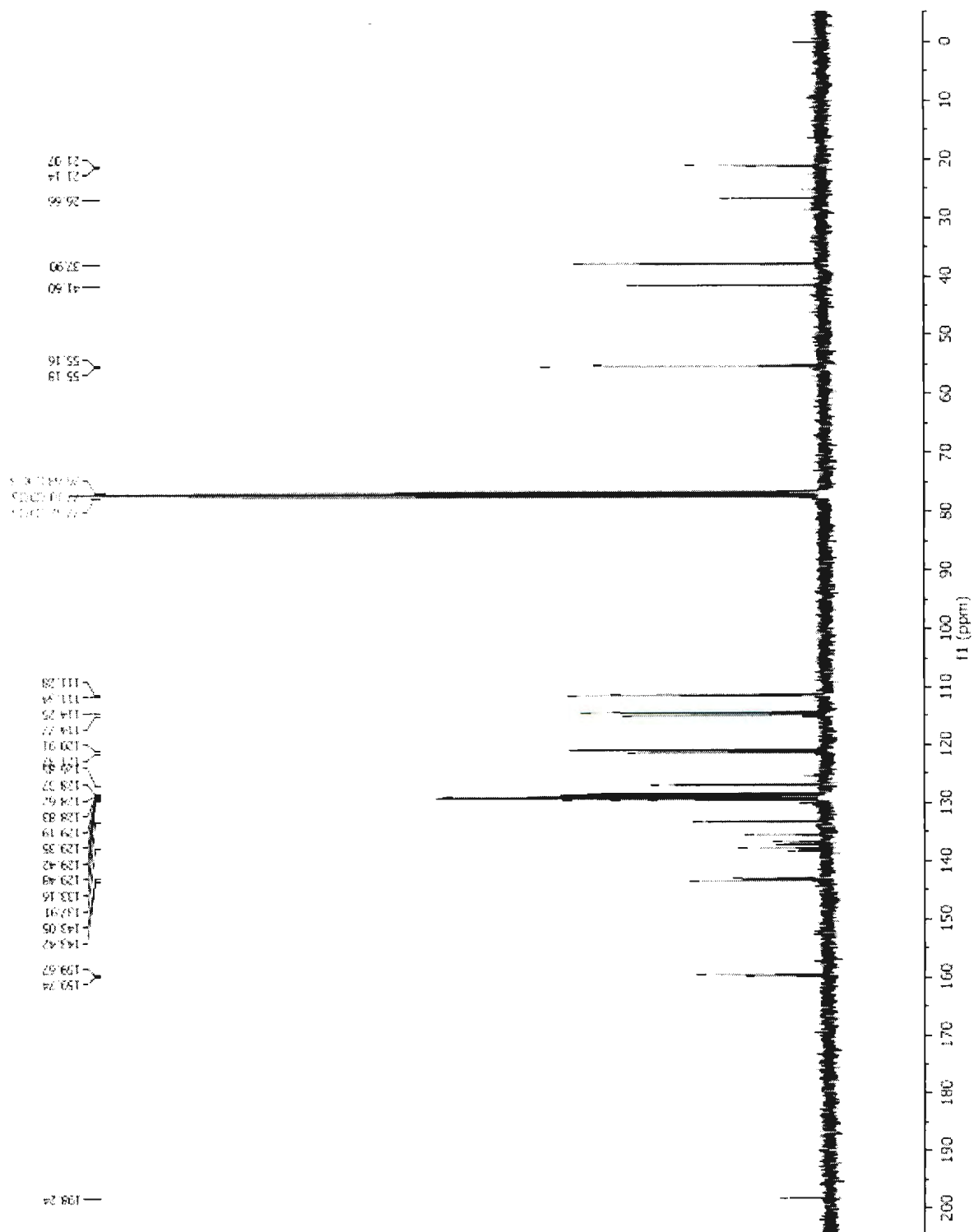
FigureA92: GC-MS analysis of 1-Methoxy-3-(4-methylbenzyl)benzene (Table 3.3, Entry 1). GC-MS retention time: 7.213 min dodecane; 10.624 min 4,4'-dimethylbiphenyl; 13.214 min 1-methoxy-3-(4-methylbenzyl)benzene; 19.639 min 3,3'-(dimethoxy)bibenzyl.



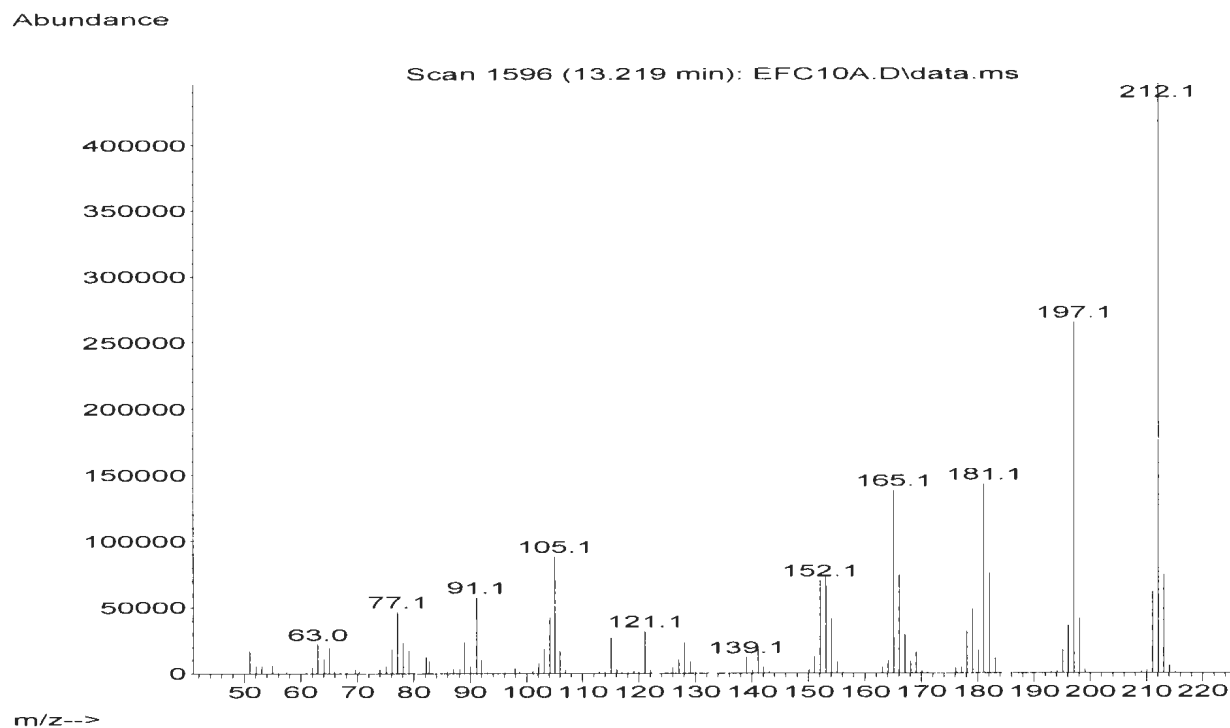
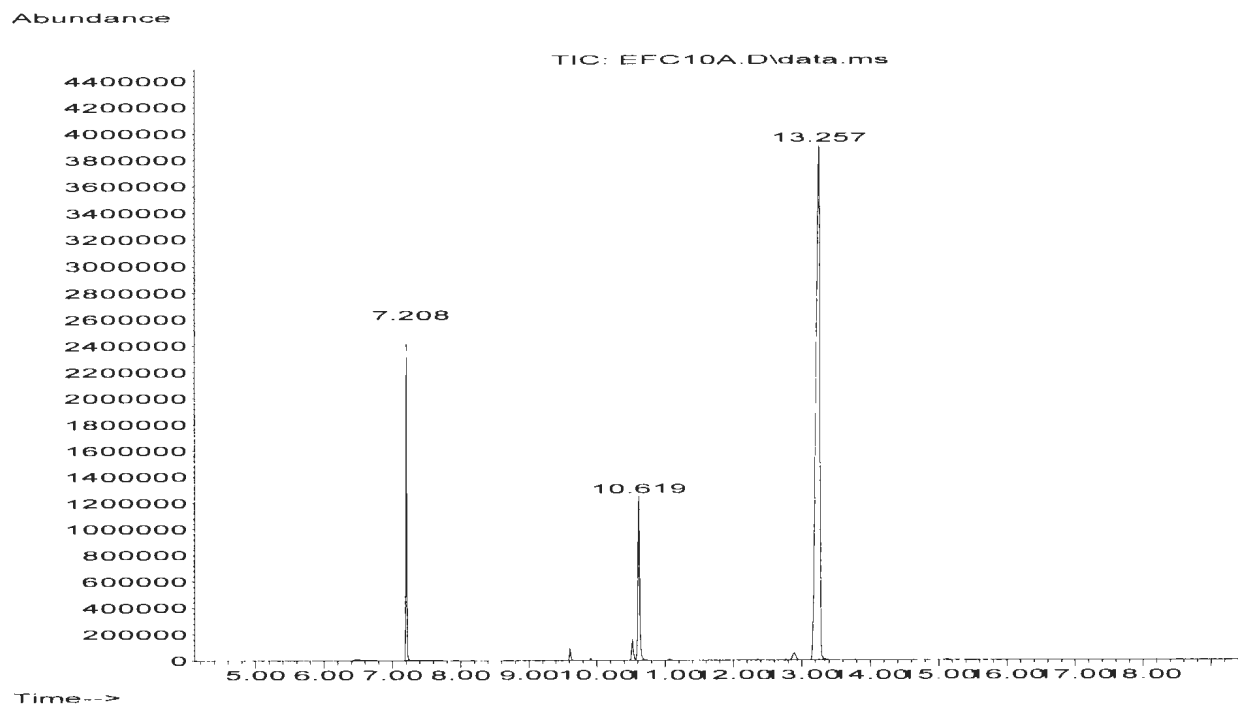
FigureA93: ^1H NMR spectrum for 1-Methoxy-3-(4-methylbenzyl)benzene (Table 3.3, Entry 1).



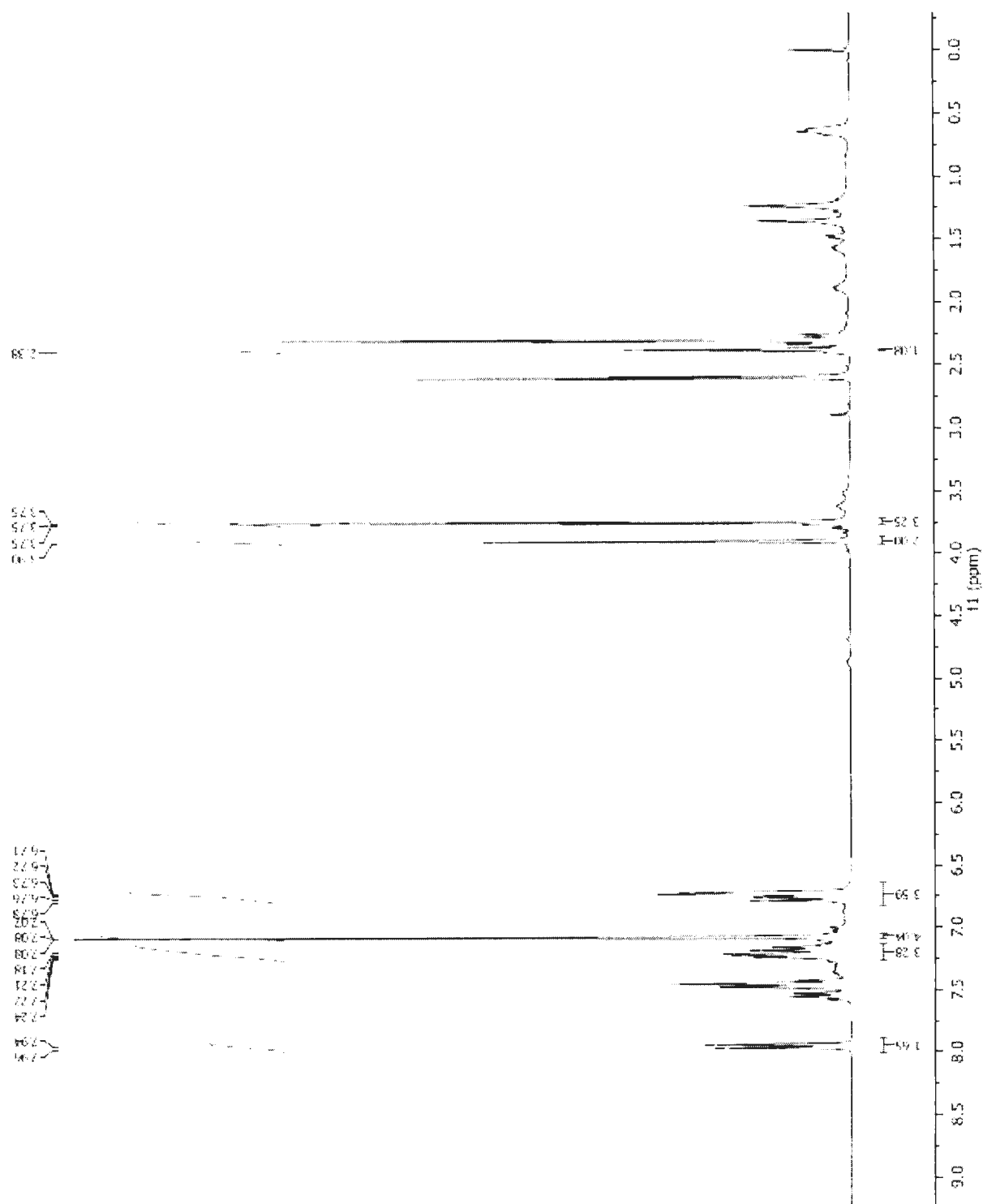
FigureA94: ^{13}C NMR spectrum for **1-Methoxy-3-(4-methylbenzyl)benzene** (Table 3.3, Entry 1).



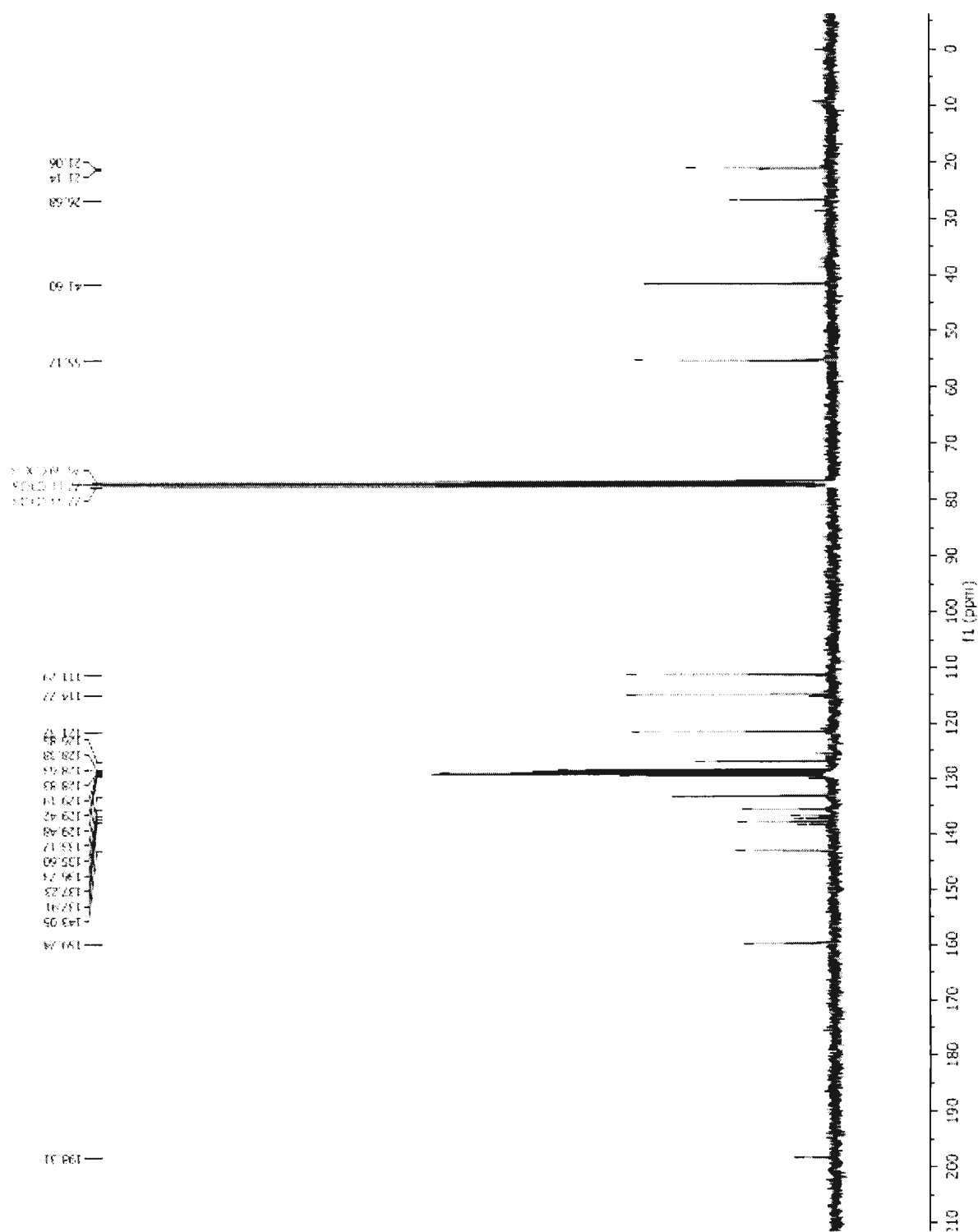
FigureA95: GC-MS analysis of **1-Methoxy-3-(4-methylbenzyl)benzene** (Table 3.3, Entry 2). GC-MS retention time: 7.208 min dodecane; 10.619 min 4,4'-dimethylbiphenyl; 13.257 min 1-methoxy-3-(4-methylbenzyl)benzene.



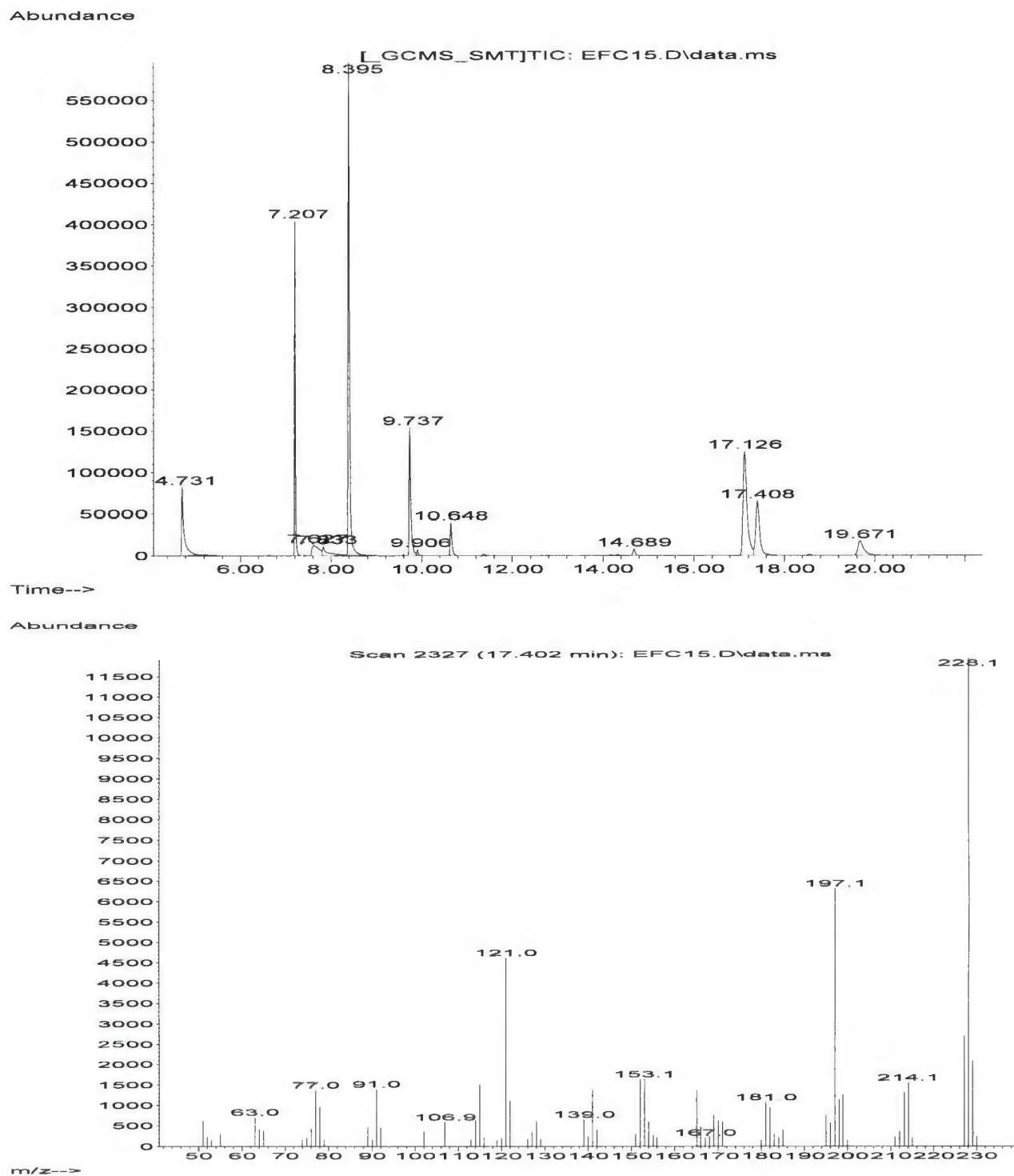
FigureA96: ^1H NMR spectrum for 1-Methoxy-3-(4-methylbenzyl)benzene (Table 3.3, Entry 2).



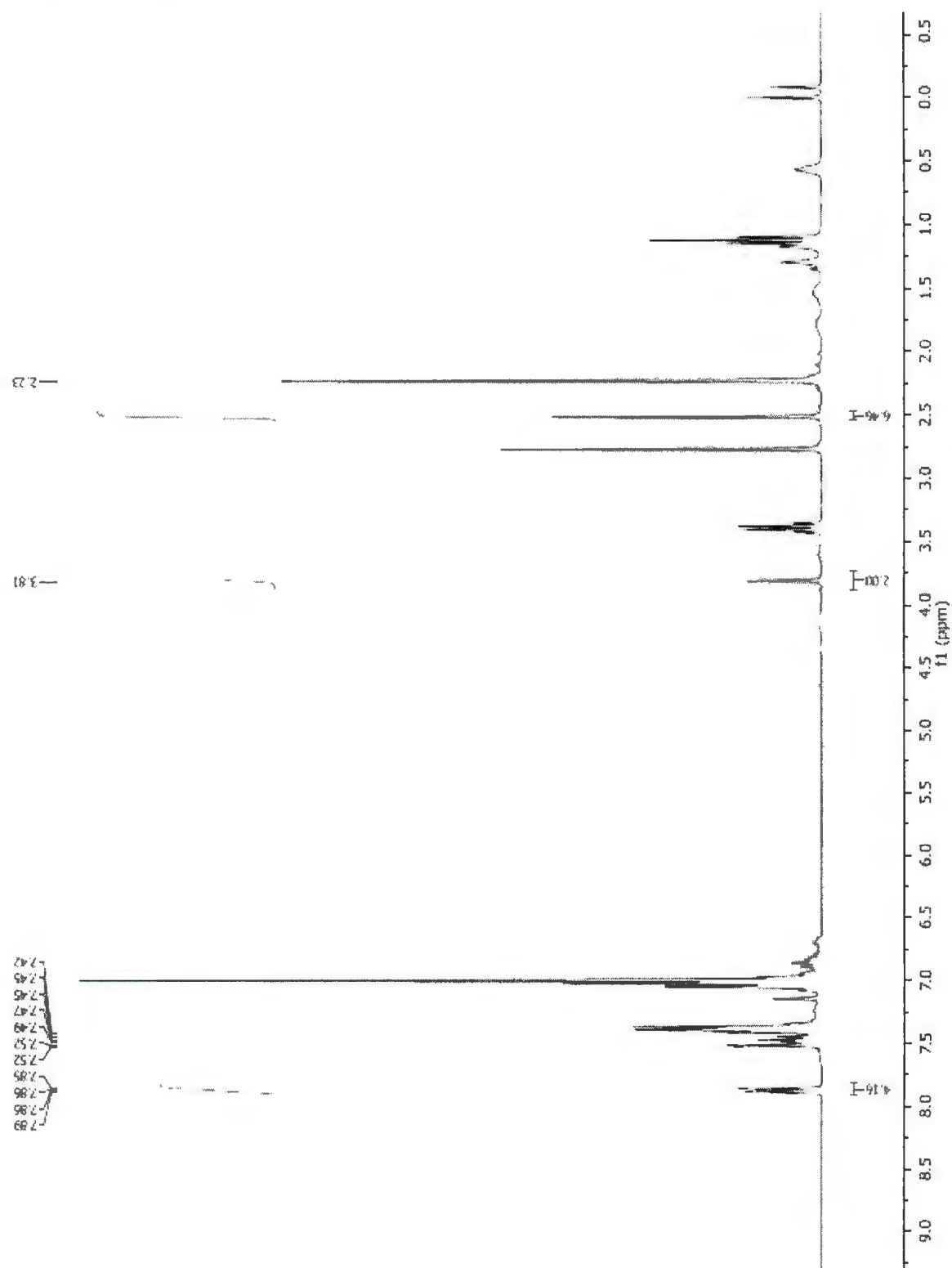
FigureA97: ^{13}C NMR spectrum for **1-Methoxy-3-(4-methylbenzyl)benzene** (Table 3.3, Entry 2).



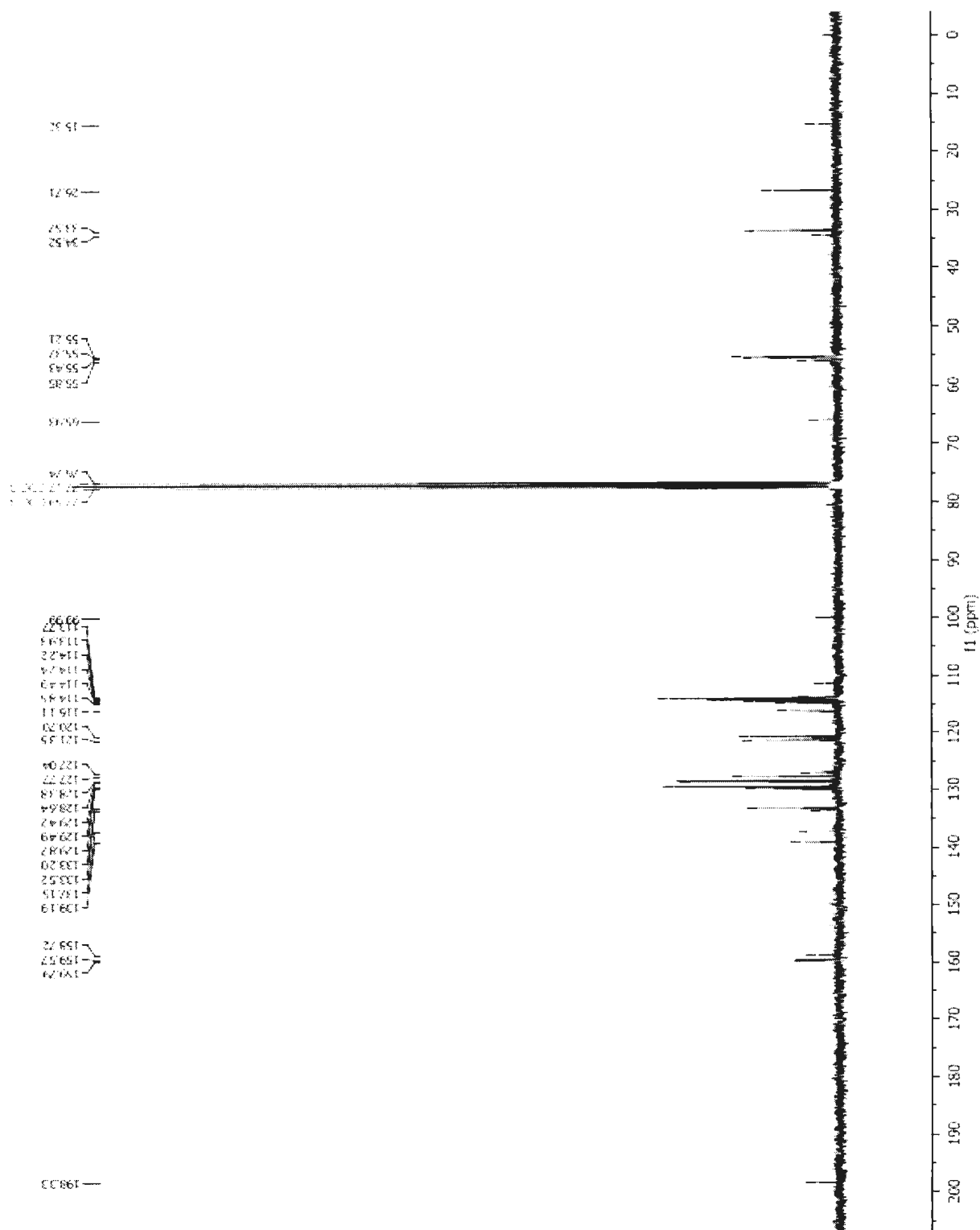
FigureA98: GC-MS analysis of 1-Methoxy-3-(4-methoxybenzyl)benzene (Table 3.3, Entry 3). GC-MS retention time: 7.207 min dodecane; 8.395 min 3-methoxybenzyl bromide; 17.126 min 4,4'-dimethoxybiphenyl; 17.408 min 1-methoxy-3-(4-methoxybenzyl)benzene; 19.671 min 3,3'-(dimethoxy)bibenzyl.



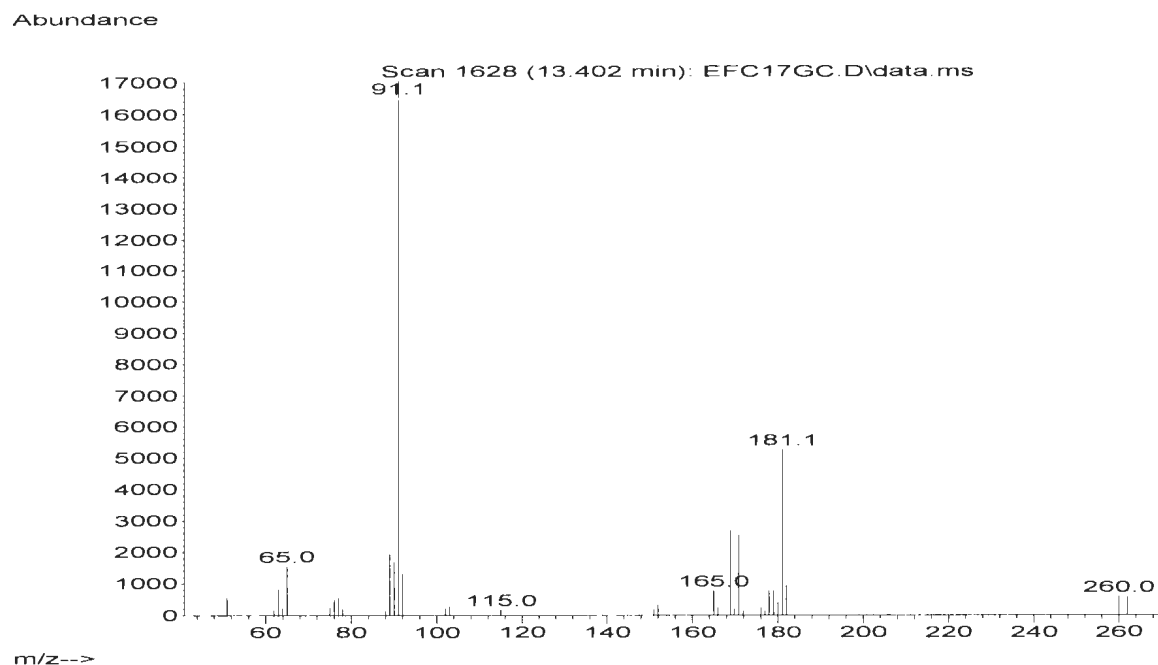
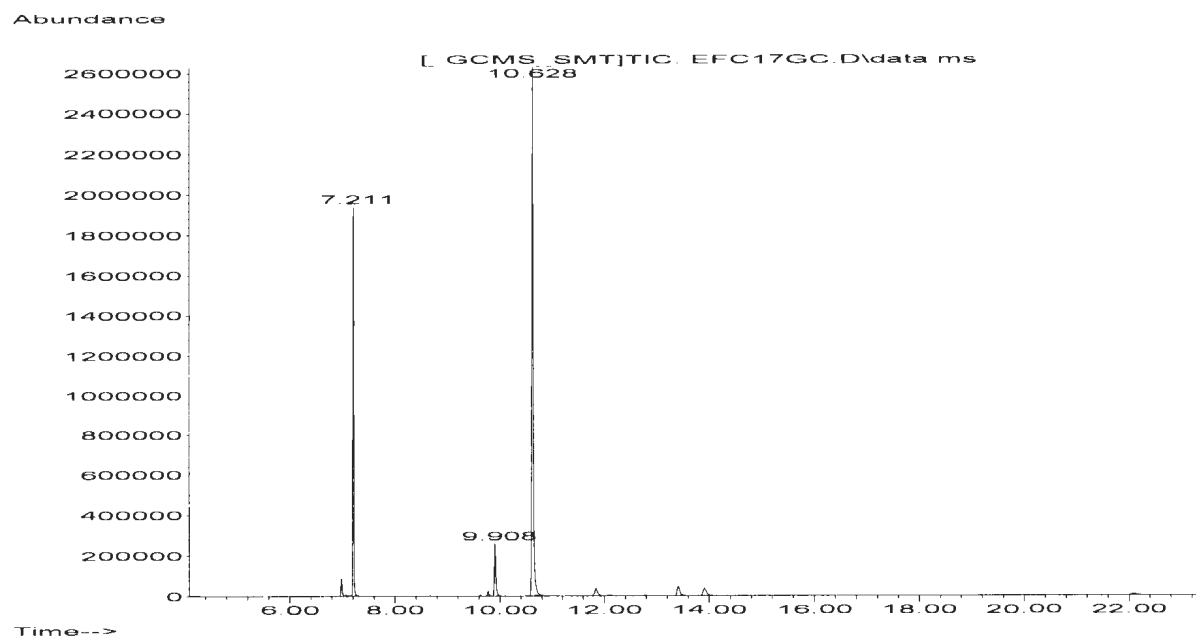
FigureA99: ^1H NMR spectrum for **1-Methoxy-3-(4-methoxybenzyl)benzene** (Table 3.3, Entry 3).



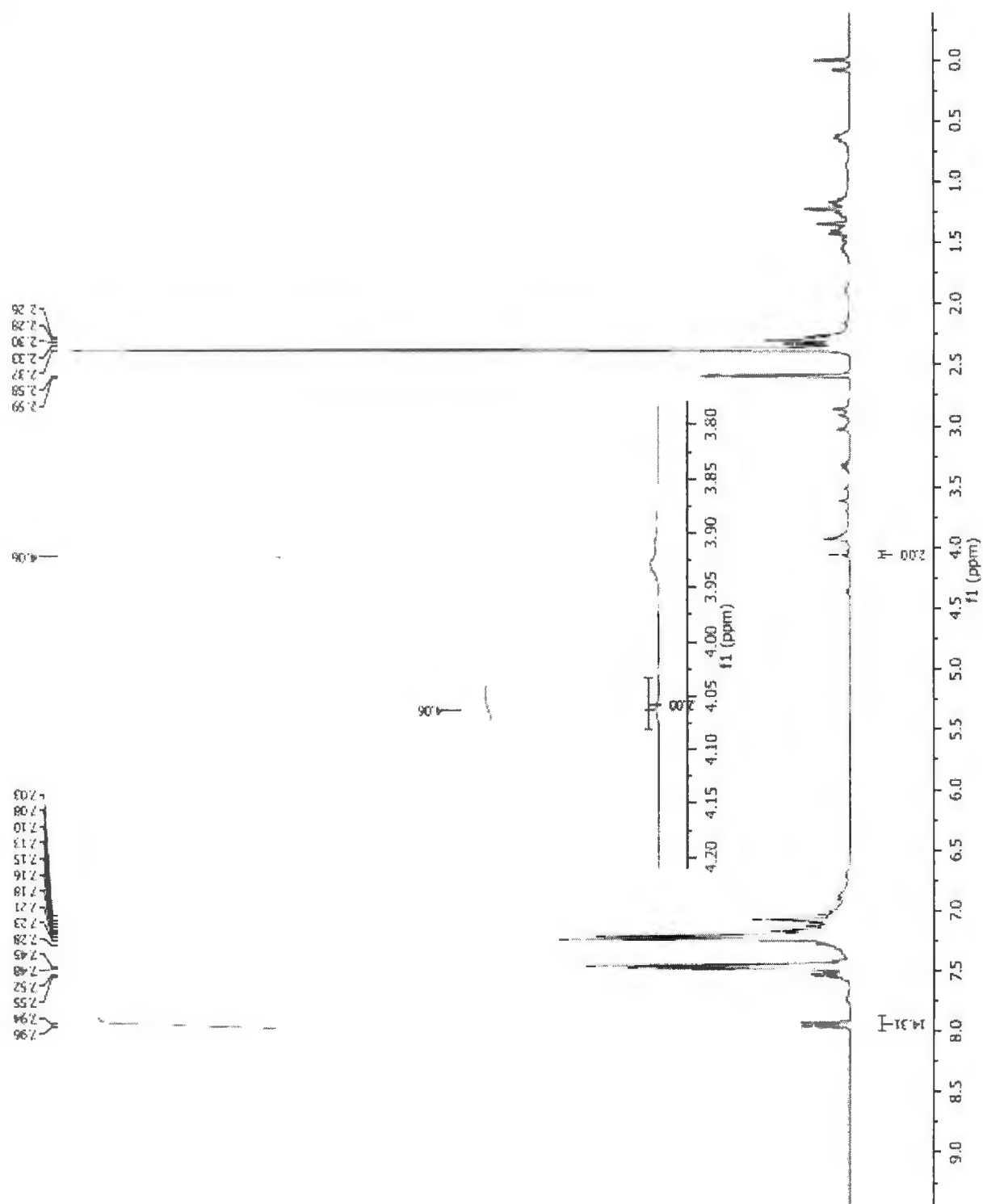
FigureA100: ^{13}C NMR spectrum for **1-Methoxy-3-(4-methoxybenzyl)benzene** (Table 3.3, Entry 3).



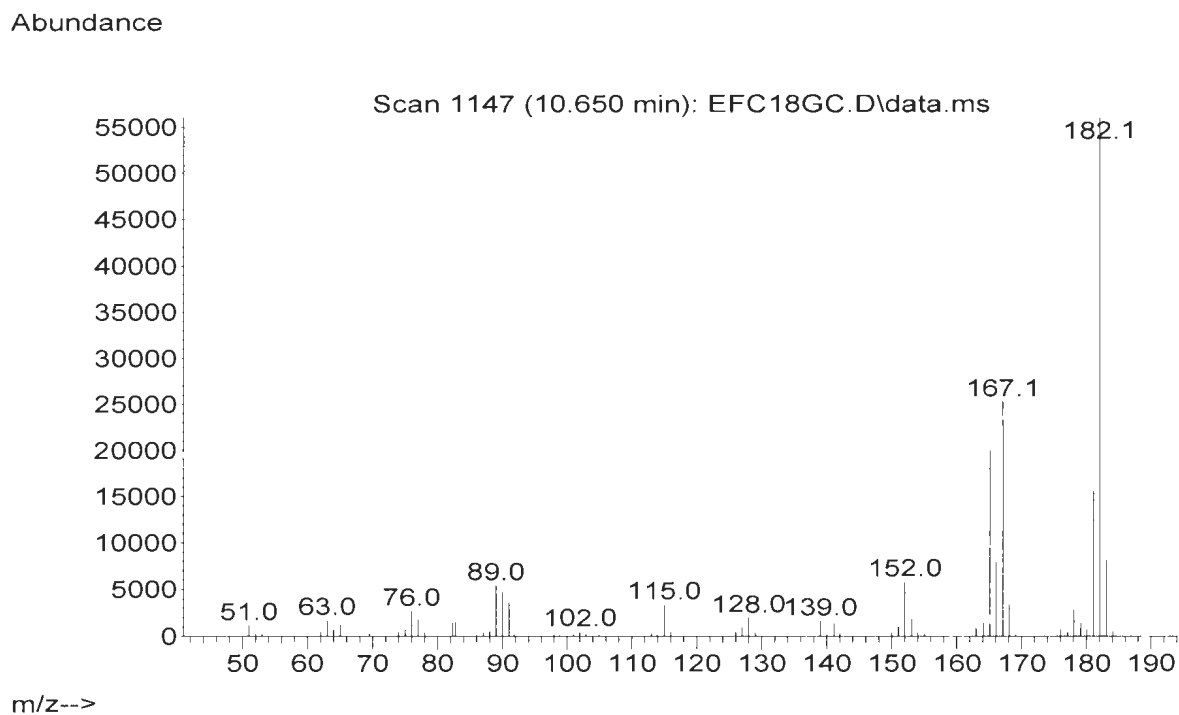
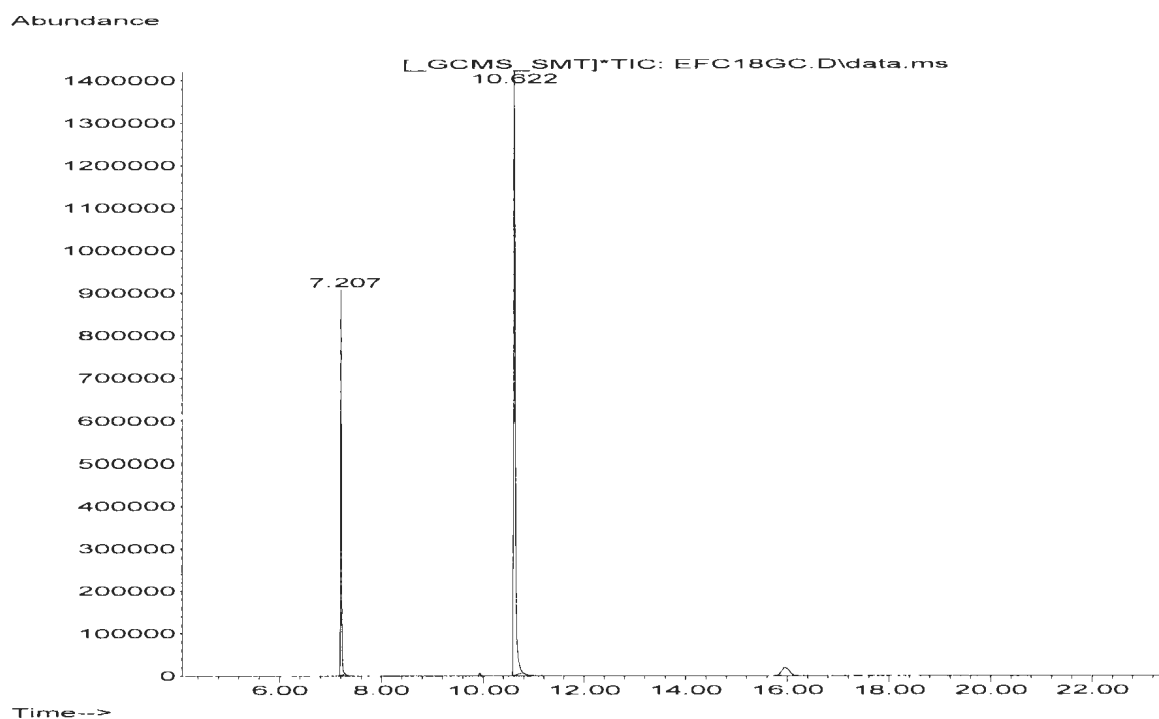
FigureA101: GC-MS analysis of **1-Bromo-2-(4-methylbenzyl)benzene** (Table 3.4, Entry 1). GC-MS retention time: 7.211 min dodecane; 10.625 min 4,4'-dimethylbiphenyl; 13.906 min 1-bromo-2-(4-methylbenzyl)benzene.



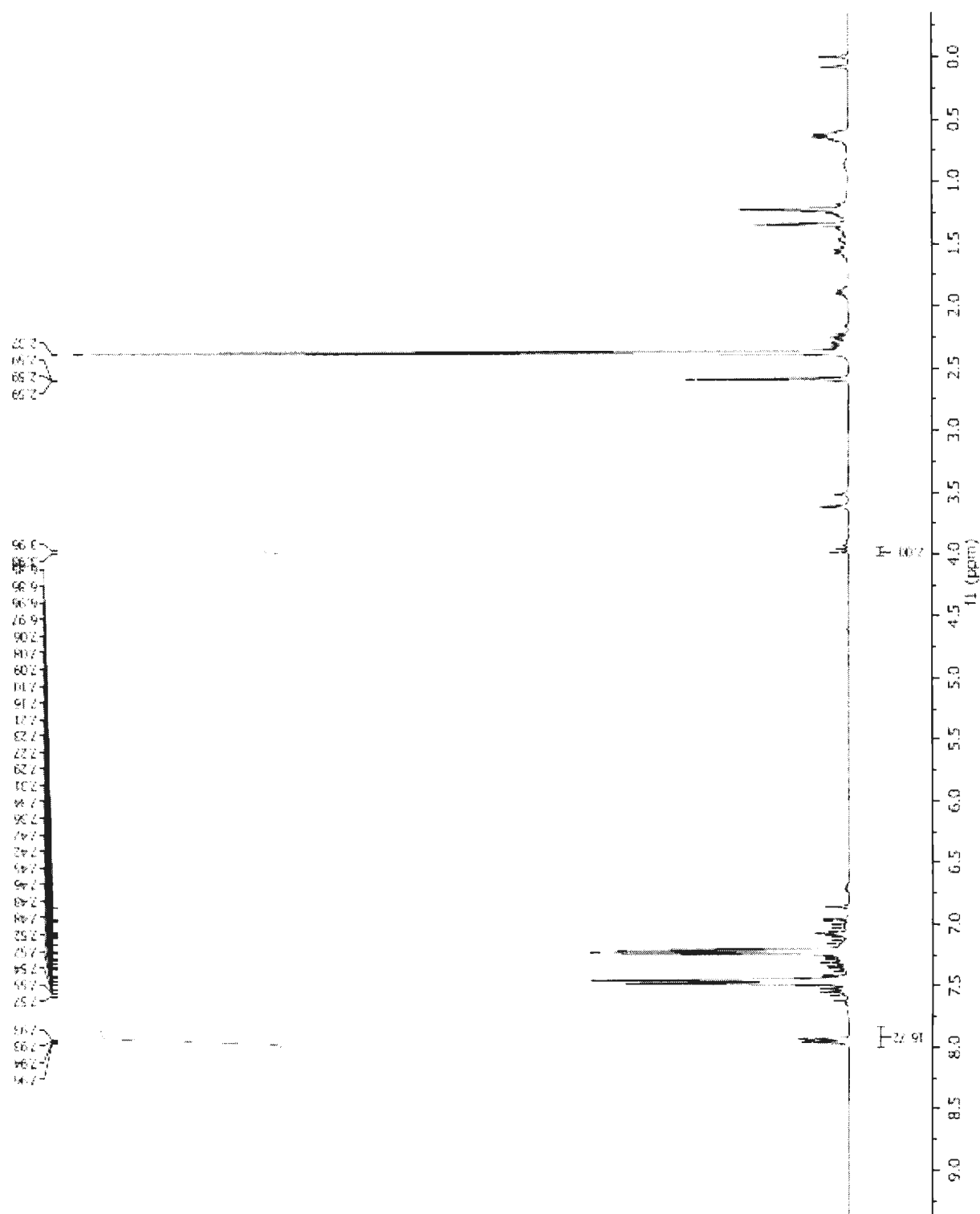
FigureA102: ^1H NMR spectrum for 1-Bromo-2-(4-methylbenzyl)benzene (Table 3.4, Entry 1).



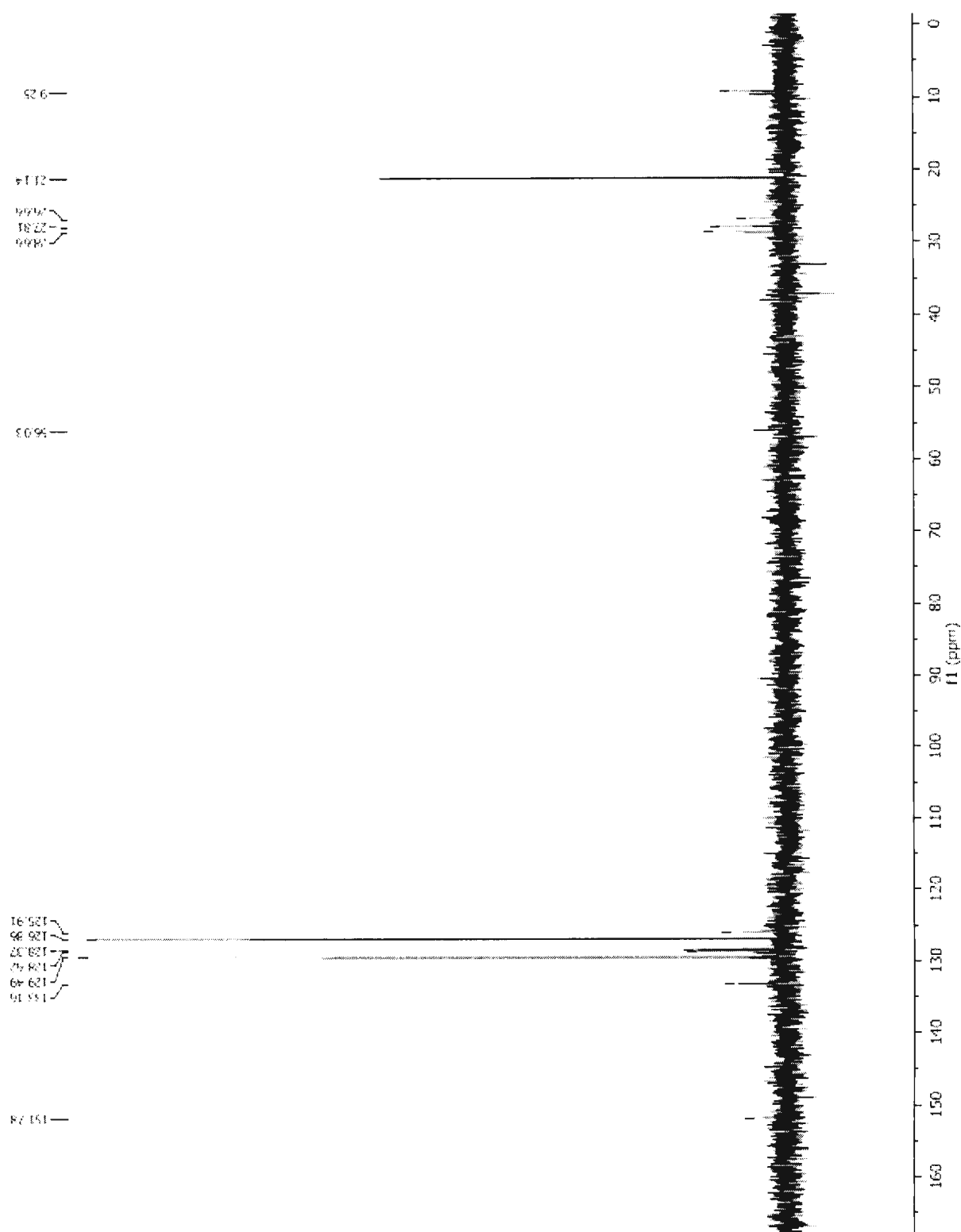
FigureA104: GC-MS analysis of **2-(4-Methylbenzyl)benzonitrile** (Table 3.4, Entry 2).
GC-MS retention time: 7.207 min dodecane; 10.622 min 4,4'-dimethylbiphenyl.



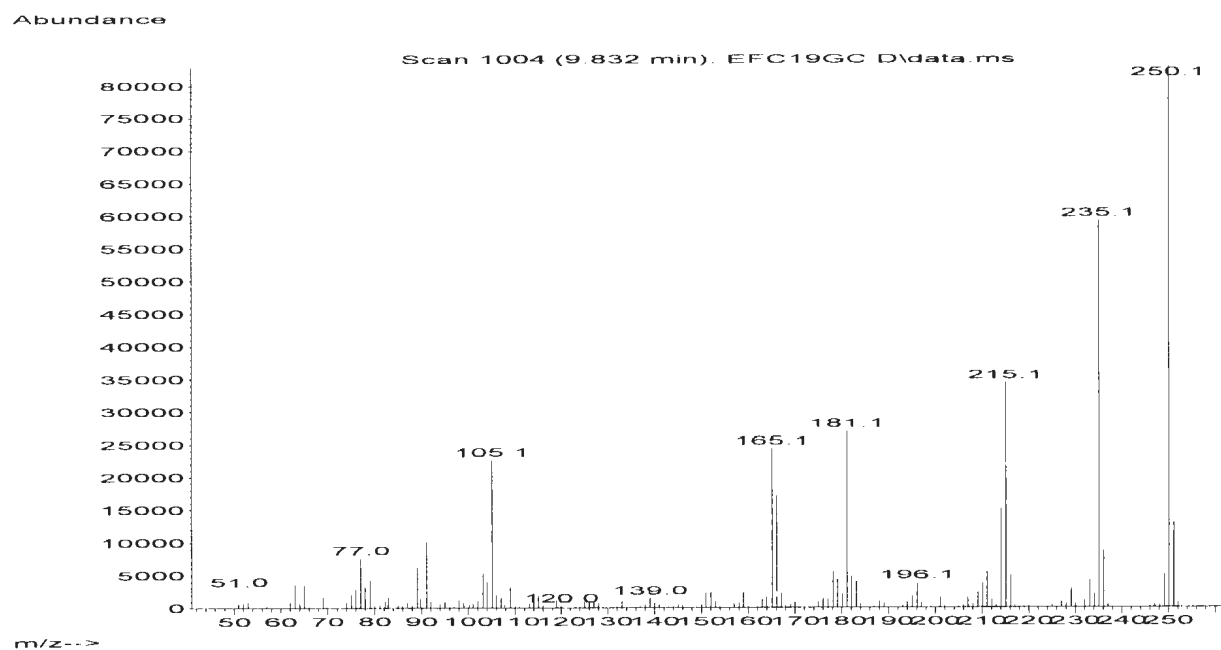
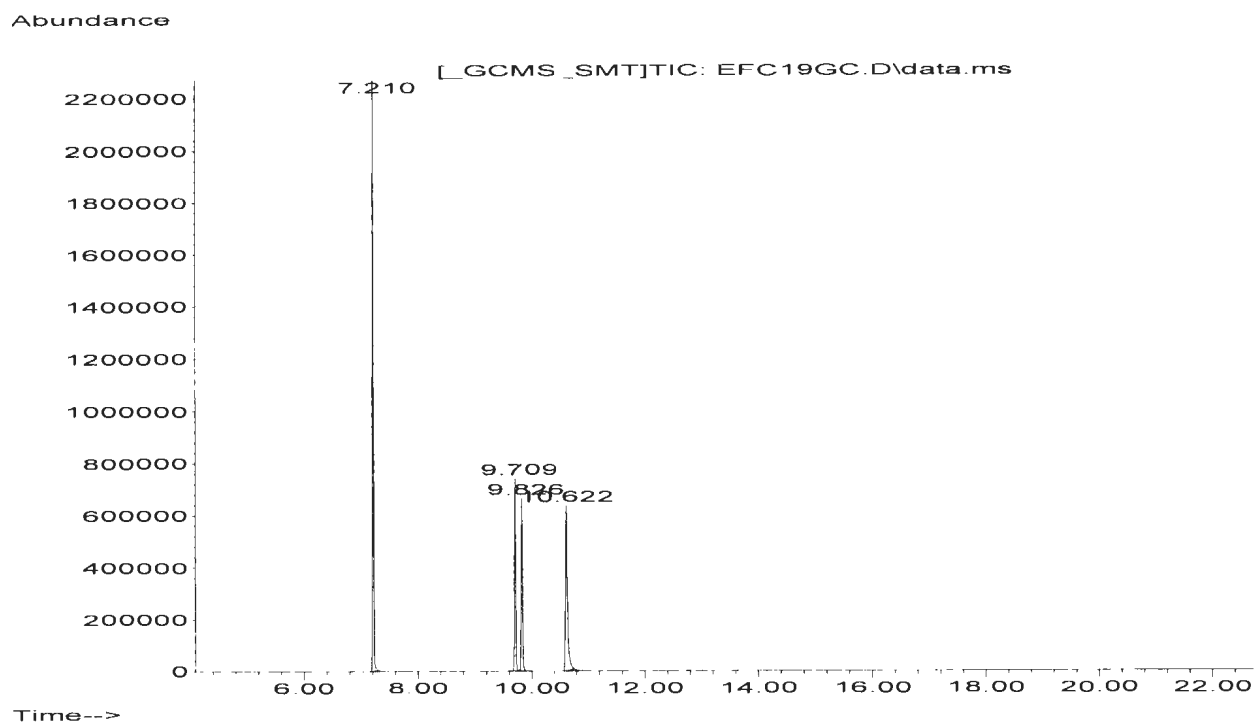
FigureA105: ^1H NMR spectrum for 2-(4-Methylbenzyl)benzonitrile (Table 3.4, Entry 2).



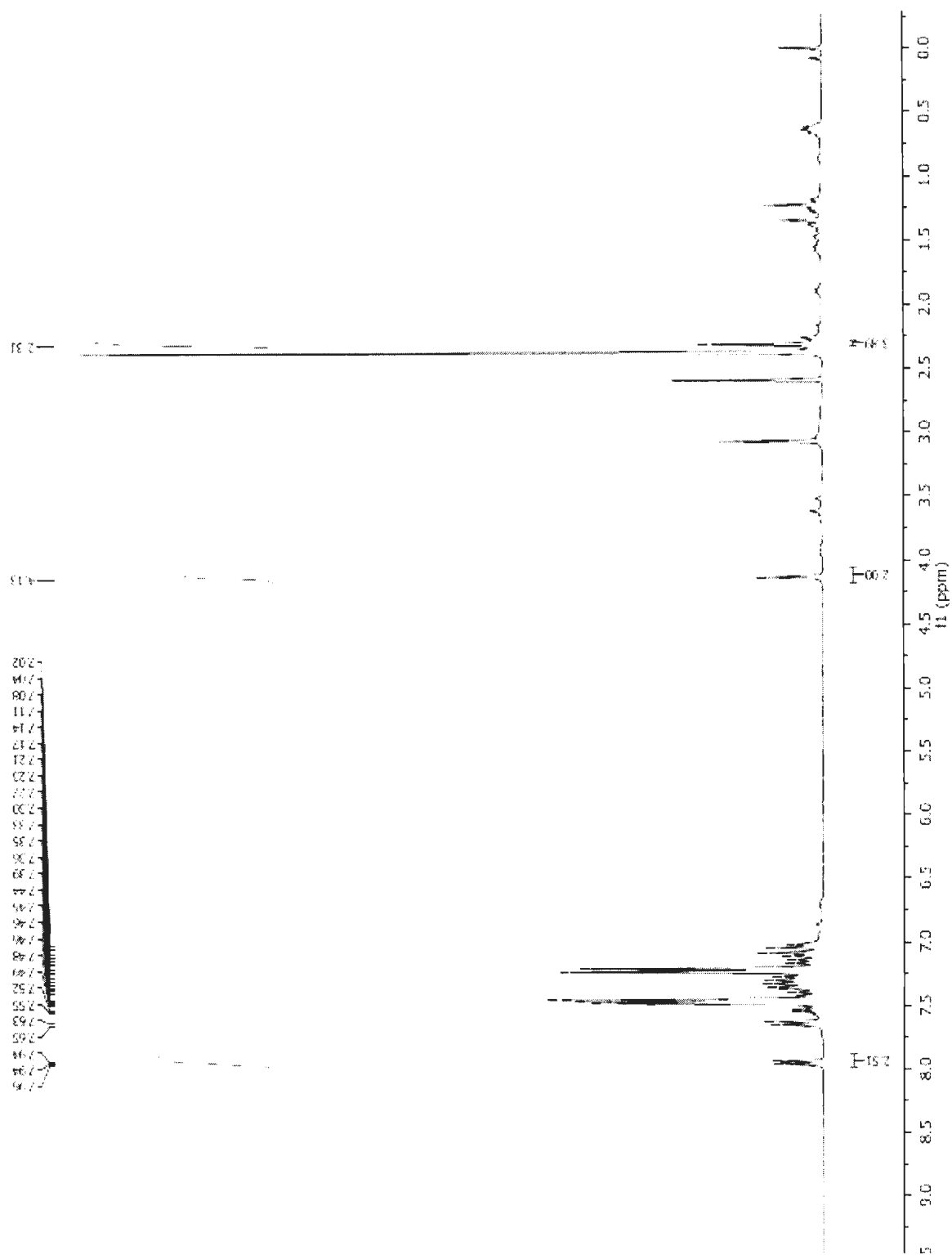
FigureA106: ^{13}C NMR spectrum for 2-(4-Methylbenzyl)benzonitrile (Table 3.4, Entry 2).



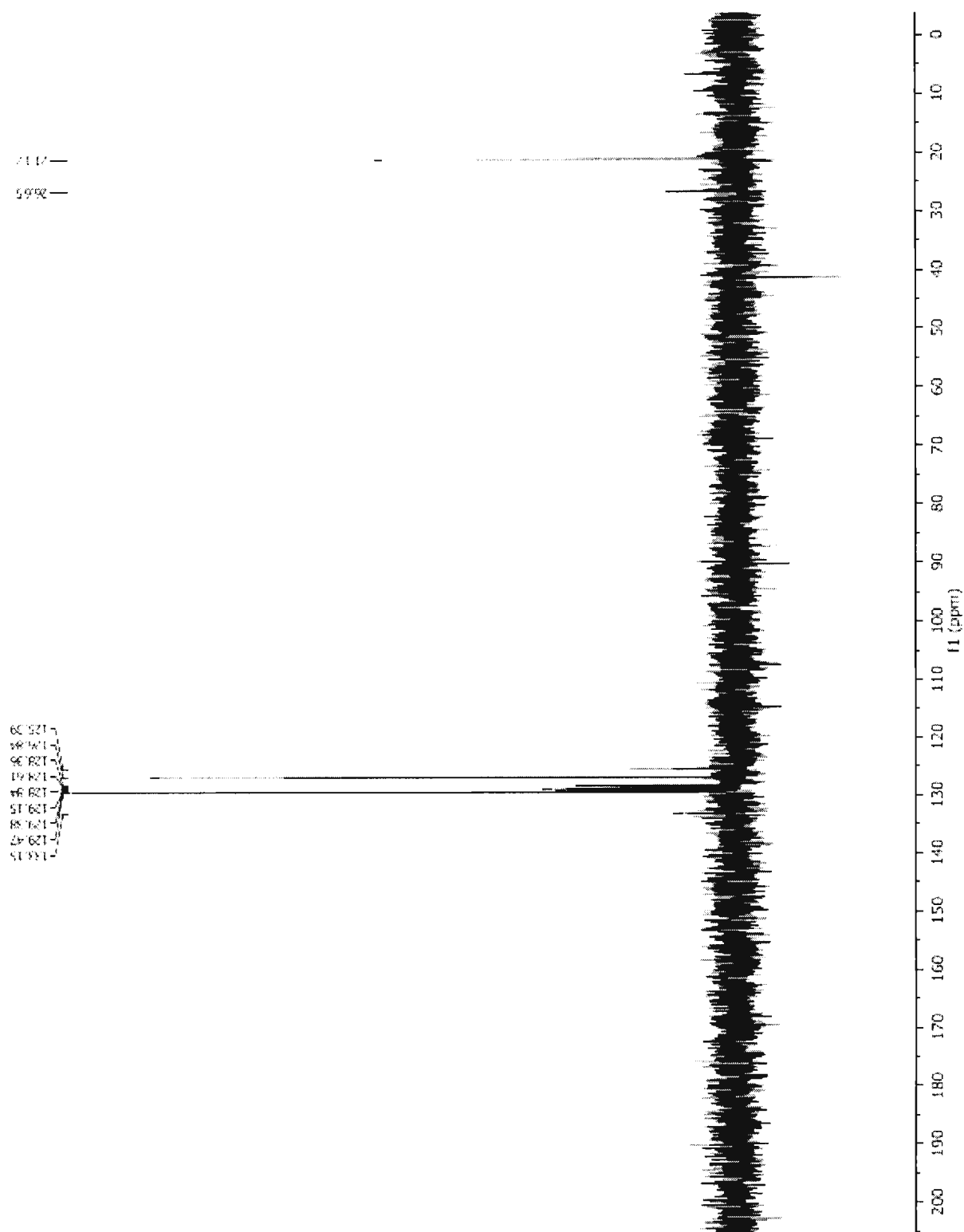
FigureA107: GC-MS analysis of **1-Methyl-4-(2-(trifluoromethyl)benzyl)benzene** (Table 3.4, Entry 3). GC-MS retention time: 7.210 min dodecane; 9.709 min 4,4'-(trifluoromethyl)bibenzyl; 9.826 min 1-methyl-4-(2-(trifluoromethyl)benzyl)benzene; 10.622 min 4,4'-dimethylbiphenyl.



FigureA108: ^1H NMR spectrum for 1-Methyl-4-(2-(trifluoromethyl)benzyl)benzene (Table 3.4, Entry 3).

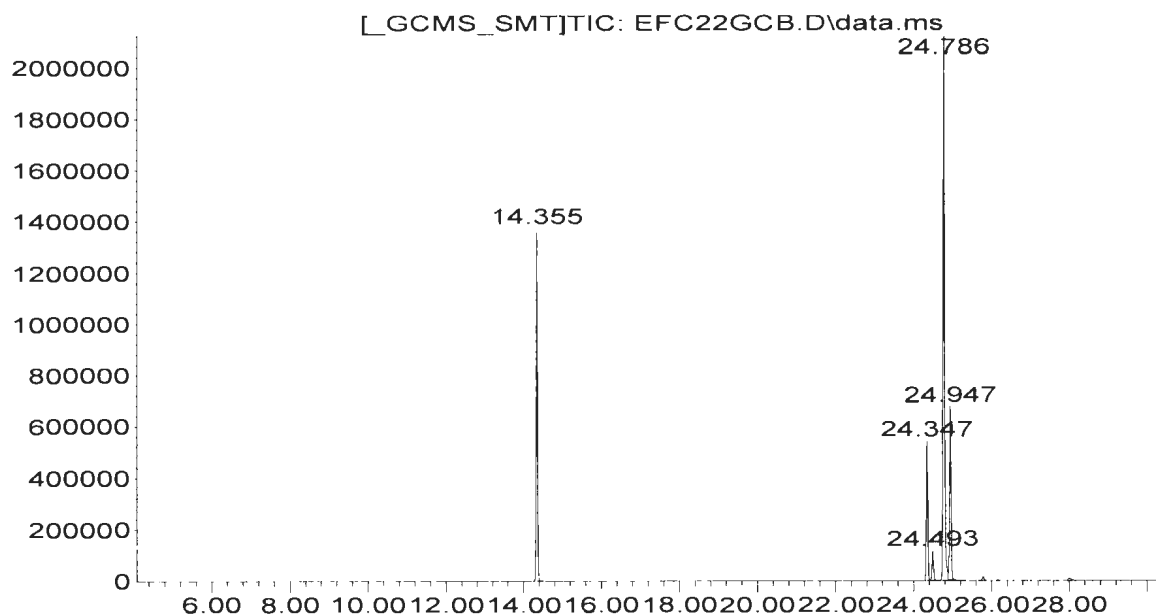


FigureA109: ^{13}C NMR spectrum for 1-Methyl-4-(2-(trifluoromethyl)benzyl)benzene (Table 3.4, Entry 3).



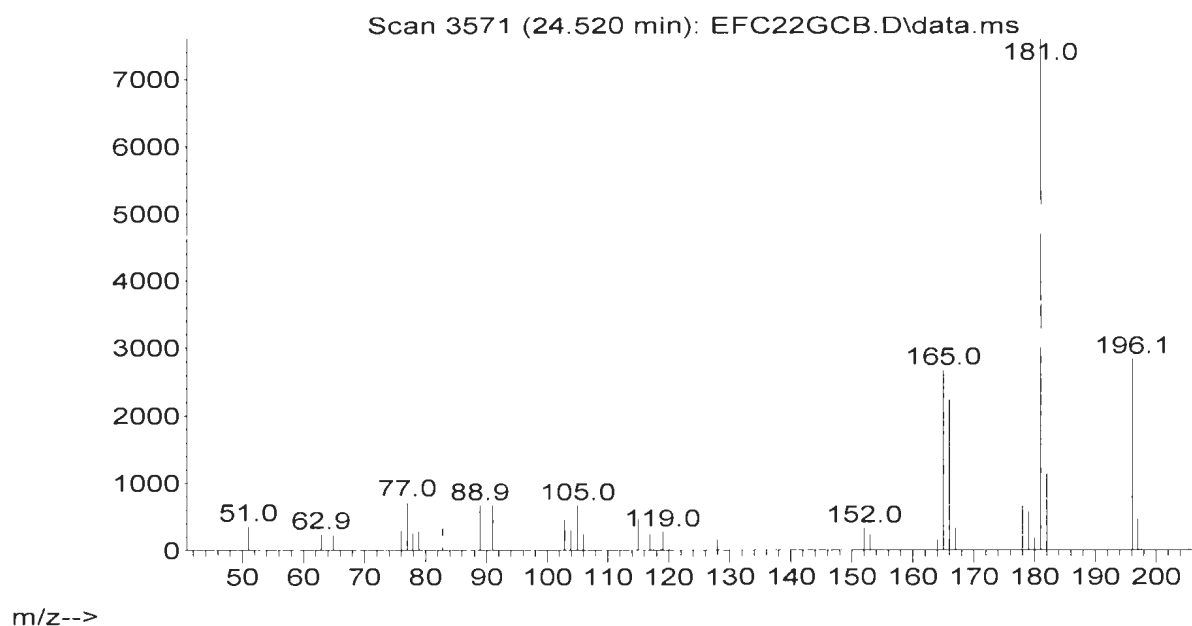
FigureA110: GC-MS analysis of 4-(1-Methyl)-1,1'-ethylidenebenzene (Table 3.4, Entry 4). GC-MS retention time: 14.355 min dodecane; 24.347 min 1,1'-(1,2-dimethyl-1,2-ethanediyl)bis-benzene; 24.493 min 4-(1-methyl)-1,1'-ethylidenebenzene; 24.786 min 4,4'-dimethylbiphenyl; 24.947 min 1,1'-(1,2-dimethyl-1,2-ethanediyl)bis-benzene.

Abundance



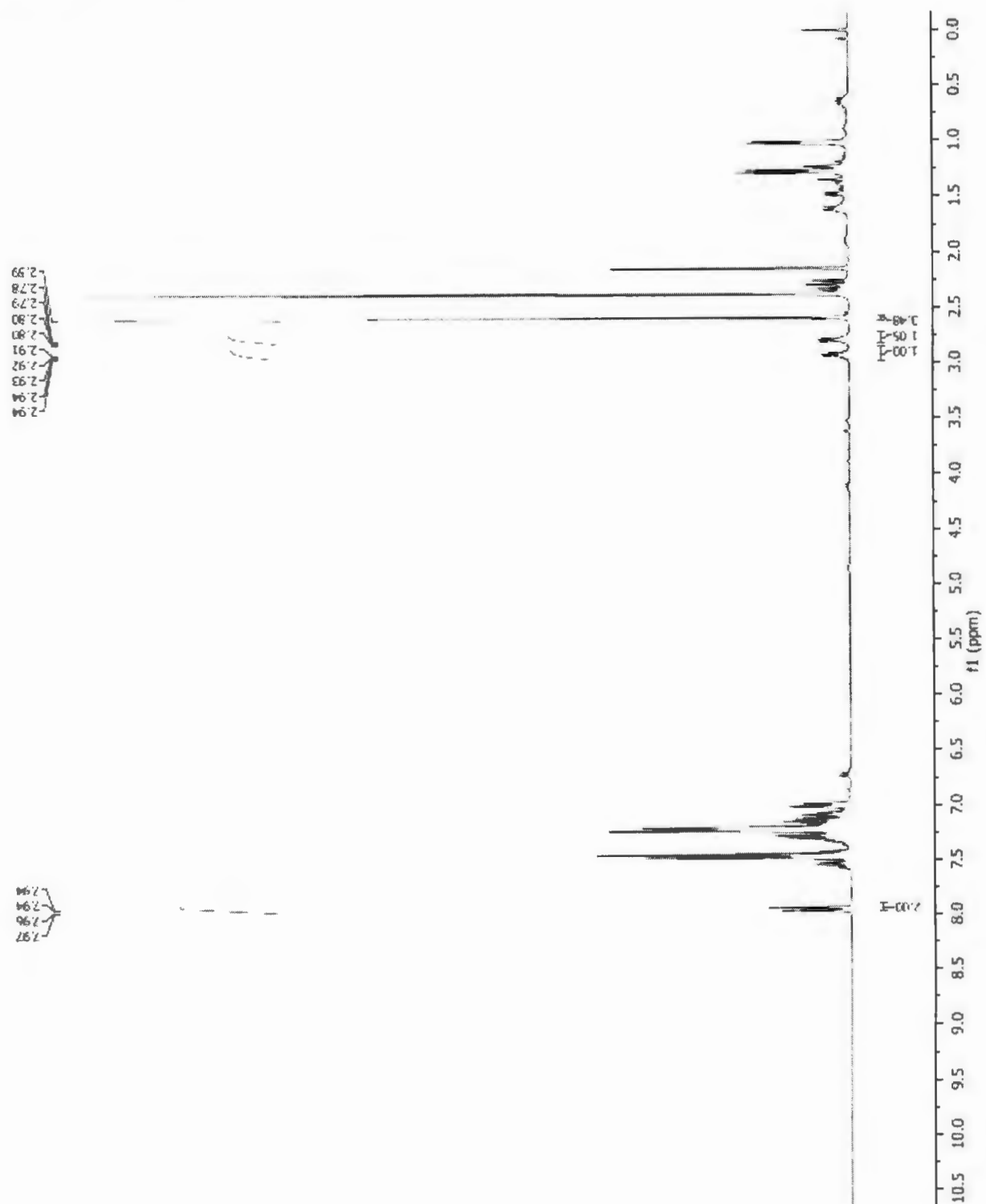
Time-->

Abundance

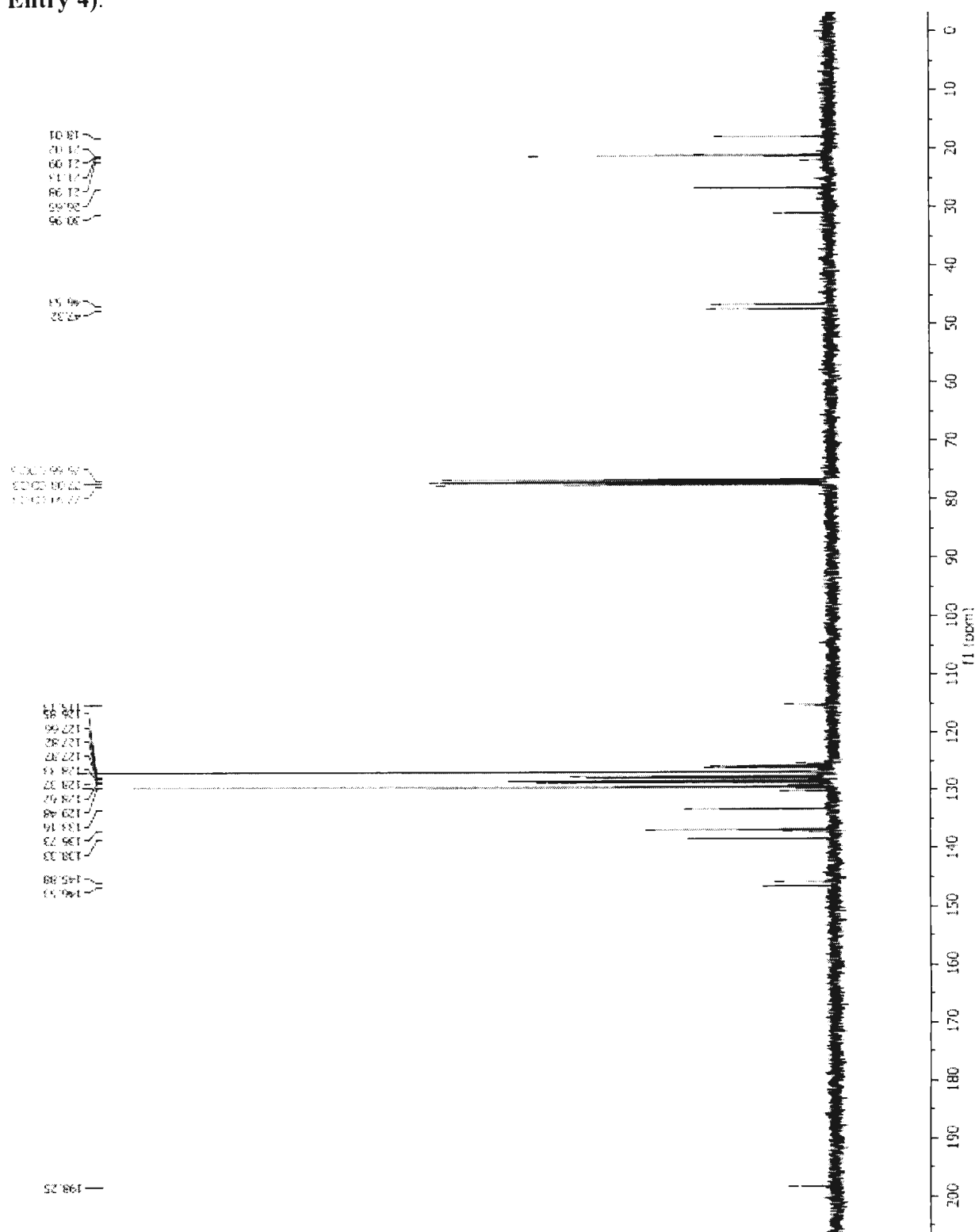


m/z-->

FigureA111: ¹H NMR spectrum for 4-(1-Methyl)-1,1'-ethylidenebenzene (Table 3.4, Entry 4).



FigureA112: ^{13}C NMR spectrum for 4-(1-Methyl)-1,1'-ethylidenebenzene (Table 3.4, Entry 4).





Request to Include Copyright Material

Adobe Reader, minimum version 8, is required to complete this form. Download the latest version at <http://get.adobe.com/reader>. (1) Save the form by clicking on the diskette icon on the upper left side of the screen; (2) Ensure that you are saving the file in PDF format; (3) Specify where you would like to save the file, e.g. Desktop; (4) Fill in the required data, save and print the file; (5) Send the completed form to the copyright holder.

Student Contact Information

Last name: Chard

Academic Unit: Chemistry

eMail Address: a36efc@mun.ca

First name: Elliott

Degree: Master of Science (M.Sc.)

Telephone No.: 709-726-1667

Copyright Material Request

I, Elliott Chard, request that you permit the inclusion of the described material in the thesis/report/practicum listed below and grant an irrevocable, non-exclusive licence to Memorial University of Newfoundland and to Library and Archives Canada to reproduce, lend or sell the material described below as part of my thesis/report/practicum. The title of the thesis/report/practicum is:

Iron(III) Complexes of Amine-bis(phenolate) Ligands as Catalysts for the C-C Cross-Coupling of Aryl Grignard Reagents with Benzyl Halides

to be submitted in partial fulfilment of the requirements for the degree of Master of Science (M.Sc.) at Memorial University of Newfoundland.

Description of the Material to be Included

For my Masters thesis, I would like to include the plot of magnetic moment vs T for complex 7 (Figure 7) as found in P. Chaudhuri, T. Weyhermüller, R. Wagner, Eur. J. Inorg. Chem. 2011, 2547-2557. Thank you!

Permission of Copyright Holder

I, _____,
(Name – please print or type)

do ☐ do not grant permission for the indicated use of the material described above.

Company/Organization: _____

Position Title: _____

Address: _____

Signature: _____

Date: _____

Note: Signature required on each additional attachment

Memorial University protects privacy and maintains the confidentiality of personal information. The information requested in this form is collected under the general authority of the Memorial University Act ([RSNL1990CHAPTERM-7](#)). It is required for administrative purposes of the School of Graduate Studies. If you have any questions about the collection and use of this information, please contact the Manager – Enrolment and Strategic Initiatives, School of Graduate Studies, at 709.864.2445 or at sqs@mun.ca.

JOHN WILEY AND SONS LICENSE TERMS AND CONDITIONS

Aug 26, 2012

This is a License Agreement between Elliott Chard ("You") and John Wiley and Sons ("John Wiley and Sons") provided by Copyright Clearance Center ("CCC"). The license consists of your order details, the terms and conditions provided by John Wiley and Sons, and the payment terms and conditions.

All payments must be made in full to CCC. For payment instructions, please see information listed at the bottom of this form.

License Number	2961240730304
License date	Aug 03, 2012
Licensed content publisher	John Wiley and Sons
Licensed content publication	European Journal of Inorganic Chemistry
Licensed content title	Asymmetrically Dibridged Diiron(III) Complexes with Aminebis(phenoxide)-Based Ligands for a Magnetostructural Study
Licensed content author	Thomas Weyhermüller, Rita Wagner, Phalguni Chaudhuri
Licensed content date	Apr 28, 2011
Start page	2547
End page	2557
Type of use	Dissertation/Thesis
Requestor type	University/Academic
Format	Electronic
Portion	Figure/table
Number of figures/tables	1
Number of extracts	None
Original Wiley figure/table number(s)	Figure 7
Will you be translating?	No
Order reference number	None
Total	0.00 USD
Terms and Conditions	

TERMS AND CONDITIONS

This copyrighted material is owned by or exclusively licensed to John Wiley & Sons, Inc. or one of its group companies (each a "Wiley Company") or a society for whom a Wiley Company has exclusive publishing rights in relation to a particular journal (collectively WILEY"). By clicking "accept" in connection with completing this licensing transaction, you agree that the following terms and conditions apply to this transaction (along with the billing and payment terms and conditions established by the Copyright Clearance Center Inc., ("CCC's Billing and Payment terms and conditions"), at the time that you opened your Rightslink account (these are available at any time at <http://myaccount.copyright.com>)

Terms and Conditions

1. The materials you have requested permission to reproduce (the "Materials") are protected by copyright.
2. You are hereby granted a personal, non-exclusive, non-sublicensable, non-transferable, worldwide, limited license to

